LT-R-XFD-CDR-0001

NSLS-II Project

CONCEPTUAL DESIGN REPORTS for the

SIX PROJECT BEAMLINES AT NSLS-II

Final Draft September 2009

This document summarizes the status of the design as of September 2009. The design continues to be refined, and the parameters contained within this report may change.

Contents

1 CHX COHERENT HARD X-RAY BEAMLINE

2 CSX COHERENT SOFT X-RAY BEAMLINE

3 HXN HARD X-RAY NANOPROBE BEAMLINE

4 IXS INELASTIC X-RAY SCATTERING BEAMLINE

5 SRX SUBMICRON RESOLUTION X-RAY SPECTROSCOPY BEAMLINE

6 XPD X-RAY POWDER DIFFRACTION BEAMLINE

7 BEAMLINES INFRASTRUCTURE AT NSLS-II

Intentionally blank.

Acronyms

3PW	3-pole wiggler beamline
ADP	Avalanche Photon Diode
APS	Advanced Photon Source
ASD	Accelerator Facilities Division
BAT	Beamline Advisory Team
Be	Beryllium
CCD	Charge Coupled Device
CDI	Coherent Diffraction Imaging
CDR	Conceptual Design Report
CFD	Conventional Facilities Division
CHX	Coherent X-ray beamline
CMPMS	Condensed Matter Physics and Materials Science
CO	Lead Collimator
CRL	Compound Refractive Lens
CSX	Coherent Soft X-ray beamline
DCM	Double Crystal Monochromator
DLCM	Double Laue Crystal Monochromator
DW	Damping Wiggler
EH	Experimental Hutch
ELS	Extended Length Straight
EPU	Elliptically Polarized Undulator
ES	End Station
EXAFS	Extended X-ray Absorption Fine Structure
FAPM	Fixed Aperture Mask
FE	Front End
FEA	Finite Element Analysis, Front End Aperture
FGV	Fast Gate Valve
FM	Focusing Mirrors
FOE	First Optics Enclosure
FWHM	Full Width at Half Minimum
FZP	Fresnel Zone Plates
GI-SAXS	Grazing Incidence Small Angle X-ray Scattering
HEG	High-Energy Grating
HMP	Horizontal Mirror Pair
HOPG	Highly Oriented Pyrolytic Graphite
HXN	Hard X-ray Nanoprobe beamline
ID	Insertion Device
IR	infrared
IVU	In-Vacuum Undulator
IXS	Inelastic X-ray Scattering
KB	Kirkpatrick-Baez
LEG	Low-Energy Grating
LOB	Lab-Office Building
LOI	Letter of Intent, Letter of Interest
MEG	Medium-Energy Grating
ML	Multilayers
MLL	Multi Layer Laue lens
NMR	Nuclear Magnetic Resonance
OA	Optical Aperture
OH	Optics Hutch
PDF	Pair Distribution Function
PGM-VLS	Planar Grating Monochromator – Variable Length spacing
PP	Phase Plate
PPS	Personnel Protection System
RSI	Requirements, Specifications and Interfaces
RSI	Requirements, Specifications, and Interfaces
SAXS	Small Angle X-ray Scattering
SBM	Side Bounce Monochromator
SGV	Slow Gate Valve
SHS	Secondary Horizontal Source
SHSA	Secondary Horizontal Source Aperture
SNR	Signal-to-Noise Ratio

SOW	Statement of Work
SRX	Submicron Resolution X-ray Spectroscopy
SS	Safety Shutter
SVS	Speckle Visibility Spectroscopy
UHV	Ultra High Vacuum
UPS	Uninterruptible Power Supply
URM	Ultrahigh Resolution Monochromator
VIPIC	Vertically Integrating Pixel Imaging Chip
WAXS	Wide Angle X-ray Scattering
WBF	White Beam Filter
WBS	White Beam Slit
XBPM	Photon Beam Position Monitor
XBPM	X-ray Beam Position Monitors
XFD	Experimental Facilities Division
XPCS	X-ray Photon Correlation Spectroscopy
XPD	X-ray Powder Diffraction beamline
ZP	Zone Plate

LT-XFD_CDR_XPD-00118

NSLS-II Project

CONCEPTUAL DESIGN REPORT for the

COHERENT HARD X-RAY BEAMLINE AT NSLS-II

final draft Sep 2009

Intentionally blank.

Approvals and Reviewers

Compiled by	Signature	Date
Andrei Fluerasu, CHX Beamline Group Leader, NSLS-II		
Approved		
Qun Shen, XFD Director, NSLS-II		
Reviewers		
Robert L. Leheny, BAT Spokesperson, on behalf of the BAT		
Andy Broadbent, Beamlines Manager		
Nicholas Gmür, ESH Coordinator, NSLS-II		
Sushil Sharma, Mechanical Engineering Group Leader, NSLS-II		

Document Updates

The Conceptual Design Report for the Coherent Hard X-ray Beamline at NSLS-II is a controlled document, revised under change control.

Version No.	Date	Changes made
A	5/13/2009	Initial draft, submitted to BAT
B	9/16/2009	Second submittal to BAT, and first to editing
1	10/1/2009	Final draft, submitted to BAT

Intentionally blank.

Contents

1 INTRODUCTION 1

1.1 Scientific Requirements 1
Glassy Dynamics in Soft Matter 2
Phase Behavior and Dynamics on Liquid and Solid Surfaces 3
Coherent Diffraction Imaging 3
New Investigation Methods; Instrumental Developments 3

1.2 Coherent Hard X-ray Beamline Team 3
Beamline Scientists 3
NSLS-II Management and Engineering Support 4
Beamline Advisory Team (BAT) 4

2 BEAMLINE LAYOUT 5

2.1 Overview 5

2.2 Insertion Device 9

2.3 Front End 11

2.4 Optical Layout 13
White Beam Mirror 13
Secondary Slits 14
Be CRLs for Vertical Focusing 14
Monochromator(s) 14

2.5 High Heat Load Optics 17

2.6 Beamline Optics and Coherence Preservation 17

2.7 Ray Tracing 18

2.8 List of Major Components 18

2.9 End Station Instrumentation 19

3 SPECIAL BEAMLINE REQUIREMENTS 21

3.1 Vacuum 21

3.2 Detectors 21

3.3 Synchrotron Filling Modes 22

3.4 Data Storage/Handling 22

4 FUTURE UPGRADE OPTIONS 23

4.1 Detector Developments 23

4.2 Specialized Sample Environments 23

4.3 Beamline Optics and Figure Control 23

APPENDIX 1 SCHEDULE 25

APPENDIX 2 REFERENCE DRAWINGS 27

Acronyms

ADP	Avalanche Photon Diode
Be	Beryllium
CDI	Coherent Diffraction Imaging
CRL	Compound Refractive Lens
DCM	Double Crystal Monochromator
DW	Damping Wiggler
EH	Experimental Hutch
FEA	Finite Element Analysis
GI-SAXS	Grazing Incidence Small Angle X-ray Scattering
LOI	Letter of Intent
ML	Multi Layers
OH	Optics Hutch
SAXS	Small Angle X-ray Scattering
SNR	Signal-to-Noise Ratio
SVS	Speckle Visibility Spectroscopy
UHV	Ultra High Vacuum
VIPIC	Vertically Integrating Pixel Imaging Chip
WAXS	Wide Angle X-ray Scattering
XPCS	X-ray Photon Correlation Spectroscopy

1 INTRODUCTION

1.1 Scientific Requirements

The Coherent Hard X-ray (CHX) beamline at NSLS-II will be dedicated to studies of nanometer-scale dynamics in materials using X-ray Photon Correlation Spectroscopy (XPCS), and to other experimental methods enabled by bright, coherent, X-ray beams. XPCS is based on measuring time correlation functions of the speckle fluctuations that occur when a coherent X-ray beam is scattered from a disordered sample. It can be used to measure equilibrium dynamics via the "usual" single-speckle intensity-intensity autocorrelation functions $g^{(2)}(q, t)$ If combined with 2D area detectors and a multispeckle technique, it can also be used to measure non-stationary, non-equilibrium dynamics via two-time correlation functions $g^{(2)}(q, t_1, t_2)$. Higher order correlation functions $g^{(n)}(q, t)$ can be used to characterize heterogeneities in the dynamical properties.

The key quantity that enables XPCS experiments is the source brightness. This determines the flux of coherent X-ray photons and ultimately the signal-to-noise ratio (SNR) of the measured correlation functions. The technique was first demonstrated in pioneering experiments that become possible at NSLS (M. Sutton et al., *Nature* **352**, 608, 1991; S. Dierker et al., *Phys. Rev. Lett.* **75**, 449, 1995) and later "moved" to brighter 3rd generation Synchrotron sources such as ESRF and APS. With the unprecedented brilliance of the NSLS-II storage ring exceeding 10^{21} photons/s/mrad^2/mm^2/0.1 % bw for a photon energy near E~8 keV (more than one order of magnitude higher than that of the Advanced Photon Source), the CHX beamline will allow studies of dynamics on time scales that can be ~10^2=100 times faster and on shorter length scales than was ever possible before (Figure 1). The experiments will be performed in a variety of scattering geometries such as small angle scattering (SAXS), wide angle scattering (WAXS) or grazing incidence small angle scattering (GI-SAXS) and the proposed instrument will provide the required flexibility to efficiently adapt to all these situations. The design of the CHX instrument is simple and robust and puts an emphasis on three key elements:

- coherence (brilliance) preservation by carefully designing and engineering key optical elements, reducing the number of windows, mirrors, etc. to an absolute minimum
- maximizing the useful signal by using the entire available coherent flux (via focusing optics)
- maximizing the mechanical stability of the instrument

With specific sample environments which will be hosted on a versatile diffractometer, and a slightly different alignment/tuning, the CHX instrument will also be ideally suited for Coherent Diffraction Imaging (CDI) and micro-beam solution small-angle scattering. Developing these techniques, especially for studies of biological systems, is an important part of the scientific program of the beamline.
There are several classes of XPCS experiments that will probe a combination of length- and time-scales that are fundamentally important, and which are very difficult or impossible to measure at other (less bright) facilities or by using other techniques. These include, but are not limited to:

- Glassy materials, driven and out-of-equilibrium systems
- Colloids, polymers, and nanostructured complex fluids
- Biological systems such as proteins in solution and biomembranes
- Dynamics at fluid surfaces and interfaces
- molecular dynamics and metallic and orientational glasses; dynamics at solid surfaces
- μ–beam SAXS studies on the kinetics of biological processes: protein and RNA folding, protein crystallization and explorations of solvent conditions
- X-ray microscopy via coherent diffraction imaging on biological systems as close as possible to their native state (frozen, hydrated)

The scientific program which will be pursued through active collaborations between the user community and the CHX group is described in detail in the XPCS LOI document, "A Coherent Hard X-ray Beamline for XPCS and Microbeam SAXS at NSLS-II" and will not be included here in its integrality. A subset of the proposed area of research, which will likely lie at the core of the in-house research program in the CHX group is briefly described below. These "in-house" studies will require instrumental developments, new sample environments, etc. and will undoubtedly become available and useful to the extended user community. Ultimately, such an approach enables new applications and results that otherwise would not be within reach.

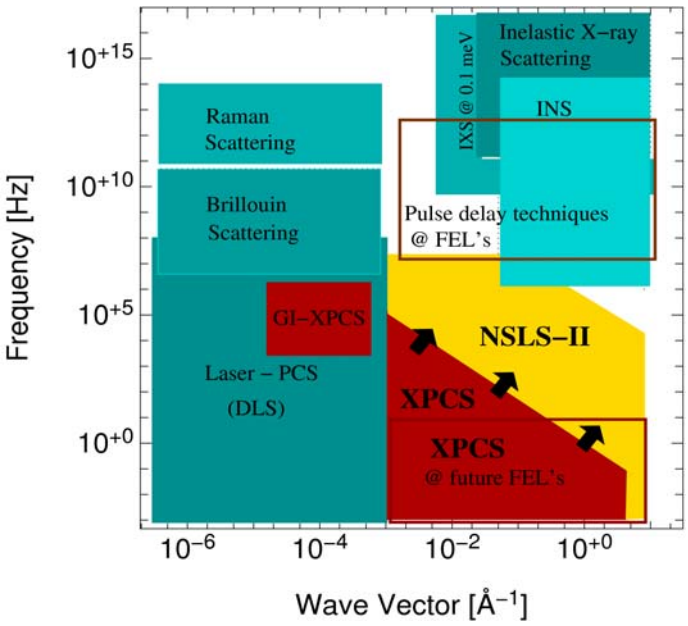

Figure 1 Wave vector – frequency phase-space currently occupied by XPCS at 3rd generation light sources. The goal of the CHX beamline at NSLS-II is to extend this region toward faster time scales and shorter length scales (gold). With its unprecedented brilliance, NSLS-II result could approach (if not match) the faster time scales accessible with neutron spin-echo and close the gap that currently exists in the phase space. This dynamic range will also fall in the gap left open by the future FELs between "classic" XPCS experiments using the high average brilliance of these sources, but being limited by their pulsed structure, and pulse delay techniques being limited by practical considerations such as the size of delay lines. This will make NSLS-II a truly unique instrument for XPCS.

Glassy Dynamics in Soft Matter

Understanding the underlying mechanism by which model systems such as highly interactive colloidal suspensions arrest to non-equilibrium states and form glasses and/or gels is a fundamental problem in condensed matter physics. As the system approaches the glass transition, the dynamics start slowing down without an obvious reason in the structural (static) properties of the system. At the same time different relaxation modes become increasingly separated in time - e.g. fast modes associated with the motion of individual constituents hindered by neighboring particles and slow modes associated with the motion of groups (cages) of particles. Understanding the glass (or gel) transition is a problem of tremendous fundamental interest in soft matter physics. Solving it will also help us in better understanding phenomena like protein aggregation, which are responsible, for instance, for the cataract formation in the human eye lens or for the neuronal cell death associated with Alzheimer's disease. With their relatively slow dynamical relaxation modes occurring on molecular length scales, glassy systems are well suited for XPCS and very recent results obtained at existing 3rd generation light sources (mainly ID10, ESRF and 8ID, APS) have provided an invaluable insight into the mechanisms associated with the slow relaxation modes. At NSLS-II it will become possible to extend the dynamic range by several decades, hence measure also the fast relaxation modes. The tremendous increase in brilliance and special sample handling techniques (e.g., using microfluidic techniques to avoid beam damage and achieve new functionalities – A. Fluerasu et al., *J. Synch. Rad.* **15**, 378, 2008) may also enable, for the first time, studies of dynamics in biological systems such as protein aggregation in a solution.

A second key advantage for the study of glassy dynamics at NSLS-II will be associated with the study of dynamical spatial or temporal heterogeneities. With the high brilliance source, it will be possible to achieve smaller beam sizes to probe smaller volumes or to go beyond analyzing the intensity fluctuations via the second order correlation functions $g^{(2)}(q\ \ t)$ and measure "fluctuations of intensity fluctuations" via higher order correlation functions $g^{(n)}(q, t)$. Such studies have been limited thus far, mainly because the even more stringent requirements they put on the source, i.e. the signal-to-noise ratio (SNR). The SNR is proportional with the square of the source brilliance B^2 for 4th order correlation functions $g^{(4)}(q, t)$, while only proportional to B in $g^{(2)}(q, t)$.

Phase Behavior and Dynamics on Liquid and Solid Surfaces
The structure, phase behavior and dynamical properties of liquid and solid interfaces can be studied using a grazing-incidence scattering geometry. Current research includes biological films at liquid-vapor interfaces, bio-membranes, etc. The CHX beamline will enable studies on faster time scales than possible today and will facilitate studies of the interplay between surface induced order and surface dynamics in systems such as alkanes undergoing surface freezing.

Coherent Diffraction Imaging
Imaging of biological systems such as a whole cell in their native state (unstained, unsectioned, etc.) in three dimensions is of a fundamental importance in cellular biology, and hard X-ray coherent diffraction imaging is arguably the best experimental tool that can achieve this task, given the high penetration depths, and the fine resolution that can be obtained (E. Lima, L. Wiegart et al., accepted *Phys. Rev. Lett*, 2009). Since the CHX instrument will be optimized to reduce to an absolute minimum any distortions to the coherent wave front, it will offer an ideal instrument for CDI experiments in the forward (SAXS) direction.

New Investigation Methods; Instrumental Developments
The continuous optimization of the CHX instrument by pushing the signal-to-noise level for XPCS and/or CDI experiments to a maximum is, and will remain, a central activity in the CHX group. At the same time, a vigorous research program aiming at developing new investigation tools will hopefully help "pushing the boundaries" of the phase space shown in Figure 1. An example of such a development is that of X-ray Speckle Visibility Spectroscopy (XSVS). This method allows the direct measurement of nanometer-scale dynamics in materials by analyzing a single "speckle pattern". The main idea, which follows the development of *speckle visibility spectroscopy* recently proposed for visible light (P.K. Dixon and D.J. Durian, *Phys. Rev. Lett.* **90**, 184302, 2003), is that the speckle contrast depends on the characteristic time scales of fluctuations in the sample, hence it is possible to resolve the dynamics over a wide range of length scales by analyzing the speckle visibility across a *single* diffraction pattern obtained with a 2D area detector. XSVS will be ideally suited to study dynamics at the high brilliance CHX beamline. As XSVS does not require a continuous time series but only single speckle patterns (with the acquisition tome determined by the software trigger of the detector or by a fast shutter), it will offer the possibility to access shorter time scales, beyond the corresponding maximum frame rate of the detector. Since it only requires single images – i.e "snapshots" - it will offer a unique way of measuring the "instantaneous" dynamics in complex systems with heterogeneous and/or intermittent behavior. In addition, it will also help avoiding beam damage in many soft matter or biological systems as the total required dose will be significantly reduced. Finally, XSVS may allow adopting a "flash approach" in measuring, for instance, the dynamics in a protein crystal. A speckle pattern can be obtained from a single pulse of intense coherent X-rays before causing irreversible damage in the sample.

1.2 Coherent Hard X-ray Beamline Team

In this section, an overview of the CHX team (as of Summer 2009) is given, as well as a brief description of the scientific and instrumentation interests of the NSLS-II Beamline Scientists, the management and engineering support and members of the Beamline Advisory Team (BAT).

Beamline Scientists

Andrei Fluerasu, Associate Physicist, NSLS-II, CHX Group Leader
Dynamics in non-equilibrium and driven systems – e.g., gels and glasses under flow/shear; Applications of XPCS, μ-beam SAXS in biophysics; Speckle Visibility Spectroscopy; Beamline optics and coherence preservation; Pushing the signal-to-noise radio in XPCS, CDI by optimizing the beamline layout; X-ray detectors; Controls and data acquisition; Statistical analysis of speckle-based methods

Lutz Wiegart, Assistant Physicist, NSLS-II
Structure and dynamics at liquid surfaces and interfaces; CDI in biological systems; Bulk dynamics associated with self-assembly of organic nanotubes; Solution scattering; Sample environments; Experimental setups adapted to coherent x-ray scattering

Lonny Berman, Physicist, NSLS (MOU)
Macromolecular and protein crystallography; Applications of coherence for imaging and studies of dynamics; Beamline optics and beamline design; Coherence preservation by beamline optics; Restoring the coherent wavefront with adaptive optics.

NSLS-II Management and Engineering Support

Qun Shen, Director, Experimental Facilities Division, NSLS-II, BNL

Andy Broadbent, Beamline Manager, Experimental Facilities Division, NSLS-II, BNL

Oleg Chubar, Beamline Scientific Support, XFD, NSLS-II, BNL

Konstantine Kaznatcheev, Beamline Scientific Support, XFD, NSLS-II, BNL

Mary Carlucci-Dayton, Mechanical Engineer, XFD, NSLS-II, BNL

Viswanath Ravindranath, Mechanical Engineer, XFD, NSLS-II, BNL

Much of the required design and engineering work is performed in a "centralized" fashion, with the whole suite of six project beamlines and the following 50+ beamlines in sight. This routinely involves tight collaborations between the scientific and engineering staff across the whole Experimental Facilities Division and even the whole NSLS-II project. The whole design of the baseline Front Ends was performed, for instance, by the Mechanical Engineering Group in the Accelerator Division. The beamline also uses resources from the same group for tasks such as FEA simulations, synchrotron and bremsstrahlung ray tracing, etc.

The Beamline Advisory Team is not only formed by world experts in XPCS but also by scientists who invented and pioneered this technique. The scientific and technical interest of all the BAT members cover a wide range of topics in condensed matter physics, biophysics, instrumental design, and the development at world-class facilities.

Beamline Advisory Team (BAT)

Robert Leheny, Associate Prof., John Hopkins Univ. (spokesperson)
Karl Ludwig, Professor, Boston University
Laurence Lurio, Associate Professor, Northern Illinois University
Simon Mochrie, Professor, Yale University
Lois Pollack, Associate Professor, Cornell University
Aymeric Robert, Instrument Scientist, LUSI/LCLS, SLAC
Alec Sandy, Physicist, 8-ID, APS, ANL
Oleg Shpyrko, Assistant Professor, University of California San Diego
Mark Sutton, Professor, McGill University

2 BEAMLINE LAYOUT

2.1 Overview

Key to performing XPCS measurements is a (partially) coherent x-ray beam. The coherence of a photon beam has two components: transverse or lateral coherence and longitudinal or temporal coherence. For a synchrotron source of x-rays, with an approximately Gaussian intensity distribution, far from the source, the transverse "one-sigma" coherence lengths in the horizontal (x) and vertical (z) direction are ξ_x, $\zeta_z=\lambda L/2\pi\sigma_{x,z}$. Here λ is the x-ray wavelength, and $\sigma_{x,z}$ are the "one-sigma" source sizes in the horizontal and vertical directions, respectively ~35 μm and ~4 μm at NSLS-II (assuming a fully damped source), and *L* is the source-to-sample distance.

It follows that, for a photon energy of E=8keV, for instance, and at a distance L=45 m from the source, near the current sample location in the CHX layout, this leads to one-sigma transverse coherence lengths in the horizontal and vertical directions of ξ_x=31.7 μm and respectively ζ_z=277.5 μm. These are both too large as the spot size has to be small enough to enable speckle detection. As a consequence, the beam has to be focused to smaller sizes in both directions. The maximum spot size that allows resolving individual speckles in determined by the detector resolution and/or working distance. Assuming a detector pixel size of 80 μm and a maximum detector distance of R=15 m (both limited by practical and/or technological limits), the spot size on the sample (*D*) corresponding to a speckle size *S*~100 μm is given by $D=\lambda R/S=23.25$ μm. Maximizing the XPCS signal-to-noise ratio (SNR) requires a spot size of "a few" one-sigma coherence lengths. It turns out that a good estimate for an "optimal" spot size is the full-width at half maximum (FWHM=$\sqrt{2\ln 2}\sigma \approx 2.35\sigma$) hence the one-sigma spot size corresponding to the speckle size mentioned above is ~10 μm. In order to perform XPCS in a SAXS geometry, the beamline optics should thus create a one-sigma spot size of 10 μm at the sample location. This can be achieved via focusing in numerous ways. In our current design, a focusing instrument consisting in a combination of Beryllium Compound Refractive Lenses (CRL) is placed in the pink beam around ~29-30 m from the source in order to provide the required "gentle" focusing. One possible layout that will provide the required beam size is shown in Figure 2. If a 2:1 demagnification geometry is used in the vertical direction with a lens placed around y=29.4 m, this will create a secondary source of 2 μm at 44.2 m which, in turn will give a one-sigma coherence length at the sample location (45 m) of ζ_z~10.36 μm (Figure 2a). Two possible layouts are presented (Figure 2b and 2c) to achieve a similar horizontal beam size. In the first one, a 1:1 lens around y=30 m is used to create a virtual source of 35 μm near the detector location at y=60 m. The horizontal coherence length determined by this source at the sample location is ξ_x~10.57 μm and, since the virtual source is behind the sample, this can be obtained by closing the horizontal gap of the secondary slits SS2. Alternatively, if a 3:1 focusing is used in the horizontal direction, a secondary source of ~11.7 μm is created at 40 m from the source which will result in the same transverse horizontal coherence length of ξ_x~10.57 μm 5 m downstream, near the sample location (Figure 2c).

By keeping the sample location close to the source, the detector distance can be sufficiently large to allow resolving relatively small speckles in XPCS-SAXS experiments. The speckle size S for a sample-detector distance R is given by S=λR/D. In the current design, R can be as large as 15 m, but can also be easily changed to any other shorter distances. With a one-sigma transverse coherence length of ~10x10 μm^2, as in the example above, the FWHM optimal beam size for XPCS experiments is about 23.5x23.5 μm^2 and, at R=15 m, this leads to a speckle size of ~92.4 μm. The SNR in the correlation functions increases when the speckles underfill the detector pixels (even though the optical contrast decreases), hence a detector with pixels of ~100 μm or smaller would be optimal. Our current expectation is that it will be possible to develop a fast (e.g., 1-10 MHz) detector with individual counters and possibly correlators for each pixel while keeping the pixel size around ~80 μm (D. P. Siddons et al., *unpublished*), and this will be suitable for XPCS experiments with the current beamline layout, provided their size will allow to cover a large-enough q-range.

For CDI experiments, the optical contrast will have to be maximized by adjusting the incident beam to a one-sigma size or smaller. In this case the speckles (at the same maximum available distance of R=15 m) will exceed ~220 μm,

which matches the assumed pixel size of 80 μm and required oversampling conditions. Often the "effective" beam size will be even smaller, as for isolated samples (e.g. a frozen cell) this is determined by the size of the object rather than the beam size. The optimal detector for CDI will be an integrating or photon counting detector with a high dynamic range and small-enough pixel size. Such detectors may become commercially available during the construction of the CHX beamline (e.g. Pilatus II).

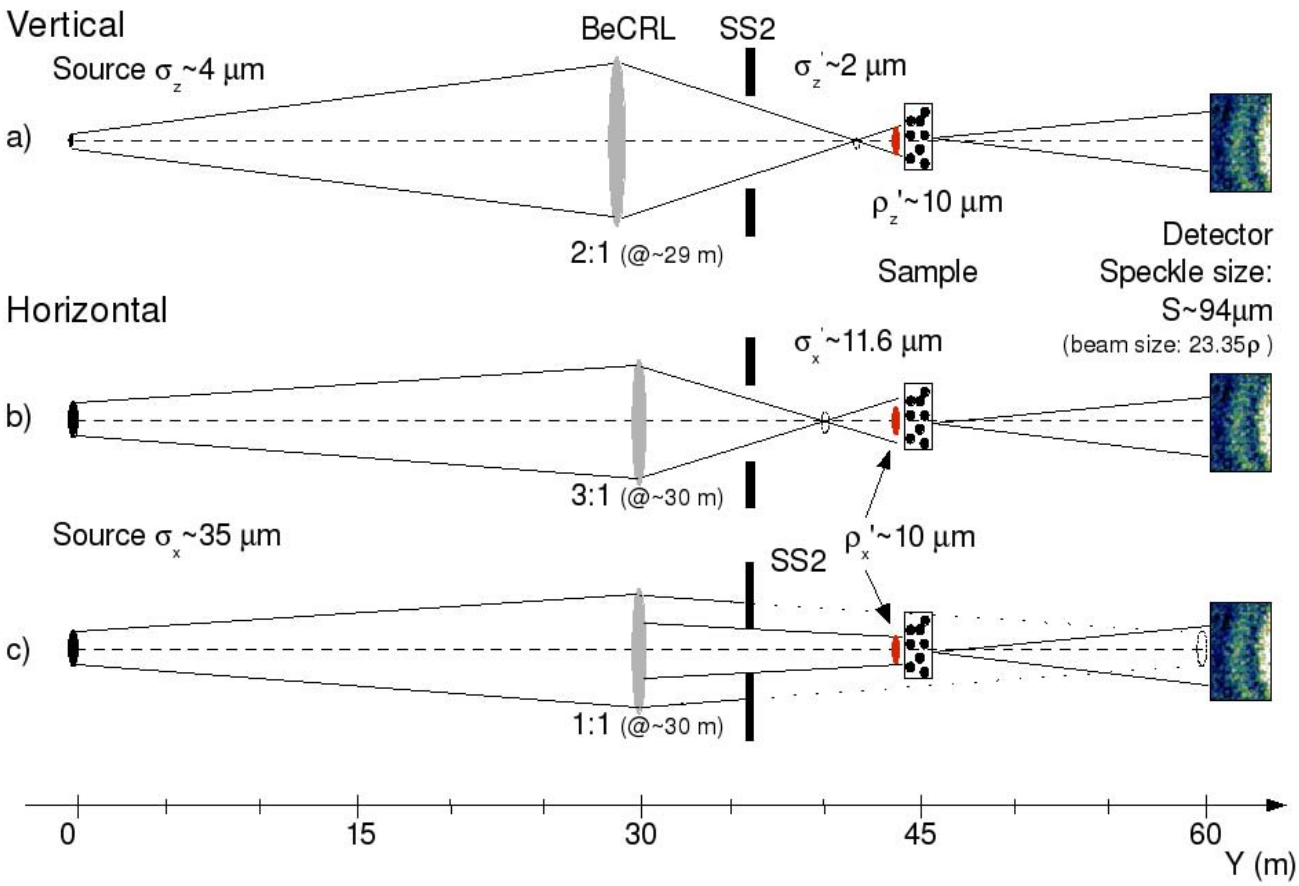

Figure 2 Possible optical layout for XPCS in a SAXS geometry. a) Vertical: A 2:1 focusing optics (represented here as a lens) placed around y=29.4 m is used to create a ~2 μm secondary source at ~44.2 m. This new source will yield a coherence length of ξ_x~10.4 μm at the sample location, (y=45 m). b) Horizontal: A similar scheme, with a 3:1 lens placed at y=30 m is used to achieve a horizontal coherence length at the sample location of ζ_z~10.6 μm. c) Horizontal: Alternatively, a 1:1 lens can be used to create a virtual source downstream of the sample around y=60 m. The corresponding coherence length at the sample location is still 10.6 μm, and the horizontal beam size can be limited by one of the available sets of secondary slits.

Wide-angle XPCS experiments will require much smaller beam sizes due to the more important effect that the finite longitudinal coherence length has on the speckle contrast in this geometry (see below) and to a much smaller detector distance limited by obvious practical reasons. A beam size of a few micrometers will be obtained in this case using horizontal and vertical focusing of the monochromatic beam with elements such as silicon kinoforms placed closer to the sample.

In addition to the transverse coherence, XPCS requires also partial longitudinal coherence (S. Mochrie, *unpublished*) The longitudinal coherence length of the beam is given by its monochromaticity $\Lambda=\lambda(E/\Delta E)$, where E is the photon energy, and ΔE is the full-width-at-half-maximum (FWHM) of the energy spectrum. Partial longitudinal coherence requires that the optical path length difference (δ) between x-rays scattered from different parts of the sample should

not be more than a few times Λ. For a transmission geometry, there are two contributions to δ. The first one, which arises because of a non-zero width (*D*) of the illuminated portion of the sample within the scattering plane, is

$$\delta_D = 2\mathrm{D}\frac{Q}{k}\sqrt{1-\frac{Q^2}{k^2}}\ .$$

The second comes from the non-zero sample thickness (*W*) and is

$$\delta_W = 2\mathrm{W}\frac{Q^2}{k^2}\ .$$

Usually, δ_W is small for typical values of *W* and may be neglected. By contrast, δ_L becomes comparable to Λ as *Q* reaches a maximum acceptable value. For a Si(111) monochromatic beam with $E/\Delta E \approx 10^4$, and a "typical" XPCS-SAXS transverse beam size D≈20 μm the maximum value of Q is about 1.5 nm^{-1}. As this is higher that needed in most SAXS experiments, many of them can be performed using a "pink" beam with $E/\Delta E \approx 10^2$, which limits the Q range to below $Q_{max} \approx 1.5\times10^{-2}$ nm^{-1}. From this analysis it is clear that longitudinal coherence requirements are more stringent in XPCS-WAXS. With the same Si(111) crystal and a beam size D≈1μm, the maximum value of Q becomes $Q_{max} \approx 3.2$ $Å^{-1}$. This also shows that a higher crystal cut with a smaller bandwidth will be beneficial for many WAXS experiments. The design of the CHX double crystal monochromator will allow the choice of several Si crystals.

The working energy range at the CHX beamline should be as large as possible, in order to offer a good flexibility in designing different experiments. A lower working energy will maximize the coherent flux which is given by $\lambda^2 B/4$ (note: B itself depends on energy and is larger at smaller energies). However, higher energies will help to reduce beam damage, allow experiments with thicker samples, allow working near or above several potentially useful edges (Mn, Fe, Co, Ni, Cu ...) etc. The proposed energy range for the CHX beamline is 6-16 keV.

The beamline layout and 3D model of the proposed CHX beamline can be seen in Figure 3. A long, pink beam compatible experimental hutch (EH) will allow a max sample-detector distance of ~15 m for SAXS experiments. The sample will be held on a versatile diffractometer which will allow also WAXS. Even though it is expected that in general an experiment will be performed either in SAXS or WAXS geometry, this arrangement opens the possibility to perform simultaneous WAXS and SAXS in certain situations (e.g., simultaneous measurement of capillary wave dynamics and structure formation on liquid surfaces).

The white-beam compatible optics hutch (OH) should be short in order to minimize the source-sample distance, but long enough to provide enough clearance to stop the bremsstrahlung while letting the pink beam deflected by a horizontal white-beam mirror go through to the EH. A choice of either a vertically deflecting "channel-cut type" monochromator offering a choice of Si crystals - e.g. Si(111), Si(311) - or a double multilayer monochromator will provide the choice of working with a high resolution monochromatic beam or a lower resolution pink beam.

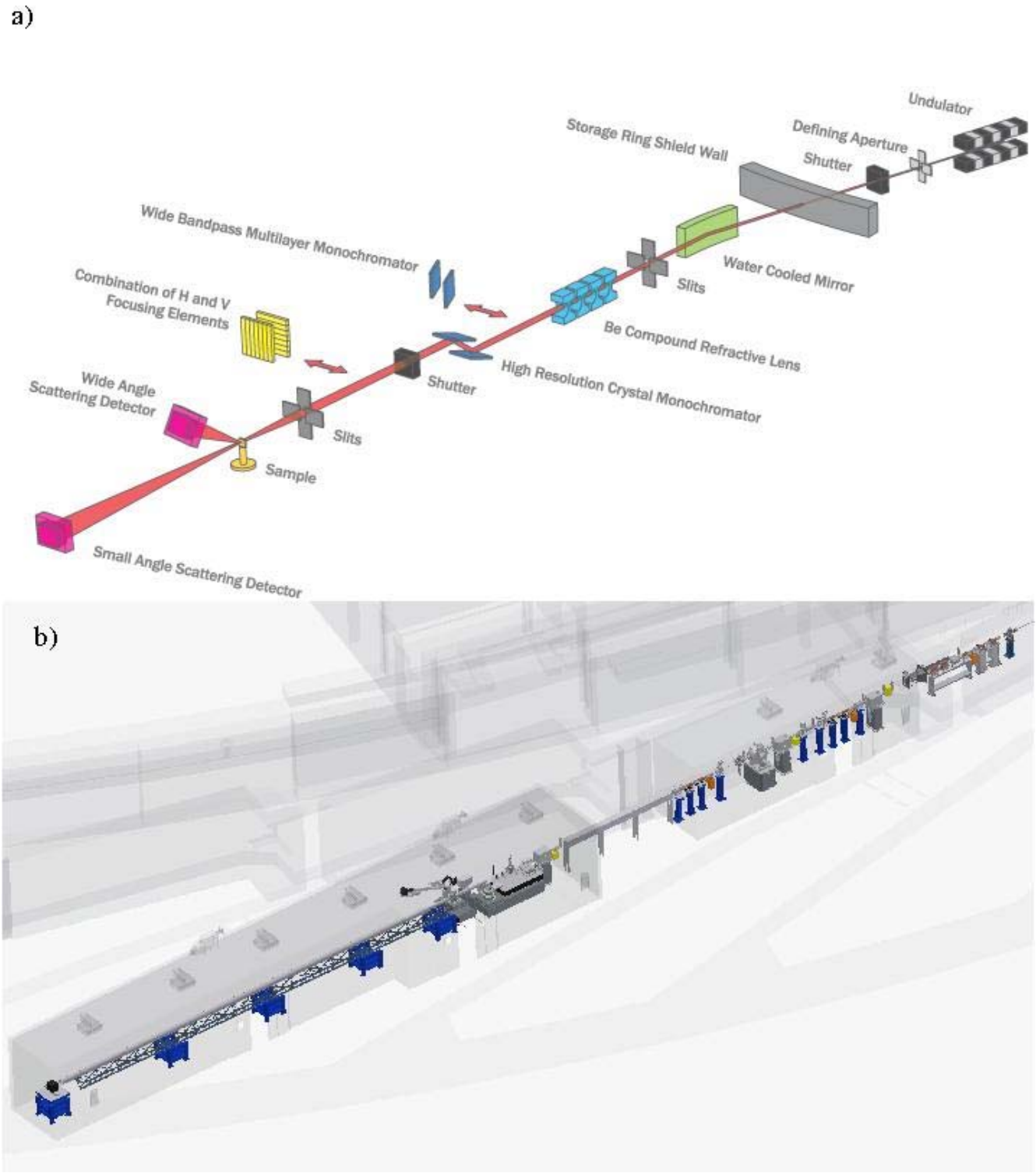

Figure 3 a) Schematic representation (not to scale) showing the optic layout of the CHX beamline; b) 3D perspective of the beamline including the Front End (FE), optics hutch (OH) and the experimental hutch (EH), which exceeds 20 m in length.

2.2 Insertion Device

Since the XPCS SNR is proportional to the source brilliance, the CHX beamline will be built on a low-beta straight section which yields the highest brilliance possible at NSLS-II. The insertion device, a 3m long U20 in-vacuum undulator (IVU) is the brightest of any devices in the NSLS-II baseline configuration. Its specifications can be seen in Table 1. The beamline will cover an energy range from 6keV to 15keV and will work most typically on the 5th harmonic of the U20 IVU but also on the 3rd, for lower energies, or the 7th harmonic for the higher energy end of the covered spectrum. For most working energies, the brilliance of the CHX source will exceed the 10^{21} ph/s/0.1%BW/mm^2/mrad^2 level, at least one order of magnitude higher than APS or ESRF. This unprecedented increase in source brightness is due to the very small emittance of the storage ring achieved with several damping wigglers (DW).

Table 1. Basic Parameters of NSLS-II U20 IVU on a Low-Beta Straight Section (Storage Ring Operating at 3 GeV and 500 mA).

U20	
Type	IVU
Photon energy range [keV]	Hard x-ray (1.9–20)
Type of straight section	Low-β
Period length, λ_U [mm]	20
Total device length [m]	3.0
Number of periods	148
Minimum magnetic gap [mm]	5
Peak magnetic field strength in linear mode, B [T]	1.03
Max K_y*, linear mode	1.81
Peak magnetic field strength in circular mode, B [T]	
Max $K_h = K_y$*, circular mode	
Minimum hν fundamental [keV]	1.62
hν critical [keV]	
Maximum total power [kW]	9.1
Horizontal angular power density [kW/mrad]	
On-axis power density [kW/mrad^2]	65.4

*K = 0.934 B[T] λ_u[cm]; effective K values listed

The fully-damped horizontal emittance value of 0.5 nm rad is assumed in all the parameters calculated by the NSLS-II Accelerator Systems Division (ASD) and reported here. This is the performance value for the NSLS-II storage ring when operating with a full complement of eight 7m damping wigglers. The initial emittance value will be greater than this value, owing to operation with fewer damping wigglers. The one-sigma electron beam size – σelectron – of the NSLS-II undulator is shown in Table 2 (source size and divergence in horizontal and vertical direction).

The diffraction-limited, "natural" photon beam size σ_{photon} is given by

$$\sigma_{photon} = \frac{1}{4\pi}\sqrt{2L\lambda}\ .$$

This is the size of a diffraction-limited photon beam for a zero emittance (and therefore zero size) electron beam. One measure of the effective photon beam size, σ_{eff}, is given by the quadrature sum of the electron ($\sigma_{electron}$) and photon (σ_{photon}) contributions:

$$\sigma_{eff} = \sqrt{\sigma_{electron}^2 + \sigma_{photon}^2}\ .$$

Table 2. Electron Beam Size and Divergence at the Center of a Low-Beta Straight Section of the NSLS-II Storage Ring.

Type of source	Low- β straight section (6.6m)
σ_h [μm]	31.8
σ_h' [μrad]	15.7
σ_v [μm]	2.9
σ_v' [μrad]	2.8

Similarly, the diffraction-limited, "natural" photon beam angular divergence σ'_{photon} is given by

$$\sigma'_{photon} = \sqrt{\frac{\lambda}{2L}},$$

and the effective photon beam angular divergence σ'_{eff} is again given by the quadrature sum of the electron ($\sigma'_{electron}$) and photon (σ'_{photon}) contributions:

$$\sigma'_{eff} = \sqrt{\sigma'^2_{electron} + \sigma'^2_{photon}}.$$

The effective photon beam size and angular divergence are shown in Figure 4 for two of the NSLS-II baseline insertion devices—EPU45 (red) and the CHX insertion device, U20 IVU (blue). The gray lines (straight, on a log-log graph) show the "natural" diffraction-limited photon beam size and angular divergence. The resulting brightness of all the NSLS-II baseline radiation sources is shown in Figure 5.

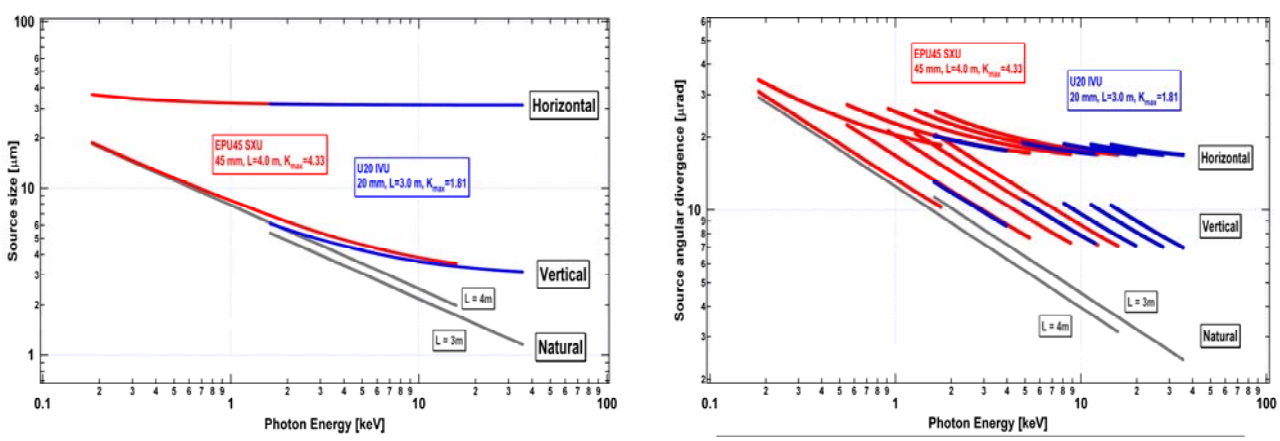

Figure 4. Vertical and horizontal photon source size and angular divergence for EPU45 soft x-ray undulator (red) and U20 IVU (blue). The gray lines show the calculated diffraction-limited size and angular divergence (see text).

To avoid unnecessarily increasing the heat load on the beamline optics, the CHX instrument will use only a small part of the beam, corresponding to one or "a few" transverse coherence lengths. This will be defined with the high heat load primary slits located at about 20m from the source, in the front end (FE). An estimate of the FWHM coherent beam size at this distance from the source is given in Table 3. The one-sigma coherence length has been estimated using ξ_x, $\zeta_z=\lambda L/2\pi/\sigma_{x,y}$ and the aperture size was considered to be FWHM~2.35σ in order to compromise between an increased SNR and a lower contrast with a larger beam.

Table 3. Coherent beam size – FWHM = 2.35σ – at the primary slits. Selecting a small beam size, corresponding to only "a few" coherence lengths, has clear advantages in terms of heat load on all the downstream elements.

E (keV)	6	8	10	12	16
λ (A)	2.06	1.55	1.24	1.03	0.77
ζ_z (μm)	447.3	335.5	268.4	223.6	154.2
ξ_x (μm)	44.7	33.55	26.8	22.4	17.6

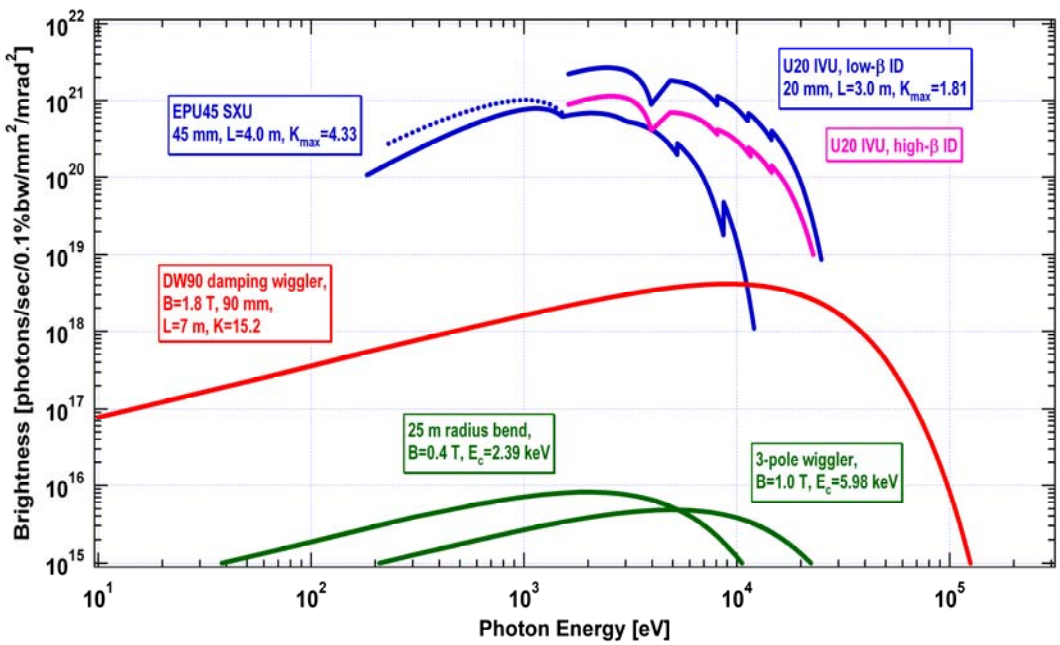

Figure 5. Brightness vs. photon energy for the baseline radiation sources at NSLS-II. Ring parameters: 3.0 GeV, I=0.5 A,ε_h=0.5 nm, ε_v=0.008 nm, energy spread=0.001; Straight section, low-β: β_h=2.02 m, β_v=1.06 m.

The filling modes and bunch uniformity will be of a particular importance for the CHX beamline. It is estimated that, in order to have clean baseline for the correlation functions that will enable measurements of sub-microsecond dynamics, the NSLS-II storage ring should provide a high current (500 mA) quasi-DC source with at least 4/5 of the buckets filled and the remaining, ion clearing buckets uniformly distributed across the ring. We estimate that a bunch-to-bunch uniformity better of 1% will lead to a structure in the correlation function safely below the noise level, while a 10% variation would be detectable in data with good statistics (hence, will require correction). More details about various synchrotron filling modes are given in section 4, Special Beamline Requirements.

2.3 Front End

The CHX beamline will use a standard NSLS-II front end configuration (see Figure 6). The key element in addition to the beam position monitors that will provide information about the transverse and angular position of the photon beam, a fixed aperture and a number of collimators, will be a set of X-Z high heat load slits with 1 μm precision/accuracy. These slits, also shown in Figure 6, are based on the design provided by the Mechanical

Engineering Group in the Accelerator System Division (ASD) and are described in more details, in the general front end section of this conceptual design report.

The slits are made out of a water cooled GlidCop body with stainless steel adapters and flanges. A set of tungsten corners will allow defining the beam (e.g., top, right with the first unit and bottom, left with the second unit). Each unit will be mounted on a motorized X-Z stage. The slit design (e.g. angle of the tapered profile in the GlidCop bodies and shape/geometry of the beam-defining Tungsten corners) has been optimized to cope with the high power load associated with white beam operation. They are a critical element in the beamline layout since by absorbing several kWs of incident power, the flux transmitted to the downstream optics will be greatly reduced. For instance, with the slits set to a "default" 500 μm (vertical) and 100 μm (horizontal) which is still larger than the coherence length at any wavelength (see Table 3), and an estimated peak power of ~90 W/mm^2 in the central cone of the U20 undulator (which is quite uniform over this reduced spatial range), the total power incident on the next optic element, in this case a horizontally deflecting flat mirror is only on the order of 4.5 W.

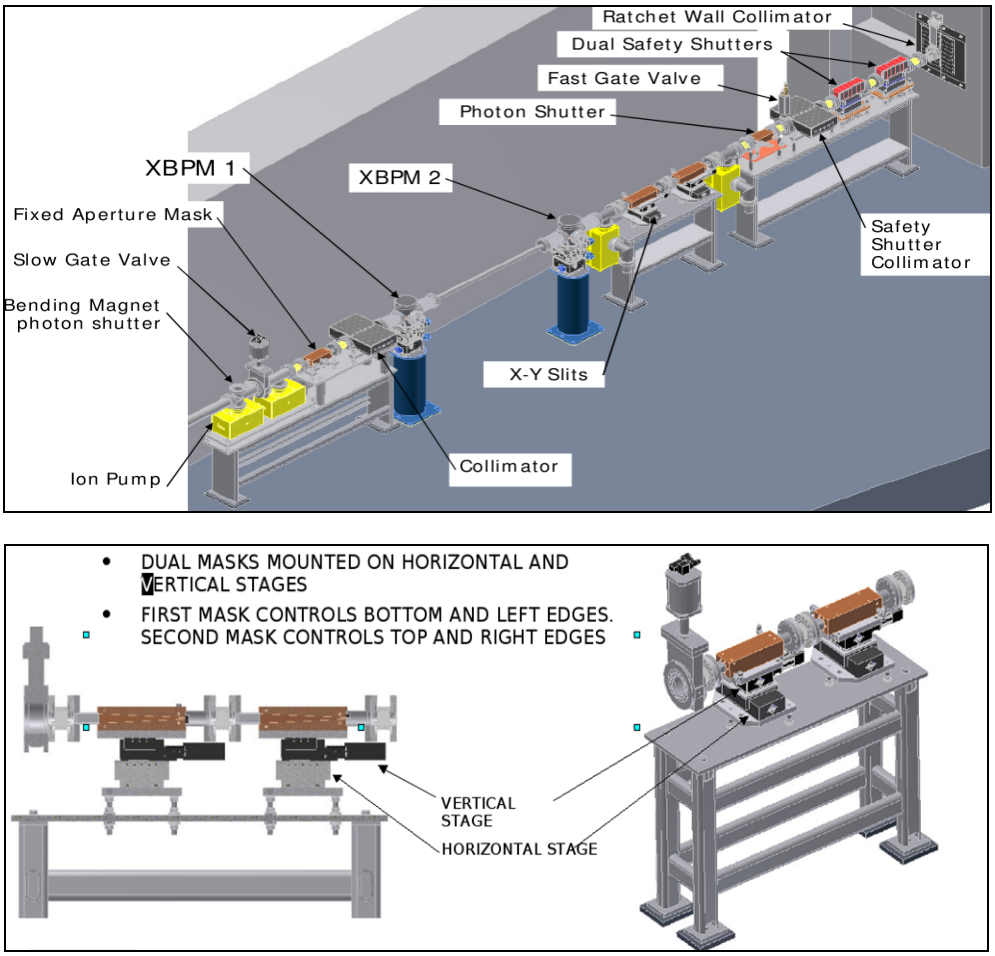

Figure 6. Front-End configuration and the high heat load X–Z precision slits, which will be used to limit the amount of power incident on the beamline optics by retaining only a few coherent modes of the photon beam.

The scannable primary slits will determine the size of the beam incident on the next optical element, which is the fixed-angle horizontally defecting mirror (a complete description can be found below in the Optical layout section). The power density on the mirror is low due to the relatively small incidence angle leading to a large footprint, hence water-cooling will be sufficient. However, since even small slope errors of a few μrad are considered to be too large, it is anticipated that the footprint of the beam on the mirror will have to be (significantly) larger that the final size of the coherent beam. It is even likely that the best performance will be obtained with a fully illuminated mirror and the coherent beam defined only further downstream by the secondary slits. For this reasons, the optical layout described below features two sets of high heat load slits placed before and after the mirror. This configuration offers

all the required heat-load management features and maximizes the flexibility for an optimal tuning of the beamline performance.

2.4 Optical Layout

The main consideration taken into account in the optical design of the CHX beamline is coherence preservation. The number of widows is reduced to a minimum and the optic elements will be polished to the best available figures. An R&D program devoted to coherence preservation by mirrors and multilayers is on-going at NSLS-II. The main goal is to identify the vendors and polishing methods that will allow optics with slope errors of 100 nrad or better.

The mechanical design of all critical elements will pay a particular attention to the overall stability. All the major elements in the proposed beamline layout are described below starting from the Front End ratchet wall and proceeding downstream.

White Beam Mirror

The first optic element in the beamline layout (apart the beam-defining X-Z slits placed in the Front End) is a horizontally-deflecting, nominally flat, white beam mirror. For simplicity and stability reasons, the incidence angle on the mirror will be fixed. A vertical translation will allow the choice between several stripes on the mirror surface. The presence of the deflecting mirror allows the possibility to stop the direct bremsstrahlung radiation in the optics hutch hence eliminates the need to build a (cost prohibitive!) white-beam compatible experimental hutch. In addition, it will also help by reducing the thermal load on the downstream optical elements and by lowering the radiation background in the Experimental Hutch. Finally, the total-reflection mirror provides a simple way to achieve high harmonic rejection in certain cases.

Increasing the angle of incidence is favorable for providing a larger deflection angle hence more room for collimators, beam stops, etc. However, decreasing the incidence angle will increase the mirror reflectivity. In the current layout, an incidence angle of 0.18 deg (3.14 mrad) will allow work with a bare Si (cutoff energy 10.4 keV) stripe for energies below ~9–10 keV or with a Rh-coated stripe (cutoff energy ~20.8 keV) for higher energies.

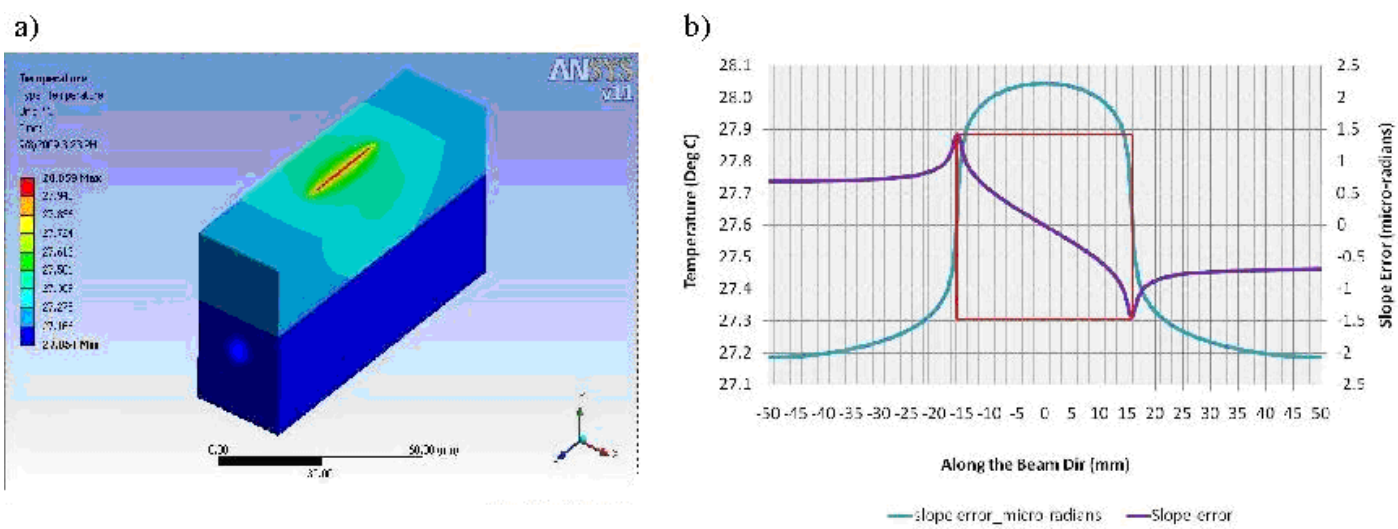

Figure 7. Finite Element Analysis for the white beam mirror assuming an indirect "back cooling" geometry. The temperature raises by less than 1°C and the maximum slope error within a "region of interest" corresponding to the coherence lengths will not exceed ~0.2 μrad.

With the small beam size at the CHX beamline and the horizontal reflection geometry, the footprint of the beam on the mirror will be quite small, e.g., the same "default" 500 μm (V) x 100 μm (H) incident beam will give a footprint of ~500 μm(V) x 3 cm (H) on the mirror. The power density will also be low, less than 0.3 W/mm^2 in this case, and can be handled by indirect water cooling of the mirror (Figure 7).

The polishing of the mirror surface and overall flatness will be of utmost importance for the coherence preservation properties of this element. In order to avoid affecting the speckle structure coming from the sample and given the fact that angular speckle sizes can be as small as ~3 μrad, it is estimated that slope errors well below 1 μrad (ideally 100–200 nrad) will be required at the CHX beamline. Obviously, the heat-induced deformations should also be kept within the same range.

Secondary Slits

A second set of water-cooled adjustable slits will follow in order to allow for collimation and further reduction of the power load on downstream components. Since the power densities can be locally high, this will also be a high heat load set of slits, based on the same design as the primary slits placed in the Front End.

Be CRLs for Vertical Focusing

All the XPCS experiments performed at the CHX beamline will require focusing in order to take advantage of the full transverse coherence lengths. This will be done using a selection of parabolic Be Compound Refractive Lenses (CRL) for vertical and horizontal focusing.

The Be CRLs are preferred over other possible focusing elements (mirrors, kinoforms, etc) because of their high reliability, tolerance to surface imperfections, and simplicity of use. Similar parabolic Be CRLs have been in regular user operation for several years at beamline ID10, ESRF. The vast majority of experiments performed there are using vertical focusing and the overall performance of the beamline improved by at least one order of magnitude with their installation.

The lenses that we plan to use – 1D focusing with cylindrical symmetry and parabolic profiles – are not available at this time, but we believe collaborations with groups that are world leaders in the fabrication of Be CRLs should enable us to obtain first prototypes for testing on a reasonably short time scale.

Preliminary heat load analysis performed using various FEA models have shown encouraging evidence that it will be possible to use them in white (or pink) beam if the (water) cooling is applied close-enough to the lenses. It is believed that it will be possible to keep the maximum operating temperature around 100-150 deg and the mechanical stresses around or below the yield stress to plastic deformation.

Monochromator(s)

Most of the experiments at the CHX beamline will be performed using a vertically deflecting double crystal monochromator (DCM). The monochromator will be designed to achieve angular stability better than 100 nrad and for this reason the vertical offset between the two crystals will be kept low – i.e. about 5-6 mm. The design will be simple and robust with a “channel-cut type” crystal cage made from two crystals cut from the same Si ingot and a piezo actuator adjusting the angular position of the second crystal to compensate for thermal offsets. In order to maximize stability the mechanical design will minimize the use of ball bearings and will mainly be based on flexure couplings.

The slope errors associated with thermal deformations of the first crystal should also be kept as low as the other “figures of merit” e.g., slope errors of the mirror or vertical stability and for this reason the DCM will use liquid nitrogen cryogenic cooling. The details of the FEA thermal analysis that proved that water cooling would not be sufficient are presented in the next section.

The fine monochromatic resolution obtained with a crystal monochromator is sometimes unnecessary in XPCS experiments working in a small-angle (SAXS) scattering geometry. In such cases, the use of broader bandwidth diffractive optics such as multilayers (ML) provide a good practical means to obtain more intense coherent beams - essentially “pink beams” - with excellent harmonic rejection efficiencies.

Here is an example of an experimental strategy that could provide a pink beam operation mode at a typical energy for XPCS experiments - E=8keV. The ML structure chosen in this simulations is a series of N=200 WSi_2/Si bilayers. Such structures are grown in the optics group at NSLS-II and have already been tested in coherent X-ray beams (see below). They are also commercially available from a number of vendors.

The simulated reflectivity curve of this structure for a photon energy of 8 keV can be seen in Figure 8. The peak value for the reflectivity is obtained for an incidence angle of 1.208 deg, R=0.81. This matches very well the measured reflectivity from a very similar ML structure (Figure 9). A sputtering deposition chamber that will allow growing such structures in-house will be installed and commissioned in the NSLS-II R&D laboratories in the very near future and it is in our plans to grow similar structures in-house.

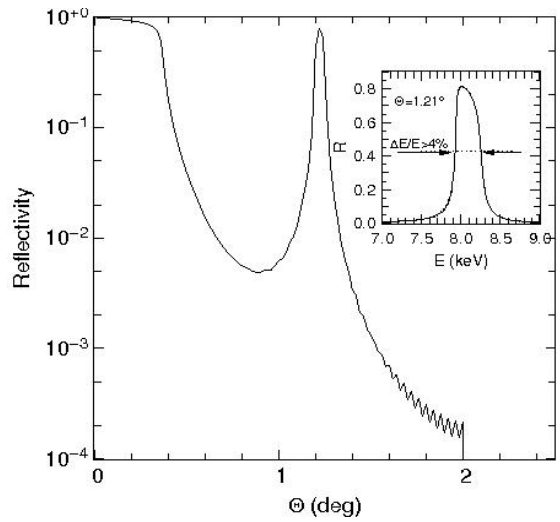

Figure 8
Simulated reflectivity from a WSi_2/Si multilayer structure for a photon energy of 8 keV. The parameters considered in this simulations are: multilayer period d=3.8 nm r=0.7 (Si layer thickness / period), thickness of inter diffusion layer s=4 Å, number of periods N=200. The inset shows the bandwidth of the 1st order E=8 keV reflection peak at an incidence angle of 1.208 deg.

The maximum intensity at 8 keV, will be obtained from the 5th harmonic of the U20 undulator. The approximate bandwidth of the undulator radiation is than $\Delta E/E=1/nN=1/750$, with n=5 for the 5th harmonic and N=150, the number of the U20 undulator periods. This approximation only takes into account the pulse length of light from a single electron resulting from the difference in travel time through the undulator between electron and photon. The results of a full calculation, taking into account diffraction effects resulting from the finite source size and angular spread is shown in Figure 10.

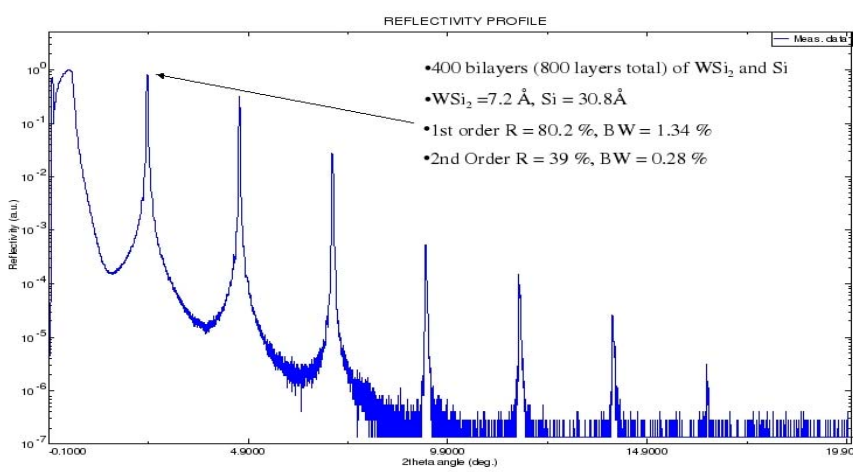

Figure 9
Measured reflectivity (E=8.04 keV, Cu-Kα rotating anode) from a WSi_2/Si multilayer structure (parameters shown on the graph).

Courtesy of Ray Conley

Figure 10. Line shape of U20 5th harmonic calculated for K=1.5 and a low-β straight section. The red curve was calculated assuming a fully damped (8 DWs) source while the black one shows the "day one" line width with only 3 DWs in the SR lattice.

Courtesy of Oleg Chubar

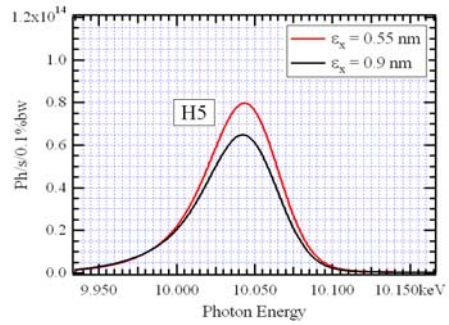

It is thus quite clear from this analysis that with the long U20 and high harmonics that will typically be used at the CHX beamline, the undulator line width will always be smaller than the bandwidth of the multilayer 1st order reflection, hence a multilayer monochromator will reflect the whole undulator harmonic providing "pink beam" operation.

The harmonic selection "efficiency" of the proposed optical layout can be seen in Table 4. Assuming a gap corresponding to the desired 5th harmonic centered around 8keV, we calculate the transmission coefficients for all the harmonics by simulating the influence of all the optical elements: total reflection mirror (reflectivity R_m), double multilayer (reflectivity R) monochromator, and a final exit window (transmission T), considered here to be a thin (100 μm) diamond. The total efficiency of the system is thus R^2TR_m. All these numbers are calculated in Table 4, showing an estimated efficiency in selecting the desired 5th harmonic larger then 50% while all other harmonics are virtually suppressed.

Table 4 Harmonic acceptance/rejection efficiency of the system consisting in: i) white beam (fixed angle) mirror; ii) multilayer monochromator; iii) 100 μm diamond exit window.

U20 Harmonic #	#1	#3	#5	#7	#9
E [keV]	1.6	4.8	8	11.2	14.4
R - ML reflectivity	0.7	7.5e-3	0.81	3.8e-4	2.7e-4
T (100 μm diamond)	1e-5	0.62	0.90	0.96	0.98
Mirror reflectivity R_m	0.94	0.96	0.96	0.13	2.5e-2
Total efficiency R^2TR_m	4.61E-06	3.35E-05	0.57	1.80E-08	1.79E-09

It is worthwhile mentioning that at low energy storage rings such as the NSLS-II, it is impossible to achieve efficient pink beam operation with a more simple harmonic selection system that would consist in an absorber working as a high-pass filter in conjunction with the total reflection mirror as a low pass filter. While this is a valid option at high energy machines such as the APS or ESRF where beamlines usually operate using the first harmonic of the undulators, it is much more difficult to select a higher harmonic (e.g., the 3rd or the 5th at the CHX beamline) and reject the neighboring ones, because they are much closer in energy. A simple calculation like the one shown before shows that in order to achieve a reasonable rejection efficiency of the "undesired" harmonics, the efficiency in accepting the desired one falls to just 1–3%. The coherent flux obtained with such a device would be the same as the one obtained from a "regular" high-resolution Si (111) monochromator, defeating the whole purpose of having a pink beam operation option.

In conclusion, the only practical way of achieving efficient pink beam operation at the CHX beamline is by using a multilayer-based wide bandpass device, and it is our belief that including this option in the baseline layout would enable important early advances in the field.

2.5 High Heat Load Optics

A comprehensive set of Finite Element Analysis (FEA) calculations were carried for the DCM using a large variety of finite element models with different cooling schemes. This exercise showed beyond little doubt that water cooling will not be sufficient for this DCM. Essentially this is the case because the small coherent beam that will be utilized at the CHX beamline will create a sharp "thermal bump" on the first crystal (a "standard" Si 111) of the monochromator. Even though the total power deposited by the small beam—e.g., 500 μm (V) x 200 μm (H) —will not exceed 10–12 W, the high thermal gradients would limit the performance of the CHX beamline by creating important distortions of the (first) Si crystal. From this analysis it was concluded that cryogenic cooling will be required in order to solve this problem. The FEA analysis shows that, unsurprisingly, any thermal distortions are almost completely eliminated by the cryogenic cooling.

2.6 Beamline Optics and Coherence Preservation

The development of the CHX beamline and other NSLS-II instruments that will focus on applications of coherence will increase the need for X-ray optics with unprecedented figure errors and coherence preservation properties. An important purpose of the NSLS-II project and later operation is to establish a vigorous research program aiming at characterizing the coherence preservation properties of optic elements such as mirrors, multilayers, compound refractive lenses, kinoform lenses, etc. and establishing the guidelines that will allow the improvement of such elements in the near future.

All the mirrors and multilayers will be carefully characterized in the NSLS-II metrology lab (described elsewhere in this conceptual design report) using multiple probes including a Long Trace Profiler, ZYGO stitching interferometer, a Micromap interferometric microscope and an atomic force microscope. Cross-correlation of multiple methods is important in understanding a wide range of spectral frequencies that are critical to the quality of the coherent wavefront. Having a wide range of metrology tools readily available will allow collaborations with selected vendors and suppliers in improving the figure errors by measuring, for instance, the quality of surfaces before and after "corrective" polishing processes.

Ultimately, the best metrology tool is arguably the X-ray beam itself. In a first "at wavelength metrology" experiment performed at beamline ID06-ESRF, we have used an "in-line holography" method (V. Kohn, I. Snigireva, and A. Snigirev, *Phys. Rev. Lett.* 85, 2745, 2000), which consists in measuring the diffraction pattern resulting from the coherent illumination of a well defined object, to evaluate the coherence preservation properties of a synthetic multilayer. As pointed out before, multilayers provide perhaps the only practical way of achieving pink beam operation at NSLS-II. At the same time it is not clear how much they perturb the coherent wavefront. Thus far, the only experience with MLs and coherent beams comes from a few experiments performed at NSLS in the mid 90s (e.g., O.K.C. Tsui S.G.J. Mochrie, *Phys. Rev. E* **57**, 2030, 1998). The contrast measured in those experiments was within 30-40% of calculated ones, indicating that the coherence of the beam is preserved, but more investigations, especially new ones using brighter X-ray beams at ESRF and/or APS are clearly needed. In the ID06 experiment we have measured the interference fringes created by a 100 um diameter Boron fiber directly with a CCD camera or after reflection by a ML structure which was used here as a "sample" (see Figure 11). The ML structure used here was a sequence of 400 WSi_2/Si bilayers structure grown in the APS deposition laboratory (R. Conley et al., *Proc. SPIE* **6705**, 670505, 2007). The ML parameters and reflectivity are shown in Figure 9. The obvious degradation of the wavefront resulting in the "horizontal stripes" (which can be seen due to the good vertical coherence of beam) is a result of slope errors distributed along the footprint along the ML surface, in this case, a few cm long and 500 μm wide. The substrate used for this test ML structure was a "non-ideal" one in terms of roughness and flatness. Once the NSLS-II deposition facility will become available, we plan to adopt a more "systematic" approach by starting with highly polished, well defined substrates that will be characterized independently before depositing the ML structure.

As shown by Souvrorov et al. (*J. Synchrotron Rad.* **9**, 223, 2002) the ``distorted'' diffraction patterns can be used to retrieve the tangential profile of the additional optical element. Our theoretical approach consists in using a full

wave propagation analysis which takes into account the partial coherent illumination (O. Chubar et al., *Proc. SPIE Int. Opt. Eng.* **4769**, 145, 2002) to retrieve the tangential surface profile of the optical element.

The proposed research program will focus on investigating a multitude of different optic elements by fostering active collaborations with a few vendors and correlating X-ray tests like the one described above with multiple metrology measurements. This will undoubtedly result in systematic and definitive correlations between the metrology data and the quantitative x-ray analysis. We believe this is an important effort that could make a considerable impact in the x-ray community, in which the x-ray optics poses a significant bottleneck to the further advancement of coherence-requiring techniques.

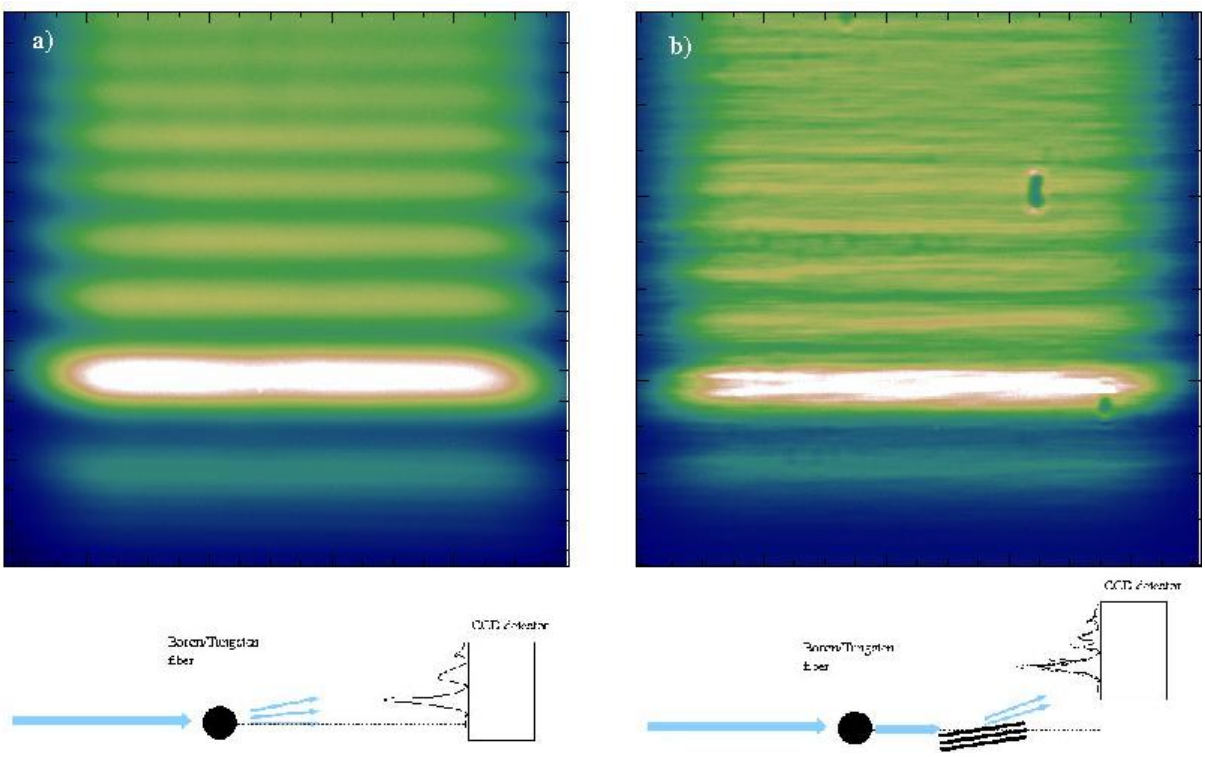

Figure 11 Interference fringes created by a Boron fiber seen directly on the CCD detector (a) or reflected through a WSi_2/Si ML structure (b). The intensity distribution with the ML was increased by 20% to compensate for losses due to a non-perfect reflectivity and "match" the color scale of the two panels for clarity purposes.

2.7 Ray Tracing

An important goal of our optical design was to achieve a large enough separation between the Bremsstrahlung radiation in the forward direction and the pink beam laterally deflected by the total external reflection fixed incidence angle mirror placed upstream. The bremsstrahlung and photon beam ray tracing for beamline optics shown in Appendix 2 demonstrate that the current separation is large enough to allow the design of a tungsten Bremsstrahlung beam stop with an opening for the pink beam about ~44.8 mm inboard of the forward direction.

2.8 List of Major Components

Table 5 shows the position and approximate size of the beamline components. The space between the main components will be filled with vacuum bellows and pipes of suitable length. The table also shows different sections of the beam line vacuum system.

A CAD drawing of the beam line and the end stations showing general layout of the beam line components is given in Appendix 2.

Table 5. List of major components.

Bement	Location (m)	Length (mm)	Description/Notes	Vacuum section
Source	0			
Fixed Front End (FE) aperture	16.21		Can be reduced to ~2 mm	
Lead collimator	16.74			
Beam Position Monitor (BPM) 1	17.43			
BPM 2	19.47			
White Beam Slit, X	20.18		water cooled high heat load	
White Beam Slit, Y	20.78		white beam slits	
Photon shutter	21.17			
Fast Gate Valve	22.1			
Safety Shutter Collimator	22.2			
Dual Safety Shutter	22.98 23.36			
Ratchet Wall Collimator	24.02			
Gate Valve 1	25.6			0/1
Differential pump	25.8			1
Gate valve 2 with x-ray window	26			1
Horizontal deflecting mirror	26.5		fixed angle 3.14 mrad, 2 stripes	1
Gate valve 3	26.9			
Bremsstrahlung collimator 1	27.2			1-2
White Beam Slit, X	27.9		“Reduced” version of white beam slits	2
White Beam Slit, Y	28.5		“Reduced” version of white beam slits	
Fluorescent screen	29.1		water cooled	2
Be CRLs	29.31			2
Gate Valve 4	29.65			2-3
Bremsstrahlung collimator	TBD			3
Fluorescent screen, H2O cooled	30.19			3
Double multilayer monochromator	31.3			3
Gate Valve 5	31.65			3-4
Dual crystal monochromator	32.36			4
Gate Valve 6	33.3			4-5
Photon shutter / Bremsstrahlung stop	33.5			5

2.9 End Station Instrumentation

A granite table placed just after the wall of the optics hutch will be the first module in the experimental hutch. The table will host a variety of local optics designed for monochromatic or pink beam operation. This will include: focusing optics such as 1D Fresnel Zone Plates or Silicon kinoforms for both vertical and horizontal focusing, local mirror to deflect the beam downwards for GI-SAXS on liquid surfaces, beam defining slits, guard slits, etc. These elements will be kept modular to allow for a certain flexibility, e.g. optimization of distances between slits, etc. All individual elements will be interfaced by vacuum pipes and bellows.

The central piece of the CHX end station (Figure 12) will be a versatile 5-circle diffractometer. A stack of motion controllers offering 3-axis (x, y, z) and 3-circle (θ, φ, χ) positioning will sit on a stable base such as a granite block.

A two-circle (δ, γ) detector arm will enable high resolution diffraction experiments in horizontal and vertical scattering geometries. The end station will feature visible on-line microscopy, provided by an on-axis microscope situated just upstream of the sample. In combination with a fluorescent screen, this microscope will also provide excellent beam diagnostic capabilities. WAXS and μ-beam SAXS experiments will be performed with the detector held on the diffractometer arm with a sample detector distance up to ~2 m and micron size focused beam (both in horizontal and vertical directions).

The SAXS detector and beamstop will be located on a long steel frame upstream of the diffractometer. A selection of working distances for SAXS (e.g. 2m, 5m, 10m, and 15m) will be available through a fast change mechanism for the sectioned flight tube, without the necessity to lift pipes. Detector and beamstop will be equipped with x and z translations for individual alignment respectively to the beam. In the most optimized setting, the setup will allow for a windowless beam path between the beam defining optics and the exit window of the SAXS flightpath.

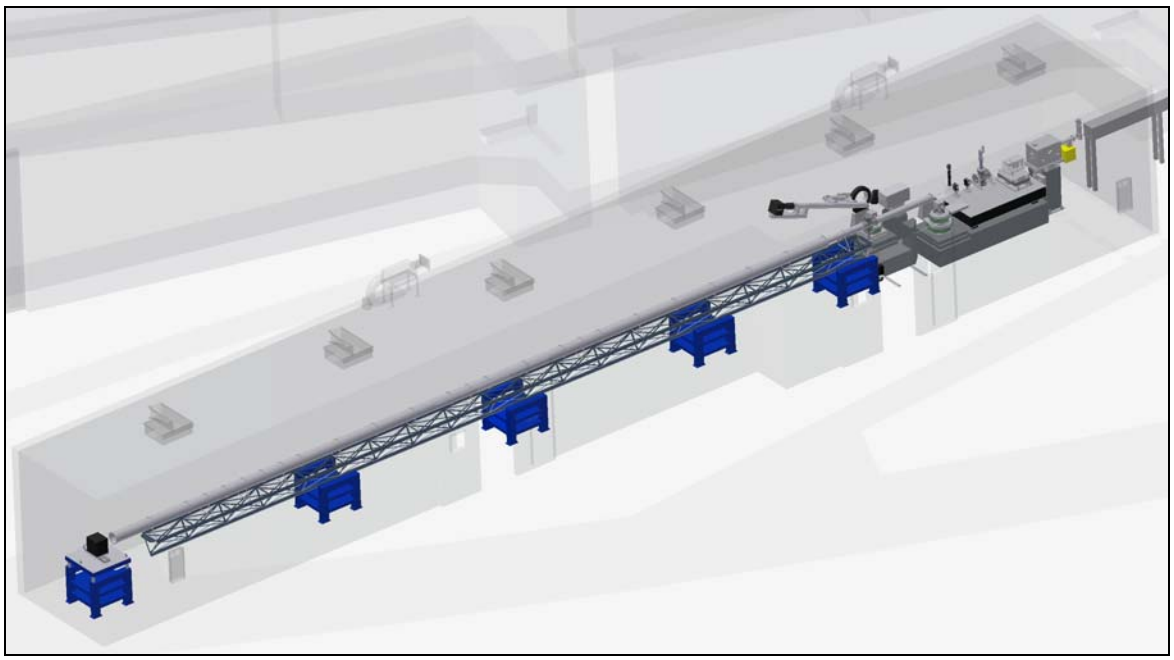

Figure 12. Sketch of a proposed end station that will allow SAXS, WAXS, and GI-SAXS experiments.

While offering optimized setups for SAXS and WAXS experiments, the end station will also allow for XCPS studies in SAXS and GISAXS geometries accompanied by (static) WAXS or GIXD measurements. This combination is of particular interest for studies of soft condensed matter systems like e.g. thin organic films or thermotropic gels of self-assembled organic nanotubes. These systems are characterized by an intimate relationship between structure and dynamics, where often the larger scale dynamics is determined by the microstructure.

The vast majority of XPCS experiments will certainly follow the current trend and will require complex sample environments. Flow cells will be used to achieve new functionalities or to avoid beam damage. Shear cells will be used to study driven dynamics in glassy systems, high precision furnaces will be required to study phase ordering processes in materials, Langmuir troughs chambers to study dynamics of ordering phenomena at surfaces, etc. In the standard setup, the diffractometer will host a sample chamber with different insets allowing for temperature control in various temperature ranges between liquid nitrogen temperature and a few hundred degrees.

The CDI setup will be a stand-alone system similar to the one recently developed at the ESRF (ID10C) featuring very high precision motion controllers. This setup could be either hosted on the diffractometer or on the last section of the granite table which supports the local optics. The letter option seems to be in particular favorable for the ptychography and Fresnel approach to CDI, where a very stable positioning of the sample in the incident beam is of utmost importance.

3 SPECIAL BEAMLINE REQUIREMENTS

3.1 Vacuum

In order to conserve the source brilliance, the beamline will have the possibility of windowless operation. As an option, a selection of "constriction valves" engineered with a window on the blade, will offer the possibility to work with more "relaxed" vacuum requirements during commissioning. In a "maximum brilliance operation" mode, only one final exit window (e.g., Diamond, Be, Si_3N_4 ...) placed just before the sample will separate the beamline UHV from the sample environment rough vacuum (or air). A vacuum sensor placed close to the end of the UHV section and a fast valve placed just after the Front End will protect the beamline optics against possible vacuum leaks. A similar system already designed in the Front End will further protect the accelerator vacuum from leaks in the Front End or Beamline Optics

3.2 Detectors

A fast 2D photon-counting area detector will be required for the XPCS experiments at NSLS-II. This detector in the most critical element that will enable pursuing the scientific program described in the first part of this document. Unfortunately, at least for the moment, no commercial detector meets our specifications. The two instruments that are the closest in doing that are the Pilatus detector (Dectris) and the Medipix (Medipix Collaboration). Out of the two, the Medipix is the one that was already successfully used in XPCS experiment and enabled results that would have not been possible otherwise (e.g., Chiara Caronna et al. *Phys. Rev. Lett* **100**, 055702, 2008). Unfortunately, the Medipix is not a commercial device and it is not clear if it will become one. More importantly, even if NSLS-II joined the Medipix project (which would perhaps be something advisable) the current maximum full frame readout rate – 1 kHz – is not sufficient for some of the experiments planned at NSLS-II. The Pilatus Detector has the advantage of being commercially available but for the moment is clearly lagging behind in terms of performance (e.g., readout speed, pixel size).

The best alternative for the CHX beamline is a XPCS detector that is currently being developed in a R&D collaboration between the BNL Detector Development Group and Fermi National Laboratory (D.P. Siddons, private communication). The so-called Vertically Integrated Pixel Imaging C... (VIPIC) detector consists in a detector chip bonded to a stack of signal processing "layers" using a "3D integration technology". A first prototype chip, with the main characteristics described in Table 6, is currently being fabricated and will be connected to a data acquisition controller designed in collaboration with the NSLS-II Controls group. The whole system could be ready for a test experiment as early as the first quarter of 2010.

Other detectors of interest that will need to be available at the CHX beamline include:

- CCD Detector
- A "standard" CCD detector with small pixel size will be used for CDI experiments and/or certain static studies (e.g., SAXS, studies of kinetics via time-resolved SAXS or WAXS, etc.)
- APD array

Fast point-like detectors to be used in conjunction with a hardware correlator will still be required for a certain class of experiment for which the dynamics time scales are typically on the order of 1μs or faster. The clearest example of such class of applications is that of capillary waves at liquid surfaces. The time scales involved in a vast majority of such experiments will likely remain too fast for the next generation of detectors like the "VIPIC" detector. These phenomena will be best studied using a linear array of Avalanche Photon Diode (APD) detectors.

Table 6. Main characteristics of the first prototype of the XPCS "VIPIC" detector.

Pixel size	80 mm
Number of pixels	64x64
Active area	5120 x 5120 mm^2
Chip size	5.5 x 6.3 mm^2
Operation: Will provide dead timeless readout: each pixels is read sequentially by 2 5-bit counters Noise well below 1 photon level (~ 100 e- vs. ~2200e- generated by a 8keV photon) Data sparsification will be provided on chip - only the detectors that had a hit will be read. Max readout speed 10 s, limited by the estimated max count rate ~0.5 photons / pixel / 10 s. Readout consists in pixel address, time no. of hits (no energy info).	

3.3 Synchrotron Filling Modes

As described before, the NSLS-II CHX beamline will be dedicated to studies of dynamics using XPCS. Obviously any intensity fluctuations coming from other sources—e.g., the filing mode—can perturb the experiment. At ESRF, for instance, the only mode that allows studies of "fast dynamics" on ~1 μs time scales - is the uniform filling one, in which all 992 buckets around the storage ring are filled, and there are no ion clearing gaps. The proposed NSLS-II baseline mode with has 1/5 of the ring empty as an ion clearing gap, and it is expected that this will not offer "optimal" conditions for this type of measurements (fast XPCS). This will most likely create, pretty much like all other time-structure modes at ESRF do, some very pronounced "spikes" in the correlation functions, precisely around the time scales that need to be measured. However, bunch trains with uniform filling structures will also be possible at NSLS-II. The NSLS-II injector will be able to support virtually any structure. The storage ring itself may operate with a uniform filling (no ion clearing gaps), but the value of the maximum achievable circulating current in this mode is difficult to estimate at this point. Having 100 ns gaps between bunches (uniformly distributed around the ring) would relax the process of ion clearing and enable a high current operation. Such a mode may be appropriate for fast-XPCS, since it should be possible to synchronize the acquisition so that the number of filled buckets within a sampling interval is constant and doesn't generate any intensity fluctuations.

3.4 Data Storage/Handling

With the advent of 2D area detectors with high quantum efficiency and single photon sensitivity, XPCS has become rapidly a technique that produces massive amounts of data. The "typical" XPCS experiment at ESRF or APS easily generates more than 50 GB of data during a single experiment. While this may be considered a "modest" rate compared to high-energy physics experiments, it starts putting a number of logistic problems. First of all, data access rates of 100 MB/s and dedicated optical fiber connection to data storage disks are considered a "minimal requirement". Data storage capabilities of many TB with automatic backups performed on a regular basis are also required.

While the next generation of XPCS detectors such as the VIPIC system designed by P. Siddons and collaborators will change the current paradigm and use data sparsification in order to increase speed and minimize the amount of unnecessary information that is saved with current systems (e.g. information about pixels that did not receive any photons in a particular time interval), it is reasonable to assume that these developments will not reduce the amount of data that is produced and/or stored, but perhaps only stop or at least reduce the exponential increase in data production that we witnessed over the past few years.

On-line, or quasi on-line data processing starts also being of a critical importance. Not only it starts being difficult for all the users to leave to their home institution with perhaps as much as 100 GB of raw data collected in a one week experiment, but processing this amount of data requires specialized software, training, etc. In many cases

users prefer to leave with semi-processed data – e.g. calculated correlation functions – which they can interpret and further analyze at a later date. For this reason it is mandatory for the CHX beamline to offer high performance and user-friendly software that can be easily used during experiments. This is of fundamental importance as partial results and analysis are actually required in most situations to decide on the optimal experimental strategy.

The strategy in the CHX group is to adopt, further develop, and package in a coherent, comprehensive way software that was designed at other facilities such as the ESRF and APS. In order to minimize problems that are always encountered with property software when new versions are being released and older versions stop being maintained, we will use open source software running on personal computers with linux platforms.

One concrete example is a environment for XPCS data analysis recently developed at ESRF (C. Caronna et. al., *unpublished*). The software is written in Python and offers a user-friendly graphics interface that can be used to calculate equilibrium correlation functions, time-dependent (two-time) correlation functions in non-stationary systems or higher order correlations in systems with dynamical heterogeneities. Such software together with other modules – e.g. for SAXS analysis, data fitting, etc – has to be integrated with the whole instrument, data acquisition, on-line monitoring, software for experimental control, etc.

4 FUTURE UPGRADE OPTIONS

4.1 Detector Developments

The detector is perhaps one of the most important parts of an instrument such as the CHX beamline. While the current development of the VIPIC detector lead by P. Siddons and collaborators will clearly push very far the current boundaries limiting the performance of detectors for XPCS, it also opens the way for a number of possible improvements: a smaller pixel size, larger detector area, faster readout, more “intelligence” on board (e.g correlation functions, two time correlation functions, on-line “dropletizing” of the detected signal, etc.).
Some of the improvements mentioned above can be more easily achievable with different types of detectors. It is clear, for instance that Avalanche Photon Diodes (APD) detectors will be much faster than other detectors, and an array of APDs will offer unique capabilities for studies of capillary-wave dynamics.

4.2 Specialized Sample Environments

Our current efforts are quite naturally centered around developing the est XPCS instrument to date. However, designing the actual experiment and the sample handling instruments and will clearly be equally important. The current trends in the community show beyond any doubt that the stage when a quartz capillary could have been simply “duct taped” in the beam are long gone. The sample environments become increasingly complex, allow for in-situ changes of experimental conditions (e.g. temperature, pressure, atmosphere, electric or magnetic fields, concentration or even composition, etc.). Often there be also an increasing need to perform other measurements in-situ – optical microscopy, rheology, light scattering, etc. or to allow new functionalities with advanced techniques – e.g. time-resolved studies in microfluidic systems (L.Pollack et al., *Phys. Rev. Lett.* **86**, 4962, 2001) or heterodyne/homodyne detection as a means to study the interplay between advective transport and dissipative motion (M. Sutton et al. *in progress,* F. Livet et al., *J. Synchrotron Rad.* **13**, 453, 2006). Last but not least, some of the techniques mentioned above (e.g. microfluidics and heterodyne detection) offer clear advantages in terms of reducing beam damage which is an issue which at NSLS-II will become even more important that in already is. From this point of view, it is clear that an instrument like the CHX beamline (or any other beamline at NSLS-II) will require continuous developments of new sample environments or improvements of existing ones.

4.3 Beamline Optics and Figure Control

The development of improved optics with better coherence preservation properties will continue to be a major preoccupation in the CHX group throughout the later operation of the beamline. The ultimate goal is to achieve an

efficiency as close as possible to 1 in using the entire coherent flux available from the NSLS-II source by improving the surface finishing of the optical elements, reducing the heat load, finding technical solutions to use new materials (e.g. better quality diamond than is available today). The use of focusing K-B mirrors for applications using coherent beams will also be investigated.

Upgraded Insertion Devices

Simulations of possibly upgraded in-vacuum undulator sources are shown (courtesy of Oleg Chubar) in Figure 13. The calculations assumed an electron current in the ring of 500 mA, a "day one" horizontal emittance of 0.9 nm (the fully damped value is 0.5 nm) and energy spread of 8.9×10^{-4}. The simulation shows the spectral brightness of a longer undulator, assuming the technology will allow an increased magnetic field to compensate for an increased vertical gap (the maximum K value is the same as for the current U20 IVU).

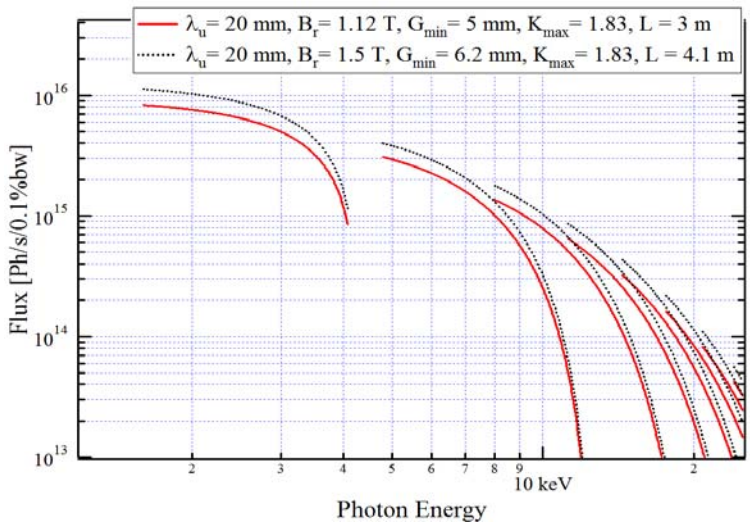

Figure 13. Spectral brightness for the odd harmonics with an (hypothetical) upgraded longer undulator with a higher magnetic field. *(courtesy of Oleg Chubar)*

APPENDIX 1 SCHEDULE

Construction of CHX beamline

Oct. 2009	Complete Conceptual Design Report
Sept. 2010	Complete Preliminary Design Report
Dec. 2010	Technical Design – Approval of Long Lead Term Procurement
Jan. 2011	Start Lead Time Procurements (monochromators, CRL, enclosures,…)
Apr. 2011	Complete Final Design of Beamline Major Components
Feb. 2012	Complete Final Design Report
Feb.2012	Approval of Start of Beamline Construction - Beneficial Occupancy of Experimental Floor
Feb. 2012	Start Installation
May 2012	Start Sub-System Testing
May 2012	Start Other Procurement
Jan 2013	Complete Long Lead Time Procurements
Aug 2013	End Procurement
Aug 2013	Start Integrated Testing
Jan 2014	Complete Installation
Feb 2014	Complete Sub-System Testing
May 2014	Complete Integrated Testing – Beamline available for Commissioning
June 2015	**CD-4**, Approve Start of Operations

Intentionally blank.

APPENDIX 2 REFERENCE DRAWINGS

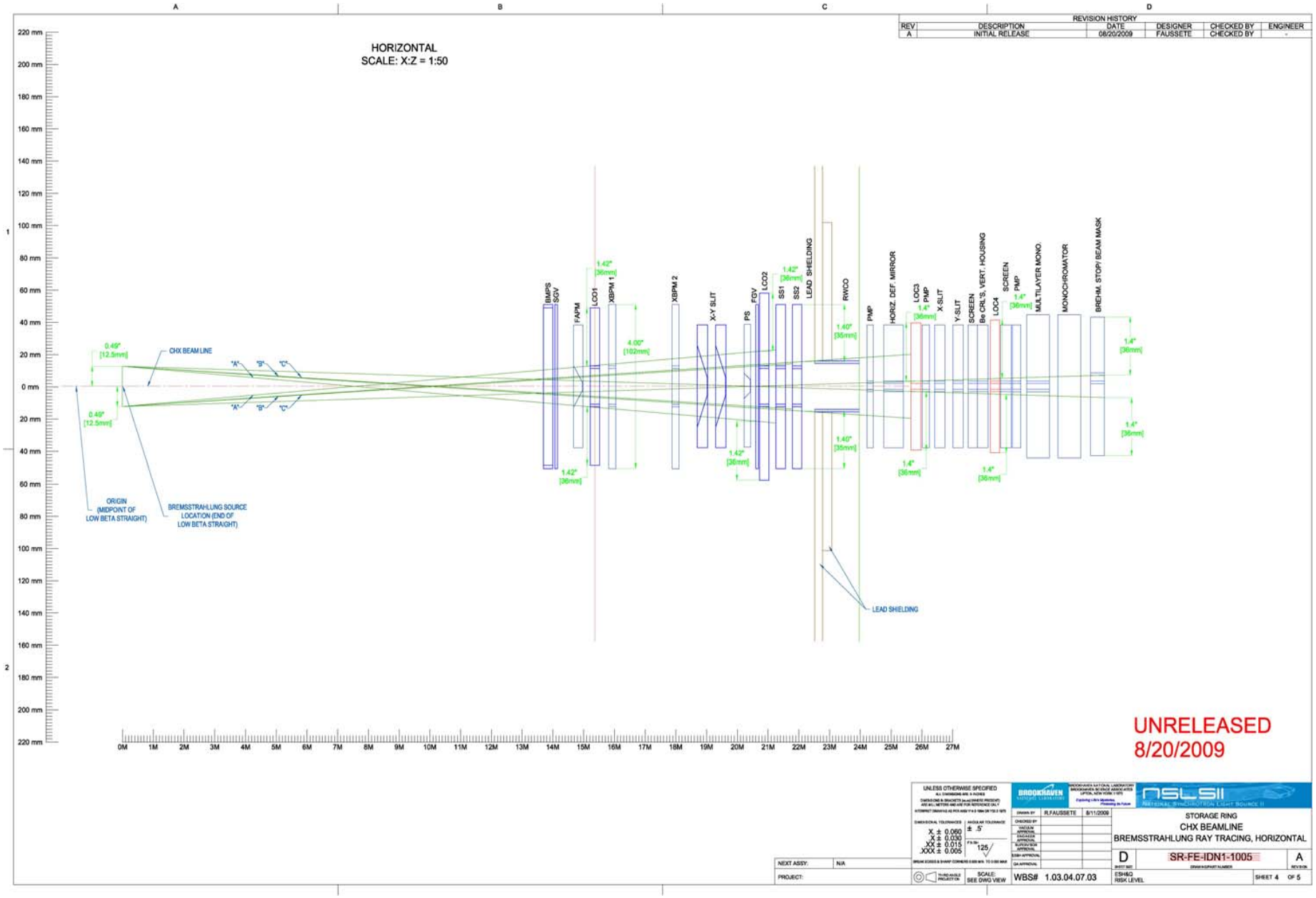
REVISION HISTORY
REV A DESCRIPTION INITIAL RELEASE DATE 08/20/2009 DESIGNER FAUSSETE CHECKED BY CHECKED BY ENGINEER
HORIZONTAL
SCALE: X:Z = 1:50
CHX BEAM LINE
ORIGIN (MIDPOINT OF LOW BETA STRAIGHT)
BREMSSTRAHLUNG SOURCE LOCATION (END OF LOW BETA STRAIGHT)
BMPS
SGV
FAPM
LCO1
XBPM 1
XBPM 2
X-Y SLIT
PS
FGV
LCO2
SS1
SS2
LEAD SHIELDING
RWCO
PMP
HORIZ. DEF. MIRROR
LOC3
X-SLIT
Y-SLIT
SCREEN
Be CRL'S, VERT. HOUSING
LOC4
MULTILAYER MONO.
MONOCHROMATOR
BREHM. STOP/ BEAM MASK
LEAD SHIELDING
UNRELEASED
8/20/2009
UNLESS OTHERWISE SPECIFIED
BROOKHAVEN NATIONAL LABORATORY
NSLS II
STORAGE RING
CHX BEAMLINE
BREMSSTRAHLUNG RAY TRACING, HORIZONTAL
SR-FE-IDN1-1005
WBS# 1.03.04.07.03
SHEET 4 OF 5

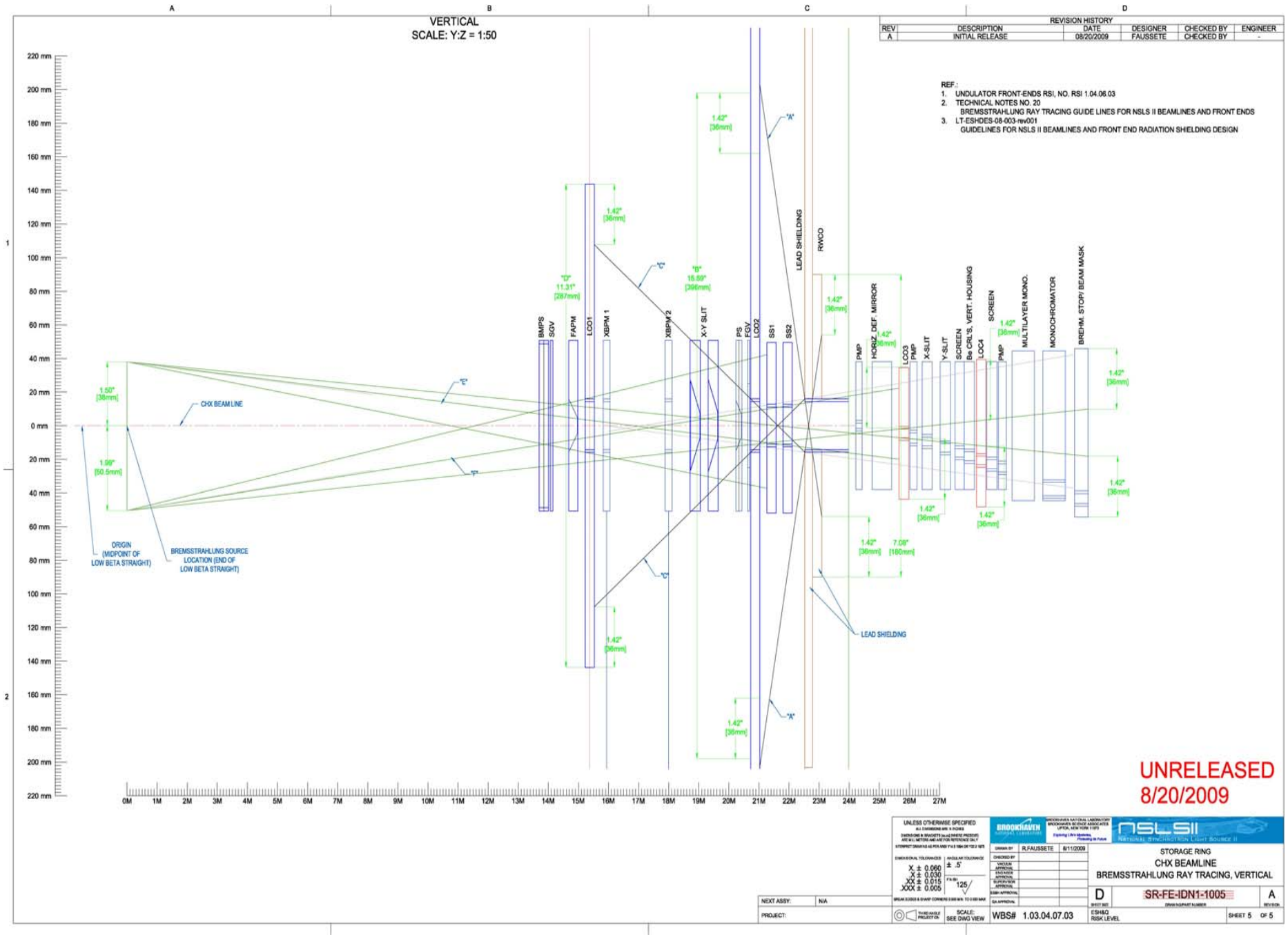
VERTICAL
SCALE: Y:Z = 1:50
REVISION HISTORY
REV A INITIAL RELEASE 08/20/2009 FAUSSETE
REF.:
1. UNDULATOR FRONT-ENDS RSI, NO. RSI 1.04.06.03
2. TECHNICAL NOTES NO. 20
BREMSSTRAHLUNG RAY TRACING GUIDE LINES FOR NSLS II BEAMLINES AND FRONT ENDS
3. LT-ESHDES-08-003-rev001
GUIDELINES FOR NSLS II BEAMLINES AND FRONT END RADIATION SHIELDING DESIGN
CHX BEAM LINE
ORIGIN (MIDPOINT OF LOW BETA STRAIGHT)
BREMSSTRAHLUNG SOURCE LOCATION (END OF LOW BETA STRAIGHT)
BMPS
SGV
FAPM
LCO1
XBPM 1
XBPM 2
X-Y SLIT
PS
FGV
LCO2
SS1
SS2
LEAD SHIELDING
RWCO
PMP
HORIZ. DEF. MIRROR
LCO3
X-SLIT
Y-SLIT
SCREEN
Be CRLS, VERT. HOUSING
LCO4
MULTILAYER MONO.
MONOCHROMATOR
BREHM. STOP/ BEAM MASK
UNRELEASED
8/20/2009
STORAGE RING
CHX BEAMLINE
BREMSSTRAHLUNG RAY TRACING, VERTICAL
SR-FE-IDN1-1005
WBS# 1.03.04.07.03

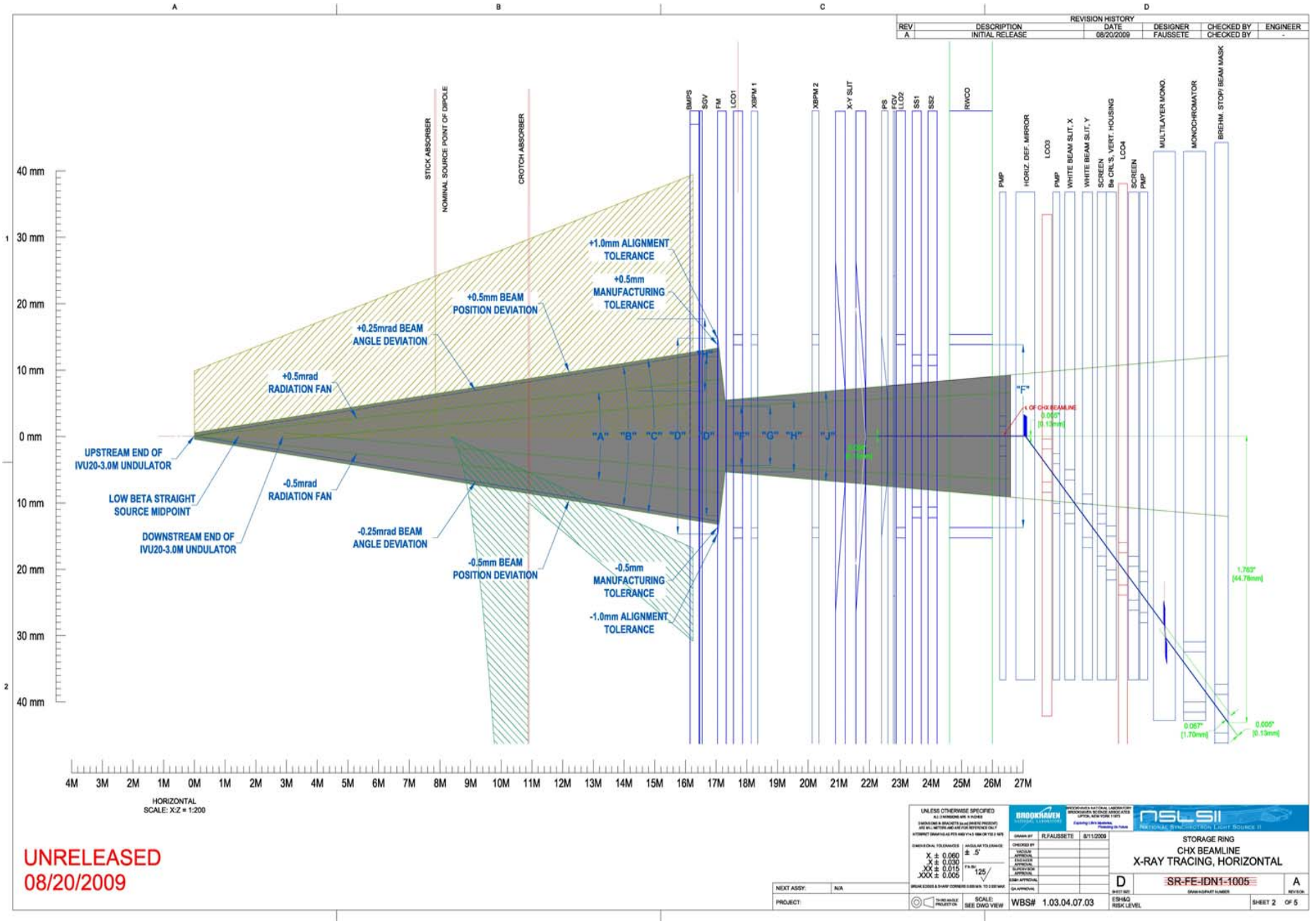
REVISION HISTORY
REV | DESCRIPTION | DATE | DESIGNER | CHECKED BY | ENGINEER
A | INITIAL RELEASE | 08/20/2009 | FAUSSETE | CHECKED BY | -
STICK ABSORBER
NOMINAL SOURCE POINT OF DIPOLE
CROTCH ABSORBER
BMPS
SGV
FM
LCO1
XBPM 1
XBPM 2
X-Y SLIT
PS
FGV
LCO2
SS1
SS2
RWCO
PMP
HORIZ. DEF. MIRROR
LCO3
PMP
WHITE BEAM SLIT, X
WHITE BEAM SLIT, Y
SCREEN
Be CRLS, VERT. HOUSING
LCO4
SCREEN
PMP
MULTILAYER MONO.
MONOCHROMATOR
BREHM. STOPJ BEAM MASK
+1.0mm ALIGNMENT TOLERANCE
+0.5mm MANUFACTURING TOLERANCE
+0.5mm BEAM POSITION DEVIATION
+0.25mrad BEAM ANGLE DEVIATION
+0.5mrad RADIATION FAN
UPSTREAM END OF IVU20-3.0M UNDULATOR
LOW BETA STRAIGHT SOURCE MIDPOINT
-0.5mrad RADIATION FAN
DOWNSTREAM END OF IVU20-3.0M UNDULATOR
-0.25mrad BEAM ANGLE DEVIATION
-0.5mm BEAM POSITION DEVIATION
-0.5mm MANUFACTURING TOLERANCE
-1.0mm ALIGNMENT TOLERANCE
"A" "B" "C" "D" "E" "F" "G" "H" "J"
"F"
℄ OF CHX BEAMLINE
0.005" [0.13mm]
1.763" [44.78mm]
0.067" [1.70mm]
0.005" [0.13mm]
40 mm
30 mm
20 mm
10 mm
0 mm
10 mm
20 mm
30 mm
40 mm
4M 3M 2M 1M 0M 1M 2M 3M 4M 5M 6M 7M 8M 9M 10M 11M 12M 13M 14M 15M 16M 17M 18M 19M 20M 21M 22M 23M 24M 25M 26M 27M
HORIZONTAL
SCALE: X:Z = 1:200
UNRELEASED
08/20/2009
BROOKHAVEN NATIONAL LABORATORY
NSLS II
STORAGE RING
CHX BEAMLINE
X-RAY TRACING, HORIZONTAL
SR-FE-IDN1-1005
D
A
SHEET 2 OF 5
WBS# 1.03.04.07.03
SCALE: SEE DWG VIEW
NEXT ASSY: N/A
PROJECT:

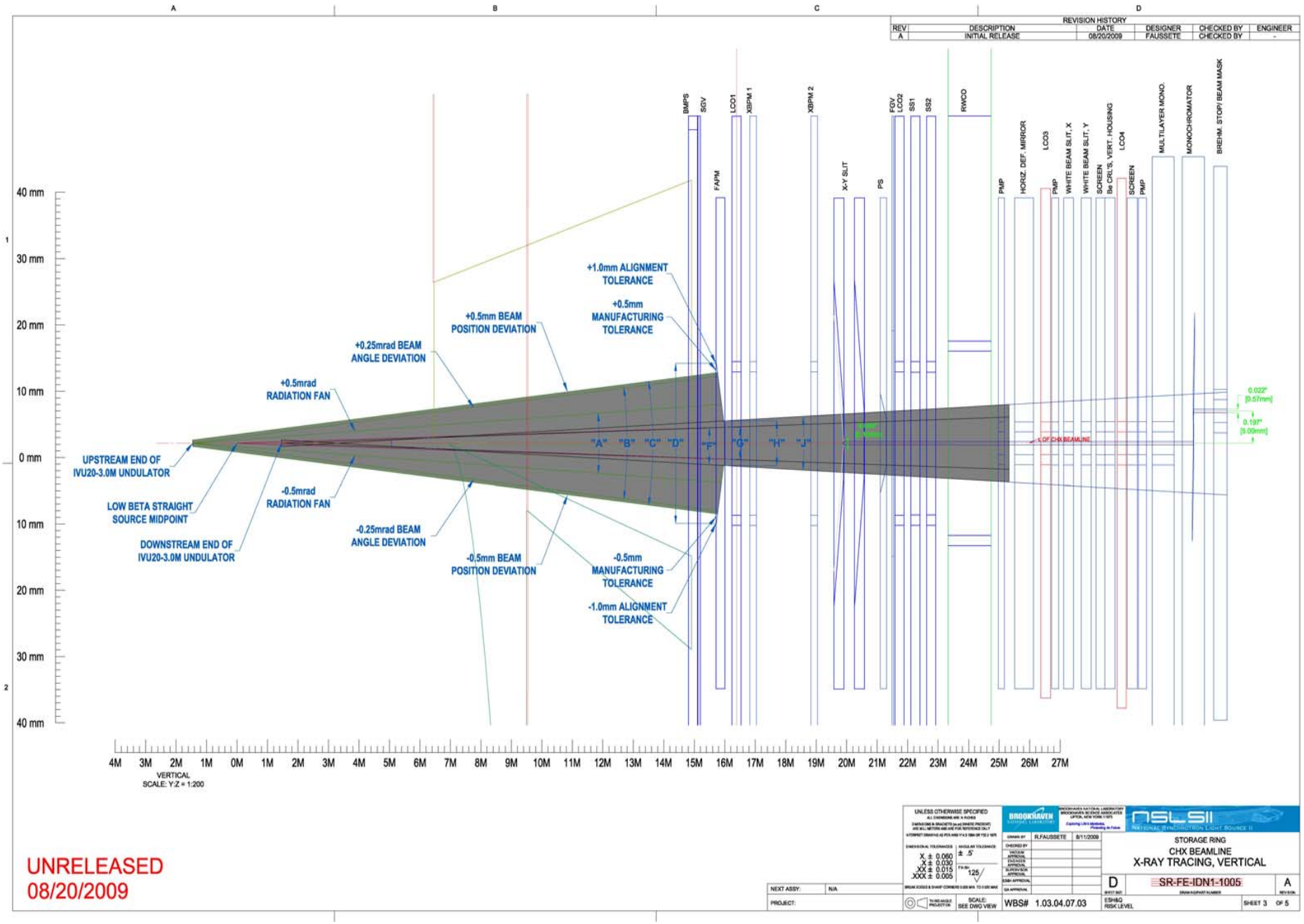
REVISION HISTORY
REV A INITIAL RELEASE 08/20/2009 FAUSSETE
BMPS
SGV
LCO1
XBPM 1
XBPM 2
FGV
LCO2
SS1
SS2
RWCO
FAPM
X-Y SLIT
PS
PMP
HORIZ. DEF. MIRROR
LCO3
WHITE BEAM SLIT, X
WHITE BEAM SLIT, Y
SCREEN
Be CRL'S, VERT. HOUSING
LCO4
MULTILAYER MONO.
MONOCHROMATOR
BREHM. STOP/ BEAM MASK
+1.0mm ALIGNMENT TOLERANCE
+0.5mm MANUFACTURING TOLERANCE
+0.5mm BEAM POSITION DEVIATION
+0.25mrad BEAM ANGLE DEVIATION
+0.5mrad RADIATION FAN
UPSTREAM END OF IVU20-3.0M UNDULATOR
LOW BETA STRAIGHT SOURCE MIDPOINT
DOWNSTREAM END OF IVU20-3.0M UNDULATOR
-0.5mrad RADIATION FAN
-0.25mrad BEAM ANGLE DEVIATION
-0.5mm BEAM POSITION DEVIATION
-0.5mm MANUFACTURING TOLERANCE
-1.0mm ALIGNMENT TOLERANCE
"A" "B" "C" "D" "F" "G" "H" "J"
0.022" [0.57mm]
0.197" [5.00mm]
℄ OF CHX BEAMLINE
VERTICAL SCALE: Y:Z = 1:200
UNRELEASED 08/20/2009
STORAGE RING
CHX BEAMLINE
X-RAY TRACING, VERTICAL
SR-FE-IDN1-1005
WBS# 1.03.04.07.03
SHEET 3 OF 5

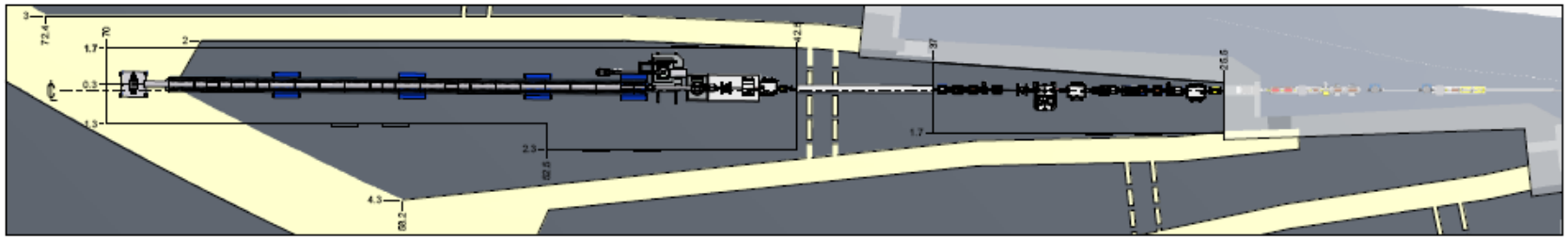

PLAN VIEW, FOE & HUTCH OUTLINED
SCALE 1 / 60

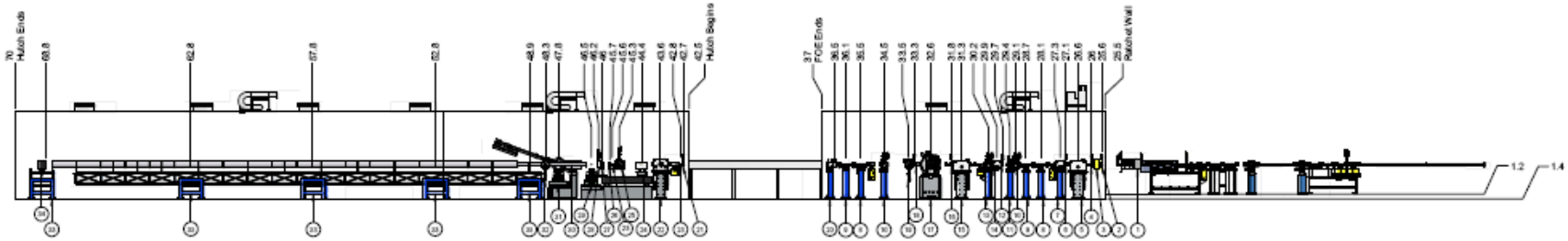

ELEVATED VIEW, FOE & HUTCH OUTLINED
SCALE 1 / 60

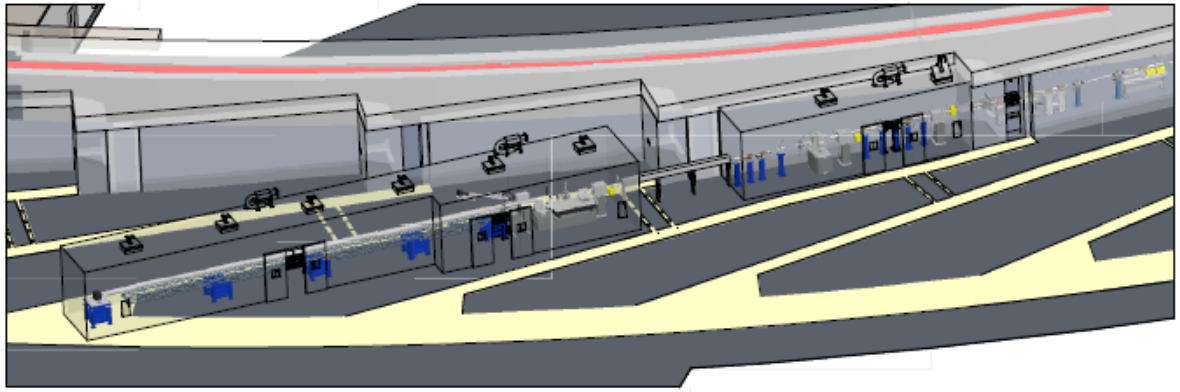

PRELIMINARY
9/25/09

Dimensions are in meters from source.

PARTS LIST				
ITEM	QTY	DESCRIPTION	PART NUMBER	VENDOR
1	1	Short Straight Front End, CHX	SR-FE-DN1-1200	
2	1	Gate Valve 1		
3	1	Differential Pump		
4	1	Gate Valve 2 with X-Ray Window		
5	1	Horizontal Deflecting Mirror		
6	1	Gate Valve 3		
7	1	Bremmstrahlung Collimator 1		
8	2	White Beam Slit, X		
9	2	White Beam Slit, Y		
10	2	Flourescent Screen, H20 Cooled		
11	1	Be CRL's, Vertical Focusing		
12	1	Gate Valve 4		
13	1	Flourescent Screen Beam Monitor		
14	1	Bremmstrahlung Collimator 2		
15	1	Multilayer Monochromator		
16	1	Gate Valve 5		
17	1	Monochromator		
18	1	Gate Valve 6		
19	1	Pink Beam Stop		
20	1	Mask, Photon Shutter & Brehm. Stop		
21	1	Gate Valve 7		
22	1	VFZP, HFZP or Kinoforms, Hor. Mirror		
23	1	Diamond (or Be/Polymer) Exit Window		
24	1	KB Mirror System		
25	1	Fast Shutter		
26	1	Beam Defining Aperture, Precision Slits		
27	1	Pink Beam Aperture, Precision Slits		
28	1	Microscope Assembly		
29	1	SAXS Goniometer		
30	1	SAXS Flight Path		
31	1	WAXS Station		
32	1	APD & Beamstop		
33	5	Detector Support		
34	1	Detector		
35	1	NSLS-II Building Assembly	XF-CF-1001	

BROOKHAVEN NATIONAL LABORATORY
NSLS-II
EXPERIMENTAL FACILITIES
BEAMLINE
LAYOUT, CHX
LT-XF-BL-CHX-1000
WBS# 1.04.05.03

LT-XFD_CDR_XPD-00121

NSLS-II Project

CONCEPTUAL DESIGN REPORT for the

COHERENT SOFT X-RAY BEAMLINE AT NSLS-II

final draft Sep 2009

Intentionally blank.

Approvals and Reviewers

Compiled by	**Signature**	**Date**
Cecilia Sánchez -Hanke, CSX Beamline Group Leader, NSLS-II		
Approved		
Qun Shen, XFD Director, NSLS-II		
Reviewers		
Stephen Kevan, BAT Spokesperson, on behalf of the BAT		
Andy Broadbent, Beamlines Manager		
Nicholas Gmür, ESH Coordinator, NSLS-II		
Sushil Sharma, Mechanical Engineering Group Leader, NSLS-II		

Document Updates

The Conceptual Design Report for the Coherent Soft X-ray Beamline at NSLS-II is a controlled document, revised under change control.

Version No.	Date	Changes made
1	30-Sep-09	final draft, submitted to BAT

Intentionally blank.

Contents

1 INTRODUCTION 1

1.1 INTRODUCTION 1
1.2 BEAMLINE REQUIREMENTS 1
1.3 BEAMLINE ADVISORY TEAM (BAT) 3
1.4 REPRESENTATIVE EXPERIMENTS 3

2 BEAMLINE LAYOUT 4

2.1 OVERVIEW 4
2.2 INSERTION DEVICE AND LOW β STRAIGHT SECTION AND OPERATION MODES 5
2.3 FRONT END 7
2.4 OPTICAL LAYOUT 8
2.5 BEAMLINE PERFORMANCE AND RAY TRACING 12
2.7 X-RAY TRACING 20

3 END STATION INSTRUMENTATION 22

4 SPECIAL BEAMLINE REQUIREMENTS 24

5 REFERENCES 26

APPENDIX 1: SCHEDULE 27

APPENDIX 2: ADDITIONAL INFORMATION 29

PREVIOUS FACILITY REPORTS 29
TIMING REQUIREMENTS FOR ULTRAFAST EXPERIMENTS (BY D. ARENA) 29
ESTIMATES FOR DATA STORAGE AND DATA PROCESSING (BY D. SHAPIRO) 30

Acronyms

ADP	Avalanche Photon Diode
Be	Beryllium
CCD	Charge Coupled Device
CDI	Coherent Diffraction Imaging
CMPMS	Condensed Matter Physics and Materials Science
DW	Damping Wiggler
FEA	Finite Element Analysis
HEG	High-Energy Grating
IVUV	In-Vacuum Undulator
LEG	Low-Energy Grating
LoI	Letter of Interest
MEG	Medium-Energy Grating
ML	Multilayers
OH	Optics Hutch
PGM-VLS	Planar Grating Monochromator – Variable Length spacing
SNR	Signal-to-Noise Ratio
UHV	Ultra High Vacuum
VIPIC	Vertically Integrating Pixel Imaging Chip
XBPM	X-ray Beam Position Monitors

1 INTRODUCTION

1.1 Introduction

This conceptual design report describes the optical design for the coherent soft x-ray NSLS-II project beamline at the ~85% completion level. The document will primarily describe optical design, including the optical layout and calculations that support the expected performance of the Coherent Soft X-ray (CSX) beamline. The ~85% completion level of the optical design refers to our intention to complete this design and achieve the 100% of completion and prepare the final design report after an in-depth beamline performance study has been completed. This study will include finite element analysis on the required optical components and a wavefront analysis of both branches of the CSX beamline. We expect to finish these studies and include them in the preliminary design report, targeted for completion one year from now.

"This document describes, in some detail, the conceptual design of the optical layout of the CSX NSLS-II project beamline. We describe a unique state-of-the-art optical design of a soft x-ray beamline with two branches, one optimized to deliver the highest possible spatially coherent flux and one optimised for the highest-performance polarization-sensitive experiments. The coherence branch maximizes flux by minimizing the number of optical reflections. The polarization experiments demand full control of the beam polarization, including the capability to switch between opposite polarization states at rates from 10 Hz to 1 kHz. The CSX beamline optical design addresses perfectly the experimental requirements for the CSX beamline, as recommended by the CSX Beamline Advisory Team (BAT), as stated in the letter of interest for this beamline "

In the search of the best possible optical layout design, the CSX beamline team has developed a very active collaboration with the beamline BAT. The design presented in this document is the result of the combined efforts of staff from the NSLS-II Project eXperimental Facilities Division (XFD) and Accelerator Systems Division (ASD), the NSLS Experimental Systems Division, and the CSX beamline BAT. The CSX beamline team would like to thank S.L. Hulbert and R. Reininger to their contributions to the content of the document and all of the collaborators for their contribution to the CDR.

Disclaimer: This document contains content from the Coherent Soft X-ray Beamline Advisory Team Letter of Interest document, as well as from the previous NSLS-II Project conceptual design reports http://www.bnl.gov/nsls2/project/CDR/Ch_11_Experimental_Facilities.pdf and preliminary design report http://www.bnl.gov/nsls2/project/PDR/2-ExFac_Ch_004_CSX.PDF] both attached to the "additional information" APPENDIX . and from documents used to prepare all of the above.

Disclaimer: This document contains sections from the coherent soft x-ray beamline advisory team letter of interest (LoI) document, as well as from other documents used in the preparation of that document.

1.2 Beamline Requirements

This report compiles technical information regarding the optical layout of the CSX beamline. This soft x-ray beamline will operate in the 270 – 1700 eV energy range and will be optimized for "photon hungry" experiments such as experiments using coherence and experiments that are sensitive to the x-ray polarization. The proposed optical layout serves two technical goals, the first being the generation of a high flux of spatially coherent photons in one branch, and the second being the generation of high photon flux with high resolving power with full control of the x-ray polarization. The proposed design requires two insertion devices in order to provide simultaneously two photon beams with opposite polarizations (for example, left- and right-circular) for the polarization control branch and also be able to operate as a single device in order to maximize the coherent flux for the coherence branch. We propose that both of the insertion devices be 49mm-period elliptically polarized undulators (EPU49) of the APPLE-II type, with two operating modes. In one of the operating modes, the IDs are in-line and phased, delivering a single beam to the coherence branch. In a second mode of operation, the two EPUs are canted in the horizontal plane by 0.16 mrad and deliver two angularly distinct beams, either to (a) serve the polarization branch

simultaneously with two beams of different polarizations or (b) deliver a single beam each of the branches for simultaneous, shared operation of both branches.

The CAD drawing below shows a 3D rendering of the CSX beamline, with its two branches, one for coherence and one for polarization control.

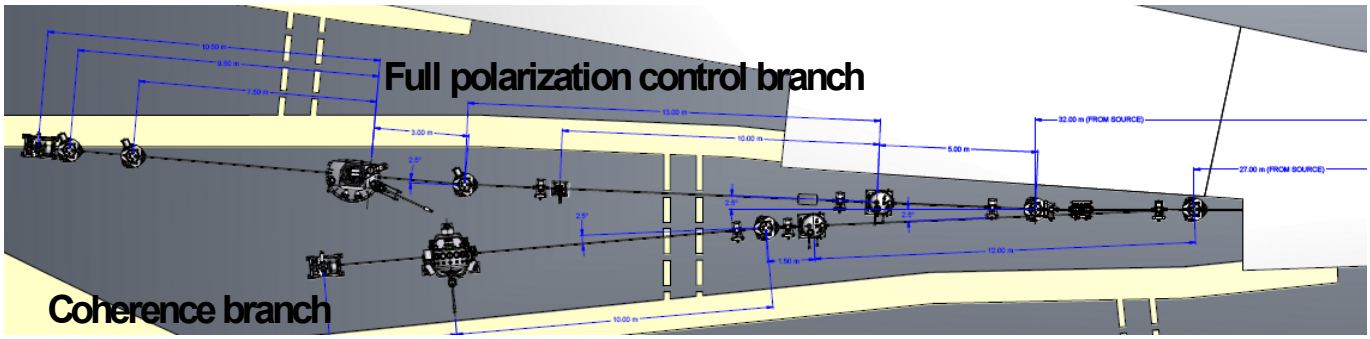

Figure 1 : Top view of CAD rendering of the CSX beamline (Courtesy Brian Mullany NSLS-II project)

The following is a list of additional requirements for the two CSX branches:

High coherent flux branch

- highest possible coherent flux
- variable focus position along the beam direction, by ±0.5m, to accommodate multiple experimental setups in the end-station, e.g. experiments using zone plates and those u sing pinholes
- beam size on sample: 5 μm x 5 μm
- possibility to have a roll-up port
- beam stability (values)
- capability of source to provide circular (left or right) or linear (sigma or pi) polarization, slow switching

Polarization control branch

- highest possible photon flux
- modulated fast-switching polarization handedness, between circular left and right, or between linear sigma and pi, or other combinations, at rates from 10 Hz up to 1 kHz.
- smallest homogeneous beam size on the sample 5 μm x 5 μm
- 95% overlap on the sample of the beams from the two undulators
- minimization of the divergence between the photon beams from the two canted undulators.

1.3 Beamline Advisory Team (BAT)

In alphabetical order…

Prof. H. Ade
Department of Physics,
North Carolina State Univ., Raleigh, NC 27695-8202
Harald_Ade@ncsu.edu

Dr. D. Arena
National Synchrotron Light Source,
Brookhaven National Laboratory, 11973 Upton NY
darena@bnl.gov

Dr. S. L. Hulbert,
National Synchrotron Light Source,
Brookhaven National Laboratory 11973 Upton NY
hulbert@bnl.gov

Prof. Y. Idzerda
Department of physics
Montana State Univ., Bozeman, 59717-3840, MT
idzerda@physics.montana.edu

Prof. S. Kevan, BAT spokesperson
Department of physics,
Univ. of Oregon, Eugene OR,
kevan@physics.uoregon.edu

Dr. S. Wilkins
Condensed Matter Physics and Materials Science department
Brookhaven National Laboratory, 11973 Upton NY
swilkins@bnl.gov,

1.4 Representative Experiments

The scope of the beamline has not change since the approval of this beamline LoI. The scientific case proposed in that document is still valid and the beamline optical design has been shaped to adapt to their technical requirements. The following text is an extract of the LoI document:

"A uniting theme of the motivation for the CSX beamline is to turn "photon hungry" coherent and polarization-sensitive experiments that are presently (2008) heroic, signal-limited experiments into high-throughput, high productivity techniques. For coherence experiments, this includes coherent diffraction (bulk and surface), phase retrieval imaging, soft x-ray photon correlation spectroscopy (XPCS), and coherent scattering. To date, these experiments have focused on the study of correlated electron systems but probably will evolve to other materials and systems, e.g. multi-ferroics. For polarization-sensitive experiments, the techniques include polarization-dependent spectroscopy, resonant scattering, time dependent and ultrafast dynamics of new materials and artificially engineered systems. Examples of these systems include highly dilute materials, micrometer-size single crystals, nanosized-materials, and interfaces. "

2 BEAMLINE LAYOUT

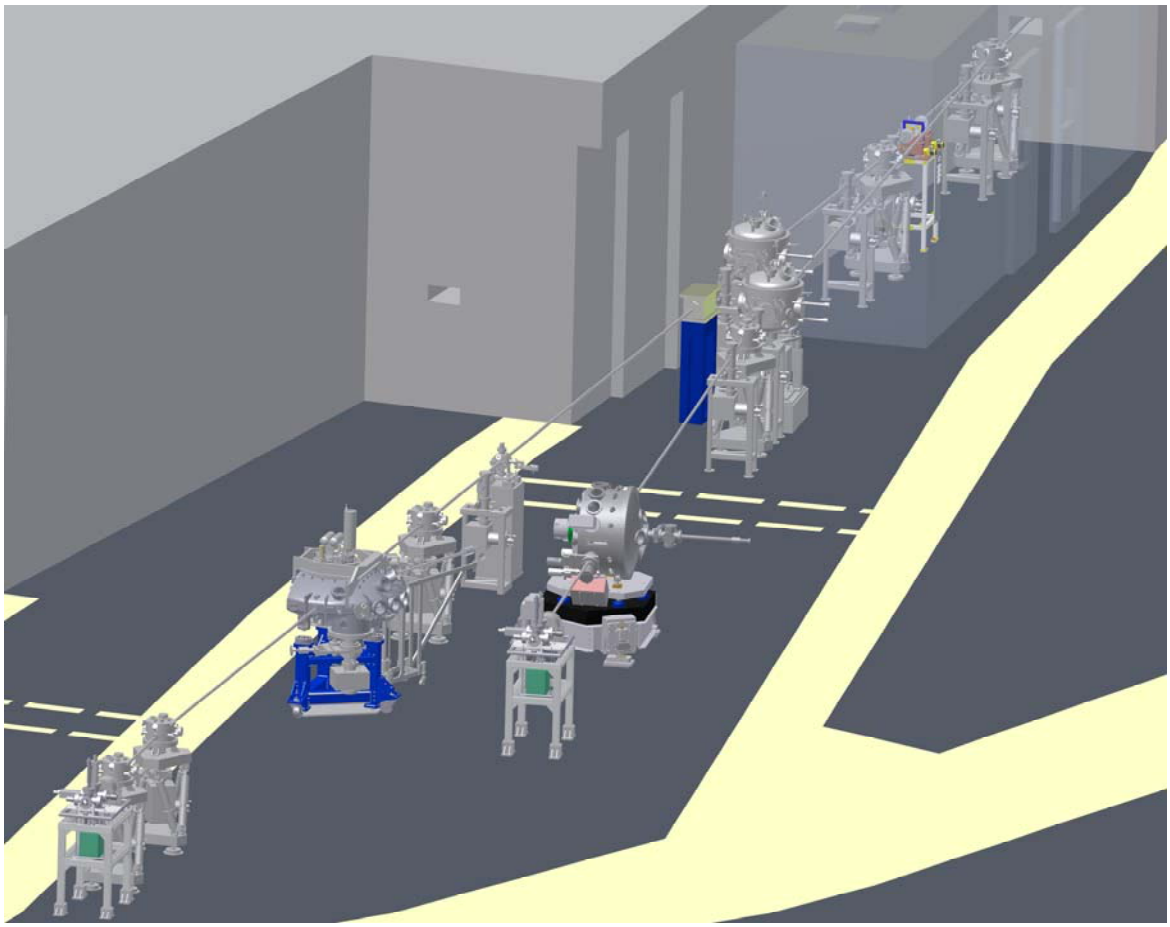

Figure 2: CAD 3D optical layout for the coherent soft x-ray beamline. (Courtesy Brian Mullany NSLS-II project)

2.1 Overview

Since the approval of the CSX beamline LoI (Sept. 2008), the scientific purpose of the beamline has not changed and the general beamline layout, consisting of two branches, one for coherence and one for polarization control, has persisted. The changes made to the beamline optical layout are a consequence of the adaptation of the beamline design to the refined experimental requirements of the beamline.

The general description of the CSX beamline, as presented originally in the CSX LoI document, is as follows:

> "The CSX beamline consists of two branches, one dedicated to the generation and uses of the highest possible spatial coherence (CB) minimizing the number of reflections and optics in the beam path and the other dedicated to the highest-performance polarization-sensitive experiments (PB). Both branches need highly coherent flux and polarization control, which unifies them in the need for the longest possible elliptically-polarized undulator (EPU) source, i.e., the 2 x 2m-long EPU45s in a low-beta straight section. One branch ("Coherence") sacrifices polarization switching rate somewhat in favor of highest possible coherent flux while the other ("Polarization") sacrifices some coherent flux in favor of optimal polarization switching rate. Additionally, during times when the polarization switching rate does not need to be fast, each of the two 2m-long undulators could serve a separate branch, thereby providing 100% operational time for both branches with good brightness/flux and slow polarization switching rate."

Changes to the CSX optical design

Since the approval of the CSX LoI, the period length of the proposed Elliptically Polarized Undulator (EPU) insertion devices has increased from 45 mm to 49 mm, as will be explained in the next section. In pursuing experimental flexibility and searching for the best possible beamline performance, the optical layout design presented in this document provides for a total of four experimental endstation locations, two for the Coherent branch (CB) and two for the Polarization branch (PB). The coherent branch optical design now provides an extended region of ± 2 meters along the beamline in the vicinity of the experimental endstation where the quality of the focused beam is almost identical, which can serve two experimental endstations without the need for an extra set of refocusing optics. In the Polarization Branch two experimental endstation positions have been provided, one optimized to have small horizontal angular divergence and a second one optimized for small spot on the sample.

2.2 Insertion Device and Low β Straight Section and Operation Modes

The insertion devices chosen for the CSX beamline, to provide elliptical, circular, and linear polarized soft x-rays are two 2 m long, 49 mm period Elliptically Polarized Undulators (EPU) of the APPLE-II type. This type of undulator is widely used in the soft x-ray community. Although earlier reports for the CSX beamline referred to an ID period length of 45 mm, the need to provide to the CSX user community with photon energies down to the Carbon K-edge (~270 eV) with linear polarization in both the horizontal and vertical directions, in addition to left- and right-hand circular polarization, required careful study to finalize this value. Figure 3 shows the results of calculations performed by O. Chubar (NSLS-II project, XFD and ASD) used to select the period length. The calculations indicate the minimum and maximum photon energies that can be achieved in the first harmonic with EPUs as a function of the period length assuming a minimum magnetic gap of 11.5 mm. Based on these results, the value of the ID period length was chosen to be 49 mm, which meets the state requirements for energy and polarization. Selecting a larger period length would enable access to lower photon energies at the price of reduced flux via reduced number of periods (in a fixed length). The panel on the right in Figure 3 shows that maximum usable photon energy from the fundamental of the EPU49 is 1700 eV.

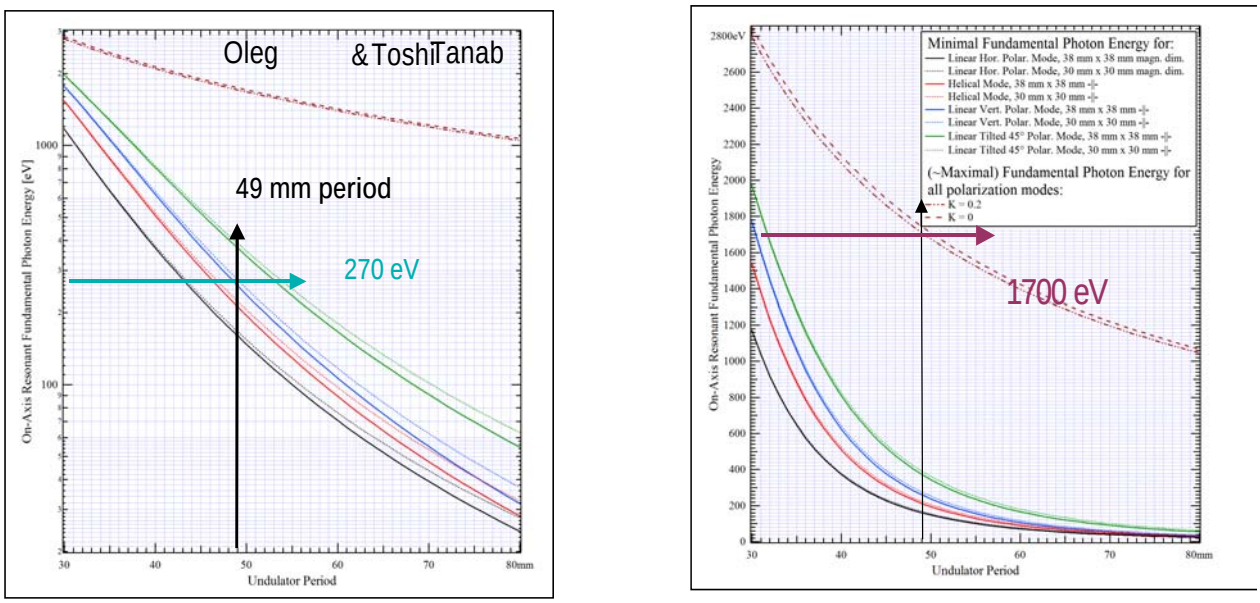

Figure 3 Calculated on-axis fundamental photon energy vs EPU period length. Left (right) panel y-axis scale is logarithmic (linear). Minimum fundamental photon energies for linear horizontal (black), circular (red), linear vertical (blue), and linear 45 degrees (green) polarizations are shown. The maximum usable fundamental photon energy is shown in brown. The 49 mm ID period length choice is marked, demonstrating that it can deliver photon energies down to 270 eV and up to 1700 eV in linear horizontal, vertical and circular polarizations. (Courtesy Oleg Chubar NSLS-II project)

ID operation modes

The CSX beamline is designed for three operation modes:

1. EPUs in-line and phased to function as one insertion device. This mode is used to deliver a single beam to the coherence branch.
2. EPUs horizontally canted by 0.16 mrad, each ID delivering a single photon beam to one branch (coherence and polarization).
3. EPUs horizontally canted by 0.16 mrad, delivering two photon beams of different or equal polarization to the polarization branch, to serve the fast polarization switching optical scheme which is described later.

Polarization control

The control of the source polarization for these Apple-II style EPUs is accomplished by mechanical adjustment of the phase of the horizontal undulator magnets with respect to the vertical ones, a process which lasts from ~1 sec to many seconds depending on the magnitude of the desired change in polarization. The technical specifications for the polarization branch require polarization switching rates from 10 Hz up to 1kHz, to reduce the signal-to-noise ratio and improve the sensitivity to smaller polarization sensitive signals. In the process of designing the optics layout two schemes where considered, both based on canted EPUs. In the first mode, the so-called static switching mode, the electron beam is shifted angularly through the insertion devices in order to deliver simultaneously two photon beams to the beamline that are separated by a fixed angular amount (0.16 mrad in the CSX case). In this mode, the polarization switching is accomplished by means of a mechanical chopper in the beamline, which alternately selects one of the two angularly-separated beams of opposite polarization. In the second mode, the dynamic switching mode, the electron beam is actively switched between the two IDs, delivering to the beamline one beam at a time with opposite polarization. The static mode requires a more complicated optical design, whereas the dynamic requires a more complicated accelerator design in the ID straight section. In addition, the dynamic mode requires fast switching of the electron beam itself, an operating mode which might lead to beam instabilities around the entire ring. And, furthermore, the simpler optical design connected with the dynamic switching mode will have poorer photon energy resolution than that of a system with optics keeping both undulators in focus. Finally, the static-switching beamline optical design presented below is in fact quite simple, consisting of only five optical elements in one branch (PB) and four in the other (CB). The decision of the CSX BAT was to adopt the static switching mode.

Phasing

The experiments to be performed at the coherent branch require as much coherent flux as possible. For that reason the soft x-ray science community is interested in being able to use both insertion devices, phased to operate as a single device. To make this operating mode possible, it is proposed to use an electromagnet located between the insertion devices to modulate the phase of the electron beam in the downstream ID to match the phase in the upstream ID. Wavefront propagation analysis will be performed to design the phasing magnet and simulate its effects on transverse coherence.

Straight section

The extremely low emittance of the electron beam in the low beta straight sections (the short straight sections) is essential to achieve the best performance of the CSX beamline. At the same time, the tiny photon beam size and angular divergence present a challenge for the mechanical design of the CSX beamline components (precision and accuracy of motions, vibration isolation, etc.). Similarly, high quality beam diagnostics are required in the ID straight section to ensure stable electron beam position and angle. The combined requirements of maximum undulator length, canting, phasing, and diagnostics could create a potential real estate problem for the layout of the CSX ID straight section. So far, this layout has been able to provide nearly all of the required

elements while preserving the desired 2 m length of the EPU49 undulators. Fig.4 is a CAD rendering of the current layout of the CSX ID straight section.

Quasiperiodicity

It is well known that higher undulator harmonics can be quite deleterious in all types of soft x-ray experiments, especially spectroscopy and scattering, and essentially impossible to remove experimentally. Various optical solutions have been implemented in soft x-ray beamlines, but always with compromises in flux and/or beam position. A much better solution is to shift the energy of the harmonics by an amount sufficient to move them out of the bandpass of the beamline monochromators. The commonly adopted solution is to introduce a small degree of quasi-periodicity to the undulator field profile. The only compromise in this solution is a 10-20% reduction in flux of the fundamental. A design study of the quasi-periodic EPU49 undulators for the CSX beamline will be undertaken in order to provide adequate harmonic rejection while minimizing the loss in flux from the fundamental.

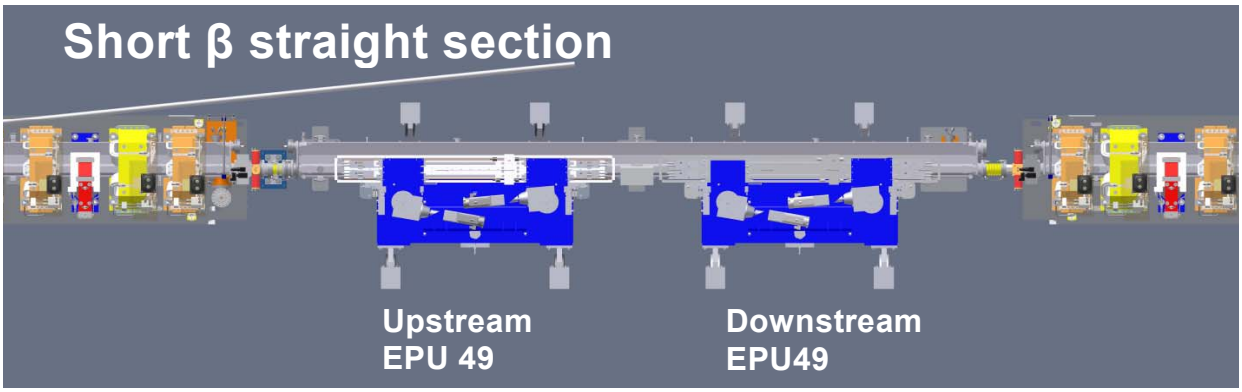

Figure 4: Layout of the CSX straight section, showing two 2m-long EPU49's, canting and phasing magnets, and beam position monitors. (Courtesy: R. Faussete, ASD, NSLS-II project)

2.3 Front End

The CSX soft x-ray beamline will operate windowless and under ultrahigh vacuum (UHV) conditions,10^{-9} Torr or better, from the insertion device all the way downstream to the endstations. All beamline components will be UHV compatible, eliminating the need for differential pumping between the beamline and the front end.

Figure 5 shows the proposed standard front-end configuration showing the names of the standard elements. Note that the CSX front end is slightly different than the standard front-end model, in ways specific to the collimation and monitoring of soft x-rays. Additional instrumentation is included to aid CSX experimenters with the alignment and characterization of the soft x-ray beam during operations.

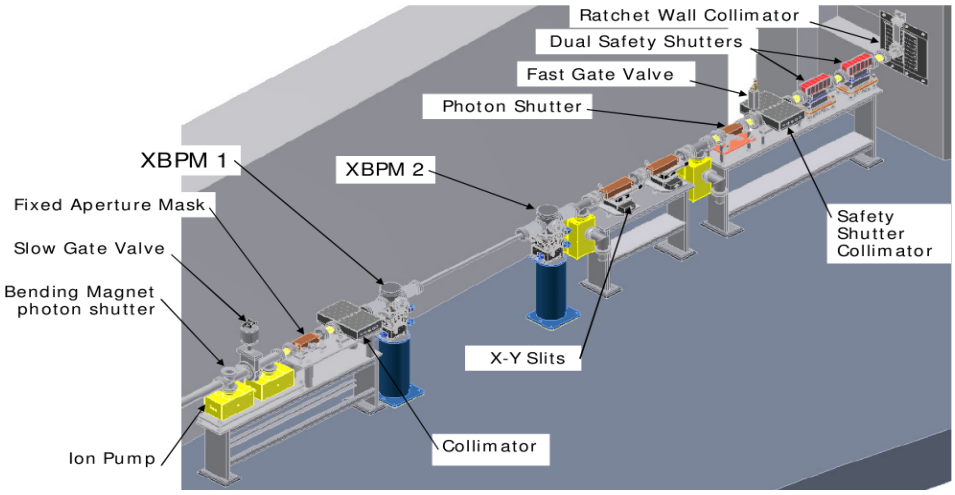

Figure 5 Proposed standard front-end configuration for the CSX project beamline. (Courtesy Lewis Doom Accelerator Systems Division, NSLS-II project).

Viewing along the beam direction from left to right, the front end components include: ion pump, photon shutter, slow gate valve, fixed aperture mask, collimator, X-ray Beam Position Monitor (XBPM) 1, XBPM 2, X-Y slits, photon shutter, safety shutter, collimator, fast gate valve, dual safety shutters, and ratchet wall collimator. The components that will be modified for the CSX front end, as compared to hard x-ray front ends, are: the fixed aperture mask, the XBPMs (1 and 2), and the X-Y slits.

The standard NSLS-II front end design will be utilized for the CSX beamline, with the following relatively minor changes: (a) the fixed aperture mask opening must be larger than the standard value, to match the maximum size of the two canted soft x-ray beams in the CSX canted undulator mode of operation, (b) it is desired to extract beam position signals from the X-Y slits, (c) the XBPMs must match the relatively soft photon energy and special polarizations of the CSX undulator beams.

Item (b) requires two engineering and design changes compared to the standard X-Y slit design: (i) the two L-shaped slit blades need to be replaced by four independent blades in order to extract separate horizontal and vertical beam position information, and (ii) each blade needs to be electrically isolated in order to sense beam position.

Item (c) requires special engineering and design of the CSX XBPMs in order to properly sense the relatively low photon energy EPU49 beams without wasting too many of them through absorption. Ideally, these XBPMs will not absorb any part of the beam that is needed at the sample positions in the endstations. The polarization sensitivity refers to the variation in beam shape for different polarization types (linear, circular, elliptical). These XBPMs also need to be able to independently sense the two angularly-separated undulator beams present in canted undulator mode. Such an XBPM has been designed at the Diamond Light Source, and may serve as a starting model for the NSLS-II dual-beam BPM.

2.4 Optical Layout

This section describes optical layout of the CSX beamline, including its major components. In addition to these major components, a number of other components will be needed. For example, instrumentation is needed for optical alignment and characterization of the photon beams, and later for efficient beamline operation. Conventional instrumentation will be needed for vacuum, interlocks, etc. A detailed design of these additional components will be initiated in the preliminary design phase.

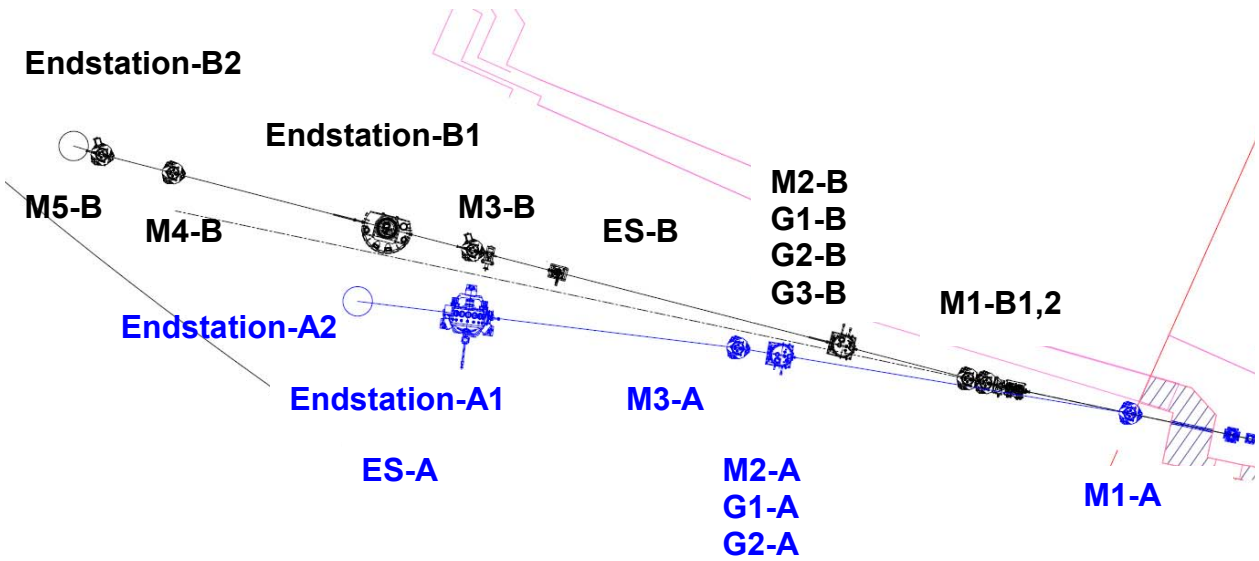

Figure 6: Top view CAD rendering of the optical layout of the CSX beamline optical layout. Major optical components are labeled.

Tables OL2 and OL3 list properties of the optical elements of the two branches of the CSX beamline, including: distance from the source, deflecting angle and direction, and the optical demagnification. In these tables, the optical components are designated as follows: M for mirrors, G for gratings, and ES for exit slits. The letters A and B are utilized to name the elements of the coherent (CB) and polarization (PB) branches, respectively. In the future and to achieve the 100% of the optical design more information will be provided such as the power dissipation or the required figure of merit.

Table 1: Optical Elements of the High Coherent Flux Branch.

Element name	Optical element	Distance (m) from source	Deflecting angle (degrees)	Direction of deflection	Demag., Hor./Ver
M1-A	Plane (water cooled)	27	88.75	Horizontal	
M2-A	Plane (water cooled)	38.7-38.9	84.5-88.6	Vertical	
	Gratings:	39	85.2-88.5	Vertical	
G1-A	LEG				/4.5-3.0
G2-A	MEG				/4.5-3.0
M3-A	Elliptical Cylinder (Bendable)	40.5	88.75	Horizontal	4.5-2.9/
ES-A	Exit Slit (sample position)	49.5 – 54.5			

A = Coherent branch item ES = Exit Slits G = Gratings M = Mirrors

The numbers are the numerical order that that element appears in the optical layout design. In the future and to achieve the 100% of the optical design, more information will be provided, such as the power dissipation or the required figure of merit. Additionally, we envision having downstream of almost each of the mirror chambers (total of 7) diagnostic chambers with enough instrumentation to help in the alignment.

Table 2 : Optical Elements of the Full Polarization Control Branch.

Element name	Optical element	Distance (m) from straight center	Deflecting angle (degrees)	Direction of deflection	Demag. Hor./Ver
M1-B1 –	Toroidal (water cooled)	31.9	88.75	horizontal	1.5/collimating
M1-B2 –	Toroidal (water cooled)	32.1	88.75	horizontal	1.5/collimating
M2-B	Plane(water cooled)	36.6-36.91	85.4-88.8	Vertical	
	Gratings:	37	84.4-88.5	Vertical	
G1-B	LEG				/4.8
G2-B	MEG				/4.8
G3-B	HEG				/7
ES-B	Exit slit	47			
M3-B	Elliptical cylinder	50	88.75	Vertical	/1
	Sample B1	53			
M4-B	Elliptical cylinder	60.5	88.75	Vertical	/2.1
M5-B	Elliptical cylinder	62.5	88.75	horizontal	10/
	Sample B2	63.5			

B = Polarization branch item ES = Exit Slits G = Gratings M = Mirrors
The numbers are the numerical order that that element appears in the optical layout design. In the future and to achieve the 100% of the optical design, more information will be provided, such as the power dissipation or the required figure of merit. Additionally, we envision having downstream of almost each of the mirror chambers (total of 7) diagnostic chambers with enough instrumentation to help in the alignment.

Not listed in tables 1 and 2 are the various beamline components that will complete the design of the beamline. These components include: (a) vacuum transport lines with vacuum components such as pumps, gauges, and hardware, (b) photon beam position monitors, (c) water-cooled white beam apertures with electrically isolated blades to dissipate the heat load and to define the external shape of the photon beams, (d) apertures for photon beam characterization, (e) diagnostic chambers containing fluorescence screens and grids for photon beam alignment and characterization, and (f) diagnostics chambers that will be used during operations to check the quality and the properties of the photon beams. In category (f) we will include instrumentation needed to characterize the degree of coherence and the degree of polarization. The designs of the diagnostics chambers will depend on the type of diagnostic and on location along the beamline.

The following is a functional listing of the major CSX beamline optical components, for both branches. Starting at the ratchet wall, the major components of the beamline are as follows:

White beam aperture — The first element after the ratchet wall. This aperture will roughly define the size and shape of the beam and will also absorb unwanted portions of the EPU49 beams, mostly from very high harmonics

High coherent flux branch — Branch designed to maximize coherent flux by minimizing the number of reflections

M1-A — Planar. internally water-cooled mirror. Its function is to absorb power from unwanted high undulator harmonics, via appropriate choice of grazing angle, and thereby reduce the heat load on downstream optics. Also directs the photon beam into the coherent branch.

Monochromator A — Variable line spacing plane grating monochromator

Plane mirror M2-A	Planar, internally water-cooled mirror, used to provide the proper angle of incidence on the grating
Grating Gn-A	Planar, side-cooled, variable line spacing diffraction grating, used both to disperse the incident pink beam and to focus it vertically at the exit slit. Two choices of grating are planned: G1-A (Low energy grating – LEG) and G2-A (medium energy grating - MEG).
M3-A	Horizontally deflecting and focusing bendable elliptical cylinder mirror. Focuses at the exit slit/pinhole/sample position.
Exit slit/pinhole A	slit/pinhole located at the beam focal point, to select photon energy and resolution as well as to define the degree of transverse spatial coherence. This slit/pinhole can be placed anywhere in an approx. 4m-long focal range of the beamline, due to the flexibility of the monochromators and the M3-A mirror.
Endstations A	The optical layout at this branch permits flexible location of more than one endstation along the beamline, over an approx. 4m-long focal range. Each endstation will need to provide its own exit slit/pinhole.
Polarization control branch	Branch designed to provide fast switching capability between photon beams with different polarizations
M1-B(1,2)	Two internally water-cooled horizontally deflecting and focusing toroidal mirrors. The minor radii are designed to collimate the beams ensuring that both beams are (vertically) focused at the exit slit by the monochromator. The major radii are slightly different from each other and are chosen to focus both beams at the sample position.
Monochromator B	Variable line spacing plane grating monochromators
Plane mirror M2-B	Planar, internally water-cooled mirror, used to provide the proper angle of incidence on the grating
Grating Gn-B	Planar, side-cooled, variable line spacing diffraction grating, used both to disperse the incident pink beam and to focus it vertically at the exit slit. Three choices of grating are planned: G1-B (Low energy grating – LEG), G2-B (medium energy grating - MEG), and G3-B (high energy grating - HEG)
Exit slit B	Vertically adjustable slit located at the beam focal point, to select photon energy and resolution. 10 μm will be the canonical vertical size, but will be variable from 5 μm to "infinity"
M3-B	Vertically focusing elliptical cylinder mirror (uncooled). Focuses the beam vertically onto the sample.
Endstation B1	Endstation location for small beam divergence.
M4-B	Vertically focusing elliptical cylinder mirror (uncooled). Refocuses the beam from endstation B1 vertically onto the sample in endstation B2.
M5-B	Horizontally focusing elliptical cylinder mirror (uncooled). Refocuses and demagnifies the beam from endstation B1 vertically onto the sample in endstation B2

Endstation B2 Endstation location for small beam spot.

It is planned that all the mirrors along both branches of the CSX beamline are supported with hexapod mounts. If possible and if the distance between the M-1B(1,2) mirrors allows it, each of these mirrors will be supported by its own hexapod.

Additionally, we envision the inclusion of diagnostic chambers to characterize the photon beams at various points along the beamline. The diagnostic instrumentation is especially useful for alignment, but will be used routinely during operation to verify beamline performance.

2.5 Beamline performance and ray tracing

The first priority for the CSX team was to converge to an optical layout to fulfill the beamline technical requirements to allow to perform as many as possible experiments proposed by the BAT in the CSX beamline LoI. The design of the beamline optics has evolved since the first proposed optical layout to the one proposed in this document. In the process of finalizing the optical, each change and variation was supported by ray tracing that will ensure that the optics keep performing in the scope of the beamline technical requirements, finite element analysis to ensure that the cooling for the first beamline optics is adequate to preserve the optics best performance and wave front analysis to ensure the efficient use of the sources.

High coherent flux branch

The suggested design for the coherence branch does not have an entrance slit, has four optical elements, and similar horizontal and vertical magnifications at the exit slit. The design and its expected performance are described in detail below.

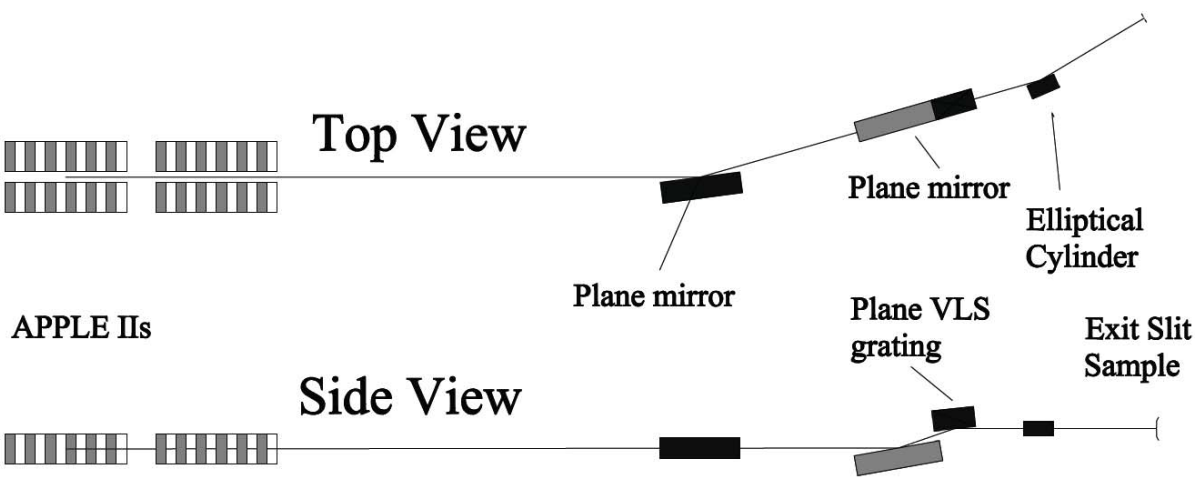

Figure 7: Top and side view of the coherence branch optics layout

Optical design

The parameters of the optical components are listed in Table 1 and a schematic layout showing the floor plan of the FPC is seen in Fig. 7

The first optical element, M1-A, is a plane mirror located outside the shield wall which deflects the beam horizontally by 2.5°. Its main function is to absorb the high photon energies emitted by the insertion device beyond the beamline range. Its angle of incidence and that of M3-A (see below) were chosen to have a reasonable horizontal separation between the full polarization control and the coherence branch.

The second optical element is a plane mirror, M2-A, which deflects the beam upwards (in the dispersion plane) towards the grating. This mirror needs to be rotated and translated in order to provide the grating with the correct angle of (normal) incidence, α, that will keep the defocus term of the grating zero at all wavelengths. The rotation and translation are actually incorporated in a simple rotation around an axis not on the mirror surface [1]. The angle of incidence on this mirror is given by $\gamma=0.5(\alpha-\beta)$, where β is the diffraction angle (negative).

The large distance between the source and the grating and the fact that the source is almost diffraction limited along the vertical direction means that a modest "resolving power" can only be achieved with a low line density grating and using a low c ($\cos\alpha/\cos\beta$) factor. To achieve the required "resolving power" of ≈2000 we chose two gratings with central line densities of 50 l/mm (LEG) and 100 l/mm (HEG) operating with c = 1.1. As mentioned above, the source will be either one or two IDs. The fact that the beamline does not have an entrance slit means that the resolving power will depend on the source in use. Furthermore, the vertical source position will vary depending on which source is used. This can be corrected by adjusting the c value. From the geometry and the chosen c value one obtains a magnification along the dispersion direction equal to 0.42 and 0.44 with two IDs and one ID, respectively.

The last element of the beamline (M3-A) is a bendable elliptical cylinder deflecting the beam horizontally by 2.5° and focusing it horizontally at the exit slit. We have chosen a bendable mirror to correct for the heat load induced slope error on the plane mirror as described in Ref.2 Its magnification is slightly lower than that of the monochromator, 0.42 with one ID and 0.41 with both IDs.

Resolving Power

The monochromator resolving power was calculated from the vector sum of all the relevant contributions to the resolution: source size, aberrations, slope errors, and exit slit.
The zeroing of the coma and spherical aberrations at 500 eV (1000 eV) for the LEG (HEG) with the quadratic and cubic term of the grating line density makes their contribution to the resolution negligible as compared to that of the source size. Meridional slope errors of 0.1 μrad in the plane elements and 0.5 μrad in the elliptical cylinder were assumed in the calculations. Their combined contribution to the resolution is comparable to that of the source size when one ID is used for photon energies ≥1000 eV, and better than the source when two IDs are used.

The exit slit width was set such that its contribution to the resolution is the same as that due to the source size. The required exit slit width is shown in Fig.8 as a function of the photon energy as well as the RMS divergence of the coherent flux for one and two IDs. Since the horizontal and vertical demagnification of the beamline are practically the same and the exit slit width was set for the same resolution as the coherent source, the horizontal aperture could be set to the same value.

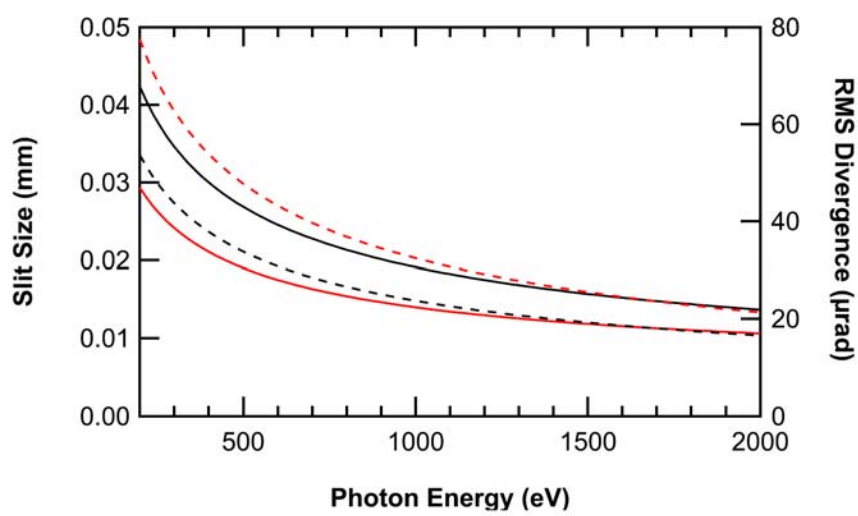

Figure 8. Left axis - Solid lines: Exit slit size yielding the same resolution as the source. Right Axes - Dashed lines: RMS divergence of the coherent flux. Red line: One ID; Black line two IDs

The total "resolving power" calculated as explained above for one and two IDs with the LEG and HEG are shown in Fig. 9. As expected, the "RP" of the two IDs is worst that that of a single ID since the coherent source size is proportional to the square root of the device length.

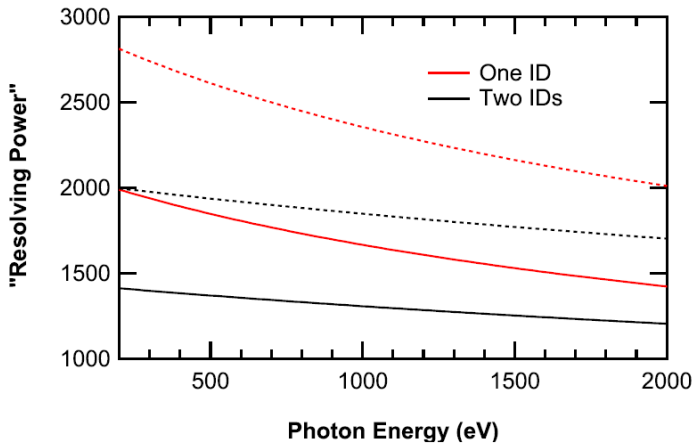

Figure 9: Total "RP". Black traces: Two IDs; Red traces: One ID. Solid lines: LEG; Dashed lines: HEG.

We ray traced the beamline for several photon energies, with sources simulating one and two IDs, and with and without slope errors on the optical elements. Two representative examples confirming the analytical calculations are described below. Evidently, the contribution of the exit slit is not included in the ray tracings and therefore are quoted as resolving power.

The spot pattern at the exit slit plane showing a RP better than 2500 when one ID and the LEG are used and the monochromator is tuned to 250 eV is seen in Fig.10. The ray tracings include the same slope errors used in the analytical calculations. Without slope errors the RMS size in the dispersion direction is 9.9 µm, only slightly smaller than the one shown in Fig. 10. Along the horizontal direction the RMS size without the slope errors is 18 µm whereas those seen in the figure are 23 µm, the value expected when one takes into account the RMS slope error on M3-A.

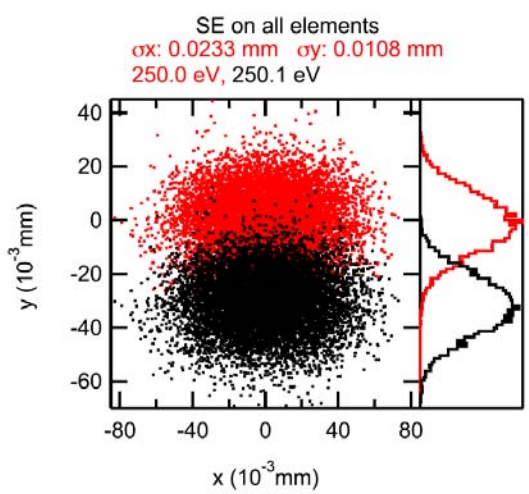

Figure 10: Spot pattern at the exit slit plane including slope errors on all optical elements. The RMS values shown above the figure are for 250 eV

The ray tracings results demonstrating a RP of ≈2000 when the upstream ID and the monochromator are tuned to 1500 eV are shown in Fig. 11. The RMS sizes without slope errors are 16 µm horizontally and 4.4 µm vertically. Since the last value is almost √2 smaller than the one in the figure means that the contribution due to the slope errors to the RP is comparable to that of the source.

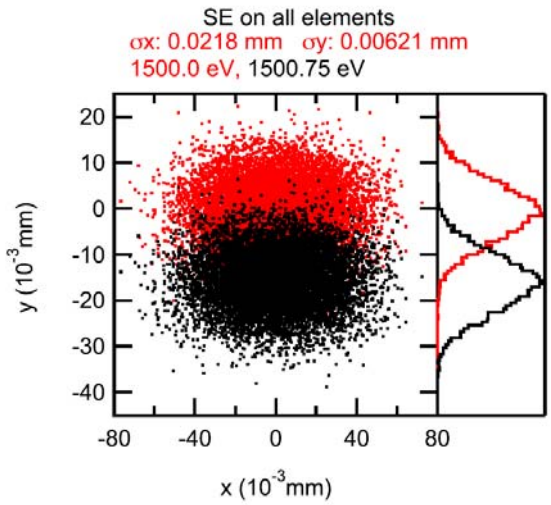

Figure 11: Spot pattern at th e exit slit plan e including slope errors on all optical el ements. The RMS values sho wn above the figure are for 1500 eV

Coherence Flux

The calculated optical efficiency of the beamline including the mirrors reflectivities and the gratings efficiencies are shown in Fig.12. The gratings efficiencies were calculated using the exact electromagnetic theory [3] assuming they are blazed at an angle of 0.1° and the optical coating is Au on all elements. As seen in the figure, the optical efficiency using two gratings is higher than 10% between 200 and 1660 eV. The other traces in the figure represent the total beamline efficiency (ε). They include, in addition to the optical efficiency, the bandwidth correction due to the exit slit resolution (same as that of the source) as well as the factor due to the increase in the horizontal spot size due to the meridional slope errors on the elliptical cylinder (M3-A). The latter factor is 0.79 at 250 eV and decreases monotonically to 0.74 (0.65) when one (two) ID is used. The total efficiencies presented in Fig.12 will be used to calculate the coherent flux. We note in passing that the reduction in coherent flux due to the meridional slope errors on M2-A and the grating are taken into account through the ``resolving power''.

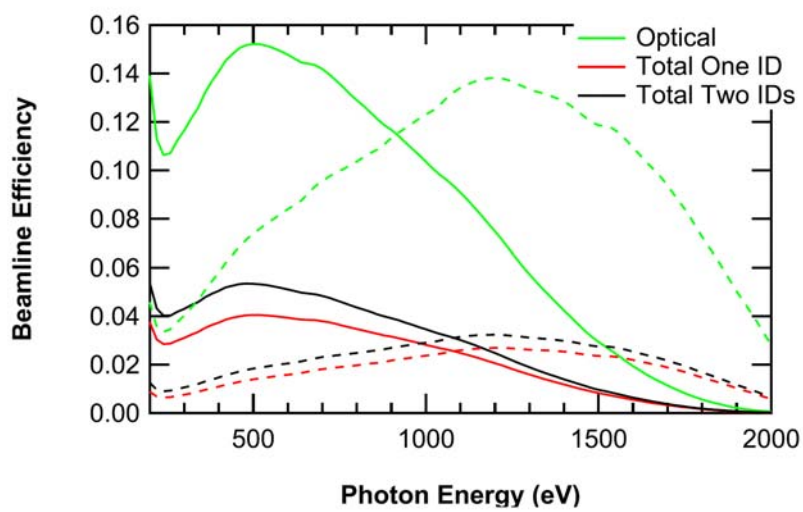

Figure 12: Green traces: Beamline optical efficiency. Red (Black) traces: Total efficiency when the source is one (two) ID. Solid lines: LEG; Dashed lines: HEG. See text.

The coherent flux transmitted by the beamline (F) for each one of the "RP" curves shown in Fig. 9 was calculated using $F=\varepsilon B \lambda^2/4$, where B is the source brightness (calculated using the spectra code) [4] and λ is the wavelength.

The results shown on the figure make clear the need for a second grating to significantly increase the coherent flux for photon energies higher than 1.1 keV. With the two gratings and with two IDs the expected coherent flux delivered by the beamline will be higher than 3×10^{12} photons/s up to 1.6 keV at a "RP" better than 1300. With one ID the coherent flux will be $\geq1\times10^{12}$ photons/s up to 1.7 keV at a "RP" better than 2000.

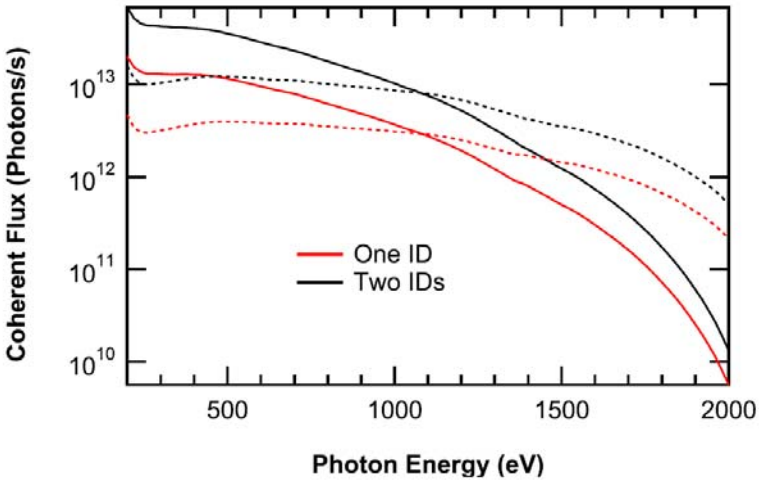

Figure 13: Coherence flux through the exit slit when using either one or two IDs.

Full polarization control branch

The description of the performance of the full polarization control branch was extracted mainly from a report/paper submitted for publication {ref RR}. The paper describes the optical design of the full polarization branch.

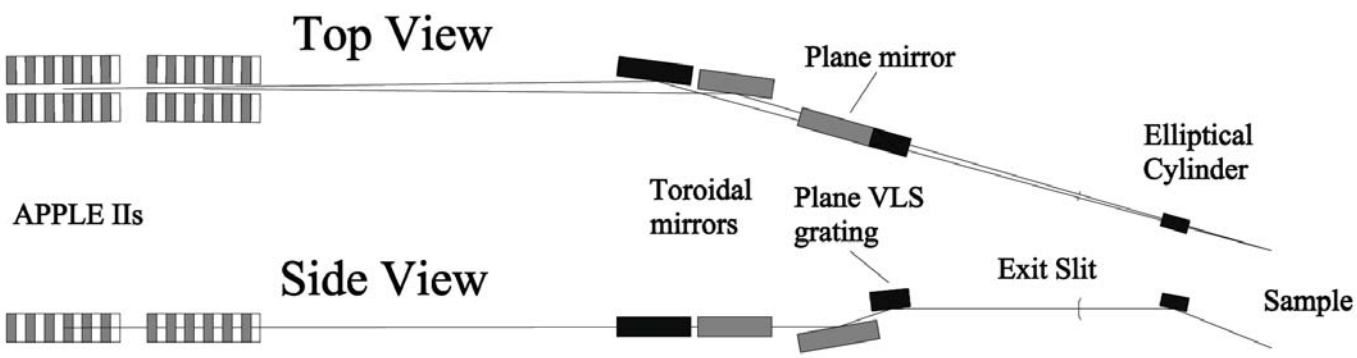

Figure 14: Schematic drawing of the full polarization control branch beamline optics

<u>Optical design</u>

Fig 14 shows the schematic drawing of the FPC branch optical layout. The distance from the source, the angles of incidence, the deflection of the optical elements, their demagnification, and the desired slope errors are listed in Table 2. The table also list the parameters of the Kirkpatrick-Baez (KB) pair (not shown in the figure) to be located downstream of the sample position and will be used to achieve a few-micron spot size for an additional experimental endstation or roll-up port to be located downstream of the scattering endstation [section 3 in this document].

The first two optical elements are a pair of internally water cooled toroidal mirrors deflecting the beam by ≈2.5° in the horizontal plane. The upstream (downstream) mirror collects the beam from the upstream (downstream) ID. Since the vertical beams waists are separated by almost 2.5 m, the sagittal radii of the toroids are designed to

collimate the photon beams along the vertical direction. This arrangement was chosen in order to have both beams focused at the exit slit of the vertically dispersing monochromator. The meridional radii of the toroids are designed to focus the source horizontally at the sample position with approximately 1.5:1 demagnification. The next optical element is a plane mirror that illuminates a variable line spacing (VLS) plane grating [5-7]. The linear coefficient term in the line spacing variation function allows focusing of one chosen wavelength, while the quadratic term corrects the coma aberration, also at one wavelength. The important point of this optical design is the fact that with the plane mirror in front of the monochromator one can focus all wavelengths in the range covered by the grating by choosing the angle of incidence on this mirror such that the reflected ray illuminates the grating at the required angle of incidence. Since the angle of incidence on the plane mirror for a given VLS grating is determined by the focusing condition and the grating equation at that energy, it is advantageous to have at least three gratings that allow trading off resolution for flux while maintaining a fixed exit slit width. The chosen gratings have central line densities of 150 (Low Energy Grating, LEG), 400 (Medium Energy Grating, MEG), and 1200 (High Energy Grating, HEG) l/mm. The LEG and MEG are operated with a *c* value ($c = \cos\beta / \cos\alpha$) of ≈ 1.5 whereas the HEG operates with c≈2.2 to allow for higher resolution [8].

An elliptical cylinder mirror (M3) downstream the exit slit deflects the beam downward by 2.5°, re-imaging the vertical exit slit onto the sample position in a 1:1 configuration. The focal spot at the sample position in the upstream experimental endstation is reimaged onto the sample position in the second endstation by a KB mirror pair consisting of elliptical cylinders. The first element of the pair deflects the beam upward by 2.5° and focuses along the vertical direction while the second deflects by the same angle in the horizontal plane and strongly demagnifies along this direction.

The beamline was ray traced using the SHADOW code [9] for several photon energies. Actually, two ray tracings were performed at each photon energy to take into account the fact that there are two sources and two different toroidal mirrors, one mirror for each source The source files were generated with a separate code to take into account the fact that the vertical and horizontal source waists are separated by almost 1.25 m. The source parameters were assumed to be Gaussian with RMS values obtained as in Eq. 1 [10]

$$\Sigma_{x,y} = \sqrt{\sigma_{x,y}^2 + \frac{\lambda L}{2\pi^2}} \text{ and } \Sigma'_{x,y} = \sqrt{\sigma'^2_{x,y} + \frac{\lambda}{2L}}, \quad (1)$$

where λ is the wavelength and L is the undulator length.

The figure errors in all the ray tracings were incorporated with SHADOW's PRESURFACE routine using a measured mirror profile scaled such as to obtain the meridional RMS slope errors specified in Table 2.

Fig 15a) shows the ray tracings of both beams at the exit slit plane of the monochromator for a photon energy of 300 eV when using the LEG. As seen in the figure, the two beams have only a small overlap. The vertical collimation means that both beams are in focus vertically at the exit slit. However, they differ in vertical focal spot size by approximately 10% owing to the 2.5m longitudinal separations of the two undulator sources.

The two beams at the sample position of the upstream experimental station when using a 10 µm exit slit opening and for 300 eV photons are displayed in Fig. 15b. For clarity, the two spot patterns have been separated in the figure. Their horizontal and vertical sizes are very close, but not identical. The difference is due to the different figure errors on the area of M3 that each beam illuminates. Nevertheless, the areas of the two spot patterns differ by less than 2%. The divergences of the two beams at the sample position in the upstream endstation are shown in Fig. 15c). Clearly, there is a larger divergence for both beams along the vertical direction compared to the horizontal direction owing to the higher vertical demagnification (see Table 2). The smaller horizontal divergence fulfills the experimental requirement of a small horizontal angular separation between the two beams.

As mentioned, the beamline will have a second branch for roll-up experiments requiring a small spot size. At this station, a spot size with a 5 µm diameter will be achieved, the beam divergences will be 1 mrad in both directions, and the horizontal angular separation between the beams will be 1.6 mrad.

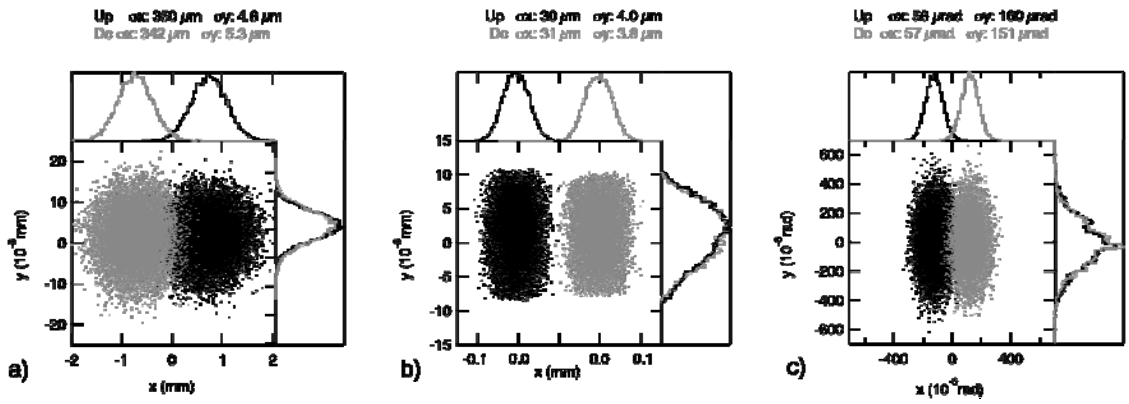

Figure 15. Ray tracings of beams from both undulators. a) At the exit slit plane; b) At the upstream endstation sample position; c) Beam divergences at the upstream endstation sample position. Photon energy 300 eV using the LEG.

Energy resolution

The expected monochromator resolution was calculated assuming the vertical spot size obtained using Eq.1, the slope errors specified in Table 2, and an exit slit width of 10 µm. All the other contributions, including coma, slope errors of the toroids, and higher order aberrations, are negligible in this design.
Fig. 16a summarizes the expected resolution of the monochromator for the three gratings when the exit slit opening is set to 10 µm. For the LEG and the MEG, the resolution term due to the source size is the largest at low photon energies whereas at higher photon energies the dominant term is that due to the exit slit. For the HEG, the largest contribution over its full energy range is that of the 10 µm exit slit. The term due to the slope errors on the grating is smaller than that of the specified exit slit contribution over the full energy range of the gratings. The instrument was not designed for ultra-high photon energy resolution. Nevertheless, as shown in the figure, the monochromator will achieve a "resolving power" [11] better than 10^4 over its full scanning range with the MEG and the HEG.

Polarized flux

The beamline flux was calculated based on the flux emitted by insertion device, corrected for the bandwidth of the 10 µm slit, the reflectivity of all optical components, and the calculated grating efficiencies. The circular polarized flux emitted by the insertion device was calculated using SPECTRA [12]. The reflectivities of all optical components were obtained using the SRCalc code [13] assuming an RMS surface roughness of 0.2 nm. The gratings were assumed to be blazed and their efficiencies were calculated using the differential formalism of the exact electromagnetic theory [2]. We included an RMS surface roughness of 0.8 nm in the grating efficiency calculations.
The expected circularly polarized flux at the upstream experimental station for each of the three gratings is shown in Fig. 16b. With the LEG and the 10 µm exit slit ("resolving power" better than 4000) we expect a flux higher than 3×10^{13} photons/sec at the sample. The flux to be delivered by the MEG is higher than 7×10^{12} photons/s up to 1.5 keV. The use of the HEG will improve the "resolving power" to over 10^4 but will reduce the flux to 10^{12} photons/s up to 1.5 keV. The flux at the downstream experimental endstation will be reduced by approximately 1/2 due to the two additional mirror reflections.

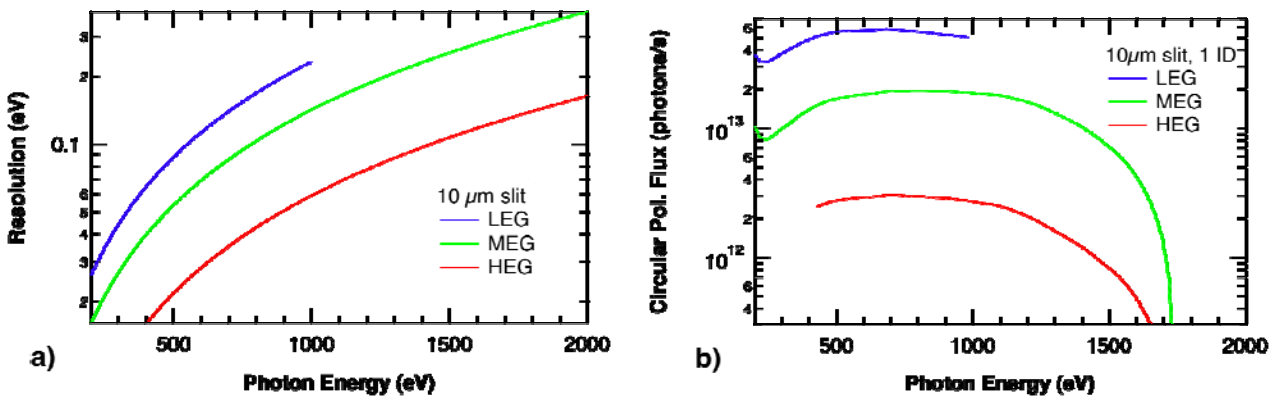

Figure 16. a) Expected resolution and b) expected flux at the upstream experimental endstation.

Other components at the beamline design also require out attention:

White beam apertures

First after the ratchet wall we find the water-cooled white beam apertures. These apertures will have the function to define the beam shape on the first optics and consequently reduce the heat load on the first optic element of each of the branches. The front end aperture will need to be able to remove in the worst case scenario of about 10 kW produced by the undulator with power densities up to 35 kW/mrad^2. A diagnostic chamber should be located directly downstream of this element.

FEA analysis of the M1 Mirror

Finite element analysis has been conducted on a generic M1 internally water cooled mirror to ensure that the effects of the heat load on that element caused by the high power photon beams delivered by the insertion devices does not jeopardize the desired performance, such as high coherent photon flux in the coherent branch, and high photon flux combined with high energy resolution in the polarization branch.
Originally the firsts FEA results for this beamline were done with considering 2 x 2 meters long EPU45 in the worst case scenario, when horizontal polarized energy at 185 eV is emitted, see report in additional information APPENDIX. That study concluded that internally water-cooling on M1 mirrors is sufficient to achieve the state of the art performance of the beamline optics. Since that report the beamline layout has gone through some modifications. The change in the period length of the IDs from 45 to 49 mm only reinforces the considerations of the report. Nevertheless we have performed new FEA analysis varying the sizes and number of cooling channels in the mirror as well as its width and thickness. These new results are even more encouraging and we are very optimistic regarding the heat dissipation and future performance of the M1 beamline mirrors. Following we show some of the most recent FEA reported analysis. The results show the performance of an internally water-cooled mirror with 11 channels and 100 mm height considering the initial conditions of total power absorbed of 1.634 kW and a power distribution of 0.86 kW/urad^2.

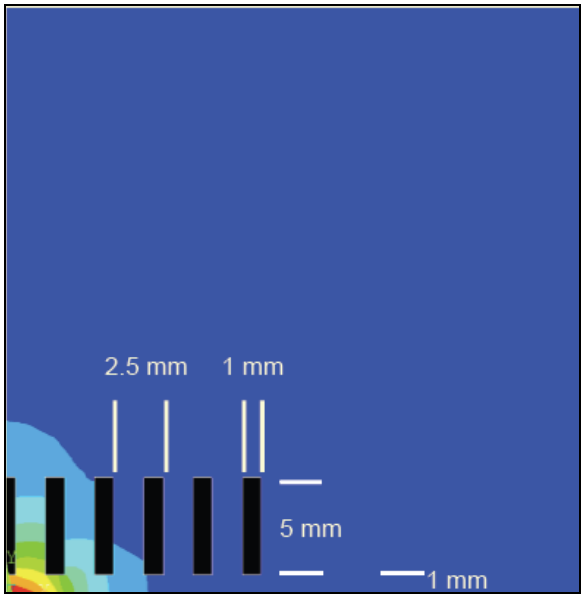

Figure 17. Partial view of a transverse section across the longest direction of the internal arrangement of the cooling channels in a 100mm x 100mm x 500mm internally water-cooled mirror with 11 channels along the beam direction (500 mm). The figure also shows that heat distribution is confined to a small region where the beam hits the mirror.
(Simulations courtesy V. Ravindranath, figure courtesy R. Reininger NSLS-II)

The results of these simulations are very encouraging, because they show, see figure 18, that in the region of the central cone (≈200 mm) the induced PV slope error of such a mirror is less than 1 μrad along the meridional direction. Furthermore, the effect of this deformation can be corrected in the CB with the bendable M3-A mirror [2]. The effects of the heat load on the M2 monochromator mirrors has been described [2]… The most important result from that study is that the deformations on this mirror can be compensated by refocusing the monochromator.

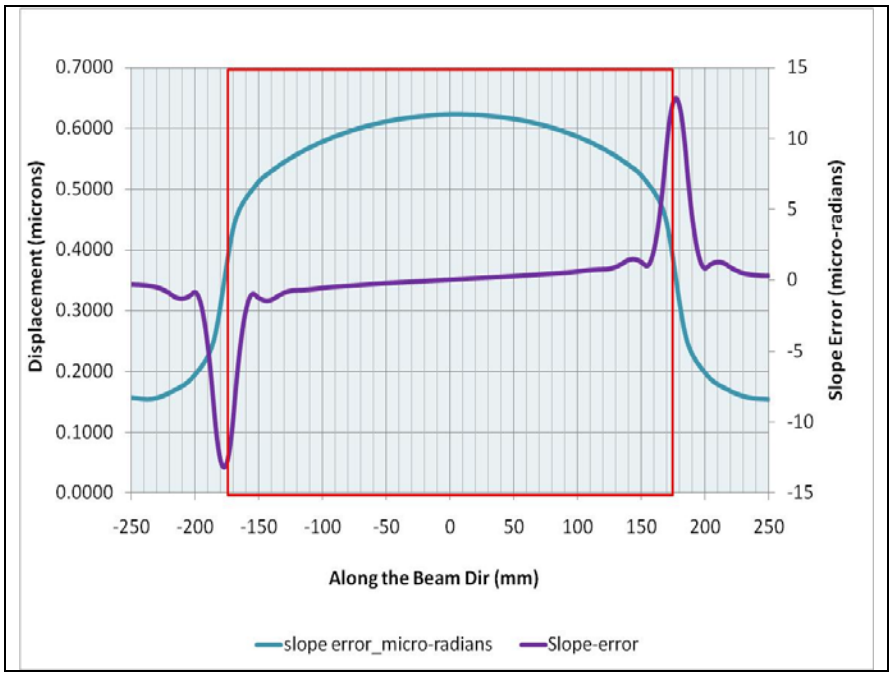

Figure 18 FEA analysis of an internally water cooled mirror with 11 channels. Inside the red box, that indentifies the size of the mirror, the deformation along the surface (light blue) is less than 300 m, meanwhile the slope error (dark blue) is > than 5 rad.
Figures and simulations and figure courtesy V.Ravindranath (NSLS-II)

2.7 X-ray Tracing

Preliminary X-ray tracing was performed at the standard configuration for the CSX beamline. . Because of the soft x-ray nature of the radiation that this beamline will be working with, it is not expected to have complications in the X-ray tracing specific for the soft x-ray beamline optical layout. Once the optical design has achieved the mark of 90% .and the approval of the review we will initiate the beamline x-ray tracing

3 END STATION INSTRUMENTATION

Two end stations are planned, one dedicated to soft x-ray diffraction and imaging for the Coherent branch, and one optimized for resonant scattering dedicated to the fast-switching Polarization branch. But these will not be the only experiments at this beamline; the flexibility of the optical design allows two roll-up ports fulfilling the conditions of beam requirements established by the BAT. The diffraction and scattering end stations are being funded through capital funds from the Condensed Matter Physics and Materials Science (CMPMS) Department and the NSLS Department, respectively. It is expected that both end stations will be commissioned and operational at NSLS and kept state-of-the-art until being transitioned to NSLS-II. The instruments that will serve in the two open roll-up ports have not yet been determined.

Soft X-ray Diffraction and Imaging Vacuum Chamber for the Coherent Branch

This end station will consist of a 6-circle, in-vacuum diffractometer equipped with x-ray focusing optics to carry out combined diffraction and imaging experiments. The end station will feature the appropriate degrees of freedom to carry out full grazing incidence diffraction experiments with large in-plane components to the momentum transfer, and zone plate focusing optics to perform imaging experiments with spatial resolutions down to 40 nm at NSLS-II. Sample cooling will be provided down to 5K and the application of a magnetic field is being actively pursued. This station will be unique, in that it will be able to perform simultaneous grazing incidence diffraction and circular and linear dichroism and diffraction contrast imaging experiments.

Table 3. Diffraction and Imaging chamber major components

Diffraction chamber	Comments
In-vacuum diffractometer	6 circles in-vacuum diffractometer
Suite of detectors	
Suite of pinholes	
Zone plate	
Sample cooling	Control and monitor
Sample transfer system	
Polarization analysis	

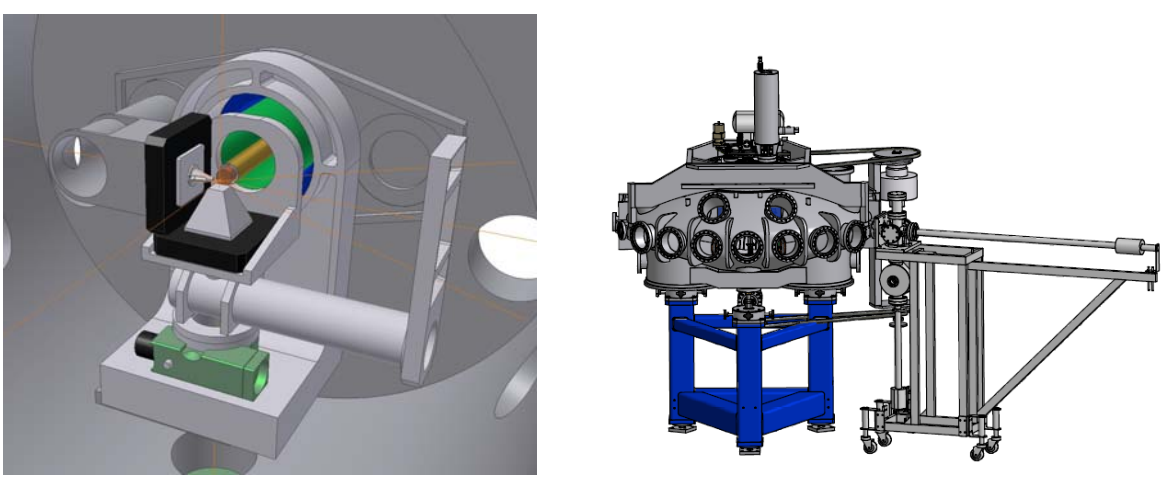

Figure 18: left, detail of in-vacuum diffractometer and sample stage in diffraction/coherent imaging vacuum chamber, right, scattering chamber with sample transfer for polarization branch.

Soft X-ray Resonant Scattering/Spectroscopy with a 1-Tesla Magnet for the Fast Switching Branch

The proposed state-of-the-art endstation will be an advanced upgrade of the NSLS X13A endstation and will have the following new features requested by the user community: (a) a new magnet, based on high temperature superconductor technology, to provide a magnetic field available at the sample position of ~1 T; (b) a more flexible scattering geometry (with magnetic field), permitting both longitudinal and transverse magneto-optical scattering geometries; (c) extension of the low-temperature limit down to ~10K; (d) full coverage of scattering angle; (e) a suite of detectors to cover the full spectral range, with large dynamic range; and (f) a sample transfer system to allow a fast sample interchange.

Table 4. Scattering chamber major components

Scattering Chamber	Comments
Superconducting magnet	1 Tesla field, along the beam direction and along the perpendicular plane
In-vaccum diffractometer	Sample stage (x, y , z) and theta , detector arm –2theta
Suite of detectors	Electron yield, photon yield, and provision for water cooled detectors and area detectors
Sample cooling (< 20 k)	Control and monitor
Sample transfer system	With parking for precooled samples
Azimuth rotation on sample	360 degrees rotation
Polarization analysis	

4 SPECIAL BEAMLINE REQUIREMENTS

This windowless soft x-ray beamline working under UHV conditions is not expected to have special requirements that are currently not common at synchrotron facilities. Nevertheless in this section it is intend to list, the requirements for the beamline regarding normal operation or for special operations.

Time request for ultrafast experiments

Timing experiments, particularly pump-probe measurements at ultrafast (picosecond-scale) timescales, are an important aspect of experiments conducted at soft x-ray beamlines. For these experiments to be performed at the CSX beamline required non-standard photon timing patterns, bunch lengths and for the experiment control signals provided by the accelerator systems.
NSLS-II current plans is to operate at a master frequency of 500 MHz with a "standard" mode of operation with a near-uniform fill pattern, this will create difficulties for pump probe type ultrafast timing experiments. We propose to have additional machine operation modes with timing patterns a) with ~ 5 times larger bunch-to-bunch separation of at least 10ns, and b) a mode where a "superbunch" or "camshaft bunch" is well separated in time from the bunch train.
Ultrafast experiments will require the delivery by the "machine signal controls group" the signals that will allow: monitoring the operation mode or fill distribution pattern, the timing signal with a resolution of 400ps and a jitter of less than 5 ps. Also important for these experiments are the signals that allow monitoring of the deleterious effect of static *rf* cavities will introduce in the bunch length, and the relative phase relative to the master frequency,
For more information we refer the reader to the APPENDIX 4.

Data storage and data processing for coherent imaging techniques

The following table provides an estimate for the need of the data storage and processing for a technique such as coherent imaging based on the detection of the diffraction pattern with a state-of-the-art CCD detector. The estimations are based on the calculated performance of the coherent scattering branch for more information about the data collection and processing estimates we refer the reader to the APPENDIX 4.

Table 5 System Data Requirements

Detector Size	2048 x 2048 pixels (larger in the future)
Detector Frame Rate	500 Hz
Peak data throughput	~ 4 GigaBytes/second
Average data throughput	~ 1 GigaByte/hour
Total daily storage capacity	10-20 GigaBytes
Total On-Sight storage	10 TeraBytes
Network Bandwidth	Gigabit ethernet
System control PC (motor control and data reduction)	Dual Quad-core CPU

These estimates do not consider the use of the simultaneous use of the two branches, what could easily add a factor 2 to the presented estimates.

With the demands of the new sources of the type of Free Electron Lasers, it is a very interesting time to observe and participate in the development of array detectors dedicated to diffraction imaging purposes. We anticipate that especially the coherent branch as de development advances the detection scheme in that branch will

be modified to incorporate one of these new detectors if this will improve the data acquisition time. In this case it is difficult to foresee the needs that the beamline will have if each of the branches will engage simultaneously in the utilization of one of these detectors. It is our intention to closely follow up the improvements in the detector technology, not only in the area of CCD detectors but also in any new type of 2D area detector that could serve the purposes of the beamline. Other areas that need follow up is in the data collection schemes as well as well as in the data processing, with the goal to achieve a best in class state-of-the-art data collection system.

Other requirements for this beamline are listed below,

- It is desirable for the operation of the beamline to have exhaust lines for the mechanical pumps to reduce the fumes and odors in the experimental floor. These should be flexible and have the capacity to handle 5 end stations simultaneously.
- Special exhaust lines with HEPA filters for experiments using "contaminant" gases that are not possible to use the normal exhaust lines. Using in the chambers elements such as chlorine and fluorine or in experiments dedicated to the observation of nanoparticles in suspension, not engineered to the substrate. With the capacity to handle two end stations at a time.
- Cabins of transparent material to cover and protect the beamline optical components from dust and accidental "bumps". These cabins, located downstream of the First optic enclosure, downstream of the monochromator will not required to be radiation safe. Their function is to protect the equipment from dust, accidental bumps, and to minimize, if possible, temperature fluctuations caused by the close location of the beamline to the experimental floor access door.
- Soundproof experimental cabin. Until the optics design has not been finalize, and because of the limited space on the experimental floor, the existence, number, size or location on the experimental floor has not been defined.

  There is also the need to keep the racks with electronics as far as possible from the beamlines to avoid vibrations, electrical noise and/or heat load transfer to the equipment.

- And regarding the utilities: the beamline will require to have: helium gas recovery, liquid nitrogen, boiled off Nitrogen gas for venting beamline components, compressed air for valves.
- Regarding the power it is very important to consider that this beamline has the capability to operate two branches at the same time, the clean power for detectors as well as the conventional power has to be sufficient to operate simulataneously two branches with their respective endstations.
- UPS up to 12 hours only for computers and area detectors at the beamline

5 REFERENCES

[1] F. Riemer and R. Torge, Nucl. Instr. Methods 208, 313(1983).
[2] R. Reininger, K. Kriesel, S. Hulbert, C. Sanchez-Hanke, and D. Arena, Rev. Sci. Instrum. 79, 033108 (2008).
[3] M. Neviere, P. Vincent, and R. Petit, Nouv. Rev. Optique 5, 65 (1974).
[4] T. Tanaka and H. Kitamura, Journal of Synchrotron Radiation 8, 1221 (2001).
[5].M. Itou, T. Harada, and T. Kita, Appl. Opt., 28, 146 (1989)
[6] R. Reininger and ARB de Castro, Nucl. Instrum. Methods A, 538, 760 (2005)
[7] R. Reininger, K, Kriesel, S.L. Hulbert, C. Sánchez-Hanke, and D.A. Arena, Rev. Sci Instrum.79, 033108 (2008)
[8] i.e., higher demagnification as seen in Table 1.
[9] C. Welnak, G.J. Chen, and F. Cerrina, Nucl. Instr. Methods A, 347, 344, 1994
[10]P. Elleaume, Undulator radiation, in Undulators, wigglers and their applications, H. Onuki and P. Elleaume, Editors. 2003, Taylor & Francis: London.
[11] We use “Resolving Power” to indicate that the contribution of the slit is also taken into account
[12] T. Tanaka and H. Kitamura. Spectra - a synchrotron radiation calculation code. J. Synchrotron Radiation, 8, 1221 (2001)
[13] R. Reininger, SRCalc, 2001-2009

APPENDIX 1: SCHEDULE

The CSX beamline main critical characteristic the total number of optics needed in this design. The CSX beamline team is aware of the difficulties and risk that this is for the construction of the beamline. Following it is a list of milestones for the CSX beamline from now up to delivery of the first beam in April 2015 and it should not surprise anybody that these milestones are centered in the on time acquisition of the optics for the beamline. We understand that other items should not be neglected and they will appear also in this list.

FY10 Finalize FEA and wavefront analysis for both branches, to confirm the performance and finalize 100% the optical design.

- Preliminary Design review: will contain all the calculations confirming the performance and feasibility of the optical layout.
- Beamline optics final specification Specification of the CSX beamline optics will allow to start an early procurement process for the optics that are currently available in the market. With 9 optical components between monochromators and mirror optics, the CSX beamline team recognize this as one of the critical aspects of the CSX beamline.
- Work closely with the ASD to specify the CSX beamline magnets: a) two times 2m long EPU49, b) phasing magnet and c) canting magnets. In all three magnetic systems the CSX team will strongly need to interact with the magnet designers and the head of the ID group in the ASD to specify all three types of magnets.
- Specification and detail design of rest of the beamline components with special focus on beam diagnostic chambers, beam characterization chambers, apertures/exit slits/pinholes and chopper chamber.
- Specification of first experiments to be performed at the beamline:
- In the following year FY10 the beamline will strongly engage in possible upgrades of the two endstations, and specify the experiments for the roll-up ports.
- Moment to start with new hiring for the CSX beamline

FY11 Final design report

- Progress with procurement process for the major/critical optical components with long lead time because of not enough vendors in the market. This is going to be very critical for many of the CSX beamline.
- Final design report : in this year we should finalize the design of all the beamline components optics chambers, diagnostics chambers and chambers for the roll-up ports, and other beamline components specially the ones that need to be engineered and build in-House.
- Start the procurement of chambers for the different optical components.

FY12 Final design report

- Start of the process of test of the optics specifications, assembly of the optical components and storage in LOB laboratories of first optical components start arriving. Keep the optics in save place until access to the experimental floor is granted.
- Construction of the First Optic enclosure
- Start of preliminary surveyors activities to precisely locate the beamline components on the experimental floor. And as soon as possible start placing optical components at the beamline.

FY13 Beamline assembly.

In this period the beamline personal will be working closely together with surveyors, utilities groups, and engineers to test the different components and safety systems before x-rays are available. Searching for beamline readiness to take beam.

FY14	Start of one year of beamline commissioning time. This will strongly depend on the availability of usable beam in the facility, presence of the IDs in the straight section and the close collaboration with the ASD.
FY15	Start of expert user access to the beamline after one year of commissioning time

APPENDIX 2: ADDITIONAL INFORMATION

Previous Facility reports

NSLS-II Conceptual design report, chapter_11 Experimental Facilities pp 11-93 to 11-100
http://www.bnl.gov/nsls2/project/CDR/Ch_11_Experimental_Facilities.pdf

NSLS-II preliminary design report, part 2, "coherent soft x-ray beamline, pp 4-1 to 4_15, and all APPENDIXES pp 16-75, http://www.bnl.gov/nsls2/project/PDR/2-ExFac_Ch_004_CSX.PDF]

The pdf files are attached to this document.

Timing requirements for ultrafast experiments (by D. Arena)

Timing experiments, particularly pump-probe measurements at ultrafast (picosecond-scale) timescales, are an increasingly important aspect of experiments conducted at soft x-ray beam lines. We present here the requirements for the CSX beamline at NSLS-II for both the photon timing patterns and bunch lengths, and the control signals necessary to mitigate potential deleterious effects and enable user timing experiments.

NSLS-II will operate at a master frequency of 500 MHz. The timing patterns are yet to be determined, but initial discussions indicate that the "standard" mode of operation will strive for a near-uniform fill pattern. This creates difficulties for ultrafast timing experiments employing a pump-probe architecture (where the x-ray pulses are the probe) as the bunch-to-bunch separation will be only 2 ns. For pump-probe experiments, the system must return to the initial state after an excitation (pump event), and characteristic damping times for many systems are longer than 2 ns. Thus the CSX beam line requires that some operating modes incorporate longer times between bunches. The two candidate timing patterns include (1) a bunch-to-bunch separation of at least 10 ns, and (2) a separate mode where a "superbunch" or ``camshaft bunch'' is well separated in time from the bunch train with 2 ns spacing.

Another aspect of the NSLS-II that affects ultrafast timing experiments is the passive *rf* cavities that may be installed to stretch the electron bunches longitudinally and hence reduce the electron emittance. This has deleterious effects for ultrafast timing experiments. First, the bunch length can increase considerably (close to a factor of two). This immediately reduces the time resolution of experiments as the minimum point-to-point resolution is determined by the photon bunch length. Second, the passive rf cavities introduce a phase delay, relative to the master rf frequency, as a function of position along the electron bunch train. After saturation, the difference in phase may be as large as 20°. The effect saturates, so that after a number of bunches after the ion clearing gaps, the change in phase remains constant. The CSX beam line requires an appropriate signal delivered to the beam line, indicating the position in time, or, equivalently, location along the bunch train where the change in the phase of the photon bunches is zero.

With regard to other control signals, the CSX beam line requires a timing signal based on the VME-EVR-230RF electronics or equivalent (or even an improved version of the system). This system can deliver a timing resolution of 400 ps and a jitter of less than 5 ps. This should be considered the minimally acceptable timing resolution. For comparison, the Advanced Photon Source delivers a timing signal with 18.5 ps resolution. The CSX project believes an improved specification is highly desirable, at the level of 5 ps or better. One possible option is to request that the controls group implement a local electronic delay line at the beam line (perhaps by use of the 10 Gb/s programmable digital delay line, model PDDL10 from Gigbaudics, Inc., or equivalent).

In addition to these signals, the CSX beam line requires a real-time distribution of the fill pattern to accommodate the selection of appropriate timing windows. Finally, blanking signals indicating fill events will also be necessary.

Estimates for data storage and data processing (by D. Shapiro)

If we assume that the coherent soft x-ray beamline delivers 10^{13} coherent photons per second and that the optical system is reasonably similar to current state-of-the-art facilities (i.e. provides the same spot size at the sample but with reduced divergence) then we can expect an increase of 10^4 in coherent flux density at the sample over those same facilities. As an example, diffraction microscopes at the ALS can record data to 10 nm resolution with exposure times of a few hundred seconds. Since the cross-section for coherent scattering goes with r^{-4}, NSLS-II should expect to produce diffraction data out to 1 nm resolution in a comparable time. This would be the ultimate experiment and not available from day one. A more conservative estimate is to expect imaging of 2 micron objects at 5 nm resolution. Using typical sampling geometries for data collection this requires a detector with 2000x2000 pixels. Imaging the same particle at 1 nm resolution requires AT LEAST 4000x4000 pixels or 10Kx10K using typical sampling rates.

Current state-of-the-art CCD detectors can produce 2 × 107 single precision data points per second. It is not unreasonable to assume that in 5 years time this will reach 2 × 109 data points per second. Thus, high throughput diffraction imaging systems will need a peak data bandwidth of 4 GigaBytes/second. This bandwidth can currently be provided by the PCI express architecture though a single 12 hour shift of data collection at this bandwidth would produce 173 TeraBytes of data! The solution to this problem is rapid on-sight data reduction since much of the recorded x-ray diffraction data is redundant and only needed to improve image statistics. Furthermore, the total data production rate will be limited by the practical problem of sample exchange. A conservative estimate would require 3 hours time for a completed tomographic dataset. Therefore, after data reduction, the total stored data per day would approach 10 GigaBytes. The data reduction itself could be performed by a reasonably fast multi-CPU desktop computer.

Efficient imaging requires near-instantaneous feedback to the scientist. One of the capabilities provided by high-brilliance light sources is high-speed imaging at high-resolution. For the case of imaging from diffraction data this requires not only a high coherent photon flux but also significant computational power. Each reconstruction requires thousands of Fourier transforms and each Fourier transform is a near TeraFLOP calculation for the three-dimensional case. This level of computational throughput can only be achieved when thousands of processing cores work in parallel. This can be provided by a multii-million dollar CPU cluster or a small cluster of massively parallel Graphical Processing Units (GPUs). A graphics card, such as the nVidia C1060 card, can provide the needed compute speed in a low-cost and low-power consuming package. A four-card compute node has a peak performance of 4 TeraFLOPS and could provide three-dimensional reconstructions in an hour. Similarly, it can provide instantaneous feedback to the microscope user by producing two dimensional reconstructions in just a few seconds.

System Data Requirements	
Detector Size	2048 x 2048 pixels (bigger later)
Detector Frame Rate	500 Hz
Peak data throughput	~ 4 GigaBytes/second
Average data throughput	~ 1 GigaByte/hour
Total daily storage capacity	10-20 GigaBytes
Total On-Sight storage	10 TeraBytes
Network Bandwidth	Gigabit ethernet
System control PC (motor control and data reduction)	Dual Quad-core CPU

LT-XFD_CDR_XPD-00122

NSLS-II Project

CONCEPTUAL DESIGN REPORT for the

HARD X-RAY NANOPROBE BEAMLINE AT NSLS-II

final draft Sep 2009

Intentionally blank.

Approvals and Reviewers

Compiled by	**Signature**	**Date**
Yong S. Chu, HXN Beamline Group Leader, NSLS-II		
Approved		
Qun Shen, XFD Director, NSLS-II		
Reviewers		
Cev Ismail Noyan, BAT Spokesperson, on behalf of the BAT		
Andy Broadbent, Beamlines Manager		
Nicholas Gmür, ESH Coordinator, NSLS-II		
Sushil Sharma, Mechanical Engineering Group Leader, NSLS-II		

Document Updates

The Conceptual Design Report for the Hard X-ray Nanoprobe (HXN) Beamline at NSLS-II is a controlled document, revised under change control.

Version No.	Date	Changes made
1	10-1-2009	final draft, submitted to BAT

Intentionally blank.

Contents

1 INTRODUCTION 7

1.1 SCIENTIFIC REQUIREMENTS 7

1.2 THE HXN TEAM 9

1.3 BEAMLINE ADVISORY TEAM (BAT) 10

2 BEAMLINE LAYOUT 11

2.1 OVERVIEW 11

2.2 INSERTION DEVICE 12

2.3 FRONT END 16

2.4 OPTICAL LAYOUT 17

2.5 HIGH HEATLOAD OPTICS 29

2.6 LIST OF MAJOR COMPONENTS 31

2.7 SUMMARY OF BEAMLINE PERFORMANCE SPECIFICATIONS 32

3 ENDSTATION INSTRUMENTATION 34

3.1 KEY REQUIREMENTS OF THE HXN MICROSCOPE 34

3.2 HXN DETECTORS 35

4 SPECIAL BEAMLINE REQUIREMENTS 36

4.1 SATELLITE BUILDING AND ENDSTATION 36

4.2 DATA TRANSFER RATES 37

5 FUTURE UPGRADE OPTIONS ..... **ERROR! BOOKMARK NOT DEFINED.**

APPENDIX 1: SCHEDULE 38

CONSTRUCTION OF HXN BEAMLINE 38

PLANNED TASKS AND MILESTONES FOR 1NM SPATIAL RESOLUTION R&D 38

PLANNED TASKS AND MILESTONES FOR NANOPOSITIONING R&D 39

APPENDIX 2: CONSIDERATIONS FOR HXN BEAMLINE SITE 40

M.1: NSLS-II SITE SPATIAL VARIABILITY OF GROUND VIBRATION 41

M.2 FIELD TEST FOR "EXTREME" TRAFFIC ON BROOKHAVEN AVE. AND INFLUENCE ON NANOPROBE 43

APPENDIX 3 LIST OF BEAMLINE COMPONENTS 48

APPENDIX 4 REFERENCE DRAWINGS 50

Acronyms

APS	Advanced Photon Source
DCM	Double Crystal Monochromator
FE	Front End
FEA	Finite Element Analysis
FOE	First Optics Enclosure
HXN	Hard X-ray Nanoprobe beamline
IVU	In-Vacuum Undulator
LOB	Lab-Office Building
LOI	Letter of Intent
MLL	Multi Layer Laue lens
RSI	Requirements, Specifications, and Interfaces

1 INTRODUCTION

1.1 Scientific Requirements

The hard x-ray nanoprobe beamline and endstation instruments (HXN) will be designed and constructed to explore new frontiers of hard x-ray microscopy applications with the highest achievable spatial resolution. Currently the available spatial resolution for scientific applications, provided by scanning x-ray microscopes in the hard x-ray regime, is limited to ~30nm, which is still insufficient for probing the nanoscale interfacial structures critical in determining properties and functionalities of material and biological systems. The HXN beamline aims to enable x-ray experiments at spatial resolutions ranging from 30 nm to its ultimate goal of ~1 nm. The proposed range of the spatial resolution will effectively bridge the current gap between x-ray microscopy and electron microscopy, opening up new scientific opportunities. The ability to adjust the spatial resolution between 1 nm and 100 nm is crucial in studying how structural hierarchy is related to the functional properties of materials. This relationship between hierarchical structure and properties is known to exist in nearly all classes of materials, from metals to biological samples, and is a key component in furthering the development of the next generation of technological materials. In order to achieve this unprecedented spatial resolution and sensitivity, the HXN beamline and endstation instruments will be designed as a scanning microscope, taking full advantage of the high brightness offered by the NSLS-II lattice.

The letter of intent (LOI) for the HXN beamline elaborated four key modalities of x-ray microscopy, which have been fully endorsed by the HXN beamline advisory team as well as the EFAC and DOE review panels. These are:

- x-ray fluorescence
- nanodiffraction
- coherent diffraction imaging
- differential phase-contrast imaging

Photon-stimulated x-ray fluorescence offers one of the most sensitive ways to detect the presence of specific atomic elements embedded within a hosting matrix. The proposed x-ray energy range of the HXN beamline, 6-25 keV, enables detection of most of the elements in the periodic table through the fluorescence process induced by K or L-edge excitation. The ability to detect extremely low quantities of isolated atoms or small clusters of atoms is extremely important in understanding how small concentration of impurities in semiconducting or condensed materials affects electronic, magnetic, or catalytic properties of the hosting matrix. In addition, the ability to image and quantify trace metal distribution in cells and tissues is extremely important in understanding metal-mediated biological processes, including understanding many diseases and the development of therapeutic and diagnostic agents to treat them. The ultimate goal is to explore the x-ray fluorescence detection with single atom sensitivity.

Diffraction is an essential structural tool to quantify crystalline phase, strain, orientation, and texture. At the atomic level, virtually all hard materials organize themselves in crystalline form at varying length scales when thermally annealed, and the spatial arrangement of the crystalline grains and grain boundaries can profoundly influence the material properties. Unlike the x-ray fluorescence process, the diffraction process channels the incident x-rays into well-defined directions, thereby providing high measurement efficiency without collecting signals over a large solid angle. Virtually all nanodiffraction investigation requires simultaneous measurement of the x-ray fluorescence signal in order to validate the positioning accuracy of the probe and quantifying the structural environment around the crystalline phase. Consequently, x-ray fluorescence and nanodiffraction are complementary tools, extremely valuable for nanoscale structural characterization of hard materials.

Coherent diffraction imaging is a powerful and fast-growing technique, with its ultimate spatial resolution limited only by the wavelength of the x-ray. There are several varieties of this imaging modality, classified by the type of sample (crystalline vs. noncrystalline) and the details on how the reconstruction is carried out. All types of coherent diffraction imaging have demonstrated extreme sensitivity for weakly absorbing specimens with a demonstrated spatial resolution below 10nm. With this potential to reach nanometer spatial resolution in the low contrast materials, coherent diffraction imaging is an important complementary technique at the HXN beamline. In

particular, it is feasible to combine x-ray fluorescence measurement with coherent diffraction imaging in a ptychography method in order to produce both spectroscopic and electronic density images from a single experiment. In addition, the far-field data collected in this way can be used for differential phase-contrast imaging by performing straightforward manipulation of the digital data set without reconstruction, to provide high-throughput direct imaging.

An important aspect of these different x-ray microscopy techniques is that they are mutually compatible with one another, providing feasibility for implementing methods to perform simultaneous or parallel measurements with two or more different techniques. This is an important instrumentation approach, because the intense photon density over the focal spot can lead to significant radiation damage for soft and even some of the hard materials. Acquiring as much information from the specimen over a given exposure time will be one of the key instrumentation principles in developing a HXN microscope.

One important scientific question regarding the ultimate performance of the HXN beamline is the feasibility for detecting single-atom fluorescence. Obviously, the answer to this question depends on the performance level of different components of this complex instrument, including the source brightness, beamline optics (i.e., mirrors and monochromator), focal spot size and focusing efficiency, structural details in the sample, stability of the beamline and microscope, solid angle and detection efficiency of the fluorescence detector. However, it would be interesting to carry out a rather crude order-of-magnitude estimate, in order to estimate the ultimate feasibility. The expected brightness of NSLS-II's U20 undulator at 10keV is 8×10^{20} ph/s/0.1%bw/mm^2/mrad^2, with horizontal and vertical emittance values of 0.5 nm-rad and 0.008nm-rad, respectively. This gives a total coherent flux of 3.1×10^{12} ph/s/0.1%bw at 10 keV. If one assumes the following conditions, the expected flux density is 2×10^{10}/nm^2.

- Beamline has 50% transmission efficiency (including mirror and monochromator reflectivity and window transmission)
- Beamline optics can deliver 50% of the available coherent flux onto the nanofocusing MLL (multilayer Laue lens) optics
- MLL optics can produce a 1nm focused beam with 20% efficiency
- MLL optics have the number of layers matched to the energy band pass of a Si(111) monochromator

The combined x-ray fluorescence cross-section of a single Zn atom excited by 10keV x-rays is 1.0×10^{4} barns or 1.0×10^{-6} nm^2. Thus, the total emitted fluorescence count rate is 2.0×10^{4} ph/s. If an energy dispersive detector can integrate 20% of 4π SR with 100% efficiency, the measured count rate would be 4,000 counts/sec. It is import to point out that the background signal due to scattering is not considered in this estimate. Of course, the greatest uncertainties in bringing the abovementioned scenario into practice reside in the ultimate performance of the nanofocusing optics. However, this estimate provides the target performance levels for different optical components at the HXN beamline that will guide the design and construction of the beamline.

Designing, building, and operating the HXN beamline are intimately connected to the two critical instrumental challenges: development of high spatial resolution nanofocusing optics, and development of an x-ray microscope with adequate positioning and scanning capabilities. In order to tackle the technical challenges, NSLS-II has launched two major R&D programs: development of 1nm spatial resolution x-ray optics and development of a nanopositioning capability adequate for 1nm x-ray microscopy. These R&D programs are making steady progress with high hopes of fulfilling the targeted goals. Recently, HXN team members, along with the collaborators at the APS and CNM, achieved the first 2D focused x-ray beam with a sub-100nm size in FWHM, which is an encouraging first experimental verification that MLL optics can be used for a 2D focused beam. The x-ray nanofocusing research is evolving rapidly and several groups in the world are developing novel technologies with the goal to achieve nm-scale focus. This includes the latest results from Japan based on multilayer mirrors, where a 15nm line focus has been demonstrated. In order to ensure the capability to accommodate these developments in the future, the conceptual design of the HXN beamline has been considerably modified in order to provide sufficient flexibility, so that the beamline does not have any potential technical limitations for taking full advantage of other types of nanofocusing optics, if a significant technical breakthrough should occur in the near future.

What separates the HXN beamline from the other existing x-ray microscopy facilities is the detailed attention paid to the vibration environment around the HXM microscope and the HXN endstation. Even at earlier planning stages, significant technical considerations were given to providing the best environment for the HXN endstation instruments. Extensive vibration measurements and numerical simulations have been performed to guide the planning of the HXN beamline site, the location and structural configuration of the satellite building, and the endstation housed within. Recently, a similar level of attention has been given to the temperature stability around the microscope and possible methods to suppress or damp out the acoustic and vibration noise from the users of the HXN beamline. The conceptual design of the HXN beamline is optimized with the physical boundary conditions required to construct a satellite building physically isolated from the potential noise sources from the NSLS-II storage ring, experimental hall, and the adjacent lab-office building.

In summary, the HXN beamline aims to become a world-leading scanning microscopy facility, enabling the highest spatially resolved structural and spectroscopic x-ray imaging techniques on day 1 with unprecedented elemental sensitivity, with the ultimate goal of achieving ~1nm spatial resolution. The x-ray microscopy techniques provided at the HXN beamline will open new frontiers of hard x-ray microscopy applications in interdisciplinary scientific fields ranging from materials science, environment science, biology, nano-catalysis, and x-ray physics. The conceptual design aims to meet extremely demanding scientific and technical requirements for achieving the highest level of detection sensitivity, delivering the highest level of available coherent flux onto the nanofocusing optics by carefully considering and optimizing the stability against the potential mechanical and thermal induced drifts.

1.2 The HXN Team

The Hard X-ray Nanoprobe beamline at NSLS-II plans to achieve scientific and technical goals that are beyond the current state-of-the-art. As mentioned earlier, development and construction of the HXN beamline is coordinated with two supporting R&D projects: 1nm Spatial Resolution R&D and Nanopositioning R&D. Consequently, the HXN Team consists of many members. It is also important to acknowledge that the effort for developing high spatial resolution multilayer Laue lenses (MLLs) initially started at the Advanced Photon Source (APS) and the Center for Nanomaterials (CNM) at Argonne National Laboratory. The HXN team members are actively engaged in continuing collaboration. The following list summarizes the HXN team and multi-faceted support and collaboration.

HXN Beamline

Yong Chu: Group leader
Lawrence Margulies: Beamline scientist
Ken Evans-Lutterodt: MOU staff from NSLS and Kinoform development
Steve O'Hara: Beamline mechanical engineer

1nm Spatial Resolution R&D

Ray Conley: MLL fabrication, processing and metrology
Hanfei Yan: MLL theory and testing
Enju Lima: MLL testing using coherent phase retrieval methods
Nathalie Bouet (postdoc): MLL processing
James Biancarosa (technician): MLL fabrication

Nanopositioning R&D

Evgueni Nazaretski: Nanopositioning development

Other Support

Andy Broadbent: Interfacial management and coordination
Nikolaos Simos: Vibration measurement, analysis and modeling
Brian Mullany: Technical drawing and designing support
Oleg Chubar: Numerical Simulations on Undulator Radiation
Viswanath Ravindranath: Numerical Simulations on High Heatload Optics

External Collaboration

Jörg Maser: APS/CNM collaboration on MLL theory and experiment
Albert Macrander: APS collaboration on MLL fabrication and metrology
Deming Shu: APS collaboration on Nanopositioning
Volker Rose: APS collaboration on x-ray characterization of MLLs
Chian Liu: APS collaboration on MLL fabrication
Nima Jihedi: APS collaboration on metrology

1.3 Beamline Advisory Team (BAT)

The beamline advisory team of the Hard X-ray Nanoprobe beamline commands significant expertise in x-ray microscopy, synchrotron instrumentation, and a wide array of x-ray microscopy applications in interdisciplinary scientific fields. The HXN BAT members not only advise on the development of the HXN beamline and its endstation instruments but also play a crucial role in representing scientific interests in different fields, including materials science, nanoscience, environmental science, and biological science. The current HXN BAT members are listed below.

Table 1.3: HXN Beamline Advisory Team

Cev Ismail Noyan (spokesperson)	Columbia University
Chris Jacobsen	Stony Brook University
Don Bilderback	Cornell University
Tonio Buonassisi	Massachusetts Institute of Technology
Ken Evans-Lutterodt	Brookhaven National Laboratory
Peter Sutter	Brookhaven National Laboratory
Tony Lanzirotti	University of Chicago
Stefan Vogt	Argonne National Laboratory
Martin Holt	Argonne National Laboratory

2 BEAMLINE LAYOUT

2.1 Overview

The conceptual design of the HXN beamline is based on a few important underlying considerations. As mentioned in the previous section, the conceptual design of the HXN beamline ensures sufficient flexibility in its optical layout to accommodate different types of nanofocusing optics. For example, multilayer Laue lenses have the potential of the reaching the highest spatial resolution with a compact design. However, the lateral dimension of the MLL is likely to be no larger than ~100 μm, due to the extreme technical challenge associated with fabricating a large optic keeping the zone placement sufficiently smaller than its outmost zone width. A Fresnel zone plate is an extremely convenient optic, adopted in many x-ray microscopes. But it requires that the source-to-optic distances in the horizontal and vertical directions are sufficiently close to each other, in order to avoid astigmatism. Astigmatism is not a problem for MLLs and nanofocusing KB mirrors, for the focal length for each direction can be chosen separately. On the other hand, nanofocusing KB mirrors tend to require a longer working distance because of the length of the two mirrors. The optical constraint of kinoforms is similar to MLLs or KBs, depending on whether they are fabricated in a short or long form. By creating a secondary source at two possible locations from the primary source, the conceptual design of the HXN beamline offers different modes of operation. These modes provide different ranges of the transverse coherence length at the plane of the nanofocusing optic, making it possible to optimize the utilization of the available coherent flux for different types of focusing optics. Section 2.4 will be devoted to elaborating how these modes can be implemented.

The second important design consideration of the HXN beamline is for overall beamline stability against possible source motion and thermal drift. The HXN beamline employs a secondary source aperture to create a secondary x-ray source with a well-defined source size in both the horizontal and vertical directions. A mechanically stable secondary source aperture will greatly reduce or even eliminate possible source motion—whether actual, or induced by the vibration or thermal drift of the high-heat load optics, located upstream. The ability to change the size of the secondary source offers an easy way to control the transverse coherence length at the plane of the nanofocusing optics, providing a straightforward way to trade the focused flux for the focus size. For example, a small secondary source size, producing a transverse coherence length larger than the lateral dimension of the focusing optic, meets a sufficient condition for a diffraction-limited spot size. On the other hand, a larger secondary source size, under the identical focusing conditions, will result in more focused flux with a larger spot size.

The third consideration is on the environment of the nanofocusing experiments. The HXN endstation will be constructed in order to provide effective means to reduce and manage the ambient vibration, acoustic noise, and temperature drift, so that the diffraction-limited beam size can be maintained over sufficiently long times (> 12 hrs). Intensive investigations have been carried out by making actual measurements of the ground vibrations at various locations around the NSLS-II site and by numerically simulating the effects of vibrations from the major sources within and around the storage ring structure and the laboratory-office-building (LOB). These results provide sufficient scientific justification that the best way to isolate or reduce the ambient vibrations is to house the HXN microscope within a satellite building, physically separated from the storage ring and nearby LOB. The conceptual design utilizes a distance of 108m from the synchrotron source to the nanofocusing optic, in order to allow a separate satellite building structure to house the HXN microscope while optimizing the utilization of the available coherent flux for nanofocusing.

The structural overview of the HXN beamline is shown in Figure 2.1.1. It will use a low beta storage ring straight section with an in-vacuum undulator with a 20 mm period (IVU20). Its FOE spans from the end of the ratchet wall at z=25.5m to z=40.0m, containing beam conditioning optical components and beam diagnostic components. The monochromatic hutch is located in the experimental hall, occupying from z=57.5m to z=64.5m. The monochromatic hutch will be primarily used for beamline diagnostics and developing beam position monitoring methods to stabilize the x-ray beam, in order to keep the focus fixed onto a constant point on a sample. The endstation will be a monochromatic hutch, spanning from z=93m to z=113m, with interior dimensions 20m long, 5m wide, and 3.5m high. The HXN microscope will be located in the endstation. A blue boundary shown in Figure 2.1.1 represents a tentative floor structure of the HXN satellite building. A specification summary on the satellite

building is found in section 4. More complete specifications on the satellite building can be found in Experimental Facilities Requirements, Specifications and Interfaces (RSI) document for the Hard X-ray Nanoprobe Beamline Satellite building. This document will be available as a reference document. Detailed descriptions of the optical layout and components are found in section 2.4.

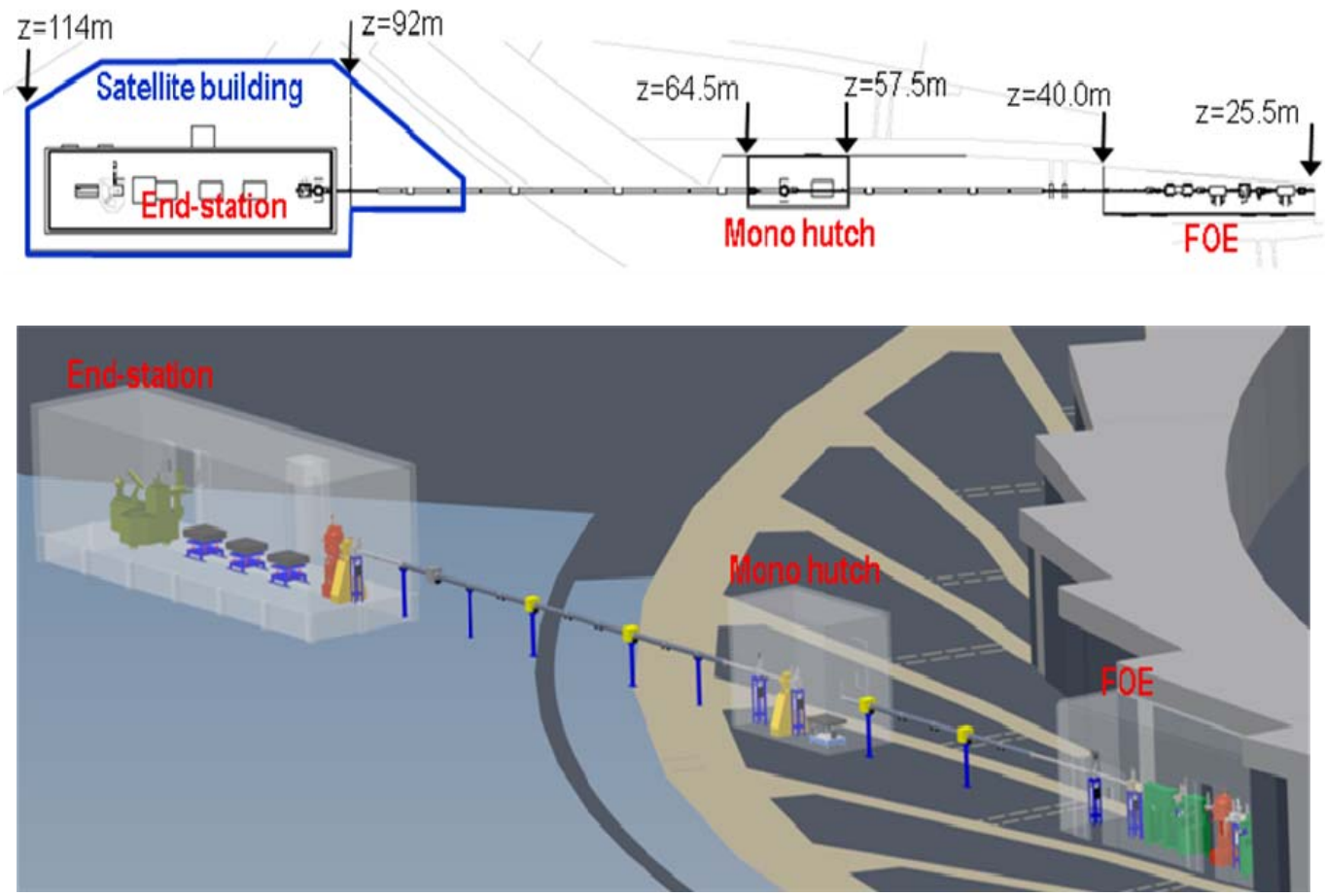

Figure 2.1.1. Structural overview of the Hard X-ray Nanoprobe beamline. The planar (top) and 3D (bottom) drawings show the position and overall size of the first optical enclosure (FOE), the monochromatic hutch, and the endstation. The endstation is located within a satellite building, physically separated from the storage ring building and a nearby lab-office-building (LOB), in order to reduce the ambient vibration. A blue boundary indicates the tentative footrprint of the satellite building.

2.2 Insertion Device

The scientific goal of the HXN beamline demands the highest achievable source brightness over its operating energy range from 6 to 25 keV. The brightness, defined as the flux output per unit bandwidth (0.1%), per unit source area, and per unit solid angular divergence, is the single most important source parameter for x-ray microscopy. The total amount of flux over the diffraction-limited focused spot is limited to the total amount of the coherent flux from a synchrotron source. The coherent flux, F_c, is related to the on-axis source brightness, B, by the following relationship, $F_c = B(\lambda/2)^2$, where λ is the x-ray wavelength. Consequently, higher source brightness gives higher coherent flux and, consequently, higher integrated flux over a diffraction-limited focused beam spot.

Among the available insertion devices as shown in Figure 2.2.1, the in-vacuum undulator (IVU20) located at the low beta section, is the most logical choice for the HXN beamline, based on the brightness comparison. The basic parameters for an IVU20 device are listed below.

- emittance: ε_H = 0.5 nm, ε_V = 0.008 nm
- beta function: $\beta_H \approx 2$ m, $\beta_V \approx 1$ m
- electron source parameters:
- σ_h=31.8μm, $\sigma_{h'}$=15.7μrad
- σ_v =2.9 μm, $\sigma_{v'}$ = 2.8 μrad
- period length: 20 mm
- number of periods: 148
- device length: 3.0m
- minimum magnetic gap: 5 mm
- peak magnetic field strength, B: 1.03T
- maximum K: 1.83
- maximum total power: 9.1 kW
- on-axis power density: 65.4 kW/mrad^2

During the initial operation phase, ε_H = 0.9 nm, ε_V = 0.008 nm will be used. A larger value of the horizontal emittance will results in σ_h=42.6μm and σ_h=21.1μm with no impact in the vertical direction.

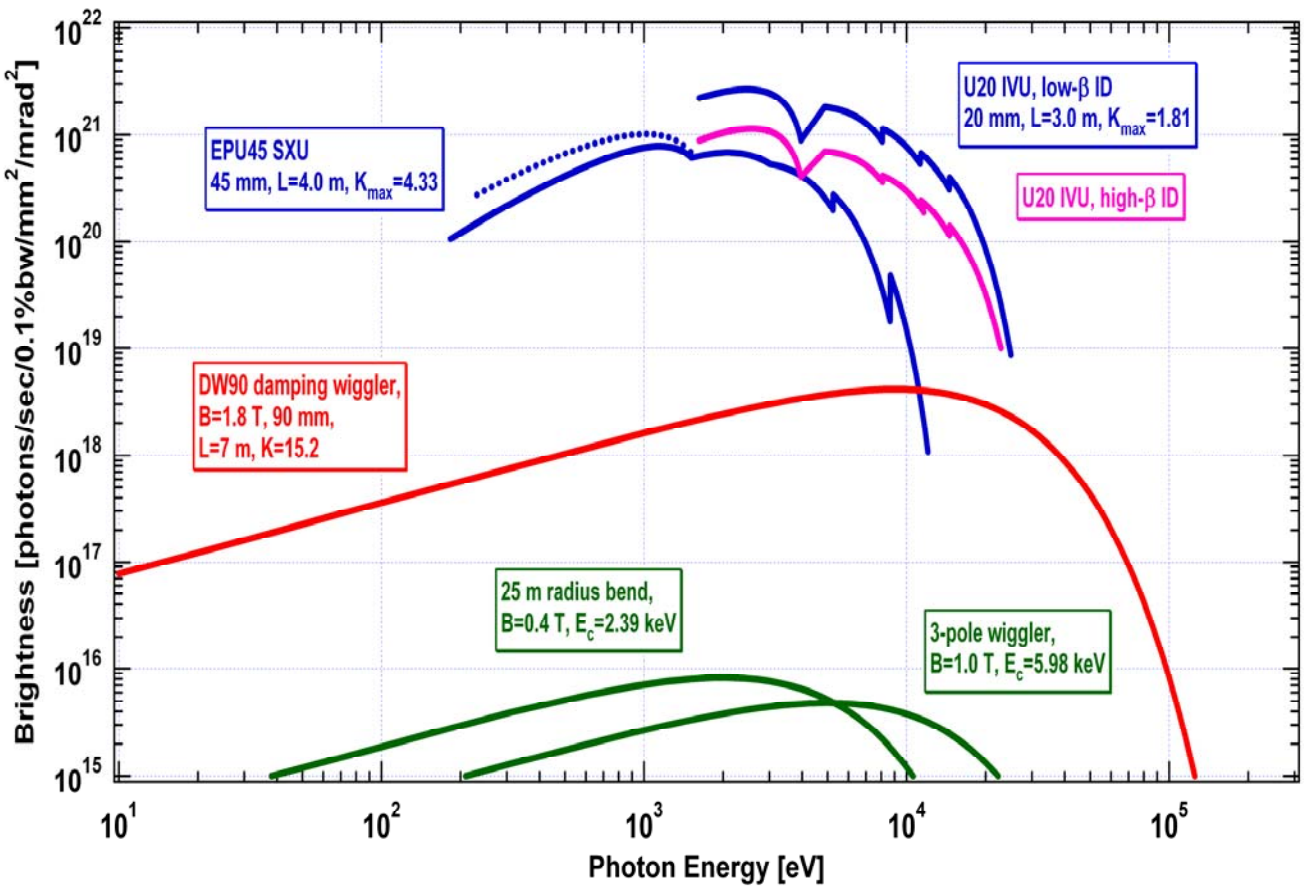

Figure 2.2.1: Brightness vs. Photon energy for the baseline radiation sources at NSLS-II. Ring parameters: 3.0 GeV, 0.5 A, ε_h=0.5 nm, ε_v=0.008 nm, energy spread=0.001; Straight section parameters: low-β: β_h=2.02 m, β_v=1.06 m; high-β: β_h=20.8 m, β_v=2.94 m; $\alpha_h=\alpha_v=\eta_h=\eta_v=\eta'_h=\eta'_v=0$. This figure was extracted from Chapter 8 of the NSLS-II Conceptual Design Report.

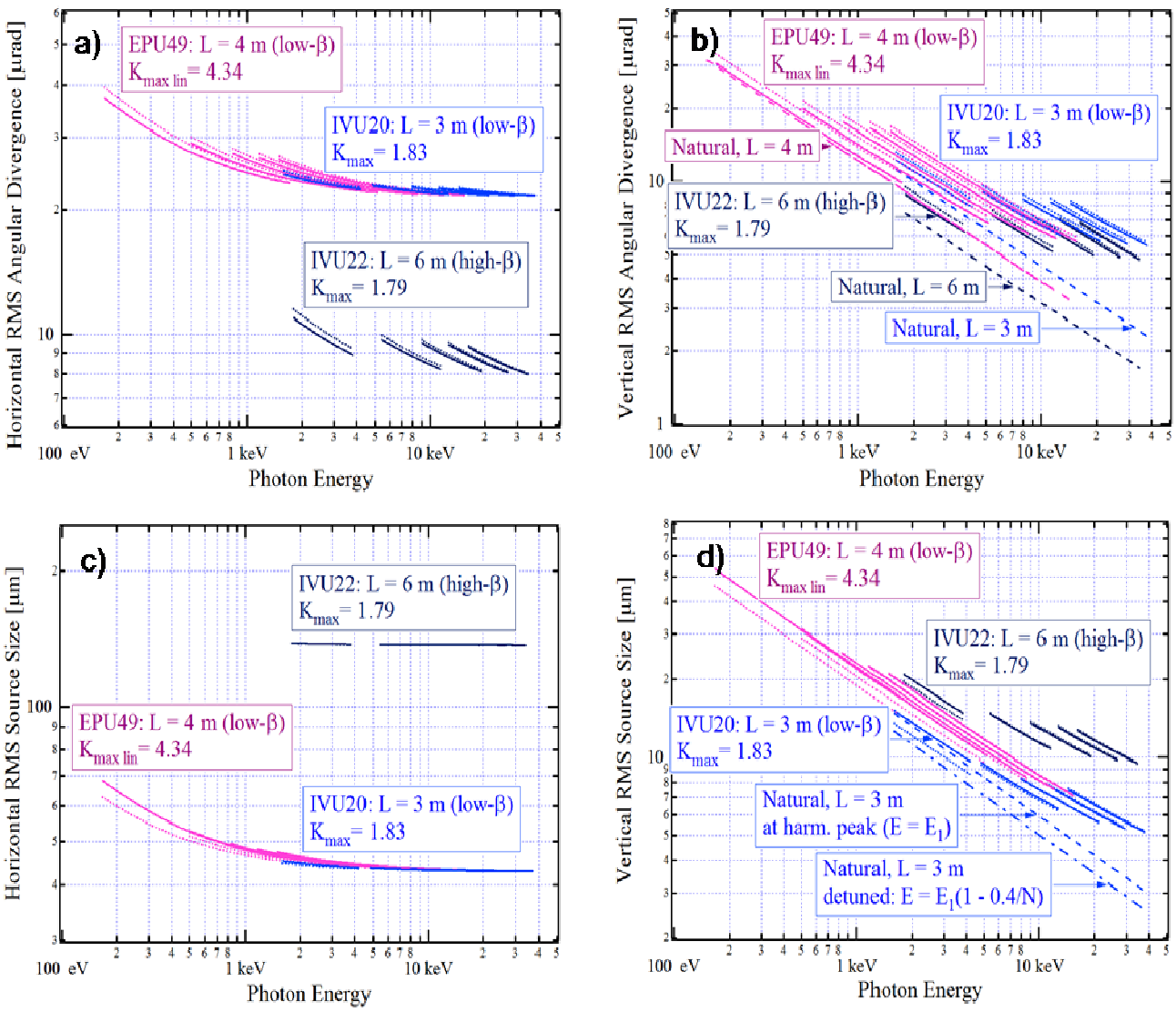

Figure 2.2.2. The RMS x-ray angular and source size of the NSLS-II undulators. a) horizontal angular divergence, b) vertical angular divergence, c) horizontal source size and d) vertical source size. The straight dashed lines represent the effective angular divergences (c) and source size (d) of the single-electron emission.

The estimated source brightness with ε_H = 0.5 nm is 8×10^{20} ph/s/0.1%bw/mm^2/mrad^2 at 10keV and 0.9×10^{20} ph/s/0.1%bw/mm^2/mrad^2 at 20keV, resulting in the total coherent flux of 3.1×10^{12} and 8.7×10^{10} ph/s/0.1%bw at the respective energies. Figure 2.2.2 shows the RMS angular and source size of a few NSLS-II undulator devices with ε_H = 0.9nm . This calculation takes into account of broadening due to finite energy spread and emittance of electron beam. At 10 keV, the estimated FWMS source size and angle are

$$S_h = 101\mu m,\ S_v = 12\ \mu m,\ \theta_H = 53\mu rad,\ \theta_V = 21\mu rad,$$

where S_h, S_v, θ_H, θ_V are the horizontal x-ray source size in FWHM, the vertical x-ray source size in FWHM, the horizontal x-ray source size in FWHM, and the vertical x-ray source angle in FWHM. In the vertical direction, the source angle and size become somewhat larger if the photon energy slightly smaller than the resonance energy of the undulator is chosen in order to increase the flux. With the horizontal emittance of 0.5 nm, the horizontal x-ray source size at 10keV reduces from 101μm to 75 μm and the horizontal x-ray source angle from 53μrad to 40μrad, with no impact in the vertical direction. The above source angle and size are used for the conceptual design as a baseline. The reduction of the horizontal source size and angle resulting from reduction of the horizontal emittance

does not have any impact on the conceptual design, other than the fact that the practical range of the horizontal source aperture will be decreased.

One of the most fundamental considerations for the conceptual design is how to handle the power delivered by the x-rays onto the beamline components, in particular to the x-ray windows, mirrors, and monochromators that are exposed to the white beam from the undulator. A brief summary on the estimated power from IVU20 is given here, so that the high heatload considerations implemented in the conceptual design can be understood easily. Figure 2.3.3 shows the total output power of the NSLS-II as a function of K and the fundamental photon energy.

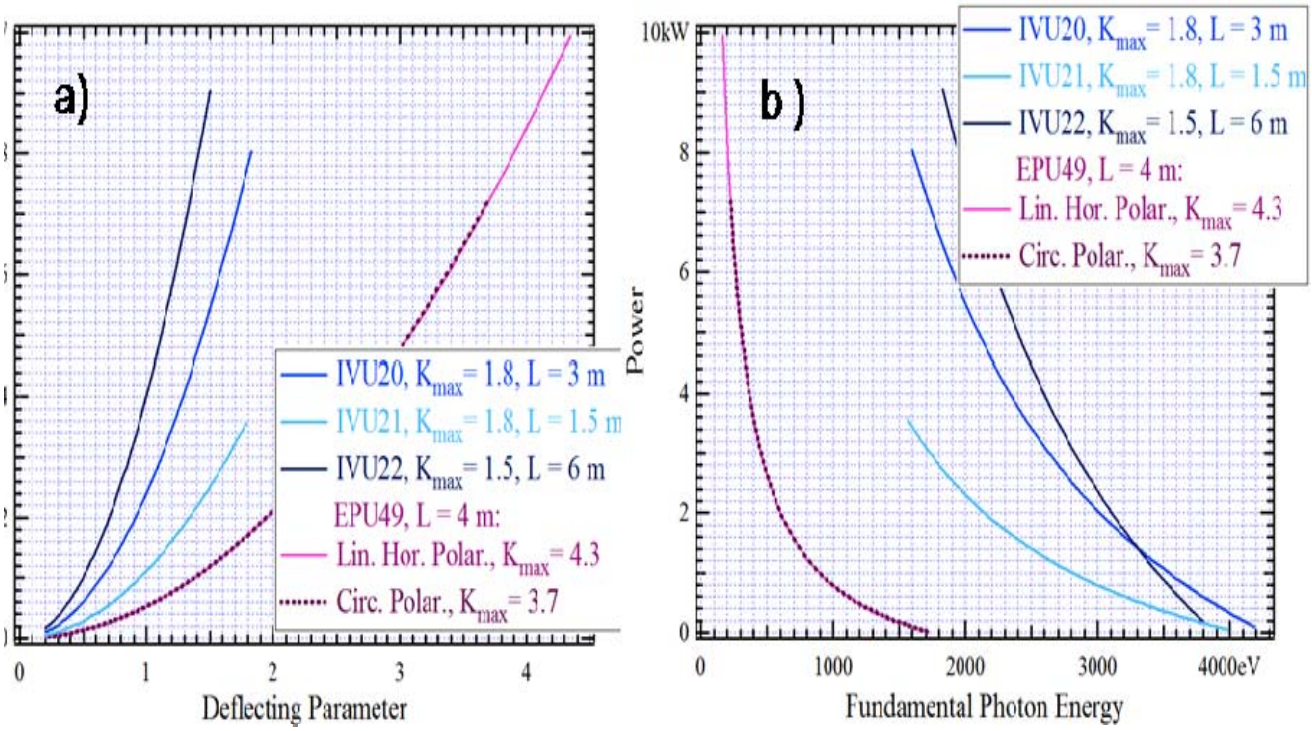

Figure 2.2.3: Total output power of the NSLS-II undulators as functions of a) the undulator deflecting parameter, K, and b) the fundamental photon energy.

For IVU20, the highest power, ~8kW, is produced at the maximum K value of 1.83, corresponding to the minimum gap of 5 mm and the fundamental photon energy of 1.6 keV. Consequently, the same high power condition is also met at higher harmonic x-ray energies, 8 (5th), 11,2 (7th), 14,4 (9th), 17.6 (11th) keV and so on. The total power output depends rapidly on the photon energy. At the fundamental photon energy of 2 keV, the total power is reduced by about 30%.

Fig 2.2.4a (next page) shows the two dimensional angular distribution of the power emitted from an IVU20 at K=1.83. The horizontal (Figure 2.2.4b) and vertical cut (Fig. 2.2.4c) through the center shows that the FWHM widths of the power distribution are ~500 μrad in the horizontal direction and ~200 μrad in the vertical direction.

These are significantly larger than the angular sizes of the central cone. Consequently, the integrated useful monochromatic flux tails off with increasing angular aperture size, while the integrated power increases almost linearly, as shown in Figure 2.2.4d and 2.2.4e. For example, with a fixed vertical angular aperture of 53μrad, corresponding to about a two FWHM angular source size, a horizontal angular aperture of 80μrad integrates more than 80% of available monochromatic flux, accepting 280W of power. On the other hand, by adjusting the horizontal and vertical angular aperture together, it is possible to optimize the acceptance of the useful flux against the accepted power. The conceptual design plans to accept 180W onto the collimating mirror with an angular aperture of 80 μrad (H) x 40 μrad (V). The HXN power management strategy is summarized in section 2.5.

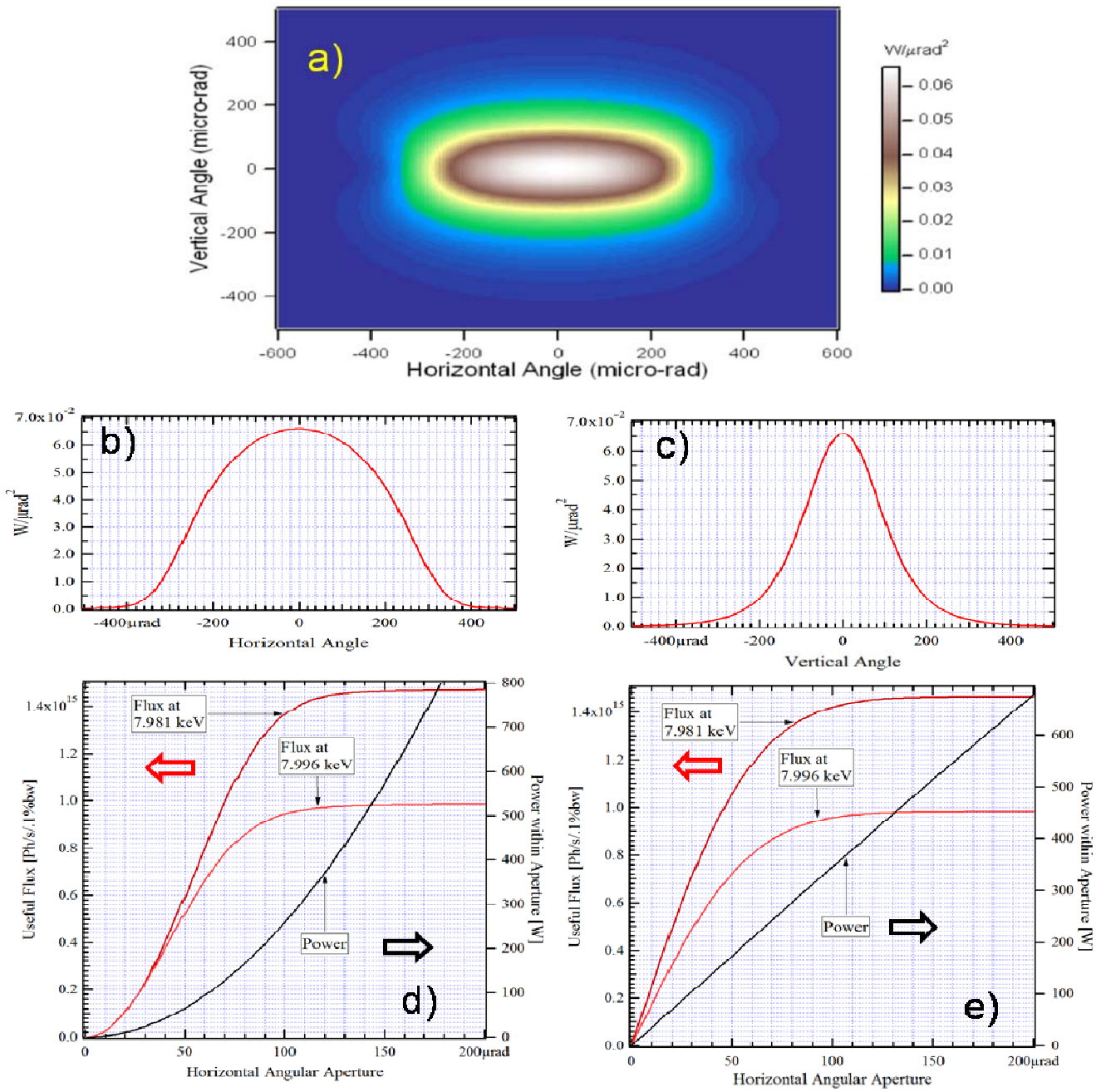

Figure 2.2.4. Angular power distribution emitted by IVU20 at K=1.83. a) 2D angular distribution, b) horizontal cut through the central axis, c) vertical cut through the central axis, d) integrate power and monochromatic flux as a function of the horizontal angular aperture with a fixed vertical angular aperture of 53 μrad, and e) integrate power and monochromatic flux while varying both aperture sizes with a fixed ratio of 1 (horizontal) to 0.4 (vertical) ratio.

2.3 Front End

A standard NSLS-II front end (FE) is shown in Figure 2.3.1. The fixed mask is designed to accept 0.5 mrad in the horizontal direction and 0.3 mrad in the vertical direction. The HXN beamline plans to use the FE XY-slits as its white beam slit. The nominal slit opening will be 50 μrad in the vertical direction and 100 μrad in the horizontal direction. A pair of typical L-shaped white beam slits results in an oval shaped beam instead of a rectangular shape. A sharper corner is needed to create a well-defined rectangular shaped illumination, useful for performing straightforward diagnostic checks for aligning the beamline optics. The standard FE will be described in a separate FE CDR document.

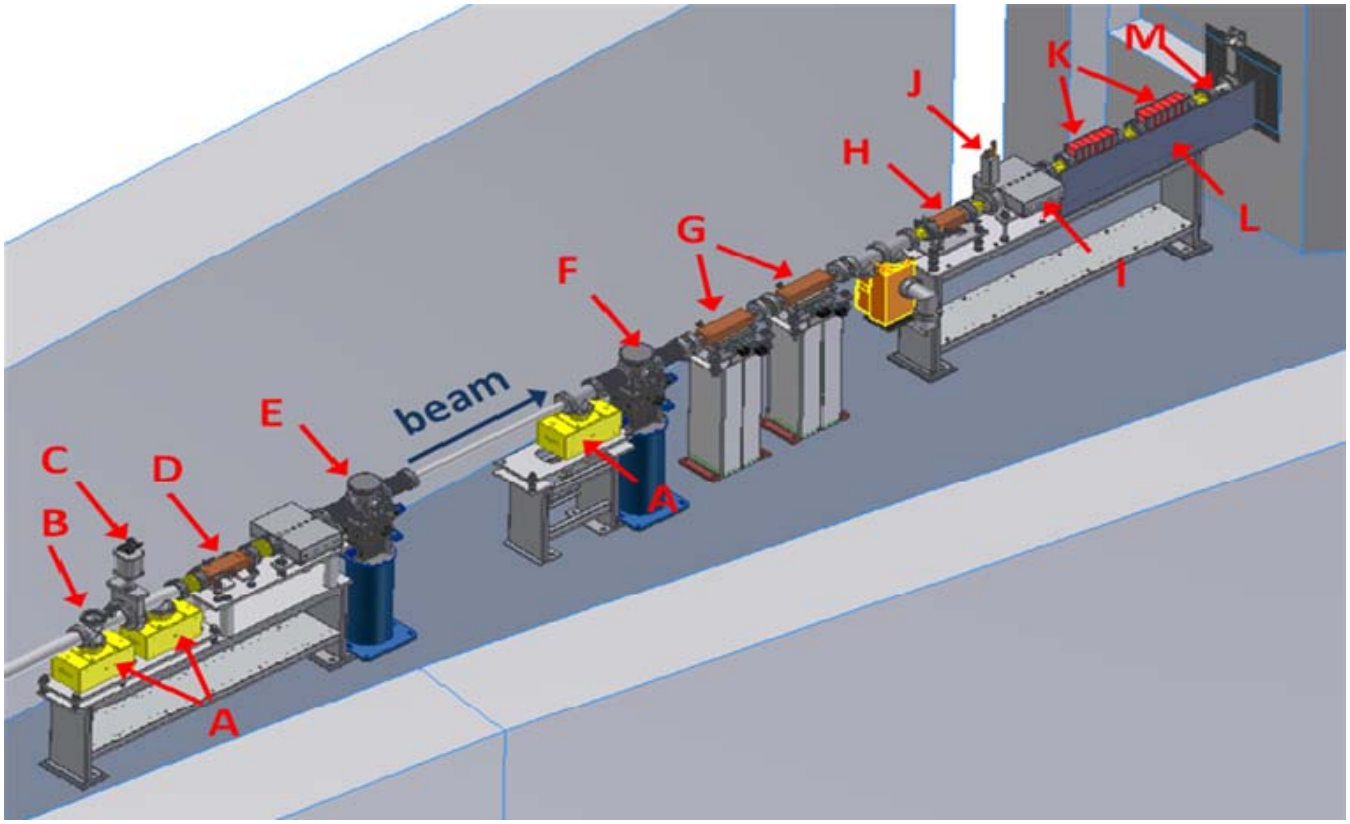

Figure 2.3.1. Configuration of a standard front end. The HXN Beamline will use a standard NSLS-II front end with one modification. The XY slits must be modified so that they have sharp corners, in order to give a square shaped beam. A: ion pump, B: bending magnet photon shutter, C: slow gate value, D: fixed aperture mask, E: X-ray beam position monitor 1, F: X-ray beam position monitor 2, G: XY slits, H: photon shutter, I: safety shutter collimator, J: fast gate value, K: dual safety shutters, L: lead shield, and M: ratchet wall collimator.

2.4 Optical Layout

This is the main section of the conceptual design report, describing the details of the optical components and the rationales for the adopted optical arrangement. Since the optical layout for the hard x-ray nanoprobe beamline is rather sophisticated, this section is subdivided into two parts, in order to provide a more effective illustration. Subsection, "Overview on Major Optical Components" will be devoted to the description of the major optical components and overall justification on why the optical components are arranged in particular ways. Subsection, "Beamline Operation Modes", will elaborate on the optical performance of three possible operations modes, along with simple model calculations.

2.4.1 Overview of Major Optical Components

The schematic overview of the major optical components is shown in Figure 2.4.1. A complete list of the beamline components is found in section 2.7. As explained in section 2.2, the HXN beamline will use an IVU20 undulator in a low-beta section. The HXN beamline will use the XY-slits in the front end (FE) as its white beam slits, in order to limit the power onto the water-cooled horizontal collimating mirror, M1, located at z=27.5m. M1 has a bending capability to collimate the incident x-rays to the horizontal monochromator, in order to reduce the energy dispersion due to the horizontal divergence from the source. M1 also serves as a low band pass filter by rejecting high order harmonics, operating at a fixed incidence angle of 2.70 mrad. With a length of 1m, M1 has a maximum angular aperture of 98 μrad in the horizontal direction. M1 has three different reflecting surfaces, Si, Rh, and Pt, corresponding to cut-off energies of ~11.3, ~22.9 and ~29.4 keV, respectively. Pink beam slits are used to define the beam footprint on a horizontally diffracting monochromator, DCM1, so that the central portion of the beam reflected from M1 will be illuminated on DCM1. DCM1 uses double Si(111) crystals to provide a fixed exit

condition to a horizontally focusing mirror M2. A very small offset value of 6 mm and a total y-travel distance of less than 1 mm will be used for DCM1, to ensure high mechanical stability. DCM1 will be cryogenically cooled using liquid nitrogen, in order to minimize the thermally induced figure errors. During the commissioning, the practicality of using the dynamical bending capability of M1 to compensate for the thermally induced slope error on both M1 and DCM1 will be explored. As will be demonstrated later, placing high-heat load optics, M1 and DCM1, in the horizontal reflection/diffraction geometry, minimizes the negative effects of thermally induced slope errors on the optical performance of the beamline. However, diffracting in the horizontal direction results in flux loss predominantly at low energies, due to the linear polarization of the incident x-rays in the horizontal plane. At 10 keV, the flux loss due to double horizontal diffraction is about 15%.

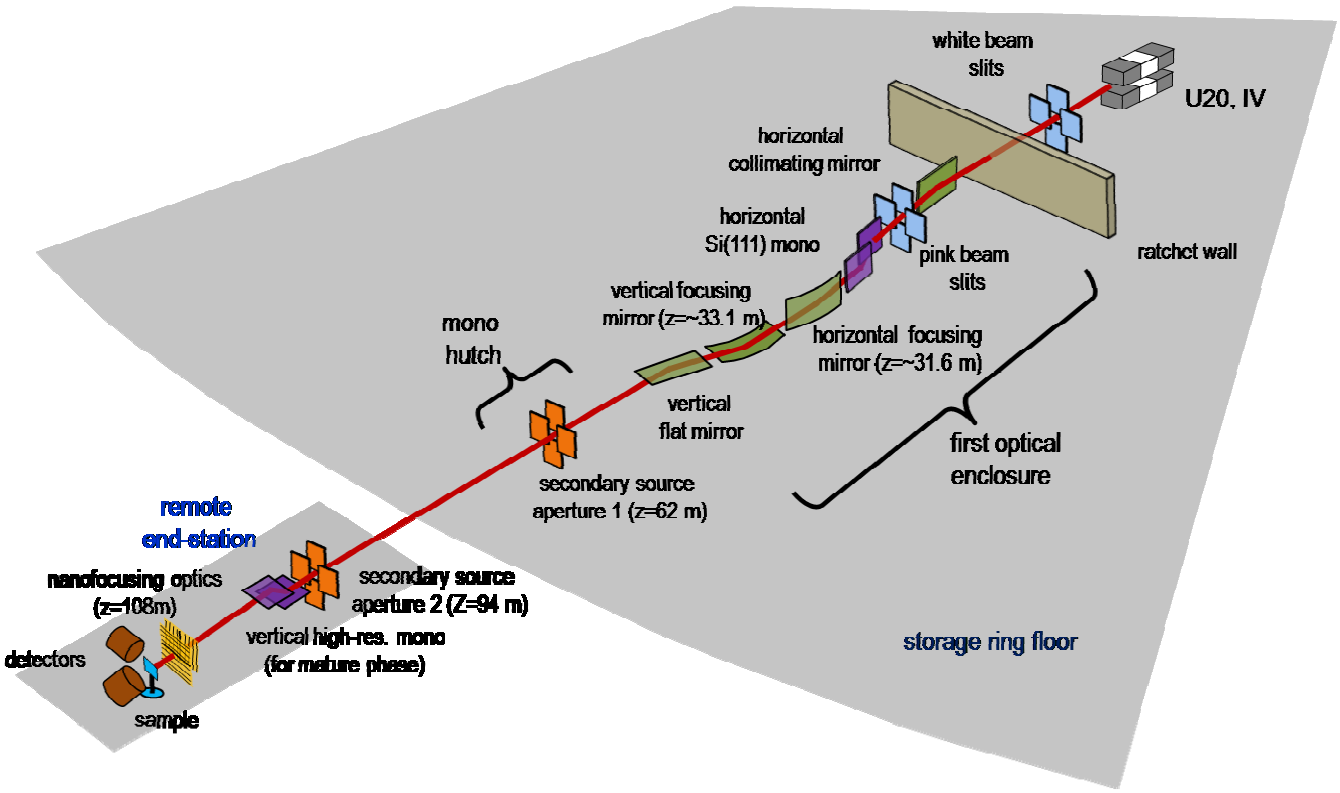

Figure 2.4.1. Overview of the major optical components of the HXN beamline. From the IVU20 undulator in the upper right corner, white beam slits (S1), horizontal collimating mirror (M1), pink beam slits (S2), horizontally diffracting Si(111) double crystal monochromator (DCM1), horizontal focusing mirror (M2), vertical focusing mirror (M3), vertical flat mirror (M4), secondary source aperture 1 (SSA1), secondary source aperture 2 (SSA2), vertically diffracting high-resolution double crystal monochromator (DCM2), and nanofocusing optics. DCM2 will be installed at the mature phase of the Beamline operation, when high-resolution nanofocusing optics requiring a higher degree of monochromaticity than Si(111) become available.

With a dynamic bending capability, a horizontally focusing mirror, M2, is used to image the source at two possible positions, in front of SSA1 (secondary source aperture 1) at z=62m or SSA2 (secondary source aperture 2) at z=94m. With the nanofocusing optics at z=108m, the secondary source at z=62m or z=94m results in an effective source-to-optic distance of 46m or 14m, respectively. Only one of the two secondary source apertures is used at a time. A larger distance between the secondary source to the nanofocusing optic is needed for a large focusing optic (>150 μm) or for coherently overfilling a smaller optic. More elaborate discussion on this topic will be presented in the following subsection.

A vertical mirror system, consisting of a focusing vertical mirror with bender (M3) and a flat vertical mirror (M4), is used to image the source in the vertical direction at the same position as the horizontal direction (i.e., either at z=62m or 94m). Rather than using a single focusing mirror, causing an angled trajectory of the x-ray beam, a double mirror system is considered. The two mirror system ensures an independent way to control focusing and positioning of the reflected beam, enabling a more straightforward method to implement a positional feedback system using beam position monitors.

The primary goal for the vertical mirror system is to maintain the same z-position for the secondary source in both the horizontal and vertical directions, completely eliminating astigmatism so that a two dimensional focusing optic such as Fresnel zoneplate can also be used without compromising its spatial resolution. For nanofocusing optical systems consisting of two 1D optics, such as MLLs, KB mirrors or Kinoform lenses, astigmatism is not important. By adopting different focal lengths in the horizontal and vertical directions, a common focal point can be achieved, even if the source-to-optic distances are different along the two directions. Nevertheless, it is important to maintain the compatibility for Fresnel zone plate optics, because low energy (< 10 keV) applications for the MLLs have not been demonstrated, to date.

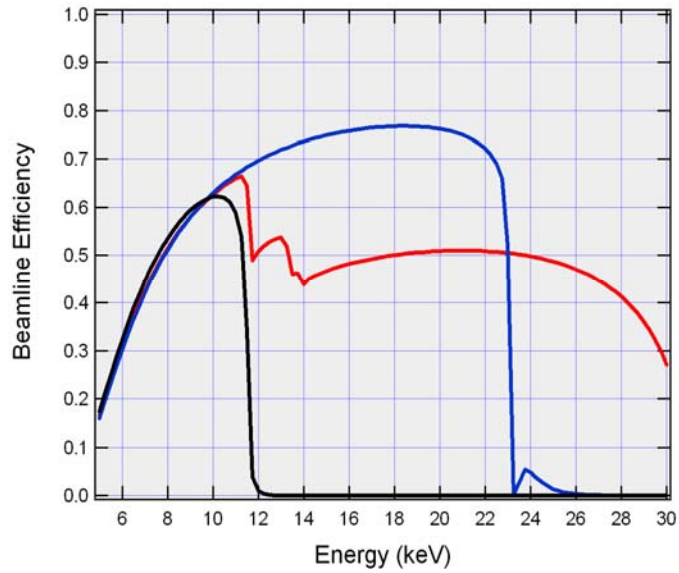

Figure 2.4.2: Beamline efficiency. The efficiency is calculated including the combined reflectivity of four mirrors, polarization due to the horizontally diffracting double-bounced Si(111) monochromators and the x-ray transmission through 1mm-thick Be. Three curves corresponds to different mirror surfaces: Si (black), Rh (blue) and Pt (red). The Beamline efficiency is better than 50% over most of its operating energies, 6-25 keV. The suppression of the beamline efficiency at low energies is primarily due to the polarization.

In order to provide effective rejection of high-order undulator harmonics, two different methods are possible: adjusting the incidence angle of M1 and M2 or implementing multiple cut-off energies at a fixed angle with different metal coatings on the silicon mirrors. Since M1 and M2 are physically separated, it is impossible to rotate them together. Thus, the conceptual design proposes to use three different reflecting surfaces, Si, Rh, and Pt, for all the mirrors with a fixed incidence angle of 2.7 mrad, to ensure adequate harmonic rejection and sufficient beamline efficiency over the operating energy of 6-25 keV. A fixed incidence angle for all the mirrors would also lead to more straightforward beamline alignment and diagnostics. Figure 2.4.2 shows the overall beamline efficiency vs. x-ray energy, taking into account the reflectivity of four mirrors, intensity reduction due to the polarization effect, and x-ray transmission through 1mm of Be windows. Except for narrow energy ranges, 6-7.5 keV and 24-25 keV, the beamline efficiency is better than 50%. The reduced efficiency at 6-7.5 keV is due to the horizontally diffracting monochromator, and lower efficiency of a Pt coating over a Rh coating is due to the multiple Pt L-edges.

The major optical components from the horizontal collimating mirror (M1) to the vertical flat mirror (M4) are housed in the FOE, while the monochromatic hutch houses the secondary source aperture 1 (SSA1). The most salient aspect of the HXN conceptual design is the endstation located within a separate HXN satellite building. The HXN endstation will house the secondary source aperture 2 (SSA2), high-resolution monochromator (DCM2), in addition to the HXN microscope.

The high-resolution monochromator, DCM2, will be implemented in the mature operating phase of the HXN when MLLs requiring a higher spectral bandwidth than that of Si(111) become available. The monochromaticity requirement states that the total number of zones of a MLL should be less than E/dE. This requirement translates into a lateral dimension smaller than 30 μm for a MLL with Δr = 1nm at 10keV or 150 μm for a MLL with Δr = 5nm. The monochromaticity requirement for a Fresnel zone plate is the same. The high resolution monochromator will consist of vertically diffracting double Si crystals with a higher index plane (i.e., 311 or 331). The selection of the spectral width for the high resolution monochromator will be based on the progress of the 1nm x-ray optics R&D.

2.4.2 Beamline Components in the First Optical Enclosure

Figure 2.4.3 shows the important beamline components in the FOE. Though specifically shown in the CAD drawings, some of the components such as gate valves, bellows, and transport pipes will not be described here. A diagnostic chamber (labeled as A) is to provide a future place holder for diagnostic elements such as an additional beam position monitor to increase the accuracy of the monitors in the FE. A white beam filter (labeled as B) is designed to house multiple x-ray absorbers. Some of the candidate materials are thin CVD diamond, Si, graphite and aluminum. The horizontal collimating mirror, M1, (labeled as C) collimates the incident x-rays to eliminate energy dispersion of the x-rays diffracted from the horizontal monochromator, DCM1 (labeled as G). A Bremsstrahlung collimator (labeled as D) and Bremsstrahlung stop (labeled as L) prevent unwanted radiation from passing down the beamline. A diagnostic chamber (labeled as H) immediately downstream of the horizontal monochromator can house both screen monitor and parasitic beam position monitor that can be used as feedback on the angle of the second crystal for DCM1. The horizontal focusing mirror, M2, (labeled as I) is used to image the primary source in front of either the secondary source aperture 1 (SSA1) or secondary source aperture 2 (SSA2). Mono beam position monitors (labeled as J and M) can operate parasitically to provide a feedback signal for correcting the drift of the mirrors and monochromator. A vertical mirror chamber (labeled as K) houses both focusing and flat mirrors. A mono shutter (labeled as N) provides the safety function for allowing safe entry into the mono hutch downstream of the FOE. The FOE is purposely designed to have some spare space. This will allow the possibility of future modifications or improvements of the beamline.

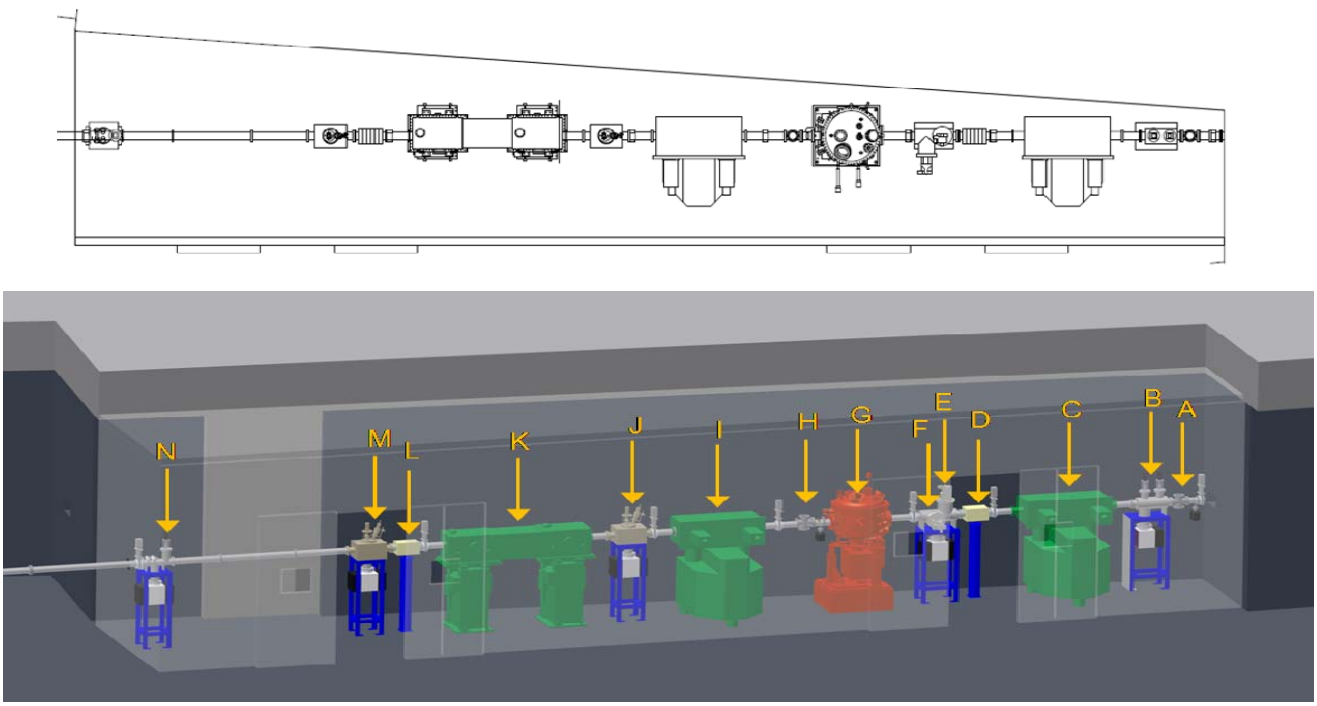

Figure 2.4.3. Planar (top) and 3D perspective (bottom) view of the first optical enclosure (FOE) and its major beamline components. A: diagnostic chamber. B: white beam filters. C: horizontal collimating mirror. D: Bremsstrahlung collimator. E: pink beam slits. F: pink beam screen monitor. G: horizontal monochromator. H: diagnostic chamber. I: horizontal focusing mirror. J: mono beam position monitor. K: vertical mirror chamber containing focusing and flat mirrors. L: Bremsstrahlung stop. M: mono beam position monitor. N: mono beam shutter. The white beam slits are located in the front end (FE).

2.4.3 Beamline Components in the Monochromatic Hutch

The monochromatic hutch houses the secondary source aperture 1 (SSA1) located at 62m from the source, as shown in Figure 2.4. It also provides 3m of space between the two Be windows (labeled as A and B). The monochromatic hutch will be used for commissioning of the FOE optics and for instrumentation development for stabilizing the beam through active feedback using the multiple parasitic beam position monitors, which are critical tasks for achieving the highest possible performance of the HXN beamline. To pass the beam to the endstation, a transport pipe will be connected between the two Be windows and evacuated the pipe. The mono beam shutter

(labeled as E) ensures safe entry into the endstation, even when monochromatic x-rays are in the monochromatic hutch. During the mature operation phase, if necessary, these two Be windows could be removed, and a permanent vacuum transport pipe can be installed, in order to reduce the x-ray absorption at low energies. To ensure a better use of the space, the hutch door will be installed on the right side of the hutch wall when looking downstream (i.e., the inboard direction).

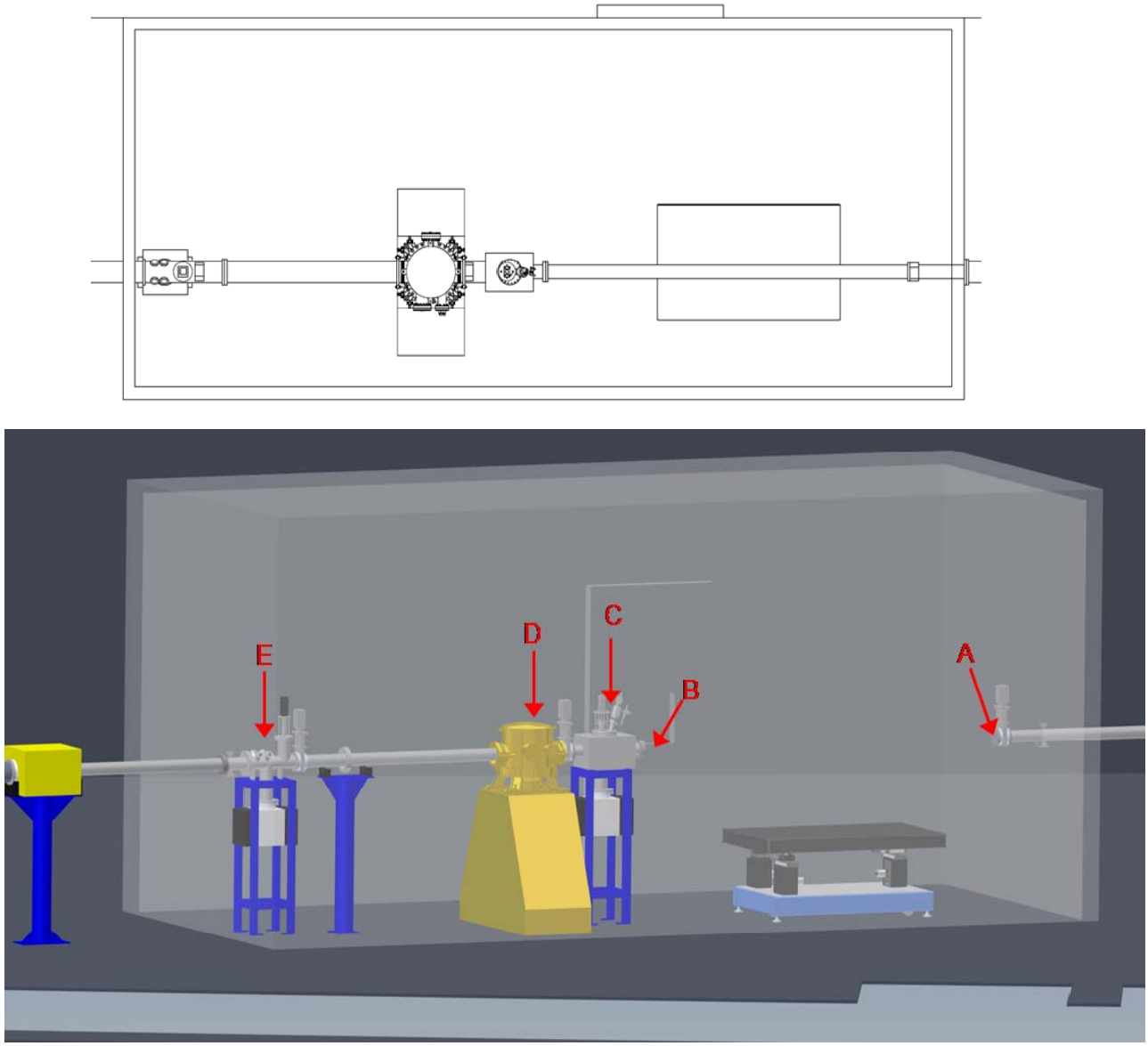

Figure 2.4.4. Planar (top) and 3D perspective (bottom) view of the monochromatic hutch and its major beamline components. A: Be window, B: Be window. C: mono beam position monitor., D: secondary source aperture 1 (SSA1). E: mono beam shutter. The monochromatic hutch will be used for commissioning of the FOE optics and instrumentation development for beam stabilization using multiple beam position monitors. To pass beam to the endstation, a vacuum pipe will be connected between two Be windows. During the mature operation phase, these two Be windows could be removed and a permanent vacuum transport pipe can be installed, in order to reduce the x-ray absorption at low energies.

2.4.4 Beamline Components in the Endstation and Satellite Building

The HXN endstation is physically separated from the storage ring building and the nearby LOB, in order to damp out the ambient vibrations originating from multiple sources. A HXN satellite workshop was held in June, 2009,

identifying the requirement for vibration and temperature stability, which is summarized in section 4. In order to maximize the structural filtering of the ground vibration at low frequencies (<10 Hz), the HXN satellite building will have a single large concrete slab with 1m-thickness under both endstation and user area, as shown in Figure 2.4.5.

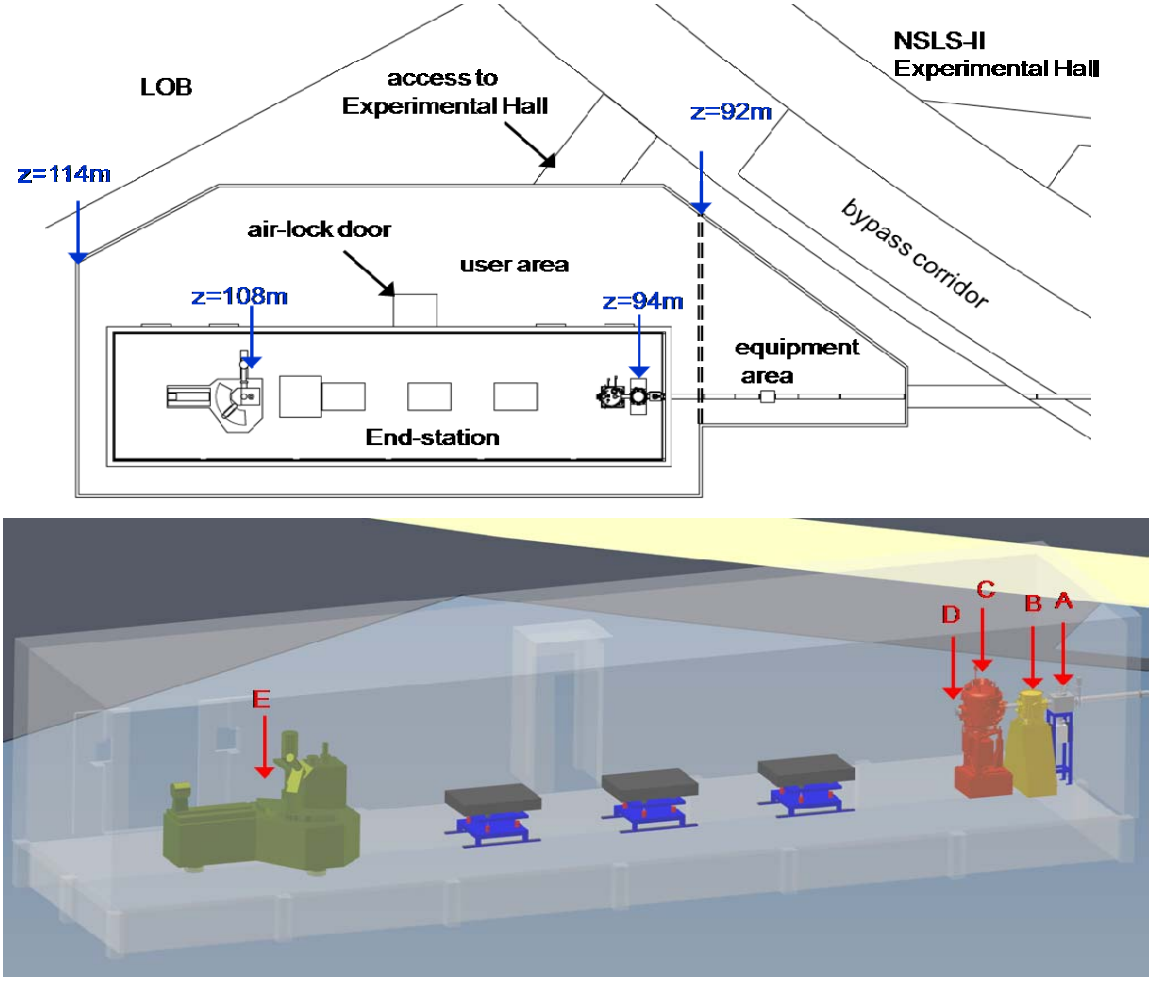

Figure 2.4.5. Planar (top) and 3D perspective (bottom) view of the endstation and its major beamline components. A: mono beam position monitor. B: secondary source aperture 2 (SSA2). C: high-resolution monochromator (to be installed in the mature phase). D: Be window. E: HXN microscope. The planar view shows a tentative satellite building floor. The satellite building will be in the corner between the NSLS-II storage ring building and the LOB. The endstation and user area will share the common concrete floor; the equipment area will have a separate concrete floor to prevent transmission of vibration and acoustic noise to the microscope. A connection to the experimental hall will be made in the upper right corner.

The beamline equipment, generating acoustic vibration and heat, will be located in the equipment area on a separate concrete slab. The utilities will be fed from the LOB with proper vibration isolation. The HXN satellite building is accessed from the bypass corridor of the experimental hall. The beam transport pipe from the experimental hall will be running through a short intermediate enclosure before entering into the satellite building. The floor structure of the satellite building shown in Figure 2.4.5 is a tentative layout. The final layout is currently under discussion.

The HXN endstation wall will be constructed with 8-inch concrete walls rather than steel walls. Concrete has superior vibration and acoustic damping properties and also provides better temperature stability, acting as a large thermal reservoir. The HXN endstation will have an air-lock entry consisting of two doors, in order to minimize the exchange of air, leading to potential temperature changes in the endstation. The dimension of the endstation will be 20m-long, 5m-wide and 3.5m-high. A one-foot deep trench with about 1 inch width will be cut outside of the endstation wall, so that high frequency noise (generated by users and computers) traveling near the surface will be scattered off by the trench and not transmitted into the endstation.

The endstation houses a mono beam position monitor (labeled as A), secondary source aperture 2 (SSA2, labelled as B), high-resolution monochromator (DCM2, labelled as C), exit Be window (labeled as D) and the HXN microscope (labeled as E). The microscope shown in the CAD drawing is a "mock" solid model taken from the nanoprobe instrument at 26-ID of the Advanced Photon Source. The design of the HXN microscope has not been carried out yet. This mock model is only for the visual purpose.

The HXN endstation length requirement of 20m is based on the need to ensure sufficient distance from the SSA2 to the nanofocusing optic. The conceptual design proposes a 14m distance. In addition, sufficient space (~5m) is needed at the downstream end of the nanofocusing optic, in order to provide space for microscope enclosure and detectors. Detectors for diffraction will be mounted on a separate granite table, isolated from the HXN microscope so that the movement of a large detector (up to a few kilograms) would not induce unwanted motions in the HXN microscope. Since an isolated satellite building will be constructed around the endstation, the dimension of the hutch must be sufficiently large to avoid a potential future need for additional space, which cannot be obtained without prohibitively expensive construction cost. Furthermore, a large interior dimension, proposed by the conceptual design, is extremely beneficial to retain a sufficiently large thermal reservoir, so that small fluctuations of local temperature due to turbulent air-flow from the ventilation system or exchanged volume of air due to entry or exit from the endstation does not influence the overall temperature stability in the endstation.

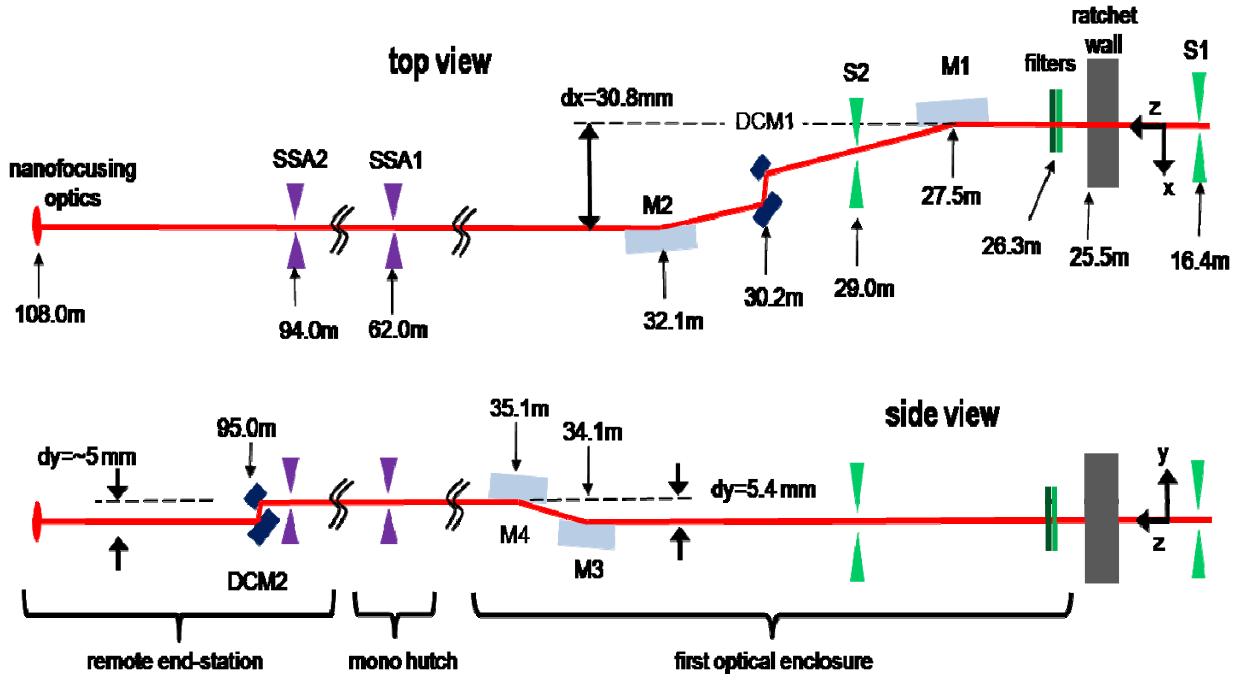

Figure 2.4.6. X-ray beam path through the major optical components of the HXN beamline. Top view shows the horizontal direction and side view the vertical direction. The coordinates are defined such that z-direction is along the beam, y-direction is up, and x-direction is the outboard direction. All the mirrors have the nominal incidence angle of 2.7mrad. The nominal offset distance for DCM1 is 6mm. The horizontal and vertical offsets are due to the reflection from the mirrors and monochromator.

<u>X-ray Beam Path through the HXN Optical Components</u>

Figure 2.4.6 shows the overall x-ray beam path through the HXN optical components. All of the optical components shown in Figure 2.4.6 have been already explained in the previous subsections. The coordinate system, adopted in this report, uses the same convention as the Advanced Photon Source, where z-direction is along the x-ray beam, y-direction is up, and x-direction is along the outboard or outward direction from the interior of the storage ring. In the horizontal direction, white beam slits, S1, limit the angular size of the incident beam onto the horizontal collimating mirror. With a nominal incidence angle of 2.7mrad at its center, M1 reflects the incident beam in the outboard direction. Pink beam slits, S2, limit the illuminated power onto the horizontal monochromator, DCM1. DCM1 operates at a fixed exit condition to position the beam onto the center of the horizontal focusing mirror, M2. M2 reflects the beam so that the central trajectory of the focused beam is parallel with the beam from the undulator. A separation distance of 4.6 m between M1 and M2 results in a horizontal offset

of 24.8mm. DCM1 adds a 6-mm offset in the same direction, resulting in a total horizontal offset of 30.8 mm. The first crystal of DCM1 diffracts in the same orientation as M1 (i.e., ++ geometry) in order to maximize the horizontal offset. A total offset of 30.8 mm is adequate for providing sufficient room for white beam Bremsstrahlung stop, which will be placed immediately outside of the DCM1.

In the vertical direction, the vertical focusing mirror, M3 (0.8m-long), reflects x-rays upward and the vertical flat mirror, M4 (0.8m-long), reflects the beam in a trajectory parallel with the x-ray beam from the undulator. A separation distance of 1 m between M3 and M4 results in a vertical offset of 5.4mm. When implemented in the future, the high-resolution monochromator, DCM2, located in the endstation will provide about a 5mm vertical offset in the opposite direction. During the initial operation phase, a total vertical offset of 5.4 mm will be used.

Beamline Operation Modes

There are three different possible operation modes for the HXN beamline, as schematically illustrated in Figure 2.4.7. In the diagram, a focusing mirror is represented as a lens. In this representation, the other optical components, such as monochromators and flat mirrors, are ignored because they do not manipulate the phase space of the beam. The three possible modes are high-coherence mode, high-throughput mode, and astigmatic high-coherence mode, distinguished by the location of the secondary source in the horizontal and vertical directions.

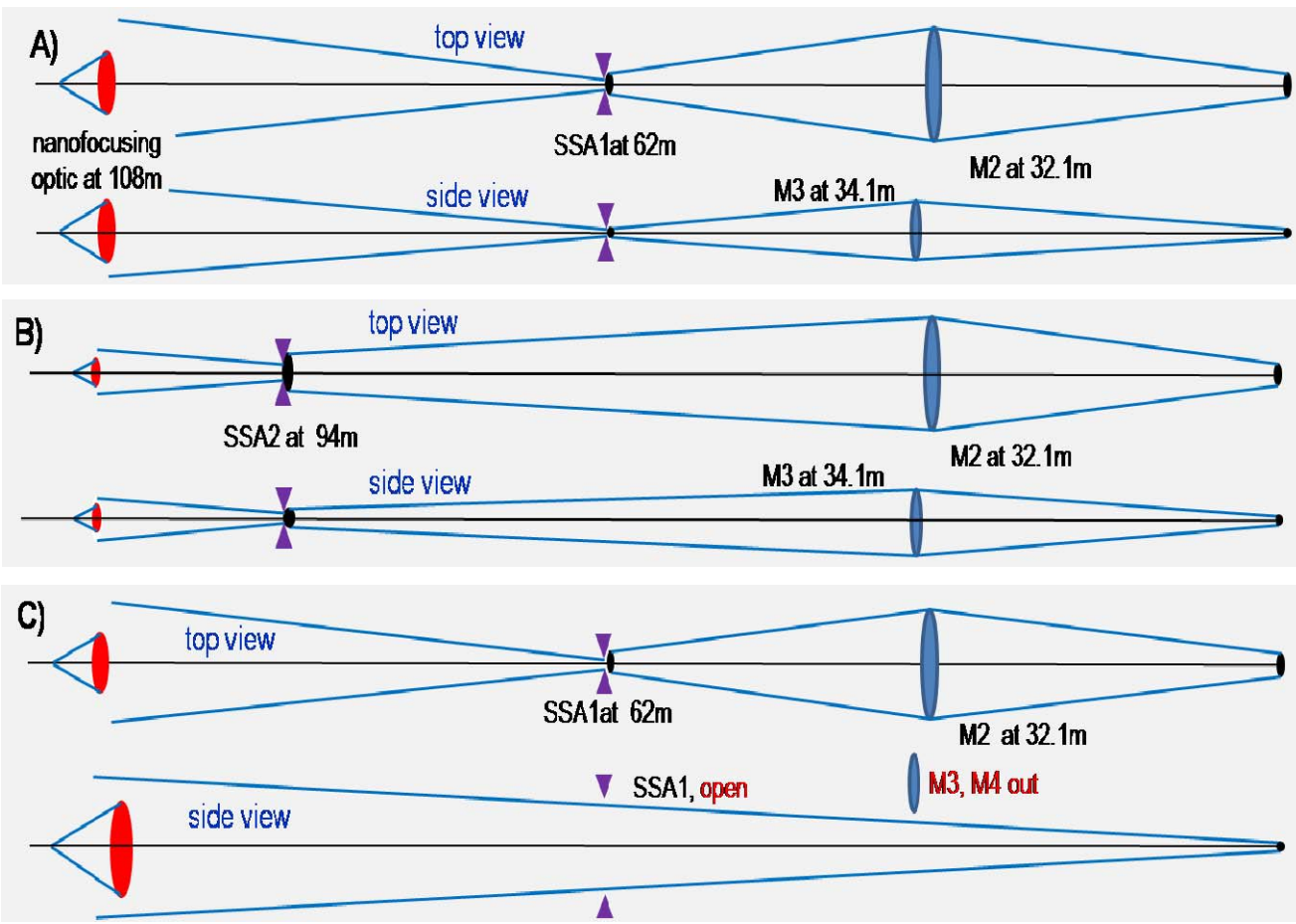

Figure 2.4.7:. Three possible operation modes for the HXN beamline. A) High-coherence mode, where the primary source from IVU20 is imaged in front of SSA1 at z=62 m by M2 (horizontal focusing mirror) and M3 (vertical focusing mirror), resulting in an effective source-to-focusing optic distance of 46 m. B) High-throughput mode, where the primary source is imaged in front of SSA2 at z=94 m, resulting in an effective source-to-focusing optic distance of 14m. C) Astigmatic high-coherence mode, where the secondary source at 62 m is used in the horizontal direction and the primary source s used in the vertical direction after moving M3 and M4 out of the beam. The beamline operation in astigmatic high-coherence mode requires lowering the vertical position of a few optical components by 5.4 mm.

High-Coherence Mode

In this mode, the x-ray source from IVU20 (this will be referred as the "primary source") is imaged in front of SSA1, located at 62 m by M2 in the horizontal direction and by M3 in the vertical direction. This geometric configuration corresponds to horizontal and vertical magnification factors of 0.93 and 0.82, respectively. At 10keV, the FWHM size of the secondary source would be 9.5 μm in the vertical direction and 94.1 μm in the horizontal direction if each mirror behaves as an ideal lens. Since the secondary source is much larger in the horizontal direction, a rather broad range of the aperture size can be selected in the horizontal direction. In order to prevent a possible source motion induced by thermal drift in the monochromator or mirrors, the secondary source aperture should not be set much larger than the FWHM size of the secondary source. This limits the range of the horizontal aperture up to about 100 μm and the vertical aperture up to about 10 μm. The low limit of the aperture depends on the quality of the polished blade of the aperture and the mechanical vibrations. A lower limit of 5 μm is expected to be feasible.

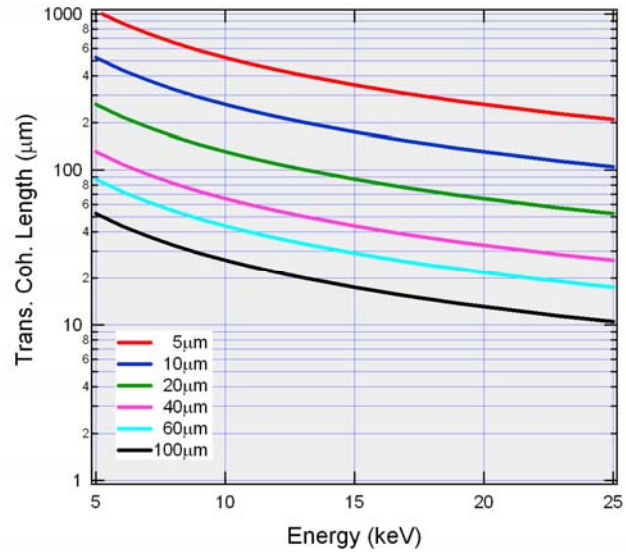

Figure 2.4.8: Transverse coherence length as a function of secondary source aperture size in high-coherence mode. The expected secondary source size at 10keV, imaged by the focusing mirrors, is 9.5 um (vertical) and 94.1 um (horizontal) in FWHM. In order to prevent source motion, the secondary source aperture should not be opened more than the FWHM beam size. Consequently, the range of aperture sizes is rather limited in the vertical direction.

A practical criterion for coherent illumination is to ensure that the transverse coherence length is larger the lateral size of the nanofocusing optic. Figure 2.4.8 shows the FWHM transverse coherence length as a function of the size of the secondary source at z = 62 m. In order to achieve a diffraction limited focus size, a nanofocusing optic must

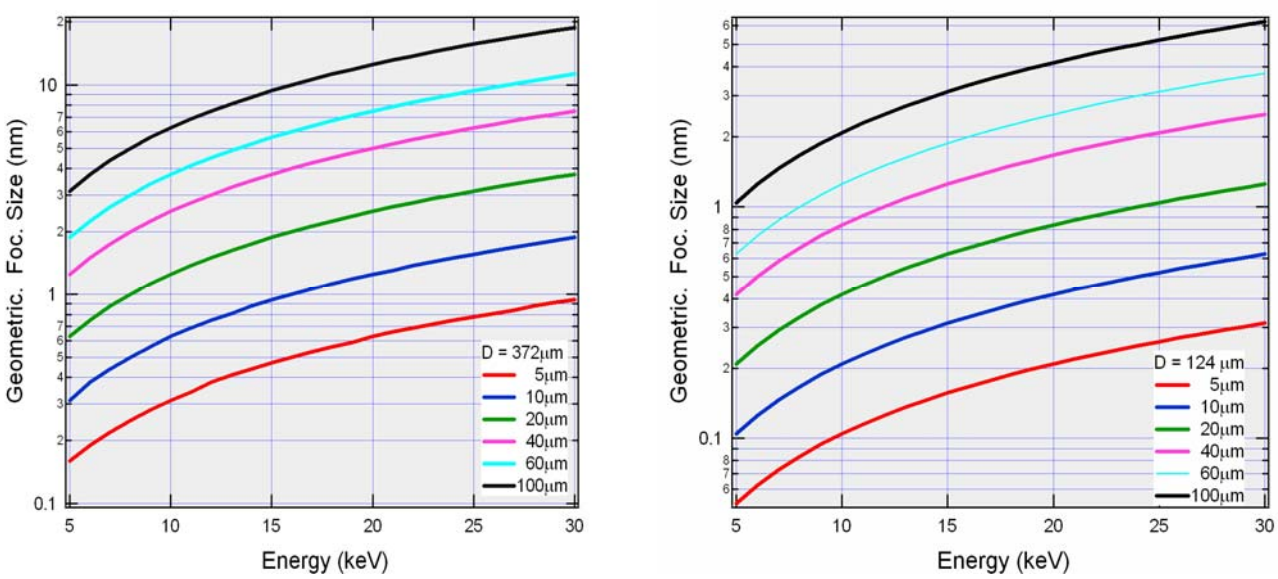

Figure 2.4.9: Expected geometric focus size based on demagnification of the secondary source size by the nanofocusing optic in high-coherence mode. Two cases are considered. A) MLL optic with a lateral dimension, D=372 μm and Δr =1nm (a focal length of 3 mm at 10keV) and B) D=124 μm and Δr =1nm (a focal length of 3mm at 10keV).

be illuminated coherently. At 10 keV, an aperture size from 5 to 100 μm produces a transverse coherence length from 500 to 25μm, respectively. However, in the vertical direction, the range of the transverse coherence length is

limited to between 250 to 500 μm, because the secondary source size is quite small in the vertical direction. Since the transverse coherence length is linear with the x-ray wavelength, the expected transverse coherence length is reduced by 50% for the same aperture size at 20 keV. A large transverse coherence length up to 500 μm is ideal for nanofocusing optics with a large lateral dimension. For example, a pair of KB mirrors with a sufficiently large working distance could be accommodated. However, for other types of nanofocusing optics such as MLLs and FZPs, fabricating a large lateral dimension is technically challenging. For example, fabricating MLL optics with a size larger than 100 μm has not been achieved, yet. The current goal of the NSLS-II 1nm x-ray optics R&D is to achieve a lateral dimension of 100~150 μm. Therefore, a considerable fraction of the coherent flux would be wasted in the vertical direction if the lateral size of MLLs or FZP is less than 250 μm.

To ensure that the proposed optical scheme can provide sufficient conditions for a 1nm focal spot, expected geometrical focal sizes are calculated for two hypothetical cases: for a MLL optic with a lateral dimension D=374 μm with the outmost zone width Δr=1nm, and for a MLL optic with D=124 μm and Δr=1nm. At 10 keV, the first MLL optic has a focal length of 3 mm, and the second optic, 1 mm. The two plots in Figure 2.4.9 show the estimated geometric focus sizes based on the demagnification factors considering a 46m-distance from the secondary source to the nanofocusing optics and their energy-dependent focal lengths. For a MLL optic with D=374 μm, a SSA size of 5 μm meets the necessary condition to achieve a 1nm focus size over the operational energy range of the HXN beamline. A SSA size of 10 μm meets the requirement up to 15 keV. For a MLL optic. In summary, the high-coherence mode can deliver a transverse coherence length up to 500 μm at 10 keV. In with D=124 μm, the 1nm requirement is met for 5~40 μm SSA sizes over most of the operating energies. The same conclusion is also valid for other nanofocusing optics.

In summary, the high-coherence mode can deliver a transverse coherence length up to 500 μm at 10 keV. In addition, it provides sufficient source-demagnification for 1nm focusing, for a nanofocusing optic with a lateral size of up to ~400 μm over the entire operational energy range. On the other hand, this mode can lead to loss of coherent flux if the size of the optic is smaller than ~250 μm.

High-Throughput Mode

In the high-throughput mode, the primary source is imaged in front of SSA2 located at z = 94 m, with a magnification factor of 1.76 in the vertical direction and 1.93 in the horizontal direction. Consequently, the expected secondary source size is 21.1 and 193.9 μm in the vertical and horizontal directions, respectively. With only a 14m distance from the secondary source to the nanofocusing optic, the transverse coherence lengths produced in this optical scheme are much smaller than those in high-coherence mode. Figure 2.4.10 shows the achievable transverse coherence length as a function of the secondary source aperture size. With an aperture size of 10 μm, the transverse coherence length at the plane of the nanofocusing optic is 75 μm at 10 keV. With an aperture size of 5 μm, a transverse coherence length of 150 μm can be achieved at 10 keV. Consequently, a small nanofocusing optic (<150 μm) can be coherently illuminated in this mode.

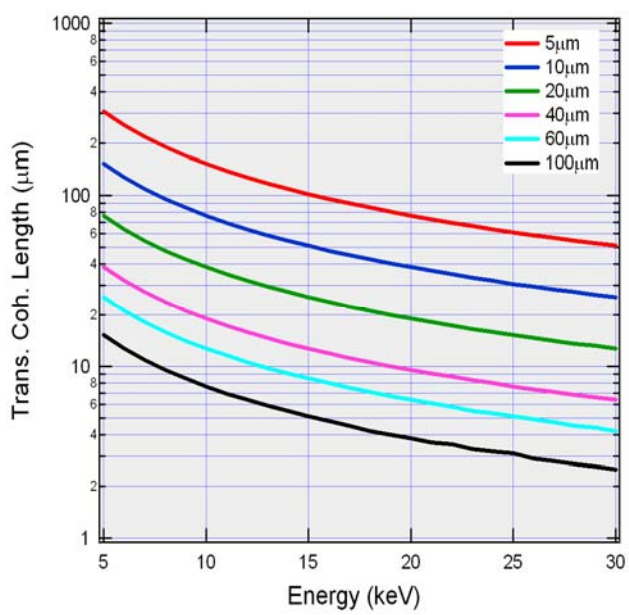

Figure 2.4.10: Transverse coherence length as a function of secondary source aperture size and x-ray energy in high-throughput mode.

The greatest utility of this mode is to achieve higher integrated flux over the focus spot by relaxing the diffraction-limited condition. In this way, spatial resolution can be traded with flux conveniently without moving the nanofocusing optic. Since the vertical size of the secondary source is 21.1μm, the range of the vertical aperture size is wider than in high-coherence mode.

Astigmatic High-Coherence Mode

In astigmatic high-coherence mode, the vertical mirrors are moved out of the beam, so that the nanofocusing optic is looking at the primary source in the vertical direction. The horizontal mirrors are still in place, creating a secondary source in front of SSA1 at 62 m from the primary source. The vertical transverse length at 10 keV is 508 μm, good for a large-size nanofocusing optic. With the vertical mirrors out of the beam, there is no optical element in the vertical direction. The source stability is unaffected, to the first degree, by the thermal drift or mechanical vibration of the beamline optics. Since the distance from the source to the nanofocusing optic is drastically different between the vertical and horizontal direction, this mode is not suited for FZPs. This mode is best utilized by a pair of KB mirrors. Unlike the MLLs, two KB mirrors must be separated by at least the length of the mirror, so that the horizontal and vertical focal lengths can differ by almost a factor of two if the same mirror length is used.
In the astigmatic high-coherence mode, the source-to-optic distance differs by almost a factor of two between the horizontal and vertical direction, providing a natural fit to nanofocusing KB mirrors. Since running the beamline in astigmatic high-coherence mode requires adjustment of the vertical position of both SSA2 and the HXN microscope, switching over to this mode of operation cannot be carried out as routinely as switching between the other two modes.

Implementing high-resolution MLLs with sufficient lateral sizes (for example, D>30μm and Δr=1nm, or D>150μm and Δr=5nm) requires a high resolution monochromator with a smaller energy band than that of the Si(111) monochromator, in order to satisfy monochromaticity requirements. A high resolution monochromator with a smaller angular acceptance can be accommodated without significant flux loss if the vertically focusing mirror, M3, is used to collimate the x-ray beam vertically. This is a variation of the astigmatic high-coherence mode described above but with M3 and M4 still in the beam. In addition, the vertical collimation helps minimize significant overfilling of the vertical transverse coherence length onto the MLL optics, in case the size of the MLL is moderately large (D~100μm). Since implementation of this mode of operation will take place after significant advance in the 1nm optics R&D, this CDR report will not elaborate further, other than stating that the current conceptual design accommodates the use of high resolution MLLs without significant flux loss. Table 2.4.1 summarizes all three possible modes of the operation:

Table 2.4.1. Summary of Three Possible Operational Modes.

Operation Modes	Source Position		Optical Components Used	Applications
	Hor.	Vert.		
High-coherence	z=6 m	z=62 m	M1, M2, M3, M4, SSA1	Diffraction-limited focusing of MLL, FZP, Kinoform or KB of lateral size up to 500 μm.
High throughput	z=94 m	z=94 m	M1, M2, M3, M4, SSA2	Diffraction-limited focusing of small (<150um) MLL or partially-coherent illumination of larger MLLs or ZP for higher focused flux.
Astigmatic high-coherence	z=62 m	z=0 m	M1, M2, SSA1	Diffraction-limited focusing of KBs with a maximum working distance.

Expected Optical Performance

Previous subsections elaborated on how to configure the HXN optical components to manipulate the transverse coherence length to match the lateral size of a nanofocusing optic that will be used for x-ray microscopy experiments. When the FWHM transverse coherence is exactly matched to a lateral dimension of a nanofocusing optic, the focusing optic accepts 76% of the coherent flux present at the plane of the focusing optic. 76% corresponds to the integral of a Gaussian curve over its FWHM. Under this condition, a nanofocusing system consisting of two linear optics such as MLLs or KBs accepts 57.9% of the available coherent flux. If the nanofocusing optic is smaller than the transverse coherence length, it accepts a smaller fraction of the coherent flux. For example, in high-coherence mode, a MLL with a lateral size of 100 μm is placed in the beam at z=108 m; the horizontal coherence length can be matched by adjusting the horizontal size of the SSA. However, in the vertical direction, the secondary source size is already much smaller than the required aperture size. Consequently, a sizable fraction of the coherent flux cannot be accepted by the nanofocusing optic. Table 2.4.2 summarizes the fraction of the coherent flux that can be accepted by nanofocusing optics with different lateral sizes.

Table 2.4.2. Fraction of the Coherent Flux Accepted by Nanofocusing Optics.

	High-Coherence Mode				High-Throughput Mode			
	at 10 keV		at 20 keV		at 10 keV		at 20 keV	
Size of focusing optic (μm)	% coh. flux accepted by focusing optic	Required SSA size (μm)	% coh. flux accepted by focusing optic	Required SSA size (μm)	% coh. flux accepted by focusing optic	Required SSA size (μm)	% coh. flux accepted by focusing optic	Required SSA size (μm)
50	13.9	50.2	27.0	25.1	57.9	13.1	62.3	6.5
100	27.0	25.1	48.9	12.5	57.9	6.5	63.3	3.2
150	38.8	16.7	57.9	8.4	57.9	4.4	57.9	2.2
200	48.9	12.5	57.9	6.3	57.9	2.2	57.9	1.6
300	57.9	8.3	57.9	4.2	57.9	2.5	57.9	1.1
400	57.9	6.3	57.9	3.1	57.9	1.6	57.9	0.8
500	57.9	5.0	57.9	2.5	57.9	1.3	57.9	0.7

The required SSA size matches the FWHM transverse coherence length to the lateral size of the nanofocusing optic. This will serve as a reference point for designing an experiment. In practice, the size of the SSA can be smaller or larger, depending on the need for more flux or more coherent illumination. In high-coherence mode, a monotonic decrease in the fraction of the accepted coherent flux with decreasing size of the nanofocusing optic is due to the fact that the vertical SSA cannot be opened further. In other words, the nanofocusing optic is becoming over coherently illuminated. The cases, requiring a SSA size less than 5 μm, are marked in light gray, indicating that these values may be hard to achieve. The feasibility to maintain aperture sizes below 5 μm needs to be explored during the beamline commissioning period. In high-throughput mode, nanofocusing optics with sizes larger than 150 μm are not feasible to use because the FWHM vertical source divergence is less than the angular size of the optics, leading to non-uniform illumination of the focusing optic.

It is important to note that all the calculations shown so far are based on ideal beamline optics free from figure errors. Since all x-ray mirrors have figure errors, the effect of figure errors must be pointed out. In the first approximation, the figure errors broaden the effective size of the secondary source. Since the vertical source size is more than 8 times smaller than the horizontal source size, the effect of figure errors is much more pronounced in the vertical direction. For example, in high-coherence mode, a combined 0.2 μrad figure error results in 50% broadening of the secondary source size in the vertical direction. On the other hand, the same figure error results in less than 1% broadening in the horizontal direction. Figure errors on the x-ray mirror are not likely to produce smooth intensity broadening of the secondary source. Consequently, the broadening of the secondary source size does not immediately translate in the ability to open up the secondary source aperture size. In this case, the secondary source aperture also works as a spatial filter to cut out the irregular part of the beam.

The broadening of the secondary source size due to the figure error results in the loss of the integrated flux through the secondary source aperture because some of the x-rays are channelled away from the central optical axis. Figure 2.4.11 shows the fraction of the flux loss due to the combined figure error in the case when the secondary source aperture is set at 10 μm. In this estimation, the Gaussian distribution is used for the secondary source broadening due to the figure errors, and the intensity loss in the central optical axis was calculated. The total figure error is the combined figure errors for the two mirrors in each direction. For the horizontal direction, a total figure error of 1μrad results in less than 10% loss of the integrated flux. On the other hand, in the vertical direction a total figure error of 1μrad leads to about 60% loss of the flux, utilized by the nanofocusing optic. This estimate provides specifications on the figure error limit on the vertical mirrors. For example, a figure error less than 0.2 μrad is required to prevent the flux loss less than 20%.

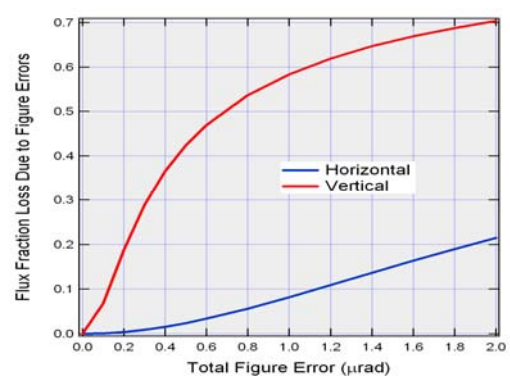

Figure 2.4.11: Effect of figure error. The fraction of the flux used for nanofocusing diminishes with increasing figure error from the beamline mirrors. The estimation shows the reduction of the integrated flux through 10 μm secondary source aperture as a function of the total figure error. The total figure error is the combined figure error due to all the mirrors in each direction. The effect of figure errors is much more dramatic for the vertical direction because the vertical source size is more than 8 times smaller than the horizontal source size. The relative impact is much larger even with

2.5 High Heatload Optics

Based on the design of the beamline optics, the power delivered to, transmitted from, and absorbed in a few key high heatload components is listed below. The calculation for the power distribution was carried out for K=1.83 corresponding to the minimum undulator gap of 5 mm and the fundamental undulator photon energy of ~1.6 keV, the condition generating the highest power output.

Table 2.5.1: Power on High Heatload Optics

Beamline component	Incident aperture size μrad (H x V)	Power delivered	Power absorbed	Power transmitted	Notes
Fixed mask	Unrestricted	~8kW	~2.4kW	~5.6kW	In the front end
White beam slits	500 x 300	~5.6kW	~5.42kW	180W	In the front end. Using an absorber can lower the incident power to M1.
Hor. col. mirror (M1)	80 x 40	180W	137W (Si) 68W (Rh) 27 W(Pt)	43W (Si) 112W(Rh) 153W(Pt)	2.7mrad incidence angle and Si, Rh, and Pt reflective surfaces. Pt coating reflects the highest power.
Si(111) mono (DCM1)	60 x 30	94W	94W	~0 W	153W is reduced to 94W by the pink beam slits (S2).

As summarized above, the power generated from the IVU20 undulator is significant but not unmanageable. By implementing incremental power reduction using the fixed mask and white beam slits, the total power delivered to the horizontal collimating mirror (M1) is about 180 W. This is an amount of power comparable to the APS undulator beamlines. The highest power loading condition for the mirror is at energies less than 11 keV, where a Si surface is used for harmonic rejection, leading to an estimated absorbed power of 137 W. On the other hand, the monochromator is exposed to the highest delivered power at energies above 23 keV, where a Pt surface is used for harmonic rejection. The illuminated aperture of the monochromator will be made smaller to reduce the delivered power to the monochromator and to reject the x-rays reflected from the region of the mirror with a high temperature gradient (i.e., edge of the beam). With an incident aperture of 60 x 30 μrad onto the monochromator, the maximum delivered power is 94 W.

Since ensuring proper management of the delivered power to the monochromator is of the utmost importance, finite element analysis (FEA) studies have been performed to quantify the amount of slope error induced by the incident x-rays. This conceptual design report summarizes the key finding in the FEA analysis. The FEA model was carried out using the following parameters:

- A Si(111) crystal, 50 mm long, 30 mm wide and 20 mm thick
- A horizontal diffraction geometry with an incidence angle of 14.04˚ corresponding the Bragg energy of 8.15 keV
- Cryogenically cooled with LN2 at 77K with a side cooling geometry with effective convection film coefficient values h_{conv}= 0.003 W/mm^2/K and h_{conv}= 0.005 W/mm^2/K, representing different effectiveness of thermal contact
- Power density corresponding to K=1.83, reflected from a Pt coating, which corresponds to the worst-case scenario in terms of delivered power density to the monochromator. This condition is met only at 24 keV but with an incidence angle of 9.48˚, resulting in 66% of the surface power density of the simulated condition

Three different angular aperture sizes were used to study the induced slope error as a function of different amounts of delivered power. The results of the FEA model are summarized in Table 2.5.1.

Table 2.5.2. Results of the FEA Analysis on horizontally diffracting Si(111) monochromator (DCM1).

Simulation #	Angular aperture H x V (μrad^2)	Power delivered	h_{conv} (W/mm^2)	Peak temp.	Min temp.	Induced slope error
1	44.4 x 22.2	53 W	0.003	98.9 K	86.5 K	4 μrad
2	66.6 x 33.3	105 W	0.003	116.5 K	95.5 K	1.2 μrad
3	88.8 x 44.4	201 W	0.003	150.0 K	109.0 K	36 μrad
4	44.2 x 22.2	53 W	0.005	94 K	82.6 K	4.6 μrad
5	66.6 x 33.3	105 W	0.005	105.8 K	88.05 K	4.8 μrad
6	88.8 x 44.4	201 W	0.005	127 K	96.1 K	4.8 μrad

As the incident energy decreases toward 6 keV, the increase in the Bragg angle is compensated by the decrease in the power density from the undulator. As the energy increases from 10 keV, the incidence angle decreases so that the power density on the surface decreases. Thus, the simulation shown here represents the worst case in terms of the power density on the monochromator surface. In all cases, a higher h_{conv} value leads to a lower peak temperature, indicating that more effective thermal contact leads to more efficient cooling. For a fixed h_{conv} value, a higher delivered power results in a higher peak temperature at the center of the beam footprint on the crystal, as expected. However, the induced slope error does not exhibit a linear relationship with respect to the delivered power or the peak temperature. This nonlinear behavior is due to the nonlinear thermal expansion coefficient of Si with temperature. In particular, near 120K, the thermal expansion coefficient of Si becomes zero. This is why simulation #6 (201W of power resulting in the peak temperature 127 K) produced the same slope error as simulation #5 (105 W of power resulting in the peak temperature 105.8 K). With the exception of simulation #3, all five cases resulted in a thermally induced slope error of less than 5 μrad. At 8 keV, the Darwin width of the Si(111) is 26.4 μrad, and a slope error less than 5 μrad is acceptable. During the actual operation of the HXN beamline, the power to the monochromator will not exceed 100 W.

Since the horizontally collimating mirror (M1) upstream of the Si(111) monochromator (DCM1) has a dynamic bending capability, it could be feasible to compensate the induced slope error on the monochromator and the collimating mirror itself by controlling the bending curvature of the collimating mirror. The practicality of this idea will be extensively explored during the commissioning of the beamline.

In the HXN conceptual design, the primary high heatload optics (the mirror and monochromator) are placed in the horizontal reflection/diffraction geometry. As mentioned in section 2.4, the optical performance degradation due to the figure errors is much less pronounced in the horizontal direction. Thus, the overall impact of the thermally

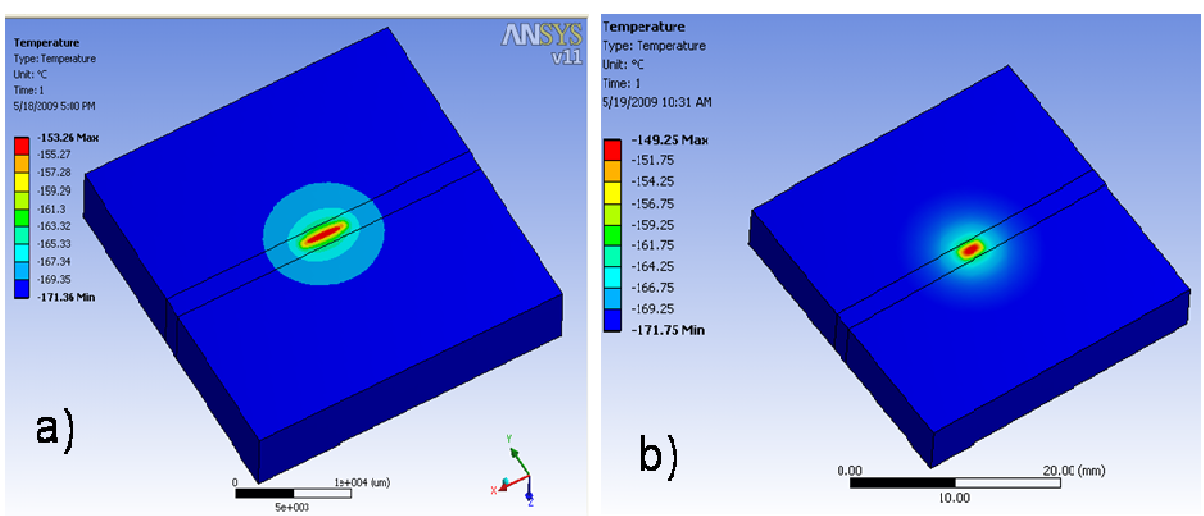

Figure 2.5.1: Comparison of the FEA simulated temperature distributions on the Si monochromator crystal placed in a) horizontal diffraction geometry and b) vertical diffraction geometry. With the identical incident angle, the horizontal diffraction geometry leads to a lower surface power density and consequently a lower peak temperature.

induced figure error is reduced by implementing a horizontal geometry. In addition, placing the high heatload optics in the horizontal geometry also results in reduction of the power density on the surface of the mirror and monochromator. Figure 2.5.1 shows the temperature distribution on a Si monochromator surface in two different diffraction geometries but under identical normal incident power. Because of the inherent asymmetry of the undulator source along the horizontal and vertical directions, the spread of the incident power density in the horizontal diffraction geometry leads to a lower power density on the surface, resulting in a lower peak temperature. For example, the FEA simulations shown in Figure 2.5.1 predicted a difference of 4 K in the peak temperature between the two cases.

In summary, the HXN utilizes incremental power management from the fixed mask to the monochromator. The initial FEA analysis indicates that the thermally induced slope error is less than 5 μrad. The FEA analysis also demonstrates that the horizontal diffraction geometry results in a smaller power density on the crystal surface. This conclusion is also applicable to the high heatload mirror.

2.6 List of Major Components

The major beamline components, along with their distance from the source, are listed in Tables 2.6.1 through 2.6.4. The HXN beamline plans to use the X–Y slits in the front end as its white beam slits. A more complete list is provided in section 8 (Appendix 2) of this report.

Table 2.6.1. Front End Components Used by the HXN Beamline.

Description	Symbol	Z (m)	Notes
White Beam Slits	S1	16.4	To limit the white beam onto M1

Table 2.6.2. Major Components in the HXN FOE. (Ratchet wall ends at 25.5 m. FOE ends at z=40.0 m.)

Description	Symbol	Z (m)	Notes
Aperture Plate	AP	25.7	~5 mm circular aperture to prevent accidental power overload to BL optics.
Diagnostic Chamber	DC1	25.9	for BL diagnostic
White Beam Filters	WBF	26.3	to provide different combination of x-ray absorbers
Be window	BW1	26.6	to isolate BL vacuum from FE
Horizontal Collimating Mirror	M1	27.5	water-cooled
Bremsstrahlung Collimator	CO	28.6	BL safety component
Pink Beam Slits	S2	29.0	to define incident illumination onto DCM1
Pink Beam Screen Monitor	PBSM	29.2	for BL diagnostic
Horizontal Double Crystal Monochromator	DCM1	30.2	Si(111), LN2-cooled
White beam Stop	WBS	30.7	placed outside of DCM1
Diagnostic Chamber	DC2	30.9	for BL diagnostic
Horizontal Focusing Mirror	M2	32.1	
Mono Beam Position Monitor	BPM1	33.3	parasitic beam position monitor
Vertical Focusing Mirror	M3	34.1	
Vertical Flat Mirror	M4	35.4	
Bremsstrahlung Stop	BS	36.3	BL safety component
Mono Beam Position Monitor	BPM2	36.8	parasitic beam position monitor
Mono Beam Shutter	MS1	39.5	BL safety component

Table 2.6.3. Major Beamline Components in the Monochromatic Hutch of the HXN Beamline.

Description	Symbol	Z (m)	Notes
Be window	BW2	58.0	to allow diagnostic experiments in the mono hutch
Be window	BW3	61.0	to allow diagnostic experiments in the mono hutch
Mono Beam Position Monitor	BPM3	61.3	parasitic beam position monitor
Secondary Source Aperture	SSA1	62.0	to define the secondary source size
Mono Beam Shutter	MS2	64.2	BL safety component

Table 2.6.4. Major Beamline Components in the HXN Endstation.

Description	Symbol	Z (m)	Notes
Mono Beam Position Monitor	BPM4	93.4	parasitic beam position monitor
Secondary Source Aperture	SSA2	94.0	to define the secondary source size
High-Resolution Monochromator	DCM2	95.0	To satisfy the monochromaticity condition for nanofocusing optic. To be installed in the mature phase.
Be Window	BW4	95.5	
HXN Microscope		108.0	The position of the focusing optic for the HXN Microscope

2.7 Summary of Beamline Performance Specifications

Spatial resolution

From 30nm down to the achievable resolution limit using a scanning x-ray microscopy. The ultimate spatial resolution is ~1nm.

Compatibility of different types of nanofocusing optics

Three different possible modes of operation ensure compatibility of all nanofocusing optics. At 10 keV, an aperture size up to 500 μm can be coherently illuminated using monochromatic x-rays.

X-ray energy range

From 6 keV to 25 keV. The lower energy range is limited by the horizontal polarization of the incident beam and the horizontal monochromator. The upper energy is tentative and will depend on the length and offset of the monochromator.

Techniques supported

- X-ray fluorescence
- Nanodiffraction
- Coherent diffraction imaging
- Differential phase-contrast imaging

Expected beamline efficiency through mirrors and monochromator

Approximately 50% for 8-22 keV

Targeted figure errors on mirrors

Vertical: less than 0.20 μrad through both mirrors, M3 and M4
Horizontal: less than 1.0 μrad through both mirrors, M1 and M2
Achieving figure below 0.5μrad is non-trivial and require intimate collaboration with the vendors.

Requirement on the slope error on monochromator induced by the power of the incident beam

Less than 20% of the Si(111) Darwin width at all energies

Targetted Beamline stability

The beam positioning feedback system must prevent loss of the intensity and the drift of the focused beam. The angular stability of the beam with an accuracy of 0.2 μrad or better is desired. The experimental methods for accurate beam positioning monitoring need to be developed during the commissioning period of the beamline.

Proposed utilization of coherent flux

Better than 50% of the coherent flux available from the source after accounting for the beamline efficiency and additional x-ray transmission due to the windows or possible air and helium path.

3 ENDSTATION INSTRUMENTATION

The most important endstation instruments are the HXN microscope with detectors and the HXN prototype. Based on the latest DOE review and inputs from the BAT, the overall strategy for constructing the HXN microscope has been recently modified. The recommendation is to design and construct an HXN microscope that can be used to carry out scientific investigations on "day 1" of the HXN operation. The primary function of the HXN microscope is to enable state-of-the-art x-ray microscopy experiments with comprehensive integration of the control system and the detector. On the other hand, the HXN prototype will be developed with a much higher level of positioning specification, in order to accommodate x-ray microscopy experiments with the highest spatial resolution down to the ultimate goal of ~1 nm. From an instrumentation point of view, combining the two capabilities into a single instrument is highly impractical, resulting in potential risks for productive scientific experiments. The HXN prototype will be developed under the Nanopositioning R&D, by incorporating the lastest advances in nanopositioning, vibration damping and advanced control feedback. Detailed design of the prototype will be finalized by FY2012 and a prototype will be constructed by end of FY2012. However, achieving its ultimate performance with subnanometer accurac may require a longer-term development beyond the initial commissioning of the HXN beamline. One the other hand, the HXN microscope will probably be constructed by a vendor through intimate interaction with the HXN team. Tentative requirements of the HXN microscope are listed below.

3.1 Key Requirements of the HXN Microscope

- Spatial resolution: from 30nm~10 nm
- The supported spatial resolution dictates not only the choices of the nanofocusing optics but also the accuracy of the positioning system. The current state-of-the-art x-ray microscopes have a positioning stability of 2~5 nm (rms). In order to accommodate the spatial resolution 30~10 nm, the HXN microscope requires a positioning/scanning accuracy of 1~2 nm.
- Short and longer term positioning stability: The HXN microscope is required to have short-term (~a few hours) and longer-term (~days) stability using close-loop differential positioning feedback between the optics and the sample.
- Fly-scan capability: A conventional method of "move, stop, and measure" imposes significant measurement overhead, because of the settling time required to stabilize on the final position with accuracy. The measurement should be carried out continuously while the sample is being scanned by adequate "hand-shake control" between the motion controller and the detectors.
- Supported techniques: x-ray fluorescence, nanodiffraction, coherent diffraction imaging, and differential phase-contrast imaging. Nanodiffraction requires a minimum of one rotation with the axial run-out error less than 1 μm.
- Supported nanofocusing optics: MLLs, FZPs, Kinoforms, and KBs. To date, the microscopes with the highest positioning/scanning performance are designed for FZPs. MLLs and KBs require a larger number of degrees of freedom for alignment. The requirement for short-format Kinoforms is similar to FZP. These optics also have different requirements for a beam stop and order-sorting aperture, and working distance from the optics to the sample. The HXN microscope requires different interchangeable optic modules to accommodate these different requirements.
- Sample environment: Materials science applications require the ability to control the temperature and atmosphere. Soft materials require cryostats to reduce the level of radiation damage. The ability to maintain and control temperatures from ~ –150˚C to ~300˚C is required.

Meeting all of the above requirements is extremely challenging. The final set of requirements will be determined through interaction with potential vendors and the scientific priorities set by the HXN BAT.

3.2 HXN Detectors

The HXN experiments require multiple detectors: an XRF detector for elemental mapping, a 2D area detector for coherent diffraction imaging and differential phase contrast, a 2D area detector for nanodiffraction, and a high-resolution (lens-coupled, ~1μm resolution) CCD detector. A multi-element silicon drift diode (SDD) detector (i.e. multi-element Vortex) is commercially avaialbe. As a commercial option, a direct detection CCD can be used for coherent diffraction imaging and nanodiffraction.

The experiments at the HXN beamline can be significantly benefited by advanced x-ray detectors that are currently being developed. Dr. Peter Siddons and his team at BNL have developed the MAIA detector for high-throughput fluorescence measurement. This detector could be a candidate for the XRF detector of the HXN. Integrating this detector with the HXN microscope requires engineering efforts, working with a potential vendor for the HXN microscope. In order to implement ptychography-based coherent diffraction imaging with fluorescence mapping, a fast forward-direction detector must be used. This detector should have a minimum of 256x256 elements with ~200 μm pixel size with the same timing response as the MAIA detector, in order for them to be used together. Development of such a detector requires close collaboration with Dr. Siddons' group. Nanodiffraction experiments can be best benefited by a pixel array detector with ~1k x 1k pixels with a pixel size of ~150 μm or smaller with a large dynamic range ($>10^4$) and a fast readout time (<10 ms) rather than a CCD detector.

4 SPECIAL BEAMLINE REQUIREMENTS

4.1 Satellite Building and Endstation

The most important requirement of the HXN beamline is the remote satellite building to house the HXN endstation, designed and constructed to meet vibration and temperature stability adequate for maintaining a 1nm-sized x-ray beam over a period longer than 12 hours. Since such a facility has not been constructed before, the specifications of the endstation floor vibration, temperature stability, and acceptable acoustic noise level can only be inferred from the requirements of state-of- the-art electron microscopy facilities.

To help define the specifications and requirements for the HXN satellite building and the endstation, a workshop was held on June 29, 2009 with scientists, engineers, and architects from HDR (the architectural firm, contracted to build the NSLS-II LOB). The following primary requirements and specifications are currently under discussion.

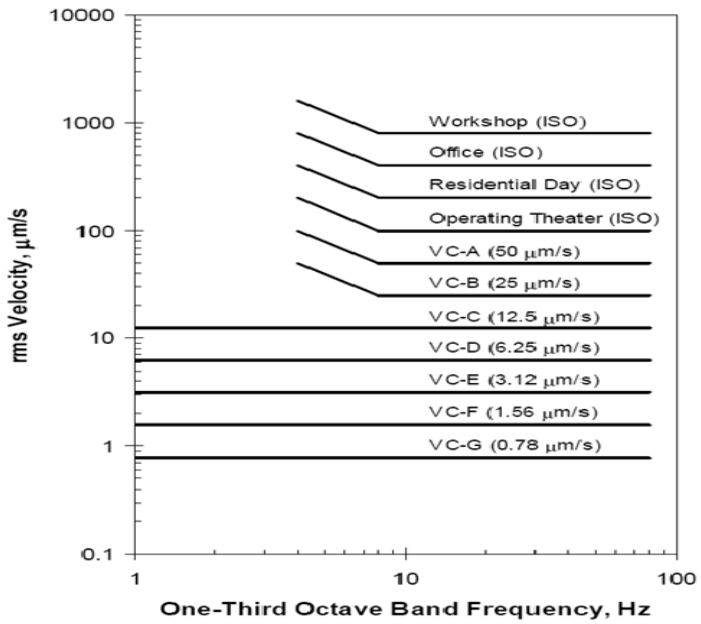

Figure 4.1: Various vibration specifications. Vibration criterion, VC-F, will be used as a vibration requirement for the HXN end-station floor.

1. The HXN satellite building must be physically isolated from the NSLS-II storage ring building and the nearby LOB.
2. The utilities (electricity, ventilation, water, and nitrogen gas) will be fed from the nearby LOB with careful consideration for vibration damping.
3. The external shell, wall, and roof structure are supported by an isolated footing structure, separated by the floor structure under the HXN endstation. The external shell and wall must have sufficient insulation to prevent temperature fluctuation of the interior due to temperature change from day to night and season to season.
4. The endstation must be constructed with a concrete wall of 8-inch thickness. The interior dimension of the endstation is 20 m long, 5 m wide, and 3.5 m high.
5. The electronic or mechanical equipment, generating acoustic vibration and heat, will be isolated from the user area and also the endstation on a separate floor structure.
6. To maximize the structural filtering of low frequency ground vibration, the user area and the endstation will share the same concrete floor. The concrete floor under the endstation will be 1 m thick. To prevent vibrations from the user area from reaching the HXN microscope, the user area will be covered with "CONCREDAMP," a concrete additive that damps vibration and noise. In addition, a small, narrow trench will be made around the outer wall of the endstation, to prevent surface vibration waves from traveling into the endstation.
7. The noise level within the endstation will be maintained at 40dBA or lower. The outer and interior wall of the endstation must be covered with acoustic damping materials. The water flow through the utility line will be regulated to meet the noise requirement.
8. Noisy or heat generating instruments will be enclosed within a water-cooled instrument rack.
9. The temperature in the user area will be maintained at 24°C ±1.0°C, at all times. The maximum temperature fluctuation over 1 hr period will be ±0.5°C. The temperature in the endstation will be 24±0.05°C. The maximum

temperature fluctuation over a 1-hr period will be ±0.02°C. A local area around the HXN microscope will be enclosed, in order to maintain higher degree of temperature stability.

10. An airlock door will be installed in order to minimize the air exchange in and out of the endstation from the user area.

More complete specifications for the satellite building can be found in Experimental Facilities **R**equirements, **S**pecifications and **I**nterfaces (RSI) document for the Hard X-ray Nanoprobe Beamline Satellite Building.

4.2 Data Transfer Rates

The HXN beamline will employ multiple detectors during the experiment. Up to 10 or more detectors can be used at the same time. The table below summarizes the estimated data production rate at the HXN beamline.

Table 4.1. Estimated Data Production Rate at the HXN Beamline.

Detector	Data production	Data rate
Multiple element energy dispersive detector	96 element operating at 100 Hz or higher	20 MB/sec
1k x 1k pixel array detector	4 MB at 100Hz	400 MB/sec
4k x 4k CCD detector	96 MB at 0.2Hz	19.2 MB/sec
Ion chambers and other 1D detectors	Insignificant	
beam position monitors	Insignificant	

APPENDIX 1: SCHEDULE

Construction of HXN Beamline

September	2009	Complete conceptual design report
September	2010	Complete preliminary design report
November	2010	Technical design – approval of long lead term procurement
January	2011	Start long lead time procurements (monochromator, mirrors, enclosures,…)
April	2011	Complete final design of beamline major components
February	2012	Complete final design report Approval of start of beamline construction - beneficial occupancy of experimental floor
February	2012	Start installation
April	2012	Start other procurements
May	2012	Start sub-system testing
November	2012	Complete long lead time procurements
August	2013	End procurement
August	2013	Start integrated testing
January	2014	Complete installation
February	2014	Complete sub-system testing
May	2014	Complete integrated testing – beamline available for commissioning
June	2015	**CD-4**, approve start of operations

Planned Tasks and Milestones for 1nm Spatial Resolution R&D

Since the conceptual design, construction, and operation of the HXN beamline are intimately connected by the outcome of the supporting R&D program, the conceptual design report summarizes planned key tasks and milestones. The dates associated with the specific tasks and milestone could change due to the unforseen technical challenges.

- MLL deposition system fully commissioned: FY10 Q4
- First wedged MLL: middle of FY11 Q2
- First 100 μm-aperture MLL with through-center growth: FY12 Q3
- First 1nm MLL deposited: FY13 Q4
- First 1nm wedged MLL with 100 μm aperture: FY14 Q2
- MLL optimized for 8-10 keV: FY15 Q2
- Develop phase-retrieval methods for accurate determination of focused beam size (< 10 nm): FY10 Q4
- Develop a robust method to assemble two MLLs into a single optic: FY11 Q2~FY14 Q4

Planned Tasks and Milestones for Nanopositioning R&D

- Establish a formal joint work project with the APS for development of the HXN prototype instrument: started in Sept, 2009.
- Commence building up Nanopositioning Lab in BNL/building 703 in order to evaluate laser interferometers and nanopositioning devices: FY10 Q3
- Evaluate vibration damping options: FY11 Q4
- Reach a critical decision on the components of the HXN prototype: FY11 Q4
- Detailed design fo the HXN prototype instrument: FY12 Q1
- Construction of the HXN prototype instrument (initial configuration for further refinement): FY12 Q4
- Reach a critical procurement decision on the HXN microscope, including detailed specifications and capabilities, for construction by a vendor: FY12 Q1
- Installation and testing of the HXN microscope: FY14 Q3
- Commissioning of the HXN microscope: FY14 Q3~FY15Q3
- User experiments using the HXN microscope: FY15 Q2
- Continue 1nm R&D at the HXN beamline using the HXN prototype after the commissioning of the HXN beamline.

APPENDIX 2: CONSIDERATIONS FOR HXN BEAMLINE SITE

Memorandum

Date: March 12, 2010
To: S. Dierker, M. Fallier, Q. Shen
From: Nick Simos
Subject: NSLS-II Nanoprobe Beamline Location Optimization – Site Vibration Aspects

This memo/technical note summarizes the results of the studies conducted to quantify the ground vibration at the two potential locations of the nanoprobe endstation (attached to LOB-2 or to LOB-3) and makes recommendations as to which of the two locations is more favorable and why.

The evaluation of the position of the nanoprobe station was based on:

1. NSLS-II site ground vibration spatial variability (affected by operating systems over the BNL site such as NSLS, CFN, etc., traffic on site, and the effect of the Long Island Expressway)
2. The effect of heavy traffic on Brookhaven Avenue (what happens at the limit of moving loads such as a 20-ton truck traveling at 30 mph?).
3. The effect of NSLS-II service building operations and the contribution toward noise reaching the nanoprobe station

The assessment of these different sources, whose combined effect should provide a clear picture as to which location for the nanoprobe end station is most appropriate, is supported by extensive field tests and accompanied by large-scale mathematical models. In particular, to address the effect of "extreme" traffic in the vicinity of NSLS-II a dedicated field test was performed that utilized a 20-ton, 3-axle large truck traveling along Brookhaven Avenue at different speeds (30 mph and 15 mph). A specially designed model describing the large truck pass as a moving source with a complicated dynamic signature was introduced as the stimuli in the dynamic model. Successful matching of such moving loads has been demonstrated in the past by the author, where simulated data/predictions compared very well with actual data.

Results associated with the three major sources indicated above are listed in three separate sections, namely M.1, M.2 and M.3. The findings are summarized as follows:

Regarding the spatial variability of the background vibration over the NSLS-II site, LOB-3 position is more favorable. In particular it was found that the "local" noise consisting of operations on site (CFN, NSLS, etc.) and BNL traffic during the day has a significant contribution which more pronounced at the LOB-2 location. The LI Expressway effect is similar for both locations.

Regarding the "occasional" extreme effect of large trucks traveling on-site and near NSLS-II, it is demonstrated through field tests and the subsequent analytical effort that location LOB-3 will be immune to such traffic while the LOB-2 location will exceed its stability requirements for the period the load will be in the vicinity of NSLS-II. In particular, ground displacements in the excess of 300 nm will be felt at the LOB-2 location for a short period, while this value will be ~15 nm at LOB-3, indicating that it will barely be felt since it will blend with the background.

Regarding the NSLS-II service building operations, the effect will be both small and similar for both choices (LOB-2 or LOB-3), given the similarity in the layout and their relative position to the SB structures.

The bottom line, based on this extensive evaluation, is that the LOB-3 position of the nanoprobe station is a more favorable position than its LOB-2 counterpart, and it is recommended as the optimal location for the vibration-sensitive endstation.

Nicholas Simos, PhD, PE
NSLS II Project

M.1: NSLS-II Site Spatial Variability of Ground Vibration

To assess the differences that may exist at the two potential locations in terms of the background ground vibration, a series of measurements were performed on the footprint of the NSLS-II and in the surrounding space, especially in terms of the NSLS-II position with the Long Island Expressway (LIE). It is expected that over the NSLS-II footprint, and thus the nanoprobe locations, will exist spatial variability of the ground vibration. In other words the vibration field will not be uniform. The deviation is expected to vary depending on the time of day and the day of the week (i.e., weekday vs. weekend). This variability, which will have an impact on the nanoprobe endstation location, is primarily the result of noise sources within BNL (CFN, NSLS, and other nearby operations), traffic-borne vibration from within BNL, and the traffic-borne ground vibrations reaching the site from the LIE.

To quantify the effects, measurements were performed both at the NSLS-II site and on the space separating LIE from NSLS-II, aiming to establish attenuation characteristics. Figure M.2-1 shows the approximate locations where measurements were performed. S1 is approximately 200 ft from the LIE, S2 ~1000 ft, S3 ~2000 ft', and S4, ~2200 ft. Site station #5 was approximately situated where the nanoprobe station will be if it is to be placed by LOB-2. Refer to figures M.1-2, 3, and 4.

The important findings are the following. The LIE effect attenuates as one approaches the NSLS-II site. There it is the locally-borne traffic and other sources that affect the background noise at the site. This is clearly demonstrated by the spectra of Figures M.1-2 and M.1-3, where the cultural noise in mid-day increases on the site. Measurements at 5 a.m. on Sunday clearly eliminate the local effect. Given that the LOB-3 option moves the nanoprobe station further from the local sources, then it is safe to assess that the effect of the local sources will be less on LOB-3 option than the LOB-2 counterpart.

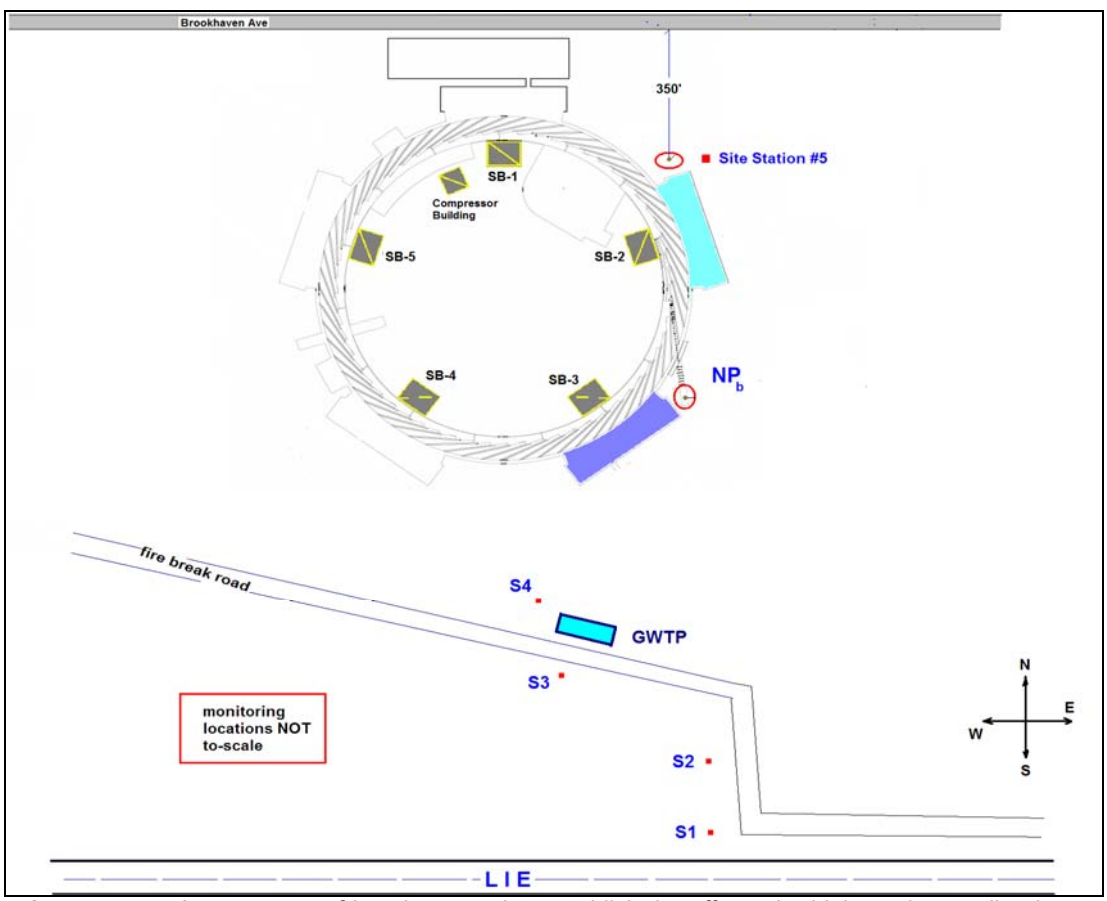

Figure M.1-1: Arrangement of locations used to establish the effects the highway borne-vibration at NSLS2 and the BNL site source contribution to NSLS2 site background noise

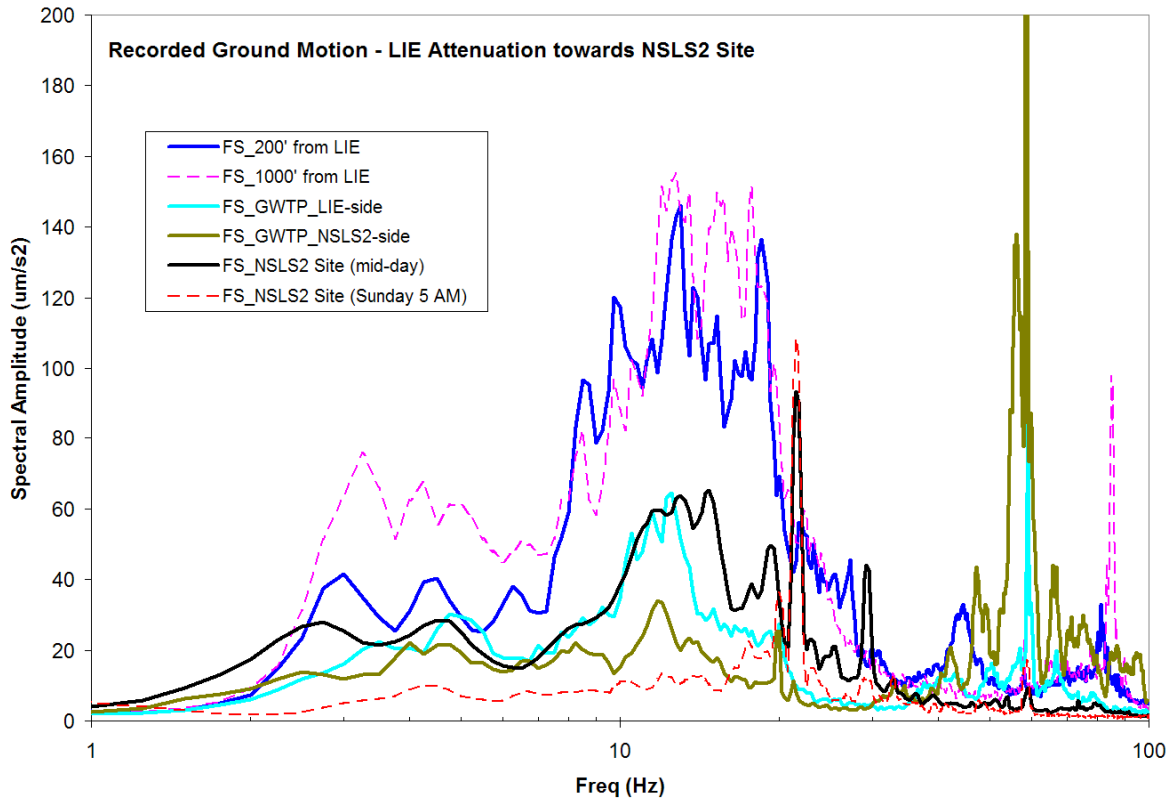

Figure M.1-2. Ground motion spectra over the different monitoring locations indicating the traffic-borne vibration (<12 Hz), as well as operating system signatures that exist in the proximity of the NSLS2 site.

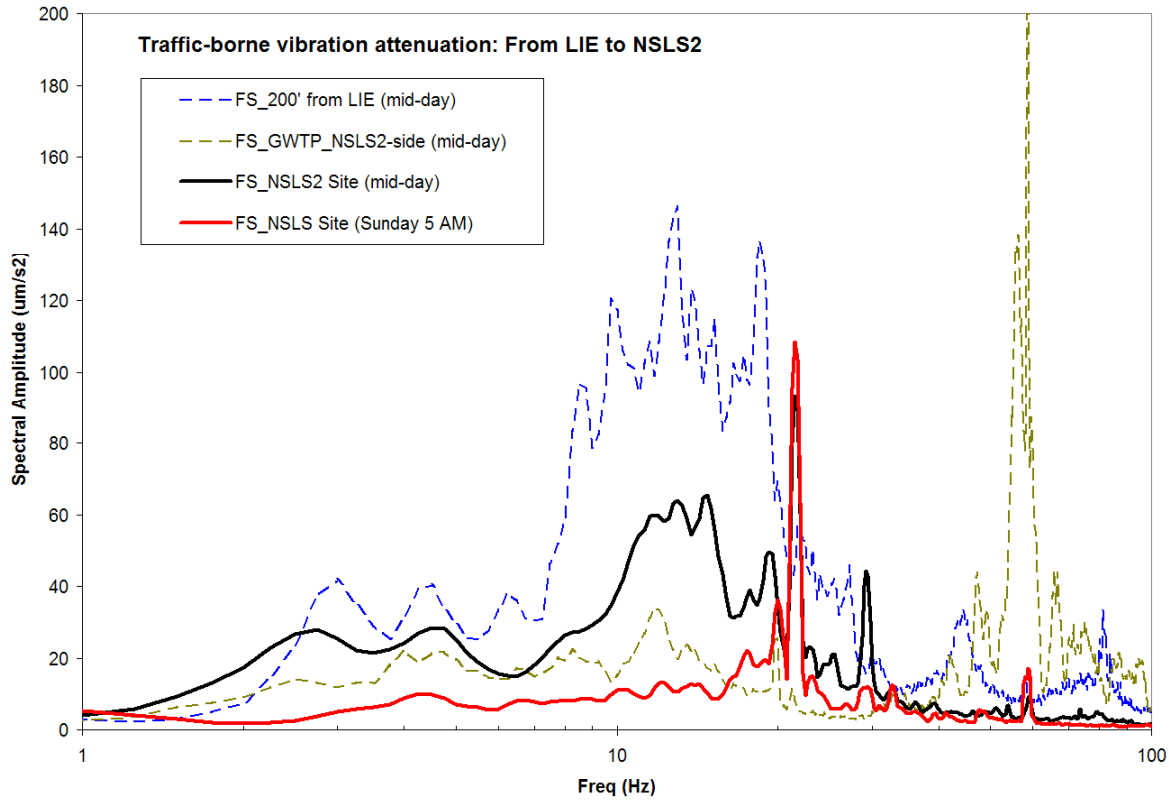

Figure M.1-3. Ground motion spectra depicting the effect of LIE and the local sources at NSLS2 site.

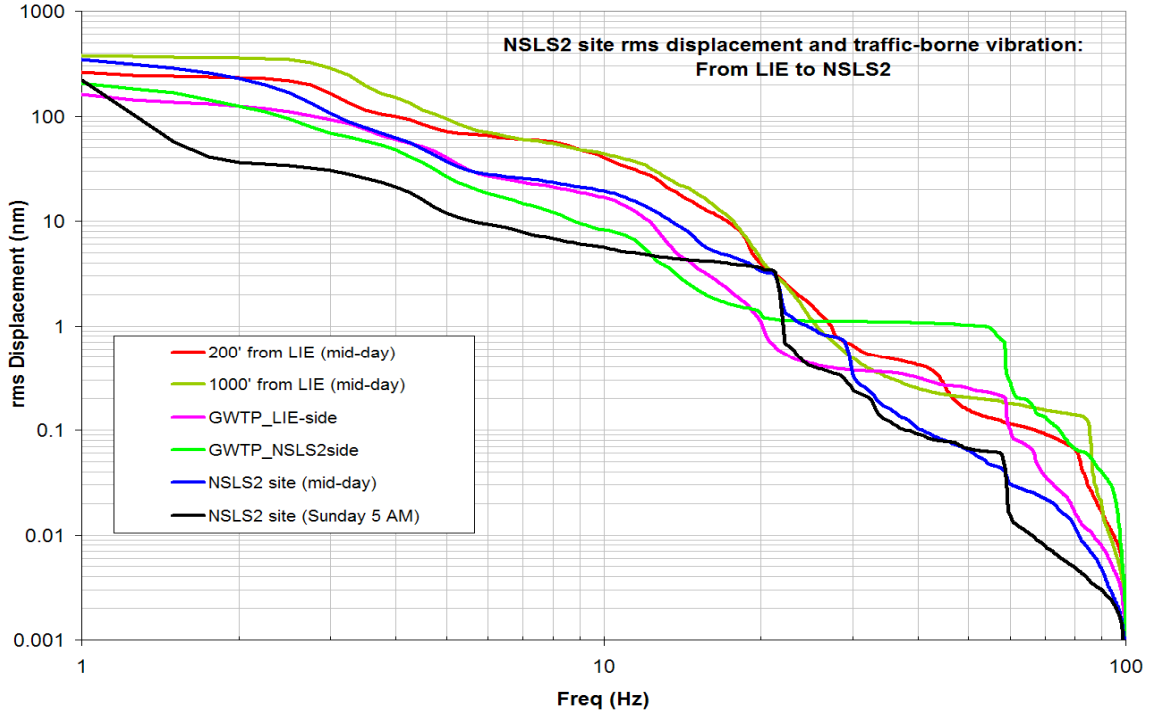

Figure M.1-4. Ground displacements (rms) at different locations relative to LIE and different times.

M.2 Field Test for "Extreme" Traffic on Brookhaven Ave. and Influence on Nanoprobe

To quantify the effect of an occasional extreme transient noise, such as a heavy truck traveling on the roads near the NSLS-II and in particular on Brookhaven Avenue, a field test was conducted. The aim was to assess the attenuation characteristics (or distance effects) of the induced ground vibration and to quantify the vibration levels that will be felt at different locations and in particular the two positions of the nanoprobe station being considered.

A 20-ton, 3-axle truck was used for the field test. The truck travelled several times on Brookhaven Avenue, as shown in Figure M.2-1, with velocities of 30 and 15 mph, and ground vibration records were captured at locations P1, P2, and P2. These ground accelerations were analyzed and the results were used in the assessment. Important to point out is that the monitoring location P3 is at approximately the same distance from Brookhaven Ave, as is the LOB-2 option for the nanoprobe (P3 is at 400 ft while LOB-2 option at ~350 ft). The LOB-3 option is ~990 ft from Brookhaven Avenue. No direct measurements were made at the LOB-3 location, since no monitoring stations existed at the vicinity. The field test records and the benchmarked numerical model were eventually used to extrapolate the effects on the LOB-3 location.

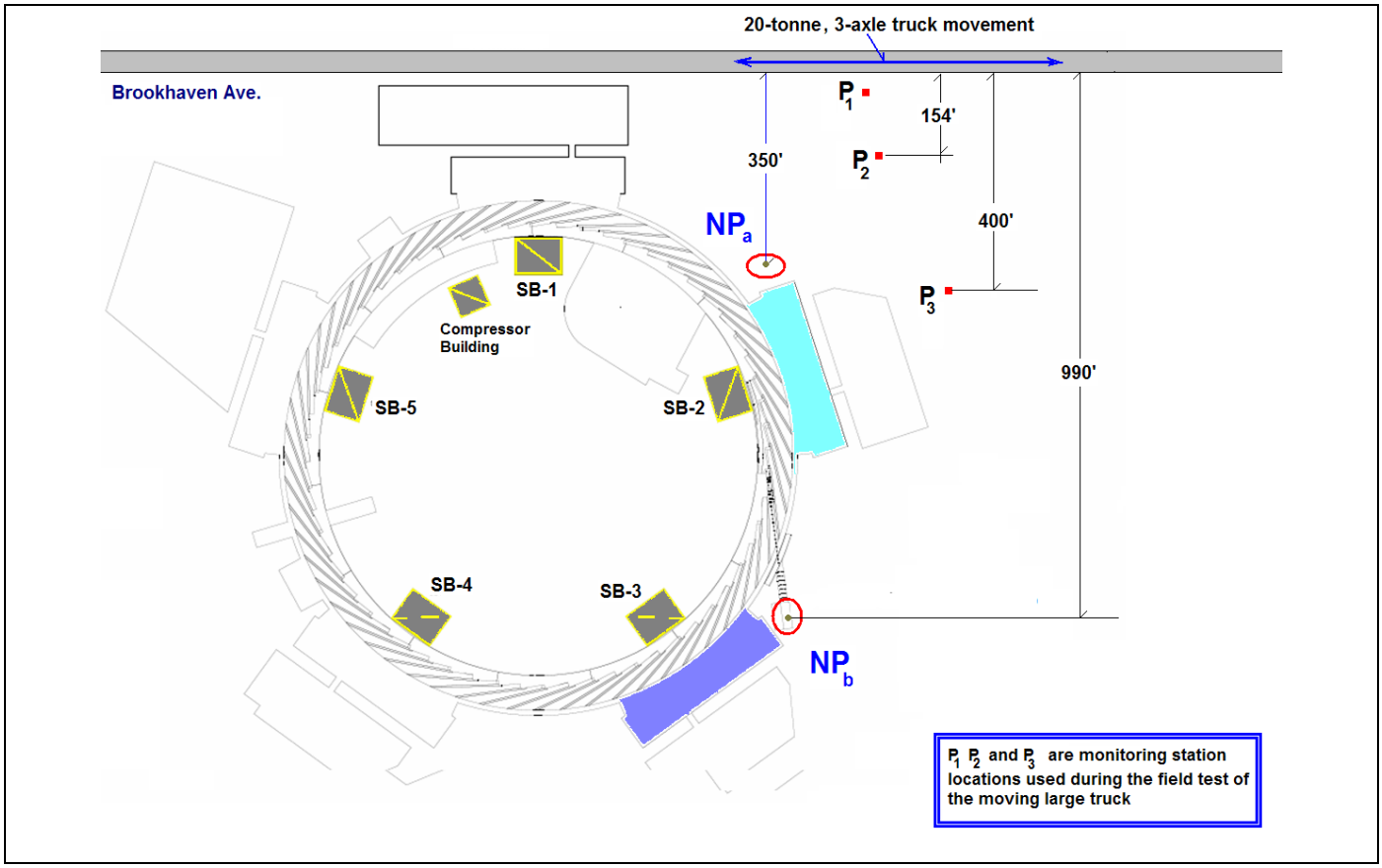

Figure M.2-1. Layout of the field test using a 20-ton moving truck and assessing the ground vibration at the NSLS-II.

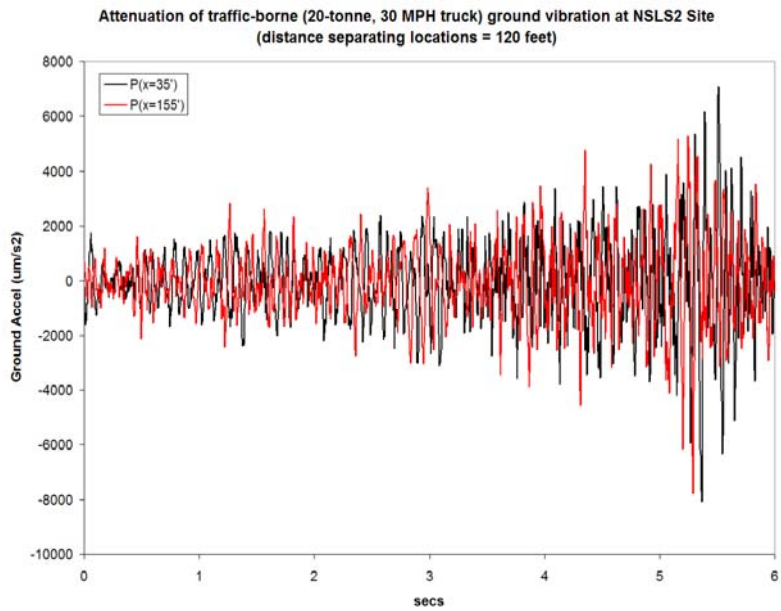

Figure M.2-2. Recorded ground motion depicting attenuation with distance of 120 ft (monitoring stations P1 and P2).

site.

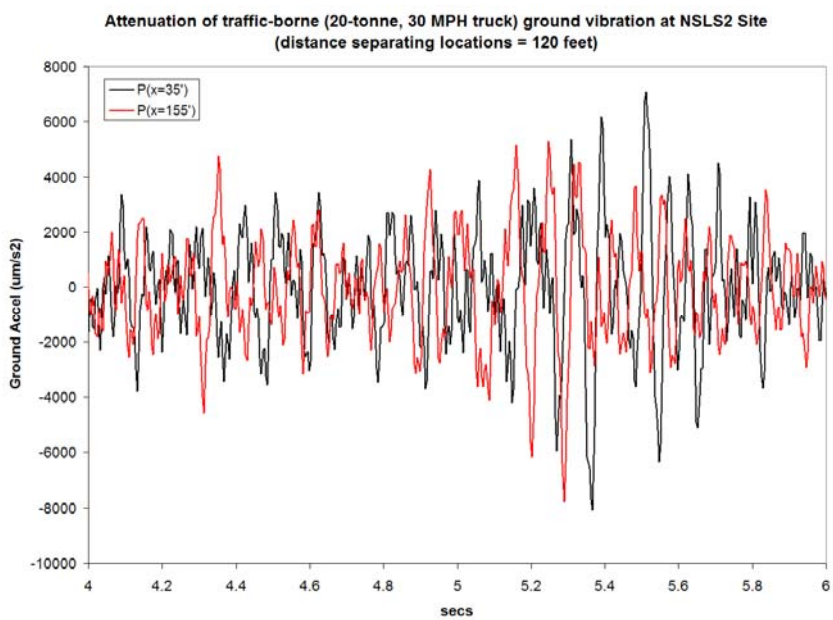

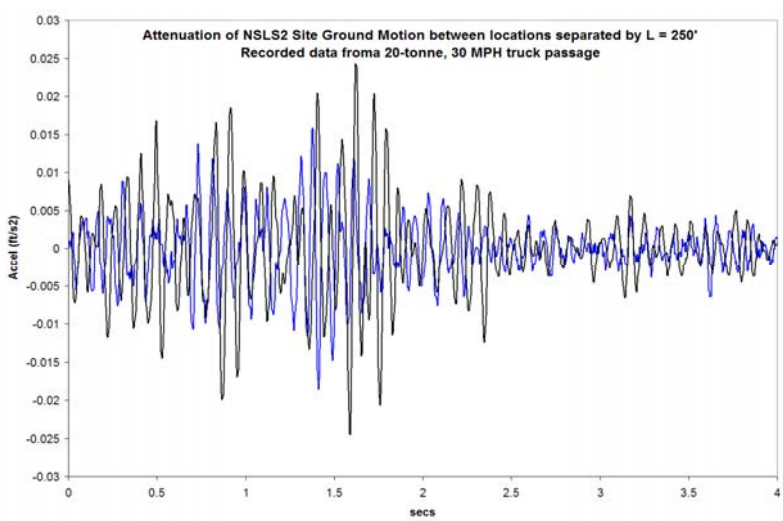

Figure M.2-3: Recorded ground motion and attenuation with distance of 250 ft (monitoring stations P2 and P3).

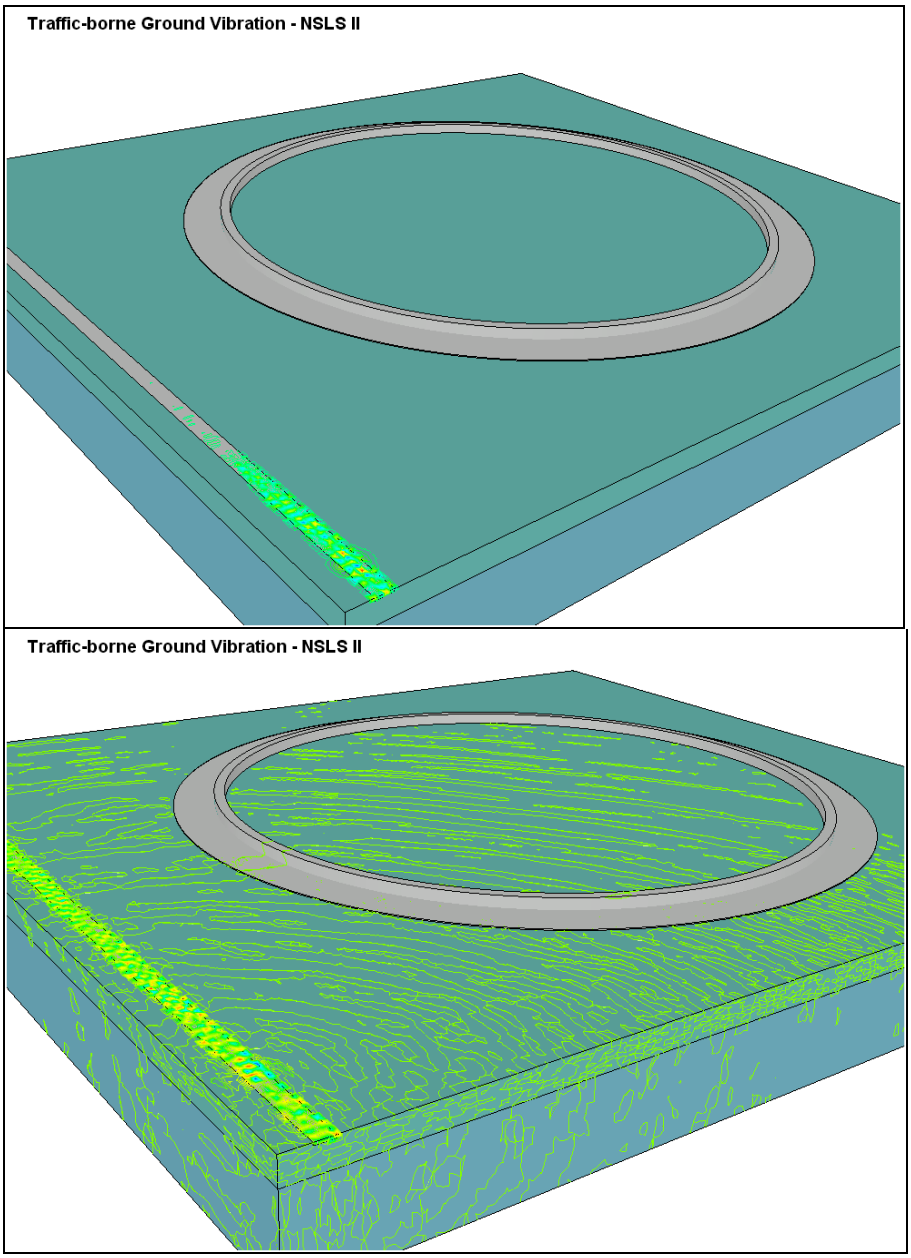

Figure M.2-4: Mathematical model used to simulate the 20-ton, 3-axle truck mph.

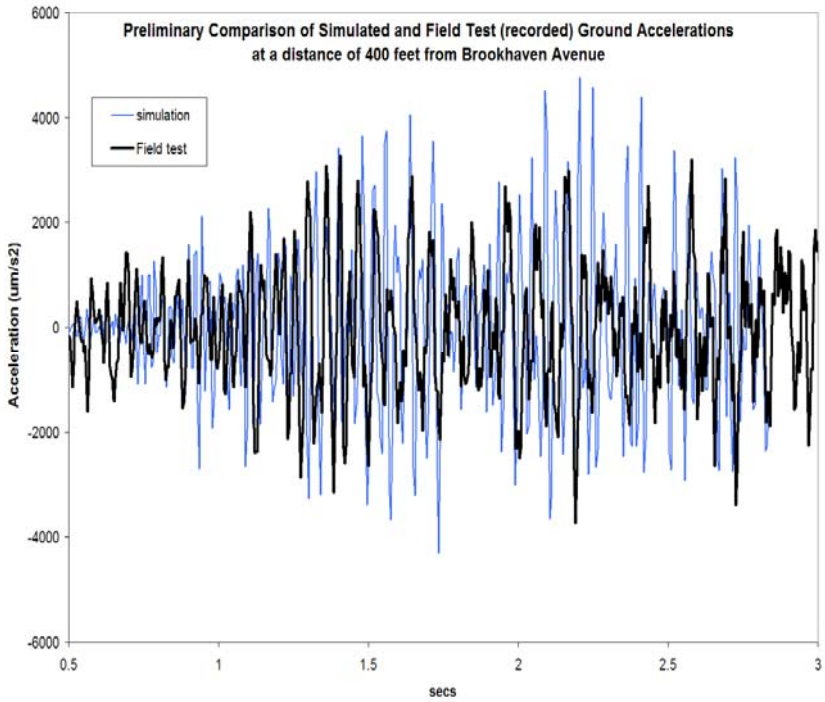

Figure M.2-5. Preliminary comparison of the ground vibration transient between the field test and the prediction through the simulation model at a distance of 400 ft from Brookhaven Avenue.

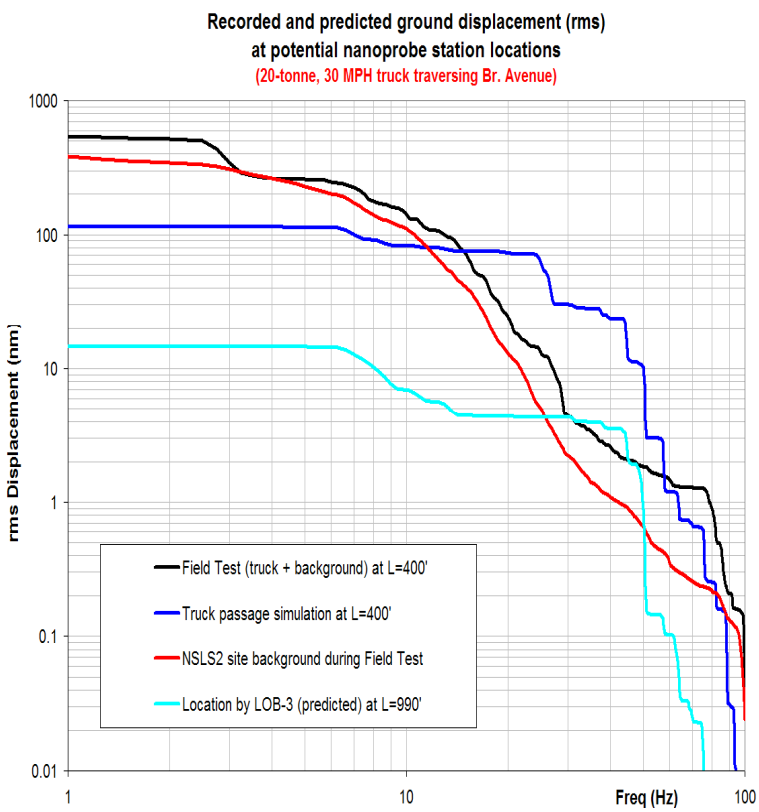

Figure M.2-6. Ground displacement (rms) based on actual test data and numerical predictions. Of importance is the extrapolation, based on the numerical model and the attenuation characteristics recorded during the field test, of the data to the LOB-3 location. Based on these findings, the effect of the large truck at that distance will be blended with the background (it shows ~14 nm for frequencies > 2 Hz). This is not the case with LOB-2 where the passage of the truck will be felt.

APPENDIX 3 LIST OF BEAMLINE COMPONENTS

Item	Description	Part Number	Symbol	Z(m)	Location
	Fixed Mask	(SR-FE-IDN1-1100)	FM		Front End
	White Beam Slits	(SR-FE-IDN1-1100)	S1	16.4	Front End
	Storage Ring Wall				
1	Gate Valve	XF-BL-HXN-GateValve	GV1	25.6	FOE
2	Aperture Plate	XF-BL-HXN-AperturePlate	AP	25.7	FOE
3	Diagnostic Chamber	XF-BL-HXN-DiagnosticChamber	DC1	25.9	FOE
4	White Beam Filters	XF-BL-HXN-WhiteBeamFilters	WBF	26.3	FOE
5	Be Window	XF-BL-HXN-Be-Window	BW1	26.6	FOE
6	Horizontal Collimating Mirror	XF-BL-HXN-Horizontal-Collimating-Mirror	M1	27.5	FOE
7	Gate Valve	XF-BL-HXN-GateValve	GV2	28.4	FOE
8	Bremsstrahlung Collimator	XF-BL-HXN-BremsstrahlungCollimator	CO	28.6	FOE
9	Pink Beam Slits	XF-BL-HXN-PinkBeamSlits	S2	29.0	FOE
10	Pink Beam Screen Monitor	XF-BL-HXN-PinkBeamScreenMonitor	PBSM	29.2	FOE
11	Gate Valve	XF-BL-HXN-GateValve	GV3	29.5	FOE
12	Monochromator, Horizontal Double Crystal	XF-CM-1028	DCM1	30.2	FOE
13	White beam Stop	XF-BL-HXN-WhiteBeamStop	BS	30.7	FOE
14	Diagnostic Chamber	XF-BL-HXN-DiagnosticChamber	DC2	30.9	FOE
15	Gate Valve	XF-BL-HXN-GateValve	GV4	31.3	FOE
16	Horizontal Focusing Mirror	XF-BL-HXN-HorizontalFocusingMirror	M2	32.1	FOE
17	Gate Valve	XF-BL-HXN-GateValve	GV5	33.0	FOE
18	Mono Beam Position Monitor	XF-BL-HXN-MonoBeamPositionMonitor	BPM1	33.3	FOE
19	Vertical Focusing Mirror	XF-BL-HXN-VerticalFocusingMirror	M3	34.1	FOE
20	Vertical Flat Mirror	XF-BL-HXN-VerticalFlatMirror	M4	35.4	FOE
21	Gate Valve	XF-BL-HXN-GateValve	GV6	36.0	FOE
22	Bremsstrahlung Stop	XF-BL-HXN-BremsstrahlungStop	BS	36.3	FOE
23	Mono Beam Position Monitor	XF-BL-HXN-MonoBeamPositionMonitor	BPM2	36.8	FOE
	Long BeamPipe				FOE
24	Mono Beam Shutter	XF-BL-HXN-MonoShutter	MS1	39.5	FOE
25	Gate Valve	XF-BL-HXN-GateValve	GV7	39.9	FOE
	Hutch 1 Downstream Wall			40.0	FOE
	Hutch 2 Upstream Wall			57.5	Mono Hutch
26	Gate Valve	XF-BL-HXN-GateValve	GV8	57.9	Mono Hutch
27	Be Window	XF-BL-HXN-BeWindow	BW2	58.0	Mono Hutch
	Long Beampipe				Mono Hutch
28	Be Window	XF-BL-HXN-BeWindow	BW3	61.0	Mono Hutch
29	Mono Beam Position Monitor	XF-BL-HXN-MonoBeamPositionMonitor	BPM3	61.3	Mono Hutch
30	Gate Valve	XF-BL-HXN-GateValve	GV9	61.7	Mono Hutch
31	Secondary Source Aperture	XF-BL-HXN-SecondSourceAperture	SSA1	62.0	Mono Hutch
32	Gate Valve	XF-BL-HXN-GateValve	GV10	63.8	Mono Hutch
33	Mono Beam Shutter	XF-BL-HXN-MonoShutter	MS2	64.2	Mono Hutch
	Hutch 2 Downstream Wall			64.5	Mono Hutch
	Hutch 3 Upstream Wall			92.9	Endstation
34	Gate Valve	XF-BL-HXN-GateValve	GV11	93.1	Endstation
35	Mono Beam Position Monitor	XF-BL-HXN-MonoBeamPositionMonitor	BPM4	93.4	Endstation
36	Secondary Source Aperture	XF-BL-HXN-SecondSourceAperture	SSA2	94.0	Endstation
37	High-Resolution Monochromator (mature phase)	XF-BL-HXN-HighResolution Monochrom.	DCM2	95.0	Endstation
38	Be Window	XF-BL-HXN-BeWindow	BW4	95.5	Endstation
	Long Beampipe				Endstation
39	HXN Microscope	XF-BL-HXN-Microscope	MIC	108.0	Endstation
	Hutch 3 Downstream Wall			113.0	Endstation

APPENDIX 4 REFERENCE DRAWINGS

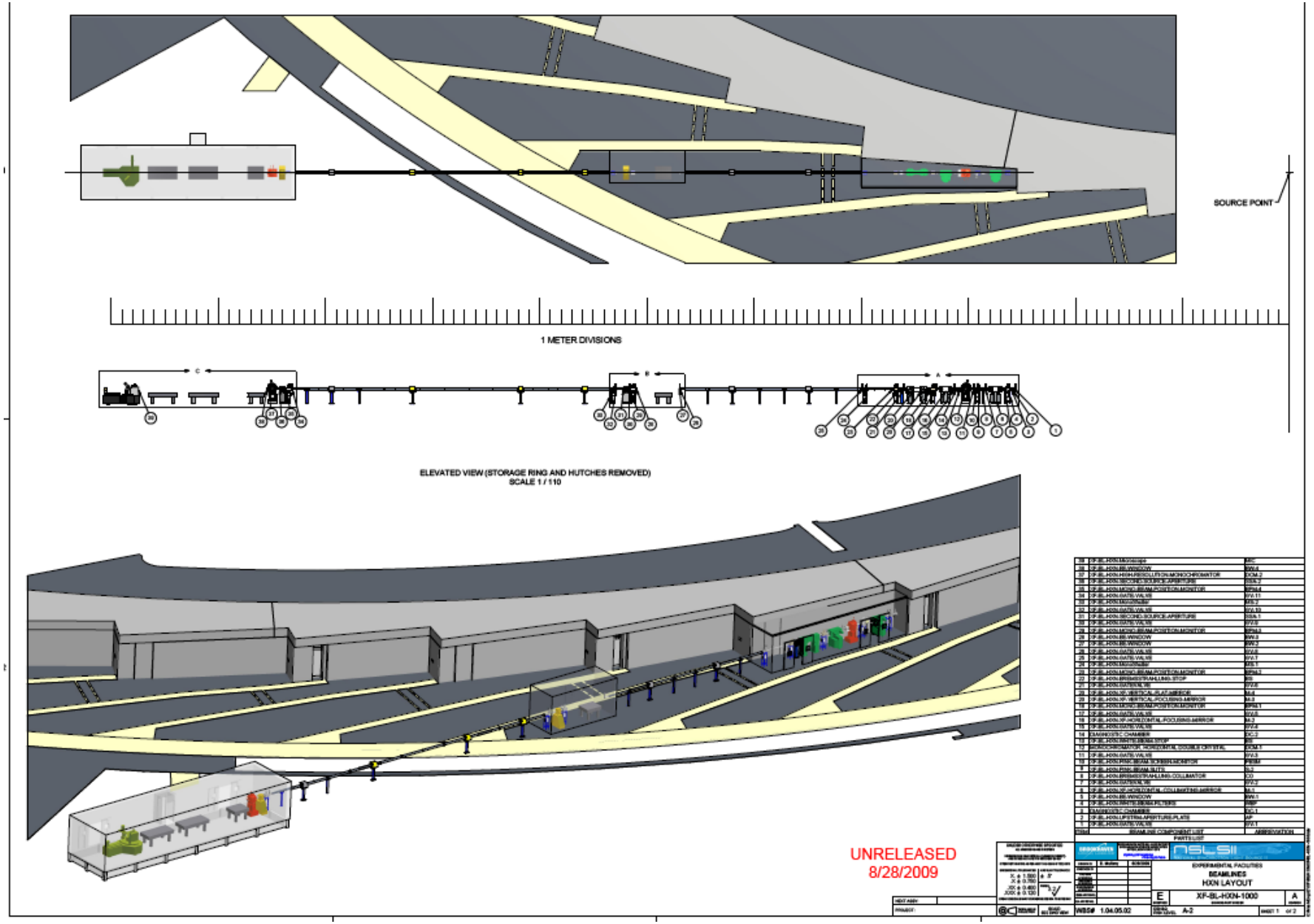
SOURCE POINT
1 METER DIVISIONS
ELEVATED VIEW (STORAGE RING AND HUTCHES REMOVED)
SCALE 1 / 110
UNRELEASED
8/28/2009
BEAMLINES
HXN LAYOUT
XF-BL-HXN-1000
A-2

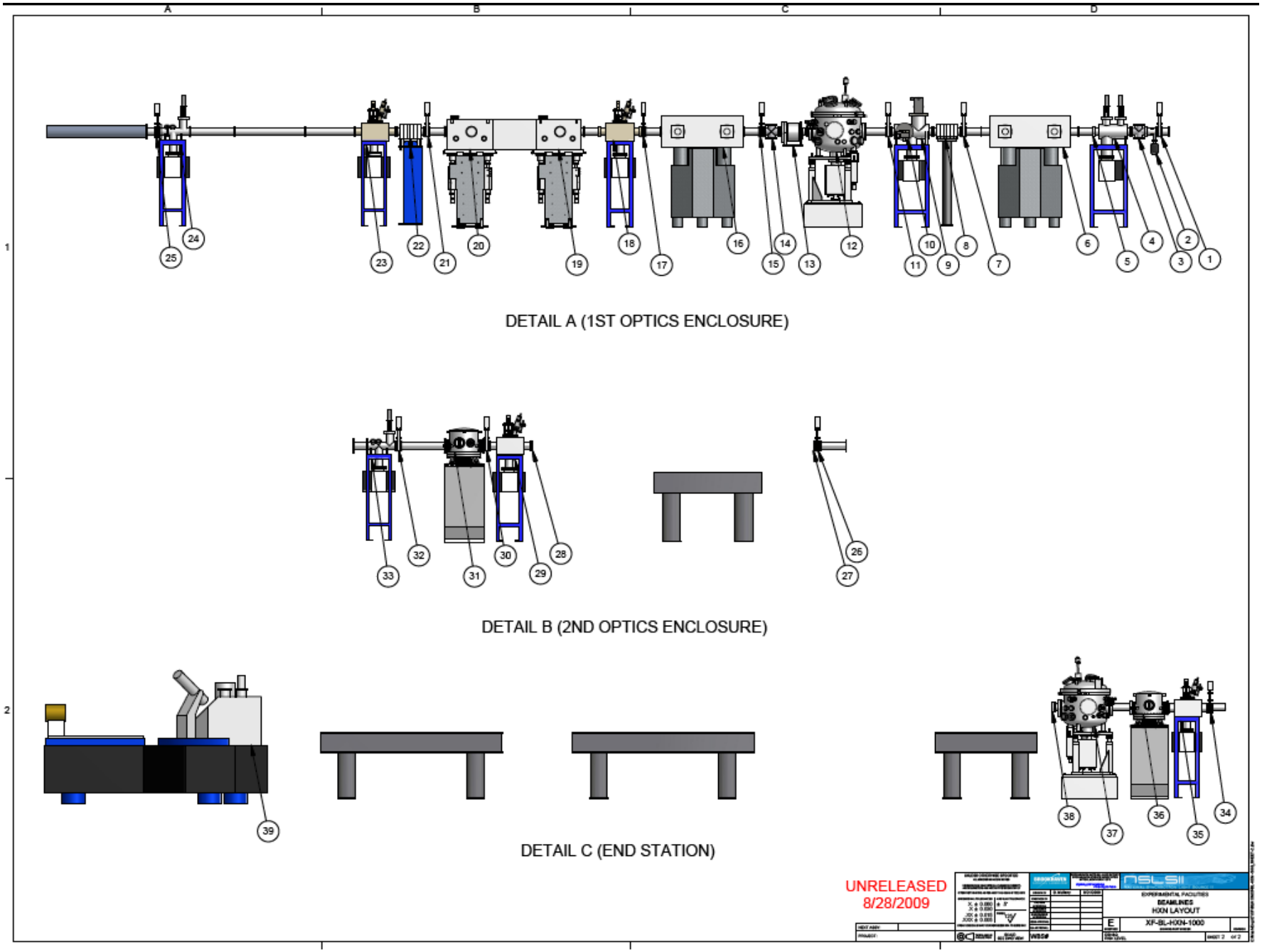
DETAIL A (1ST OPTICS ENCLOSURE)
DETAIL B (2ND OPTICS ENCLOSURE)
DETAIL C (END STATION)
UNRELEASED
8/28/2009
BEAMLINES
HXN LAYOUT
XF-BL-HXN-1000

Intentionally blank.

LT-XFD_CDR_IXS-00123

NSLS-II Project

CONCEPTUAL DESIGN REPORT for the

INELASTIC X-RAY SCATTERING BEAMLINE at NSLS-II

Final draft September 2009

Intentionally blank.

Approvals and Reviewers

Compiled by	**Signature**	**Date**
Yong Cai, IXS Beamline Group Leader, NSLS-II		
Reviewers		
Clement Bums, BAT Spokesperson, signing on behalf of the BAT		
Andy Broadbent, Beamlines Manager		
Nicholas Gmür, ESH Coordinator, NSLS-II		
Sushil Sharma, Mechanical Engineering Group Leader, NSLS-II		
Approval		
Qun Shen, XFD Director, NSLS-II		

Document Updates

The Conceptual Design Report for the IXS Beamline at NSLS-II is a controlled document, revised under change control.

Version No.	Date	Changes made
1	10-2-2009	final draft, submitted to BAT
2	1-28-2010	final version approved by the BAT

Intentionally blank.

Table of Contents

1. INTRODUCTION 1

1.1 Scientific Requirements 1
1.2 Beamline Advisory Team (BAT) 3
1.3 The IXS Project Team 4
1.4 Acknowledgements 4

2. BEAMLINE LAYOUT 5

2.1 Overview 5
2.2 Insertion Device 6
2.3 Front End 11
2.4 Optical Layout 12
CDW/CDDW Monochromators 12
Focusing Configurations 18
Alternative Monochromators 20
2.5 High Heatload Optics 21
2.6 Beamline Component Layout 23
First Optical Enclosure 23
Experimental Hutches 24
2.7 List of Major Components 26

3. SPECTROMETER LAYOUT 28

3.1 Design Considerations 28
3.2 Multilayer Mirror 29
Layer Materials and Thickness 29
Figure Parameters 30
Mirror Configurations and Performance 30
3.3 Overall Performance and Count Rate Estimate 34

APPENDIX 1: SCHEDULE 37

A1.1 Construction of the IXS beamline 37
A1.2 Critical Decisions and Milestones of the 0.1 meV Optics R&D 37

APPENDIX 2: REFERENCE DRAWINGS 39

APPENDIX 3: REPRESENTATIVE EXPERIMENTS 42

A3.1 Studies of Liquids and Disordered Systems 42
A3.2 High-Pressure Vibrational Dynamics 43
A3.3 Phonons and Phonon-Damping in Bio-Materials 43
A3.4 Phonons in Crystalline Systems 44

Acronyms

BAT	Beamline Advisory Team
CDR	Conceptual Design Report
CRL	Compound Refractive Lens
DCM	Double-Crystal pre-Monochromator
EH	Experimental Hutch
FM	Focusing Mirrors
FOE	First Optics Enclosure
IXS	Inelastic X-ray Scattering
K-B	Kirkpatrick-Baez
PP	Phase Plate
URM	Ultrahigh Resolution Monochromator

1. INTRODUCTION

1.1 Scientific Requirements

Momentum-resolved Inelastic X-ray Scattering (IXS) with meV energy resolution provides a powerful technique for studying vibrational dynamics and excitations in condensed matter systems. The scientific objective of this beamline is focused on very high-resolution (1 meV ~ 0.1 meV) IXS experiments. The ultimate goal is to achieve an energy resolution of ~ 0.1 meV, which represents an order of magnitude improvement over the best currently operating instruments in the world.

As elaborated in the Letter of Intent[1], two classes of experiments are envisioned for this beamline:

- 0.1 meV resolution experiments

  The focus is on viscous-elastic crossover behaviors of disordered systems and fluids, and new low-energy modes in complex fluids and confined systems that would require the 0.1 meV resolution to be resolved. Another important area of research is the collective dynamics of lipid membranes and other biological systems, where correlated molecular motions and density fluctuations on the meV energy scale play a significant role in determining their physical and biological properties. The 0.1 meV resolution would also be potentially useful for mapping out the superconducting band gap with phonons.

- 1 meV resolution experiments

  Examples include relaxation dynamics, sound propagation and transport properties in disordered systems such as glasses, fluids, polymers, etc. The higher available flux and small focused beam achievable from the NSLS-II sources will be highly valuable for studying phonons in single crystals, surfaces, thin films, confined liquids, small samples down to micrometer sizes, systems under extreme pressure, phonons in excited states (pump probe), and exotic excitations in strongly correlated systems.

Some specific examples of these experiments as proposed in the Letter of Intent are listed in Appendix 3 for reference.

With the ~ 0.1 meV energy resolution, we anticipate in particular improved understanding of the low-energy excitations in liquid, disordered, and biomolecular systems, where atomic motions due to the naturally occurring inhomogeneity and/or density fluctuations dominate the scattering in the forward direction, for which very high momentum transfer (Q) resolution (< 0.1 nm^{-1}) would also be required. Together, the NSLS-II IXS beamline is expected to bridge, at least partially, the dynamic gap (0.1 nm^{-1} < Q < 2 nm^{-1} and 0.1 meV < E < 5 meV) between various existing inelastic scattering probes (see Figure 1-1). This is the area where potential new science may be expected.

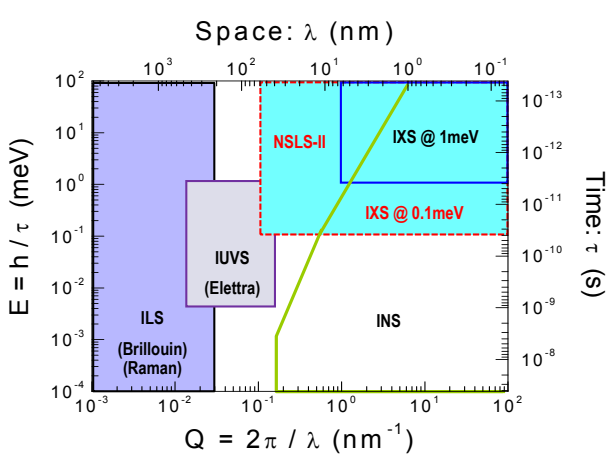

Figure 1-1. Representation of the dynamic regions currently accessible by various inelastic scattering probes including visible and UV light, neutron, and x-ray. The region the NSLS-II IXS beamline will aim to bridge is indicated.

To achieve the 0.1 meV resolution goal, the optical design of the NSLS-II IXS beamline employs a newly proposed monochromator design – the so-called CDW[2,3] or CDDW[4] monochromator – based on the angular dispersion effect in asymmetric Bragg reflections[2,5]. These newly proposed monochromators are implemented at the Si(008) back reflection at a medium energy of 9.13 keV, where the NSLS-II undulator sources will have superior performance in both brightness and spectral flux. It differs fundamentally from the symmetric Bragg back reflection optics – the spherical backscattering crystal analyzers – employed in all existing IXS instruments which must work with high index Bragg reflections at higher energies (> 20 keV) in order to achieve ~ meV resolution[6]. The unusually large angular acceptance of the CDW/CDDW monochromator makes it possible to use as crystal analyzers by combining with collimating optics. The CDW/CDDW monochromator offers also a much cleaner resolution function with sharper tails compared to the symmetric Bragg back reflection optics, which will help eliminate spurious backgrounds and increase contrast. This novel design, albeit yet to be demonstrated in a working instrument for which active R&D are currently being pursued by the project team, provides a unique opportunity for NSLS-II to build a fundamentally new instrument with unprecedented performance for experiments that are not yet feasible on any existing IXS instruments to date.

The design of the CDW/CDDW monochromator can be optimized to deliver 0.1 – 1 meV resolution. For scientific problems that do not require the ultimate 0.1 meV resolution, the 1 meV resolution will offer at least a factor of 10 higher incident flux. Coupled with the sharper tails, the NSLS-II IXS instrument operating with 1 meV resolution is expected to provide enhanced counting efficiency and much improved contrast and will be highly competitive in existing scientific areas performed by current instruments operating with similar energy resolution in the world. In fact, the current state-of-the-art meV IXS spectrometers operating at all three high-energy synchrotron sources (ESRF, APS and SPring-8) in the world have had a profound impact in the study of vibrational dynamics in liquids and disordered systems, phonons and phonon softening in crystalline materials, vibrational dynamics under extreme environments, and phonons and phonon damping in biomolecular systems. However, currently the best workable energy resolution of these instruments is limited to ~ 1.5 meV with slowly decaying resolution tails. Although technically sub-meV energy resolutions have been demonstrated, they are rarely used for experiments due to insufficient intensity. In many cases, the slowly decaying resolution tails hinder the clear identification of low-energy excitation features at energies as high as 10 meV[7]. The development of the NSLS-II IXS instrument having the 1 meV resolution with much sharper resolution tails is therefore of considerable interest, and will benefit many areas of research mentioned above.

The resolution of the momentum transfer Q plays also an important role in some experiments, particularly in the study of vibrational dynamics in liquids, disordered and biomolecular systems where the physical processes of interest occur mostly in the low Q region. The Q resolution is determined by the acceptance angle of the analyzers used in the spectrometer. Currently this is limited to ~ 0.5 nm^{-1} in the directions parallel and perpendicular to the scattering plane for existing meV IXS instruments. The ability to work with a medium energy of ~ 9.1 keV provides naturally a higher Q resolution by at least a factor 2 with the same acceptance angle compared to experiments performed at > 20 keV. Further improvement of the Q resolution to less than 0.1 nm^{-1} is required for some of the most demanding experiments at very low Q, and will be considered in the design of the spectrometers.

The ultimate success of the NSLS-II IXS beamline depends on the success of the 0.1 meV optics R&D program. The IXS project team is well aware of the tremendous technical challenges associated with this new monochromator design and has staged an aggressive R&D plan to address all these challenges. In many of the technical areas such as the required lattice homogeneity, temperature uniformity and stability, and surface quality, the technical challenges associated with the new optics scheme increases inversely proportionally with the targeted energy resolution. So far, a total resolution of 3.1 meV has been demonstrated with the CDW design[3]. Our brute force preliminary test using a rather primitive setup demonstrated a total resolution of 10 meV using the CDW design[8]. Even though the 1 meV resolution with the CDW design has not been demonstrated, strong R&D effort is ongoing.

The current design of the IXS beamline and spectrometers presented here is based on our current understanding of the operating principles of these new optics. The design is made compatible with energy resolutions of both 0.1 and 1 meV using the CDW/CDDW monochromator design. In the latter case, the design is also compatible with a proven alternative inline 4-bounce monochromator design which delivers 1 meV resolution at 9.4 keV[9]. This monochromator has also the advantage of a sharp resolution tails through multiple high index Bragg reflections, although the smaller angular acceptance may limit its efficiency for use as a crystal analyzer. Nevertheless, this alternative monochromator design provides a valid alternative to minimize risks and to ensure that a best in class user instrument can be built on day one of NSLS-II operation.

1.2 Beamline Advisory Team (BAT)

The IXS Beamline Advisory Team (BAT) is made up by a group of world-class scientists having a broad range of complementary scientific expertise and experiences in areas relevant for the NSLS-II IXS beamline. Current membership includes:

Clement Burns (spokesperson)	Western Michigan University
Sow-Hsin Chen	Massachusetts Institute of Technology
Alessandro Cunsolo*	Argonne National Laboratory
John Hill	Brookhaven National Laboratory
Michael Krisch	European Synchrotron Radiation Facility
Ho-kwang Mao	Carnegie Institution of Washington
Tullio Scopigno	Universita' Roma "Sapienza"
Stephen Shapiro	Brookhaven National Laboratory
Yuri Shvyd'ko	Argonne National Laboratory

* Member until September 2009.

A short summary of their expertise and experiences is given below:

Clement Burns, Professor at WMU; IXS on highly correlated systems; Principal Scientist (until 2006) for the Medium Resolution IXS Instrument at Sector 30 of APS; PI on DOE Proposal for Inelastic X-ray Scattering Sector (Sector 30) at APS.

Sow-Hsin Chen, Professor at MIT; Distinguished expert in neutron, laser, inelastic x-ray scattering of soft condensed matters, and molecular dynamics of these systems; Expert in dynamical properties of water with strong current emphasis on biological systems.

Alessandro Cunsolo*, Scientist at APS (until September 2009); Specialist in glassy and disordered systems; Experience with neutron, UV, visible light, and Brillouin scattering; has joined the IXS project team from September 2009.

Michael Krisch, Scientist at ESRF; Spokesperson for the high resolution IXS beam line ID28 at the ESRF since 1996; Expert in ~ meV resolution IXS studies, both in instrumentation and experiments.

John Hill, Physicist at BNL; IXS experience at NSLS and APS studying electron dynamics in simple metals and strongly correlated electron systems, using resonant and non-resonant techniques; Director of the IXS-CAT (Sector 30) at APS (2002 – 2008); Director of the Experimental Facilities Division of NSLS-II (2006 – 2008).

Ho-kwang (David) Mao, Senior Scientist at Geophysical Lab of CIW; Vast experience in high pressure studies of all sorts; Expert in use of numerous spectroscopies (including IXS) to study vibrational excitations under high pressure and extreme temperature conditions; Director of the high pressure beam line (HP-CAT) at the APS.

Tullio Scopigno, Professor at University of Roma "La Sapienza"; Expert in spectroscopy (including time resolved Brillouin and Raman spectroscopy) of glassy, fluid, polymer and soft matter systems, and conceptual methodologies for describing these systems.

Steve Shapiro, Senior Scientist at BNL; Expert in neutron scattering, high resolution studies of phonons and phonon linewidths in single crystals, and studies of phase transitions.

Yuri Shvyd'ko, Senior Scientist at APS at ANL; Expert in x-ray optics, including work on x-ray interferometry, Mössbauer, and asymmetric Bragg reflections; Originated and tested the basic idea for the new inelastic x-ray spectrometer described here.

1.3 The IXS Project Team

Advised by the BAT, the NSLS-II IXS Project Team is responsible for the R&D of the ultrahigh resolution optics and the design, construction and commissioning of the NSLS-II IXS beamline and spectrometers.

List of current members (as of September 2009) and their individual responsibilities:

Yong Cai, Physicist, NSLS-II IXS Group Leader

Scott Coburn, Engineer (matrixed with the Beamline Support Group, XFD)

Alessandro Cunsolo, Associate Physicist, NSLS-II IXS Beamline Scientist

Marcelo Honnicke, Assistant Physicist, multilayer collimating mirrors, crystal optics R&D

Xianrong Huang, Associate Physicist, x-ray dynamic diffraction theory, crystal optics R&D

Jeff Keister, Associate Physicist, NSLS-II R&D Beamline Scientist

Nalaka Kodituwakku, Postdoctoral Fellow, crystal optics R&D

Kevin Kovacs, Technician, NSLS-II R&D beamline support (temporary)

Leo Reffi, Mechanical Designer (matrixed with the Design Group, ASD)

Bill Struble, Technician, crystal fabrication and lab support

Zhong Zhong, Physicist, NSLS D&I Beamline Spokesperson (MOU)

1.4 Acknowledgements

The following BNL staffs are acknowledged for their contributions to the materials presented here.

Andy Broadbent, Beamlines Manager (XFD, NSLS-II)

Oleg Chubar, Beamline Scientific Support, insertion device optimization, wave front propagation (XFD, NSLS-II)

Lewis Doom, Engineer, Front-end design (ASD, NSLS-II)

Viswanath Ravindranath, Engineer, Heat load analysis (ASD, NSLS-II)

Kathleen Robinson, Editor (NSLS-II)

Qun Shen, Director of XFD (XFD, NSLS-II)

In addition, **Michael Krisch** of ESRF, France, and **Alfred Baron** of SPring-8/RIKEN, Japan are acknowledged for their contributions to the count rate estimates presented herein and their insightful comments and helpful discussions on a number of occasions on the issues.

2. BEAMLINE LAYOUT

2.1 Overview

A CAD drawing showing the layout of the beamline is given in Figure 2-1. A reference drawing with dimensions is provided in Appendix 2. The layout is driven by the scientific requirements of the beamline and is based on our best understanding of the working principles of the new CDW/CDDW monochromator designed for achieving the ultimate resolution of ~ 0.1 meV[2-5,8]. Inelastic x-ray scattering is a photon-hungry experiment; the IXS beamline is therefore designed to maximize the spectral flux deliverable to the sample, maintaining at the same time the momentum transfer resolution required for the experiments by appropriate focusing schemes. Optimization of the design begins with the insertion device, which is discussed in section 2.2. The rationale for the optical layout is discussed in section 2.4.

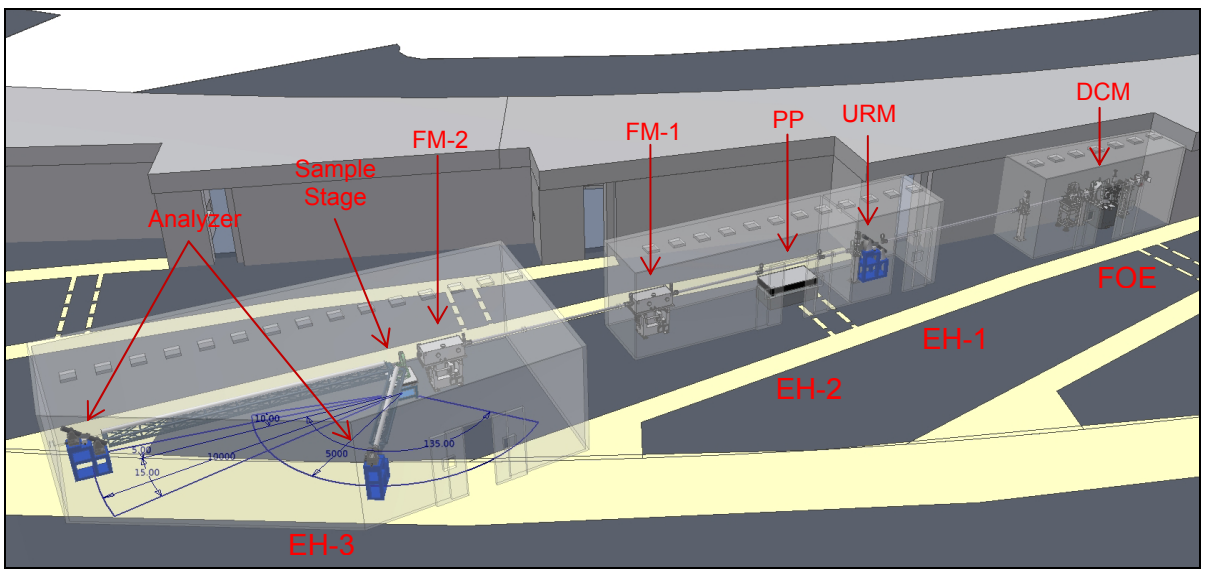

Figure 2-1. Layout of the Inelastic X-ray Scattering (IXS) beamline, showing (right to left) the first optical enclosure (FOE) containing the double crystal pre-monochromator (DCM), the first experimental hutch (EH-1) housing the ultrahigh resolution monochromator (URM), the second experimental hutch (EH-2) for additional optics such as the phase plate (PP) for conditioning the beam, and the third experimental hutch (EH-3) where the IXS spectrometers are located. Two sets of focusing mirrors (FM-1 and FM-2) provide two focusing configurations for the beamline.

The beamline occupies a long, high-β straight section of the NSLS-II storage ring on a sector with the extended experimental floor space made available by the by-pass corridors. The extra floor space allows the beamline to extend to ~ 70 m from the source point, which is needed in order to accommodate the 0.1 meV spectrometer with an anticipated arm length of ~ 10 m. Further considerations for the optimal location of the beamline include 1) the possibility to extend the straight section for more insertion devices to further increase the spectral flux, and 2) the possibility to go beyond the storage ring building to accommodate possible new optical schemes that may require an extended beamline in the future. These possibilities should be taken into consideration when the beamline location is decided.

As shown in Figure 2-1, the major optical components include the high heat-load double crystal pre-monochromator (DCM), an ultrahigh resolution monochromator (URM) based on the new inline CDDW monochromator design[4], and two sets of Kirkpatrick-Baez (K-B) focusing mirrors (FM). Together with a set of Be compound refractive lenses (CRLs)

installed in the front end (see section 2.3), these mirrors provide two focusing configurations for the beamline, which will be discussed in detail in section 2.4. In addition, a diamond phase plate (PP) may be inserted into the optical path to rotate the polarization to the vertical to compensate intensity loss when the scattering angle is greater than ~ 50 deg. Apart from the focusing configurations and without the ultrahigh resolution monochromator, this layout is generic and can be combined with most inline high resolution monochromator designs to deliver a highly monochromatized beam to the sample.

All these optical and other beamline components are housed in four enclosures. The first one (the first optical enclosure: FOE) is for the white beam components including the high heat-load DCM. The DCM will be cryogenically cooled and designed to take the entire central cone of the undulator beam. All other hutches are designated as experimental hutches taking only monochromatic beam. The first experimental hutch (EH-1) houses the URM with its own photon shutter. This ensures temperature stability by keeping the x-ray beam on the monochromator while access to the downstream hutches is required. The second experimental hutch (EH-2) houses the PP and the first set of FM (FM-1). This hutch includes an optical table and is designed for future optics R&D to further enhance the capabilities of the IXS beamline. The last experimental hutch (EH-3) houses the second set of FM (FM-2) and has space for two IXS spectrometers, one designed for ~ 1 meV resolution with a 5 m arm and a large scattering angle range (-10 to 135 degree) and the other for ~ 0.1 meV resolution with a 10 m arm and a limited scattering angle range of (-5 to 15 degree). A detailed conceptual layout of the IXS spectrometers is under development, which consists of analyzer optics for the collection and detection of the scattered photons from the sample based on the CDW/CDDW monochromator design. Some details will be discussed in section 3.

2.2 Insertion Device

Due to the weak scattering cross section, IXS is a flux-limited experiment. Sufficient photon flux is essential in order to obtain useful count rate for a realistic experiment. Experiences with the current state-of-the-art instruments show that the required photon flux for studies of vibrational dynamics should be at least on the order of 10^9 photons/sec/meV at ~ 1 meV resolution[10]. Assuming that the overall beamline optics efficiency of the IXS beamline is at least 10%, and that the optics efficiency of the spectrometer is as efficient as the current instruments, the required photon flux at the source would need to be at least 10^{15} photons/sec/0.1%bw at the working energy of ~ 9.1 keV in order to perform experiments with the ultimate 0.1 meV energy resolution.

Optimization of the insertion device for the IXS beamline therefore looks for the best possible device with the current NSLS-II lattice design using state-of-the-art room temperature permanent magnets, the NEOMAX-32AH magnet NdFeB (B_r = 1.12 T), to deliver the highest possible spectral flux at the working energy of ~ 9.1 keV. The minimal goal is to achieve a spectral flux of 10^{15} photons/sec/0.1%bw at the source. A number of devices with a magnet period ranging from 20 – 26 mm have been investigated (see Figure 2-2) [11], where the gap value required for generating the 9.13 keV photons with the 5th harmonic for each period is used to determine the maximum undulator length satisfying the "stay-clear" criterion. The resulted undulators are then compared in performance by calculating the spectral flux delivered through an aperture of 100(H) × 50(V) μrad^2 in Figure 2-3. Clearly, the undulator with a magnet period of 22 mm and 6 m in length (named IVU22-6m thereafter) in a high-β straight section delivers the maximum spectral flux of 1.6×10^{15} photons/sec/0.1%bw at 9.1 keV, meeting the minimum goal of the optimization, and is the best choice for the IXS beamline. Figure 2-3 also illustrates some tuning range from 7 – 11 keV with the IVU22-6m meeting the 10^{15} photons/sec/0.1%bw goal using the 3rd and 5th harmonics. This allows the use of possible alternative optical schemes for the beamline and spectrometer. Further discussion will be given in section 2.4. Table 2-1 summarizes the basic performance parameters of the device.

Physically only the high-β straight section with an active length of 7 m can accommodate the IVU22-6m. Due to the difference in the β functions (see Table 2-2), however, there is another important reason for choosing the high-β instead of the shorter low-β straight section for the IXS beamline, despite the bigger beam size: The smaller beam divergence in the high-β straight (in the horizontal, the difference is more than a factor 3!) produces an x-ray beam with a smaller beam cross section and divergence than in the low-β straight, and yet the spatial distribution of the power density is essentially the same in both cases. This has multiple benefits for the optics design in maximizing the optical throughput, including better acceptance by the optics, shorter lengths for the optical elements, particularly for the mirrors, and possibly less integrated power over the central cone of the x-ray beam. This is illustrated in Figure 2-4, where we

compare the spectral flux and power density distribution of the IVU22-6m in a high-β straight with the baseline device, the IVU20-3m, in a low-β straight section. Expectedly the power density is higher for the IVU22-6m in the high-β straight section but the total integrated power of the central cone is lower compared to the IVU20-3m in a low-β straight section.

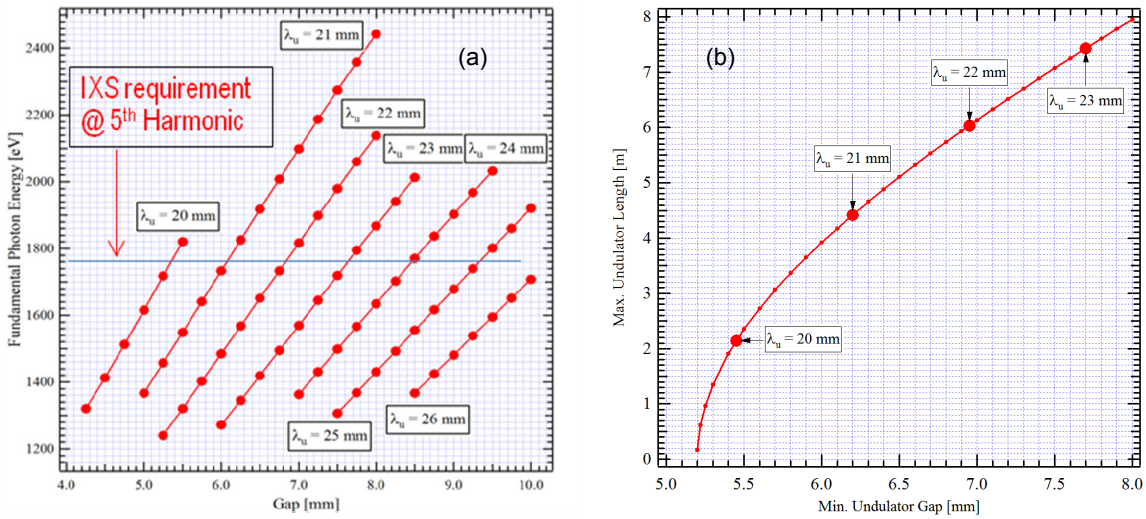

Figure 2-2. (a) The fundamental energy as a function of the magnetic gap for a number of magnet periods for NSLS-II. The NEOMAX-32AH magnet NdFeB with B_r = 1.12 T at room temperature is assumed. This provides the gap value needed to generate the 9.13 keV photons with the 5th harmonic. Note that the minimum allowable gap is 5mm. (b) The maximum undulator length as a function of the "stay-clear" aperture or the minimum undulator gap for a high-β straight section. The gap values required to generate the 9.13 keV photons for the chosen magnetic periods are marked by the red dots, which indicate the maximum length of the undulator for the corresponding period. For a period of 22 mm, for example, the maximum length is 6 m.

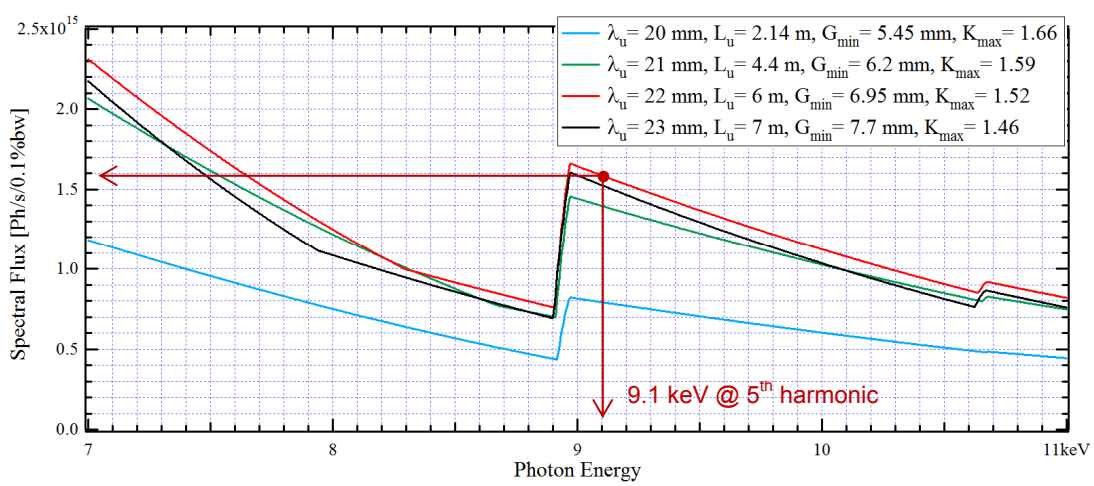

Figure 2-3. Comparison of the spectral flux of several undulators meeting the "stay-clear" criterion in a high-β straight of the NSLS-II storage ring filled with 500 mA current. At the working energy of ~ 9.1 keV, the undulator with a magnetic period of 22 mm and 6 m in length (named IVU22-6m) delivers the maximum spectral flux of 1.6 × 10^{15} photons/sec/0.1%bw.

Table 2-1. Basic parameters of the IVU22-6m Undulator.

Device Type	PMU / in vacuum planar
Br [T] (NEOMAX-32AH magnet NdFeB)	1.12
Period [mm]	22
Length [m]	6
Number of Periods	270
Minimum Gap @ High-β Straight [mm]	6.95
Maximum Field Bmax [T]	0.81
Maximum Deflection Kmax [T]	1.52
Total Power [kW]	11.1
On-axis Power Density [kW/mrad2]	94.1

Table 2-2. Beam parameters assuming three damping wigglers installed with 0.87 nm-rad horizontal emittance[12]. The electron beam size and angular divergence are calculated values based on the formula $\sigma_{x,y} = \sqrt{\varepsilon_{x,y}\beta_{x,y} + \delta_{x,y}^2}$ and $\sigma'_{x,y} = \sqrt{\varepsilon_{x,y}/\beta_{x,y} + \left(\delta'_{x,y}\right)^2}$, where $\delta_{x,y} = \eta_{x,y}\left(\delta E/E\right)$ and $\delta'_{x,y} = \eta'_{x,y}\left(\delta E/E\right)$, with $\eta_{x,y}$ and $\eta'_{x,y}$ being the energy dispersion functions, are the energy dispersion widths of the electron beam. $\eta_{x,y}$ and $\eta'_{x,y}$ are both assumed zero in the calculation.

Parameters		Low β	High β	Units
Emittance	ε_x (horizontal) ε_y (vertical)	0.87 0.008		nm · rad
Beta function	β_x (horizontal) β_y (vertical)	2.02 1.06	20.8 2.94	m
Energy spread $\Delta E / E$		0.102%		-
Beam size	σ_x (horizontal) σ_y (vertical)	41.92 2.913	134.5 4.851	μm
Angular divergence	σ'_x (horizontal) σ'_y (vertical)	20.75 2.748	6.467 1.65	μrad

Based on the x-ray beam characteristics of the IVU22-6m, the opening aperture of the beamline should be optimized to make use of most of the flux while keeping the heat load on the optical elements as low as possible. The photon source size and divergence are also required to determine the optimal locations of the mirrors and the footprint of the beam at optical elements. Taking into account the emittance of the electron beam, the rms source size and the angular divergence of the photon beam from the IVU22-6m calculated for 9.13 keV with the 5th harmonic (K ~ 1.5) are summarized in Table 2-3. Distance scalings of the photon beam size and divergence as it propogates downstream of the beamline are summarized in Table 2-4. Based on these numbers, an aperture size of 1 mm diameter at 20 m or 50 μrad angular openning covers more than 4Σ of the photon beam.

In Figure 2-5 the spectral flux and power as a function of the horizontal aperture size given in angle are examined. The vertical aperture is fixed at 50 µrad, corresponding to 1 mm opening at 20 m from the source. Clearly the flux reaches a plateau at ~ 60 µrad, whereas the power increases linearly with the horizontal aperture size, which is expected given the flux and power density distributions shown in Figure 2-4.

We note that the calculations reported above assume a damped horizontal emittance of 0.87 nm·rad with three 7 m damping wigglers installed. The ultimate damped horizontal emittance of 0.55 nm·rad with eight 7 m damping wigglers is expected to improve the horizonal source size and divergence. In terms of the total deliverable flux, however, no improvement would be expected as long as the aperture is set to collect the full central cone of the beam (see Figure 2-5).

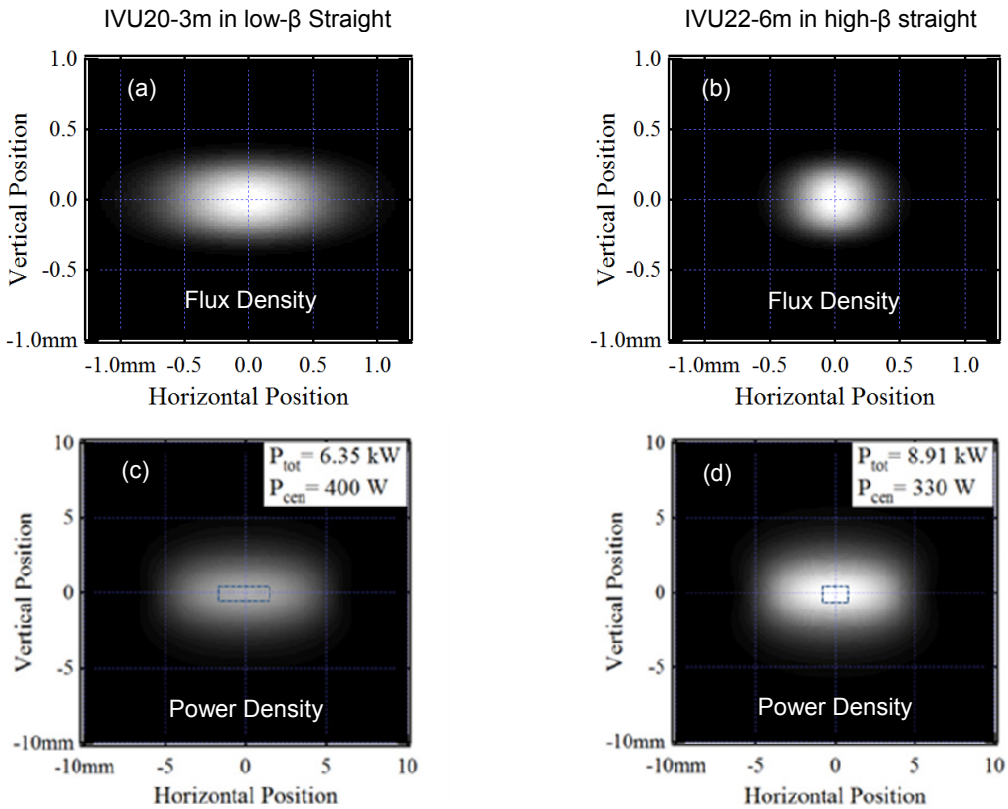

Figure 2-4. Comparison of the spatial distribution of the spectral flux and power density of the baseline undulator IVU20-3m in a low-β straight (a and c) and those of the IVU22-6m in a high-β straight (b and d) at ~ 9.1 keV, observed at 20 m from the center of the straight section. Note the different scales between the flux and the power density distribution. The extent of the central cone is indicated by the blue dotted rectangle in (c) and (d).

For further improvement that could lead to a significant increase of the spectral flux, one of the options being considered is to explore the LN2 cooled NEOMAX-45AH magnet with a B_r = 1.4 T at 120 K[13]. An in-vacuum undulator using these cooled magnets with a magnetic period of 17 mm and up to 5.5 m long, for example, would still satisfy the "stay-clear" criterion in producing the 9.1 keV photons. With this device, one would be able to work at the 3rd harmonic for the 9.1 keV photons, potentially gaining ~ 75% more flux compared to the IVU22-6m and reducing the power load on the optics (the total power generated by this cooled device is 8.1 kW). Other possible cooled devices based on PrFeB with Br ~ 1.5 T at 77K have also been considered, which provide still better performance in spectral flux and/or tuning range while the power generated is comparable or below that of the IVU22-6m[11]. However, these devices will require substantial R&D effort to address the technical challenges associated with the cryogenic cooling of the device. Strong non-linear effects on the dynamic aperture of the storage ring are also expected and need to be resolved. If these

challenges associated with the cryogenic cooled undulators can be met, an even more dramatic improvement may be obtained by modifying the NSLS-II storage ring to accommodate an extended long straight section that doubles the length of the current high-β straight section, where one could potentially install two of these cryogenic devices and be able to more than triple the spectral flux compared to the IVU22-6m.

Table 2-3. The rms photon source size and divergence of the IVU22-6m at 9.13 keV with the 5th harmonic (K ~ 1.5). Here $\sigma_{Tx,Ty} = \sqrt{\sigma_r^2 + \sigma_{x,y}^2}$ and $\sigma'_{Tx,Ty} = \sqrt{\left(\sigma'_r\right)^2 + \left(\sigma'_{x,y}\right)^2}$, where $\sigma_r = \sqrt{2\lambda L}/4\pi$ is the diffraction limited photon beam size and $\sigma'_r = \sqrt{\lambda/2L}$ is the rms width of the central cone. λ is the wavelength and L is the undulator length. $\sigma_{x,y}$ and $\sigma'_{x,y}$ are electron beam size and divergence given in Table 2.

K	E (keV)	σ_{Tx} (μm)	σ_{Ty} (μm)	σ'_{Tx} (μrad)	σ'_{Ty} (μrad)
1.5017	9.13	134.7	8.66	9.928	7.711

Table 2-4. Distance scaling of the photon beam size and divergence of the IVU22-6m at 9.13 keV with the 5th harmonic (K ~ 1.5). Here $\Sigma_{x,y} = \sqrt{\sigma_{Tx,Ty}^2 + (\sigma'_{Tx,Ty} \cdot p)^2}$ and, $\Sigma'_{x,y} = \sqrt{(\sigma'_{Tx,Ty})^2 + (\sigma_{Tx,Ty}/p)^2}$. $S_{x,y}$ and $S'_{x,y}$ are values given in full width at half maximum ($FWHM = 2\sigma\sqrt{2\ln 2}$)

Distance p (m)	Σ_x (μm)	Σ_y (μm)	Σ'_x (μrad)	Σ'_y (μrad)	S_x (mm) (FWHM)	S_y (mm) (FWHM)	S'_x (μrad) (FWHM)	S'_y (μrad) (FWHM)
10	167.3	77.6	16.7	7.8	0.394	0.183	39.41	18.27
20	239.9	154.5	12.0	7.7	0.565	0.364	28.25	18.19
30	326.9	231.5	10.9	7.7	0.770	0.545	25.66	18.17
40	419.3	308.6	10.5	7.7	0.987	0.727	24.69	18.16
50	514.3	385.6	10.3	7.7	1.211	0.908	24.22	18.16

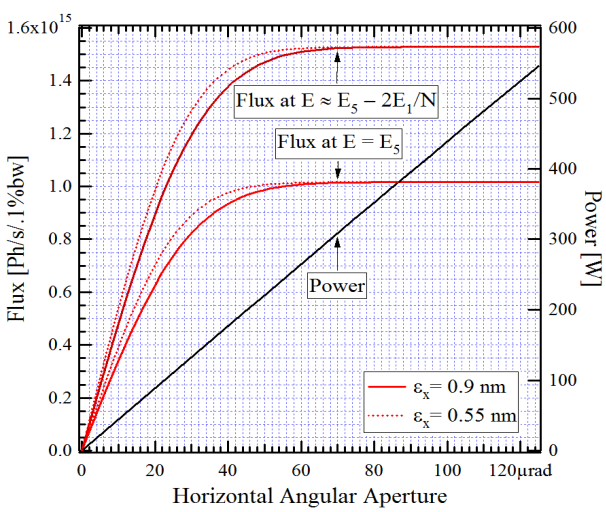

Figure 2-5. Partial spectral flux and power of the IVU22-6m in the high-β straight operating with 5th harmonic at ~ 9.1 keV. The curves are calculated as a function of the horizontal angular aperture. The vertical aperture is fixed at 50 μrad or 1 mm at 20 m from the source.

2.3 Front End

The IXS beamline front end will follow the generic front end of NSLS-II designed for the high-β straight section with modifications that meet the needs of the IXS beamline. A schematic layout of the generic front end is shown in Figure 2-6. The Front End Conceptual Design Report should be consulted for the design details and considerations in radiation safety, heat load management and functionality[14]. A component layout drawing showing the location of the components is included in Appendix 2 for reference.

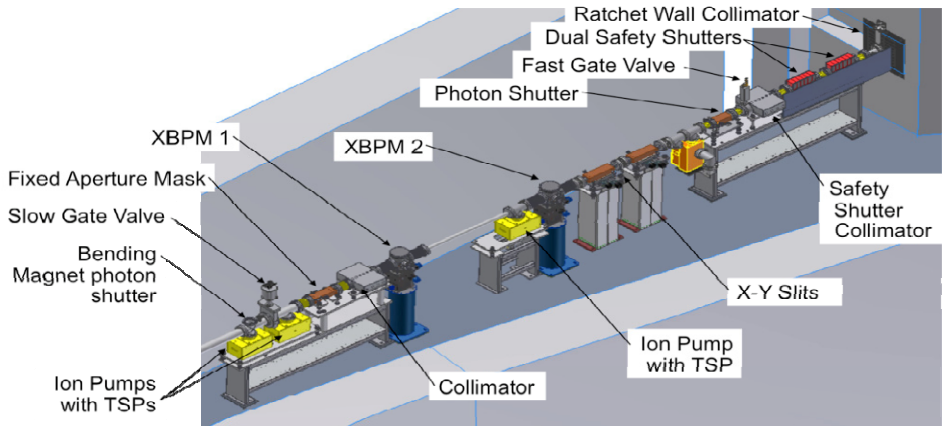

Figure 2-6. Schematic layout of the generic front end for the high-β straight section.

Specific to the IXS beamline, the fixed aperture mask will have an opening of 0.5 mrad in the horizontal and 0.3 mrad in the vertical. The X-Y slits are designed to handle the total power and power density of the IVU22-6m. The slits are constructed by two independent L shape water cooled tapered Glidcop blocks motorized on two X-Y stages, which allow full control of the opening and position of the slits. The opening can be adjusted continuously from fully closed to a maximum opening of 0.2×0.2 mrad^2, whereas the positioning covers possible excursion of the beam up to 0.5 mrad with a positioning resolution of better than 1 µm and stability of better than 5 µm. Under normal operation, the opening of the slits defines the x-ray beam for the beamline and will be limited to no more than 50 µrad in both the vertical and horizontal directions.

As a part of the optical design for the beamline (see section 2.4), a set of Be CRLs will be inserted between the two x-ray beam position monitors (XBPM-1 and XBPM-2) at ~ 20 m from the source to provide 1:1 focusing of the beam for the ultrahigh resolution monochromator. Preliminary heat load analysis suggests that it is feasible for such Be CRLs to withstand the heat load of the central cone from the IVU22-6m, provided that proper water cooling can be applied to the lenses. A water-cooled conical or a rectangular tapered aperture of no more than 50 µrad opening will be designed as an integrated part of the Be CRLs assembly to protect the CRLs from being exposed to excessive heat power. We will also evaluate the use of graphite filters before the Be CRLs to remove the low energy heat power if necessary. This will be done with the aim to minimize absorption loss of the flux.

With the Be CRLs in place, the XBPM-2 would no longer function properly and could be removed. In the generic front end design, XBPM-2 is intended to provide monitoring of the x-ray beam exit angle from the undulator source and as a redundancy to XBPM-1. Its removal is not expected to affect the performance of the front end for the IXS beamline. Further beam position monitoring will be provided in the FOE, upstream of the DCM. Also, no adverse effects on x-ray and Bremsstrahlung shielding by the Be CRLs are expected. Nevertheless, once the Be CRLs assembly design is finalized, a new x-ray and Bremsstrahlung ray tracing will be done to ensure safety compliance.

2.4 Optical Layout

In this section, the rationales for the optical layout and the details of the optical components will be presented and discussed. A schematic rendering of the optical layout for the beamline and spectrometer is shown in Figure 2-7. As mentioned in section 2.1, starting from the undulator, the optical components include the 1D Be compound refractive lens, the high heat load pre-monochromator, and the ultrahigh resolution monochromator based on the inline CDDW monochromator design, followed by two sets of focusing mirrors in two configurations (Mode A and B). After the sample, the optical components for the spectrometer include the multilayer collimating mirror and the ultrahigh resolution CDDW analyzer, followed by the detector. For the analyzer, the CDW monochromator design can also be used, which will be discussed in section 3. In order to discuss the rationales of this layout, it is useful that we first review the working principles and discuss the characteristics and technical challenges of the CDW/CDDW monochromator.

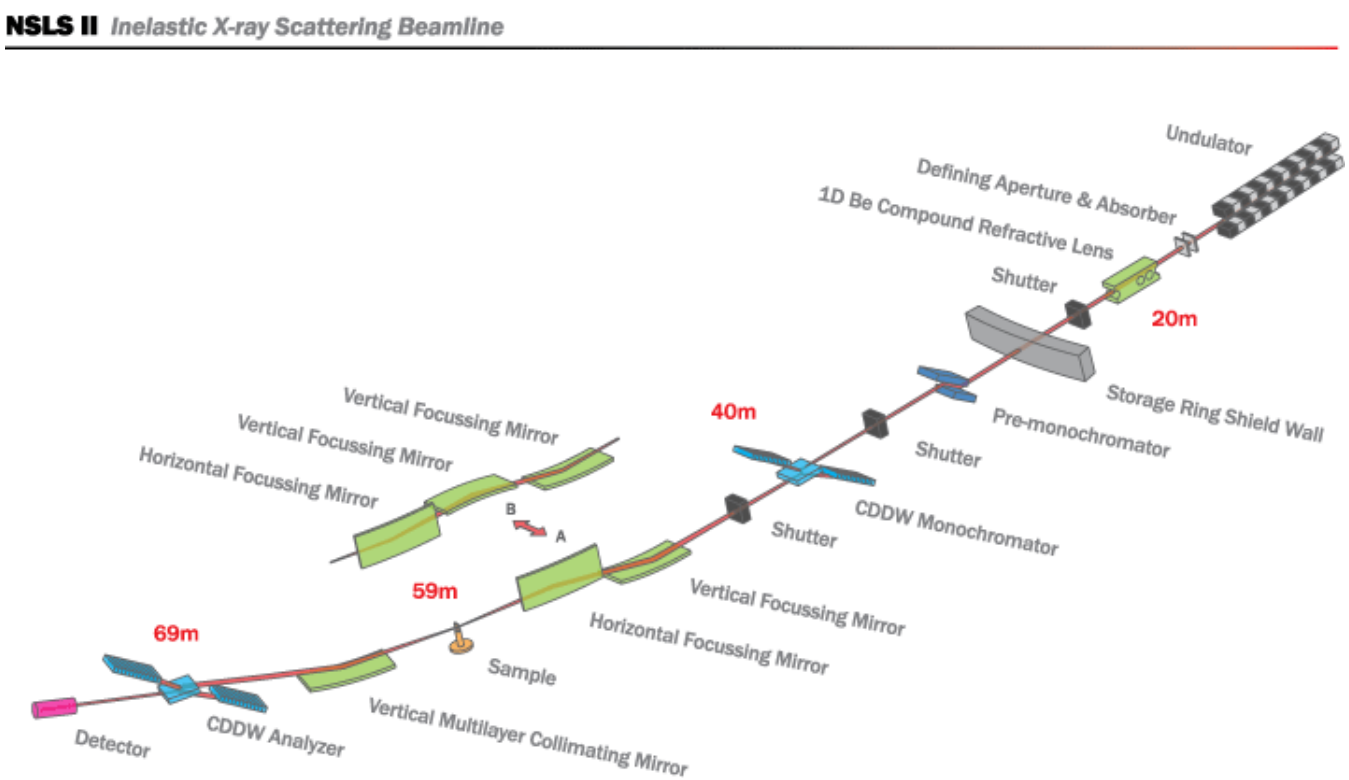

Figure 2-7. A schematic rendering of the optical layout of the IXS beamline and spectrometer. Starting from the undulator, the optical components include the 1D Be compound refractive lens, the pre-monochromator, the CDDW monochromator, followed by two sets of focusing mirrors in two configurations (Mode A and B). After the sample, the optical components include the multilayer collimating mirror, the CDDW analyzer, followed by the detector. See also, Ref 4.

CDW/CDDW Monochromators

The CDW/CDDW monochromator designs[2-4], as shown in Figure 2-8 and Figure 2-10, are based on the angular dispersion effect in asymmetric x-ray diffraction[2,5]. Detailed treatment of the theory can be found in Refs 2-5, which was confirmed by independent calculations in Ref 8. For an ideally collimated and polychromatic incident beam, the dispersion effect is maximized with extreme glancing incidence and at exact backscattering. It can be shown that in this case the relative energy width of the reflected beam is determined only by the angular width of the selected dispersion fan $\Delta\theta_e$ and the glancing incident angle θ_e (= 90˚- φ, where φ is the asymmetric angle of the crystal):

$$\frac{\Delta E}{E} \approx \frac{\Delta\theta_e}{2\tan\varphi} \approx \frac{\theta_e \Delta\theta_e}{2}.$$

By choosing appropriate values for θ_e and $\Delta\theta_e$, it can be shown that sub-meV resolution can be obtained for hard x-rays. And for a given set of θ_e and $\Delta\theta_e$, the lower the energy E, the better the absolute resolution ΔE can be. This makes the CDW/CDDW monochromator design fundamentally different from the symmetric Bragg backscattering optics.

The design of the CDW monochromator implements the dispersion effect through the long dispersing crystal D using the Si(008) reflection at exact backscattering (Figure 2-8). This sets the working energy at 9.13 keV. The required collimation of the incident beam to the D crystal is obtained using a Si(220) asymmetric crystal – the Collimator (C) – with an asymmetric factor of ~ 20 and an incident angle θ_1 of ~ 1.7˚. The C crystal collimates the beam to ~ 5 µrad, and at the same time provides a large angular acceptance of ~ 100 µrad for the monochromator. The collimated beam then transmits through the thin Wavelength selector (W) which has the same reflection and asymmetric angle as the C crystal. The transmission is enhanced anomalously by the Borrmann effect with a detuned angle η of ~ 5 µrad. The transmitted beam is then dispersed by the D crystal to form a dispersion fan back to the W crystal. The W crystal, now in glancing exit geometry with a narrow angular acceptance $\Delta\theta_e$ of ~ 5.15 µrad, selects a sub-meV energy band from the fan to produce a highly monochromatic beam. From a practical point of view, the W crystal also serves the important function of separating the exit beam from the incident beam, so that the exit beam can be utilized for experiments. One could also reverse the optical path of the incident and exit beam of the CDW design as illustrated by the CDW-2 layout shown in Figure 2-8. The two layouts are almost identical with only one exception: The Borrmann effect is introduced after the D crystal dispersion in the CDW-2 layout which results in even sharper resolution function tails. This is shown in Figure 2-9 where the resolution functions for the two layouts are compared. The resolution of the CDW-2 layout can be further improved and the bump can be further suppressed by increasing the thickness of the C crystal at the expense of a small decrease of efficiency[15].

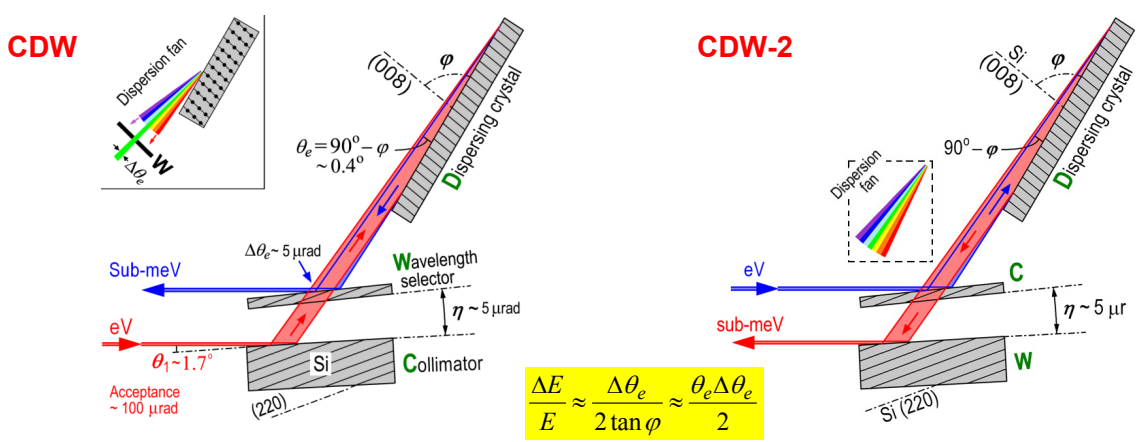

Figure 2-8. Conceptual design of the CDW monochromator[2,3,5] based on the angular dispersion effect in asymmetric Bragg diffraction. The design utilizes the exact back scattering from Si(008) reflection at 9.13 keV to maximize the dispersion effect. The energy resolution achievable is given by $\Delta E / E \approx \Delta\theta_e / 2\tan\varphi \approx \theta_e \Delta\theta_e / 2$. The optical path of the incident and exit beam can be reversed as shown for CDW-2 compared to the CDW.

If the W crystal in the CDW-2 layout is replaced with another D crystal, the exit beam can be reflected to the forward direction as shown in Figure 2-10. This is the so-called CDDW monochromator[4]. In this design, the thin crystal in the middle acts both as the collimator and wavelength selector by reflecting off the two faces, respectively. The additional D crystal increases the resolution by a factor of 2 due to the additional angular dispersion. This inline design is particularly convenient for use as a monochromator for the beamline.

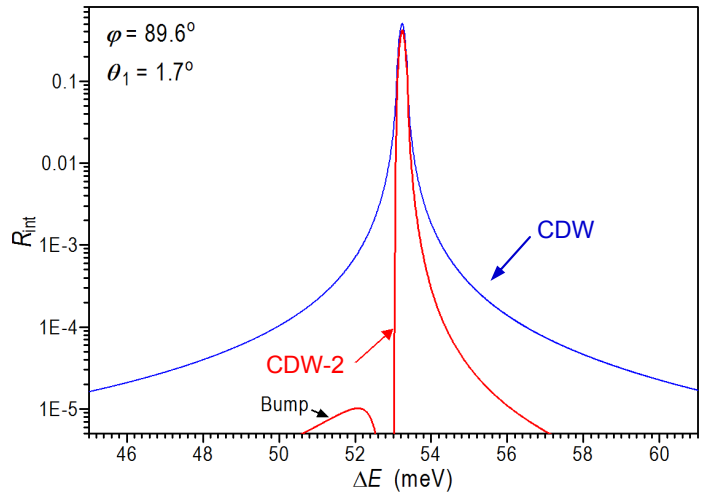

Figure 2-9. Comparison of the resolution function between the CDW and CDW-2 layout in Figure 2-8, both are designed for energy resolution of 0.2 meV. For CDW-2 layout, the resolution can be further improved and the bump can be further suppressed by increasing the thickness of the C crystal at the expense of a small decrease of efficiency.

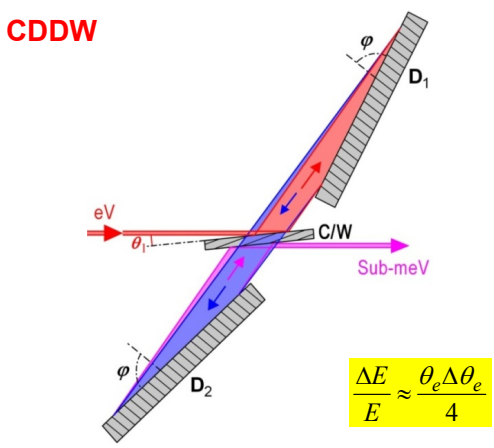

Figure 2-10. The CDDW design[4]. The resolution is improved by a factor of 2 due to the use of two angular dispersive reflections (two D crystals). The thickness of the C/W crystal is ~ 200 μm.

The design parameters of the CDW/CDDW monochromators presented in Figure 2-8 and Figure 2-10 are summarized in Table 2-5. With the parameters of the C/W crystals fixed, the energy resolution of the monochromators can be adjusted by choosing the glancing incident angle θ_e of the D crystal to an appropriate value. A set of energy resolutions along with the required θ_e are listed. The convoluted resolution of two CDDW monochromators represents the total resolution of the IXS instrument. To obtain 1 meV total resolution, two identical CDDW monochromators with 0.7 meV resolution and a θ_e value of 3.41 degree would be needed[16]. For 0.1 meV resolution, both numbers become 10 times smaller with θ_e being at 0.34 degree. Note that the critical angle for Si at 9.1 keV is ~ 0.2 degree.

This small value of glancing incident angle has severe consequences for the design to reach 0.1 meV resolution. As can be seen from Table 2-5, assuming a vertical incident beam height of 0.5 mm, to achieve 0.1 meV resolution, the required D crystal length is more than 1.8 m long!

This is one of the major technical challenges facing the CDW/CDDW monochromator design. The challenge arises from the required lattice homogeneity to obtain 0.1 meV resolution as $\Delta d / d = \Delta E / E \sim 10^{-8}$. Furthermore, due to the

thermal expansion of silicon ($\Delta d / d = \alpha \Delta T$, $\alpha = 2.56\times10^{-6}$ K^{-1}), a 4 mK change in temperature gives rise to an energy change of ~ 0.1 meV. The temperature stability and uniformity of the crystal should therefore be 10 times better at 0.4 mK for 0.1 meV. The use of extreme glancing incidence puts also stringent requirements on the surface roughness and slope errors of the diffracting surface. Our preliminary modeling of diffuse scattering due to surface roughness based on the distorted wave Born approximation (DWBA) suggests that, in order to achieve 80% of the reflectivity of a flat surface, the surface roughness should be less than 2 nm (RMS) for 0.1 meV[15]. Due to the dependence of the energy resolution on the asymmetry angle, the slope error (or the straightness) of the diffraction surface should be better than 10 µrad for 0.1 meV. Strain-induced crystal bending as a result of the mounting schemes as well as the positioning angular stability of the optics must be better than 0.2 µrad (see later). To achieve these technical specifications is already a formidable task for a crystal length of 180 mm. To do that for a crystal length of more than 1.8 m seems almost impossible.

Table 2-5. Design parameters for the CDW and CDDW monochromators in Figure 2-8.

- D crystal: Si(008) at exact backscattering
  - E = 9.132437 [keV] (d = 0.678813 [Å])
- C/W crystal: Si(220) reflection
  - Bragg angle: θ_B = 20.70481 [deg]
  - Asymmetric angle: φ_C = 19.0 [deg]
  - Incident angle: θ_1 = 1.7 [deg]
  - W angular acceptance: $\Delta\theta_e$ = 5.15 [µrad]
- Geometry parameters
  - Incident beam height: h = 0.5 [mm]
  - Footprint on C/W: l_C = 16.85 [mm]
  - Exit beam width: h_D = 10.77 [mm]

ΔE of CDW [meV]	ΔE of CDDW [meV]	ΔE of 2 CDDW convoluted [meV]	$\theta_e = 90 - \varphi$ [deg][16]	D crystal length [mm]
2.00	1.00	1.41	4.87	127
1.40	0.70	**0.99**	3.41	181
0.70	0.35	0.49	1.71	362
0.30	0.15	0.21	0.73	844
0.20	0.10	0.14	0.49	1266
0.14	0.07	**0.10**	0.34	1809

To address this challenge, we will consider two approaches:

(1) On the beamline side, we will use the idea of a CDDW monochromator designed for 1 meV resolution plus a channel cut (CC) crystal to reach the final goal of 0.1 meV. This is illustrated in Figure 2-11. For this scheme to work, the incident beam divergence needs to be smaller than 20 µrad. Since the central cone vertical divergence of the beam from the IVU22-6m is less than 20 µrad in FWHM (see Table 2-4), this scheme provides a natural solution. Even with the Be CRLs providing the 1:1 vertical focusing, this vertical divergence will be maintained. Furthermore, this approach provides the possibility of switching the energy resolution of the beamline between the 1 meV and 0.1 meV. A detailed calculation of the efficiency between this approach and a CDDW monochromator designed for 0.1 meV is presented in Figure 2-12. Based on the calculation, the peak efficiency of the CDDW+CC scheme is only about 20% less than that of a single CDDW monochromator designed for 0.1 meV. Both schemes also display sharp tails – largely due to the Borrmann transmission – compared to a Lorentzian curve of the same width, which is the typical shape of the resolution function from symmetric Bragg back reflections.

(2) The same approach however will not work well for the analyzer of the spectrometer, since the incident divergence (or more precisely, convergence) of the scattered photons onto the CDW/CDDW analyzer must be optimized to match their angular acceptance of ~ 100 μrad (in order to maximize the count rate). As noted above, the channel cut requires the divergence be less than 20 μrad to work. In the spectrometer design (see Section 3), this is done by coupling the CDW/CDDW analyzer with a multilayer collimating/focusing mirror which collects up to 5 mrad of the scattered photons in both the vertical and horizontal (the scattering) planes and collimates them to within 100 μrad. To solve this problem, we will develop the so-called "comb crystal" to replace the long D crystal in the CDW/CDDW design.

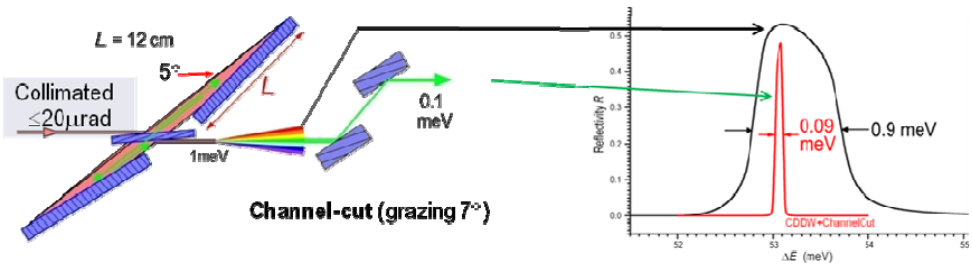

Figure 2-11. The optical scheme of using a CDDW monochromator[4] designed for 1 meV resolution plus a channel-cut crystal to obtain the 0.1 meV resolution. The scheme provides also a natural way of switching the energy resolution between 1 and 0.1 meV.

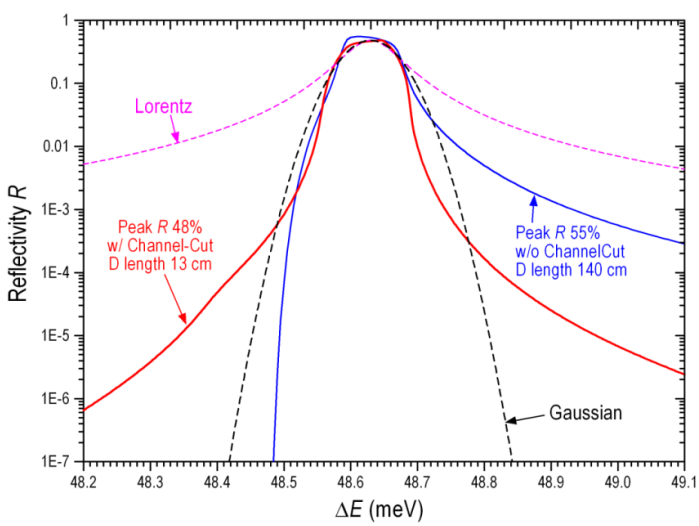

Figure 2-12. Comparison of the reflectivity of the CDDW monochromator designed for 0.1 meV and that designed for 1 meV plus a channel cut to reach the 0.1 meV resolution, both showing a resolution function much sharper than a Lorentz curve.

Proposed by Shvyd'ko[17], the idea of the comb crystal is essentially to reduce the physical length of the long D crystal by sectioning it into segments and stacking them together (see Figure 2-13). The individual segments have a thickness of a few hundred microns, a width of ~ 5 – 10 mm and a length of ~ 100 mm. The thickness of the fins should be chosen to be greater than the extinction length of the x-ray diffraction but minimized to reduce loss of diffracting area. It should be thick enough to provide sufficient strength to withstand the gravity sag. The separation between the fins obviously depends on the glancing incident angle for the desired resolution and should be optimized together with the length of the fins. Clearly, it would be ideal if such crystals can be fabricated as a monolithic block as shown in Figure 2-13(a), as this helps to maintain the crystalline alignment of the individual fins. There is however considerable technical challenge in doing so due to the difficulty in polishing the diffraction surface inside the grooves to the required level of roughness and slope errors. Another approach would be to first fabricate the fins individually and then put them back together by

mechanical means. In this way, preparing the diffraction surface is relatively easier as conventional CMP polishing machineries and techniques can be utilized to obtain the high quality crystal surface needed for the individual fins. However, putting them back together afterward with the crystalline planes aligned and maintained becomes an engineering challenge. Both approaches therefore have their pros and cons. In any case, the successful implementation of the CDW/CDDW analyzers requires the comb crystal. The comb crystal therefore is one of the key components for the success of this new spectrometer. Dedicated R&D effort is currently underway.

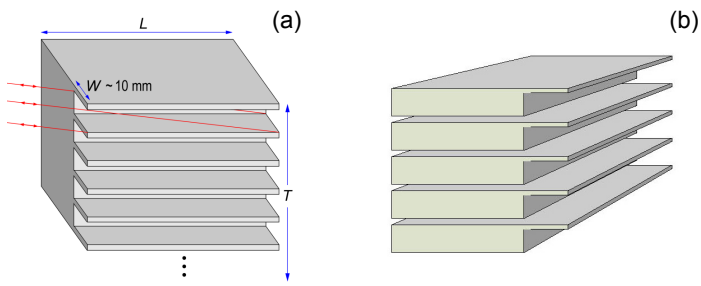

Figure 2-13. Two possible ways of fabricating the comb crystal: (a) as a monolithic block[17]; and (b) as individual fins joined together by mechanical means

Another major technical challenge of the CDW/CDDW monochromators and analyzers is about maintaining the angular stability of the D crystal. This is due to a useful feature of the CDW/CDDW designs in which energy tuning can be carried out through rotation of the D crystals (relative to the C/W crystals). Figure 2-14 shows the calculated spectra for a range of rotation angle ($\Delta\Theta$) of the D crystal from the central position for the CDW design. The tuning rate depends on the energy resolution of the design. Two examples are shown here: one was designed for a resolution of 0.62 meV which has a tuning rate of 0.24 meV/µrad; the other was designed for 0.16 meV with a tuning rate of 0.07 meV/µrad. In both cases, a rotation of 0.2 µrad corresponds to an energy tuning of ~ 1/10 of the designed resolution. While this feature provides a fast way of scanning the monochromator energy for the experiment, it also requires an angular stability of the D crystal relative to the C/W crystals to within 0.2 µrad in order to maintain the energy stability during data acquisition.

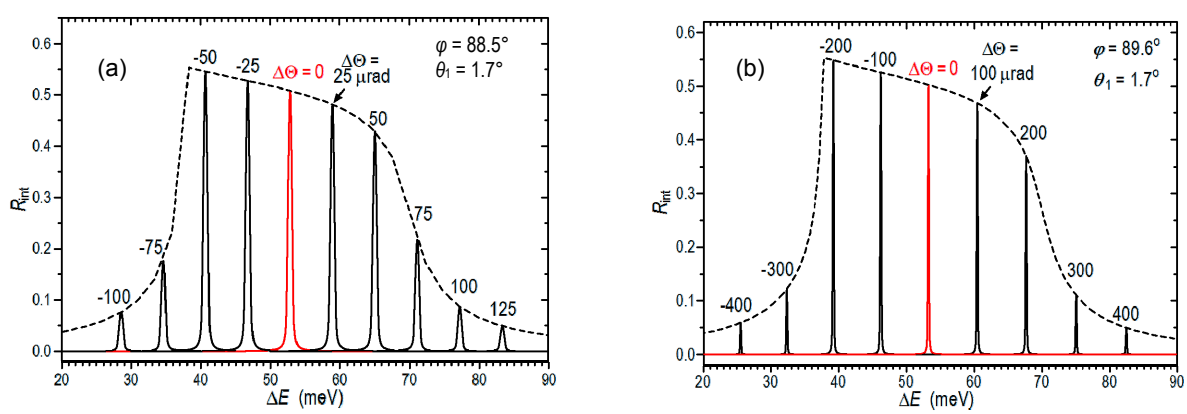

Figure 2-14. Energy tuning of the CDW monochromator through rotation of the D crystal. (a) is designed for an energy resolution of 0.62 meV with a tuning rate of 0.24 meV/µrad. (b) is designed for an energy resolution of 0.16 meV with a tuning rate of 0.07 meV/µrad. In both case, a rotation of the D crystal by 0.2 µrad corresponds to an energy tuning of ~ 1/10 of the designed resolution.

The energy tuning range in this case is given essentially by the Darwin curve width of the Si(008) back reflection of the D crystal, i.e., the width of the entire dispersion fan, which is about 34 meV. For a wider scan range, temperature scan of the D crystals is necessary. For experiments performed at the 0.1 meV resolution, it is anticipated that a scan range of 34 meV would be sufficient for most cases.

Finally, we discuss the broadening of the source size by the CDW/CDDW optics. This is an important issue as it influences the design of the optical layout of the beamline, particularly the focusing configuration. As illustrated in Figure 2-15, the effect is due to the angular dispersion in asymmetric Bragg reflections employed in the optics. Essentially, for a monochromatic beam reflected from an asymmetric crystal with an asymmetric factor of $|b| = \sin\theta_e / \sin\theta$, the virtual source size stays the same, but the distance of the virtual source is modified by the asymmetric factor: $L' = L \cdot |b|$ (Figure 2-15 (a)). In the case of a polychromatic beam, because different color traces to a different virtual source point due to the angular dispersion (Figure 2-15 (b)), it produces a virtual source size given by the virtual source distance multiplied by the angular divergence of the exit beam: $\Delta Z = L' \Delta\theta_e$. In the case of the CDW/CDDW optics, the D reflections are at exact backscattering with $|b| = 1$; the C and W reflections act as a (+, -) channel cut crystal which brings the virtual source also back to the same location. The angular dispersion in the exit beam of the CDW/CDDW monochromator therefore dominates the broadening effect. Tracing through the CDDW optics (Figure 2-15 (c)) indeed indicates that the virtual source is located almost at the same location as the real source, but with substantial source size broadening in the dispersion plane due to the angular dispersion and divergence of the exit beam, which is as much as ~ 100 µrad for the CDDW monochromator. If the CDDW mono is located at ~ 40 m from the source, the vertical virtual source size can be more than 4mm! This is much bigger than desired, and will impact severely the performance of the beamline if not corrected.

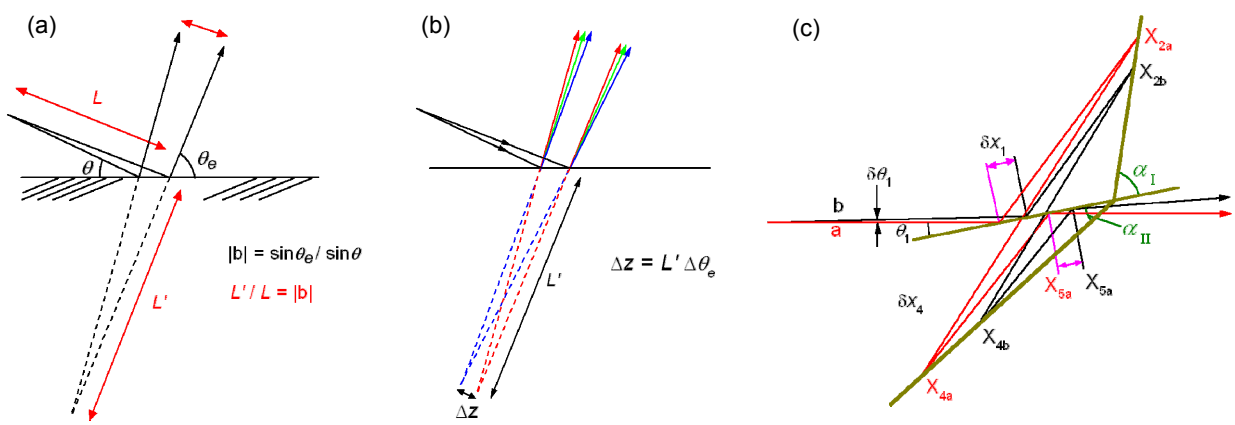

Figure 2-15. Effect of the angular dispersion in asymmetric Bragg reflection on the virtual source size: (a) for a monochromatic beam, and (b) for a polychromatic beam. The virtual source size is amplified and is given by the virtual source distance multiplied by the angular divergence of the reflected beam. (c) A trace through the CDDW optics confirms that the virtual source is located almost at the same location as the real source, but the source size is broadened by the angular divergence of the exit beam (~ 100 µrad) multiplied by the distance of the source.

Focusing Configurations

Since the vertical virtual source size of the CDDW monochromator scales with the distance of the source, in order to reduce the virtual source size of the CDDW monochromator, a 1D Be CRL is used in the front end at 20 m from the source to provide a 1:1 focusing *only* in the vertical direction. This creates a secondary vertical source point to 40 m for the CDDW monochromator (see Figure 2-16), while the horizontal source location remains at the undulator. The latter is important in order to retain the necessary distance to create the needed demagnification for horizontal focusing. The CDDW monochromator is then located at a nominal position of 40.2 m giving a new source distance to the CDDW

monochromator at 0.2 m. One could perhaps even focus the beam on to the CDDW monochromator, although this creates a divergent term in our beam size estimate. Further optimization of the positions of the Be CRL and the CDDW monochromator will be considered during the preliminary design, when the actual location of the Be CRL in the front end can be decided.

Subsequent amount of focusing applied to the beam takes into account the requirements of the IXS experiments, and is determined by optimal positioning of the focusing optics that sets the demagnification factors. Two configurations have been considered and are shown in Figure 2-16:

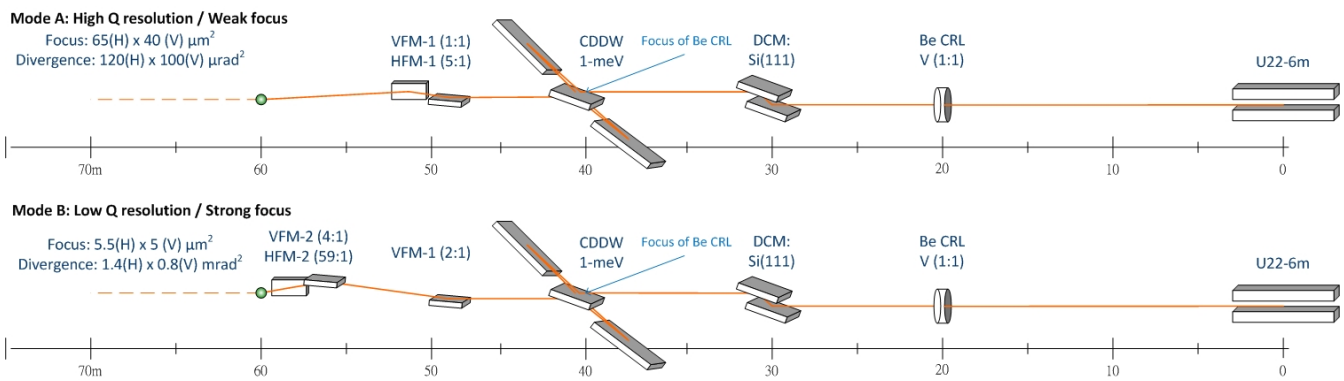

Figure 2-16. Schematics of the two focusing configurations of the beamline. The horizontal axis indicates the distance from the undulator source. Mode A uses one set of K-B mirrors located around 50 m from the source with weak demagnifications in order to achieve high Q resolution, small divergent beam. Mode B uses a second set of K-B mirrors located at ~ 58 m with strong demagnifications to achieve fine focus. In both configurations, the Be CRL located at 20 m provides a 1:1 focusing of the source in the vertical in order to reduce the vertical virtual source size of the CDDW monochromator.

(1) Mode A: High Q Resolution / Large Focus

This configuration takes into account the best Q resolution of ~ 0.01 nm^{-1} required for some of the most demanding experiments on disordered systems in low Q. In the scattering plane, the total Q resolution Δq is determined by the Q spread of the incident and the scattered beam as illustrated in Figure 2-17 by the vector sum: $\Delta\mathbf{q} = \Delta\mathbf{Q}_i + \Delta\mathbf{Q}_s$, where the magnitude ΔQ_i is determined by the divergence of the incident beam onto the sample, and ΔQ_s by the angular acceptance of the analyzer of the spectrometer. This requires an incident beam divergence on the sample of less than or ~ 0.2 mrad and can be achieved with a K-B mirror set located at ~ 50 m, providing a 1:1 focusing in the vertical (since the vertical source point is at 40 m) and 5:1 in the horizontal onto the sample located at ~ 60 m. The estimated focal size is 65(H) × 40(V) μm^2 with a beam divergence of 0.12 (H) × 0.10 (V) $mrad^2$, considering only geometric contributions of the optics (i.e., slope errors) and distance scaling of the source size and divergence from the IVU22-6m. The large focus would be helpful to reduce beam damage for soft mater and biomolecular systems, but would be detrimental to the acceptance of the analyzer system. Preliminary calculation shows that the ML mirror needs to be more than 0.5 m away from the sample in order to collimate the scattered photons to ~ 0.1 mrad for the acceptance of the CDDW analyzer. The actual detection efficiency obtainable on the spectrometer design may put an upper limit on how high the Q resolution can be for this configuration.

(2) Mode B: Low Q Resolution / Small Focus

In this configuration, the horizontal mirror in Mode A is removed from the optical path, whereas the vertical mirror is detuned to provide a 2:1 focusing to ~ 55 m. A second set of K-B mirrors is then introduced at ~ 59 m to provide a 4:1 focusing in the vertical, which combined with the first vertical mirror, provides a total demagnification of 8:1 for the vertical focus. This double focusing scheme is necessary in order to obtain a vertical focal size of around 5 μm as a result of the new vertical source position at 40 m after the Be CRL. In the horizontal, only the second

horizontal mirror is used which provides a 59:1 focusing for the horizontal focus. This is necessary in order to produce a horizontal focal size of ~ 5 µm due to the large horizontal source size of the high-β straight section. The estimated focal size is 5.5(H) × 5(V) μm^2 with a beam divergence of 1.4(H) x 0.8(V) $mrad^2$. This configuration provides stronger focusing at the expense of the Q resolution, and should be suitable for HP systems, small single crystals and samples in confined geometries (such as surfaces and interfaces), for which high Q resolution is not required. In this case, the Q resolution contribution from the horizontal divergence of the focused beam would be ~ 0.05 nm^{-1}, which limits the best total Q resolution can be achieved.

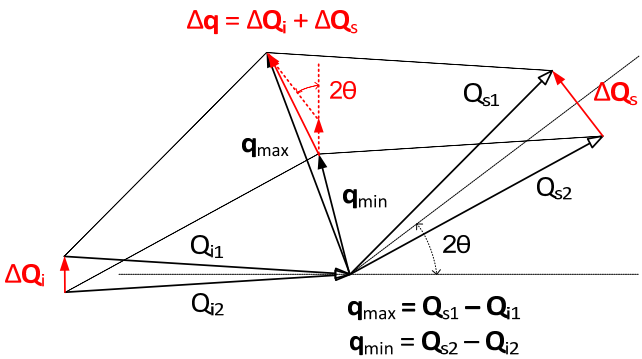

Figure 2-17. Schematic illustration of the total Q resolution in the scattering plane. Here $\Delta\mathbf{Q}_i$ and $\Delta\mathbf{Q}_s$ are the momentum spread of the incident and scattered beam, respectively. The spread of the momentum transfer $\Delta\mathbf{q}$, which represents the total momentum resolution in the scattering plane, is given by the vector sum of $\Delta\mathbf{Q}_i$ and $\Delta\mathbf{Q}_s$. It is obvious that $\Delta q = (\Delta Q_i + \Delta Q_s)\cdot\cos(\theta)$. At very low Q or in the plane perpendicular to the scattering plane (corresponding to $\theta \approx 0$), $\Delta q = \Delta Q_i + \Delta Q_s$.

A third possible configuration is to remove the 1st set of the K-B mirrors completely from the beam and use only the 2nd set of the K-B mirrors for the focusing. A stronger demagnification factor for the vertical can be obtained which gives potentially a better vertical beam size. The efficiency and performance of all these configurations will be studied in greater details by Shadow ray tracing during the preliminary design.

All these configurations call for bendable prefigured or adaptive mirrors, which provide the highest flexibility in adjustment needed for these configurations. The adaptive mirrors can in principle be used to correct tangential slope errors of its own and those induced by other optics. All these mirrors will be of bare Si without coatings as it provides the highest reflectivity of ~ 95% at 9.1 keV with an incident angle of ~ 2.5 mrad. The use of Si will also help to eliminate possible higher harmonics penetrating through the CDDW monochromators.

Alternative Monochromators

The CDW/CDDW monochromators are chosen for the IXS beamline because of their novel design that gives *a large angular acceptance and the potential to lead us to the ultimate resolution of 0.1 meV*. For this reason, they remain at present the focus of our R&D effort. However, there are considerable technical challenges as we have presented in the previous sections. In order to ensure that a workable, best in class user instrument can be built on day one of NSLS-II operation, a number of alternative monochromator designs have been considered. In choosing an alternative design, our main considerations include (1) the practically achievable energy resolution, (2) the angular acceptance or compatibility to be used as analyzer optics, and (3) compatibility with the current beamline design. Among the alternatives we have examined, the inline 4-bounce scheme designed by Yabashi et al[18] and Toellner et al[9] is the most applicable. The monochromator by Toellner et al (Figure 2-18) in particular was designed and proven to deliver 1 meV resolution at the ^{83}Kr nuclear resonant energy at 9.403 keV with an overall efficiency of 36% using four Si(008) reflections. The asymmetry factors (*b*) are 0.13, 0.174, 5.76 and 7.6, respectively. The working energy is very compatible with the current beamline design, including the choice of the undulator. This monochromator has also the advantage of a sharp resolution tails due to the multiple high index Bragg reflections, compared to a Lorentzian shape[9,19]. This is compared in Figure 2-18 with the CDW monochromator. Both are designed in this case to achieve an angular acceptance of ~ 93 µrad with an energy resolution of ~ 1 meV. The resolution function of both designs has a comparable tail on one side. The CDW has a sharper tail on the other side due to the Borrmann effect, and a higher theoretical efficiency. However,

we should note that the angular acceptance of ~ 93 µrad is near its maximum for this alternative monochromator design as the incident angle gets close to the critical angle. It would be difficult also to improve the energy resolution further.

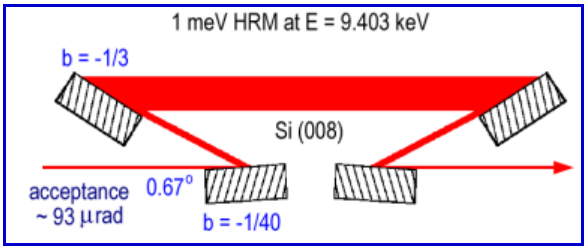

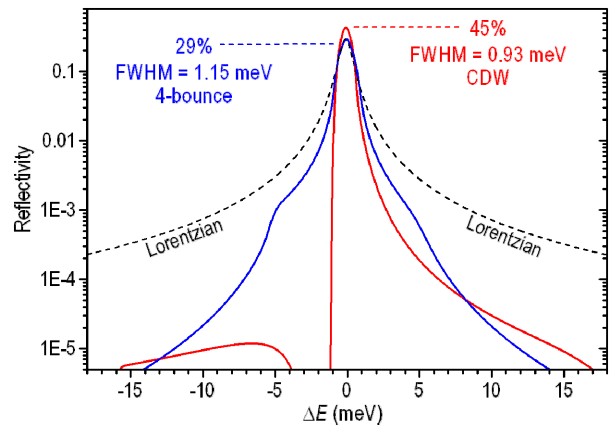

Figure 2-18. An alternative monochromator design by T. Toellner[9]. This design has been demonstrated to deliver an energy resolution of ~ 1 meV with an overall efficiency of 36% (at smaller angular acceptance than shown). A comparison of this monochromator designed to achieve ~ 93 µrad angular acceptance is made with the CDW design (right panel).

2.5 High Heatload Optics

Based on the optical design presented above, the power delivered to, absorbed by and transmitted through the high heat load components in the front end and the beamline are summarized in Table 2-6. The calculations were performed for the IVU22-6m operating at 9.13 keV with the 5th harmonic (K ~ 1.5). Two scenarios are considered here based on whether or not the Be CRLs are used in the front end. In the case without the Be CRLs, the X-Y slits opening corresponds to 4Σ of the central cone as defined in Table 2-4, whereby ~ 133 W of power is transmitted through with ~ 95% of the total available flux. In general, this is the optimal condition to operate the beamline when the Be CRLs are not in use. Opening further the XY-slits to allow the entire central cone flux through will result in a substantial increase of heat power as can be seen from Figure 2-5. The maximum power for the full central cone beam corresponds to a minimum opening of ~ 60 µrad × 50 µrad (H × V) with a transmitted power of ~ 267 W. This would be the worst case scenario for the power load onto the double crystal pre-monochromator (DCM).

Table 2-6. Calculated power load from the IVU22-6m operating at 9.13 keV with the 5th harmonic (K ~ 1.5) on various components in the front end and on the double crystal monochromator (DCM)

Beamline Component	Aperture (H×V) µrad^2	Incident Power	Power Absorbed	Power Transmitted	Notes
Fixed Mask	500 × 300	~9.1 kW	~2.3 kW	~6.8 kW	Generic front end component
Be CRL Collimator	Φ50	~6.8 kW	~6.635 kW	~175 W	Without filters upstream
2D Be CRLs	Φ50	~175W	~95 W	~80 W	Z = 20 m from source
X-Y Slits	50 × 50	~80 W	~0	~80 W	With Be CRLs
	48 × 30.8	~6.8 kW	~6.67 kW	~133 W	Without Be CRLs, aperture opening corresponds to 4Σ of the central cone
DCM	50 × 50	~80 W	~80 W	~0 W	With Be CRLs
	48 × 30.8	~133 W	~133 W	~0 W	Without Be CRLs, aperture opening corresponds to 4Σ of the central cone

To ensure that the DCM crystal can handle these heat powers, finite element analysis (FEA) has been performed to quantify the amount of slope error induced by the incident x-rays for these two cases using the following parameters:

- The Si(111) monochromator crystal dimension is 90 mm long, 50 mm wide and 35 mm thick
- The crystal is located at 29.3 m from the source with a vertical diffraction geometry and an incidence angle of 12.506˚, corresponding the Bragg angle for 9.13 keV
- The crystal is cryogenically cooled with LN2 at 77K with a side cooling geometry with effective convection coefficient of h_{conv}= 0.003 W/mm^2/K representing the effectiveness of thermal contact

The results are summarized in Figure 2-19. In these cases, a slope error of < ± 4 µrad was obtained. This is ~ 25% of the rocking curve width of Si(111) reflection at 9.13 keV, and therefore is believed to have minimal effect on the performance of the DCM.

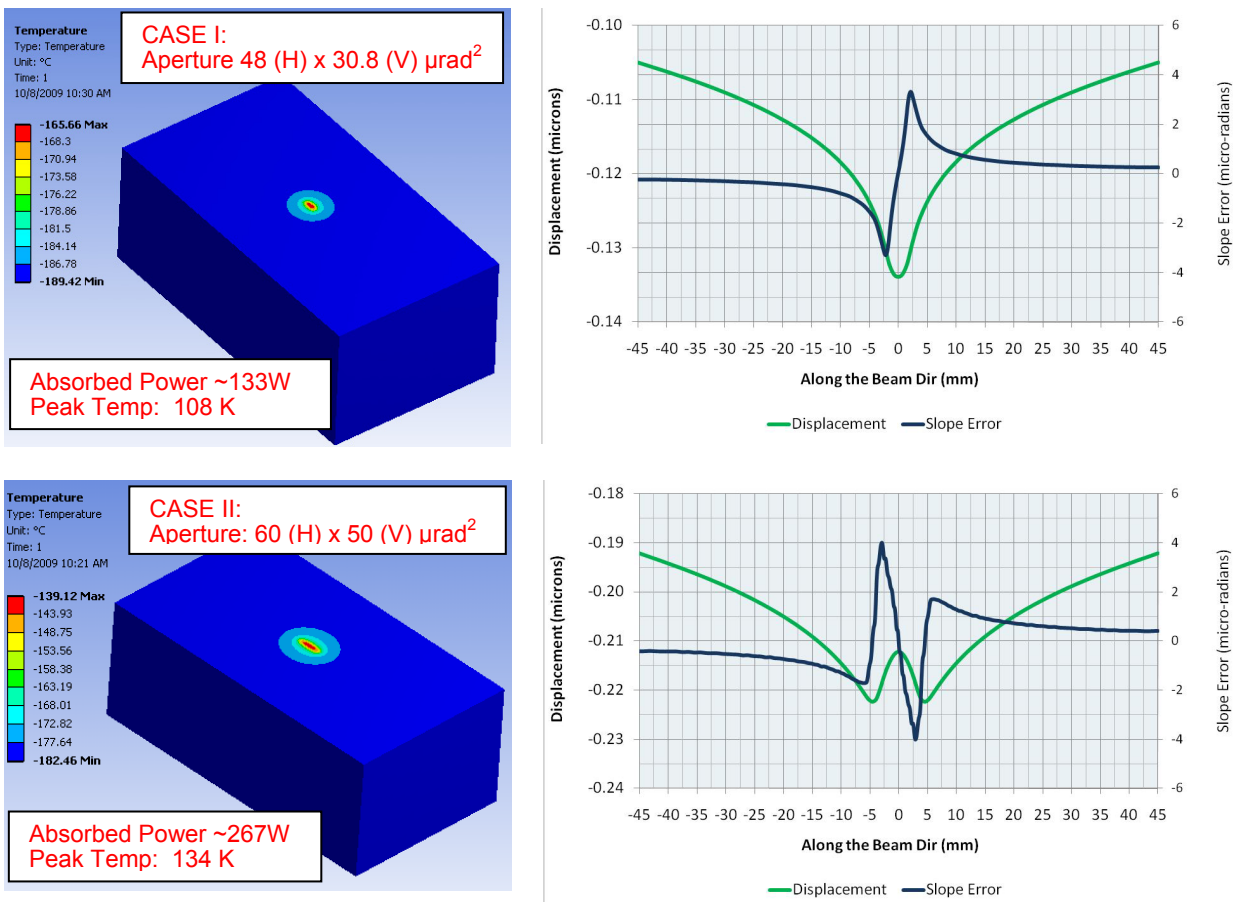

Figure 2-19. Finite element analysis (FEA) of the 1st DCM Si(111) crystal. Two cases of heat power were considered: Case I aperture opening corresponds to 4Σ of the central cone; Case II corresponds to the minimum aperture opening for the entire photon flux to go through. The left panels show the temperature distribution on the crystal. The right panels show the vertical displacement and slope error induced by the heat load.

In the case with the Be CRLs, preliminary heat load analysis has been performed for a 2D Be CRL with a focal length of $f = R/2\delta = 30$ m, where $\delta = 1 - n = 4.11552355\times10^{-6}$ for Be at 9.1 keV with R = 0.2469 mm defining the apex radius of the parabolic shape. For 1:1 focusing at 20 m away from the source, three lenses will be required. The power

absorption and transmission shown in Table 2-6 were calculated for one such lens with an apex thickness of 100 µm. With a uniform boundary condition of 27 °C, a maximum temperature rise is ~ 95 °C (Figure 2-20). This result is encouraging, suggesting that it should be feasible for the Be CRLs to withstand the heat power of the IVU22-6m white beam. Further FEA analysis will be performed to aid the cooling design for 1D Be CRLs which will be used for the beamline. In case that the Be CRLs could not withstand the heat load under reasonable doubts, pre-filters will be considered. The power transmitted through to the DCM with the Be CRLs in place would then be substantially less. Further FEA analysis for the DCM crystal for these cases will also be performed to ensure that the cooling design with LN2 of the DCM crystals is adequate to handle the remaining heat power.

Finally, we note that the power transmitted through the DCM as shown in Table 2-6 is not exactly zero, but is on the order of ~ 10 mW. This power will be delivered to the thin C crystal of the CDDW monochromator. Albeit small, the effect of this power load on the C crystal should be studied and will be examined during the preliminary design.

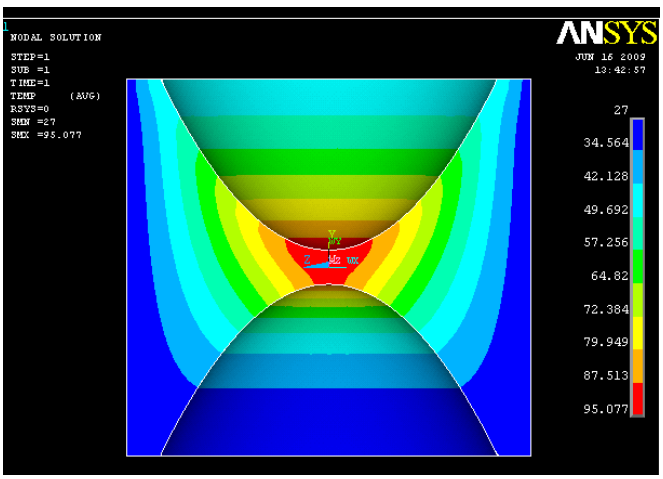

Figure 2-20. Preliminary FEA analysis of a 2D Be CRL designed with *f* = 30 m for 9.1 keV photons. Apex thickness is 100 µm. The apex radius of parabolic shape is 0.2469 mm. With a uniform boundary condition of 27 °C and a close to uniform power density deposited on the lens of ~ 225 W/mm^2 from the IVU22-6m, the maximum temperature rise is ~ 95°C.

2.6 Beamline Component Layout

In this section, some details of the beamline component layout will be presented and discussed.

First Optical Enclosure

As can be seen from Figure 2-21, the first major component in the first optical enclosure (FOE) is a differential pumping unit (labeled as DP) that separates the beamline vacuum from the front end. This was designed to minimize the number of windows in order to reduce unnecessary loss of flux due to absorption. This is followed by a Bremsstrahlung collimator (BC) which prevents unwanted radiation from passing through. A blade type beam position monitor (BPM) with water cooled fluorescent screen provides the needed diagnostic tool during initial commissioning. The BPM can be used further to provide beam position monitoring and feedback during operation. The main optical component in this enclosure is the double crystal pre-monochromator (DCM). It will be cryogenically cooled using LN2. Its design will be based on commercially available models with modifications that meet the requirements of this beamline. For example, it can be designed with a reduced energy tuning range compared to most commercial devices, which will result in a more compact design, less cost and higher stability. The DCM will have a built-in white beam stop to stop the high-energy white beam from passing through. Another Bremsstrahlung collimator or stop then follows. A quadrant BPM after the DCM provides the needed diagnostics for the alignment and feedback control of the DCM, which is important to maintain the stability of the DCM. The monochromatic beam slit (MS) then defines the monochromatic beam from the DCM before it is delivered further downstream. A photon shutter (PS) is installed at the end of the enclosure to maintain the heat load on the DCM while access to the downstream experimental hutches is needed. Finally, a 1.5m long space upstream of the PS is reserved in case it becomes necessary to install a mirror there to collimate/focus the beam before it is delivered to the downstream high-resolution optics.

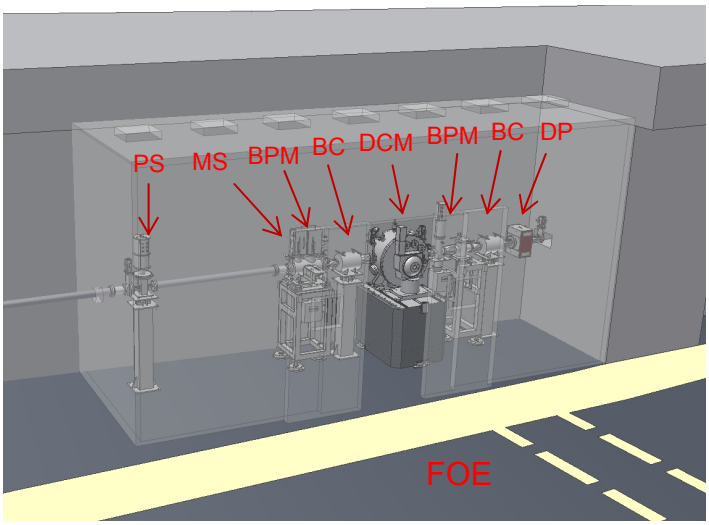

Figure 2-21. 3D perspective view of the first optical enclosure (FOE) and its major beamline components. From right to left we have DP: differential pump; BC: Bremsstrahlung collimator; BPM: beam position monitor; DCM: double crystal pre-monochromator; MS: monochromatic beam slit; and PS: photon shutter.

Experimental Hutches

The experimental hutches EH-1 and EH-2 and their major components are shown in Figure 2-22. EH-1 houses the ultrahigh resolution monochromator (URM). This can be the CDDW+CC monochromator or one of the alternative monochromator designs. The goal here is to achieve the 1 and 0.1 meV resolution for the experiment. Maintaining the temperature stability is extremely important here. EH-1 is therefore designed to house only the URM. A photon shutter (PS) is included to maintain the heat load (a few mW) on the optics while access to the downstream hutches is required.

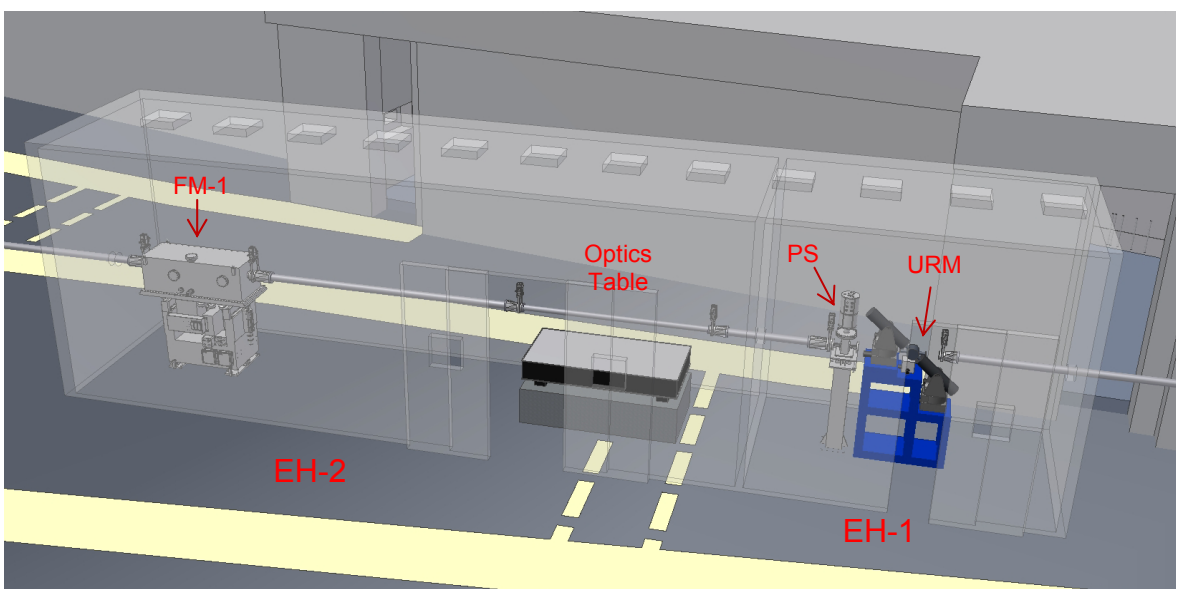

Figure 2-22. Experimental hutches EH-1 and EH-2 and their major components. EH-1 houses the ultrahigh resolution monochromator (URM) with a photon shutter (PS). EH-2 has an optics table where additional conditioning optics and diagnostics can be installed. The first set of K-B mirrors (FM-1) is located at the downstream end of EH-2.

In EH-2, the main components include an optical table and the first set of focusing K-B mirrors (FM-1). The hutch is made relatively large (~ 9 m long) with open space designed for future optics development. We anticipate in particular that this may become essential for realizing the ultimate 0.1 meV resolution goal. The optical table will be used to house additional optics for conditioning the beam for the experiment, such as a phase plate to rotate the polarization from the horizontal to the vertical. This will be necessary when the scattering angle of the experiment is more than ~ 50 deg, where the polarization loss begins to outweigh absorption loss by the phase plate. Additional diagnostics setup may be installed also on the optical table. It is possible also that a removable beam stop be installed at the end of the EH-2. This will enable access to the last experimental hutch (EH-3) for sample preparation and instrument setup while EH-2 is being used for experiments.

Finally, the last experimental hutch EH-3 and the major components are shown in Figure 2-23. These include the second set of focusing K-B mirrors (FM-2), and the two spectrometers. One spectrometer has an arm length of 5 m and covers a scattering angle from -10 to 135 deg. The corresponding momentum transfer (Q) range covers -8 to 85 nm^{-1}. It is designed to achieve 1 meV resolution and a Q resolution of ~ 0.1 nm^{-1}. It will be coupled with a phase plate installed in EH-2 when the scattering angle is close or larger than ~ 50 deg where the polarization loss becomes greater than the intensity loss due to absorption by the phase plate. The other spectrometer has an arm length of 10 m and covers a scattering angle from -5 to 15 deg, corresponding to a Q range of -4 to 12 nm^{-1}. It is designed to achieve 0.1 meV resolution and a Q resolution of much less than 0.1 nm^{-1}. The two spectrometers share the same sample stage. All conventional sample environments will be supported, including high pressure diamond anvil cells, low temperature (4K) with He cryostats, high temperature (1000K) and alignment capability for single crystals. A beam conditioning unit with clean-up slits, absorber wheel, and beam monitor etc, will be installed between the FM-2 and the sample stage. In Section 3, we will present and discuss the basic optical concept of the spectrometers.

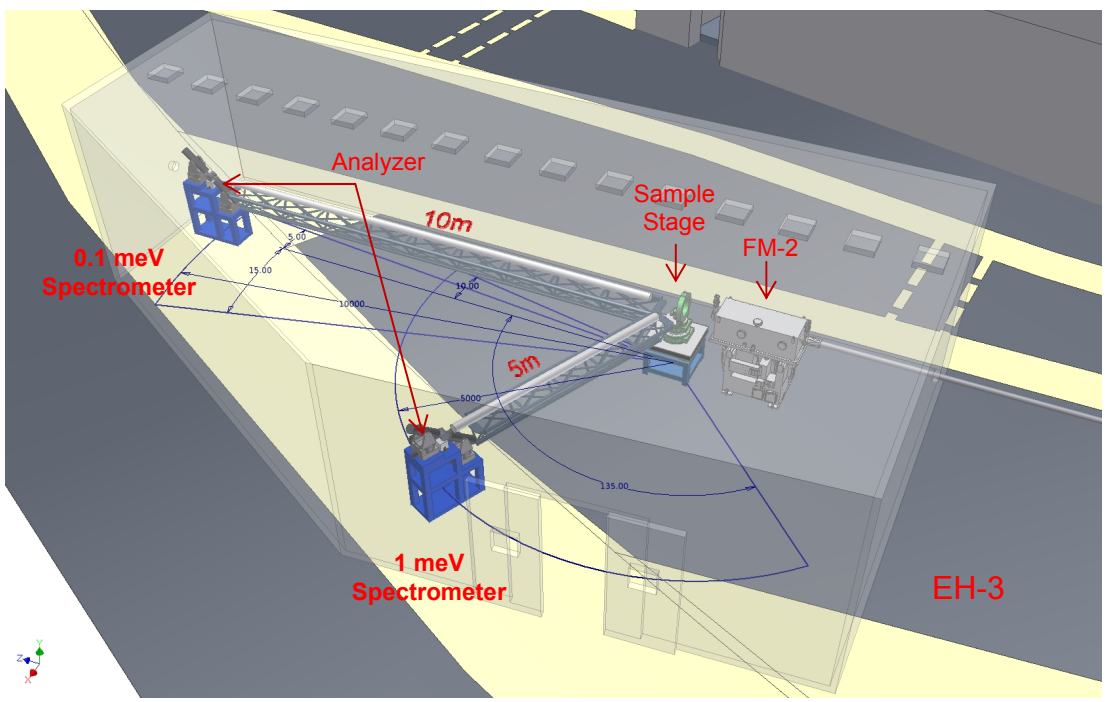

Figure 2-23. Experimental hutch EH-3 and the major components. These include the second set of focusing K-B mirrors (FM-2) and two spectrometers. One spectrometer has an arm length of 5 m and covers a scattering angle from -10 to 135 deg and is designed to achieve 1 meV resolution. The other spectrometer has an arm length of 10 m and covers a scattering angle from -5 to 15 deg and is designed to achieve 0.1 meV resolution. The two spectrometers share the same sample stage.

2.7 List of Major Components

The major beamline components, along with their distance from the source are listed in Table 2-7 through Table 2-10.

Table 2-7. Major components in the first optics enclosure (FOE starts at 26.7 m, and ends at Z = 33.7 m)

Description	Start Position (m)	Length (mm)	Notes
Beamline isolation valve	26.720	70	Vacuum isolation for beamline
Differential pump	26.965	325	For windowless operation
Bremsstrahlung Collimator	27.465	387	Beamline safety component
Blade BPM	27.989	320	Beam position monitor
Cooled Fluorescent Screen	28.446	210	Beamline diagnostics
Gate valve	28.793	70	Vacuum isolation for DCM
DCM	28.863	748	Beamline optics
Gate valve	29.611	70	Vacuum isolation for DCM
Bremsstrahlung Stop	29.818	387	Beamline safety component
Quadrant BPM	30.342	35	Beamline diagnostic
Monochromatic Slits & Fluorescent Screen	30.377	550	Beamline diagnostic and aperture
Monochromatic Beam Shutter	32.877	320	Beamline safety component
Gate valve	33.197	70	Vacuum isolation for beamline

Table 2-8. Major components in the first experimental hutch (EH-1 starts at 38.3 m, and ends at 42.0 m)

Description	Start Position (m)	Length (mm)	Notes
Gate valve	39.804	70	Vacuum isolation
URM (CDDW+CC)	39.874	965	Beamline optics
Monochromatic Beam Shutter	40.839	320	BL Safety component

Table 2-9. Major components in the second experimental hutch (EH-2 starts at 42.0 m, and ends at 51.0 m)

Description	Start Position (m)	Length (mm)	Notes
Gate valve	42.399	70	Vacuum isolation
Optical Table	42.606	2442	For additional beamline conditioning optics, two Be windows will be added if necessary.
Gate valve	45.185	70	Vacuum isolation
Gate valve	48.755	70	Vacuum isolation
VFM-1 & HFM-1	48.825	1525	Beamline optics
Gate valve	50.350	70	Vacuum isolation

Table 2-10. Major components in the second experimental hutch (EH-3 starts at 54.5 m, and ends at 70.0 m)

Description	Start Position (m)	Length (mm)	Notes
Gate valve	56.595	70	Vacuum isolation
VFM-2 & HFM-2	56.665	1525	Beamline optics
Gate valve	58.190	70	Vacuum isolation
Be window	58.260	150	Beam exit port
Beam conditioning and monitor unit	58.410	635	Beam conditioning and clean-up
Sample motion stage	59.045	0	Spectrometer center
Sample entrance slit and Be window	59.145	25	Sample slit/pinhole with Be window
Multilayer collimating mirror x 2	59.170	150	Analyzer system
Spectrometer arm-1 (5 m)	59.320	4516	Spectrometer arm
Analyzer-1 (CDDW)	63.836	965	Crystal analyzer for 1 meV
Spectrometer arm-2 (10m)	59.170	9516	Spectrometer arm
Analyzer-2 (CDDW)	68.836	965	Crystal analyzer for 0.1 meV

3. SPECTROMETER LAYOUT

3.1 Design Considerations

In this section, we outline the optical concept and discuss a few possible layouts for the spectrometers. Common to all existing high-resolution inelastic x-ray scattering spectrometers, after the incident beam impinges on the sample, one must collect the scattered photons and determine their energy in the most efficient way pertaining to a given set of energy and momentum transfer resolution. This is done using spherically bent crystal analyzers in all existing spectrometers with a typical angular acceptance of 5-10 mrad in both the vertical and horizontal directions[10]. These analyzers operate at a fixed energy determined by the Bragg back reflection used, typically at Si(hhh), where h = 7, 8, 9, 11, 12, and 13, with a total energy resolution ranging from 7.6 – 1.0 meV[10]. Energy scan is performed by scanning the incident energy so that the difference between the incident energy and the Bragg reflection of the analyzers gives the energy loss or gain of the incident photons in the inelastic scattering process. Obviously the analyzer optics should match the monochromator optics both in energy and resolution in order to perform the experiment most efficiently. Also, the angular span of the analyzer determines the minimum span of the momentum transfer (Q_s) of the scattered photons as seen by the analyzer, hence the resolution of the spectrometer ΔQ_s. For a given acceptance angle $\Delta\theta$ in the scattering plane, ΔQ_s depends on the scattering angle θ as illustrated in Figure 3-1. Perpendicular to the scattering plane, ΔQ_s remains constant and is determined only by the acceptance angle of the analyzer in that direction. For the current state-of-the-arts spectrometers operating at > 20 keV, the typical momentum transfer resolution ΔQ_s in both directions is ~ 0.5 nm^{-1}.

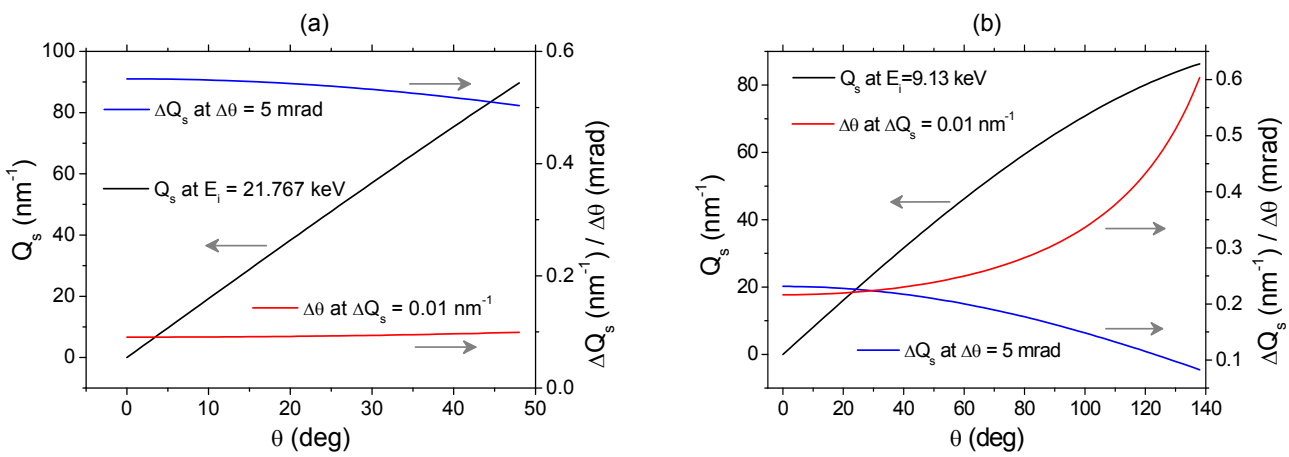

Figure 3-1. Range of momentum transfer Q_s, resolution ΔQ_s at a constant angular acceptance $\Delta\theta$ of 5 mrad of the analyzer in the scattering plane, and the angular acceptance required for ΔQ_s = 0.01 nm^{-1} as a function of the scattering angle θ for (a) the current state-of-the-arts spectrometers operating at 21.767 keV (a), and (b) for the NSLS-II IXS spectrometer operating at 9.13 keV. Here the momentum transfer Q_s is given by $Q_s = 4\pi/\lambda \sin(\theta/2)$, where λ is the wavelength of the incident x-ray, and ΔQ_s for a given $\Delta\theta$ is given by: $\Delta Q_s = 4\pi/\lambda\left[\sin(\theta/2)[\cos(\Delta\theta/2)-1]+\cos(\theta/2)\sin(\Delta\theta/2)\right]$

With the CDDW monochromator design being used for the beamline, in principle we must use the same optical scheme for the analyzer optics in order to match the energy and resolution of the incident beam. This applies to all possible alternative monochromator designs that we will consider for the beamline. However, despite the relatively large angular acceptance of ~ 0.1 mrad for the CDDW monochromator design, it is still far less than the spherically bent backscattering crystal analyzers, and will severely limit the number of scattered photons that can be collected. To increase the angular acceptance to a comparable level, one must use collimating optics in conjunction with the CDDW

monochromator for the analyzer. This is illustrated in Figure 3-2 where a multilayer mirror is used to collect ~ 5 mrad of scattered photons and collimate them to ~ 0.1 mrad in order to be accepted by the CDDW monochromator for energy analysis. This multilayer mirror therefore holds the key for this analyzer scheme to work[2]. Its performance influences the design of the spectrometer, including the optical layout and the dimension.

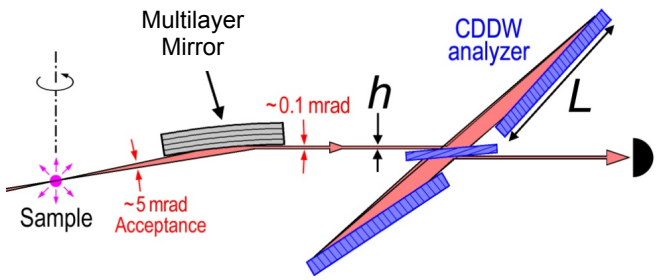

Figure 3-2. Optical scheme for the analyzer system of the spectrometer[2,4].

3.2 Multilayer Mirror

The main design objective for the multilayer mirror is to have an angular acceptance of 5 mrad (H) × 5 mrad (V) and collimate the beam to within 0.1 mrad in both directions. In the vertical, the 0.1 mrad would be required to match the acceptance of the CDDW monochromator. In the horizontal, however, there are two considerations:

(1) Near backscattering, the energy of the reflected beam follows a dispersion relation $E(\varphi) = E_0(1-\varphi^2/2)$, where φ is the incident divergent angle in the non-dispersive plane (i.e., the horizontal plane) and E_0 is the energy of the central rays. This is equivalent to $\Delta E/E_0 = (E-E_0)/E_0 = \varphi^2/2$. In order to maintain 0.1 meV resolution, therefore, the horizontal angular divergence of the incident beam to the CDDW monochromator must be smaller than ~ 0.15 mrad. For 1 meV resolution, this can be relaxed to ~ 0.5 mrad.

(2) The horizontal divergence of the beam before the multilayer mirror determines the momentum transfer resolution ΔQ_s in the scattering plane as illustrated in Figure 3-1. For 9.1 keV photons, a 5 mrad acceptance angle of scattered photons produces a ΔQ_s range from ~ 0.23 nm^{-1} at Q_s = 0 to ~ 0.12 nm^{-1} at Q_s = 80 nm^{-1} at a scattering angle of ~ 120 deg. In order to improve this further to substantially better than 0.1 nm^{-1} at low Q_s as required by some experiments, one must reduce the horizontal acceptance or divide the accepted fan into smaller segments through the use of position sensitive detectors after the CDDW analyzer. The best obtainable Q_s resolution will therefore depend on the best collimation achievable with the multilayer mirror in the horizontal direction and the size of the sensitive elements of the detector.

This sets the minimum required horizontal divergence of the collimated beam from the mirror according to the required energy and momentum transfer resolutions for the experiment. The optimization of the multilayer mirror is then based on an in-house ray-tracing program[20] involving the optimization of the layer materials, thickness and the mirror figure (parabolic or elliptic), taking into consideration the source size and divergence, mirror errors (slope errors, roughness, and interlayer thickness fluctuation) and imperfections, and so on. We report some of the details here.

Layer Materials and Thickness

The best combination of the layer materials and their thickness is determined for a flat mirror that produces the best reflectivity, large angular acceptance and an incident angle that allows a reasonable working distance and mirror length at 9.1 keV. The result is either a W/Si or W/B_4C multilayers deposited on a Si substrate with a layer thickness of ~ 1 nm

for W and ~ 1.5 nm for the Si or B_4C. Figure 3-3 compares the reflectivity curves for a 100 bi-layers of W/Si or W/B_4C with that of Mo/Si, showing a peak value of 0.85 and a FWHM of ~ 5 mrad for the W/Si or W/B_4C.

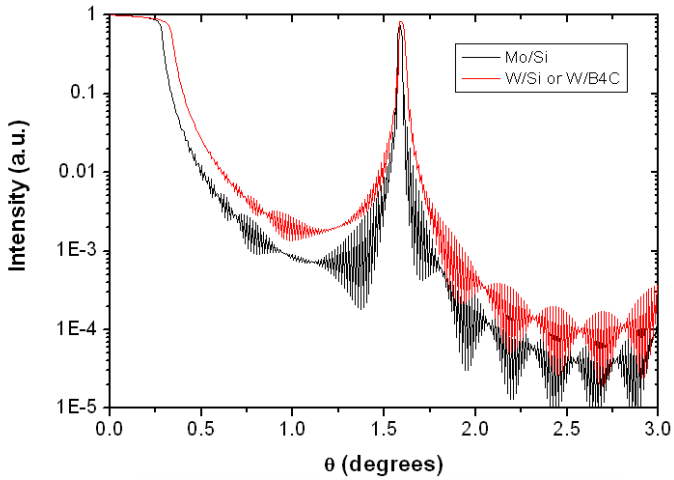

Figure 3-3. X-ray reflectivity at 9.1 keV for 100 bi-layers of Mo/Si (black) and W/Si or W/B_4C on a Si substrate (red). The layer thickness is 1 nm for W, and 1.5 nm for Mo, Si, or B_4C.

Figure Parameters

In the present applications, the layer thicknesses are laterally graded to take into account the different incident angle of the beam at different locations along the mirror in order to increase the reflectivity and acceptance. The ideal figure and mirror size depend on the distance of the mirror from the sample and the incident angle. We have chosen to position the center of mirror at 200 mm from the sample in order to leave reasonable amount of space for sample environments. Since a 50:1 demagnification is required to collimate 5 mrad of scattered photons to 0.1 mrad, the focal point should be at 10 m away from the mirror. This sets the ideal dimension of the spectrometer. Two mirror figures have been considered, one parabolic for collimating and the other elliptic for focusing. The optimized figure parameters are summarized in Figure 3-4 and Table 3-1.

Mirror Configurations and Performance

These mirror figures provide only one dimensional collimating or focusing, respectively. In order to collimate or focus in two dimensions, one can combine two such mirrors mounted at 90 deg to each other[21]. This type of "L-shaped" multilayer mirrors has been used in commercial powder diffractometers, and has been proven to work well[22,23]. Several combinations are shown in Figure 3-5 to illustrate the versatility of the setup as (a) collimator in both directions; (b) focusing optics in both directions; and (c) focusing in one but collimating in the other direction. To provide the same functionality using a single toroidal mirror would require a rather complicated surface figure, which would be extremely difficult to fabricate. The only advantage of a single toroidal mirror compared to these "L-shaped" mirrors is that every ray reflects only once in the former, whereas they reflect twice in the latter, resulting in some additional loss due to the finite reflectivity.

The performance of these mirrors has been examined using our in-house ray tracing code[20]. In the simulations the source size (beam size on the sample), the designed acceptance, and the gap between the two mirrors were kept constant with the following values: 5×5 μm^2, 5×5 mrad^2 and 2 μm, respectively. Also, four different parameter sets were considered for each mirror: (a) no slope error, no roughness and no random variations in the lattice parameter ($\Delta d/d$) (perfect mirror); (b) slope error of 5 μrad, roughness of 0.2 nm and $\Delta d/d = 7\times10^{-4}$; (c) slope error of 10 μrad, roughness of 0.2 nm and $\Delta d/d = 7\times10^{-4}$ and; (d) slope error of 15 μrad, roughness of 0.2 nm and $\Delta d/d = 7\times10^{-4}$. The results are summarized in Table 3-2. The simulated images for condition (c) with a slope error of 10 μrad are shown in Figure 3-6.

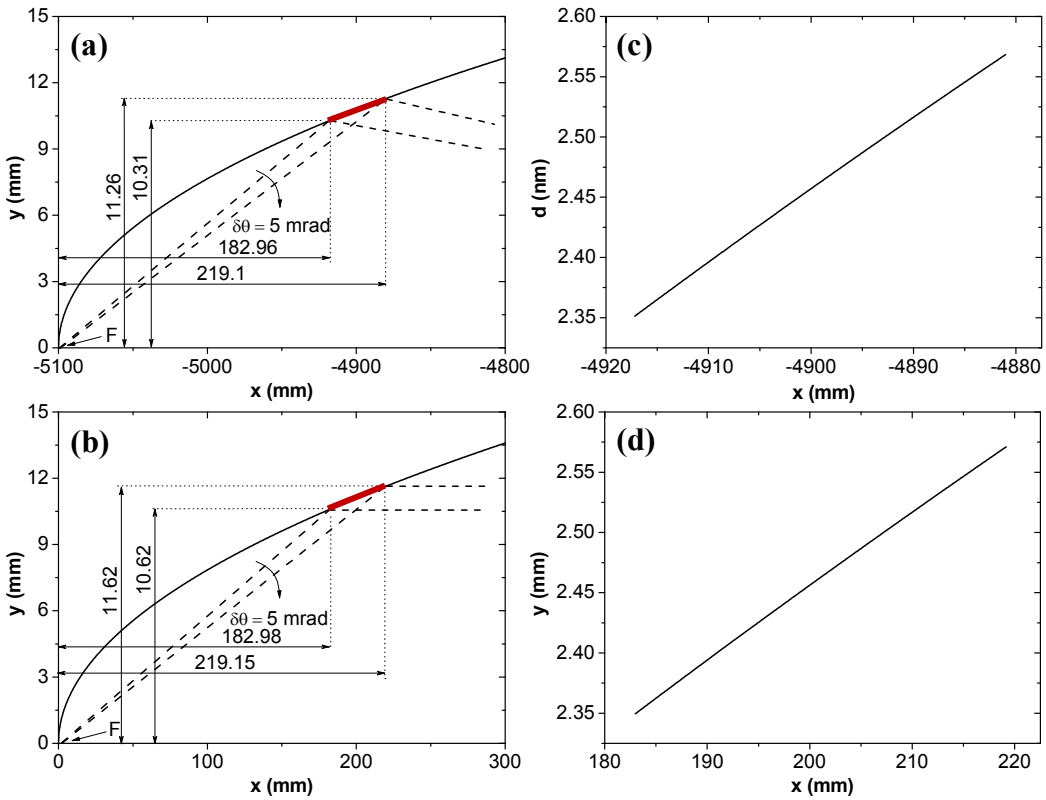

Figure 3-4. Mirror figures and parameters optimized for the chosen working distances of 200 mm from the sample. The numbers are used as input in the ray tracing program: (a) parabolic; (b) elliptic; (c) variation in the lattice parameter *vs.* distance on the mirror surface for the parabolic laterally graded multilayer; and (d) variation in the lattice parameter *vs.* distance on the mirror surface for the elliptic laterally graded multilayer mirror.

Table 3-1. Parameters of the parabolic and elliptic mirror figure shown in Figure 3-4. P is the focal parameter corresponding to the apex radius, θ_m the medium incident angle, δx and δy the dimension in X and Y direction respectively, and d_i and d_f the initial and final layer periods.

Figure	P (mm)	θ_m (mrad)	δx (mm)	δy (mm)	d_i (nm)	d_f (nm)
Parabolic	0.30796	27.75	36.17	1.002	2.3495	2.5710
Elliptic	0.30193	27.75	35.94	0.953	2.3513	2.5683

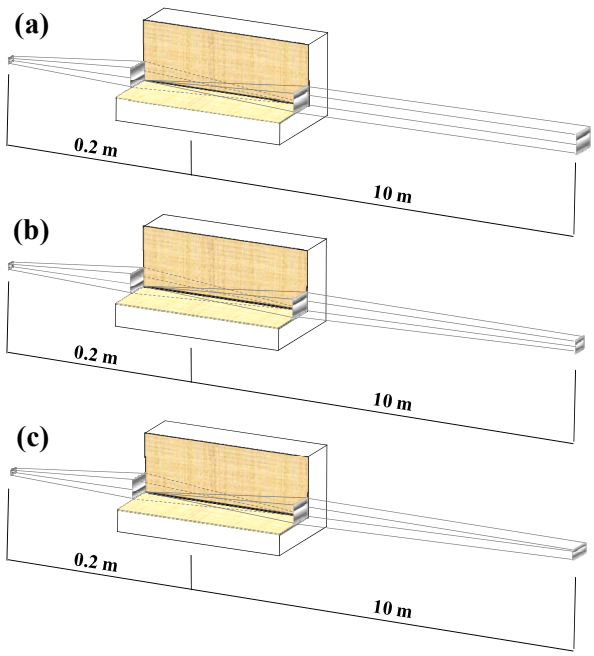

Figure 3-5. Schematic representation of the L shaped double bounce x-ray mirror used as: (a) collimator (parabolic figure); (b) focusing optics (elliptic figure) and; (c) focusing/collimating optics (combination of parabolic and elliptic figure)

Table 3-2. Simulated focus beam size and divergence assuming different slope errors for the "L-shaped" mirrors shown in Figure 3-5. In the simulations, the source size is set to 5×5 μm^2. Four sets of parameters were considered for each mirror: (a) no slope error, no roughness and no random variations in the lattice parameter ($\Delta d/d$) (perfect mirror); (b) slope error of 5 μrad, roughness of 0.2 nm and $\Delta d/d = 7\times10^{-4}$; (c) slope error of 10 μrad, roughness of 0.2 nm and $\Delta d/d = 7\times10^{-4}$ and; (d) slope error of 15 μrad, roughness of 0.2 nm and $\Delta d/d = 7\times10^{-4}$.

Simulation conditions (slope error)	Parabolic + Parabolic		Elliptic + Elliptic		Parabolic + Elliptic	
	Focus Size H×V (mm)	Divergence H×V (μrad)	Focus Size H×V (mm)	Divergence H×V (μrad)	Focus Size H×V (mm)	Divergence H×V (μrad)
(a): (0 μrad)	1.0 × 1.0	19 × 19	0.16 × 0.16	84 × 84	1.0 × 0.16	19 × 84
(b): (5 μrad)	1.1 × 1.1	37 × 37	0.35 × 0.35	63 × 63	1.1 × 0.35	37 × 63
(c): (10 μrad)	1.2 × 1.2	57 × 57	0.5 × 0.5	44 × 44	1.2 × 0.5	57 × 44
(d): (15 μrad)	1.4 × 1.4	77 × 77	0.76 × 0.76	19 × 19	1.4 × 0.76	77 × 19

As can be seen, the divergence is strongly dependent on the source size and on the slope error. The divergence of 19 μrad from a perfect parabolic mirror is entirely caused by the source size. As the slope error increases, the divergence from the parabolic mirror also increases. On the other hand, for a perfect elliptic mirror, the divergence of 84 μrad caused by the source size is the strongest due to strong focusing by the elliptic figure. With increasing slope error, however, the divergence decreases, showing opposite behavior than that of the parabolic mirror. This can be understood as a consequence of compensation effect introduced by the slope error which effectively improves the overall divergence of the beam. Based on these simulated results, the best combination appears to be an elliptic-elliptic or a parabolic-elliptic "L-shaped" mirror with 10 μrad of slope error. This slope error is in fact what commercial vendors could deliver now. A test "L-shaped" elliptic-elliptic mirror with the corresponding specifications has been ordered in order to test the performance, which can be used to verify the simulated results.

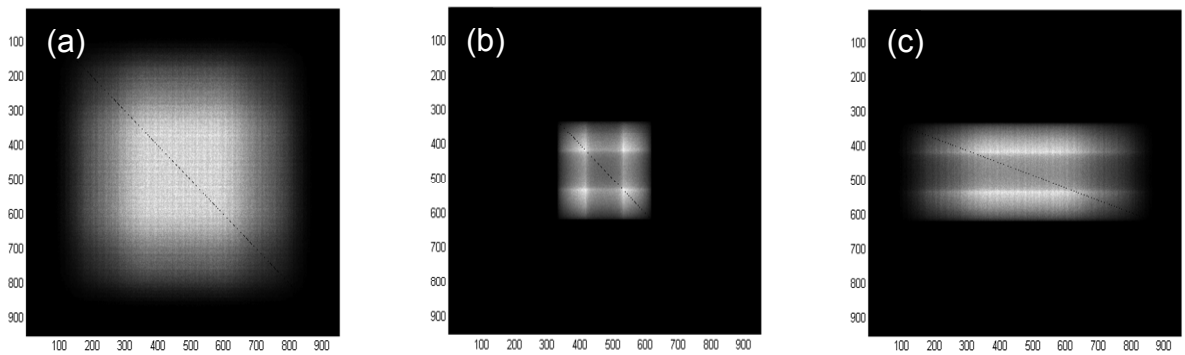

Figure 3-6. Spot sizes for the "L-shaped" mirror combinations shown in Figure 3-5. The images were taken at 10 m from the mirrors with the (c) simulation conditions listed in Table 3-2. The dark diagonal line is the missing intensity due to the corner gap. The axes labels are in pixel size, which is 2×2 μm^2.

Based on these results, we can examine the best possible Q_s resolution obtainable with these mirrors. We consider only the horizontal scattering plane. Clearly in all the simulated cases, the incident divergence to the CDDW analyzer is well within the 0.1 mrad in both directions, and therefore the entire beam can be accepted. If all the photons go to the same detector and are integrated, the Q_s resolution obtainable would be given by the angular acceptance of the mirror, which is 5 mrad, or ~ 0.23 nm^{-1} at Q_s ~ 0, which is the worst case (see Figure 3-1).

In order to improve the Q resolution while maintaining the total angular acceptance of the mirror, a position sensitive detector may be used after the CDDW analyzer to divide the incoming radiation fan into smaller segments. The smallest segment depends on the detector used. Currently a strip detector of Peter Siddons' design has a pitch value of 125 μm, which sets the limit to how small a segment can be. If there is a one-to-one correspondence between the incident rays into the mirror and the outgoing rays into the CDDW analyzer, this segmenting can be used to improve the Q resolution. For example, assuming no figure error, a parabolic mirror delivers an almost parallel beam (limited only by the source size) to the CDDW monochromator with a beam cross section of ~1 mm. With a pitch size of 125 μm, the strip detector would be able to improve the Q resolution by a factor of 8, to a value of ~ 0.03 nm^{-1}, again at Q_s ~ 0 . We note that there is a 180 deg rotation of the incident beam after the "L-shaped" mirror which swaps the Q_s position of the rays. Also, any compaction of the beam in the horizontal direction by the multilayer mirror (e.g., with an elliptic mirror), or by the change of divergence due to source size or figure errors will worsen the Q resolution in this scheme. In this context, a parabolic-elliptic combination presents the best choice among these "L-shaped" mirrors in order to improve the Q_s resolution for the IXS spectrometer.

A more attractive solution for improving the Q_s resolution is illustrated in Figure 3-7. Here, we use a single multilayer mirror collimating only in the vertical direction. In the horizontal direction, the scattered rays are allowed to propagate in their original direction. Due to the energy dispersion relation $E(\varphi) = E_0(1-\varphi^2/2)$ mentioned earlier, there is a natural angular acceptance of ~ 3 mrad by the CDDW analyzer within the rocking curve width of the Si(008) reflection. If one places a strip detector after the CDDW analyzer, the segmenting will retain directly the Q information of the scattered photons. In this case, as illustrated in Figure 3-1, the required angular width to obtain a Q_s resolution of ~ 0.01 nm^{-1} would be ~ 0.2 mrad at low Q_s. If the detector is positioned at 1 m from the sample, this gives a strip size of 200 μm, or 1 mm if the detector is placed at 5 m from the sample, in which case, one could even use a conventional multi element detector. This angular width increases with increasing Q_s to about 0.5 mrad at Q_s = 80 nm^{-1}.

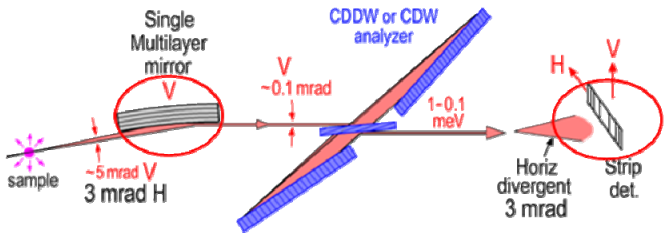

Figure 3-7. An optical scheme for the analyzer system which makes use of the natural angular acceptance of the CDW/CDDW monochromator, with a single multilayer mirror collimating only in the vertical direction.

This scheme does force us to position the CDDW analyzer closer to the sample, away from the focal point of the multilayer mirror. This is due to the fact that the transverse size of the beam corresponding to the 3 mrad fan increases rapidly with the distance from the sample. Positioning the CDDW at 1m seems ideal as the horizontal beam size would be ~ 3 mm. The vertical beam size (~ 1 mm) is expected to be twice as big as at the focal point at 10 m, which again calls for a very long D crystal or the comb crystal.

Finally, we note that in the one-dimensional scheme illustrated in Figure 3-7, due to the energy dispersion relation $E(\varphi) = E_0(1-\varphi^2/2)$, in addition to having different scattering momentum Q_s, the energy of the scattered photons landing on different strips of the detector will have different energies over the energy width (~ 34 meV) of the Si(008) back reflection. This is a unique feature of this scheme, whereby an energy-momentum dispersion map can be obtained in one energy scan.

3.3 Overall Performance and Count Rate Estimate

In this section, we discuss the overall performance of the NSLS-II IXS instrument by comparing it with existing state-of-the-arts IXS instruments in the world, and provide a count rate estimate based on the actual count rates obtained at ID28 of ESRF on a few representative systems[24]. This should provide useful guidance on the overall feasibility of the science programs envisioned for the beamline.

The performance of the NSLS-II IXS instrument depends on the overall optical efficiency of the beamline and the efficiency of the analyzer system. The optical efficiency of the beamline can be estimated based on the optical layout discussed in Section 2, and is summarized in Table 3-3 for two possible configurations corresponding to the 1 and 0.1 meV resolution, respectively. In the estimate, we consider only the theoretical peak reflectivity and transmissivity, and neglect other possible efficiency losses due to filtering, slitting, figure errors and/or surface roughness, etc. In both configurations, the combined efficiency obtained is 28% and 22%, respectively, which can be regarded as the best possible efficiency obtainable from the beamline.

Table 3-3. Beamline optical efficiency estimates based on the layouts presented in Figure 2-16, and discussed in Section 2. For optical components, the theoretical peak reflectivity is used. For the Be exit window, the transmission is calculated for a thickness of 250 μm. To obtain the 0.1 meV resolution, a channel-cut monochromator (CCM) is used after the CDDW monochromator. The combined efficiencies obtained can be regarded as the best possible efficiency obtainable from the beamline.

Components Optical Efficiency	Be CRLs	DCM	CDDW	CCM	FM-1 (VFM only)	FM-2	Be Exit Window	Combined Efficiency
Configuration I (1 meV, strong focus)	0.9	0.85	0.45	--	0.95	0.9	0.95	0.28
Configuration II (0.1 meV, strong focus)	0.9	0.85	0.45	0.8	0.95	0.9	0.95	0.22

In reality, additional losses can be caused by absorption, diffuse scattering from surface roughness or reduced acceptance due to figure errors, etc, which will be studied in details later by proper modeling using Shadow during the preliminary design. For the present purpose, we assume that a 10% total efficiency of the entire beamline optical system can be obtained for 1 meV resolution and compare the performance with the other existing facilities in Table 3-4. Clearly, in addition to having sharper resolution function tails from the CDDW optics, higher intensity at the same 1.0 meV resolution is expected for NSLS-II.

Table 3-4. Performance comparison between the NSLS-II IXS beamline and those at other facilities. Incident intensity is given at the corresponding incident beam energy (E_{inc}) and bandwidth (ΔE_{inc}). For the NSLS-II instrument, the incident intensity for 1 meV resolution is estimated with an overall beamline optical efficiency of 10% and the IVU22-6m delivering 1.6×10^{15} phs/sec/0.1%bw.

Facility	ΔE_{inc} (meV)	E_{inc} (keV)	I_{inc} (phs/sec/ΔE_{inc})	Sharp Resolution Tails
ESRF (ID28)	1.0	21.7	4.0×10^9	--
SPring-8 (BL35XU)	1.0	21.7	4.5×10^9	--
APS (Sector 30)	1.0	23.8	2.8×10^9	--
NSLS-II	1.0	9.13	~1.6×10^{10}	Yes
NSLS-II	0.1	9.13	~1.0×10^9	Yes

For the count rate estimate, we further assume that the new analyzer system has comparable efficiency as that of the ID28 (ESRF) spectrometer operating at 17.8 keV with the Si(999) back reflection. For higher photon energies the efficiency of the spectrometer at ID28 is estimated based on measurements on Plexiglas at Q = 10 nm^{-1}. The estimated efficiency loss is about a factor of 2.5 at 21.7 keV with the Si(11,11,11) reflection compared to measurements performed at 17.8 keV with the Si(999) reflection[24]. The experimental data from ID28 are summarized in Table 3-5.

Table 3-5. Experimental data obtained from ID28 of ESRF on four sample systems (courtesy of Michael Krisch).

Sample	Thickness (μm)	E_{inc} (keV)	ΔE_{inc} (meV)	Intensity (phs/sec/ΔE_{inc})	Acceptance ($mrad^2$)	ΔE_{total} (meV)	Count Rate (cnts/sec)
H_2O (HP)	~1000	21.7	1.0	4×10^9	27	1.6	~1.0
Solid O_2 (HP)	~10	17.8	2.0	1.0×10^{10}	27	3.3	~1.5
v-SiO_2	~2100	21.7	1.0	4×10^9	27	1.6	~0.2
La_2CuO_4	~75.3	17.8	2.0	2.7×10^{10}	27	3.3	~0.5

We then follow the formalism detailed by Harald Sinn[25] which provides a scaling of the relative scattering intensity (I/I_0) for a given sample system as a function of the incident energy E_i, the Q resolution of the analyzer $(\delta q)^2$ and the absorption length l_{abs} or the actual sample thickness along the beam path:

$$\frac{I}{I_0} = \frac{r_e^2 \hbar^2 c^2 (\delta q)^2}{2eE_i^2} Z^2 \rho l_{abs} \frac{k_B T}{M\upsilon^2}.$$

Since $(\delta q)^2 / E_i^2 = (2/\hbar)^2 (\delta\theta)^2$, where $(\delta\theta)^2$ is the angular acceptance of the analyzer, we have $(I/I_0) \propto (\delta\theta)^2 l_{abs}$. The scattering intensity is therefore proportional to the incident beam intensity, the analyzer angular acceptance and the absorption length or the actual sample thickness (whichever is smaller).

Based on all these considerations, the expected count rate (CR) for the NSLS-II spectrometer operating at 1 meV resolution can be calculated by:

(Estimated CR) = (Measured CR) × (I_0 Gain) × (l_{abs} Gain) × ($(\delta\theta)^2$ Gain) × (Efficiency Gain) × (Absorption Correction)

The results are summarized in Table 3-6.

Table 3-6. Estimated count rate for the NSLS-II spectrometer operating at 1 meV based on the measured count rate at ID28 of ESRF (see Table 3-5). l_{abs} gain for high pressure (HP) systems is based on the actual sample thickness available. Absorption correction is calculated assuming transmission through a Be gasket of 3mm diameter.

Sample	I_0 Gain	l_{abs} Gain	$(\delta\theta)^2$ Gain	Efficiency Gain	Abs. Correction	Est. CR (cnts/sec)
H_2O (HP)	1.6/0.4	1000/1000	25/27	2.5	0.68/0.90	~7.0
Solid O_2 (HP)	1.6/1.0	10/10	25/27	1.0	0.68/0.89	~2.0
v-SiO_2	1.6/0.4	190/2100	25/27	2.5	1	~0.2
La_2CuO_4	1.6/2.7	7.13/75.3	25/27	1.0	1	~0.03*

*Count rate for low lying optical phonons in the range of 20-40 meV.

From Table 3-6, it is clear that the NSLS-II spectrometer will perform better in general for low Z materials where spectrometers operating at higher energies are unable to capitalize on the gain on the absorption length due to the fact that the available sample volume is limited either by the sample environment (e.g., the high pressure diamond anvil cell), or by the source size contribution to the resolution function in the back reflection spherical analyzer scheme[6]. In the present analyzer scheme, similar limitations may also be at work due to the source size contribution to the divergence of the collimated beam after the multilayer collimating mirror. The effects are mainly due to the projection of the sample volume at a given scattering angle which may either render the scattering source size outside the acceptance of the analyzer in the dispersion plane, or broaden the divergence of the collimated scattered photons in the horizontal direction which worsens the resolution. These effects will be studied in greater detail during the preliminary design phase.

APPENDIX 1: SCHEDULE

A1.1 Construction of the IXS beamline

September	2009	Complete conceptual design report
September	2010	Complete preliminary design report
November	2010	Technical design – approval of long lead term procurement
January	2011	Start long lead time procurements (monochromator, mirrors, enclosures,…)
April	2011	Complete final design of beamline major components
February	2012	Complete final design report
		Approval of start of beamline construction - beneficial occupancy of experimental floor
February	2012	Start installation
May	2012	Start sub-system testing
April	2012	Start other procurements
November	2012	Complete long lead time procurements
August	2013	End procurement
August	2013	Start integrated testing
January	2014	Complete installation
February	2014	Complete sub-system testing
May	2014	Complete integrated testing – beamline available for commissioning
June	2015	**CD-4**, approve start of operations

A1.2 Critical Decisions and Milestones of the 0.1 meV Optics R&D

Since the conceptual design, construction, and operation of the IXS beamline are intimately connected to the outcome of the 0.1 meV optics R&D program, we summarize the planned key tasks and milestones. The dates associated with the specific milestone could change due to unforeseen technical challenges.

- FY10 Q2: 1 meV optics fabrication and test complete; critical decision on how to proceed with 1 meV prototype
- FY11 Q2: 1 meV prototype spectrometer construction complete and begin testing
- FY11 Q4: 0.5 meV CDDW optics fabrication and test complete; critical decision on the CDDW scheme
- FY11 Q4: 0.5 meV alternative optics fabrication and test complete; critical decision on alternative scheme
- FY12 Q1: Start of 0.2 meV optics fabrication and test based on chosen optical scheme
- FY12 Q2: Demonstration experiments using 1 meV prototype spectrometer
- FY12 Q3: Critical decision on the IXS spectrometer
- FY13 Q2: Start of 0.1 meV optics fabrication and test
- FY14 Q4: Continue 0.1 meV optics R&D at IXS BL using prototype

APPENDIX 2: REFERENCE DRAWINGS

The following drawings are provided here for reference:

1 Beamline layout in legal format

2 Front End Component Layout

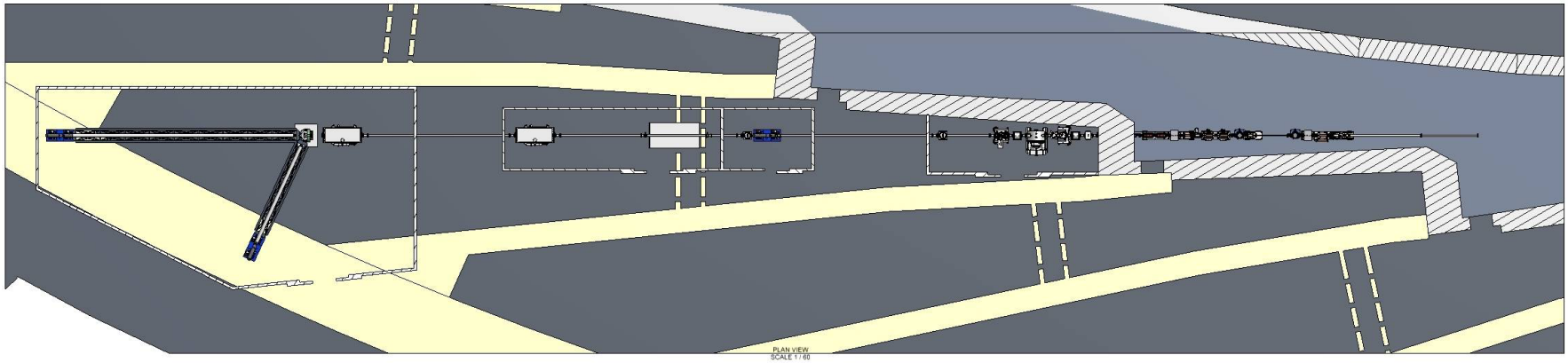

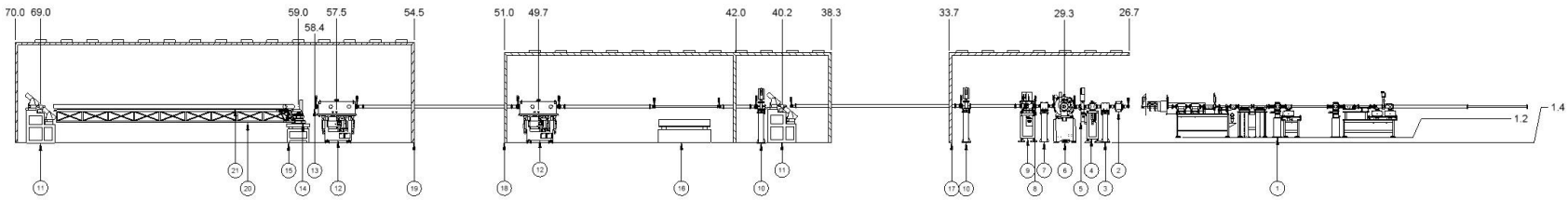

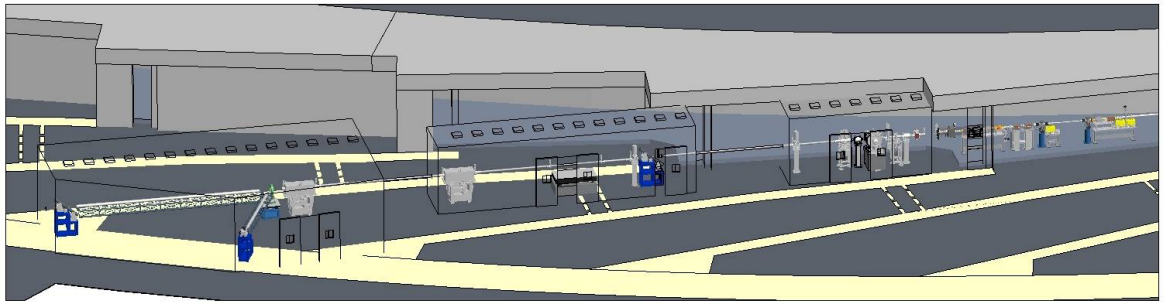

PARTS LIST

ITEM	QTY	PART NUMBER	DESCRIPTION
1	1	SR-FE-IDN0-1100	FRONT END ASSEMBLY (IXS);(6.9mm X 5.3mm)
2	1	XF-BL-IXS-DiffPump0	Differential Vacuum Pump
3	1	XF-BL-IXS-BremsCollimator0	Bremsstrahlung Collimator
4	1	XF-BL-IXS-BladeBPM0	Beam Position Monitor, Blade Type
5	1	XF-BL-IXS-FluorScreen0	Fluorescent Screen, Diagnostic
6	1	XF-BL-IXS-Oxford-DCM0	Monochromator, Double Crystal
7	1	XF-BL-IXS-BremsWhiteBeamStop0	Bremsstrahlung and White Beam Stop
8	1	XF-BL-IXS-QuadrantBPM0	Beam Position Monitor, Quadrant Type
9	1	XF-BL-IXS-MonochromaticSlits-FluorScreen0	Monochromatic Slits & Fluorescent Screen
10	2	XF-BL-IXS-MonochromaticShutter0	Monochromatic Shutter
11	3	XF-BL-IXS-Deci-Mono	High Resolution Monochromator/Analyzer
12	2	XF-BL-IXS-KBMirrorPair0	Mirror, KB Focusing Pair
13	1	XF-BL-IXS-BeWindow0	Window, Beryllium
14	1	XF-BL-IXS-Sample-Motion	Sample Motion Stages
15	1	XF-BL-IXS-TableA	Optical Table
16	1	XF-BL-IXS-RDTable0	Optics Table
17	1	XF-BL-IXS-HutchFOE2	First Optical Enclosure
18	1	XF-BL-IXS-HutchG	Second Optical Enclosure
19	1	XF-BL-IXS-HutchJ	Experimental Hutch
20	1	XF-BL-IXS-Tube10mArmTruss	Truss Weldment, 10m
21	1	XF-BL-IXS-Tube10mArm	Analyzer Flight Path, 10m
22	1	XF-BL-IXS-Tube5mArmTruss	Truss Weldment, 5m
23	1	XF-BL-IXS-Tube5mArm	Analyzer Flight Path, 5m
24	4	XF-BL-IXS-GateValve1	Gate Valve, 4.5 inch
25	8	XF-CM-1011	Gate Valve, 6 inch

UNLESS OTHERWISE SPECIFIED
DIMENSIONAL TOLERANCES
X. ± 1.500
.X ± 0.750
.XX ± 0.400
.XXX ± 0.120
ANGULAR TOLERANCE ± .5°
BREAK EDGES & REMOVE BURRS TO 0.1 MAX
BROOKHAVEN NATIONAL LABORATORY
NSLS II
Drawn by: Coburn 10 Sep 09
EXPERIMENTAL FACILITIES
BEAMLINES
LAYOUT, IXS
E
XF-BL-IXS-1000
1
SHEET 1 OF 1
NEXT ASSY
PROJECT:
SCALE SEE DWG VIEW
WBS#
ESH&Q RISK LEVEL

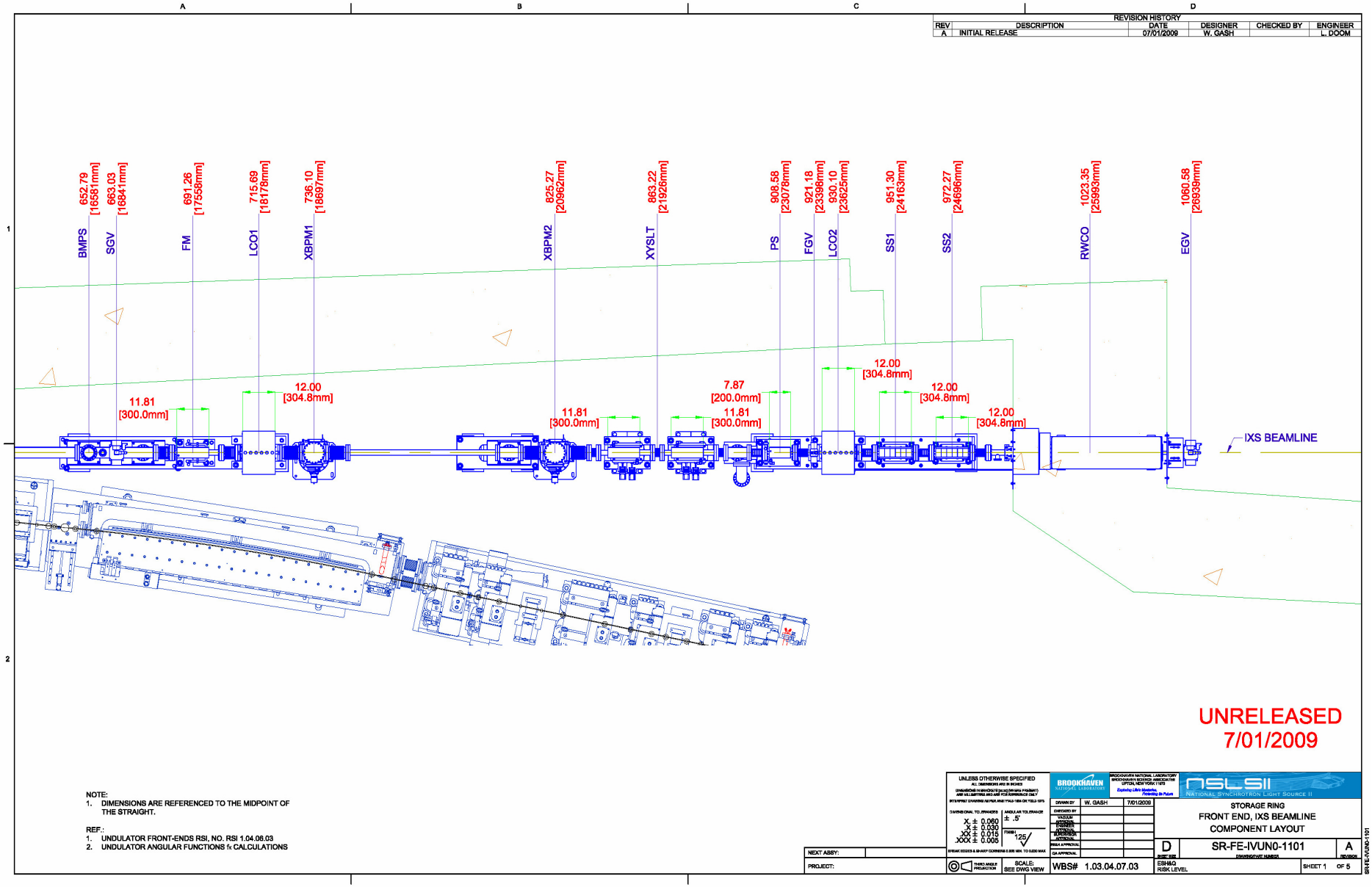
REVISION HISTORY
REV | DESCRIPTION | DATE | DESIGNER | CHECKED BY | ENGINEER
A | INITIAL RELEASE | 07/01/2009 | W. GASH | | L. DOOM
652.79 [16581mm]
663.03 [16841mm]
691.26 [17558mm]
715.69 [18178mm]
736.10 [18697mm]
825.27 [20962mm]
863.22 [21926mm]
908.58 [23078mm]
921.18 [23396mm]
930.10 [23625mm]
951.30 [24163mm]
972.27 [24696mm]
1023.35 [25993mm]
1060.58 [26939mm]
BMPS
SGV
FM
LCO1
XBPM1
XBPM2
XYSLT
PS
FGV
LCO2
SS1
SS2
RWCO
EGV
11.81 [300.0mm]
12.00 [304.8mm]
11.81 [300.0mm]
7.87 [200.0mm]
11.81 [300.0mm]
12.00 [304.8mm]
12.00 [304.8mm]
12.00 [304.8mm]
IXS BEAMLINE
UNRELEASED
7/01/2009
NOTE:
1. DIMENSIONS ARE REFERENCED TO THE MIDPOINT OF THE STRAIGHT.
REF.:
1. UNDULATOR FRONT-ENDS RSI, NO. RSI 1.04.06.03
2. UNDULATOR ANGULAR FUNCTIONS fx CALCULATIONS
UNLESS OTHERWISE SPECIFIED
BROOKHAVEN NATIONAL LABORATORY
NSLSII NATIONAL SYNCHROTRON LIGHT SOURCE II
DRAWN BY W. GASH 7/01/2009
STORAGE RING
FRONT END, IXS BEAMLINE
COMPONENT LAYOUT
D SR-FE-IVUN0-1101 A
NEXT ASSY:
PROJECT:
SCALE: SEE DWG VIEW
WBS# 1.03.04.07.03
ESH&Q RISK LEVEL
SHEET 1 OF 5
SR-FE-IVUN0-1101

APPENDIX 3: REPRESENTATIVE EXPERIMENTS

The following lists representative experiments as proposed by the BAT in the Letter of Intent. They are grouped into four subject areas including liquids and disordered materials, high pressure systems, biomolecular materials, and crystalline systems:

A3.1 Studies of Liquids and Disordered Systems

(1) Sound propagation and transport properties in metallic systems:

The focus here is on the non-hydrodynamic behavior of longitudinal acoustic (LA) sound excitations in the uncharted energy-momentum region between the hydrodynamic region (explored by light scattering or ultrasounds) and microscopic regime (explored by INS and current IXS). For instance, an interesting question is whether the high thermal conductivity of metallic fluids may be responsible for an intermediate isothermal regime bridging the gap between adiabatic sound propagation and high frequency, solid-like regime[26].

(2) Search for Non-Longitudinal/Non-Acoustic modes in disordered systems:

Based on symmetry arguments from crystalline physics, transverse acoustic modes are not expected to appear in the first (quasi) Brillouin zone. Higher frequency excitations of optic origin are, in turn, often difficult to distinguish from fast sound-like acoustic modes arising from positive dispersion of LA branch (interaction with structural relaxation and/or disordered structural configuration). Although a few possible observations have been recently reported[27], no convincing evidence of transverse or optic modes has been provided so far.

(3) Acoustic properties and dynamical heterogeneities in glasses:

The frequency and wavelength dependence of the sound attenuation in glasses and its connection with the vibrational density of states (Boson Peak) is one of the most important unsolved questions in the physics of disordered systems. The low frequency (Brillouin Light Scattering) and high frequency (IXS) behaviors of the damping coefficient are apparently inconsistent. Recently, Inelastic UV Scattering has shown that a crossover occurs in between the two regimes. But the $0.1 < Q < 1$ nm^{-1} region is still unexplored and the 0.1 meV goal will allow access to this region.

(4) The relaxation dynamics in liquids and glass formers:

The study of relaxation phenomena in simple fluids[28] and glass formers[29] is presently the focus of thorough investigations. The use of IXS spectrometers has moved these studies towards a new era. Spectral lineshape analysis giving direct insight on relevant physical parameters (such as viscosity, relaxation time, elastic and viscous sound speeds) are nowadays achievable on a routine basis. Unfortunately, rather interesting systems such as glass formers at melting or in the supercooled phase still elude firm IXS investigations, mainly owing to the rather slow relaxation processes in these materials. Their proper observation will require both sub-meV resolution bandwidth as well as the access to a Q window (0.1 – 1 nm^{-1}) well below the range covered by present instrumentation.

(5) Is a sound bifurcation observable in the spectrum of binary mixtures?

According to modern theories the dispersion curve of a binary gas mixture at relatively low *Q*'s would split into two different branches (sound bifurcation) corresponding to the acoustic propagation of two modes: the fast one propagating essentially through the lighter component and the slow mode traveling essentially within the slow background formed by the heavier one. Such bifurcation, though predicted theoretically[30], has never been properly observed, mainly owing to severe resolution limitations.[31] These limitations will be overcome once next generation 0.1 meV instrument will be available.

(6) The dynamics of confined liquids

Mesoscopic and microscopic properties of confined liquids are of crucial interest in domains as different as materials science, microfabrication, adhesion and lubrication, biology, geology, the novel fields of nanoscience and nanotechnologies, as well as the development of hydrogen fuel cells. The main difficulty faced by IXS when

dealing with these systems is the usually huge quasi-elastic contribution coming from the confining substrate, which hides almost completely the spectral contribution of the confined liquid. A much narrower and sharper resolution function would represent a decisive improvement to definitely solve this problem.

A3.2 High-Pressure Vibrational Dynamics

Recent advances in high-pressure sciences, to a large degree, can be accredited to our abilities to study optical phonons by Raman and infrared spectroscopy and acoustic phonons by Brillouin spectroscopy at high pressures. These optical probes, however, have a very small *q* range, essentially limited to the Brillouin zone center, and are unable to reveal important phonon dispersion information. They are also very much restricted by selection rules of IR and Raman, energy windows of the instrument and pressure vessels, absorption and fluorescence backgrounds of the samples, etc. IXS is, in principle, not subject to any of these constraints, and potentially can provide the most powerful probe for the fundamental information of vibrational dynamics if the energy resolution is comparable to that of optical Raman spectroscopy (1 to 10 cm^{-1} or approximately 0.1 to 1 meV).

Due to the low efficiency of IXS and the high demand of beam time, high-pressure IXS phonon study must focus on truly significant scientific issues with far-reaching implications. One example is the high pressure vibron dynamics of hydrogen. Numerous exotic behaviors have been predicted for hydrogen under compression[32]. Decades of high-pressure experimental efforts using Raman and IR spectroscopy have led to discoveries of a plethora of novel phenomena in hydrogen, including the vibron turnover[33], the greatly increased intermolecular coupling energy[34] from 3 to 510 cm^{-1}, bound-unbound transition in the quasiparticle bivibron[35], the charge-transfer state with intense infrared vibron absorption[36], and the quantum and classic orientational ordered phases II and III.[37] High-pressure IXS determination of vibron dispersion, which is currently only available at ambient pressure, will provide the key missing information for overall understanding.

In addition to high resolution, other requirements for high-pressure IXS include maximized flux, microbeam focus <5 μm, integration of pressures with high and cryogenic temperatures, and analyzer probe with high spatial resolution. The sample stage design must consider both the radius clearance and solid angle clearance for the analyzer probe.

A3.3 Phonons and Phonon-Damping in Bio-Materials

Study of collective wave propagation and damping is expected to increase our understanding of some aspects of biological functions which are not directly related to the structure of bio-molecular assemblies. Examples are: phonon assisted transport of water molecules across lipid bilayers; the base pair opening of DNA double helices; and the anomalous density of states in a protein below its glass transition temperature.

(1) IXS is a coherent scattering, irrespectively of atomic composition of a bio-molecule. There is no need to deuterate the bio-molecule as in an INS experiment. This factor alone results in a major saving of cost of the deuteration. For coherent INS at thermal energies ΔE is at best 0.25 meV and the Q range is not as broad as in IXS. An energy resolution of ΔE=0.1 meV will allow us to greatly increase the ability to investigate low-energy phonons.

(2) While the number of x-ray photons or neutrons at the sample are roughly comparable (3×108 photons or neutrons per sec), an IXS beam size is much smaller (200 ×100 μm) than that in an INS spectrometer. Thus the required biomaterial is in mg quantity. This is an absolute requirement for any systematic investigation of biomaterials.

(3) Even if one deuterates a bio-molecule, the dynamic structure factor as measured in an INS experiment is a weighted sum of contributions from partial structure factors of deuterium, carbon, oxygen, nitrogen and phosphor, etc. Fortunately, the dynamic structure factor measured in an IXS of DNA is practically dominated by the phosphate-phosphate (high Z atoms) PSF coming from the backbones of the DNA molecules. In the case of lipid bilayers the scattering is dominated by that from carbon atoms of the lipid molecules. Therefore, the interpretation of the nature of the collective modes measured is simpler.

(4) An IXS spectrum measured with an energy resolution of ΔE = 0.1 meV can be calculated from the corresponding intermediate scattering function (ISF) computed with a time window of 15 ps. This allows the investigation of the alpha relaxation at high Q in the ISF. Furthermore, modern MD simulations of bio-

macromolecules are routinely pursued up to 100 ps. Thus measured IXS spectra of bio-macromolecules can be used to critically test the force field models of proteins, lipid bilayers, and DNAs.

In summary, IXS has a major advantage in studying phonon propagation in biomaterials compared to INS. For many circumstances, resolution of 1 meV with an improved resolution function will be sufficient. However, the availability of 0.1 meV resolution is predicted to have a major impact on investigations of relaxational dynamics of bio-molecular assemblies in their glassy states.

A3.4 Phonons in Crystalline Systems

The study of phonons in crystalline media has traditionally been the domain of inelastic neutron scattering (INS). IXS has important advantages that make it extremely attractive to complement neutron measurements of phonon behavior in solids, mainly the very strong intensity of the sources and the extremely small spot size. In contrast to INS, IXS is free of any kinematic limitations. Since the x-ray cross section is mostly dominated by photoelectric absorption, the optimum scattering signal can be obtained for sample volumes as small as 10^{-4} to 10^{-6} mm^3. This allowed previously impossible studies on single crystals only available in small sizes such as MgB_2 and plutonium[38], or on materials for which homogeneous stoichiometry and/or doping can only be ensured within a small volume. Since most new and novel materials can only be grown as small single crystals, IXS is expected to become the probe of choice for these materials.

Furthermore, the typical x-ray beam sizes are well compatible with the sample volume constraints of diamond anvil cells, and lattice dynamics studies at very high pressures – to 40 GPa for single crystals and above 100 GPa for polycrystalline materials – have been conducted.

(1) A problem of growing interest is the study of phonon line widths, which is inversely related to the phonon lifetime. Phonons interacting with other collective excitations – other phonons, spin waves, or electrons – give rise to a finite line width whose measurement provides detailed information about the collective behavior of the solid. A recent example[39] is the study of Kohn anomalies in the superconductors Nb and Pb using a novel neutron method with resolution < 0.1 meV. This experiment measured the change in phonon linewidth on entering the superconducting state, which is a direct measurement of the electron-phonon coupling. With the high resolution it was possible to measure other Kohn anomalies and show that the superconducting energy gap extracted from the line width measurements converges towards a sharp Kohn anomaly originating from Fermi surface nesting.

This study has an order of magnitude better resolution than previous work on Nb[40] and demonstrates how an order of magnitude increase in performance yields new physics. With the 0.1meV IXS instrument one can extend these measurements to other materials, such as organic superconductors, where large single crystals are not available. It would also be possible to probe the pressure dependence of the e-p coupling by measuring the pressure dependence of line widths.

(2) Another exciting opportunity offered by IXS is the study of lattice dynamics in the near-surface region. This is accomplished in grazing incidence geometry for which the X-rays impinge onto the sample below the critical angle of total reflection, α, and consequently penetrate only 30-40 Å into the material under study. As a matter of fact, as the glancing angle of incidence can be tuned (from below to well above), IXS offers the unique possibility to study bulk and near-surface dynamics, using the same experimental set-up. The high brilliance of NLSL-II would benefit such measurements. For these materials, a more moderate resolution (~ 1 meV) is probably adequate.

(3) For polycrystalline materials IXS allows the determination of the orientation averaged longitudinal sound velocity of polycrystalline materials at low momentum transfers, Q, typically in the 1 – 10 nm^{-1} momentum transfer range, where the dynamics are dominated by longitudinal modes.

REFERENCES

[1] C. Burns, S.-H. Chen, A. Cunsolo, M. Krisch, H.-K. Mao, T. Scopigno, S. Shapiro, and Y. Shvyd'ko, *A Letter of Intent for an Extremely-High Resolution Inelastic X-ray Scattering Beamline for NSLS-II* (Submitted to NSLS-II Project on April 22, 2008)

[2] Yu. V. Shvyd'ko, *X-Ray Optics, High-Energy-Resolution Applications* (Springer, Berlin, 2004)

[3] Yu. V. Shvyd'ko et al, AIP Conf. Proceedings Series, CP 879 (2006)

[4] Yu. V. Shvyd'ko. *Advanced Designs of Angular Dispersive X-ray Monochromators*, to be published. See also *Conceptual Design Report for NSLS-II* (http://www.bnl.gov/nsls2/project/CDR) Section 11.5.2: *Conceptual Design for the Inelastic X-Ray Scattering Beamline*.

[5] Yu. Shvyd'ko et al., Phys. Rev. Lett. **97**, 235502 (2006)

[6] C. Masciovecchio et al., Nucl. Inst. Meth. Phys. Res., **B111**, 181 (1996)

[7] D. Liu and S.-H. Chen et al, Phys. Rev. Lett. **101**, 135501 (2008)

[8] X.R. Huang, Z. Zhong, Y.Q. Cai, and S. Coburn, Proceedings of SPIE **7077** (Advances in X-Ray/EUV Optics and Components III, San Diego, August 11-13, 2008, USA), 70771A (2008)

[9] T.S. Toellner et al, NIM A557, 670 (2006); and NSLS-II presentation

[10] See, for example, G. Monaco, C.R. Physique **9**, 608 (2008).

[11] O. Chubar, J. Bengtsson, A. Broadbent, Y.Q. Cai, Q. Shen, and T. Tanabe, AIP Conference Proceedings for SRI2009.

[12] Parameters extracted from the NSLS-II Storage Ring Parameters database: http://groups.nsls2.bnl.gov/acceleratorsystems/interface/Lists/ProjectParameters/Summary.aspx

[13] T. Tanabe, private communication. See also *Conceptual Design Report for NSLS-II* (http://www.bnl.gov/nsls2/project/CDR) Section 12.7: *Insertion Devices*.

[14] L. Doom, B. Gash, S. Sharma et al, see http://groups.nsls2.bnl.gov/acceleratorsystems/mech/frontends/default.aspx.

[15] X.R. Huang, unpublished.

[16] It is suggested by Yu. V. Shvyd'ko that, for glancing incident angles $\theta_e > 2°$, multiple beam diffraction may become possible which would reduce considerably the performance of the CDW/CDDW monochromators. We intend to carry out theoretical and experimental verification of the issue.

[17] Yu. V. Shvyd'ko, *Advanceds in X-ray Optics for IXS Spectroscopies*, Workshop on Inelastic X-ray Scattering at NSLS-II, February 7-8, 2008, http://www,bnl.gov/nsls2/workshops/docs/IXS/IXS_15_Shvydko.pdf.

[18] M. Yabashi, K. Tamasaku, S. Kikuta, and T. Ishikawa, Rev. Sci. Instr. **72**, 4080 (2001)

[19] T.S. Toellner, private communication. The measured resolution function shows substantially sharper tails compared with a Lorentz function of the same width (FWHM), and compares well with theoretical simulation.

[20] M. Honnicke, X. Huang, J. Keister, C.N. Kodituwakku, and Y.Q. Cai, J. Syn. Rad. (submitted).

[21] R. Dietsch and T. Holz, United State Paten 7298822 – X-ray optical element

[22] F. Hertlein et al., Part. Part. Syst. Charact. **22**, 378 (2005)

[23] U. Shymanovich et al., Appl. Phys. B **92**, 493 (2008)

[24] M. Krisch, private communications.

[25] H. Sinn, J. Phys.: Condens. Matter **13**, 7525 (2001).

[26] T. Scopigno et al. Rev. Mod. Phys **77**, 881 (2005).

[27] S. Hosokawa et al., J. Phys.: Condens. Matter **20**, 114107 (2008); L.E. Bove et al, Eur. Phys. Lett. **79**, 16002 (2007).

[28] A. Cunsolo et al., J. Chem. Phys. **114**, 2259 (2001); T. Scopigno et al., Phy. Rev. E **66**, 031205 (2002).

[29] C. Masciovecchio et al., Phys. Rev. Lett. **80**, 544 (1998).

[30] A. Campa and G. D. Cohen, Phys. Rev. **A39**, 4909 (1989).

[31] P. Westerhuijs et al., Phys. Rev. **A45**, 3749 (1992); W. Montfrooij et al. Phys. Rev. Lett. **61**, 2155, (1988).

[32] See for example, C. J. Pickard, R. J. Needs, Nature Phys. **3**, 473 (2007); E. Babaev, A. Sudbø, N. W. Ashcroft, Nature **421**, 666 (2004).

[33] H. K. Mao, P. M. Bell, R. J. Hemley, Phys. Rev. Lett. **55**, 99 (1985).

[34] M. Hanfland, R. J. Hemley, H. K. Mao, G. P. Williams, Phys. Rev. Lett. **69**, 1129 (1992).

[35] J. H. Eggert, H. K. Mao, R. J. Hemley, Phys. Rev. Lett. **70**, 2301 (1993).

[36] R. J. Hemley, Z. G. Soos, M. Hanfland, H. K. Mao, Nature **369**, 384 (1994); M. Hanfland, R. J. Hemley, H. K. Mao, Phys. Rev. Lett. **70**, 3760 (1993).

[37] I. I. Mazin, R. J. Hemley, A. F. Goncharov, M. Hanfland, H. K. Mao, Phys. Rev. Lett. **78**, 1066 (1997); H. K. Mao, R. J. Hemley, Rev. Mod. Phys. **66**, 671 (1994).

[38] J. Wong et al., Phys. Rev. B **72**, 064115 (2005).

[39] P. Aynajian et al., Science **319**, 1509 (2008).

[40] S. M. Shapiro, G. Shirane, and J. D. Axe, Phys. Rev. B **12**, 4899 (1977).

Intentionally blank.

LT-XFD_CDR_XPD-00124

NSLS-II Project

CONCEPTUAL DESIGN REPORT for the

SUBMICRON RESOLUTION X-RAY SPECTROSCOPY (SRX) BEAMLINE AT NSLS-II

final draft Sep 2009

Intentionally blank.

Approvals and Reviewers

Compiled by	**Signature**	**Date**
Juergen Thieme, SRX Beamline Group Leader, NSLS-II		
Approved		
Qun Shen, XFD Director, NSLS-II		
Reviewers		
Antonio Lanzirotti, BAT Spokesperson, signing on behalf of the BAT		
Andy Broadbent, Beamlines Manager		
Nicholas Gmür, ESH Coordinator, NSLS-II		
Sushil Sharma, Mechanical Engineering Group Leader, NSLS-II		

Document Updates

The Conceptual Design Report for the Submicron Resolution X-ray Spectroscopy (SRX) beamline at NSLS-II is a controlled document, revised under change control.

Version No.	Date	Changes made
A	9/18/2009	Initial draft
1	10/1/2009	Final draft, submitted to BAT

Intentionally blank.

Contents

1 INTRODUCTION 1

1.1 SCIENTIFIC REQUIREMENTS 1
1.2 BEAMLINE ADVISORY TEAM (BAT) 2
1.3 REPRESENTATIVE EXPERIMENTS 2
1.4 COMPARISON TO OTHER INSTRUMENTS 6

2 BEAMLINE LAYOUT 8

2.1 OVERVIEW 8
2.2 INSERTION DEVICE AND LOW β STRAIGHT SECTION AND OPERATION MODES 10
2.3 FRONT END 13
2.4 OPTICAL LAYOUT 13
2.5 HIGH HEATLOAD OPTICS 17
2.6 RAY TRACING 28
2.7 LIST OF MAJOR COMPONENTS 32

3 END STATION INSTRUMENTATION 39

3.1 HUTCH MECHANICAL, ENVIRONMENTAL AND UTILITIES REQUIREMENT 39
3.2 SAMPLE MOUNTING, ENVIRONMENTS AND MANIPULATION 40
3.3 DETECTORS 42

4 SPECIAL BEAMLINE REQUIREMENTS 44

5 FUTURE UPGRADE OPTIONS 44

APPENDIX 1: SCHEDULE 45

APPENDIX 2: REFERENCE DRAWINGS 47

Acronyms

FEA	Front End Aperture
FOE	First Optical Enclosure
FWHM	Full Width at Half Minimum
HMP	Horizontal Mirror Pair
IVU	In-Vacuum Undulator
KB	Kirkpatrick-Baez
MLL	Multi Layer Laue Lens
OA	Optical Aperture
SHS	Secondary Horizontal Source
SHSA	Secondary Horizontal Source Aperture
SRX	Submicron Resolution X-ray Spectroscopy beamline
WBF	White Beam Filter
WBS	White Beam Slit
ZP	Zone Plate

1 INTRODUCTION

1.1 Scientific Requirements

Scientific communities (such as Earth, Environmental, and Life sciences, Hard Condensed Matter and Materials sciences, Chemical and Energy sciences) have all identified analytical resources that must be developed to advance our understanding complex natural and engineered systems that are heterogeneous on the micron to submicron scale. These groups in particular specified a need for higher intensity focused x-ray probes and made it clear in the Letter of Interest they submitted to the NSLS-II Project for the Sub-Micron Resolution X-Ray (SRX) Spectroscopy Beamline, that NSLS-II would provide one of the best sources in the world for such instruments. The research topics these scientific communities hoped to better address using such an instrument require characterization of elemental abundances and speciation in samples that are heterogeneous at the sub-micrometer scale. The targeted scientific issues show a wide gamut of environmental and health issues of high societal impact. Interactions between micro-organisms and minerals control the speciation, migration and toxicity of contaminated materials produced by human activity. Micro-organisms and particulates are likely major players in the cycling of nutrients and metals in the Earth's oceans, processes that can have a significant impact on conditions at the planetary scale, such as global climate change. The properties of airborne particulates can have a profound effect on the toxicity of atmospheric dust introduced to the human body by inhalation. The study of how genetic variations in organisms affect their interactions with contaminant and nutrient metal species in the environment is in its infancy but likely to be greatly advanced with this new technology because of the ability to observe in detail the chemical modifications in organisms caused by genetic modification. Equally significant will be studies of the varied sources, pathways and functions of metals in organisms, in particular their role in human health. Some metals are required for normal metabolic function, with optimal amounts for maximum benefit. Others are only known to cause toxic effects. Metal ions are also used both as treatments for disease and as image contrast agents within the body. Yet, in order to understand at the molecular level how metal ions function in life, disease, and therapy, a multi-dimensional approach is necessary. Such an instrument will allow studies of catalysis and chemical processes at the scale of a single particle using coupled μXAS/μXRD of catalytic particles and interfaces to follow processes such as oxidation. In the materials sciences scientists will be able to research the elemental partitioning in microelectronics and elemental diffusion into microcrystalline domains that occur due to aging of plastics and alloys and tracking redox changes of single particle contaminants in batteries and silicon solar cells.

The SRX sector with its unique combination of high spectral resolution over a very broad energy range and very high beam intensity in a sub-micrometer spot will be a tool very well suited for the study of the scientific issues mentioned above. The design envisions a canted undulator sector that will consist of two beamlines, each optimized for a specific energy range that will allow the scientific community to cover the spectroscopic range they identified was needed for the research. Two beamlines are required to cover the large energy range and spatial resolution of interest in an optimal way. The first beamline is optimized to access higher energy and is included in the initial budget scope for the SRX sector. It will access an energy range of E = 4 keV to E = 25 keV. The second low energy beamline, accessing spectroscopic edges from E = 2 keV to E = 15 keV, will require additional funding to be completed.

The high energy cut-off of E = 25 keV of the first beamline is determined by the energy at which the brightness of the NSLS-II undulators has dropped by approximately two orders of magnitude from that of the third harmonic at closed gap. Also, the K absorption edge of rhodium, the likely mirror coating, will begin to interfere at about E = 23 keV. The low energy cut-off of E = 4 keV is the energy at which the undulator third harmonic is likely to begin. It will still give access to elements down to the Ti K edge.

The low energy cut-off of E = 2 keV of the second beamline is set by the limits of the Si (111) monochromator, while still reaching the K absorption edge of phosphorus. The high-energy cut-off of E = 15 keV is determined by the need to access the LIII absorption edge of lead at E = 13 keV.

1.2 Beamline Advisory Team (BAT)

Peter Eng: Senior Research Associate, University of Chicago
Jeffrey Fitts: Assistant Geochemist, Brookhaven National Laboratory
Chris Jacobsen: Professor, Stony Brook University
Keith Jones: Senior Physicist, Brookhaven National Laboratory
Antonio Lanzirotti (BAT Spokesperson): Senior Research Associate, University of Chicago
Lisa Miller: Biophysical Chemist, Brookhaven National Laboratory
Matt Newville: Senior Research Associate, University of Chicago
Paul Northrup: Associate Environmental Scientist, Brookhaven National Laboratory
Richard Reeder: Professor, Stony Brook University
Mark Rivers: Senior Scientist, University of Chicago
Stephen Sutton: Senior Scientist, University of Chicago
Stefan Vogt: Beamline Scientist, Advanced Photon Source, Argonne National Laboratory
Gayle Woloschak: Professor, Northwestern University

1.3 Representative Experiments

There are a number of research areas where the SRX beamline will enable significant advances. Largely this will be due to the world leading flux density the SRX probes will provide, their unique sub-micrometer x-ray fluorescence and x-ray spectroscopic capabilities and the plan to develop these hard x-ray methodologies as imaging modalities by utilizing both the beamline's optical characteristics and advanced detector technologies. This holds true for both branches of this beamline, the Kirkpatrick-Baez (KB) based instruments as well as the zone plate (ZP) based instrument. Only the KB branch is part of the original scope of the NSLS-II project, however it is expressly desired by the scientific community to establish the ZP branch as contemporary as possible. An exhaustive list of potential experiments that could be conducted on this beamline and their scientific significance is presented in the original Letter of Interest (LOI) submitted by the beamline advisory team (BAT). Some of the experiments discussed in the LOI include:

- How SRX will extend x-ray elemental analysis, spectroscopy, and scattering to spatial resolutions suitable for the analysis of aerosols.
- Applications of coupled sub-micrometer XRF, XAFS and XRD methods to access to the details of microbial-mineral interactions in-situ.
- Sub-micrometer XRF, XAFS and XRD studies of how micro-organisms fixate and cycle carbon and nitrogen in the Earth's oceans using metalloenzymes.
- Evaluation of how specific genes influence the uptake of metals in plants and animals at the cellular level using the highest spatially-resolved XRF and XAFS computed microtomography available *in-vivo*.
- Characterization of how metallic-DNA nanocomposites target individual cells to determine specific localization.
- Sub-micrometer XAFS studies to constrain the speciation of metallic species that may contribute to the oxidative damage of cells from redox processes.

At this point an example of how the unique optical characteristics of the Kirkpatrick-Baez (KB) instrument at the SRX beamline, the advanced energy scanning capabilities of the beamline's monochromator and in-vacuum undulator, and the synergistic development of advanced energy dispersive detectors at BNL will help formulate new methodologies for sub-micrometer hard x-ray spectroscopy. Given the predicted intensity of the KB instrument, many spectroscopic experiments will benefit from being conducted in an 'event driven' or 'image stack' modality utilizing fluorescence detectors that support fast on-the-fly scanning modes working in conjunction with high precision monochromator and undulator energy scanning. This must all be done with suitable feedback to maintain focused beam position on the sample within a few nanometers. A preliminary evaluation of how such experiments can be designed an implemented was conducted by members of the BAT (P. Eng, A. Lanzirotti, and M. Rivers – U. Chicago in collaboration with Emily Knowles and Alexis Templeton – U.C. Boulder) at the

Australian Synchrotron's X-ray Fluorescence Microspectroscopy beamline (5ID). This Kirkpatrick-Baez mirror based beamline shares a great deal of commonality with the proposed design of the KB based instrument at the SRX beamline including a high stability horizontally diffracting monochromator design, the use of a harmonic rejecting horizontally focusing mirror, an in-vacuum undulator that is designed to synchronize with the monochromator to keep the undulator tuned to the maximum of its emission peak, and an evaluation program of a prototype 96-element BNL-CSIRO *Maia* detector system. Photon flux of the 5ID KB instrument at E = 10 keV is ~ $4x10^{12}$ ph/sec. The KB instrument at the SRX beamline is expected to deliver more than a factor of 10 higher flux to the sample in a spot size that is up to a factor of 10 smaller.

This experiment sought to examine the redistribution of metals and changes in metal speciation associated with microbial alteration of deep-sea volcanic glasses. There is considerable interest in understanding the microchemistry of these organisms and their environment since they may constitute a significant fraction of the global biomass (and are thus relevant in modelling climate change) and are relevant to the development of the earliest life on Earth (and potentially models for the evolution of life on other planets). The granular alteration left by these microbes in deep sea basaltic glasses are typically only a few microns in diameter, requiring highly resolved spectroscopic probes for evaluating the chemistry of the alteration products.

Figure 1 shows in the left a plane light photomicrograph of a sample of the Troodos Ophiolite, a 170 million year old sample of obducted oceanic crust. The box marked in blue delineates an area that was compositionally mapped using the prototype *Maia* X-ray fluorescence detector. The dark filamentous areas in the center left of the figure show areas of microbial alteration. An Fe compositional map is shown in the upper right and a composite Fe-Ti-Mn RGB map in the lower right of Figure 1. These maps were collected as on-the-fly continuous scans with a dwell time that translates to 16 msec per pixel at a pixel size of 1.25 µm. The *Maia* detector is operating in an event-driven list mode, counting each individual photon as a function of its energy and motor position. These images, collected over roughly 6 hours, represent almost 1.5 Megapixels of full energy dispersive data. The rapid detector readout coupled with high instrument brightness and precise energy control then allows for Fe K-edge spectroscopy to be conducted in an image stack mode similar to what has been developed by Chris Jacobsen to STXM instruments. The smaller area of the section marked in a red box on the photomicrograph shows one specific area that was interrogated using this image-stack approach. Each individual image in the stack contains 14,400 pixels collected at 16 msec dwell time and a pixel resolution of 1.25 µm. After each image the monochromator and the IVU adjust energy in unison, scanning through the Fe K absorption edge (compare Figure 2) to produce a stack of images from which high-resolution Fe K-edge XANES data can be extracted (Figure 3). This data set required approximately 4 hours of instrument time at this resolution but the planned 384-element *Maia* detector planned for SRX-KB should yield 4x higher data rates. Coupled with the significantly higher brightness of this KB instrument and the stability of the horizontally deflecting monochromator and IVU, it can be expected that this likely will be the most common mode in which sub-micrometer resolution X-ray absorption spectroscopy will be conducted at the beamline.

Figure 4 shows as an example what could be achieved with the zone plate (ZP) branch of the SRX beamline results achieved when studying the annually laminated sediments of a lake in Germany using beamline Id21 at the storage ring ESRF. The top left image is an image taken with an optical microscope, showing the lamination of the sample. This lamination originates from the precipitation of carbonates during summer and early autumn and the sedimentation of clay minerals and organic matter during winter and spring. Such laminae are only preserved, when bioturbation is prevented and thus evidence anoxic conditions. Even though, XANES at the sulfur K-absorption edge was able to determine a different sulfur species distribution in different laminated sediment sections. The lamination is also reproduced when looking at the sample in the X-ray fluorescence light at E = 2490 eV, just above the K-absorption edge of sulfur. Sulfur-rich and sulfur-poor layers alternate. To identify the sulfur speciation within the layers, a sequence of XANES spectra has been taken, following the trajectory from A to B, indicated in the top images. The lower image of Figure 8 is a three-dimensional representation of this set of spectra. It shows, that the amount of reduced sulfur species decreases when going from A to B, whereas the oxidized species gets more prominent.

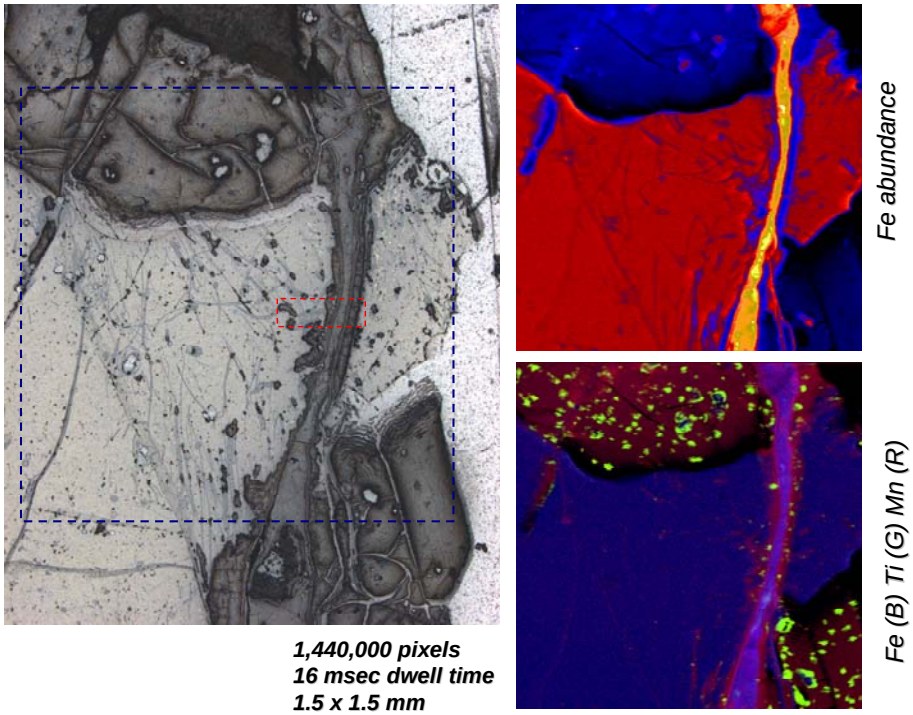

Figure 1. (Left) plane light photomicrograph of a sample of the Troodos Ophiolite, a 170 million-year-old sample of obducted oceanic crust. The box marked in blue delineates an area that was compositionally mapped using the prototype *Maia* X-ray fluorescence detector. The area delineated in red shows where Fe K-edge image stack XANES data were collected. The dark filamentous areas in the center left of the figure show areas of microbial alteration. (Top Right) Fe compositional map of the blue area. (Bottom Right) Composite Fe-Ti-Mn RGB map of the blue area. These were collected as on-the-fly continuous scans with a dwell time that translates to 16 msec per pixel at a pixel size of 1.25 µm. (Knowles, Templeton, Eng, Lanzirotti, Rivers. Unpublished data)

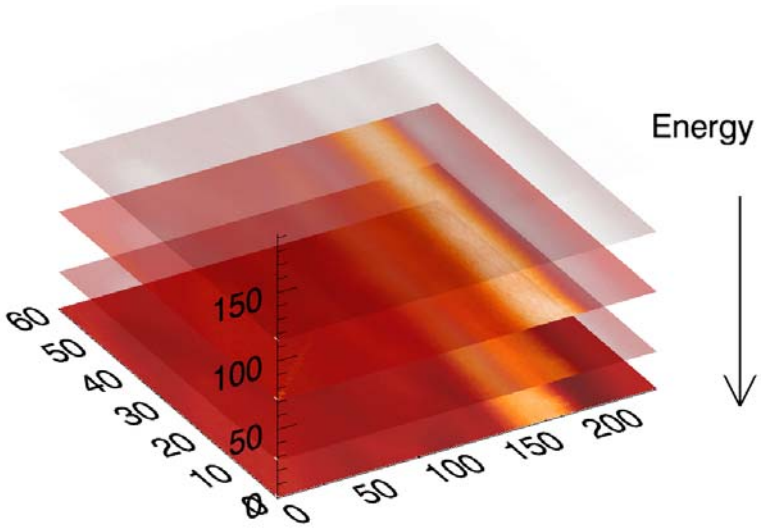

Figure 2. Selected Fe K-edge image stacks as a function of incident beam energy for the area marked in red in Figure 1. (Knowles, Templeton, Eng, Lanzirotti, Rivers. Unpublished data).

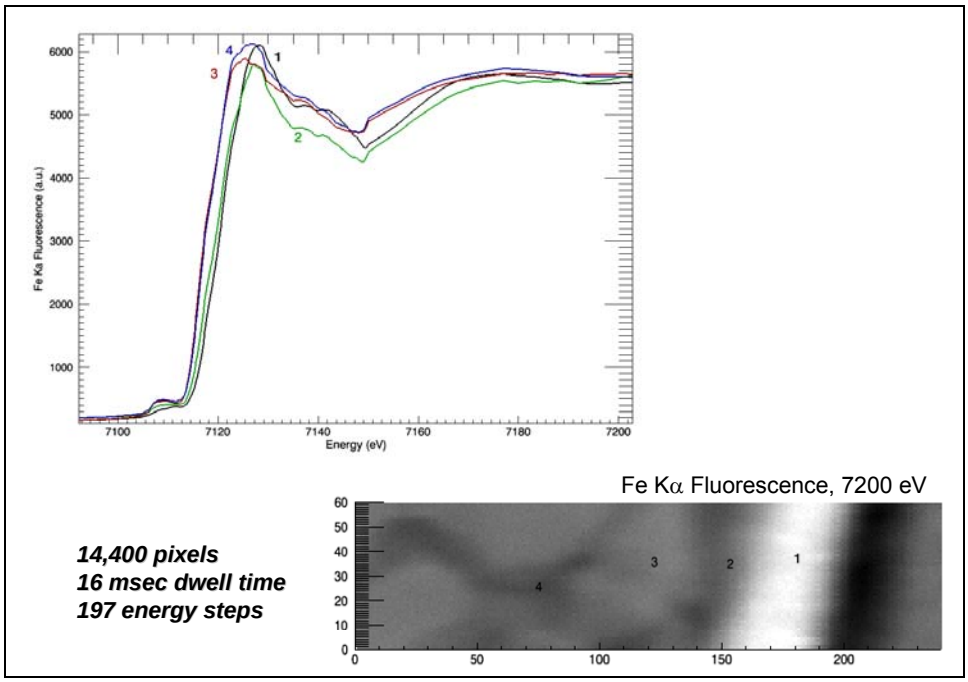

Figure 3. (Bottom) Fe K-edge image stack of the area marked in red in Fig. 1, collected at 7200 eV incident beam energy. Each map contains 14,400 pixels collected with 16 msec dwell time and 1.25 µm pixel resolution. 197 energy steps were collected for the entire stack. (Top) Extracted Fe K-edge XANES spectra from the image stack at pixel locations (1-4) marked on the bottom image. (Knowles, Templeton, Eng, Lanzirotti, Rivers. Unpublished data)

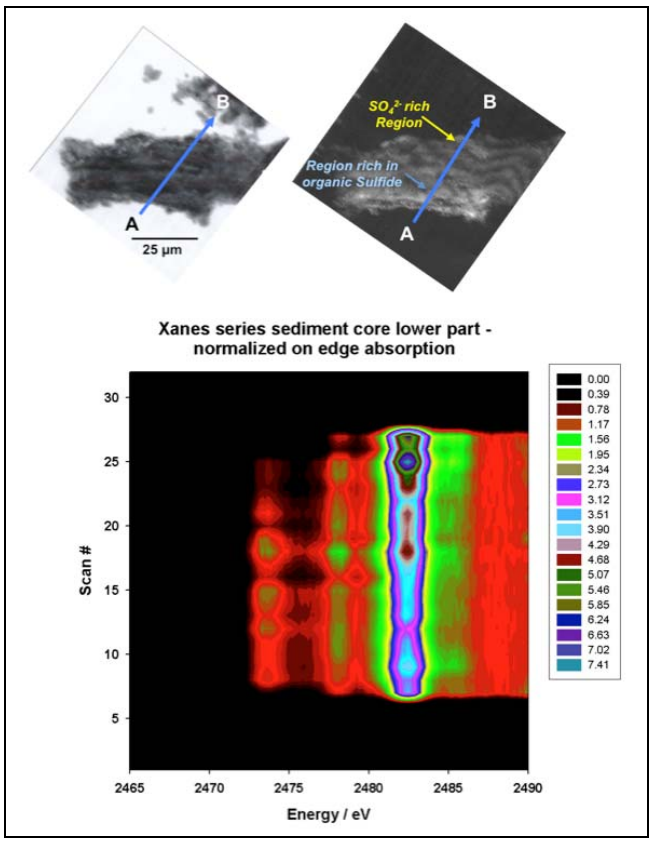

Figure 4. (top left) Optical microscope image of a section of a laminated sediment core from the lake Steisslinger See. (top right) X-ray fluorescence image of the same sediment core taken at E = 2.490 keV, showing the same lamination. (bottom) 3D-representation of the XANES spectra across the sediment core, scan numbers increasing from A to B.

1.4 Comparison to Other Instruments

The following list might be far fom complete but shows exemplary the scientific environment in which the SRX beamline would evolve delivering the highest photon flux in the smallest spot.

1. Beamline ID21 at electron storage ring ESRF in Grenoble, France

   This scanning transmission x-ray microscope is designed for using the spectral range from E = 6.5 keV to E = 18 keV for spectromicroscopy experiments in life, materials and environmental sciences. The instrument is capable of absorption contrast imaging, fluorescence imaging and XANES imaging. Using a zone plate or a KB mirror system as focusing optics the spatial resolution lies in the range of 0.2 – 1 µm.

2. Beamline ID22 at electron storage ring ESRF in Grenoble, France

   This x-ray microprobe scope is designed for using the spectral range from E = 2 keV to E = 7.5 keV. It provides a focused x-ray beam of about 3.5 x 1.5 μm^2 at a flux of up to 10^{12} ph/s. The instrument offers access to absorption, fluorescence and diffraction, fluorescence-tomography, XANES imaging, holography and phase-contrast micro-tomography, focusing optics are KB mirrors and compound refractive lenses.

3. Beamline 2-ID-B at the Advanced Photon Source in Argonne, IL

   This beamline is built for scanning x-ray microscopy and coherent diffraction x-ray microscopy in the energy range from E ≤ 1 keV up to E = 4 keV. Phase contrast, micro-fluorescence imaging and XANES are supported as well as coherent x-ray scattering and diffraction imaging. A photon flux up to 10^9 phot/sec and a spot size of 60 x 60 nm^2 using a Fresnel zone plate can be utilized for experiments.

4. Beamline 2-ID-D at the Advanced Photon Source in Argonne, IL

   That beamline is built for sub-micron high-resolution x-ray imaging studies. Most of the work centers on fluorescence analysis of biological samples and micro-diffraction of a variety of materials. Micro-fluorescence, micro-diffraction and micro-XAFS are available for experiments. The usable x-ray energy ranges from E = 5 keV up to E = 30 keV, flux can be expected as high as 4 x 10^9 phot/sec, the spatial resolution goes down to 0.2 x 0.2 μm^2.

5. Beamline 2-ID-E at the Advanced Photon Source in Argonne, IL

   This beamline is built as a micro-fluorescence imaging station. The energy usable for experiments ranges from E = 7.5 keV up to E = 10 keV. A photon flux up to 5 x 10^9 phot/sec and a spot size of 0.5 x 0.3 μm^2 using a Fresnel zone plate optics can be utilized for experiments.

6. Beamline 13-ID-C,D at the Advanced Photon Source in Argonne, IL

   This beamline is specialized on earth and environmental science research. The reachable energy ranges from E = 4 keV to E = 45 keV. A KB mirror system focuses the beam into a 2 x 2 μm^2 spot with a photon flux of up to 1 x 10^{11} phot/sec. Inelastic x-ray scattering, micro-XAFS, micro - diffraction, x-ray absorption fine structure (XAFS), and micro-fluorescence are supported techniques. High pressure diamond anvil cell and high pressure multi-anvil press (LVP) are available for sample treatment.

7. Beamline 20-ID-B,C at the Advanced Photon Source in Argonne, IL

   This beamline is specialized on material science, environmental science, chemistry and geoscience. When focused using KB mirrors, it covers energy range from E = 4.3 keV to E = 27 keV delivering the beam into a 2 x 2 μm^2 spot with a photon flux of up to 1 x 10^{11} phot/sec. X-ray absorption fine structure (XAFS), surface diffraction, x-ray raman scattering, micro-XAFS, micro-fluorescence time resolved XAFS, and x-ray emission spectroscopy are supported techniques.

8. Beamline X26A at the National Synchrotron Light Source in Brookhaven, NY

The beamline covers an energy range in a focused mode from E = 4 keV to E = 30 eV, using a KB setup, which focuses the monochromatic beam down to 5 µm x 10 µm size. Photon flux is then in the range of 3 x 10^9 phot/sec. The beamline can be utilized as a microprobe and is as well suited for microdiffraction imaging.

9. Beamline X27A at the National Synchrotron Light Source in Brookhaven, NY

The beamline covers an energy range in a focused mode from E = 4.5 keV to E = 32 eV, using a KB setup to focus the monochromatic beam down to 15 µm x 10 µm size. Photon flux is then in the range of 1-5 x 10^9 phot/sec. This beamline is a microprobe being used by researches from environmental science, geoscience, physics, chemistry, and biology.

10. XFM beamline at the Australian Synchrotron Project

The X-ray Fluorescence Microprobe at the Australian Synchrotron is a microprobe station with either a KB mirror system with a spot size down to 2 x 1 μm^2 or a ZP showing a spot size of about 0.06 x 0.06 μm^2. The energy range scales from E = 4.1 keV up to E = 25 keV, the photon flux can reach 4 x 10^{11}phot/sec for the KB and 10^{10} phot/sec for the ZP optics.

11. MicroXAS beamline at the Swiss Light Source

This beamline focuses on x-ray fluorescence imaging and XAS spectroscopy with a spatial resolution in the 1 x 1 μm^2 range. The energies available for experiments range from E = 5 keV up to E = 20 keV. A photon flux up to 2 x 10^{12} phot/s will be delivered.

12. LUCIA beamline at the synchrotron SOLEIL, Gif-sur-Yvette, France

The beamline LUCIA covers the energy range from E = 0.8 keV up to E = 8 keV. It is an x-ray microprobe with capabilities for chemical speciation by x-ray absorption spectroscopy (µXAS) and for elemental mapping by x-ray micro-fluorescence (µXRF). The focusing is done with a "Kirkpatrick-Baez" (KB) reflecting mirrors system, yielding a focal spot of about 2.5 x 2.5 μm^2. A photon flux up to 2 x 10^{11} phot/s can be expected.

2 BEAMLINE LAYOUT

2.1 Overview

The general concept of the SRX beamline is to offer stations where x-ray spectromicroscopy experiments can be performed with a spatial resolution in the sub-micrometer range. The energy range covered should extend from E = 2 keV up to E = 28 keV. This concept will be realized by dividing this beamline into two branches, each served by an optimized, in-vacuum undulator with the two insertion devices arranged in a canted geometry. One branch will be equipped with focusing mirrors in a Kirkpatrick-Baez (KB) setup, aiming at a spatial resolution down to 100 x 100 nm^2, working in the energy range from E = 4.65 keV up to E = 28 keV, and delivering a flux of up to 5 x 10^{12} phot/sec in that spot. The other branch will use a Fresnel zone plate to reach a spatial resolution down to 30 nm in the energy range of E = 2 keV up to E = 15 keV, where the expected flux will be up to 7 x 10^9 phot/sec. Photon flux and spatial resolution in that energy range will be unprecedented as can be seen when comparing these key parameters to similar beamlines as listed on the previous page. The KB branch is a project beamline of the NSLS-II project; the ZP branch is not in the original scope. To ensure that a reasonable design and layout for the latter will be available when an approving decision will be due, the conceptual design of both branches will be found in this report. A schematic view of the sector starting with the two canted undulators and showing major optical components of the two branch lines is seen in Figure 5. Note, that the angle between the two branches is exaggerated for illustration purposes.

The optical layout of the KB-branch is shown in Figure 6. Due to heat load reasons (see chapter 2.5), the double crystal monochromator will be the first optical element downstream of the storage ring shield wall, followed by the horizontally focusing mirror. The Secondary Horizontal Source Aperture will define the source point for the KB mirrors located downstream in the hutch. The KB mirrors will create a demagnified image of this source point as a focal spot through which the sample will be scanned. A variety of detectors will be available for fluorescence, transmission and diffraction measurements.

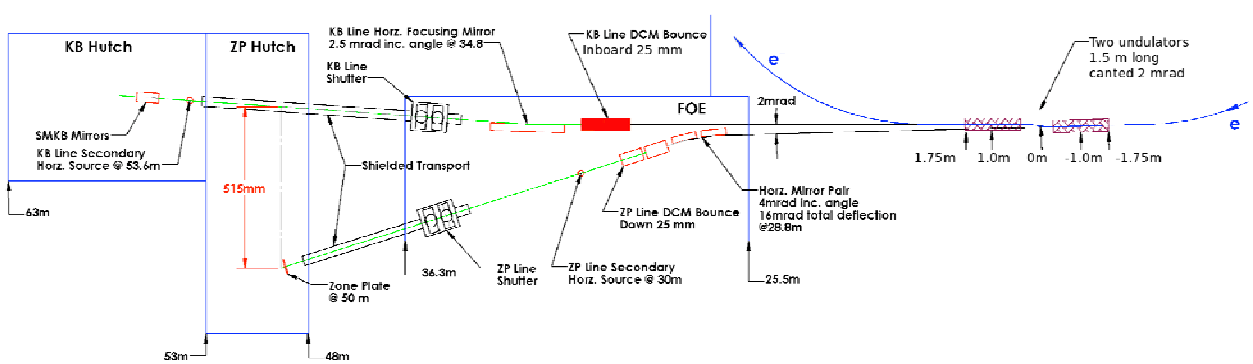

Figure 5. Schematic layout (top view) of the SRX beamline. The angle between the two beamlines is exaggerated for illustration purposes. A canting angle of 2 mrad will be used.

Figure 6 shows a layout of the KB branch of the SRX beamline itself including the hutches, major optical elements and the beam pipes. The first hutch, starting at the ratchet wall, will be the First Optical Enclosure (FOE). Here, the double crystal monochromator and the horizontally focusing mirror of the KB-branch, and the mirror pair and the double-crystal monochromator of the ZP-branch will be found. Due to the canted design of the undulators the x-ray beams for the two branches are very close. Therefore, the optical components for the KB branch have to be constructed in a way that room is available for the x-ray beam feeding the ZP-branch, which may be implemented at a later time. The hutch in the middle will be housing the endstation of the ZP branch, the hutch farthermost downstream will be the place for the endstation of the KB branch, including the KB mirror, the sample holder and the detectors. The Secondary Horizontal Source Aperture will be at the upstream end of this hutch.

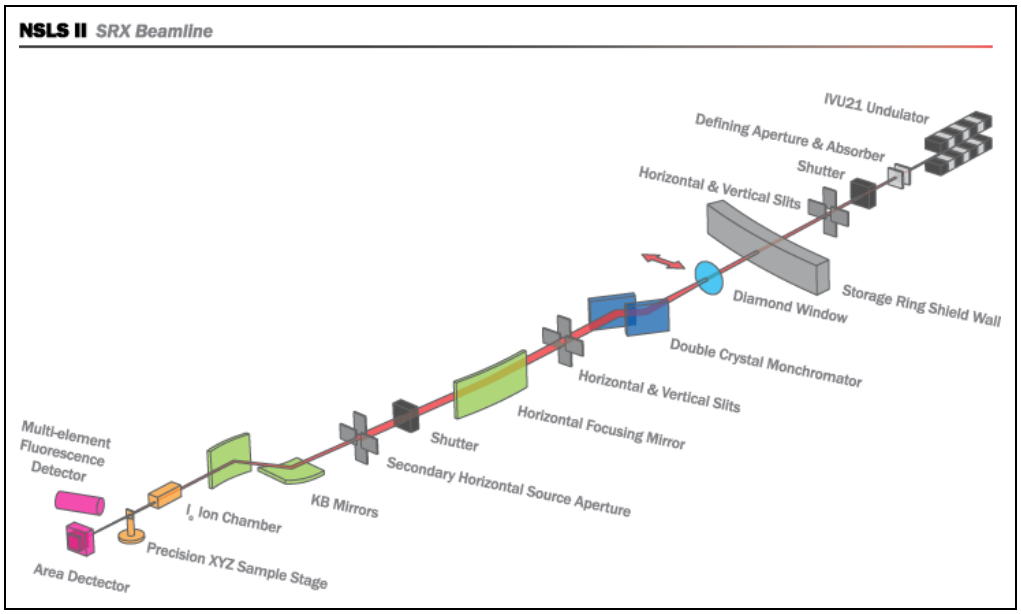

Figure 6. Optical layout of the SRX beamline. Here, only the branch with the Kirkpatrick-Baez mirrors is visible.

Figure 7 shows the layout of the complete beamline, starting at the ratched wall. Three hutches are visible, the first optical enclosure on the right, the zone plate endstation in the middle, and the KB endstation on the left.

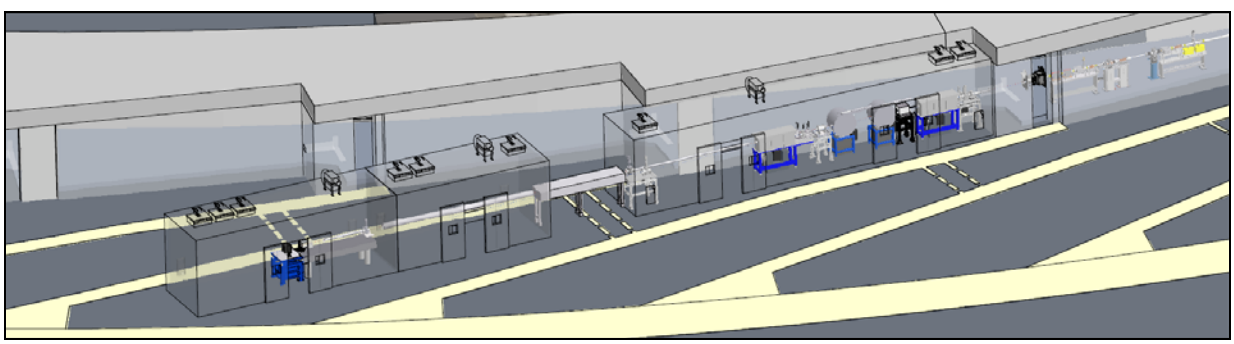

Side view

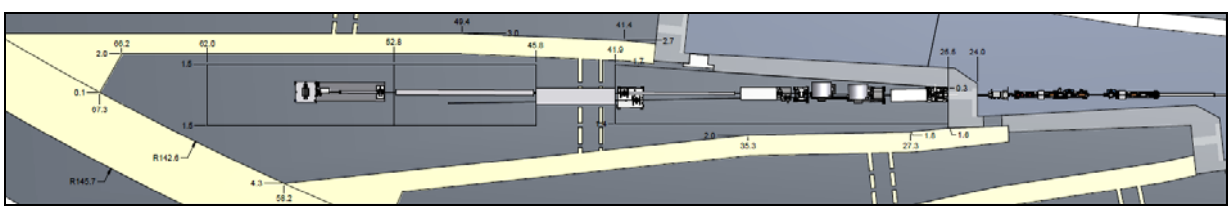

Top view

Figure 7. Beamline layout of the SRX beamline. Hutches (from right to left: FOE, ZP-branch, KB-branch) are indicated.

2.2 Insertion Device and Low β Straight Section and Operation Modes

Table 1. Source Parameters Used for the Calculations within this Document.

Electron Energy	E = 3 GeV
Stored Current	I = 500 mA
Electron Beam Emittance:	
Horizontal	$\varepsilon_x = 0.55 \times 10^{-9}$ m rad
Vertical (1.5% Coupling)	$\varepsilon_y = 8.25 \times 10^{-12}$ m rad
Betatron Function:§	
Horizontal	$\beta_x = 1.5$ m
Vertical	$\beta_y = 0.8$ m
Electron Beam Size:§	
Horizontal	$\sigma_x = 28.7$ μm
Vertical	$\sigma_y = 2.57$ μm
Electron Beam Divergence:§	
Horizontal	$\sigma'_{y\,x} = 19.2$ μrad
Vertical	$\sigma'_{y\,y} = 3.21$ μrad
Intrinsic Photon Size*	$\sigma_r = 1.95$ μm
Intrinsic Photon Divergence*	$\sigma'_y = 4.08$ μrad
Total Photon Source Size:§*	
Horizontal	$\Sigma_x = 28.8$ μm
Vertical	$\Sigma_y = 3.2$ μm
Total Photon Source Divergence:§*	
Horizontal	$\Sigma'_{y\,x} = 28.8$ μrad
Vertical	$\Sigma'_y = 5.19$ μrad

§ Low b straight.
*Quantities evaluated for 12.4keV x-rays and a 3m-long undulator.

The two branches of the SRX beamline are designed for different energy ranges, making the undulator design unusual amongst the suite of insertion devices at NSLS-II. Two undulators in canted geometry on this short (low beta) straight section will serve the two instruments as light sources. As there is the need to do spectroscopy at the titanium K-absorption edge, the specified lowest energy the undulator for the KB branch should reach is E = 4.7 keV. There are a couple of restrictions applied to the choice of the insertion device as a light source for the SRX beamline. The length of the device and the minimum gap have to be adjusted to the limitations stemming from the beta function of the short straight section. A length of 0.5 m minimum has to be removed from the total length of the straight section available for the two undulators to give room for the canting magnets as well as room has to be given to transition pieces and a full canting magnet at the end of the straight, which is also assumed to be 0.5 m long.

The optimized period of an undulator for the KB branch will depend on the gap (itself related to the length of the device through the beta-function restrictions) and the minimum photon energy (E = 4.7 keV). Oleg Tchoubar from NSLS-II has performed the calculations presented below, which are the basis for the decision on the actual undulator for the KB branch.

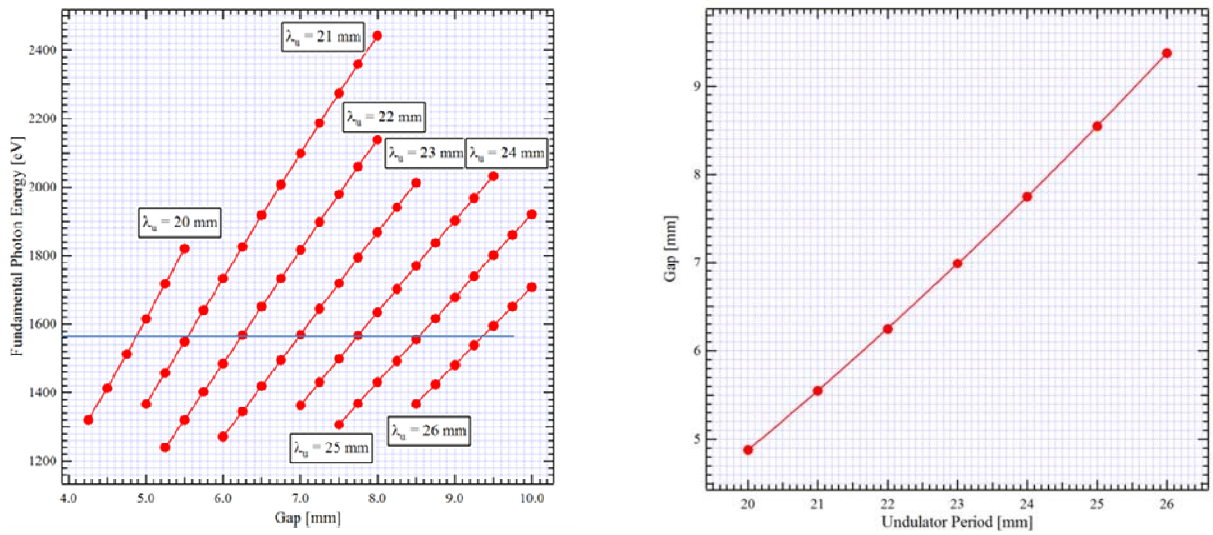

Figure 8. Fundamental photon energy as a function of the gap for different IVU periods (a) and (b) the gap as a function of the IVU period, when the minimum resonant photon energy of the 3rd harmonic is set to E = 4.7 keV.

In Figure 8 the fundamental photon energy as a function of the gap for different in-vacuum undulator (IVU) periods are plotted as well as the gap as a function of the IVU period, when the minimum resonant photon energy of the 3rd harmonic is set to E = 4.7 keV.

The geometry used for the calculations was: Pole Width: 40 mm, Pole Height: 25 mm, Pole Thickness: 3 mm, (for λ_u = 20 mm).Magnet Width: 50 mm, Height: 29 mm, Pole: Va Permendur NEOMAX, Magnet: NdFeB, Br = 1.12 T. These data were supplied from Toshi Tanabe from NSLS-II.

From the graphs in Figure 8 it becomes visible that for a minimum gap of 4.9 mm a period of 20 mm would be allowable, a minimum gap of 5.5 mm would relate to a period of 21 mm and for a gap of 6.2 mm the period would be 22 mm.

The maximum device length for a given minimum gap is determined by the beta function for the straight. Toshi Tanabe from NSLS-II calculated the possible lengths, assuming a canted device placed into a half-straight, as listed in Table 2.

Table 2. Maximum Canted Device Lengths for Given Gaps in a Canted Device Setup.

Gap	Maximum canted device length.
5.0mm	1.25m
5.5mm	1.5m
6.0mm	1.75m
6.26mm	1.85m
6.6mm	2.0m
7.2mm	2.25m

As a result of these calculations three realistic possibilities have been studied more thoroughly, an undulator with 20 mm period and 1.25 m length at a gap of 4.9 mm, an undulator with 21 mm period and 5.5 mm gap and 1.5 m length, and an undulator with 22 mm period and 6.2 mm gap and 1.8 m length. For these further calculations the center of the device is located approximately 1m from the center of the low-beta straight.

Figure 9 shows the spectral flux in phot/sec/0.1%BW of the three possible configurations at odd harmonics as a function of photon energy, and Figure 10 shoes for the same configurations the calculated spectral flux through an aperture of 0.1 x 0.1 mrad^2 at minimal gap.

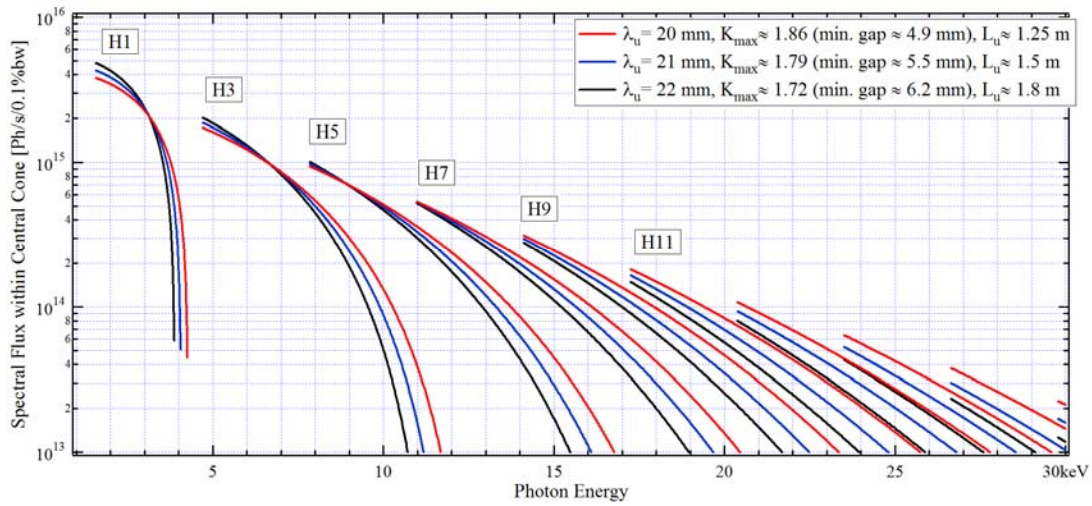

Figure 9. Spectral flux at odd harmonics for three undulator setups as seen in the legend.

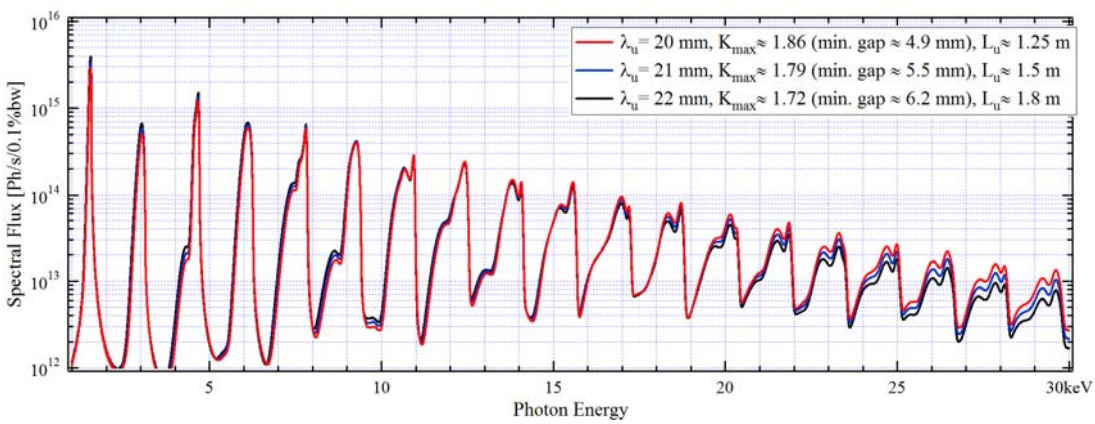

Figure 10. Spectral flux through an aperture with 0.1 x 0.1 mrad^2 size at minimal gap for three undulator setups as seen in the legend.

As the result of the above described calculations an in-vacuum undulator U21 has been chosen to work as the light source for the KB mirror branch. The parameters are listed in Table 3.

Table 3: Parameters in-vacuum undulator U21.

Undulator length	1.5 m
Period length	21 mm
Minimum gap	5.5 mm
Lowest energy in 3rd harmonic (E=3GeV)	4.65 keV
Maximum energy	28 keV
K-Value 1.79	

ZP Branch

The ZP branch is dedicated to an energy range from E =2 keV up to E = 15 keV. When looking at the parameters of the standard undulators IVU 20, IVU 21, or IVU 22 and at the minimum allowable gap of 5.0 mm, it becomes clear that due to these limitations there will be an energy range between E = 4 keV and E = 5 keV, where no radiation can be delivered. From the viewpoint of scientific applications this cannot be accepted, therefore a solution has to be found to close this energy gap. Two ways to solve this problem are possible. The first solution would be to shorten the length of an undulator IVU 22 to 1.2 m. This would allow the minimum gap to be reduced without deteriorating the electron beam. Due to the resulting higher magnetic field strength the full desired energy range would be covered. However, due to the shorter length, the overall performance in terms of photon flux will be poorer. The other solution would be to insert a cryo-cooled IVU 22 undulator. Due to cryo-cooling a higher K-value would be achievable resulting in a full coverage of the desired energy range without hampering the electron beam even at the full length of 1.5 m.

2.3 Front End

A typical layout of a standard front end designed by NSLS-II can be seen in Figure 11. In principle, the components are comparable to the needs of the SRX beamline, however, due to the canted design several modifications are necessary. All elements have to be prepared for accommodating both beams from the two undulators. This is taken into account in the list of components that is found in chapter 2.7 of this report. The layout incorporating these constraints and special demands is work in progress.

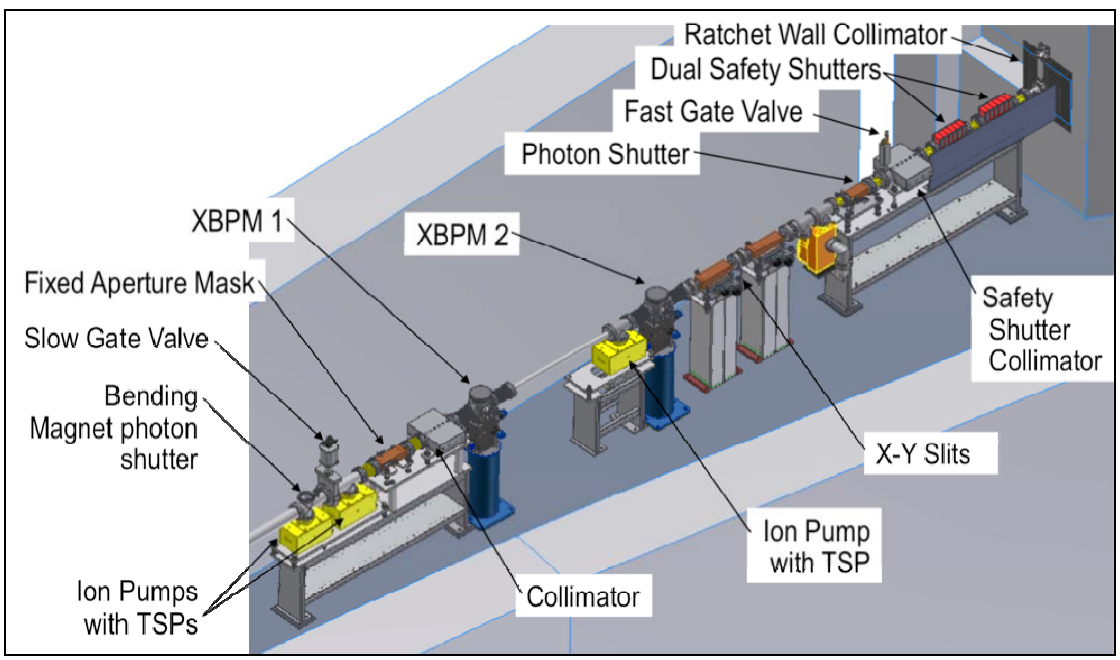

Figure 11. Layout of a standard front end of the NSLS-II SRX.

2.4 Optical Layout

The proposed optics plan is designed to provide state of the art x-rays, to accommodate a wide range of measurement needs and to maximize availability of beamtime for the earth, environmental and life science user communities. By canting two undulators and separating the optics into a lower energy line using zone plate (ZP) optics and a higher energy line with a Kirkpatrick-Beaz (KB) mirror system an extraordinary amount of new science will be accomplished by a very active and large user community. The complementary nature of the two lines together with a sector staffed with scientists possessing a wide range of synchrotron expertise will allow fluid and agile investigation of complex problems that often require a multitude of measurement types to solve.

In the following section the description of the optical layout starts in the front end and follows the beam downstream branching in the FOE, describing the optics of each line separately. This optics plan is based on the source parameters inserted as Table 1 in this document.

2.4.1 Common Components

Figure 5 shows a schematic of the sector. Located in the straight section are two undulators canted by 2 mrad. The midpoint between these undulators is used as a zero point for the distance values described in the following text. The 2 mrad separation in the center line of each undulator beam provides sufficient space to place separate apertures around each beam even before they exit the shield wall. It is proposed that a front end aperture (FEA) acting as a power and conductance limiter be placed as close the storage ring as possible. Such an aperture should be adjustable in both horizontal and vertical position and width and will most likely consist of two apertures one that is fixed and large designed to stop most of the unwanted power followed by a motorized second aperture exposed to a power load of 300 watts or less. This FEA will save space by acting as a differential pump and significantly reducing the x-ray power that enters the FOE. The reduce power will improve optics stability, a critical design requirement for this beamline. Once the beams enter the FOE front wall at 25.5 m they will pass through a pair of white beam filter (WBF) racks at 26 m that can be used to filter out low energy power as well as aid in diagnosing the performance of the beamline optics. Following the white beam filters will be a pair of horizontal and vertical white beam slits (WBS) that will further define the beam and be used as the beamlines primary storage ring diagnostic by configuring them as a pinhole camera and white beam profiler. Following the WBS the optics for the ZP line and KB line separate.

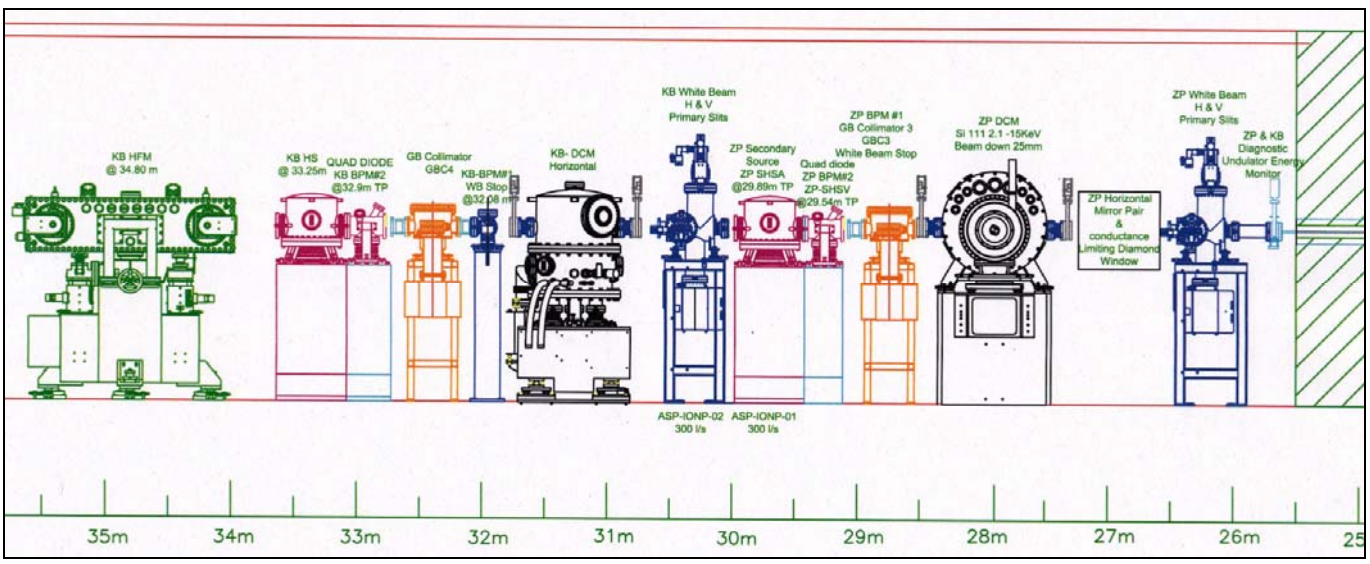

Figure 12. Layout of the beamline components in the First Optical Enclosure (FOE). For a detailed description of the components see chapter 2.7.

2.4.2 KB Branch

Figures 31 and 32 illustrate the horizontal and vertical optics layout for the KB line respectively. The KB line FEA will allow 4 sigma of the source to be delivered to a LN_2 cooled Si (111) / (311) double crystal monochromator. The monochromator, located at 34.8 m, will bounce the beam inboard 25 mm over an energy range of E = 4 keV to E = 25 keV. This monochromator is a horizontally deflecting design. The advantage is of course the larger separation of the two branches of this beamline. This happens to the expense of a potentially somewhat lower spectral resolution of this monochromator when using the full beam, as the horizontal divergence of the incoming beam is larger than the vertical. Accepting a trade-off in photon flux this can be compensated for by closing the slits and so not having to deal with the full divergence. The monochromatic beam illuminates a 1.2 m long water cooled Si horizontal focusing mirror (HFM) half coated with rhodium and operating at a fixed incident angle of 2.5 mrad. The HFM is located at 34.8 m and deflects the beam inboard forming a secondary horizontal focus at 56.5 m with a

demagnification of 1.85. The KB line beam passes by the experimental table of the ZP line endstation approximate 0.5 m inboard contained in a narrow profile shielded transport pipe.

Located at the upstream wall in the KB line endstation is a secondary horizontal source aperture (SHSA). The SHSA will be identical to the one used on the ZP line with a BPM used to stabilize the secondary horizontal source by controlling the HFM pitch. Inserted into Figure 31 at the secondary horizontal source location is a scatter plot of the 37 μm FWHM focal spot created by the HFM, also inserted is a scatter plot of the beam transmitted through a SHSA set to 2.7 μm horizontal width. The secondary horizontal focus is re-imaged by a 100 mm long horizontal KB mirror with a focal length of 80 mm, demagnification of 35 and a divergence of 3 mrad. Inserted into Figure 31 at the final focus location are two scatter plots, one showing the final horizontal focus of 1099 nm FWHM with the SHSA full open (transmitting 95% of the source) and the other showing a final focus of 71 nm FWHM with the SHSA set to 2.7 μm width (transmitting 7%).

The vertical focusing optics plan exploits the low vertical divergence of the source by utilizing a single 280 mm long vertical focusing mirror at 56.23 m (see Figure 32). This mirror is capable of collecting nearly the full vertical source divergence and focusing it 270 mm away to a focal spot of 70 nm with a divergence of 2.5 mrad. Figure 33 shows scatter plots and histograms for the SHSA full open (left panel) and set to 2.7 μm (right panel). By adjusting the SHSA the size of the final horizontal source can be tuned to best match the requirements of the experiment, allowing a trade off of flux for beam size. The vertical source can be made larger by defocusing the mirror using the bender. The ray traces were performed using ideal elliptical mirrors and in order to achieve the 100 x 100 nm goal the total RMS slope errors needs to be under 0.2 μrad. A total RMS slope error this low will require advances in mirror manufacturing and figuring technology but giving the recent progress in reflective x-ray optics it can be expected that mirrors of this quality will be available in the next five years.

Using a source brightness at 0.1 nm of $7x10^{20}$ phot/sec/0.1%bw/mm^2/mrad^2, a 0.4 correction for a 1.2 m long device, a triple mirror reflection efficiency of 70%, and an open SHSA collecting 95% of the full source the total flux delivered to 1000 x 100 nm (HxV) FWHM focus is 7 x 10^{13} phot/sec and with the SHSA set to 2.7 μm collecting 7% of the full source the flux delivered to a 100 x 100 nm focus is 5 x 10^{12} phot/sec.

2.4.3 ZP Branch

The goal of the FOE optics for the ZP line is to provide a stable coherent source to illuminate a zone plate located on the endstation optical table. The goal of the ZP line is to produce a focal spot that is 30 nm with maximal intensity. The ZP line should be able to utilize a zone plate with an outer zone width ΔR_n = 25nm and a diameter D = 330 μm under optimum conditions. Working at a wavelength of λ = 0.1 nm the focal distance of such a zone plate is f = 83 mm. A zone plate with these parameters is not readily available but given the numerous development efforts underway on zone plates and other nano-focusing optics, it is anticipated that optics with this kind of capability will be available in the next five years. Promisingly, it has been shown recently (published by Y.-T. Chen et al. in Nanotechnology in 2008) that gold zone plates for x-ray energies higher than E = 8 keV can be used for spatial resolutions below 30 nm.

For a nanoprobe beamline utilizing a zone plate as a focusing optic it is important to consider the coherent divergence of the source, given by $S'_{coh} = \lambda / 2S_{coh}$ where S_{coh} is the FWHM of the source. At a wavelength of λ = 0.1 nm the NSLS II source is within a factor of 2 of being fully coherent in the vertical direction whereas the horizontal source is more than 30 times less coherent then the vertical. If the full source size is used this astigmatism in the coherence would require astigmatic optics that are incompatible with a planar, radial symmetric focusing lens such as a zone plate. Figure 34 in chapter 2.6.2 illustrates the case of using the full horizontal and vertical source size showing a ray trace at 50 m – a typical final optic focusing location. The intersection of the horizontal and the vertical red lines (Figure 34 a) mark the coherent area of the un-apertured source. Figure 34 b shows all the incoherent rays and Figure 34 c shows that a 37 x 329 μm (H x V) aperture would be required at the optic for coherent illumination and that such an aperture would transmit 0.7% of the full undulator source. Though this is incompatible with a ZP lens it may be compatible with crossed linear lenses such as Multilayer Laue Lenses

(MLL) and kinoform lenses, both of which are candidate lenses for creating focal spot sizes down to 1 nm and which are subject of extensive development efforts.

The typical approach to lifting the astigmatism in coherence is to place a pinhole aperture as close to the source as possible. For the NSLS II only the horizontal beam size would need to be reduced by such an aperture. Figure 35 in chapter 2.6.2 illustrates an optics layout that provides nearly symmetric coherent illumination for an optic located at 50 m. In this case a 6 x 96 μm (H x V) front end aperture (FEA) is located at 14.5 m. Such an aperture will produce a coherent horizontal divergence of 9.3 μrad and allows the full coherent vertical divergence to pass. The pair of scatter plots inserted at 14.5 m in the Figure 35 shows the incoherent rays that would be lost and coherent rays that pass through the aperture. The inserted scatter plot at 50 m shows that 0.4% of the total undulator source is available to coherently illuminate a zone plate lens with a diameter of D = 330 μm. Such a zone plate would then focus the beam 83 mm away to a spot size of 30 nm with a divergence of 4 mrad. Figure 36 shows a scatter plot along with the horizontal and vertical histograms of the source at the zone plate location.

The use of a small horizontal FEA (or one as close to the source as the storage ring and beamline optics allow) is often used on zone plate beamlines. An aperture this close also has the advantage of significantly reducing the power passed to the remaining optics.The disadvantage of this aperture is the significant technical challenge of designing a small and stable aperture subjected to such high power loads, as well as that it is relative inaccessible and the likelihood that it will need to be moved further downstream due to front end design constraints. As an alternative approach and one that works well in our canted beamline design is to use a horizontal mirror pair (HMP) as close as possible to the shield wall in the FOE. The HMP will both, deflect the beam horizontally creating beam separation at the endstation and form a secondary horizontal source (SHS) that can be manipulated by a secondary horizontal source aperture (SHSA). Figure 33 in chapter 2.6.2 illustrates this arrangement showing an FEA that is now much larger (60 x 96 μm) and only acting as a power limiter and differential pump (its exact location is also now flexible).

The HMP would be located at 28.8 m and focuses the horizontal source with a demagnification of 9 at 32 m. The HMP can be compact since the coherent horizontal divergence is low (4.1 μrad), requiring only an optical aperture (OA) with a diameter of 120 μm. The mirrors will be water cooled silicon, each half coated with rhodium and operating at a fixed 4 mrad incident angle for a total horizontal deflection of 16 mrad. The second mirror will have a dynamic bender that will correct for the thermal bump on the first mirror and focus the beam to approximately 7 μm FWHM at the SHSA. Located after the HMP and before the SHSA will be an indirectly LN_2 cooled Si (111) double crystal monochromator that bounces the beam down by 25 mm with an energy range of E = 2 keV to E = 15 keV. In this arrangement the SHSA will see no power load, eliminating the thermal stability concerns of locating such an aperture in the front end.

The SHSA will be an ultra stable horizontally adjustable aperture with an integrated beam position monitor (BPM) utilizing active feedback of the HMP deflection angle to produce a stable, small coherent horizontal source with approx. 3 μm FWHM for the zone plate located at 50 m. The insert in Figure 33 at the SHS location is scatter plot showing the full focus of the HMP of 6.6 μm FWHM and a scatter plot with the SHSA set to 2.7 μm. With the SHSA set to 2.7 μm the coherent horizontal divergence of this source is 19 μrad. This secondary source diverges to 330 μm at the zone plate located at 50 m (18 m downstream form the SHSA) thus symmetrically illuminating the final focusing optic (see inserted scatter plot at 50 m in Figure 35). Figure 34 shows an evenly illuminated 330 μm aperture at 50 m that transmits 0.8% of the full source. The experimental table mounted zone plate is expected to focus the beam to a 30 nm spot. Using a source brightness at 0.1 nm of $7x10^{20}$ phot/sec/0.1%bw/mm^2/$mrad^2$, a 0.4 correction for a 1.2 m long device, a double mirror reflection efficiency of 80%, a zone plate efficiency of 10%, together with the 0.8% of the full source results in a total flux delivered to the sample of $7x10^9$ phot/sec. One the main benefits of this optics plan for the ZP line is its flexibility in accommodating future developments in nano-focusing optics while at the same time allowing the specification and procurement of major beamline components.

2.5 High Heatload Optics

To maintain the stability of the focused beam and to ensure that the energy resolution of the SRX-KB monochromator is not significantly degraded for spectroscopic studies, we carefully evaluated the positioning of possible white beam components in the first optical enclosure so as to minimize errors resultant from heating. Two arrangements are proposed for the horizontally focusing mirror (HFM) design, a monochromatic beam mirror located downstream of the double crystal monochromator (DCM), and a mirror capable of accepting the white beam. It turns out, that the first crystal of the DCM will be better able to master the heat load stemming from the undulator than the horizontally focusing mirror, at the same time keeping the optical performance of the beamline in its desired limits. Therefore, solution II will be pursued further on. Details of the calculations and the results leading to this conclusion will follow in this chapter.

2.5.1 Horizontally Focusing Mirror

The mirror has a total length of 1390mm, width 50mm and depth 50mm, with an optical area of 1200mm. The white beam option includes symmetric channels cut into the side faces along the length of the mirror, which are used for liquid gallium cooling. Both mirror options have two reflective stripes (rhodium & bare silicon) covering the length of the optical face of the mirror. Figure 13 shows the calculated reflectivity of the rhodium and silicon stripes at an incidence angle of 2.5mrad. For low energy reflection, silicon is shown to give high reflectivity and suppression of higher order harmonics. The rhodium stripe is used at the higher energies to maintain mirror reflectivity. The latter might be the option used almost all the time, as the desired energy range is fully covered with high reflectivity.

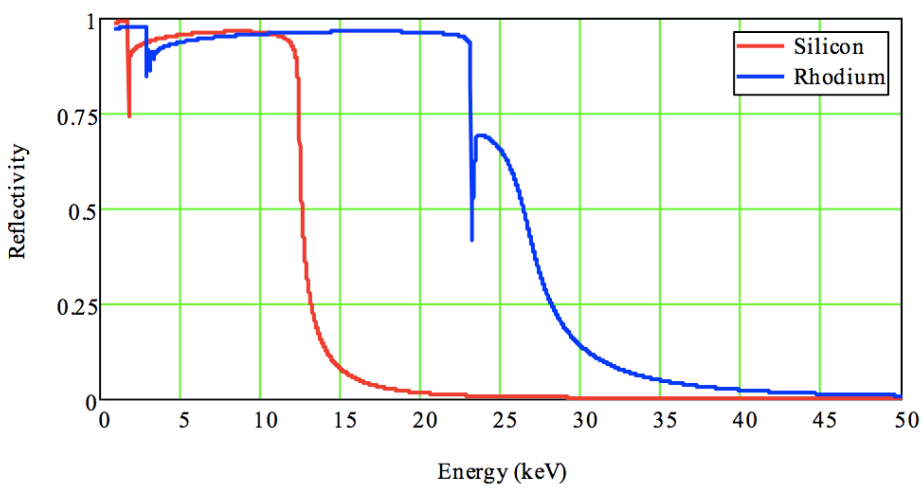

Figure 13. Reflectivity of silicon- or rhodium-coated mirror surfaces as a function of incident x-ray energy.

Based on the source, beam and undulator parameters the source spectral power distributions for the bare silicon and rhodium stripes are shown in Figure 14 and Figure 15 respectively. The transmitted spectral power distribution for each stripe is superimposed with the source distribution profile. The transmitted distribution is calculated by multiplying the source spectral distribution with the coating absorption characteristic (Figure 13). The sum of transmitted power at each energy is then divided by the sum of the source power at each energy to give the percentage transmission from the mirror. Relative to the source distribution at a grazing angle of 2.5 mrad, the power absorption for the bare silicon stripe has been calculated at 56.0%, while the rhodium stripe has been calculated at 18.4%.

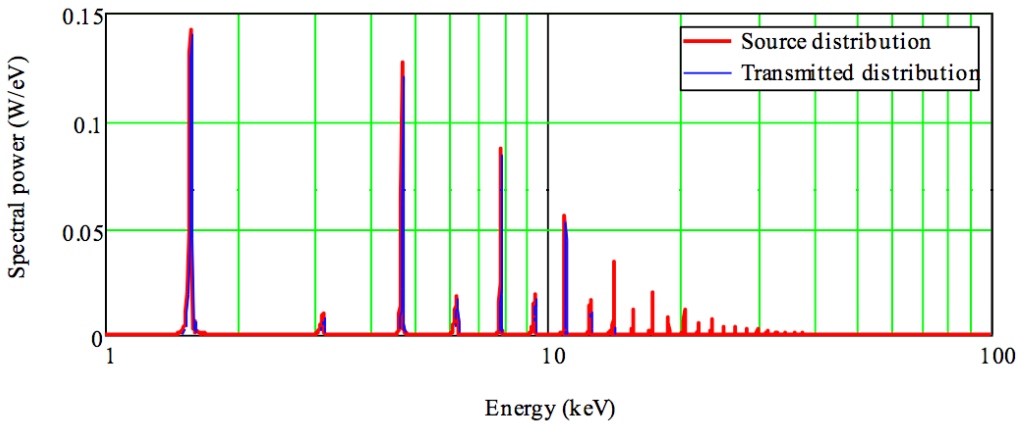

Figure 14. Spectral power absorption distribution for a bare silicon stripe.

The mirror is a super polished flat cut silicon mirror to horizontally collimate the beam using differential bending to figure the mirror to an approximation of the ideal collimating shape. To achieve this, two independent moments are applied to either end of the mirror producing a linear moment distribution along the mirror length. Although a uniform radius of curvature can readily be achieved with the two-moment bender, a key advantage in offering differential moment is that even a small deviation from ideal can be reduced or eliminated as desired. The principle of the bending mechanism is shown schematically in Figure 16. Applying the bending forces to the mirrors through bending holes below the surface allows any distortions resulting from contact strain to dissipate before reaching the optical surface.

The tangent point of the monochromatic beam mirror is that given in NSLS-II documentation. For the purposes of this study the white beam mirror option is treated as the first optical component, with the tangent point taken as 31.7m (that of the DCM). The mirror operates at a fixed incident angle of 2.5mrad.

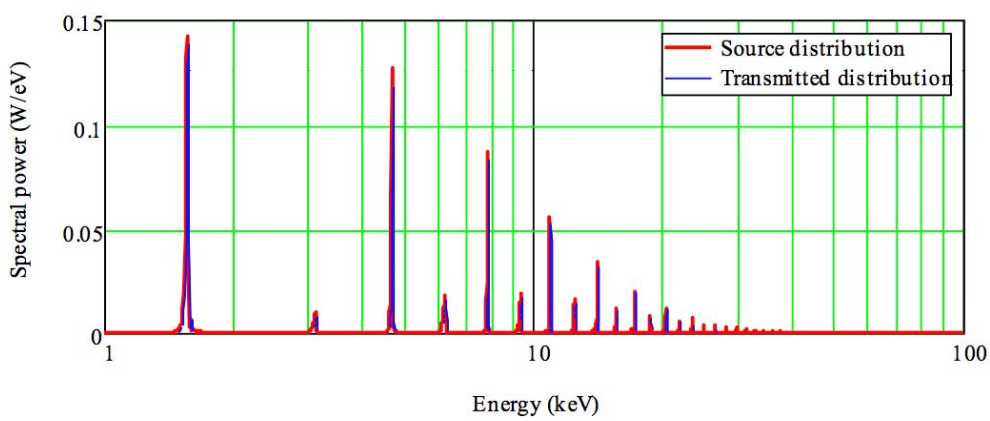

Figure 15. Spectral power absorption distribution for the rhodium stripe.

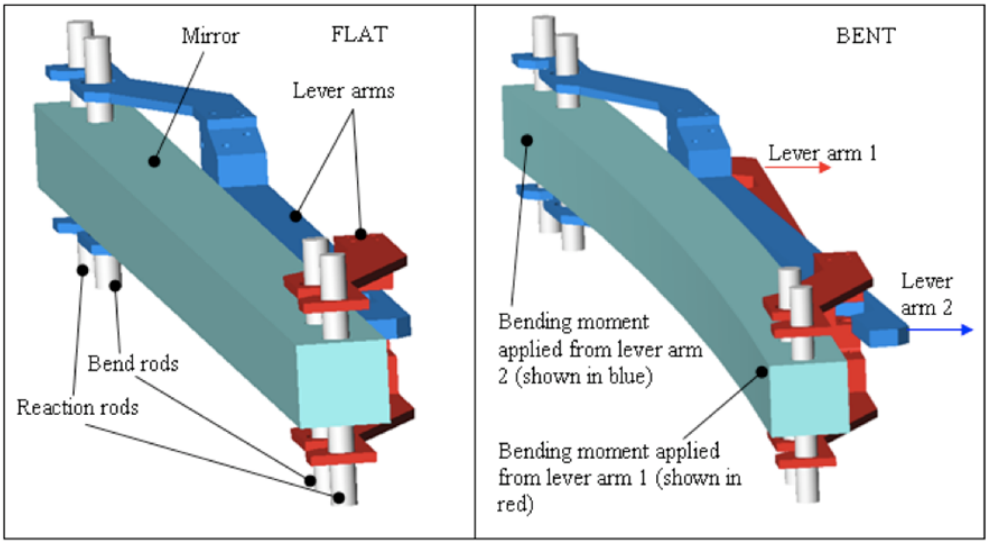

Figure 16. Bending principle suggested for the horizontally focusing mirror.

For the white beam mirror option, a finite element analysis model of the mirror is run to determine the mirror displacement due to the thermal heat load. The beam size incident on the white beam mirror has been set at 94.6µrad horizontally by 100µrad vertically. Based on this size, the transmitted power through the slits and incident on the mirror is calculated at 248.7W. The 'worst case' mirror absorption has been calculated at 56% when using the bare silicon reflective stripe.

To apply the thermal load, an area representative of the beam footprint is projected onto the optical surface. The undulator angular power density distribution is fitted with a Gaussian function, which is projected onto the optical surface at the appropriate incident angle. An optically active length of 1200 mm corresponds to a beam acceptance of 94.6µrad (horizontally) x 100µrad (vertically). The total heat load incident upon the crystal is 139.3W, with an on-axis power density of 15.6kW/mrad^2.

Convective cooling is applied through the top gallium groove, with an applied heat transfer coefficient of 1W/cm^2/ºC. Calculations indicate that a heat transfer coefficient of 1.5W/cm^2/ºC would be achievable inside the coolant pipe with a diameter of 6 mm bore. The heat transfer coefficient value applied inside the gallium grooves is lowered to account for the larger wetted area of the grooves relative to the internal area of the coolant pipe.

The results from the thermal model (shown in Figure 17) are then loaded into a structural model, with appropriate constraints applied to the mirror to allow free expansion. Material properties for silicon are taken from the Material Property Database program.

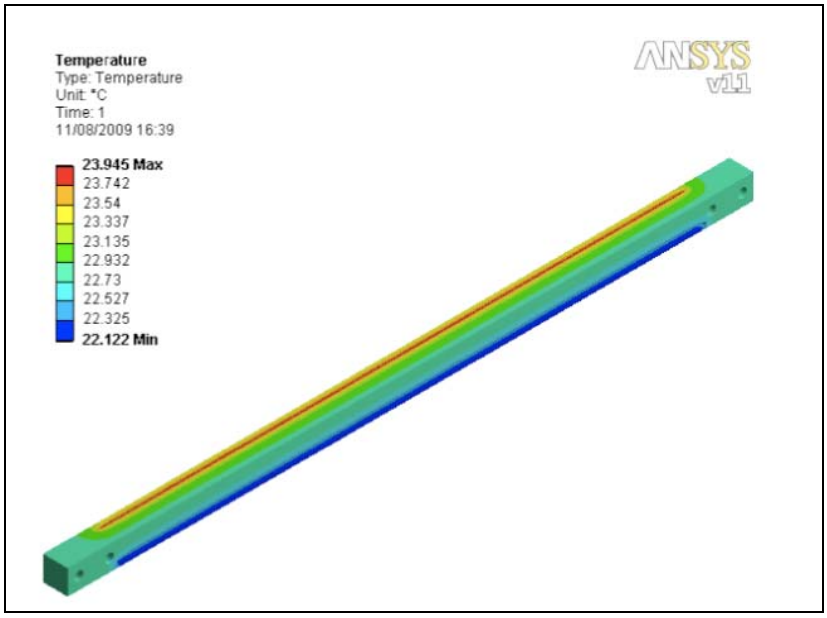

Figure 17. Temperature distribution on a mirror in white beam.

The focal length, the incidence angle and the optical length of the mirror define the ideal mirror bend profile. To induce the bend and achieve the required central deflection, which is determined from the ideal bend profile, loads are applied at either end of the mirror through the bending mechanism. For the monochromatic beam mirror a load of 113.9 N applied at each end is calculated to give the required deflection at the mid-span location. Figure 18 superimposes the calculated mirror bend profile using this bending load with the ideal profile.

For the white beam mirror option, the effects of the thermal heat load of the white beam must also be considered. In this case, the applied bending load is calculated to compensate for the effect of the thermal bend to give the correct mirror profile. A bending load of 131.7 N is required by the white beam mirror to give the correct profile. The bend profiles for the white beam mirror are shown in Figure 19.

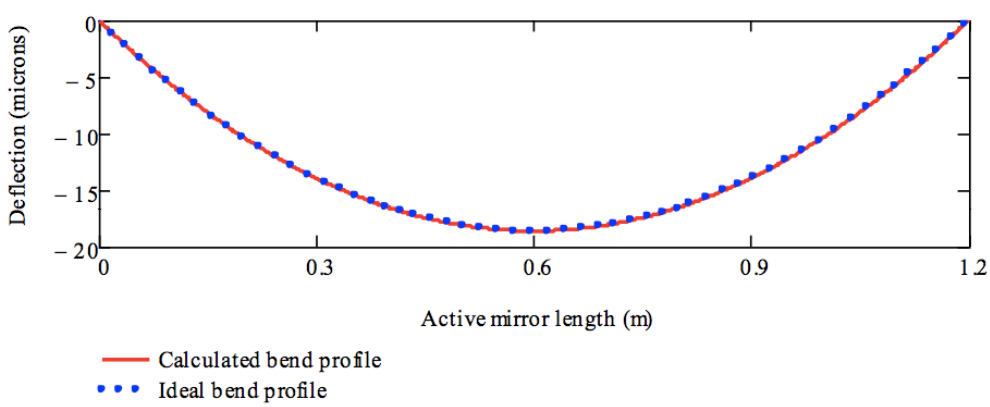

Figure 18. Comparison of the calculated and the ideal mirror bend profiles for a mirror in monochromatic beam downstream of the monochromator.

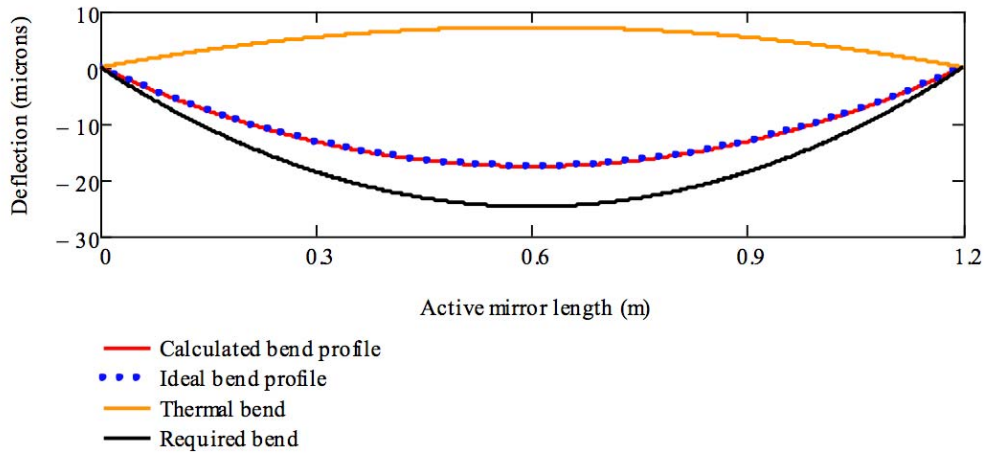

Figure 19. Comparison of the required, the calculated, the ideal, and the thermally induced mirror bend profiles for a mirror in white beam.

The bending loads determined from the ideal bend profile are applied to the finite element analysis model of the mirror (along with the thermal load in the case of the white beam mirror) to determine the actual bend profile.

The residual (uncorrectable) slope error is defined as the difference between the actual mirror slope profile (given by differentiation of the bend profile determined by the finite element analysis model) and the ideal slope profile. The residual slope errors for the monochromatic and white beam mirrors, calculated over the optically active length, are shown in Figure 20 and Figure 21 respectively. A root mean square (RMS) slope error of 0.076μrad is calculated for the monochromatic beam mirror, and 0.599μrad for the white beam mirror.

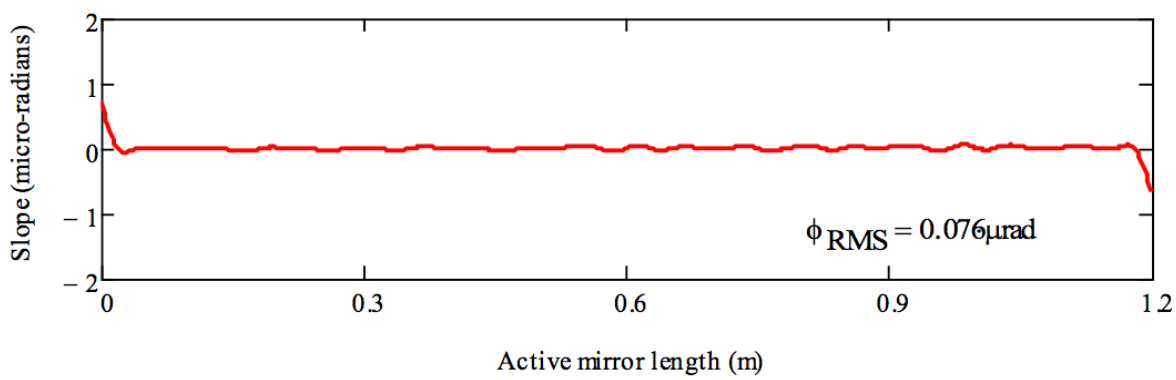

Figure 20. Residual slope error along the length of the mirror for monochromatic beam downstream of the monochromator.

A summary of the key criteria of the mirrors is given in Table 4. The monochromatic beam mirror design, gives negligible residual slope errors. The white beam mirror option on the other side gives slope errors, which would affect the performance of the SRX beamline.

Table 4. Key criteria for Horizontally Focusing Mirror Options

Description		Focussing mirror, reflecting horizontally
Substrate material		Single crystal silicon
Substrate dimensions		1390mm long x 50mm wide x 50mm deep
Reflective coatings		Silicon (<12keV), Rhodium (10-28keV)
Optically active length		1200mm
Incidence angle	θ	2.5mrad
Monochromatic beam mirror		
Focal lengths	F_1	33.8m
	F_2	18.8m
Beam acceptance		86μrad (h) x 100μrad (v)
Radius of curvature	$R = \frac{2}{\left(\frac{\sin(\theta)}{F_1} + \frac{\sin(\theta)}{F_2}\right)}$	9.66km
Calculated bending load		113.9N
RMS slope error		0.076μrad
Calculated bending stress	$\sigma = y \cdot \frac{E}{R}$	0.34MPa
White beam mirror option		
Focal lengths	F_1	30.7m
	F_2	21.9m
Beam acceptance		94.6μrad (h) x 100μrad (v)
Radius of curvature	$R = \frac{2}{\left(\frac{\sin(\theta)}{F_1} + \frac{\sin(\theta)}{F_2}\right)}$	10.23km
	Calculated bending load	131.7N
	RMS slope error	0.599μrad
Calculated bending stress	$\sigma = y \cdot \frac{E}{R}$	0.32MPa

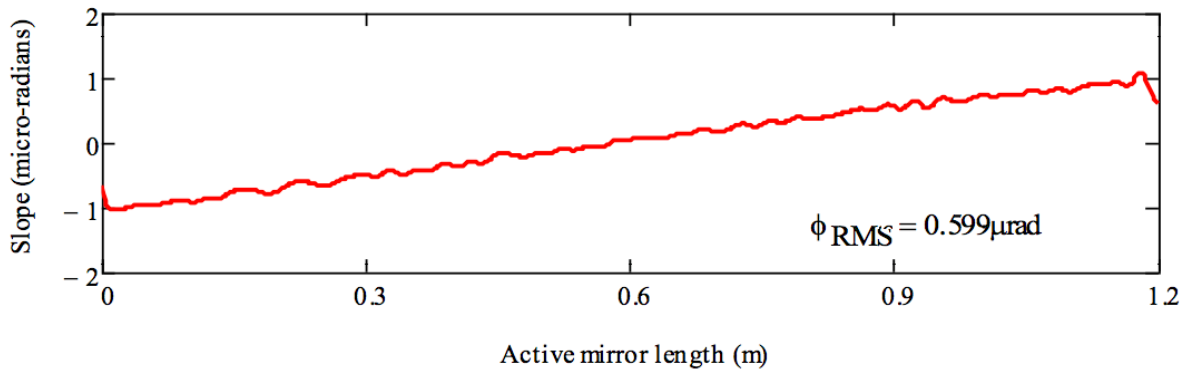

Figure 21. Residual slope error along the length of the mirror for white beam.

2.5.2 Double Crystal Monochromator

Heat load calculations have been made for the first crystal of the double crystal monochromator to evaluate whether it will be possible to have the monochromator as a first optical element in front of the horizontally focusing mirror without harming the spectral and optical performance of the beamline.

An indirect cryogenic cooling arrangement is proposed for the crystal design. The design of the crystal holder is similar in principle to a design successfully implemented by the company IDT at the Australian Synchrotron, with the 1st crystal sandwiched between two cooled copper blocks. To improve vibrational stability, short lengths of copper braid will be used to connect the LN_2 coolant pipe to the copper blocks, mechanically decoupling the crystal from the cooling circuit. The design accommodates four crystals (Si (111), Si (311) and two multilayer crystals).

To provide good thermal contact, Indium foil is used between the sides of the silicon and copper blocks. The indium foil has a secondary benefit of absorbing the differential expansion between the copper blocks and silicon crystal and limits the resulting stress and strain transmitted to the optical surface of crystal.

To determine the crystal displacement due to the thermal heat load, an FEA model of the crystal was run. This chapter shows the finite element analysis results for the silicon crystal only.

Previous thermal analysis of monochromator crystals has shown that the primary design case for selecting the crystal design is generally fixed by the optical performance at the higher energies as a result of the narrower Rocking Curve widths. Figure 22 shows that the narrowest Rocking Curve width is 9.9μrad for Si (111) at E = 28 keV, and 3.8μrad for Si (311) at E = 28 keV. These high energies are used as the primary design case for finite element analysis modeling.

A secondary design case of Si (111) at E = 4.65 keV is also implemented in this study. This low energy configuration requires the largest Bragg angle, which gives the smallest beam footprint and therefore the highest incident power density.

The crystal size used for the finite element analysis model is similar to that used on the Australian synchrotron monochromator. The crystal has length 80 mm, width 30 mm and depth 30 mm.

The second crystal length and the beam offset determine the workable range for the Si (111) and Si (311) crystals. A beam offset of 25mm and a second crystal length of 180mm allows Si (111) to operate over the full energy range from E = 4.65 keV up to E = 28 keV.

Figure 22 shows that for the low energies Si (311) requires a very large Bragg angle, which limits the lowest energy accessible to Si (311). For a 25 mm beam offset, the minimum energy of Si (311) is E = 6.5 keV. This minimum can be lowered by increasing the beam offset value.

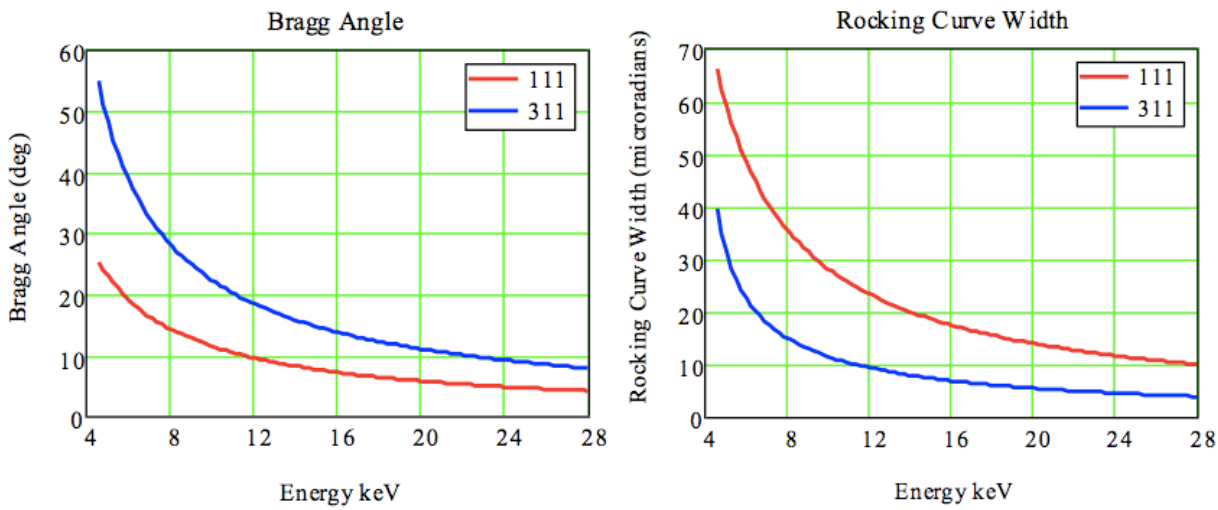

Figure 22. Bragg angle (left) and width of rocking curve (right) for Si (111) in red and Si (311) in blue.

To apply the thermal load, an area representative of the beam footprint is projected onto the optical surface. The undulator power density distribution is fitted with a Gaussian function, and this Gaussian is then projected onto the optical surface at the appropriate Bragg angle. For a beam acceptance of 100 µrad x 100 µrad, the total heat load incident upon the crystal is 263W, with an on-axis power density of 27.8kW/mrad^2.

Convective cooling is applied to the cooled contact area between the crystal and the copper heat exchangers. Based on a hydraulic diameter of 10mm and a LN_2 flow rate of 4litres/min, a heat transfer coefficient at the LN_2 heat sink of 2360W/m^{2}K is calculated using the Dittus-Boelter correlation. With the inclusion of thermal contact and conduction resistances, an effective heat transfer coefficient at the crystal contact of 1700W/m^{2}K is calculated by considering the entire cooling circuit, with the bulk temperature on the contact surface set to 80 K.

Material properties for silicon are taken from the Material Property Database program.

The results of the thermal model are loaded into a structural model, with restraints applied to simulate clamping and allow free expansion.

Figure 23 shows the temperature and displacement distribution for Si (111) at E = 28 keV, while Figure 24 shows the slope error profile of the crystal at this energy.

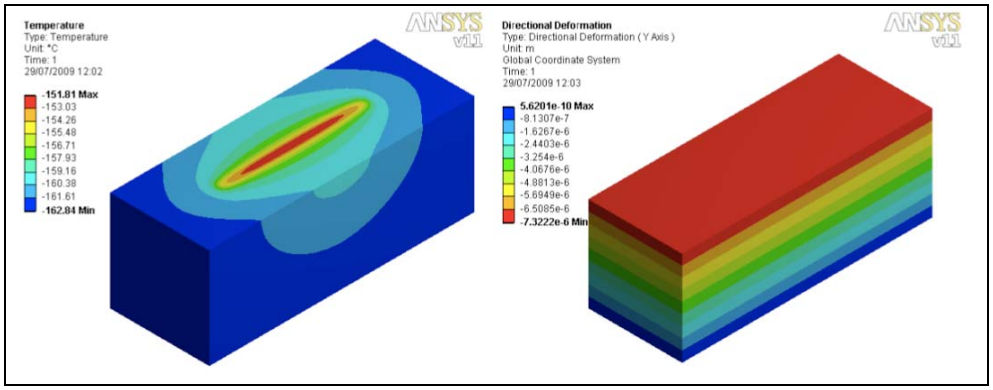

Figure 23. Spatial distribution of temperature (left) and deformation along the vertical axis (right) for Si (111) at E = 28 keV.

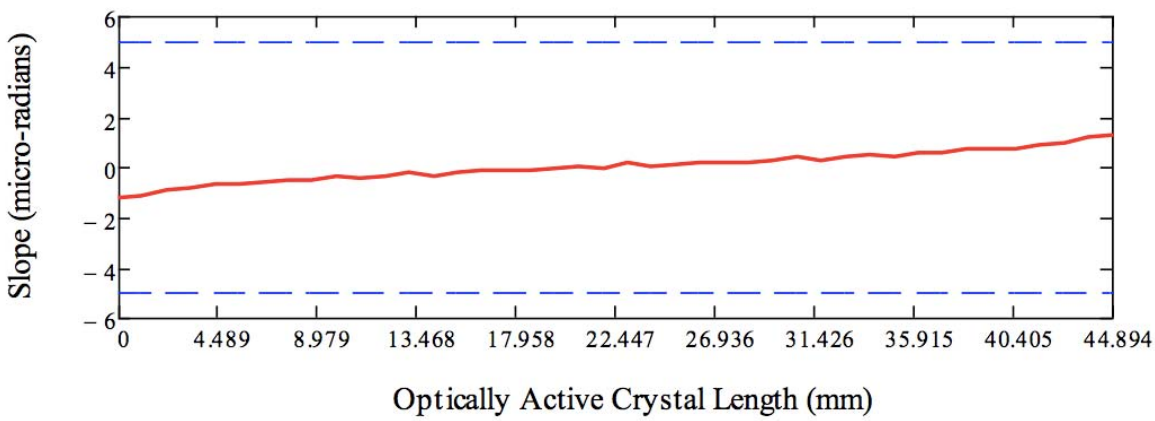

Figure 24. Tangential slope profile for Si(111) at E = 28 keV. The dashed blue lines show the rocking curve limits.

The case of Si (111) at E = 4.65 keV gives the highest incident power density. This energy has a large rocking curve width of 65.8 μrad. The results for this energy, given in Figures 25 and 26, show that the slope error is easily under the rocking curve limit at this energy.

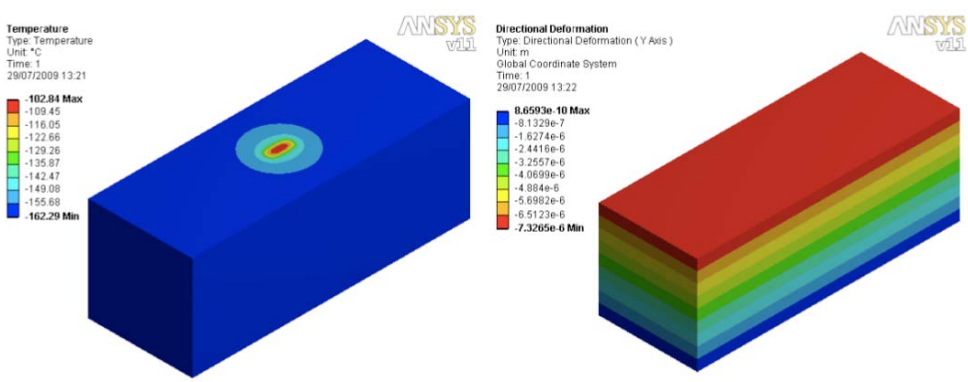

Figure 25. Spatial distribution of temperature (left) and deformation along the vertical axis (right) for Si (111) at E = 4.65 keV.

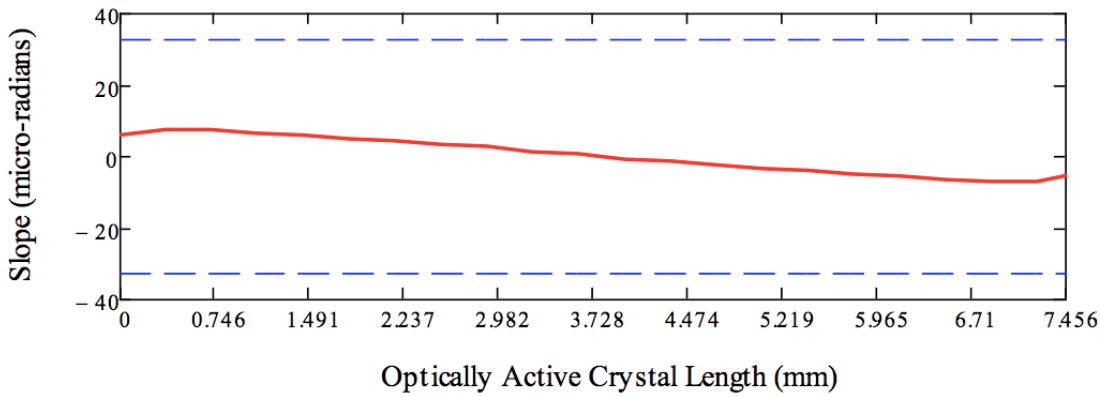

Figure 26. Tangential slope profile for Si (111) at E = 4.65 keV. Dashed blue lines show the rocking curve limits.

Figure 27 shows the temperature and displacement distribution for Si (311) at E = 28 keV, while Figure 28 shows the slope error profile of the crystal at this energy.

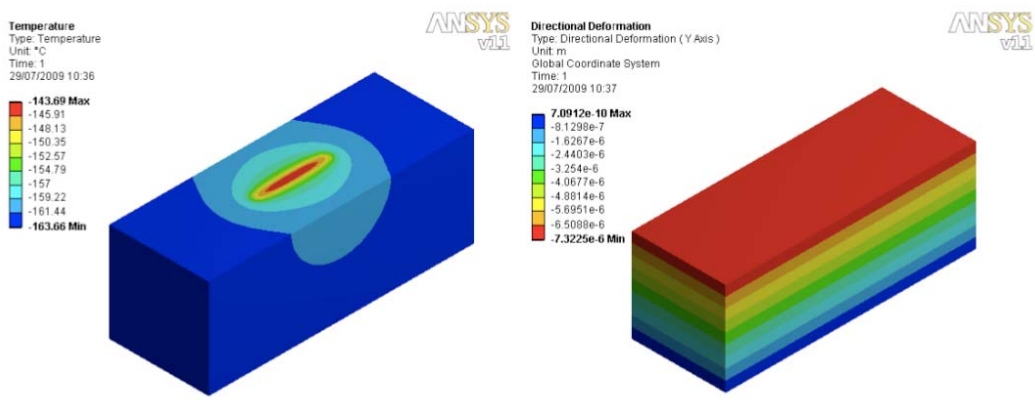

Figure 27. Spatial distribution of temperature (left) and deformation along the vertical axis (right) for Si (311) at E = 28 keV.

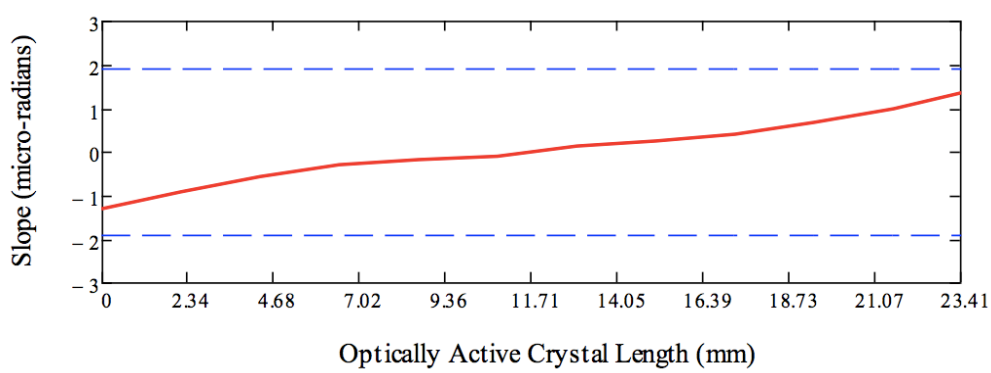

Figure 28. Tangential slope profile for Si (311) at E = 28 keV. The dashed blue lines show the rocking curve limits.

Figures 29 and 30 show the results for Si (311) at the lowest energy attainable with the 25mm beam offset design (E = 6.5 keV). The rocking curve width here is 20.1 µrad.

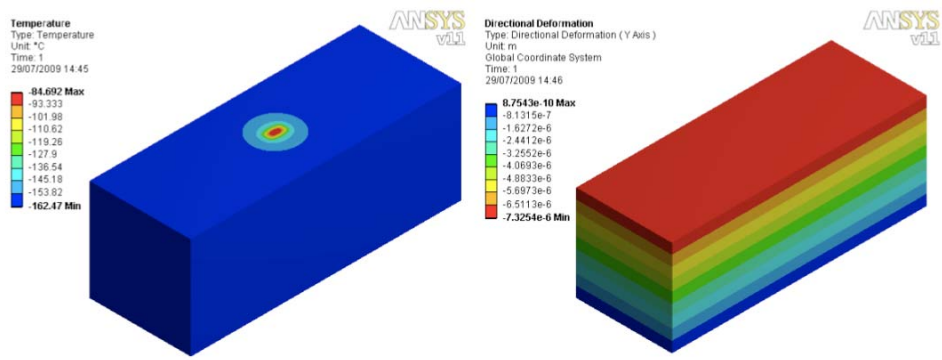

Figure 29. Spatial distribution of temperature (left) and deformation along the vertical axis (right) for Si (111) at E = 6.5 keV.

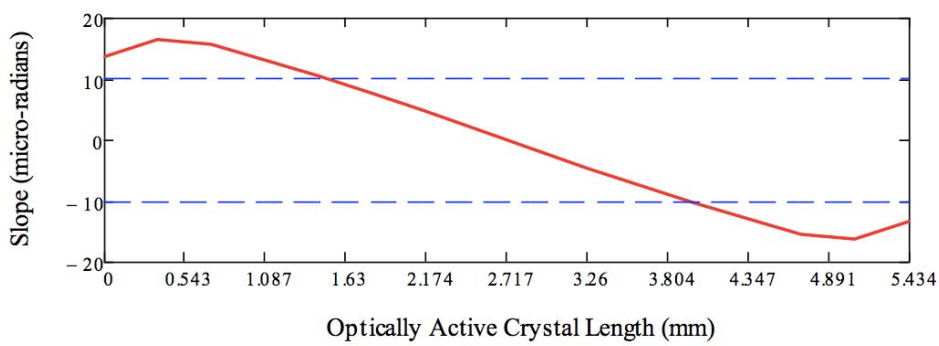

Figure 30. Tangential slope profile for Si (311) at E = 6.5 keV. Dashed blue lines show the rocking curve limits.

It is clear from these results that the slope error at this energy is larger than the rocking curve width. Figure 22 shows that the Bragg angle necessary to access this energy is much larger than that required for Si (111). A much larger Bragg angle gives a much higher incident power density. It is this high power density that will limit the lowest energy of Si (311) within the slope error requirements. The lowest energy of Si (311) giving both tangential and sagittal slopes under the rocking curve width is E = 8.5 keV.

Table 5, which also gives the sagittal slope errors for the energy configurations discussed, summarizes the findings of this study.

Table 5. Slope Error Summary.

Crystal Face	Energy	Rocking Curve Width	Tangential Slope Error	Sagittal Slope Error
Si(111)	4.65 keV	65.8 µrad	11.6 µrad	20.9 µrad
Si(111)	28 keV	9.9 µrad	2.5 µrad	1.0 µrad
Si(311)	6.5 keV	20.1 µrad	26.9 µrad	35.1 µrad
Si(311)	28 keV	3.8 µrad	2.6 µrad	0.8 µrad

The result of this study is that a braided cryo-cooled crystal of size 80 mm x 30 mm x 30 mm is feasible for the SRX beamline. The Si (111) crystal can operate over the full energy range from E = 4.65 keV to E = 28 keV within slope error requirements, while the Si (311) crystal operates over the reduced range of E = 8.5 keV to E = 28 keV.

2.6 Ray Tracing

2.6.1 KB Beamline

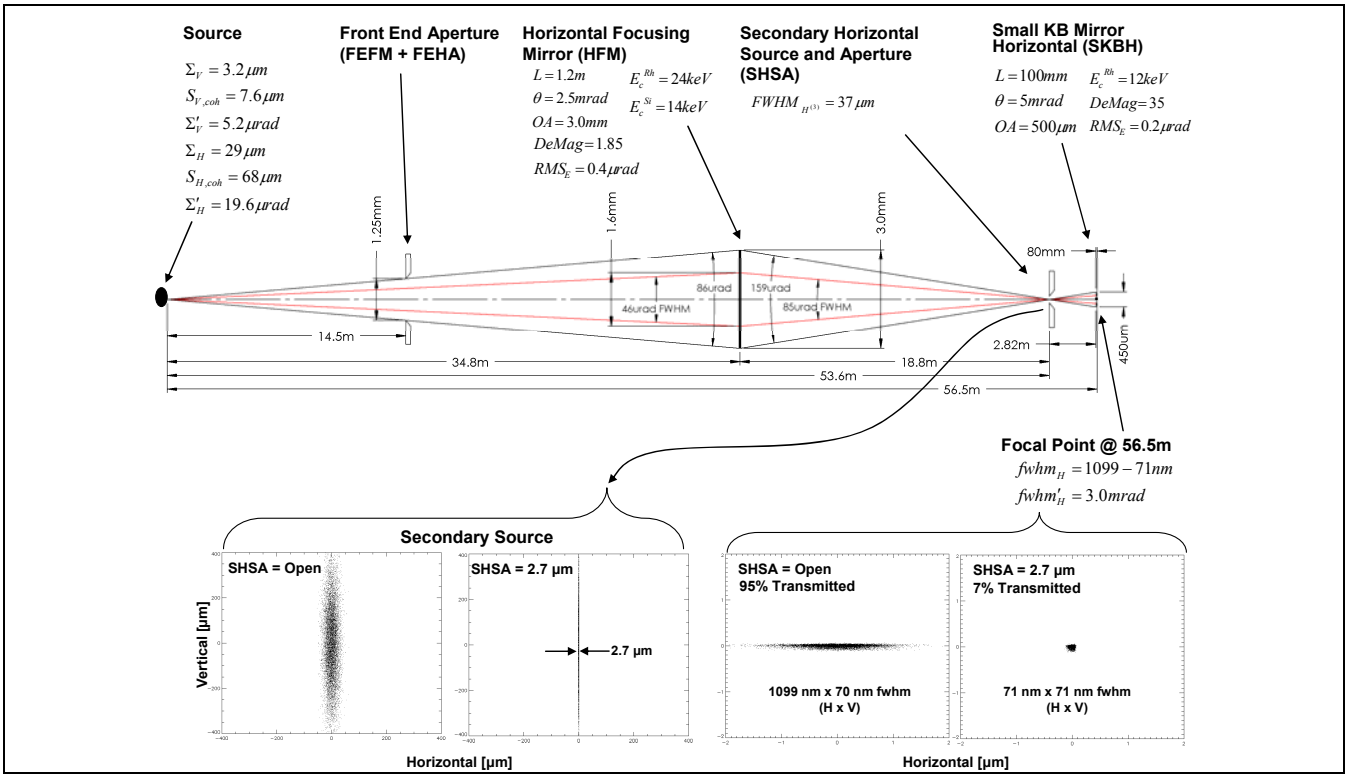

Figure 31. Horizontal optics layout and scatter plots for the KB beamline with a secondary horizontal source at 53.6 m, produced by a 1.2m long horizontal focusing mirror at 34.8 m at a fixed incidence angle of 2.5 mrad. Working distance ~ 30 mm

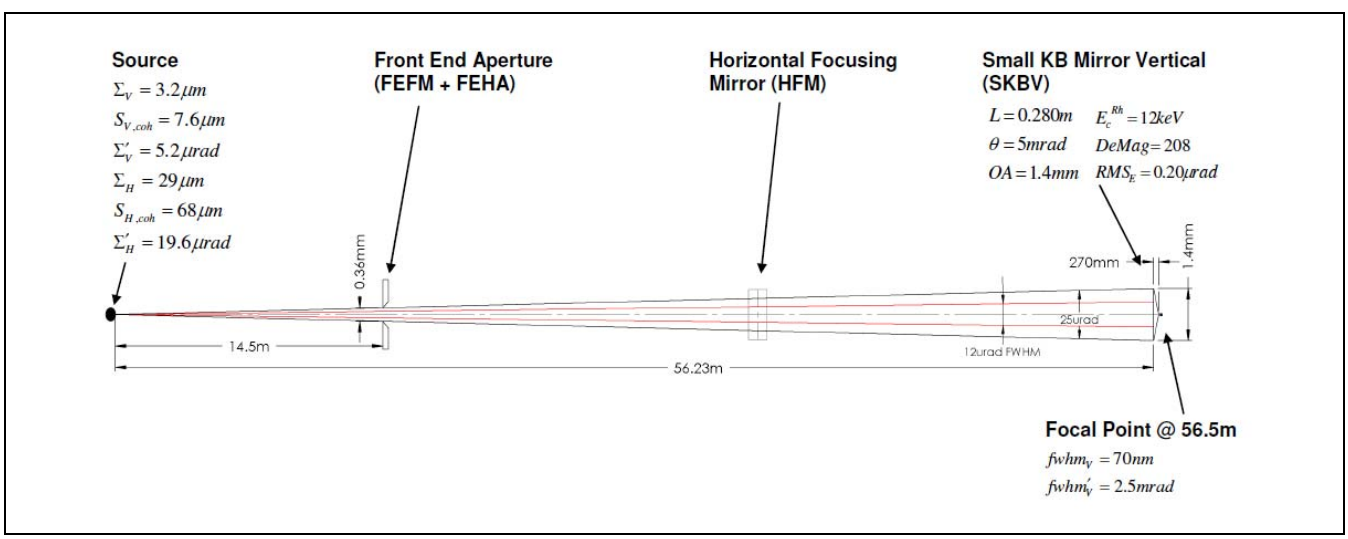

Figure 32. Vertical optics layout for the KB beamline showing a single 280 mm long vertical focusing at 56.23 m.

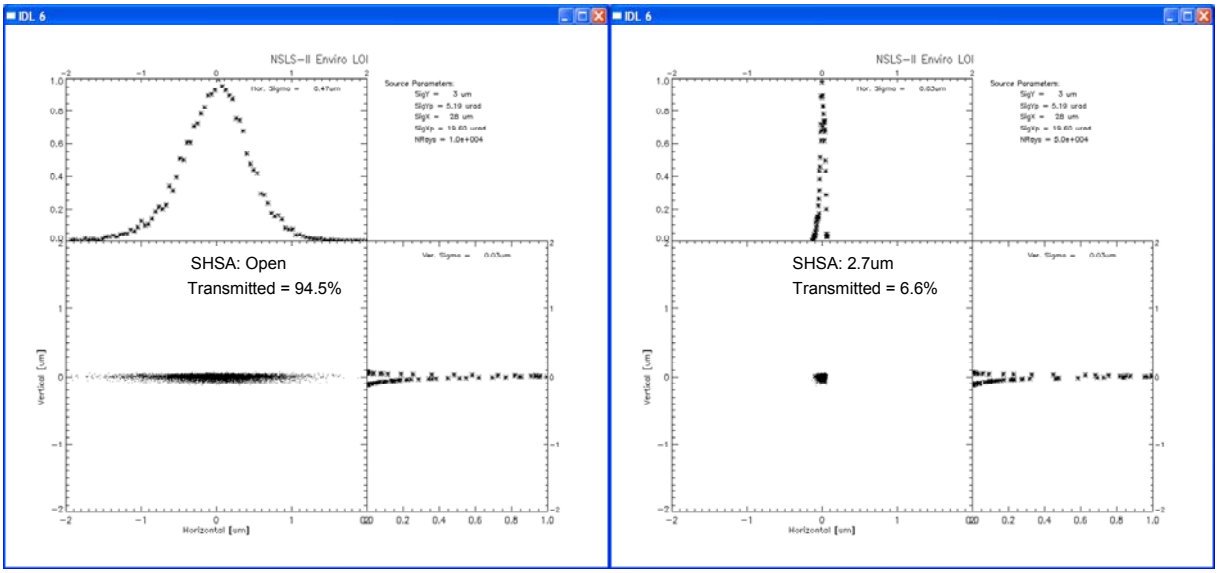

Figure 33. Scatter plots and horizontal and vertical histograms for the KB beamline showing two extreme settings of the secondary horizontal source aperture: full source (left panel) and set to 2.7 μm (right panel).

2.6.2 Zone Plate Beamline

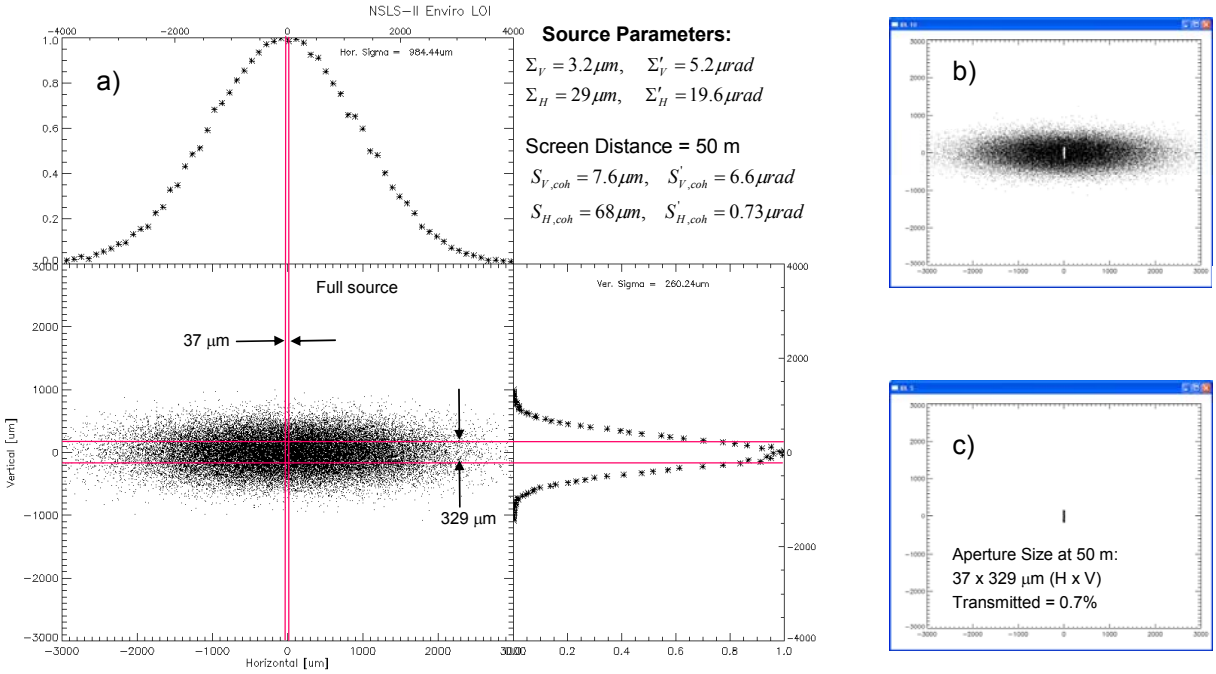

Figure 34. Scatter plot of a full source ray-trace at 50 m. a) Shows the horizontal and vertical histograms with the intersection of the red lines marking the coherent section of the source. b) Shows all the incoherent rays and c) the coherent rays into a 37 x 329 μm (H x V) aperture.

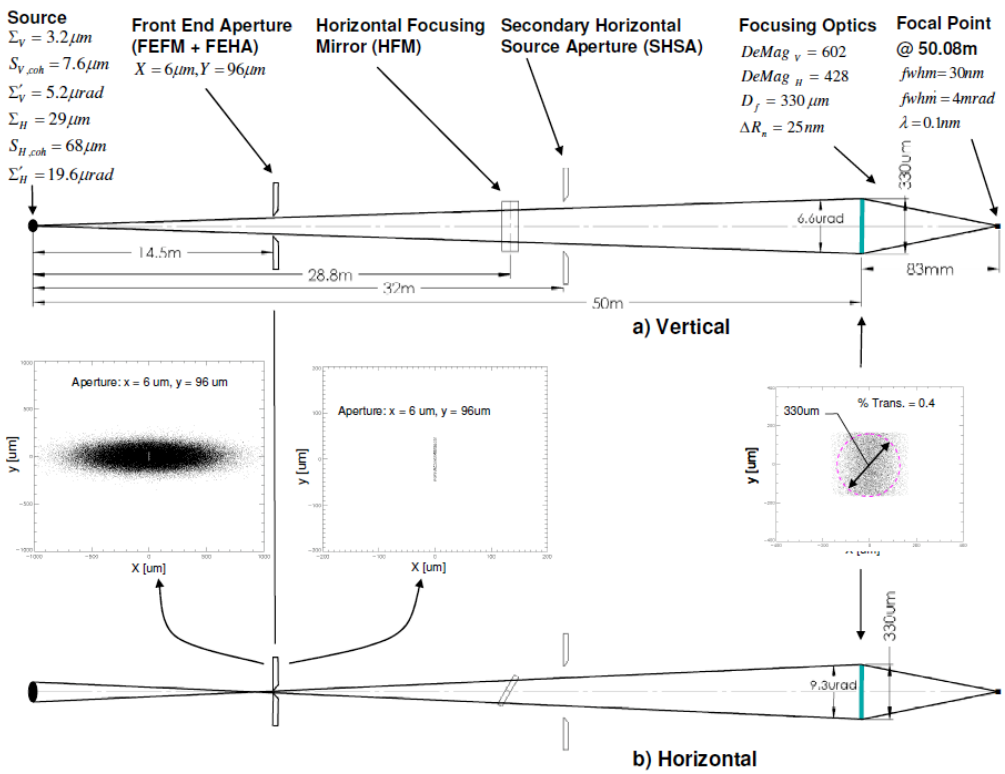

Figure 35. Optics layouts, ray trace and scatter plots for a ZP beamline utilizing a front end aperture to select the coherent fraction of the beam to illuminate a linear symmetric lens such as a zone plate.

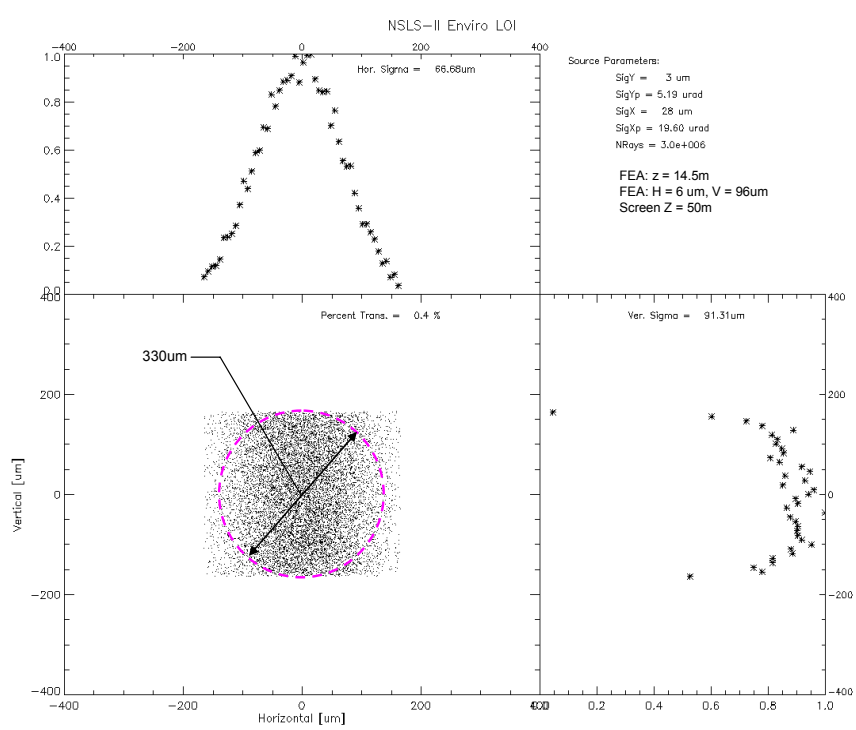

Figure 36. Scatter plot and horizontal and vertical histograms at the location of the zone plate at 50 m of the optics layout illustrated in Figure 35.

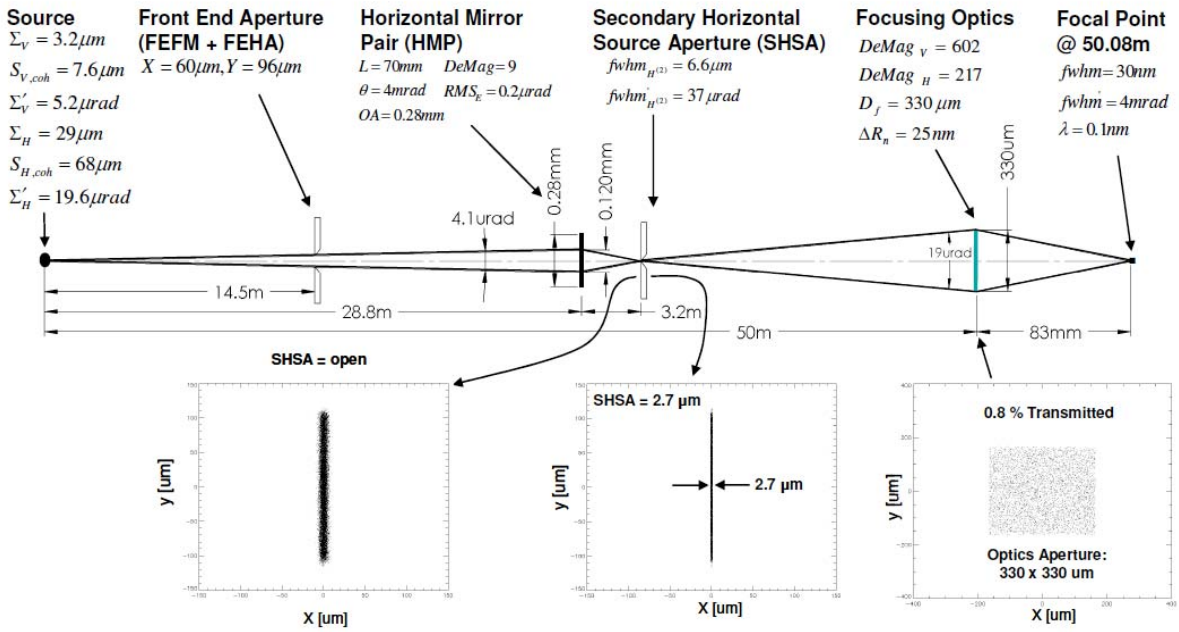

Figure 37. Horizontal optics layout and scatter plots for the ZP beamline with a secondary horizontal source point at 32 m produced by a horizontal focusing mirror.

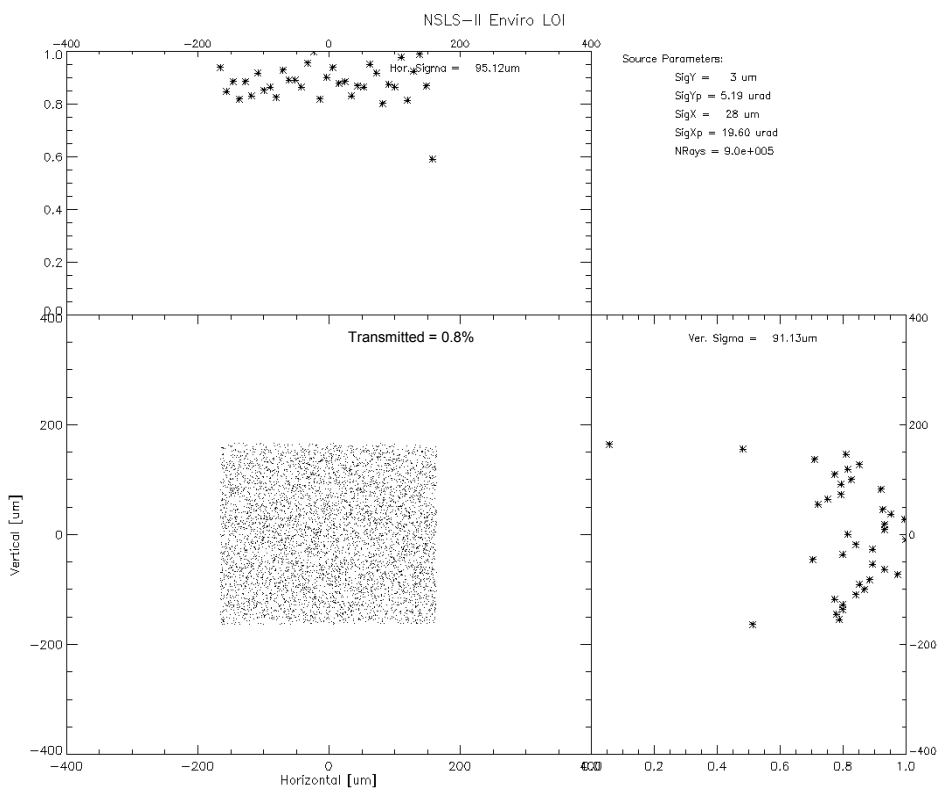

Figure 38. Scatter plot Horizontal optics layout and scatter plots for the ZP beamline with a secondary horizontal source point at 32 m produced by a horizontally focusing mirror.

2.7 List of Major Components

2.7.1 Tabular list of components

Table 2 lists all components for the SRX beamline in their spatial order from source to detector. The distances are in meters relative to center of low-beta (short) straight section. Items in *italics* are for the second canted ZP-branch, which is not in the original scope. A detailed description of key components will follow this table.

Table 2: List of Components for SRX Beamline.

Item	General	KB-branch	*ZP-branch*	Center pos.	Beam sep.
CD 1	Canting Dipole 1				
IVU 22			*Undulator IVU22*	- 1.0 m	
CD 2	Canting Dipole 2			0.0 m	
IVU 21		Undulator IVU21		1.0 m	
CD 3	Canting Dipole 3				
SGV	Slow Gate Valve			15.77 m	31.5 mm
FDAM	Fixed Dual Aperture Mask			16.41 m	32.8 mm
FEXBPM	Front End X-ray Beam Position Monitor			17.4 m	34.8 mm
GBC 1	Gas Bremsstrahlung Collimator 1			18.0 m	36.0 mm
PS-ZP			*Photon shutter*	18.835 m	37.47 mm
PS-KB		Photon shutter		19.4 m	38.8 mm
FGV	Fast Gate Valve			20.2 m	40.4 mm
ALA	Adjustable L Aperture			22.1 m	44.2 mm
GBSS	Gas Bremsstrahlung Safety Shutter			23.35 m	46.7 mm
	Ratchet Wall			24.625 m	
GBC2	Gas Bremsstrahlung Collimator 2			23.9 m	48.1 mm
	FOE Front Wall			25.5 m	
FOE-GV1	First Optical Enclosure – Gate Valve 1			25.57 m	51.2 mm
FOE-B1	FOE Bellows 1			25.71 m	51.6 mm
DV1	Diagnostic Vessel 1			26.13 m	
ZP-WBS			*White beam slits*	26.18 m	52.4 mm
FOE-B2	FOE Bellows 2			26.54 m	53.1 mm
ZP-HMP			*Horizontal mirror pair*	1st 26.745 m 2nd 26.865 m	53.6 mm center line
FOE-B3	FOE Bellows 3			27.02 m	
CLDW	Conductance Limiting Diamond Window			27.14 m	60.72 mm
ZP-DCM			*Double crystal monochromator*	27.9 m	73.2 mm
FOE-B4	FOE Bellows 4			28.66 m	88.1 mm
ZP-BPM1			*Beam Position Monitor 1*	28.82 m	91.7 mm
ZP-WBES			*White Beam End Stop*	28.97 m	93.5 mm
GBC3	Gas Bremsstrahlung Collimator 3			29.22 m	100.7 mm
FOE-B5	FOE Bellows 5			29.48 m	102.8 mm
ZP-BPM2			*Beam Position Monitor 2*	29.665 m	107.3 mm
ZP-SHSA			*Secondary Horizontal Source Aperture*	29.89 m	109.2 mm
ZP-SHSV			*Secondary Horizontal Source Viewer*	30.065 m	113.7 mm
FOE-B6	FOE Bellows 6			30.2 m	115.8 mm
KB-WBS		White Beam Slits		30.29 m	119.1 mm

continued…

Table 2: List of Components for SRX Beamline *(continued)*

FOE-B7	FOE Bellows 7			30.5 m	121.2 mm
KB-DCM		Double Crystal Monochromator		31.26 m	133.8 mm
FOE-B8	FOE Bellows 8			32.02 m	173.6 mm
KB-BPM1		Beam Position Monitor 1		32.18 m	177.2 mm
KB-WBES		White Beam End Stop		32.33 m	179.0 mm
GBC4	Gas Bremsstrahlung Collimator 4			32.58 m	186.2 mm
FOE-B9	FOE Bellows 9			32.84 m	188.3 mm
KB-BPM2		Beam Position Monitor 2		33.025 m	192.8 mm
KB-HS		Horizontal slit		33.325 m	197.3 mm
FOE-BP1	FOE Beam Pipe 1			33.623 m	205.3 mm
FOE-B10	FOE Bellows 10			33.905 m	207.5 mm
KB-HFM		Horizontally focusing mirror		34.8 m	222.5 mm
FOE-B11	FOE Bellows 11			35.695 m	244.5 mm
FOE-BP2	FOE Beam Pipe 2			38.378 m	365.1 mm
ZP-PS			*Photon Shutter*	41.0 m	365.1 mm
KB-PS		Photon Shutter		41.6 m	379.0 mm
	FOE End Wall			41.9 m	385.9 mm
	Shielded Beam Pipes				
	ZP Endstation Front Wall			45.8 m	475.6 mm
ZP-BPM3			*Beam Position Monitor 3*	49.0 m	549.2 mm
ZPL			*Zone Plate*	50 m	572.2 mm
ZP-SS			*Sample Stage*	50.8 m	574.0 mm
	Endstation Mid Wall			52.8 m	
KB-BPM3		Beam Position Monitor 3		53.5 m	
KB-SHSA		Secondary Horiz. Source Aperture		53.6 m	
KB-SHSV		Secondary Horiz. Source Viewer		53.7 m	
SMKBV		Vertical KB mirror		56.23 m	
SMKBH		Horizontal KB mirror		56.42 m	
KB-SS		Sample Stage		56.5 m	
	KB Endstation Rear Wall			58.5 m	

2.7.2 Detailed description of key components

Note: The optical components of the ZP branch are listed in *italic* to distinct quickly between the two branches.

Canting Dipole 1 (CD1)

This is an electromagnet dipole designed to steer the beam 1 mrad outboard. It will work in series with two additional dipoles - CD2 (2 mrad inboard) and CD3 (1 mrad outboard) - together providing the angular deflection required to separate the center line of the KB and ZP branch and bringing the electron beam back to the uncanted straight section centerline. The three dipole magnets will likely operate from a common power supply in series resulting in a zero deflection summation. The exact location, the bending radius and/or the field length need to be defined so that accurate source locations and center lines can be determined for the ZP and KB branch. For example, the ZP undulator source for raytacing purposes would effectively originate from the center of CD1

deflecting the beam outboard from this point 1 mrad. With CD2 located at the center of the low beta straight, the horizontal location of the KB source would be displaced outboard by the distance between CD1 and CD2 times 1 mrad. With the upstream end of the ZP undulator approximately -1.75 m from the center, it can reasonably be estimated that CD1 would be located about -2 m from CD2, resulting in an outboard horizontal displacement of 2 mm for the KB branch source. Therefore for synchrotron raytracing purposes the KB branch source would originate at an X = 2 mm and Z = 0 mm deflected inboard from this point by 1 mrad. Note that there will be a small correction for the outboard horizontal displacement of the KB branch that will depend on the bending radius of CD1.

Zone plate branch undulator
The discussion over the properties of t his device is still ongoing. The goal i s to have a f ull coverage of x-ray energies extending from just below the phosphorous K – absorption edge up to approx. E = 15 keV. The ZP source ray originates at the intersection of a ray making a 1 mrad outboard angle with the straight section centerline and the tangent to CD1 bending radius.

Kirkpatrick-Baez mirror branch undulator
The KB branch in-vacuum undulator is optimized to allow access on the 3rd harmonic to just below the titanium K – absorption edge as well as to minimize drop offs at harmonic transition points. It will be extremely important to control the upstream and downstream gap of this device precisely and reproducibly to 0.5 micron. The development of the motion control of this device will be a significant technical challenge. The ultimate goal is to be able to scan the undulator and monochromator synchronously maintaining the monochromator alignment with the undulator harmonic to better than 1 % or (depending on harmonic used) from around 1 to 5 microns gap accuracy. One possible approach is to design and install before the FOE WBS (see below) a real-time energy monitor that intercepts a horizontal edge of the undulator fan. This real-time energy monitor consisting of a channel cut crystal and photo diode could be operated in a phase locked loop that constantly determines the peak energy of the harmonic. Once calibrated (with aperture dependent offsets) the monochromator crystal angle can be slaved to its output. This control approach places the more difficult to control device – the undulator – as the master. Energy scans would be performed – on the fly – by driving the undulator along a gap speed time trajectory. It is recommend to leave space in the FOE layout between the shield wall and FOE WBS for such a device.

Fixed Dual Aperture Mask (FDAM)
This is a fixed dual missteer, power limiting and differential pumping aperture. Centered on each branch is a rectangular 20 sigma divergence aperture with a size at 16.41 m of 6.56 x 1.64 mm^2 (H x V). It will act to protect downstream components in case orbit control loss as well as limit the total power delivered to downstream components. It will also act a conductance limiter and together with upstream and downstream pumps should achieve about three orders of magnitude of differential pumping. The aperture size is dictated mostly by requirements for initial beam alignment. Once a good orbit is established a much smaller aperture could be used. By combining this dual fixed aperture with adjustable “L” apertures both, initial orbit control can be established and the power delivered to the FOE can be greatly reduced. The actual size of this slit will be dictated by the machine physicist’s requirements for initial orbit control.

Front End X-ray BPM (FEXBPM)
This x-ray BPM will be used to adjust and stabilize the orbit by feeding back to storage ring trim magnets. These devices and their control systems are in the domain of the machine physicists. One set will be needed for each undulator. It’s not clear up to now if there will be a set of trim magnets for each undulator – they may operate in an either or mode.

Gas Bremsstrahlung Collimator 1 (GBC1)
This in-air gas bremsstrahlung collimator will consist of lead blocks arranged around a rectangular beam pipe with a lead length along the beam of 300 mm. The ID of vacuum beam pipe is 51.2 x 9.8 mm (H x V). Allowing for a 3 mm wall thickness the ID of the lead collimator is 58 x 16 mm (H x V). The outside dimensions of the collimating blocks must overlap the inside dimensions of the GBC2 located inside the ratchet wall. Since this is an in air

collimator its aperture must in the horizontal encompass the separation of the two branches resulting in a wide aperture. When a full GB study is performed for the beamline it will be worth considering breaking this collimator up to two parts. The first part would be a in vacuum tungsten collimator with two holes sized to be 3 mm all around larger then the extremal ray of the missteered beam at the collimator location. The second part would be an in air lead collimator with an ID that overlaps the OD of the first collimator and who's OD overlaps the ID of the ratchet wall collimator (GBC2). This would result in a much greater collimation potentially simplifying the collimators and stops needed in the FOE.

Photon Shutter ZP and KB (PS-ZP and PS-KB)
These are movable glancing incidence thermal stops capable of absorbing the full power passed by either the ZP aperture or the KB aperture in the FDAM. They will allow either the KB or the ZP branch beam to pass.

Fast Gate Valve (FGV)
This gate valve is design to protect the ring vacuum should there be a failure of the downstream vacuum. It will be triggered by both, a beamline vacuum fault and a front end vacuum fault. Both PS-ZP and PS-KB would rapidly close together with this valve. The storage ring RF should not need to be tripped as long as the ring vacuum stays in acceptable limits.

Adjustable L Apertures (ALA)
A pair of these adjustable L apertures will be centered on each branch. When fully open they will act as a synchrotron missteering mask and when closed they will have a -4 mm overlap. The main purpose of these adjustable masks is to reduce the size of the beam passed to the FOE to a minimum required by the x-ray optics. Typically they will be set slightly larger than the precision FOE white beam slits. By reducing the power absorbed by the FOE white beam slits to a minimum the stability of these precision slits will be greatly improved.

Gas Bremsstrahlung Safety Shutter (GBSS)
The present proposal is to build this shutter out of a pair of in-air lead blocks each 300 mm long mounted on separate vertical actuators (redundant shutters). The blocks are connected in the direction of the beam to hollow beam tubes and bellows that allows the beam to pass when the blocks are lower and the bellows flexible enough to allow the blocks to be moved into the gas bremsstrahlung fan. The OD of the lead blocks will over lap the ID of ratchet wall GBC2.

Gas Bremsstrahlung Collimator 2 (GBC2)
This in-air gas bremsstrahlung collimator will consist of 300 mm long lead blocks arranged around a rect-angular beam pipe that passes through the ratchet wall. The upstream edge of this collimator starts at the upstream edge of the ratchet and it is built into the wall. The ID of vacuum beam pipe is 65.8 x 10.4 mm^2 (H x V). Allowing for a 3 mm wall thickness the ID of the lead collimator is 71.8 x 16.4 mm^2 (H x V).

Diagnostic Vessel 1 (DV1)
Located upstream in the vessel will be an outboard and inboard port for mounting the ZP and KB branch undulator harmonic energy monitor. Downstream will be the ports for mounting the horizontal and vertical ZP branch white beam slits.

ZP White Beam Slits (ZP-WBS)
These slits are of the relative open and center type allowing a preset aperture to be scanned across the beam. The upstream edges water-cooled copper wedges backed on the downstream edge with a beam defining tungsten edge. The resolution and repeatability for the centering stage should be 0.1 µm with a range of +/- 3 mm. The relative opening stage should have a resolution and repeatability of 0.1 µm and a maximal opening of 10 mm.

ZP Horizontal Mirror Pair (ZP-HMP)

The ZP-HMP is located as close as possible to the shield wall in the FOE. It will both, deflect the beam horizontally outboard and thus create a beam separation at the endstation, and form a secondary horizontal source (SHS) that can be manipulated by a secondary horizontal source aperture (SHSA). The center of the ZP-HMP is located at 26.78 m. The mirror pair focuses the horizontal source with a demagnification of 9 at 29.89 m. The ZP-HMP will be compact since the coherent horizontal divergence is low (4.1 μrad), requiring only 120 μm optical aperture (OA). The mirrors will be water cooled silicon, each half coated with rhodium and operating at a fixed incident angle of 4 mrad for a total horizontal deflection of 16 mrad. The second mirror will have a dynamic bender that will correct for the thermal bump on the first mirror and focus the beam to approximately 7 μm FWHM at the SHSA. Each mirror will be 110 mm long (separated by 10 mm) with an optical aperture of 70 mm, a thickness of 30 mm and 25 mm wide. A water-cooled copper mask located on the upstream leg of the first mirror (travelling with the mirror pitch and height displacement) will protect the mirrors from the normal incidence beam as well as shadow all the support and bender components downstream. This mask will also have an aperture to allow the KB branch beam to pass inboard of the backside of the mirrors. The mask will have a copper edge leading to the optical surface. The total horizontal travel will be limited to +2mm and -4 mm. A 10 mm vertical displacement of both mirrors together, will move the beam between the rhodium and the silicon stripe. The ZP branch centerline is now deflected an additional 16 mrad outboard.

Conductance Limiting Diamond Window (CLDW)
This is a diamond window mounted inside a movable water-cooled copper frame. When the window is in the beam the copper frame makes a small gap with a stationary frame. The small gap acts as a differential pump The main function of the CLDW is to help isolate potential poor vacuum from the upstream optics and storage ring vacuum. Both branches with travel through this window.

ZP Double Crystal Mono (ZP-DCM)
This is an indirectly L N_2 cooled Si (111) double crystal monochromator that bounces the beam down 25 mm with an energy range of E = 2.1 keV to E = 15 keV (the incident angle ranges thus from 70 to 7 deg). It will allow the KB branch beam to pass 73.2 mm inboard in a common vacuum.

ZP Beam Position Monitor 1 (ZP-BPM1)
This beam position monitor is for setup and alignment only. During operation it will be moved to an open aperture. This BPM will be mounted on a vertical through-vacuum actuator in a four way cross. In the outboard horizontal port will be a window that will allow a CCD camera to image on the BPM screens. In the lower outboard corner will be an eclectically isolated tungsten blade mounted through a ceramic insulator to a water-cooled copper mask. This tungsten blade will allow measuring the total beam current striking it and can be used to center the upstream white beam slits, the mirrors and the monochromators 1st crystal on the white beam. Just above the tungsten blade will be a diamond scintillation screen. This screen will allows to view the white beam and will also aid in alignment of upstream slits mirrors and monochromator first crystal. Both, the tungsten blade and the diamond window, should be wide enough to intercept the beam off one or both mirrors. Offset vertically by 25 mm and centered on the double mirror defected beam centerline will be a doped YAG screen that will allow us to optically monitor the diffraction condition of the monochromator second crystal. Two apertures above the diamond screen and the YAG screen will allow the white / pink and monochromatic beam to pass by translating the actuator down 10 mm.

ZP White Beam End Stop
This water-cooled, wedged copper block will be capable of absorbing the full white beam power passed by the FDAM. This thermal stop will be mounted in the same vacuum vessel as the in-vacuum tungsten GBC3. It serves to protect the tungsten GBC.

Gas Bremsstrahlung Collimator 3 (GBC3)
This in-vacuum 200 mm long tungsten block will block the GB fan and will have a hole aligned with the double mirror deflected monochromatic beam.

ZP Beam Position Monitor 2 (ZP- BPM2)
This is a thin foil back fluorescence quad di ode BPM. It will provide vert ical and hor izontal beam position information that will allow the mirrors and the monochromator optics to be stabilized with a feedback loop. It will have six apertures on a rotary stage to allow up to five differen t foils to be placed into the beam with the sixth aperture blank.

ZP Secondary Horizontal Source Aperture (ZP-SHSA)
This will be a pair of relative open and center XY-slits. Th e slit blades will be made of polis hed tungsten carbide rods. Since these slits will act as the so urce for the ZP optics they must be extremely stable both to vibration and long period drifts.

ZP Secondary Horizontal Source Viewer (ZP-SHSV)
Located just downstream of the ZP-SHSA will be a removable YAG screen. The screen will be mounted with a 45 degree pitch relative to th e beam and a re-entrant tube with a gl ass window will allow a long working distance CCD microscope with 20x magnification to view t he beam focus. This visual system is crucial for beamline alignment and horizontal focus optimization.

KB White Beam Slits (KB-WBS)
These slits are identical to the ZP-WBS with the ability to allow the outboard ZP beam to pass.

KB Double Crystal Monochromator (KB-DCM)
This is a vertical axis double crystal monochromator that offsets the beam inboard by 25 mm. It will have three indirectly LN_2 cooled crystals, a Si (111), Si (311) and a place holder for a multilayer. Its energy range will be from E = 4.1 keV to E = 28 keV.

KB Beam Position Monitor 1 (KB-BPM1)
This beam position monitor is for setup and alignment only. During operation it will be moved to an open aperture. This beam will be mounted on a vertical through vacuum actuator in a four way cross. In the inboard horizontal port will be a window that will allow a CCD camera to image on the BPM screens. At the lower edge of the BPM will be an eclectically isolated tungsten blade mounted through a ceramic insulator to a water-cooled copper mask. This tungsten blade will allow measuring the total beam current striking it and can be used to center the upstream white beam slits and monochromator first crystal on the white beam. Just above the tungsten blade will be a diamond scintillation screen. This screen will allow viewing the white beam and will also aid in alignment of upstream slits and the first crystal of the monochromator. Offset horizontally inboard by 25 mm will be a doped YAG screen that will allow optically monitoring the diffraction condition of the second crystal of the monochromator. Translating the actuator up by 10 mm will remove them from beam.

KB White Beam End Stop
This water-cooled, wedged copper block will be capable of absorbing the full white beam power passed by the FDAM. This thermal stop will be mounted in the same vacuum vessel as the in-vacuum tungsten GBC4. It serves to protect the tungsten GBC.

Gas Bremsstrahlung Collimator 4 (GBC4)
This in-vacuum 200 mm long tungsten block will block the GB fan and will have a hole aligned with the monochromatic beam.

KB Horizontal Slit (KB-HS)
These are the same as the ZP-SHSA but without the vertical slit.

KB Horizontally Focusing Mirror (KB-HFM)
The KB monochromator illuminates a 1.2 m long water-cooled silicon horizontally focusing mirror (HFM) half coated with rhodium and operating at a fixed incident angle of 2.5 mrad. The HFM is located at 34.8 m and deflects

the beam inboard by 5 mrad forming a secondary horizontal focus at 53.6 m with a demagnification of 1.85. The KB line beam passes by the ZP line endstation experimental table approxi-mate 0.5 m inboard contained in a narrow profile shielded transport pipe

KB Secondary Horizontal Source Aperture (KB –SHSA)
This is the same as the ZP-SHSA.

KB Secondary Horizontal Source Aperture (KB –SHSV)
This is the same as the ZP-SHSV.

SMKB Vertical Mirror (SMKBV)
The vertically focusing optics plan exploits the low vertical divergence of the source by utilizing a single 280 mm long vertically focusing mirror at 56.23 m. This mirror is capable of collecting nearly the full vertical source divergence and focusing it 270 mm away to a focal spot of 70 nm with a divergence of 2.5 mrad.

SMKB Horizontal Mirror (SMKBH)
The secondary horizontal focus is re-imaged by a 100 mm long horizontal KB mirror with a focal length of 80 mm, a demagnification of 35 and a divergence of 3 mrad.

3 END STATION INSTRUMENTATION

3.1 Hutch Mechanical, Environmental and Utilities Requirement

The experimental hutch of the high energy SRX-KB branch will be a monochromatic beam enclosure with its upstream wall positioned at 52.8 m from the second canting bend source point. This wall is shared with the lower energy SRX-ZP experimental hutch that sits upstream (Figure 7). The end wall of the SRX-KB hutch is designed to sit at 58.5 m. There are a number of mechanical, engineering, and utility requirements that are both generally and specifically necessary to support the user science program at the beamline and to ensure optimal instrument stability and performance. The hutch should be designed with the following:

- *User and Equipment Access* : Convenient access needs to be provided to support both beamline and user instrumentation that will be utilized at this station. Access to the SRX-KB hutch should be through sliding doors which are double width for equipment and single capability for personnel. The roof of the enclosure should be surrounded by a railing to permit safe personnel access and there should be convenient access to the roof areas via access ladders to permit equipment installations. Precise positioning and remounting of equipment within the hutch should be provided through the placement of laser tracked floor and wall fiducials. A number of experiments will likely require interfacing between permanent beamline instrumentation and user equipment. Setup and utilization of such equipment will be significantly enhanced by providing interlocked user labyrinths to allow for easy transfer of equipment cabling out of the hutch without the need to engage floor coordinators. Crane access will also be required, but a mobile crane rather than a fixed overhead system will likely be acceptable and less invasive.

- *Hutch Environment*: The spatial resolution requirements of the instrument will necessitate careful control of hutch temperature, humidity and airflow. Although a careful evaluation of thermal requirements should be modelled, it is reasonable to assume that air temperature control of ± 0.1 °C will be required to limit spatial drift to approximately 10 nm per 1 cm. The hutches should provide baffled airflow to minimize air currents and the "windsock" design that has been implemented at PETRA III for their experimental endstations has high merit as an implementable design here. Deviations in hutch temperature and humidity would also be likely minimized by providing airlocked access to the hutch. Airlocks on the hutch access doors, however, are potentially cumbersome to implement and could prove a nuisance for frequent user access to the hutch. An alternative is to provide an environmentally controlled user-control cabin, which is accessed through an airlock that shares similar environmental parameters as the hutch. The hutches need to provide particulate filtering (possibly HEPA filtering for the instrumentation area) for air entering the hutch. It is also anticipated that some experimental work will involve the analysis of manufactured nanomaterials, which will likely require HEPA filtering on air outflow for safety.

- *Signal and Utilities requirements:* There are a number of specific signal and utilities requirements for the SRX beamline that need consideration. A liquid N_2 tap must be provided for cooling detectors and the sample cyro-stage. It is desirable to utilize SEMIFLEX/Triax type delivery systems to deliver low pressure liquid nitrogen so that no gas is vented through the equipment. A chilled water panel should be provided to cool electronics and temperature sensitive experimental cells supplied by users. A compressed air panel nominally rated at 75-100 psi pressure for pneumatic valves and devices will likely be required for equipment shutters that may be utilized in XRD applications, etc. Video monitoring of the hutch and sample via Ethernet CCD camera systems will be required (i.e. high-speed CCD's). Hutch monitoring should utilize pan-tilt-zoom systems. It is also required to have access to various standard signals for monitoring beam position and intensity, but also have requirements specific to the nature of this experiment. A signal patch panel into the hutches must be provided that should be configured to allow for multiple plugin of:
    - BNC connectors (estimate 32, required for beam position readout, binary I/O, TTL, etc.)
    - Lemo (estimate 32, similar equipment need as BNC)

- HV (estimate 8, for providing clean power to ion chambers and detectors, many of these HV supplies will be in the hutch, but it's prudent to allow for some externally powered equipment outside of the hutch), We would reiterate here the need for clean power to maintain high precision focus on beamline optics.
- RS232 (minimally 8, required for serial devices)
- RJ45 and fiber optic (connector types to-be-determined) ethernet connectors (estimate 16, required for modern detector interfaces and high speed CCD's).

An experimental gas farm and station patch panels with flowmeters must be provided minimally to supply high purity He, N_2, Ar gases.

3.2 Sample Mounting, Environments and Manipulation

The types of samples required for the anticipated scientific applications are variable and therefore the specimen mounting, environment and manipulation apparatus must have flexibility. This flexibility will greatly challenge the design of an instrument with high performance and ease of use.

It is likely that the majority of the experiments will operate at the highest available spatial resolution and that specimen sizes will necessarily be small (~mm) compared to those typically used at currently operating x-ray microprobes (~cm). Nonetheless, it is critical that the SRX-KB probe provide sufficient flexibility to accommodate high-impact experiments that will require relatively large specimens (~cm) and large travel dimensions (~cm). The instrument must accommodate the following sample types:

- Microtomed and Focused Ion Beam (FIB) milled sections: This category includes both geological and biological specimens. While many can be accommodated on TEM grids and SiN windows, biological specimens may require several millimeters of scanning range. Examples include plant specimens (sections of roots, stems, seeds, and leaves with ~mms cross sectional dimensions) and sections from higher order organisms (i.e., human tissue sections, transgenic mice sections). Accommodating sections that are up to 25 mm in diameter is required.
- Individual sub-micron particles: These specimens will likely be mounted on TEM grids or Si3N4 windows.
- Dispersed powders: Traditionally these samples are mounted on Kapton, Mylar, and polypropylene films, but will likely be prepared on TEM and Si3N4 substrates here for higher substrate stability. Some particulate matter will be on filters, such as aerosol collectors, that cannot be easily removed from the collection material.
- Mineral chip polished mounts: These specimens are epoxy embedded polished mounts or polished chips mounted to pure silica glass slides. Accommodating mounts up to 25 mm rounds is required
- Rock and soil thin sections: These are 30 µm standard thickness, mounted on high purity silica slides (i.e., Suprasil). At the smallest size these can be mounted on 25 mm diameter rounds, but conventional rectangular sections are mounted on glass with dimensions of 27 x 46 mm2.
- Intact geologic and biologic specimens: Some specimens will need to be studied whole without sectioning, primarily geological and biological samples for fluorescence microtomography imaging. These samples are large enough to allow element distributions to be determined rather than only bulk compositions (as for sub-micron particles). Typical dimensions will be in the 0.1 mm to 1 mm range.

A variety of sample environments is required to optimize the trade-offs between low-energy x-ray detection, accommodation of water-bearing samples and reduction of photochemical beam effects. Specimen compartment(s) should be available that operate in air, helium or vacuum. Cryogenic capability (down to LN_2 temperatures) will be required for many biological and wet geological materials (such as soils) to minimize radiation damage. Such damage can alter chemical speciation, for example. This capability will probably be best implemented through a cold finger approach. Such systems are being commercially developed (e.g., Xradia) but some facility R&D will likely be required to develop a customized apparatus. High temperatures (up to 1300K) are also of interest in

studying fluid inclusion above homogenization temperatures, for example. However, it remains to be seen if this capability can be implemented without compromising the performance of the instrument for the "mainstream" experiments. Humidity control may also be desirable. One of the big challenges is to design environmental chambers where the specimen can be viewed optically, at least at some moderate magnification (~100x) for analysis targeting purposes. Higher magnification viewing is probably unnecessary because coarse x-ray imaging can provide this targeting guidance. Reasonable sample exchange time (~10 mins) is also desirable with multiple sample cassettes being used where possible and feasible.

The sample mounting assembly needs to incorporate motorized stages that are capable of translating samples with high precision vertically (Y), horizontally (X, inboard-outboard), along the direction of the incident beam (Z, upstream-downstream), and of rotating samples about the focal point (θ). Because of the requirement for a relatively wide range of sample sizes, the motion requirements are best accomplished using a dual, coarse-fine motor stack. The underlying coarse stack will use high resolution linear motors (2 cm travel; 100 nm resolution) whereas the overlying fine stack uses nano-positioning devices (20 μm travel; 10 nm resolution). It will be necessary for the coarse stack to maintain 10 nm stability when stationary (i.e., high rigidity).

Existing, mirror-based hard x-ray microprobes, most commonly have utilized an instrument geometry that places the sample surface at 45° to the incident beam with the detector at 90° to the incident beam. This geometry is optimum for minimizing background from scattered radiation and maximizes space for ancillary equipment, such as optical microscopes. However, it is likely that the focusing optics that will be used to achieve the targeted spatial resolution for the SRX-KB instrument will have reduced working distance to the sample. Additionally, the desire to collect larger solid angles of fluorescence given the likely choice of energy dispersive detector that has been identified for this instrument will also make a 45° sample geometry non-optimal. Consequently, the SRX-KB instrument will be designed to work primarily in normal incidence. In addition to allowing the greatest beam demagnification, this approach will reduce the horizontal footprint of the beam on the sample and place the microscope optic axis coincident with (or at least parallel to) the x-ray beam.

Fluorescence microtomography applications will be accommodated using a high precision rotation stage (0.01°) with the rotation axis aligned with the focal point of the beam. With this rotation stage placed between the fine and coarse x-y-z translation stacks, the fine stages can be used to center the specimen on the rotation axis and for translations during data collection. Another approach is to have the rotation stage as the topmost stage in the fine stack and allow sufficient vertical space for mounting a small goniometer head. The horizontal translations need to account for the full horizontal travel of the sample through the beam to generate a sinogram using the first generation (pencil-beam) approach. For low density biological specimens that are being imaged for emission lines above 12 keV, self-absorption can be corrected for samples that are greater than 1 mm in diameter. Thus, at least 1 mm, high precision (10 nm), horizontal translation will be required for this application.

Next generation experiments utilizing the BNL-CSIRO MAIA detector system will dominantly operate in a continuous scanning mode. As currently designed, this system interfaces with stage motion control in one of two modes. One is an event driven modality where the detector drives the stage directly. The other modality reads the encoder position of the stage as it is being scanned. Both modes of operation are required, thus encoder-enabled stages and controllers are required. Stage scan rates must be able to achieve 1-10 mm/second.

The sample mounting, environment and manipulation requirements cover a fairly wide range of requirements. However, these requirements can be largely met with a few specialized modules which will be designed to be exchangeable on an experiment basis using a fiducial registry system. We envision the following modules listed in order of development:
Module A: Designed for highest flexibility in terms of sample mounting and sample size. Will operate in air and thus will be best suited for initial commissioning and work with high energy fluorescence lines (≥ 5 keV).
Module B: Designed for highest spatial resolution on small samples (TEM grids, FIB sections). Will have helium gas environment to allow efficient detection of low energy fluorescence lines (e.g., down to Al).

Module C: Similar to Module B but with cryogenic capability and vacuum environment. Designed primarily for studies of biological specimens. Likely will not have optical viewing.
Module D: High temperature module with heating stage designed primarily for fluid inclusion work.

3.3 Detectors

The KB branch will be optimized for sub-micrometer x-ray fluorescence imaging, spectroscopy and diffraction. Our choices for detectors at this early design stage reflect our desires to foster and develop next generation data acquisition approaches that best utilize the unique characteristics of the instrument. These approaches include:

- Detectors and spectroscopy amplifiers capable of rapid on-the-fly x-ray fluorescence acquisition. This is requires to allow for imaging of large sample areas while maintaining high pixel resolution and to minimize radiation dose to photo-redox sensitive samples.
- Spectroscopy amplifiers that can provide near real-time elemental analysis will be required due to the large data sets such scans will produce. Even moderately sized datasets can be expected to be tens or hundreds of Gigabytes in size, which are generally unmanageable by users utilizing current consumer level computers and data storage options.
- Imaging mode spectroscopy will likely be the manner in which most near edge spectroscopy data is collected. This has the benefit of allowing for more unambiguous evaluation of differences in speciation at the sub-micron scale. Efficient detectors capable of rapid data collection, with high throughput and large solid angles are required. Typically this capability is best achieved with detector arrays.
- Tomographic fluorescence, absorption and diffraction imaging will be high demand analytical techniques. Rapid fluorescence detectors are required, but additionally calibrated photodiodes with high sensitivity to measure absorption through the sample are needed as well as high sensitivity and rapid readout CCD area detectors for diffraction imaging and tomography.
- Sub-micrometer x-ray diffraction analysis has also become a high demand technique on hard x-ray microprobes, it can be estimated minimally 20% of users will wish to utilize the instrument's spot and imaging XRD capabilities. High sensitivity, low noise area detectors will be required with relatively large 2q coverage and along-beam adjustable position for optimizing angular range and phase-contrast

Considering detector technologies that are either currently available or in advanced stages of development, the following specific systems should be considered for the beamline at a minimum:

- Silicon-drift Detector Array: Multi-cathode detectors area variant of silicon drift diode detector technology. SDD detectors are becoming increasingly popular choices for synchrotron x-ray fluorescence analysis as the technology for SDD detectors has greatly improved over the past few years. While more conventional lithium-drifted silicon (Si(Li)) or high-purity germanium (HPGe) offer substantial x-ray efficiency for a wide range of x-ray energies, they do have their drawbacks, such as the physical limitation due to the presence of a large LN2 dewar attached to the detector. SDD systems, by contrast, operate efficiently at near room temperature yielding a much more compact and flexible system. Another disadvantage of conventional Si(Li) and HPGe detectors is that their capacitance is relatively high, which limits their use at short peaking times and high count rates, and thus are not optimal for the fast scanning modes we wish to develop at SRX-KB. The SDDs, by contrast, exhibit extremely low capacitance (~0.06 pF) and very low leakage current (~10-9 A) due to the unique structure and small anode size, virtually independent of the detector area, providing a system with high throughput and very good energy resolution even when operated at extremely short peaking times. The 4-element multi-cathode X-ray detector arrays are also available featuring large active area per element (~50 mm2) and excellent energy resolution. The detector system will incorporate 4 preamplifiers, one 4-channel digital pulse processor (DPP), power supplies necessary to operate the full spectrometer, an electronic crate for the 4-channel DPP), PCI interface cards and fiber optic communication cables. The DXP spectrometers offer full spectrum or multi-SCA acquisition at sub-millisecond dwell times, which supports the beamline requirement for fast on-the-fly scanning. In mapping mode assuming 1 msec dwell times, the 4-element array will stream full channel spectra

at about 32 Mb/second. The cPCI bus is rated to stream up to 50 Mb/sec. This translates into 113 Gb per hour. Assuming round the clock data collection, storage will be required for up to 2.7 Tb per day.

- Maia detector array: The Maia large solid angle Si detector array is a joint BNL/CSIRO development which utilizes an alternative data acquisition strategy that uses a multiparameter approach in which each photon event is tagged by sample XY position and detector identity and then streamed as 'events' for further processing or storage. The advantage of this strategy is that it exhibits zero read-out overhead and enables faster raster scanning, again, very much in line with the desired performance characteristics of SRX-KB. The Maia system allows complex full-spectral SXRF data to be decomposed into elemental components using a matrix transform method called Dynamic Analysis which in a mature form will permit its execution on the event stream in real-time, again…a desired capability for the beamline. Physically, the Maia utilizes a large planar monolithic silicon detector array and dedicated application specific integrated circuits (ASICs) for signal processing offering large solid-angle collection and high count rates spread over a large number of detectors. A 96 element version of the Maia is currently in commissioning at the NSLS microprobe beamline X27A and at the AS microprobe beamline 5ID and a 384 element final design is in construction for both facilities. Tests at NSLS beamline X27A using the 96 element prototype demonstrated count rates up to 6 M/s, image sizes up to 4.3 megapixels, and dwell times as short as 0.8 ms (limited by stage speed for 7.5 μm pixels). The 384 element final design minimally will generate 4x larger data streams of ~8 24 M/s. As pileup rejection improves on the detector this will likely be larger since they will be able to operate at higher rates. This translates to data rates of roughly 2 Tb/day with round the clock operation.
- Wavelength Dispersive Spectrometer: There may be analyses that require better resolution in separating fluorescence emissions that overlap strongly when detected using energy dispersive detectors (i.e. overlap of rare earth element L emission lines with K emission lines of Ti, V, Cr, Mn, and Fe). These analyses benefit from wavelength dispersive spectrometers utilizing high-resolution fluorescence analyzer crystals lying in a Rowland circle geometry. Commercial devices do exist that are designed to attach to scanning electron microscope systems. Instruments are also being deleloped specifically for x-ray microprobe use, such as that available at the ESRF's ID21. While some experiments might benefit, these systems do have some significant disadvantages as well in that they are difficult to align, must operate in vacuum and minimally have detection sensitivities 10x lower than what is achievable with energy dispersive spectrometers. Thus while useful for a small subset of experiments, other detector technologies listed above must take priority for this instrument.
- Diffraction Area Detector: Microfocused synchrotron x-ray diffraction has proved to be valuable in the in-situ identification of phases in minute amounts of sample. On microprobes, these instruments generally rely on Bragg techniques with a fixed detector position and monochromatic radiation. Two primary limitations need to be considered in selecting suitable detectors for this application. Increased 2θ coverage is generally provided by placing the area detector slightly offset to the incident beam. This offset provides partial coverage of powder diffraction rings over a larger 2θ range than could be achieved with the detector centered. Additionally, while many samples with large numbers of crystallites within the incident beam are strongly diffracting, many samples require longer dwell times to achieve sufficient sensitivity for phase identification. Image Plate area detectors are very effective in allowing users to identify phases in low abundance since they can be operated with little detriment at very long dwell times, often over periods of hours. Modern CCD based area detectors provide short read-out times (a few seconds) with good signal-to-noise for short exposures (<1 minute) which are needed at SRX-HE for the rapid analyses required for phase mapping and tomography. At highest resolution these CCDs output 8 Mb files. Generally μXRD studies are conducted as single point analyses. However, increasingly there is demand for diffraction imaging analysis integrated with coupled with μXRF imaging. We expect that 1 second readouts would be the shortest exposures that are likely to yield analyzable results. In an imaging mode this would result in data rates of ~ 8Mb/sec and for a relatively small 500 x 500 pixel image would generate 2Tb of data.

4 SPECIAL BEAMLINE REQUIREMENTS

As written in section 3 of this report, there are several special requirements this beamline has to comply with. They are described there in detail, therefore here only found as a bulleted list.

- Air temperature control (± 0.1 °C; 10 nm/1 cm)
- Baffled air flow to minimize air currents
- Particulate filtering (possibly HEPA filtering for instrumentation area)
- Signal patch panel (BNC, HV, RS232, ethernet, etc.)
- Experimental gas farm and station patch panels with flowmeters (He, N2, Ar)
- LN2 tap (detectors, cyro-stage)
- Chilled water panel
- Compressed air
- Video monitoring
- Floor access (mobile rather than overhead)
- Floor fiducials

A significant part of future experiments could deal with materials under extreme environments, especially with radioactive samples. Nuclear fuels, containment and waste management are just a few keywords. Therefore, the beamline should be able to handle this kind of material.

5 FUTURE UPGRADE OPTIONS

Only the KB branch of the SRX beamline is in the original scope of project beamlines at the NSLS-II. It is of course desirable to build up the ZP branch within the same timeframe. The advantages would be from the construction side not to interfere with later user activities at the KB branch and from the experiments side the access to a high resolution station where lower energies and thus important elements such as phosphorus, sulfur and calcium are in reach simultaneously to experiments at the KB branch.

APPENDIX 1: SCHEDULE

This Conceptual Design Report will be finished	September 30,2009.
Work on the Preliminary Design Report will begin	October 1, 2009,
and will be finished	October 1, 2010.
Approval of long-lead time procurement will be given	November 3, 2010.
Work on Final Design Report will start	October 4, 2010.
The final design of major components will be ready	April 14, 2011,
and the full report will be finished	February 7, 2012.
Long lead time procurement will begin	January 11, 2011,
and should be finished	November 5, 2012.
Procurement will start	April 20, 2012,
and should end	August 14, 2013.
Beneficial occupancy of the experimental floor will be possible	February,2012.
Installation will start	February 10, 2012,
and should be complete	January 07, 2014.
Sub-system testing will begin	May 15, 2012,
and will be done	February 03, 2014.
Integrated testing will start	August 19, 2013,
and will finish	May 27,2014.
All beamlines should be available for commissioning	May 27, 2014.

Intentionally blank.

APPENDIX 2: REFERENCE DRAWINGS

The following drawings are provided here for reference:

1 Beamline layout in legal format

LT-XFD_CDR_XPD-00119

NSLS-II Project

CONCEPTUAL DESIGN REPORT for the

X-RAY POWDER DIFFRACTION BEAMLINE AT NSLS-II

final draft Sep 2009

Intentionally blank.

Approvals and Reviewers

Compiled by	**Signature**	**Date**
Eric Dooryhee, XPD Beamline Group Leader, NSLS-II		
Reviewers		
Simon Billinge, BAT Spokesperson, signing on behalf of the BAT		
Andy Broadbent, Beamlines Manager		
Nicholas Gmür, ESH Coordinator, NSLS-II		
Sushil Sharma, Mechanical Engineering Group Leader, NSLS-II		
Approvals		
Qun Shen, XFD Director, NSLS-II		

Document Updates

The Conceptual Design Report for the Beamlines Infrastructure at NSLS-II is a controlled document, revised under change control.

Version No.	Date	Authorized by	Changes made
A	9/30/2009	E. Dooryhee	Final release
1	10/1/2009		final draft, submitted to BAT

Intentionally blank.

Contents

1. INTRODUCTION 1
   - 1.1 Scientific Issues 1
   - 2.2 Beamline Advisory Team (BAT) 1
   - 1.3 Representative Experiments 2
   - 1.4 Acknowledgments 2
2. BEAMLINE LAYOUT 3
   - 2.1 Overview 3
   - 2.2 Insertion Device 6
   - 2.3 Front End 9
   - 2.4 Optical Layout 11
     - 2.4.1 Main Branch 16
     - 2.4.2 Side-Branch 16
     - 2.4.3 Sector Layout 16
   - 2.5 High Heatload Optics 16
   - 2.6 Major Components 18
     - 2.6.1 Horizontal Deflecting Side Bounce Monochromator 19
     - 2.6.2 Sagittally-Focusing Double-Crystal Laue Monochromator 20
     - 2.6.3 Focusing optics 22
   - 2.7 Summary of Beamline Performance Specifications 24
3. END STATION INSTRUMENTATION 25
   - 3.1 High Energy X-ray Detectors 26
   - 3.2 High-Resolution Analyzer Stage 26
   - 3.3 Software Development 27
   - 3.4 Complementary Experimental Stations 27
   - 3.5 Sample Environment 28
4. SPECIAL BEAMLINE REQUIREMENTS 29
5. FUTURE UPGRADE OPTIONS 30
6. SUMMARY 31
7. REFERENCES 32

APPENDIX 1 SCHEDULE 33
APPENDIX 2 REFERENCE DRAWINGS 34
APPENDIX 3 REPRESENTATIVE EXPERIMENTS 38
APPENDIX 4 THERMAL CALCULATIONS 40
APPENDIX 5 LAUE MONOCHROMATIZATION 42
- Horizontal Deflecting Side Bounce Monochromator 42
- Sagittally-Focusing Double-Crystal Laue Monochromator 43

APPENDIX 6 REFRACTIVE OPTICS 46
APPENDIX 7 DETECTOR DEVELOPMENT 47

Acronyms

Be	beryllium
CDR	Conceptual Design Report
CO	Lead Collimator
CRL	Compound Refractive Lens
DLCM	Double Laue Crystal Monochromator
ES	End Station
EXAFS	Extended X-ray Absorption Fine Structure
FAPM	Fixed Aperture Mask
FE	Front End
FEA	Finite Element Analysis
FGV	Fast Gate Valve
FOE	First Optics Enclosure
FZP	Fresnel Zone Plates
HOPG	Highly Oriented Pyrolytic Graphite
NMR	Nuclear Magnetic Resonance
PDF	Pair Distribution Function
SBM	Side Bounce Monochromator
SGV	Slow Gate Valve
SS	Safety Shutter
XBPM	Photon Beam Position Monitor

1. INTRODUCTION

1.1 Scientific Issues

The primary purpose of this beamline is the quantitative characterization of the atomic structure of complex materials; not just carefully-prepared ideal systems, but materials as they are actually used. Detailed knowledge of atomic structure is a prerequisite to understanding material properties, and essential in any rational materials design and synthesis effort. Development of meaningful structure/property correlations requires simultaneous measurement of structure and properties.

The scientific grand challenge is to obtain robust and quantitative (micro)structural information about materials that are complex, nanostructured and often heterogeneous. As well as studying structure in the ground state at ambient conditions, it is increasingly important to study structure in systems that are evolving in time (for example, after excitation or while undergoing chemical reaction), and materials that are in a metastable state. These situations are becoming the norm rather than the exception in frontier science and technology, but we are far from having robust tools for studying structure in such systems. Finally, an important scientific goal is the study of materials under extreme conditions of temperature, pressure, magnetic/electric/stress field, chemical environment, etc. Such study presents special challenges to the experimentalist, not only in generating the extreme conditions, but in getting the x-ray probe into and out of the apparatus.

The proposed X-ray Powder Diffraction (XPD) beamline will provide unique capabilities for addressing these problems, and is designed with Total Structure Studies in mind. High-throughput, high-resolution powder diffraction (with well-defined peak shapes and extremely low background) will be carried out using hard x-rays, with a beam size (tens to hundreds of microns) adjustable to match the graininess and heterogeneity scales. The need for high resolution applies either in reciprocal space or in direct space or more rarely in both. The combination with a complementary parallel operation side-station for high-throughput, high-Q, Pair Distribution Function studies (also with small beams) will permit determination of both long- and short-range structures. Moreover the beamline will pay special attention to sample environments, allowing for time-resolved and in situ measurements.

The XPD beamline will build upon active programs at the NSLS (and elsewhere), concentrating on higher energies (40-100 keV). In conventional x-ray diffraction, any energy greater than 20keV is considered exotically high. The beamline must address future scientific challenges in (for example) hydrogen storage, CO2 sequestration, advanced structural ceramics, catalysis, and materials processing—all in situ/in operando experiments difficult at other national user facilities. The beamline will also be of novel optical design, making use of techniques and instrumentation pioneered at the NSLS (Laue monochromators and Ge strip array detectors), as well as being perfectly matched to the high flux of a full 7m NSLS-II damping wiggler.

2.2 Beamline Advisory Team (BAT)

The XPD Beamline Advisory Team (BAT), formed in March 2008, is a group of expert scientists with common interest and experience in the XPD scientific program and the beamline optics and endstations needed to carry out this forefront program. The members are as follows:

Simon Billinge (spokesperson)	Columbia University and BNL
Peter Chupas	Argonne National Laboratory
Lars Ehm	Stony Brook University
Jon Hanson	Brookhaven National Laboratory
James Kaduk	Poly Crystallography Inc.
John Parise	Stony Brook University
Peter Stephens	Stony Brook University

Sign-up agreement between NSLS-II Project Director Steve Dierker and the Beamline Advisory Team, 11/24/2008.

1.3 Representative Experiments

The source for the beamline will be a full length 7m long damping wiggler to obtain the highest possible flux in the desired energy range of 40-100keV, with optimization at ~50keV and ~80keV. The advantages of hard x-rays are the ability to penetrate thick samples and environmental chambers, to provide access to a larger portion of reciprocal space, and to access reciprocal diffraction vectors Q as large as 60Å^{-1}. The scattering geometry is also simplified because of the large Ewald sphere and allows for transmission diffraction. Most importantly, absorption corrections are minimal and yield more accurate diffracted intensities.

Recent examples of high-energy x-ray research include measurements of stress/strain in materials, powder diffraction of compounds containing heavy elements, diffuse scattering of defects in complex oxides, high/small-angle scattering from thermal-barrier coatings, imaging and tomography. In short, the major proposed XPD beamline scientific program areas are:

- Complexity and the nanostructure problem
- Extreme environments
- Time resolved studies
- Total structure studies

In particular, next-generation technologies will place increasing demands on materials, requiring enhanced functionality and performance under extreme environments. The ability to design functional materials at the atomic level, taking advantage of new synthetic approaches and computational modeling, unavoidably requires dedicated characterization tools with an increasing level of sophistication and hardware/software integration. Specific examples are given in Appendix 3.

1.4 Acknowledgments

All BNL staff below are acknowledged for help, support, and discussion and for providing relevant material (calculations, figures, drawings, etc.). ACCEL (now Bruker) is also thanked for providing the preliminary case study and design for the XPD project beamline.

Qun Shen, Director, Experimental Facilities Division (XFD), NSLS-II, BNL

Lonny Berman, Head of the Beamline R&D Section, Experimental Systems Division (ESD), NSLS, BNL

Andy Broadbent, Beamlines Manager, XFD, NSLS-II, BNL

Mary Carlucci-Dayton, Mechanical Engineer, XFD, NSLS-II, BNL

Oleg Chubar, Beamline Scientific Support, XFD, NSLS-II, BNL

Lewis Doom, Mechanical Engineering Division, NSLS-II, BNL

Kenneth Evans-Lutterodt, physicist, ESD, NSLS, BNL

Konstantine Kaznatcheev, Beamline Scientific Support, XFD, NSLS-II, BNL

Paul Northrup, physicist, Environmental Sciences Department, BNL

Viswanath Ravindranath, Mechanical Engineering Division, NSLS-II, BNL

Kathleen Robinson, Editor, NSLS-II, BNL

Xianbo Shi, intern, NSLS-II, BNL

Peter Siddons, Head of the Detectors Section, ESD, NSLS, BNL

Zhong Zhong, physicist, ESD, NSLS, BNL

Much of the required design and engineering work is performed in a "centralized" fashion, involving the whole suite of six project beamlines and the anticipated 50+ beamlines. This routinely involves tight collaborations between the scientific and engineering staff across the Experimental Facilities Division and the entire NSLS-II project. The design of the baseline front ends was performed, for instance, by the Mechanical Engineering Group in the Accelerator Systems Division. The beamline also uses resources from the same group for tasks such as FEA simulations, synchrotron and bremsstrahlung ray tracing, etc.

2. BEAMLINE LAYOUT

2.1 Overview

The technical design issues are:

- Energy range 50-90keV
- Energy resolution (mode 1: $\Delta E/E \sim 2 \times 10^{-4}$; mode 2: $\Delta E/E \sim 1 \times 10^{-3}$)
- Intensity ($>10^{13}$ photons/sec/0.1%BW)
- Flexibility of focal lengths and sizes (2mm-500μm, down to 10μm)
- Beam stability (intensity and position)
- Low background and high filtering of forward, parasitic scattering and of low energy photons
- Employ proven technology whenever possible
- Ease of use
- Independent operation (shuttering) for the different hutches

The x-ray optics and beamline layout, shown in Figs. 1 and 2, are designed to operate two independent branch lines simultaneously. The angle deviation between the two beam axes is ~7.5 degrees, depending on the setting of the first monochromator. The first (upstream) endstation (ES1) covers most powder diffraction measurements, while the second endstation (ES2) is specialized in more elaborate/complex setups (large pressure cells, non routine reaction chambers, combined spectrometry, gas handling, user-defined specific devices). The downstream side station (ES3) will operate at a fixed high energy with very limited adjustability, and focuses on total scattering measurements over a large Q range. One main beamline target is the study of real samples in real time and in real conditions. By using a modular design for the endstations, special environments can be designed and inserted at different locations into the beamline with compatible interfaces. It is important all stations share the expertise, equipment, and software, and be operated more as a single entity. This is the reason why the floor occupation plan of the beamline allows us to easily move equipments and samples back and forth, in particular between ES1 ("standard" powder diffraction) and ES3 (PDF). The considerable divergence of the wiggler source, its high power output, and the low reflection angles in the x-ray high energy range are carefully handled in the present proposal: all three features put additional constraints on the optics and overall performance.

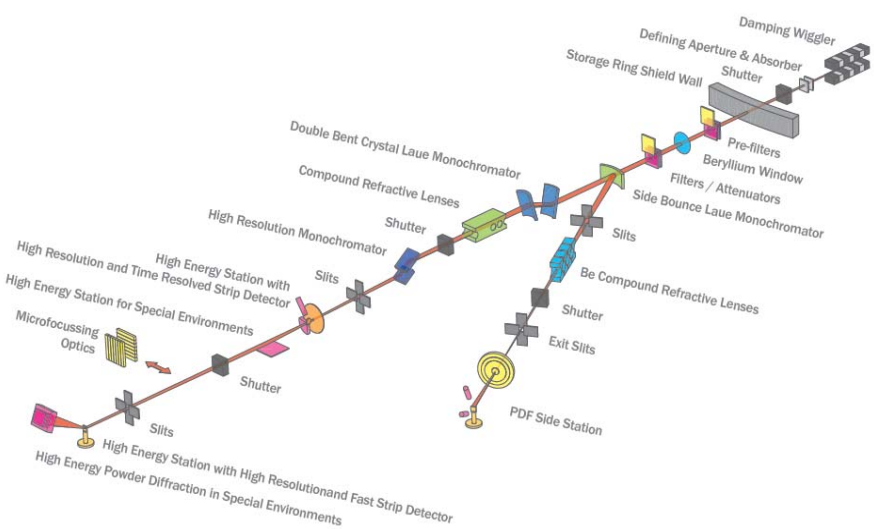

Fig. 1. Schematic layout of the beamline.

The horizontal radiation fan is more than 2mrad wide (FWHM). Focusing of the x-rays is thus crucial to collect the large fan in order to increase the available flux at the sample. Recent developments in sagittal focusing Laue optics make it possible to focus a large divergence of high-energy x-rays. The DOE review committee in June 2009 strongly recommended to "*include secondary optics into the design of the XPD beamline to provide 1-2micrometer focus.*" The DOE committee underlines: "Adding such optics should not have a significant impact on the beamline design while greatly broadening the user base for experiments that can be performed at the beamline. One example is the use of high-pressure cells." We are therefore carefully considering the ability to tune the beam size at will, in particular to resolve some particular inhomogeneities or for diffraction mapping. We propose here to achieve this goal by combining the sagittally bent double-Laue monochromator with CRL-based optics. A set of accurate hard x-ray slits and secondary focusing optics in hutch ES2 should allow a 10μm focus; this would be exceptional at these energies, and particularly suited for layered structures and heterogeneous compounds. The present design is provisioned for optimizing the beam size and beam intensity with 4 distinct focal lengths: at the sample or at the 2D detector either in hutch ES1, or in hutch ES2.

Fig. 2. Conceptual layout for the powder diffraction beamline. Top image, view from above. Scale 1/50.

2.2 Insertion Device

The powder diffraction beamline will be located at the damping wiggler source DW90 (12.5mm fixed gap), in a high-β straight-section of the NSLS-II ring. Unlike the NSLS-II undulator, bending-magnet and 3-pole wiggler sources, the NSLS-II damping wiggler extends the range of x-ray energies well beyond 50keV, thus allowing the study of samples under real conditions, i.e. in environmental chambers. This requires a dedicated strategy for handling the exceptional power output as well as significant shielding and thick enclosure walls. The power output of 65kW is unprecedented for a permanent magnet wiggler (the APS sector 11 wiggler produces 8kW for K=14, SPring-8 BL08W wiggler produces 14kW for K=10). The power density is about half that of the 14mm period superconducting undulator at its highest K. Power reduction (filtering) and high heat load optics merit careful investigation (see section 2.5).
The basic parameters for the damping wiggler source used in this design are shown in Tables 1 and 2.

Table 1. NSLS-II Machine and Damping Wiggler Parameters.

Electron energy, Eo	3 GeV
Electron current, Io	500 mA
Number of periods	70
Period length, λu	9 cm
Magnetic field	1.85 Tesla
Deflection parameter, k	15.8
Critical energy	10.8 keV

Table 2. RMS Electron Beam Values at the Center of the High-β Straight Section (9.3m).

Horizontal electron beam size, σ_x	137 μm
Vertical electron beam size, σ_z	4.9 μm
Horizontal electron beam divergence, σ_x'	6.6 μrad
Vertical electron beam divergence, σ_z'	1.6 μrad

Figs. 3 and 4 show the flux per unit horizontal angle and brightness values for the various NSLS-II sources. Fig. 4 shows the flux and brightness and compares the NSLS-II damping wiggler source and the existing NSLS X17 super-conducting wiggler (at the high-pressure diffraction beamline). The NSLS-II damping wiggler source exceeds the X17 source output and thus makes the proposed high-energy high-resolution powder diffraction beamline at the NSLS-II machine a very powerful facility.

Table 3. Brightness and flux of the Damping Wiggler source at NSLS II.

keV	Brightness (ph/sec/0.1%BW/mrad^2/mm^2)	Flux (ph/sec/0.1% BW/mrad)
40	6.8×10^{17}	4.5×10^{14}
60	1.7×10^{17}	8.8×10^{13}
80	3.8×10^{16}	1.7×10^{13}
100	7.9×10^{15}	3.1×10^{12}

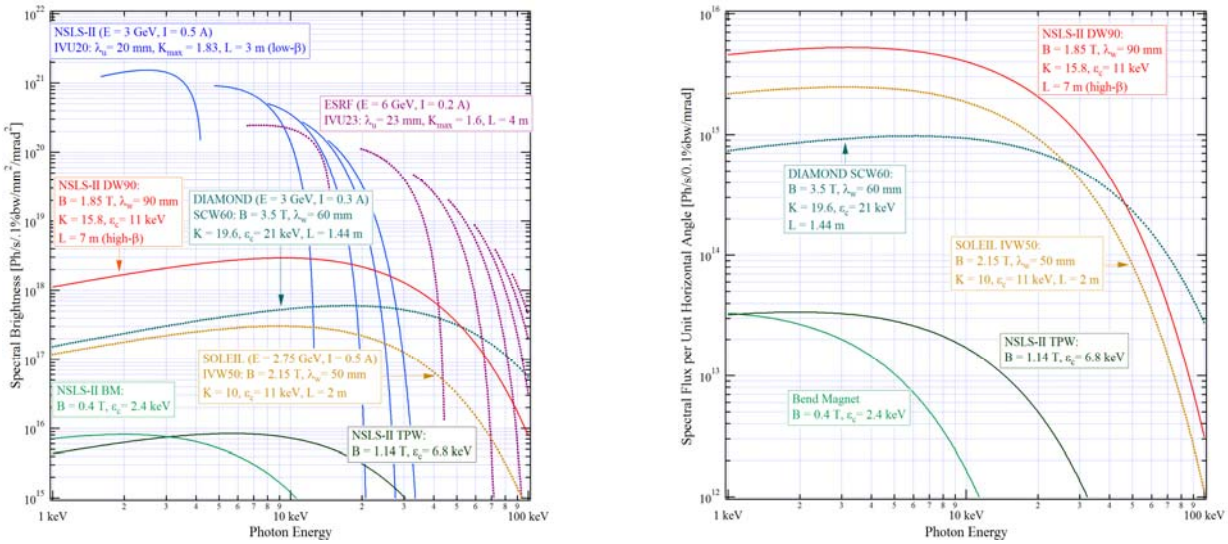

Fig. 3. Comparison of spectral brightness and spectral flux per unit of horizontal angle. (O. Tchoubar, NSLS-II)

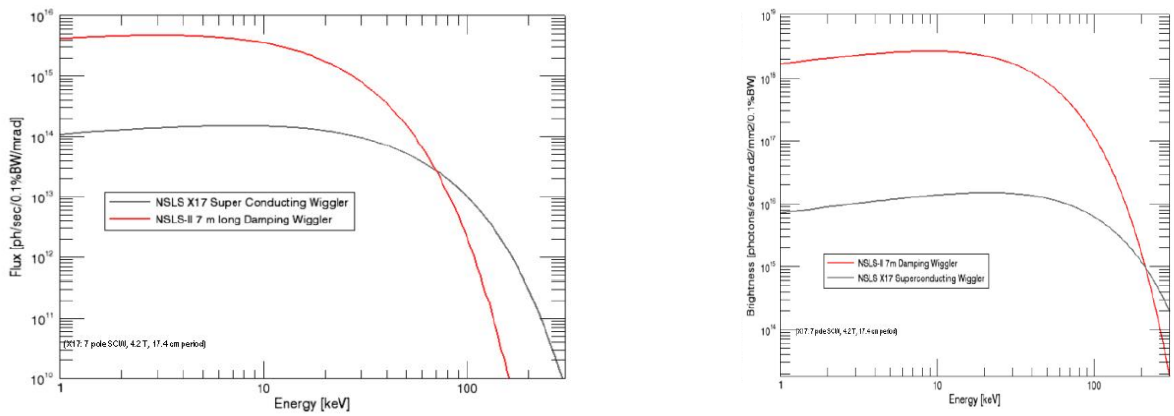

Fig. 4. Flux and brightness comparisons between the NSLS-II 7m-long DW source and the NSLS super-conducting wiggler.

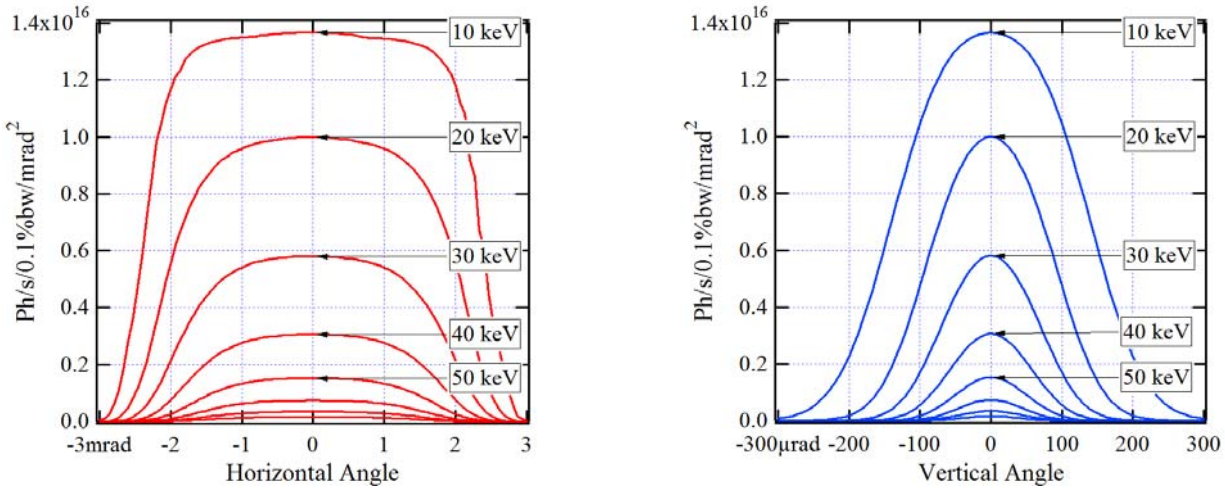

Fig. 5: Horizontal (left) and vertical (right) angular Profiles of DW Emission at Different Photon Energies. (O. Tchoubar, NSLS-II)

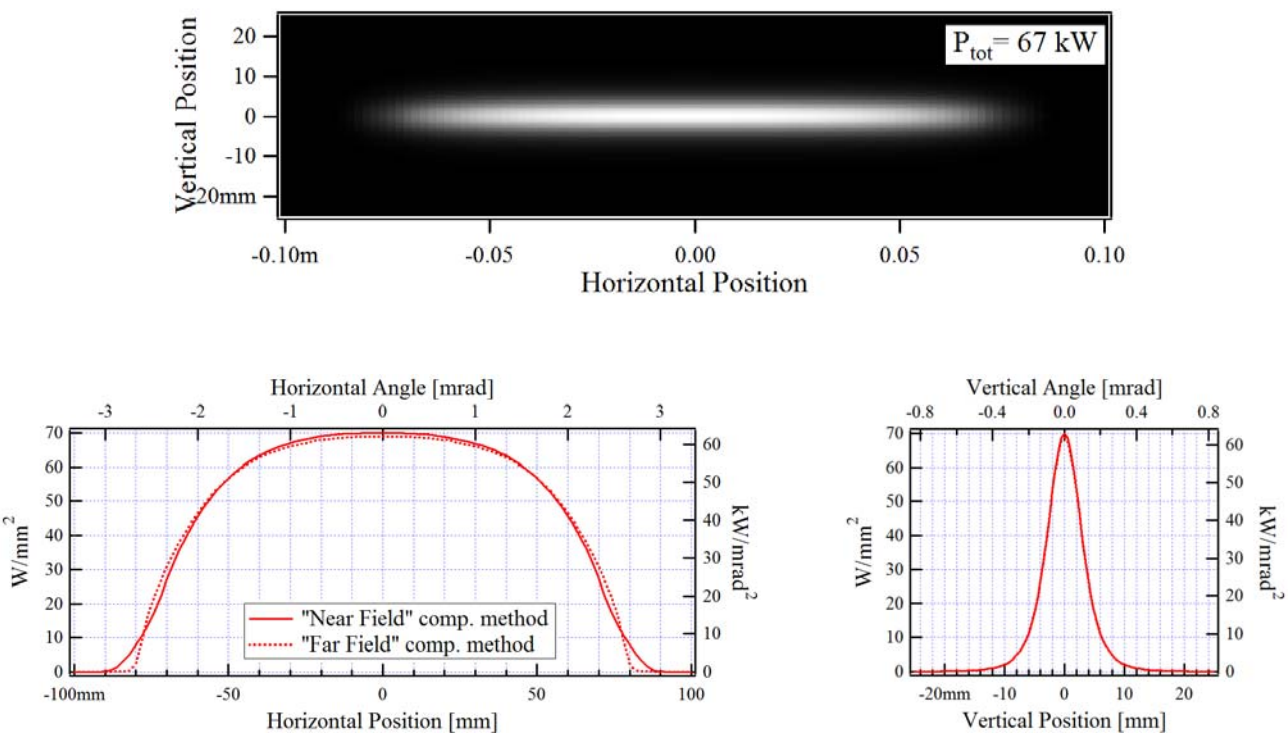

Fig. 6. Power Density Distribution in Transverse Plane at 30 m from Center of Straight Section. (O. Tchoubar, NSLS-II)

2.3 Front End

A layout of the standard NSLS-II front-end is shown in Fig. 7 and in appendix 2, and comprises: slow gate valve (SGV); fixed aperture mask (FM); photon beam position monitor; lead collimators (LCO and RCO); fast gate valve (FGV); safety shutters (SS, BMPS and PS); X,Y slits (XYSLT). The layout is shown in Appendix 2.

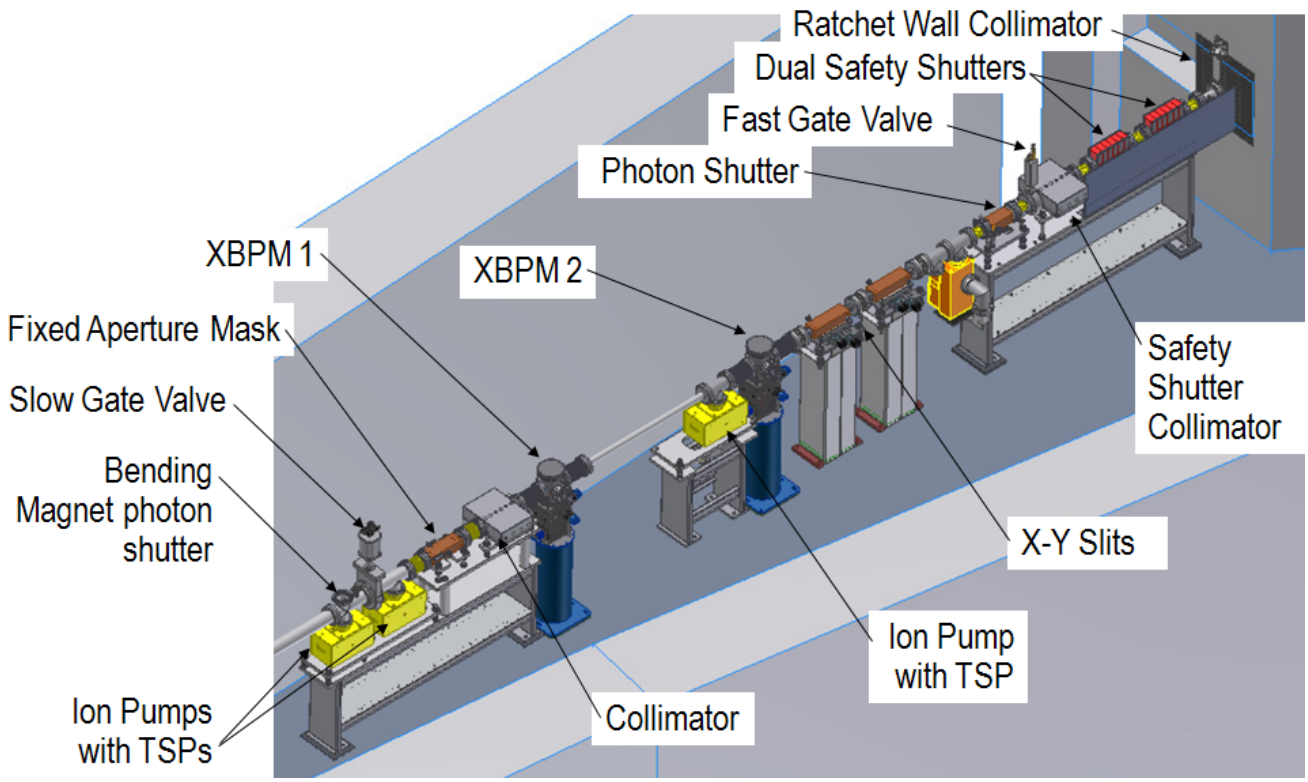

Fig. 7. Typical Front End Configuration at NSLSL II.

The basic configuration of the Damping Wiggler Front End is similar to the In-Vacuum Undulator front ends but must be able to accept the higher heat load and increased beam size. An absorber capable of trimming the sides of the damping wiggler beam will be mounted on the outlet of the bending magnet vacuum chamber immediately upstream of the Front end. This absorber is required to trim the beam from ±2.6mrad down to below ±1.7mrad in order to allow it to pass the sextupole and quadrupole magnets at the upstream end of the storage ring section four girder assembly. A maximum drift pipe size of 1.75" OD is allowable in this area.

The Front End Fixed aperture mask will be constructed as two masks in order to simplify manufacturing of the assembly. When trimming the beam from 3.4mrad down to the specified 1.1mrad, the mask will absorb 55kW of power. 60cm of length at a 1.6 degree angle in the vertical direction and 3.9 degree angle in the horizontal direction is required to keep the water cooled Glidcop surface below 315°C.

The absorber is cantilevered from the upstream flange to allow thermal expansion during bakeout. A formed bellow will be mounted between the masks to allow for alignment and thermal movement during bakeout.

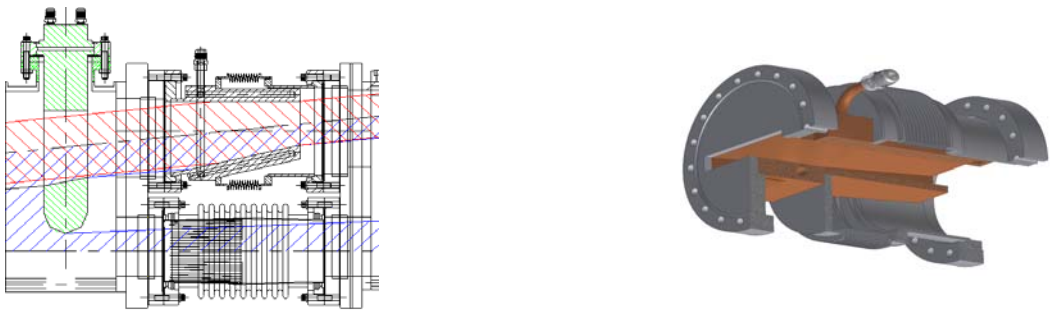

Fig. 8. Principle of the Glidcop wiggler absorber.

In Fig. 9, the thermal calculations show a peak power density ~ 200W/mm^2 at the mask, corresponding to a peak temperature ~315 °C.

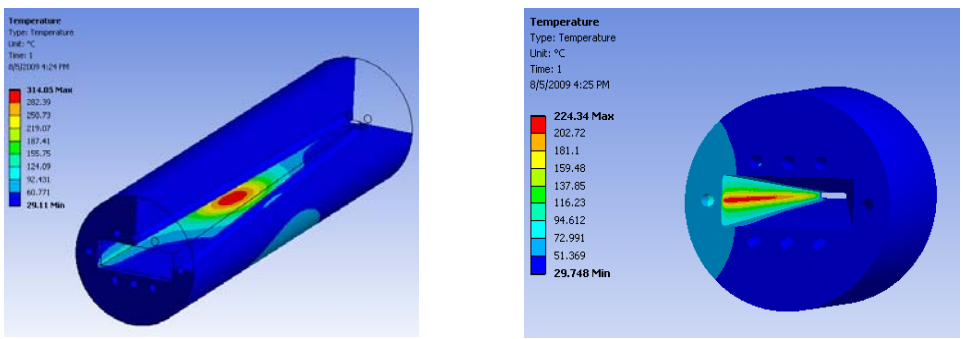

Fig. 9. Thermal calculations on the glidcop mask. (Courtesy of V. Ravindranath)

A pair of white-beam X-Y slits is located immediately down stream of the second XBPM, to further reduce power loads and reduce the angular acceptance, if required. These slits will increase in length and aperture in order to accept the damping wiggler beam. In addition to the increased size of the Glidcop slit bodies the stages supporting the slit assemblies require larger horizontal strokes.

The Photon shutter length will be increased from 20cm for an Undulator Beamline to 30cm and the horizontal aperture will increase from 20mm to a minimum of 39mm. The same actuator and position sensors will be used as on the Undulator front ends to reduce spare part requirements.

The Lead collimator length does not change but the horizontal aperture increases from 20mm to 36mm.

The safety shutter aperture will be increased from 21mm to 38mm. In addition to the primary aperture the edge welded bellows will be increased in size to 1.5” ID. Prior to final design of the damping wiggler safey shutter, cycle tests will be completed to confirm the fatigue life of the larger bellows.

Preliminary Front End X-Ray tracings have been developed for the Damping Wiggler Beamline to confirm the apertures and locations of the various front end components. The horizontal Ray tracing is shown in Appendix 2.

The effect of vertical aperturing on the overall spectral distribution and power output is shown in Fig. 11.

2.4 Optical Layout

The layout of the beamline consists in two branches and three endstations (see referenced drawings in Appendix 2).

- The first endstation will allow high energy powder diffraction studies to be conducted. A range of sample environments will be provided, and the emphasis will be on maximizing the throughput of the station; a robot will be included to assist with this and software developed for on-line data pre-analysis and quick assessment of the data. The data collection strategy and the continuation of the experiment need to be continuously guided by the on-line fast data-assessment.
- The second in-line endstation is for ´long setup time´ experiments. Beam will be delivered to the hutch, but the endstation is not fitted out within the Project scope. Much equipment for this station is expected to be transferred from NSLS and/or purchased with funds and grants from other sources.
- A parallel operating fixed energy side station for pair distribution function (PDF) experiments at ~80keV will be constructed. This equipment is not part of the present project scope either.

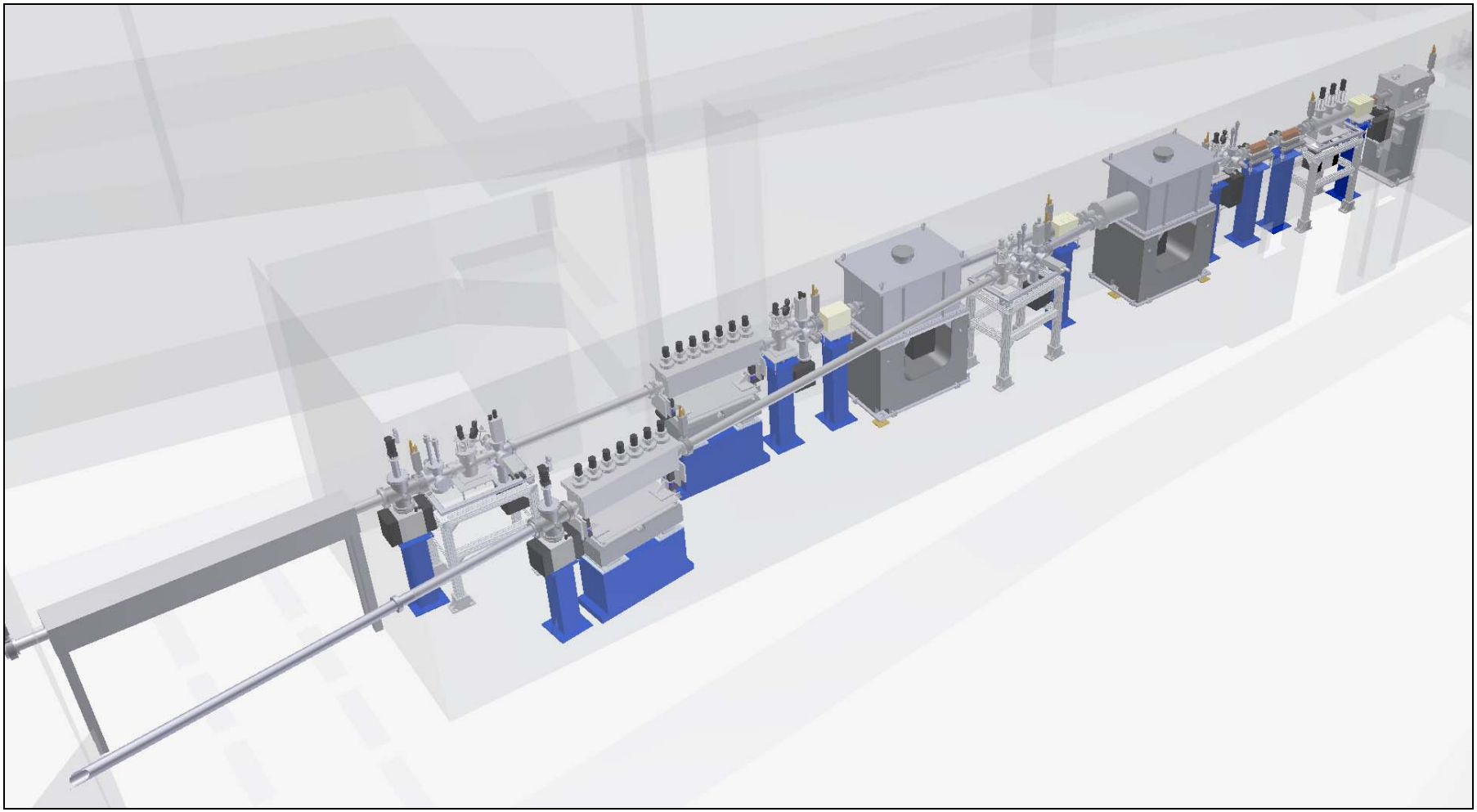

Fig. 10a. Conceptual layout for the powder diffraction beamline FOE.

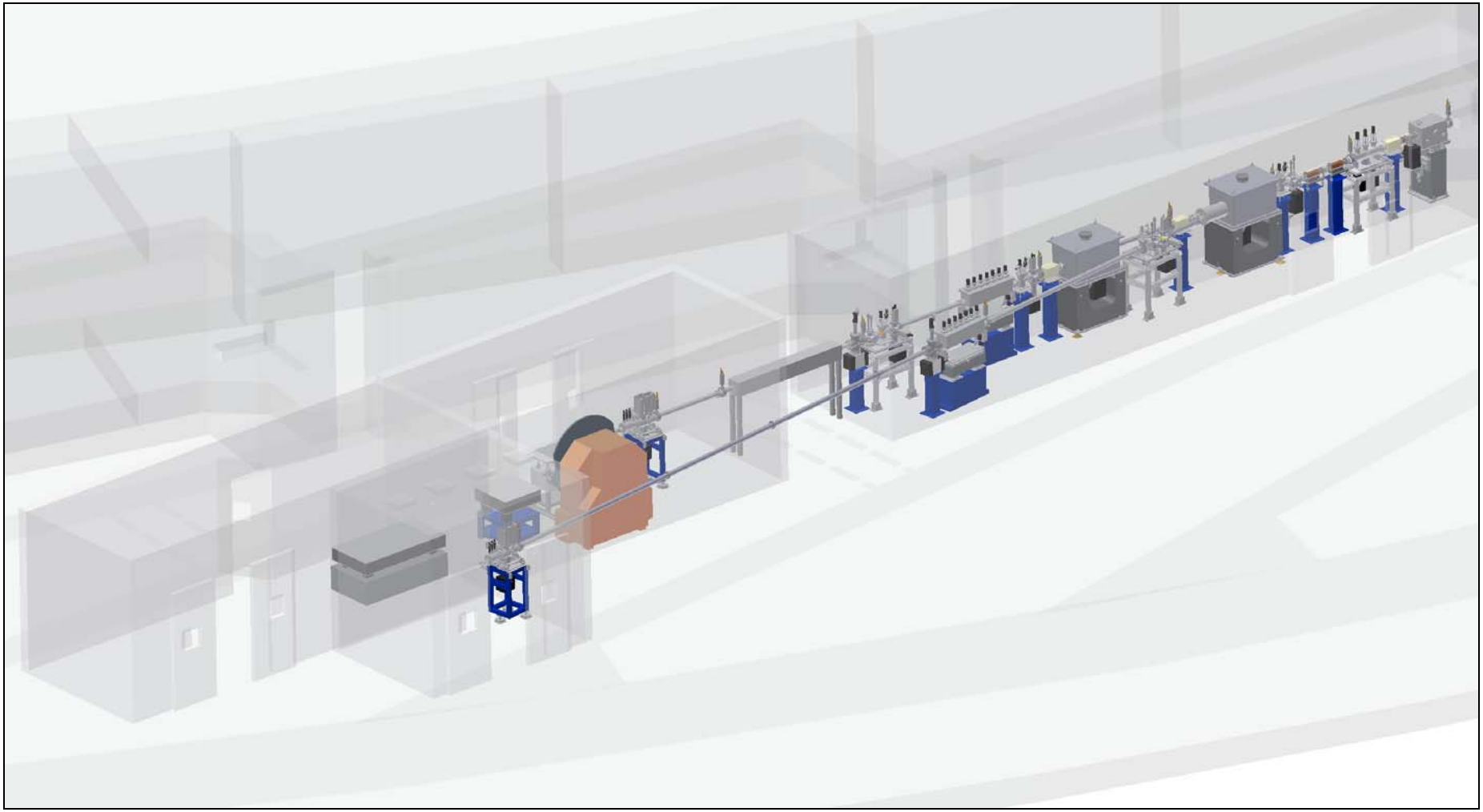

Fig. 10b. Conceptual layout for the powder diffraction beamline: FOE and all three endstations.

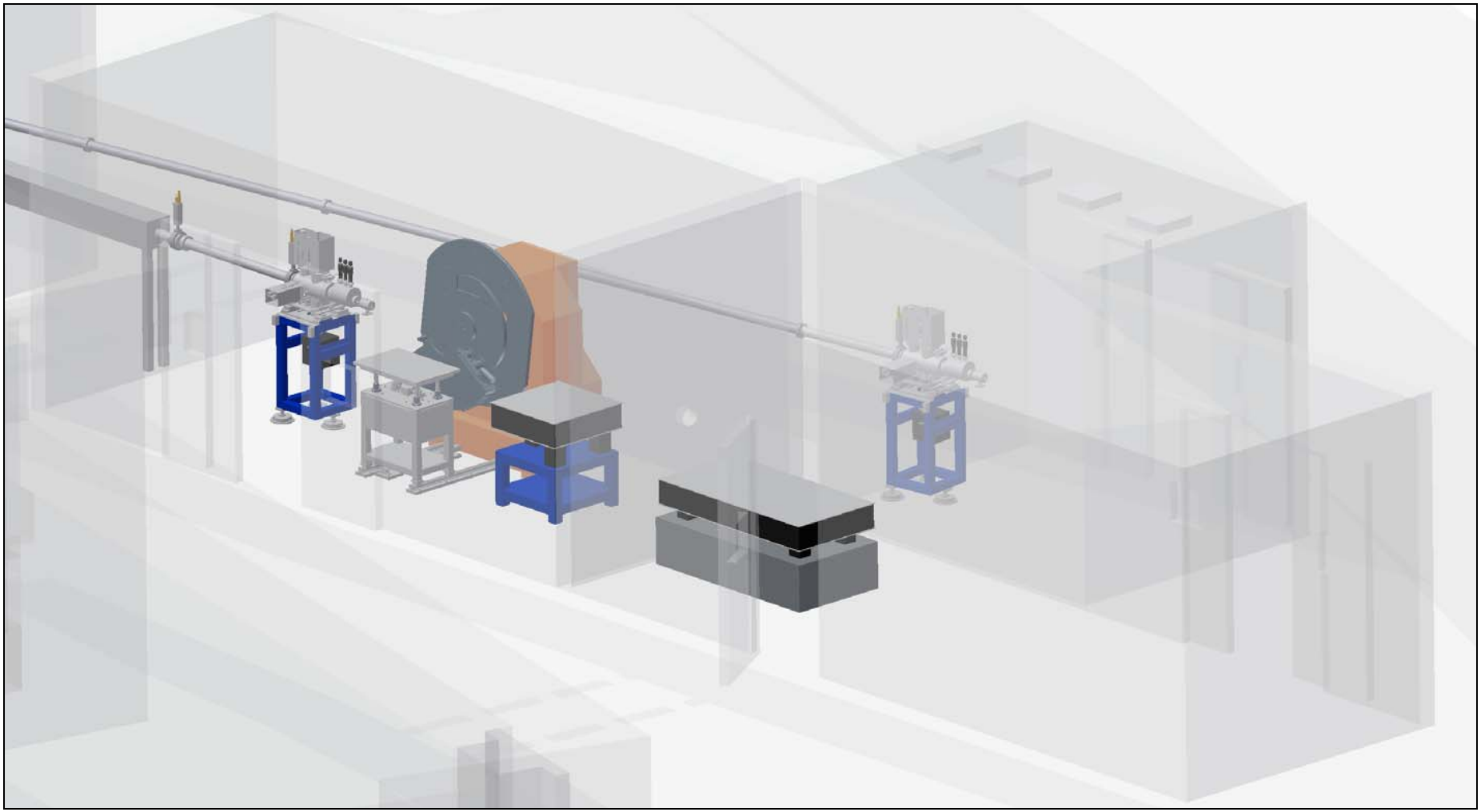

Fig. 10c. Conceptual layout for the powder diffraction beamline endstations.

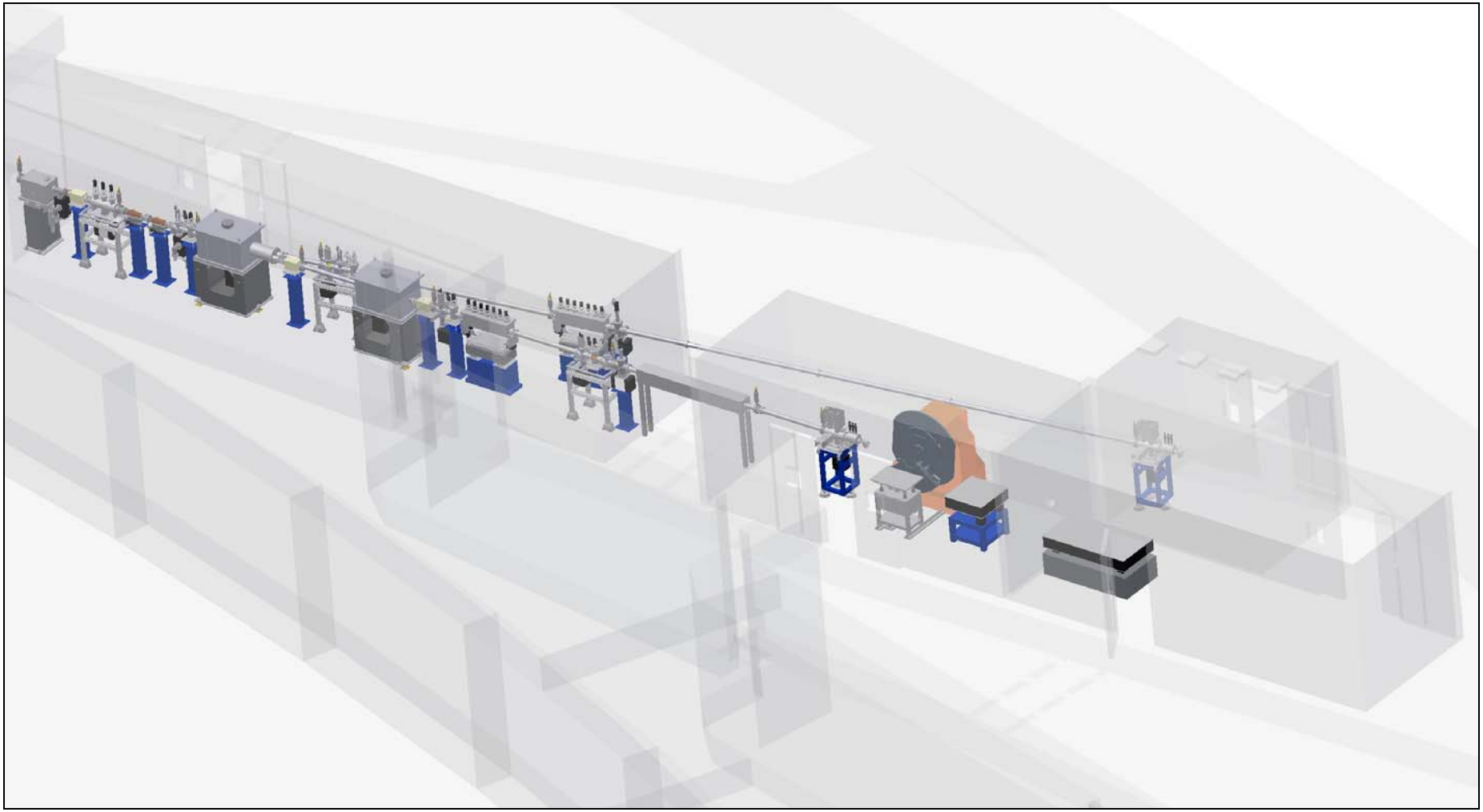

Fig. 10d. Conceptual layout for the powder diffraction beamline.

2.4.1 Main Branch

The upstream part comprises: the high-heat-load filter assembly combined with white beam slits. A single-bounce Laue monochromator, deflecting the beam sideways toward the PDF station, and a double Laue crystal monochromator (DLCM) operate simultaneously in the FOE. The DLCM geometry is based on proven technology used at NSLS at X17 and X7B (see section 2.6). The goal of the DLCM is to produce an horizontal focus with sagittal focusing around a photon energy of 40-60keV, and to deliver high flux in a small focus (less than 0.5x0.5mm^2) for small samples. The bent Laue system provides over an order of magnitude more flux, for lattice strain increases the integrated reflectivity by 1-2 orders of magnitude compared to perfect crystal. The anticlastic bending preserves a reasonable energy-resolution and increases the photon flux, given that all rays make the same incidence angle with respect to the crystal planes (the so-called Rowland condition). For many experiments, with a vertical scattering plane geometry, a beam divergence of the order of 0.1-0.2mrad at the sample and a 10^{-3} energy spread will be tolerable. Refractive optics is placed downstream and designed to either collimate or focus the beam in the vertical direction.

2.4.2 Side-Branch

A horizontally focusing Laue single-crystal monochromator produces a larger photon energy bandwidth which is related to the horizontal divergence of the beam (polychromatic focusing). The bandwidth then can be tuned by selecting an appropriate horizontal aperture. For a combination of good energy resolution and good focusing, a horizontally focusing Bragg monochromator would be better. The side-bounce monochromator will operate at a fixed nominal energy, typically 80keV. The Laue monochromator design has the option of implementing more than one crystal reaching different energies.

2.4.3 Sector Layout

The conceptual layout for the NSLS-II powder diffraction beamline is shown in Fig. 10 and in Appendix 2. The optical components are listed in Table 4 in section 2.6. Distances from the source are shown.

2.5 High Heatload Optics

Most of the thermal power of the wiggler source inherently is with the low energy spectrum (50% lies below the critical energy of 10.8 keV). *Reduction of heat load needs to be carefully considered*, addressing earlier requests from advisory/review committees for reduced technical risk. A lower power will always improve the performance of white beam optical components such as the Laue monochromators. In addition to severely *aperturing* and *filtering* the incident beam, appropriate cooling needs to be considered and integrated in the design of the white-beam optical elements (see section 2.6):

- the single Laue-crystal monochromator (section 2.6.1)
- the double Laue-crystal monochromator (section 2.6.2)

Fig. 11 shows the variation of the flux outputs at 50keV and 80keV as a function of the vertical opening, versus the total power output. It basically reflects the dependence of the vertical distributions on the x-ray energy. The nominal mask aperture is 1.1mrad × 0.22mrad, with the option to reduce the vertical aperture using the white beam slits in the FOE. A 0.22mrad vertical aperture of the mask lets all the 50keV photons through, given that the FWHM of the flux vertical distribution is 0.116mrad. A larger aperture increases the total power, but not the useful flux at 50keV. At 80keV, the useful vertical aperture is ~0.13mrad (FWHM of the flux vertical distribution is 0.09mrad). The horizontal aperture can usefully be reduced in order to keep the beam footprint on the crystal to a reasonable size.

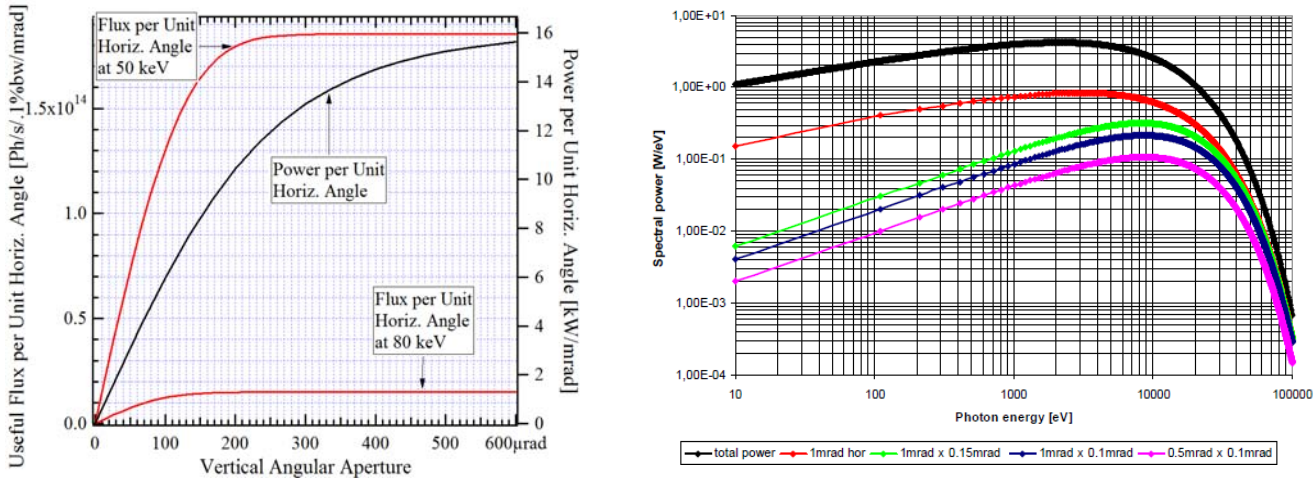

Fig. 11: (left) The variation of the flux outputs at 50keV and 80keV as a function of the vertical opening, versus the total power output; (right) The variation of the spectral power versus the aperture. The total power is: 65kW (full); 16.7kW (1mrad horizontal); 10kW (1x0.22mrad^2); 8kW (1x0.15mrad^2); 5.7kW (1x0.1mrad^2); 2.9kW (0.5x0.1mrad^2).

In hard x-ray beamlines, one typically uses a beryllium (Be) window to separate the beamline vacuum from the machine vacuum. Such a window has also the advantage that it absorbs a fraction of the unused low energy x-ray spectrum, therefore reducing the overall power on the downstream components. The 30x5x0.25mm^3 beryllium window is supported on an absorber with tapered walls, in a similar design as the FE mask. However, in a wiggler beamline such as NSLS-II DW 90 described in section 2.2, the calculation of the absorbed power indicates that a Be window in the direct white wiggler beam would simply fail: considering that the incident power is 10kW and the peak power density is 6.3W/mm^2, the calculated peak temperature in the Be window is at 890°C!

Due to carbon high thermal conductivity and mechanical stability, carbon foils are typically used as a protective filter material in front of the Be window. Our approach is to design a filter assembly that can be safely used to protect the vacuum isolation window, and that reduces the power levels on the optical components. Considering that the maximum acceptable temperature for Be is 100°C, the pre-filter is designed for reducing the incident power on the window by a factor of ~10. The upfront filters need to be very thin. 5µm of pyrolitic graphite absorb ~450W and the resulting peak temperature in the graphite foil is ~1160°C. As a first approximation, assuming the power absorption is kept constant in each foil, 20 foils are needed to reduce the incident power on the Be window from 10kW down to 1kW.

The current design of the pre-filter assembly is very similar to the setup already in use at several beamlines at NSLS (see thermal calculations in Appendix 4). It consists of a water-cooled frame that holds the different filters. The radiation-cooled foil is held in a tantalum frame, since it must withstand the extremely high contact temperature, and will become hot itself. The power then is dissipated into the surrounding environment and is absorbed by a water-cooled OFHC copper surface positioned around the tantalum frame. PT100 temperature sensors and IR pyrometers will be installed and interlocked. The final carbon filter combination has to be realized with a larger number of filter foils and a combination like the following one is a possible solution: 5 / 5 / 5 / 25 / 25 / 50 / 50 / 100 / 135 / 300 / 300 / 500 / 500 / 1000 / 1000 / 1000µm. The power density on the first foil is critical, while heat conduction and physical integrity under thermal stress limit the thickness. In case the first foil fails, the subsequent foil needs to hold the same power and should have a similar design.

As shown in Fig. 12, a set of carbon filters with a total length ≈5mm, located in the FOE, significantly reduces the heat load while decreasing the photon flux only by 19% and 17% at 50keV and 80keV, respectively.

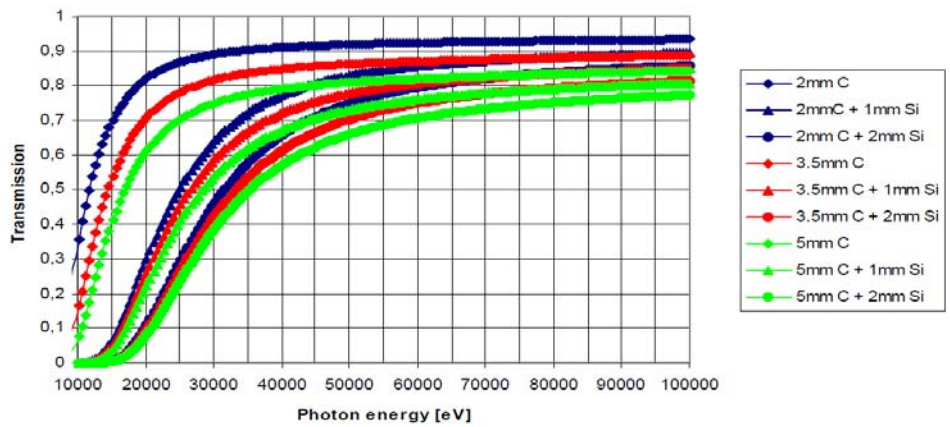

Fig. 12. Transmission of various filter combinations at the powder diffraction beamline.

After the pre-filter, the beam needs to be further attenuated to reduce the total incident power to a sustainable level (~200W). A combination of 5mm carbon, 0.25mm beryllium (vacuum isolation window) and 8mm silicon yields levels of absorbed power less than 30W that become manageable for white-beam x-ray optics. The photon flux changes by 64% and 46% at respectively 50keV and 80keV (see Appendix 4). The proposal for this beamline is to use one more fixed filter in a conservative approach for protecting the downstream optics, and one filter system that leaves the option of tuning the attenuation factor depending on the experimenter's needs. The attenuation must be adjustable in certain cases, for instance in the small beam operation mode or in case work at lower energies is required. The design of the first fixed filter, as in operation at ESRF-ID15, could consist of a water-cooled bulk rotating SiC disk. The second filter assembly consists in a controllable attenuator design and carries silicon foils of 2mm thickness each. This unit allows tailoring the power load on the optical elements to the right level of operational mode of the beamline. The water-cooled mounts are motorized and attached to a pneumatic drive.

2.6 Major Components

Table 4. The various components in the conceptual layout of the powder diffraction beamline.

Components	Distance from Source (m)
1. Front End Assembly (see appendix 2)	
2. Gate Valve (downstream of ratchet wall)	26.8
3. Pre-filter Assembly (graphite foils)	27.3
4. Beryllium insulation window	28.0
5. Bremsstrahlung Collimator	28.1
6. Second filter unit: limits the power load on the downstream optical components	28.9
7. White beam X,Y slits	29.3
8. White beam XBPM	31.0
9. White beam Fluorescent CVD screen	31.1
10. Horizontally diffracting monochromator (single Laue crystal): serves the side-branch for high-Q measurements	32.0
11. Sagittally focusing double-crystal Laue monochromator: wavelength selection, with the required band-pass	35.9
12. Bremsstrahlung stop	36.7
13. Monochromatic X,Y slits	37.5
14. Phosphor screen	37.6
15. Proposed location for 1D CRL: vertical divergence and demagnification tuning	38.5

16.	Monochromatic X,Y slits	40.8
17.	Fluorescent screen	41.1
18.	High precision BPM	41.4
19.	Safety shutter (monochromatic beam)	41.7
20.	End of FOE	
21.	Transfer tube, shielded, FOE to ES1	
22.	Hutch, EndStation 1	44.8
23.	Provisional place for second monochromator (for high-resolution operation mode)	45.1
24.	High resolution monochromatic slits	46.9
25.	Beam diagnostics, fluorescent screen	47.1
26.	Cartridge assembly: pinholes, filters, diode	47.5
27.	Exit window	47.6
28.	Ion chamber	47.8
29.	Multi-modal diffractometer in ES1 (white beam operation allowed)	48.9
30.	Support table for detectors	50.5
31.	Hutch, EndStation 2 (dedicated to long setups)	
32.	Provisional place for secondary focusing optics, used in conjunction with the CRLs	53.5
33.	Refractive Optics in branchline: 2D focusing	40.1
34.	Transfer tube, FOE to ES3	
35.	PDF side-banch station operating at 80keV (ES3)	

See referenced drawings in Appendix 2.

2.6.1 Horizontal Deflecting Side Bounce Monochromator

Horizontally focusing monochromators have been frequently used in the past (ESRF, APS, Spring8) to benefit from sources with a large horizontal divergence, like a bending magnet or a wiggler. The target photon energy for the side-bounce monochromator is beyond 80keV, while the Bragg angle will be almost fixed around 7.5 degrees (10% tunability) by the beamline geometry. Such a requirement implies the use of a high order reflection.
At the high-energy diffraction beamline at the APS, sector 11, there have been studies on horizontally diffracting Laue and Bragg monochromators [1]. A bent Bragg diffracting crystal is most suited to focus while preserving a narrow bandwidth of 10^{-3} [1]. However, such a crystal becomes very long at such a shallow angle, and it would not be practical to accept more than a 10mm wide beam (which represents a horizontal acceptance of only 0.3mrad).

In the case of Laue diffraction, the small Bragg angle is not a geometrical challenge any more: the length of the beam footprint on a Laue crystal is small and insensitive to energy. Although crystal bending preserves the natural bandwidth of the crystal to some degree while focusing a divergent beam, a white beam of large divergence on the monochromator typically implies a large energy band pass. As a consequence the bandwidth is much larger than the one obtained in Bragg diffraction. For instance, a beam divergence of 1mrad at a Bragg angle of 4 degrees produces a bandwidth of 10^{-2}. This bandwidth can be reduced to 10^{-3} when reducing the divergence to less than 0.3mrad. Appendix 5 shows our preliminary calculations. The monochromator is focusing on the slits located before the CRL assembly along the branch line. This forms a secondary source, which is re-imaged by the refractive optics at the sample position 14m downstream in ES3.

The proposed design of the monochromator assembly will ultimately need stability and reliability. The side-bounce crystal and mechanics will sit in a (UHV) vacuum vessel. A picture of a side-bounce monochromator from ACCEL is shown in Fig. 13. There is the possibility of implementing more than one crystal, leaving the choice of two

different pre-aligned crystal reflections for different energies. In such a case, one must consider a translation stage to swap between different crystals. Depending on the cooling design, that can be either a horizontal stage, or a vertical stage. On top of such translations we propose to build the rotation stages for theta (coarse), roll (coarse), and pitch (fine) (see table 5).

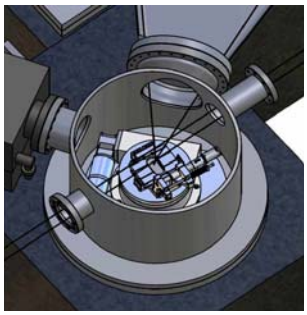

Fig. 13. CAD drawing of a side bounce monochromator. ® ACCEL-Bruker

Table 5. Possible Adjustments for the Horizontally-Focusing Single-Crystal Laue Monochromator. (Bending adjustments are not shown in this table.)

Movement	Range	Resolution	Repeatability
Whole optic assembly:			
Transversal (Y)	150 mm	≤ 0.1 mm	≤ 50 µm
crystal units:			
Roll rotation	-10 – 10°	≤ 10 µrad	≤ 20 µrad
Bragg rotation (θ_{coarse})	Full turn	≤ 10 µrad	≤ 20 µrad
Bragg rotation (θ_{fine})	± 50 µrad	≈ 0.01µrad	≈ 0.06" (uni-directional)

NSLS X17A side station (currently under design) is due to operate at 75keV and will be using a Si(311)<511> Si crystal ($\Delta E/E \approx 10^{-3}$ and angle deflection ≈7.4°). The 3mm × 3mm beam is expected to be focused to <0.5x0.5mm^2, using both the sagittal and the meridional bendings of the crystal mounted on a specially-designed two-axis bender. A silicon crystal on a cryo-cooled Glidcop bender (incident power is 40W) is being implemented at ESRF-ID24 (energy-dispersive EXAFS) with a 30:1 demagnification at 7keV. PETRA III (beamline P07) is also considering the horizontally deflecting Laue geometry for energies > 60keV [2]: the diffraction efficiency and bandwidth are controlled by a silicon crystal with either a Ge composition-gradient or a thermal gradient .

2.6.2 Sagittally-Focusing Double-Crystal Laue Monochromator

Sagittal focusing using Laue crystals was pioneered at NSLS [3-6]. The concept is shown in Appendix 5, and is increasingly used at high energy x-ray beamlines [7]. The focusing capability is similar to that of sagittal focusing by a Bragg crystal, except for a factor related to the asymmetry angle. This monochromator concept is very attractive at high energies for its flux, energy resolution, tunability and in-line-geometry properties. The good performance is imparted to some compensation effect whereby the second crystal significantly undoes the substantial brilliance degradation of the first crystal. In relaxing the bend radius of the first crystal, one finds an optimal setting where a much closer compensation occurs [8, 9].
From the current beamline geometry and distances, the demagnification ratios typically are 2.8:1 (ES1) and 2:1 (ES2), which would then give a theoretical spot size of ~60µm to ~100µm FWHM Ve.

From a first evaluation by Z. Zhong using crystal cuts with an asymmetry angle of 35.3°, it seems that a Si(311) reflection from a <100> crystal would be a good candidate at 80keV. A Si(311) reflection from a <511> crystal would be a good candidate for ≤ 50keV (see table 6). The resulting bending radii are feasible and a fixed beam

vertical offset of 20mm or more is possible. The exit beam offset has to be large enough (≥ 20mm) to provide enough clearance for bremsstrahlung shielding that is needed for personnel safety. Table 6 shows the expected flux and resolution depending on the choice of the diffracting lattice plane, crystal orientation, crystal thickness and crystal bend.

Table 6. Expected Flux and Resolution at NSLS Beamlines (Z. Zhong).

	(111)<100>	(311)<100>	(311)<511>	(111)<511>
thickness (mm)	0.4	0.4	0.6	
bending radius (m)	0.4	1.3	1.0	0.6
$\Delta E/E$ (10^{-3})	2.0	0.2	1.2	0.4
Flux (s^{-1})	5.4e+10	2.0e+09	5.6e+09	6.7e+09
		X17B1	X7B	

As seen in Fig. 14, the conceptual design consists of two pre-aligned crystal mounts with appropriate offset angles for operation. Starting from these positions, a fine tuning is available for the second crystal. The reduced Bragg angle tuning is maintained through a longitudinal translation of the second crystal having a linear attachment arm to the first crystal.

Fig. 14. NSLS Laue DCM designed by Z. Zhong.

The two sets of crystals will be sitting inside a UHV chamber, with a long lateral translation. Discussions with vendors even assume design the Laue monochromator for two or three energies, with lateral translation of crystals. It may be sensible to have one “central” setup with full tunability in bending, and side holders on kinematic mounts for “fixed” bending crystals with small adjustments possible (±5 keV). Interestingly, a single crystal bent and optimized for 80keV in the second downstream station will also focus at a lower energy in the first hutch, without changing the bend radius but only the Bragg angle.

Table 7. Possible Adjustments for the Sagittally-Focusing Double-Crystal Laue Monochromator. (Bending adjustments are not shown in this table.)

Movement	Range	Resolution	Repeatability
Whole optic assembly:			
Transversal (Y)	200 mm	≤ 0.1 mm	≤ 50 μm
2nd crystal units:			
Longitudinal (X)	300 mm	≤ 0.5 mm	≤ 1 mm
Roll rotation (χ_1)	-10 – 10°	≤ 10 μrad	≤ 20 μrad
Bragg rotation ($\theta 1_{coarse}$)	-5 – 35°	≤ 10 μrad	≤ 20 μrad
Bragg rotation ($\theta 1_{fine}$)	± 50 μrad	≈ 0.01μrad	≈ 0.06" (uni-directional)
(rotating table for the 1st crystal and cross links between the two crystals)			

As outlined before, the monochromator cooling should be carefully considered. Simple side-clamp water-cooling has shown to be inadequate through finite element analysis (FEA, see Appendix 5). Other simple methods (e.g., immersed in an In/Ga bath as in the designs at APS BESSRC CAT and ESRF ID11) are being considered before using much more demanding cryo-cooling techniques. Cryo-cooled Laue-Laue monochromator operates at APS 1-ID [7]. Similar principles could be used for XPD, if compatible with sagittal bending. Gravity fed cryocooling probably is a low-cost, low-technology, and probably an effective alternative for handling the temperature rise at the monochromator. The large acceptance (~100μrad) of the bent crystal is also relatively forgiving regarding the cooling efficiency.

In addition, the present layout is following the flexible approach taken at beamline APS 1-ID for achieving higher energy resolution, when necessary. Keeping the high resolution performance requires a low energy band-pass, typically 2×10^{-4}. This is not easily achievable with a monochromator in the Laue geometry. The current proposal is to fit the beamline with a channel-cut monochomator in ES1, which can be translated in and out of the beam. The large-bandwidth double-Laue monochromator (in the FOE) is thus followed with a high-energy/resolution monochromator (in ES1). Owing to the small (a few microradians) vertical angular acceptance of the high-resolution flat-crystal system, the beam divergence needs to be reduced by placing some collimating optics between the two monochromators (see description of the CRL in section 2.6.3). This method keeps the white beam optics fixed, and permits the subsequent high-resolution system to operate in a stable fashion without thermal load and in a more convenient room environment, where it can also be easily adapted. The monochromator at APS 1-ID consists in a four-reflection Si(111) crystal system resembling two channel-cuts in a dispersive arrangement, reducing the bandwidth to less than 10^{-4}. Another possibility under consideration is to keep the option of an additional set of unbent crystals to gain back the 10^{-4} resolution.

2.6.3 Focusing optics

High energy focusing with mirrors is extremely difficult due to the very small angle of reflection. Efficient focusing of hard x-rays using diffractive optics such as Fresnel zone plates (FZP) is limited by the ability to manufacture diffracting structures with small outermost zone width and large thicknesses. Stacked FZP or sputtered-sliced FZP can be considered, but refractive optics prove to perform better in the high energy range [10].

The purpose of one-dimensional compound refractive lenses (CRL) at this beamline will be to either vertically collimate or focus the beam at the sample. CRL are being used at other high-energy x-ray beamlines at the ESRF [11] and APS [7,8]. High energy x-ray operation overcomes the main weakness of the CRL, i.e. the attenuation of the beam through the CRL is no longer critical although a large number of lenses is required to accumulate a significant focusing effect. This relaxes the constraints on the fabrication of the lenses. At very high photon energies, the refractive index is small and therefore the preferred choice of material is silicon or aluminum instead of beryllium, or a combination of both. Approximately 15% of the available flux is absorbed at 50keV and 80keV through 5mm of Be.

Commercial CRL of high quality are available. Such lenses are shown in Fig. 15 from the Technical University of Aachen, Prof. Dr. Lengeler. Such CRL are simple to align, very stable, immune to vibrations and relatively forgiving for misorientation errors. It is recommended to use guard slits in front of the samples to avoid tails from imperfections (blurred focus etc.) and to minimize small-angle scattering halos.

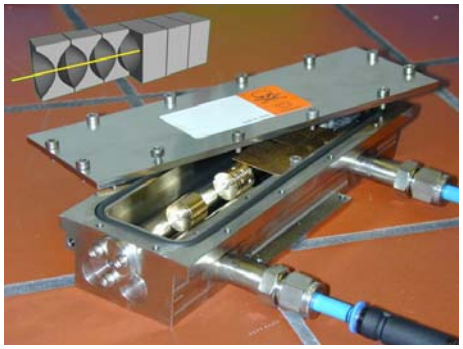

Fig. 15. Photo of the commercially available CRL setup of Prof. Lengeler, University of Aachen.

A tunable x-ray focusing apparatus based on CRL has been recently designed and tested at the ESRF (referred to as a transfocator [11]). By varying the number of lenses in the beam, the energy focused and the focal length can be varied continuously throughout a large range of energies and distances, e.g. focusing 50keV x-ray beam and partially collimating the 80keV photons. At ESRF-ID11, the transfocator is used either as a stand-alone instrument in both white and monochromatic beams to vertically focus, pre-focus or collimate the beam, or in conjunction with another focusing element downstream (CRL or multilayer mirror). Substantial gains in flux ($\geq 10^4$) are observed. In addition, the CRL can deliver a vertically-collimated beam, instead of a naturally diverging beam (0.1-0.2mrad), which better matches the acceptance of some secondary optics downstream (ES1), including a high-resolution monochromator or a secondary focusing device.

The current proposal is to use a similar design after the monochromators, consisting of highly flexible arrangements of pneumatic vertical actuators supporting a variety of cartridges containing filter foils, pinholes and masks, Al and Be lenses. The CRL are key components of the beamline which offer flexibility and different operational modes, without too much increasing the complexity of the optical setup:

- Routine work where focal length and focal spot size can be tuned
- High spatial resolution mode: the beam is sagittally focused by the Double Laue Crystal monochromator and meridionally by the CRL. An additional set of CRL or a multilayer placed closed to the sample in ES2 will tentatively produce a focal beam size of the order of 10μm.
- High 2θ resolution mode: the beam is collimated in the vertical diffraction plane, and impinges an optional channel-cut monochromator which is placed in ES1. Both the resulting low vertical divergence and low energy band pass (10^{-4}) will contribute into the resolution performance.

Those configurations are implemented at APS and ESRF [9,11], and we believe that they can be implemented at NSLS-II, for enhanced flexibility in flux/resolution and keeping the change in the setup configuration relatively easy and automated.
However, a significant drawback is the limited horizontal/vertical aperture (~1mm), which limits the gain in flux for long-focal-length (low demagnification) focusing. Table 8 shows the reduction in overall incident power and useful flux at 50 and 80keV, respectively, assuming the overall angular acceptance is ultimately defined by a 1mm effective aperture of the CRL at 30m and not by the mask in the FE. Parabolic Al lenses of 3.5mm H × 1mm V now become available.

Table 8. Reduction in Overall Incident Power and Useful Flux.

	1x0.22mrad^2	1x0.03mrad^2	0.03x0.22mrad^2
Total power (kW)	11	1.8	0.04
Flux (10^{14} ph/s/.1%bw) at 50keV	1.8	0.45	0.06
Flux (10^{14} ph/s/.1%bw) at 80keV	0.15	0.05	0.005

Alternatively, a 1m long Pt coated mirror at a glancing angle of 89.9427° (critical energy = 80keV) would ensure a good reflectivity and could also capture 0.03mrad of the vertical fan. Since it will be placed after the monochromator, a simple design (no heat load) can be considered with a substrate made of glass or metal. Multilayered mirrors $(W/B_4C)_{300}$ with periods as small as 2nm could offer an even better option, considering their higher incidence angle.

2.7 Summary of Beamline Performance Specifications

Powder diffraction experiments will be performed in both the high-resolution (angle-scanning) and area (fixed) detector modes. The crystal analyzer [12,13], in use at the diffactometer in ES1, is the most demanding in terms of angular stability, since it aims to provide high d-spacing resolution and precision. The area detector mode is primarily affected by position stability. Both modes are sensitive to beam energy changes.

In the crystal analyzer mode [12,13], the critical requirement is angular stability. A typical powder peak width using an analyzer Bragg crystal is in the range of 0.005^o to 0.01^o in the 10-30 keV range, depending on the sample quality. 0.001^o is unusually good. Let us consider 0.005^o as typical. Then, the photon beam stability should be 10% of this value i.e. 0.0005^o, or 8μrad.

A related concern is the energy stability, since energy maps directly to d-spacing in a diffraction experiment. Using Si(111), its intrinsic energy resolution, $\Delta E/E \sim 10^{-4}$, sets a limit on what can be achieved. If we assume we can find centroids to a few percent of this, we end up with an energy stability requirement of at least 10^{-5}. This requires an angular stability of 1 or 2 μrad (Si(111) at 17keV has a Darwin width of 15μrad), and a monochromator temperature stability of 10°K.

All of the above arguments are directed in the vertical plane of diffraction.

The resolution using an area detector typically is 10 times lower than that using scintillation counter with a crystal analyzer, so angular stability is not the limiting case. In contrast to the crystal analyzer mode, position stability is important, since position is used as an angle analogue. If we assume a focused beamline with a focal spot of 100μm and a detector with a 100μm spatial resolution, then using the '10% rule', beam stability should be on the 10μm level. Similar arguments apply to energy stability. In this case, the spatial stability requirements are in both the horizontal and vertical directions.

3. END STATION INSTRUMENTATION

The first endstation will be ~3m wide × 7.5m long and very similar to modern, highly productive, stations at the ESRF, SLS, APS, ASP and will cater to a wide range of users interested in higher energies (>50keV). The core instrument consists of a highly accurate 3-axis diffractometer (Fig. 16): The "inner" stage will be for sample rotation, but will have a capacity of 35kg at a distance of ~200mm from the interface plate; this will allow the rotation of heavy samples with environmental cells where applicable. The interface plate is fitted with "spherolinders" (heavy duty kinematic type mountings with cylindrical rather than spherical attachments); these will allow sample environments to be swapped over easily and with minimal alignment. A Euler cradle and a x-y-z stage can be fitted on that circle, with appropriate sample positioning (metrology, alignment) and beam position monitoring. Opposite the diffractometer, a translating table can support larger loads such as large cryostats and furnaces and high pressure cells. In addition, a robot for fast and automated sample changing is recommended for high-throughput measurements for combinatorial investigation and screening purposes.

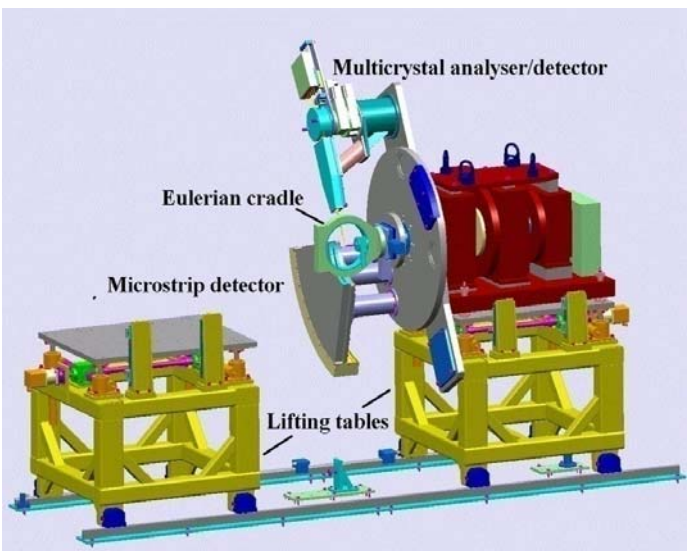

Fig. 16. Conceptual design of the NSLS-II high-energy high-resolution powder diffraction beamline. For clarity, sample environments (such as cryostats, furnaces and diamond-anvil cells) and a robotic sample changer for high-throughput applications are not included in the figure.

The second axis holds a fast read-out position sensitive silicon strip detector for in-situ time-resolved studies and remains essentially fixed. The implementation of a fast position-sensitive strip-array detector allows the real-time, microsecond timescale study of phase transitions, transformations, and catalytic reactions as a function of temperature, chemical gradients, and pressure. The third axis is essentially used to hold a multi-crystal array analyzer system that can be rotated in the vertical diffraction plane, and meant for high-resolution high-energy studies. This arrangement proves to work satisfactorily and to cover a wide range of users' needs on several PD endstations. In the present scope, it is envisaged to mount a second angle-scanning stage for scanning over the high-angle range with a medium resolution (larger angle step size and longer count time are required over the far-Q range). In this unique arrangement, both angle-scanning stages could operate simultaneously, recording complementary parts of the diffraction diagram. They will run in a continuous scanning mode, replacing the usual step-by-step "move and count" mode for better efficiency (minimal overhead). The resolution of the rotary stages and the encoder readings need to be accurate to obtain exact peak positions and reliable data. The Newport and RPI systems have the necessary resolution to enable the operation of this facility.

The most advanced powder diffraction machines now provide instrumental peak widths (FWHM) as low as <5 milli-degrees in the 10-30keV energy range, thus allowing accurate peak profile measurements and minizing the peak overlap effect. The former is essential for the study of strain, microstructure and lattice defects. The latter is required for peak indexing and peak intensity extraction (using the Le Bail approach) in structure solution. The high resolution operation is achieved using a bank of analyser crystals on the diffracted beam paths. To our knowledge, all existing designs rely on the concept developed at the ESRF by J-L. Hodeau et al [12] and use Bragg crystals.

This cannot be transposed to the present case. High energy diffraction imposes very shallow Bragg angles (extended footprint of the impinging beam on the analyzer crystals) and higher shielding and collimating for reducing the cross-talk and noise level. Such a stage would need to accommodate long Bragg crystals, and x-ray tracing shows that it would be extremely difficult to keep the design compact and light-weight. Moreover any energy change will cause important drift of the sample-diffracted beam impact point over the surface of each analyzer crystal, making the alignment extremely difficult [13].

The DOE review committee of last June recommended that novel detection schemes such as Ge Strip detectors and Laue Crystal Analyzers should continue to be explored. These issues are addressed in the following sections.

3.1 High Energy X-ray Detectors

Powder diffraction often requires different data collection strategies, and make use of such detectors as:

- High count-rate high-energy scintillation counters
- upgrade from baseline Si-based strip array (e.g. Mythen, XSTRIP) to Ge-based detectors
- MAR 345
- CCD–fiber tapers are now routine e.g. Frelon ESRF
- Pilatus II, MediPix, XPAD (PAD with in-pixel processing)
- Pixium (ESRF, Thales) or GE Healthcare (APS)

The route to high efficiency, high energy detectors and energy-discriminating area detectors should lead to many more exciting opportunities in high energy x-ray diffraction science in the coming years. *But the lack of detectors that perform well at high x-ray energies is a real concern and this development will noticeably impact the performance of the beamline* (see appendix 7).

3.2 High-Resolution Analyzer Stage

The overall design of the diffractometer is relatively standard, although a significant R&D effort is needed for optimized performance above 40keV. By employing a high-resolution crystal analyzer array, this new instrument will enhance the quality of the diffraction data, through suppression of the fluorescence and Compton components (including diffuse scattering). This is a prerequisite to evaluate technologically important disordered materials. Due to the inherent small instrumental (and source) broadening, the high resolution of the crystal array will enable the measurement of accurate peak-profiles, thus allowing the investigation of strain, lattice defects, and micro-structure.

Low Bragg angles at short working wavelengths make it less suitable to use an array of parallel post-sample crystals in the reflection geometry. The analyzer stage would better work in the transmission geometry using Laue crystals. To our knowledge, such a design does not exist nowadays [13]. A solution is proposed by Siddons et al. in reference [13] as a relatively simple 16-element crystal analyzer based on a single monolithic piece of Si (Fig. 17), elastically bent in a pseudo-Rowland circle geometry and combined with a compact 16-channel pulse-counting detector. This detector could be a custom multi-element germanium or CdZnTe detector, made inhouse by the NSLS Detector Development Group. This particular device requires some x-ray tracing simulation and prototype-testing.

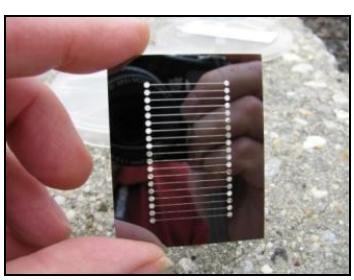

Fig. 17. The Laue crystal array from [13]. The rectangular slats in the center of the crystal are the diffracting elements. The wide side plates are the elastically defornung part. The crystal is clamped at top and bottom, and a bending moment applied to curve the object into a segmented cylinder. The strain induced by the bending is isolated from the diffracting elements by the small cross section of the connecting fillets.

3.3 Software Development

More and more, users expect to find a user-friendly "expert" software that insures they walk away from experiments with data sufficiently processed for analysis at their home institution. For the sake of beamline efficiency and reliability, this is desirable and achievable, provided significant software development accompanies the implementation of the endstation instruments. This includes:

- On-line quick data assessment for rapid evaluation and as an easy assistance of the user in his decisions regarding the subsequent measurements.
- Data reduction and analysis to handle the large amount of 1D and 2D data the beamline is likely to produce in the future. The user comes back home with pre-processed data and preliminary results, rather than with DVD disks of 2D raw data.

The SR user community more and more often points at data handling and data analysis as being a recurrent bottleneck for producing science from SR measurements. Therefore this particular issue should be addressed right from the start of the project conception, and should be an integrated part of the beamline design.

Table 9. A list of detectors and their requirements in terms of data storage and data rate.

Detector / station	Data production	Data rate
CMOS flat panel detector for PDF station	50MB image size, 10 Hz.	500 MB/sec
Strip detector in high throughput station	13 x 80mm modules with 125 micron strips (8320 elements) running at 1kHz	6 MB/sec
Crystal analyzer detectors	Very low data rate	
CCD for special setup enclosure	30MB image size, 1 Hz	30 MB/sec

3.4 Complementary Experimental Stations

Although not in the scope of the present NSLS-II project, the **second hutch** (~3 × 9m^2) is meant for special sample environments and long setups. The second station (ES2) will be built as large as the existing floor allows. The access and facilities will be designed to allow very flexible setups with reasonably easy changeover of experiments. It could be partially populated by existing NSLS equipment and will be able to accommodate a variety of users' designed chambers and cells using heavy-duty supports and a crane. We anticipate such a facility would also be in high demand at NSLS-II. A graded bendable multilayer system or a 2D focusing CRL may be used to focus the beam to ~10 microns for studying small samples (e.g. for high-pressure diamond-anvil cell research). This focusing optics is located relatively close to the sample position to minimize beam motion. This secondary focusing device can be used in conjunction with the "transfocator" (see section 2.6.3).

Local and nanostructure studies are often referred to by the method name, pair distribution function (PDF) analysis, or total scattering, which refers to the fact that all the scattering (Bragg and diffuse) is utilized. Hard x-rays are well suited to PDF studies of nanostructures in particular. Current approaches for studying nanostructure utilize the PDF method combined with full profile fitting structural modeling. Efforts are under way to incorporate information from complementary methods (anomalous diffraction, EXAFS, x-ray and neutron data, NMR, quantum chemistry, etc.) in a rational way when the problem is under constrained. A recent breakthrough was the first demonstration of ab initio structure solution of a nanoparticle from PDF data. However, there is still a long way to go to develop these tools to the level of confidence enjoyed by crystallographic methods. Beyond the present baseline proposal, we are considering combining the structural Q-dependent measurement with a space-resolved probe. Recently, it was shown how diffraction and the tomographic method could be combined for 3D phase imaging [14]. The PDF work can be accommodated in the **third hutch**; its instrumentation is not in the scope of the present project.

The PDF side station shall be ~3 × 4m^2. The concept for this station is based on APS beamline 11-ID-B and NSLS beamline X17A, which feature a single horizontal bounce design. A thin bent Silicon crystal in the Laue geometry will kick the beam sideways and simultaneously provide horizontal focusing, it should be noted that this is at the

expense of bandwidth, although this will not be an issue as 10^{-3} bandwidth is sufficient for PDF studies (see section 2.6.1).

- Energy needed is ~80keV (as high as possible but giving sensible beam separation).
- The CRL could be common to both branches, but there is a preference to put independent CRLs on each branch, after the individual monochromators.
- The horizontal focus is <300 microns.
- The energy will be switchable through the implementation of a double crystal setup (one on top of the other, which just translate vertically through the beam to switch over).

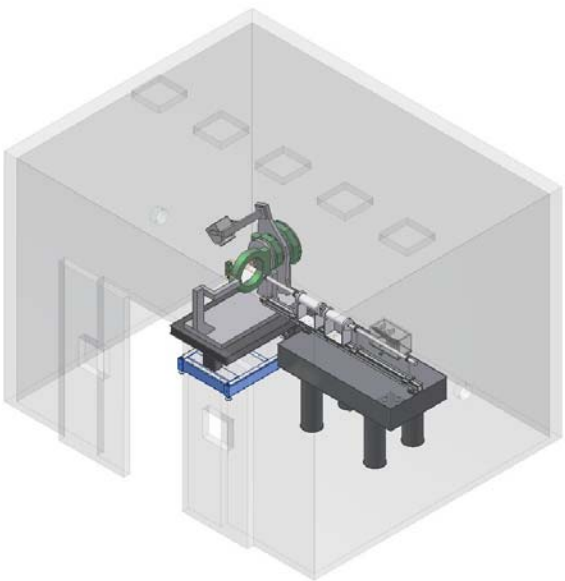

Fig. 18. Conceptual layout for a second powder diffraction beamline, downstream of the high-energy high resolution NSLS-II powder diffraction beamline. Note that this endstation is not in the current scope of the NSLS-II project.

3.5 Sample Environment

Considerable efforts will be made to ensure that a wide range of sample environments are made available to the user community. The access and facilities will be designed to allow very flexible setups with reasonably easy changeover of experiments. For easy configuration changes, we are considering the use of "towers" mounted on rail paths, instead of granite table benches: sample tower, detector tower, optics tower (filters, slits, shutter, laser, collimator,…). The user can come along with his own custom setup, and put it on the top of a heavy-duty (200kg)

Huber table (rotation φ, translations X and Y, coarse and fine Z), supported on a granite base plate and motorized on rails. A variety of sample environments (not shown) are included in the budget, consisting of cryostats, furnaces, laser heating and diamond-anvil cells for high-pressure research. A typical suite of ancillary equipments on modern powder diffraction instruments includes:

- Stoe capillary furnace (T = 300 – 1700K)
- MRI flat plate furnace, (T=300 - 2000K)
- Bruker Humidity chamber (-5°C up to 75°C dew-point, T= 25 – 90°C)
- Linkam DSC (T = 77 – 870K)
- Cyberstar Hot air blower (T = RT-1300K)
- PheniX He Cryostat (T = 11 – 300K)
- ASI cryostat (T= 4 -300K)
- Oxford Cryosystem 700+ cryostream (T = 80 – 500K)

To support modularity, rapid interchange of sample environments, and extensibility in the future, instrument interfaces and software will be carefully designed and specified. The scattering from sample environments often

compromises the data quality in experiments at non ambient conditions. Tight collimation and/or small focus are necessary to minimize or totally exclude parasitic scattering from the sample environment.

Table 10. List of ancillary equipments and sample environments.

Technique and equipment	Size of equipment (typical)	Weight (approx)
HP Earth and Materials Sciences: 2000T press to give routine 50 GPa at sample.	4m x 4m plus plumbing (hydraulics) plus accessories.	2000 kg
HP Earth and Materials Sciences: Double sided laser heating (2500K) for routine experiments up to 200 GPa.	3m x 2m plus plumbing and accessories.	100 kg including laser and stand.
Catalysis cells with goniometer and detector on 1m arm.	2m x 2m plus gas handling and analysis equipment.	500 kg
Carbon sequestration and catalysis. High pressure CO2 cell.	1m x 2m plus accessories.	1000 kg including cell, rotation stages, area detector etc.
Engineering applications (white beam, fixed angle EDX, high capacity 0.5μm resolution x/y/z translating table, for scattering in the vertical and horizontal).	3m x 3m	2000 kg
Single-crystal setup concentrating on higher energy experiments and heavier loads (complements standard set up beamline proposed on adjacent BM line).	~2m x 2m	1000 kg

4. SPECIAL BEAMLINE REQUIREMENTS

Although a plethora of user-friendly ultra-high temperature, high pressure and apparatus are designed and built for the study of materials *in operando*, it is critical that the 5-year horizon to the construction of XPD be accompanied by efforts to prototype environmental chambers, and to push ahead with ever more suitably high time, angular and spatial resolution optics and detectors.

Because the beamline is intended to study materials under operational conditions, we can anticipate that most (if not all) of the 241 substances in CAA 112R, the EPA list of Regulated Toxic, Explosive, or Flammable Substances, will be used at some time - fortunately in small quantities. Many of them are involved in catalytic processes and/or semiconductor manufacturing, two key areas of beamline science. A ventilated cabinet for dangerous gas bottles is required, and the gases will be piped to the first hutch.

Many catalytic studies will involve multiple reagents. It is easy to imagine feeding a mixture of gas, gaseous hydrocarbon, and liquid hydrocarbon into a reactor. Systems to control the flows of such materials (including mass flow controllers interfaced to data collection software), as well as to monitor the composition of the products (online GS/MS, also interfaced to the data collection software) will be required from the outset. Because each experiment will have different requirements, modularity of the endstation equipment will be critical, but as much common infrastructure as possible needs to be provided to maximize the productivity of the beamline.

Table 11. List of potential catalysis applications and chemicals involved.

Reaction	Potential "interesting" compounds involved
Ammoxidation	NH_3, air, propylene/propane, acrylonitrile, acrolein (avoid flammability limits)
Partial oxidation	Butane, air (flammability limits)
Xylene isomerization	Hydrogen, xylenes, toluene, ethylbenzene, benzene, ethane/ethylene
Hydrotreating	H_2S, NH_3, H_2 (P < 5000 psig)
Offgas treating	CO_x, NO_x, SO_x, HCl, HBr
Oxychlorination	Cl_2, HCl, vinyl chloride monomer
Olefin Polymerization	Metal alkyls, metal chlorides, HCl, BF_3
Alkylation	H_2SO_4, H_3PO_4
Many reactions	H_2O (steam)
Hydrogenation	H_2, aromatic acids, acetic acid

The proximity of the Center for Nanomaterials and trends in current frontier science suggest that many experiments involving nanomaterials will be performed at the beamline. A HEPA filtration system needs to be an integral part of the endstations.

5. FUTURE UPGRADE OPTIONS

Operating the beamline with "extremely" small (1-2µm) beams, especially in the context of one of the major scientific goals to study heterogeneous samples *in operando*, opens more scientific possibilities. *1-2µm focusing is an untried technological challenge to deliver from a wiggler source*. Whilst highly desirable, this is not a design goal of the beamline: 5–20µm vertical and 20–50µm horizontally focusing are in the base design, and the 1–2µm focusing is kept in mind as a long term goal with enough room left in the beamline to accommodate possible optics (CRL, KB, ML) for this purpose in the future. The capability of delivering small beams (below 10µm) is thus being considered as part of the mature scope of the project, below the build-out of the PDF side-station in priority. The current layout keeps the option of a primary focus and slits at the first hutch position and then refocusing optics to produce a 10µm focus in the second hutch; this would be unique at these energies.

An important and unique feature of the beamline will be the ability to combine the angle-dispersive setup with energy step scans. Alternatively, we can use a so-called "pink" beam or a large energy band-pass beam. This is particularly important when the grain statistics of the sample is insufficient. This well-known sampling problem in powder diffraction impairs the diffraction intensities and introduces significant biases in the resolution of the diffraction pattern. This occurs for a non-spinning sample (as it frequently happens for a sample confined inside an environmental cell in a fixed geometry) or when the beam does not probe a sufficient number of randomly oriented crystallites. This is very common for spatially-resolved measurements using a focused beam below 10 microns size (small gauge volume) or with a poor powder or not quite a powder. Varying the energy of the monochromatic beam or using a non-monochromatic beam often helps overcome this grain problem. Combining the energy scan with an area detector will probably develop in the future years: a relevant example is shown by Wang et al. [15] in an energy-dispersive measurement, whereby the Ge solid-state detector is angle-scanned (and not at a fixed angle as usual) for covering a larger fraction of the reciprocal space.

An interesting option is to use the transfocator as a broad energy band-pass (1%) monochromator, simply using the longitudinal chromatic dispersion of the focused beam. This acts as a *longitudinally dispersive monochromator*, and will prove to be particularly useful for powder diffraction on "poor" powders, non spinning specimens, dilute or extremely small samples or time resolved work. Provided focal length is kept relatively short (a few meters), the depth of focus is sufficiently short that only a narrow band pass is focused at a given longitudinal point. At the focal point, this leads to a substantial increase in the flux at this selected energy with respect to the rest of the spectrum. The first experimental hutch could therefore be designed for accepting an in-going white beam. The desirability to

change from a monochromatic beam (as in the current baseline design) to a white beam hutch is under investigation.

6. SUMMARY

Powder diffraction has widespread scientific interest, such as in the fields of metallurgy, solid-state chemistry, nanomaterials, microelectronics, mineralogy, and the biological and pharmaceutical sciences. In addition, the study of condensed matter at extreme conditions is developing into a very rich field of research. In situ elastic scattering provides the data required to derive structure models, which is essential to systematic searches for new classes of materials and to rationalizing their desirable properties.

The proposed powder diffraction beamline at NSLS-II will be a tunable high-resolution facility with the ability to collect data at high energies (50keV-100keV), offering exceptional capabilities such as fast (milli-second) readout rates and high angular resolution on the same instrument. The high-energy x-rays will be able to propagate through environmental cells, and are suitable for powder diffraction measurements in difficult environments, e.g., stainless steel reaction tubes and high temperature capillaries. It also allows for the investigation of materials made up of high-Z components, and enable high-Q accessibility, which is crucial for atomic pair distribution function analysis and high-pressure cell research. This will be an outstanding research facility for studying the structure and kinetics of materials under real conditions, and the beamline will meet the needs of the powder diffraction user community.

This report has presented a conceptual design of the XPD project beamline. Additionally, we have described proceeding hutch ES2 and hutch ES3 build-outs in a preliminary stage of development. The beamline components are based on proven concepts. The combination of high-heat load double-Laue crystal with refractive optics is or will be used in particular at ESRF-ID15, ESRF-ID11, APS-11ID and PETRA-P07. This design proves to be a stable configuration and performs well in the high-energy range. The present proposal is adopting a similar strategy tailored to the characteristics of the Damping Wiggler source, in particular for handling the large horizontal fan.

Because of the nature of complex materials research, the scientific impact depends equally on beamline characteristics and on the existence and usability of appropriate software and special environments, and on the success with which researchers can combine data from complementary approaches (such as conventional powder diffraction and PDF).

More information regarding the experimental facilities and the standard beamline components can be found at the NSLS-II Conceptual Design Report web page.

7. REFERENCES

1 M.A. Beno, U. Rütt, C. Kurtz, G. Jennings. Synchrotron Radiation Instrumentation: Eight International Conference on Synchrotron Radiation Instrumentation, CP705, p.675, 2004, San Francisco.

2 U. Rütt, J. Heuer, H. Schulte-Schrepping. Private communication. Work based on R. Smither, K. Abu Saleem, M. Beno, C. kurtz, A. Khounsary, N. Abrosimov. Rev. of Sci. Insstrum. 76 (2005) 123107.

3 Z. Zhong, C.C. Kao, D.P. Siddons and J. B. Hastings. J. Appl. Cryst., 34 (2001) 646-653.

4 Z. Zhong, C.C. Kao, D.P. Siddons and J. B. Hastings. J. Appl. Cryst. 34 (2001) 504-509.

5 Z. Zhong, C. Kao, D.P. Siddons and J.B. Hastings. Acta Cryst, A 58 (2002) 487-493

6 Z. Zhong, C. Kao, D.P. Siddons, H. Zhong, and J.B. Hastings. Acta. Cryst. A 59 (2003) 1-6.

7 S. D. Shastri, K. Fezzaa, A. Mashayekhi, W.-K. Lee, P. B. Fernandez and P. L. Lee J. Synchrotron Rad. 9 (2002) 317.

8 S.D. Shastri. J. Synchrotron Rad. 11 (2004) 150–156.

9 S. D. Shastri. J. Almer, C. Ribbing and B. Cederstrom. J. Synchrotron Rad. 14 (2007) 204–211

10 A. Snigirev, I. Snigireva, M. Grigoriev, V. Yunkin, M. Di Michiel, S. Kuznetsov, G. Vaughan. Advances in X-Ray/EUV Optics and Components II, ed. by Ali M. Khounsary, Christian Morawe, Shunji Goto, Proc. of SPIE Vol. 6705 (2007) 670506.

11 http://www.esrf.eu/news/spotlight/spotlight85/spotlight85/

12 J.L. Hodeau, P. Bordet, M. Anne, A. Prat, A. N. Fitch, E. Dooryhée, G. Vaughan, A. Freund, SPIE Conference on Crystal and Multilayer Optics, San Diego 1998 SPIE Vol. 3448 p 353.

13 D. P. Siddons, Zhijian Yin, L. Furenlid, P. Pietraski, Zheng Li, R. Harlow. A. Freund2, SPIE Conference on Crystal and Multilayer Optics, San Diego 1998 SPIE Vol. 3448 p120.

14 P. Bleuet, E. Welcomme, E. Dooryhee, J. Susini, J-L. Hodeau, P. Walter. Nature materials 7 (2008) 468.

15 Y. Wang, T. Uchida, R. Von Dreele, M. L. Rivers, N. Nishiyama, K. Funakoshi, A. Nozawa and H. Kaneko. J. of Applied Ccrystallography 37 (2004) 947.

16 P. Suortti, S. Fiedler, A. Bravin, T. Brochard, M. Mattenet, M. Renier, P. Spanne, W. Thomlinson, A. M. Charvet, H. Elleaume, C. Schulze-Briese and A. C. Thompson J. Synchrotron Rad. 7, p.340, 2000

17 C. Schulze, U. Lienert, M. Hanfland, M. Lorenzen and F. Zontone. J. Synchrotron Rad. 5, p. 77, 1998

18 C.G. Schroer, M. Kuhlmann, B. Lengeler, T.F. Günzler, O. Kurapova, B. Benner, C. Rau, A.S. Simionovici, A.A. Snigirev, I. Snigireva. Proc. SPIE, 4783 (2002) 10–18.

19 A. Stein, K. Evans-Lutterodt, N. Bozovic, A. Taylor. J. Vac. Sci. Technol. B 26 (2008) 122

20 A. F. Isakovic, A. Stein, J. B. Warren, S. Narayanan, M. Sprung, A. R. Sandyd and K. Evans-Lutterodt. J. Synchrotron Rad. 16 (2009). 8–13

21 Jark,W., Perennes, F. & Matteucci, M. J. Synchrotron Rad. 13 (2006) 239–252.

22 E. Dooryhée, M. Anne, I. Bardiès, J.-L. Hodeau, P. Martinetto, S. Rondot, J. Salomon, G.B.M. Vaughan and P. Walter. Appl. Phys. A 81 (2005) 663.

23 P.J. Chupas, K.W. Chapman and P.L. Lee. J. Appl. Cryst. 40 (2007) 463–470

24 J.H. Lee, J. Almer, C. Aydiner, J. Bernier, K. Chapman, P. Chupas, D. Haeffner,K. Kump, P.L. Lee, U. Lienert, A. Miceli, G. Vera. Nuclear Instruments and Methods in Physics Research A 582 (2007) 182–184

25 J. E. Danielsa and M. Drakopoulos. J. Synchrotron Rad. 16 (2009) 1

26 J.-F. Berar, L. Blanquart, N. Boudet, P. Breugnon, B. Caillot, J.-C. Clemens, P. Delpierre, I. Koudobine, C. Mouget, R. Potheau, I. Valin. J. Appl. Cryst. 35 (2002). 471-476

27 P. Pangaud et al. Nuclear Instruments and Methods in Physics Research A 591 (2008) 159–162.

28 V.A. Wright, A. Blue, M. Horn, I. Johnston, E. Koskiahde, L. Lea, J. Melone, S. Nenonen, V. O'Shea, M. Rahman, P. Roy, K. Smith. Nuclear Instruments and Methods in Physics Research A 531 (2004) 56.

29 B. Schmitt, Ch. Bronnimann, E.F. Eikenberry, F. Gozzo,C. Hormann, R. Horisberger, B. Patterson. Nuclear Instruments and Methods in Physics Research A 501 (2003) 267–272

30 S. Basolo et al. J. Synchrotron Rad. (2007). 14, 151–157.

31 J-C. Labiche et al. Rev. of Scientific Instruments 78 (2007) 091301

APPENDIX 1 SCHEDULE

September 30	2009	Complete Conceptual Design Report
September 28	2010	Complete Preliminary Design Report
November 03	2010	Technical Design – Approval of Long Lead Term Procurement
January 11	2011	Start Lead Time Procurements (monochromators, CRL, enclosures,…)
April 14	2011	Complete Final Design of Beamline Major Components
February 07	2012	Complete Final Design Report Approval of Start of Beamline Construction - Beneficial Occupancy of Experimental Floor
February 10	2012	Start Installation
May 15	2012	Start Sub-System Testing
April 20	2012	Start Other Procurement
November 05	2012	Complete Long Lead Time Procurements
August 14	2013	End Procurement
August 19	2013	Start Integrated Testing
January 07	2014	Complete Installation
February 03	2014	Complete Sub-System Testing
May 27	2014	Complete Integrated Testing – Beamline available for Commissioning
June	2015	**CD-4**, Approve Start of Operations

APPENDIX 2 REFERENCE DRAWINGS

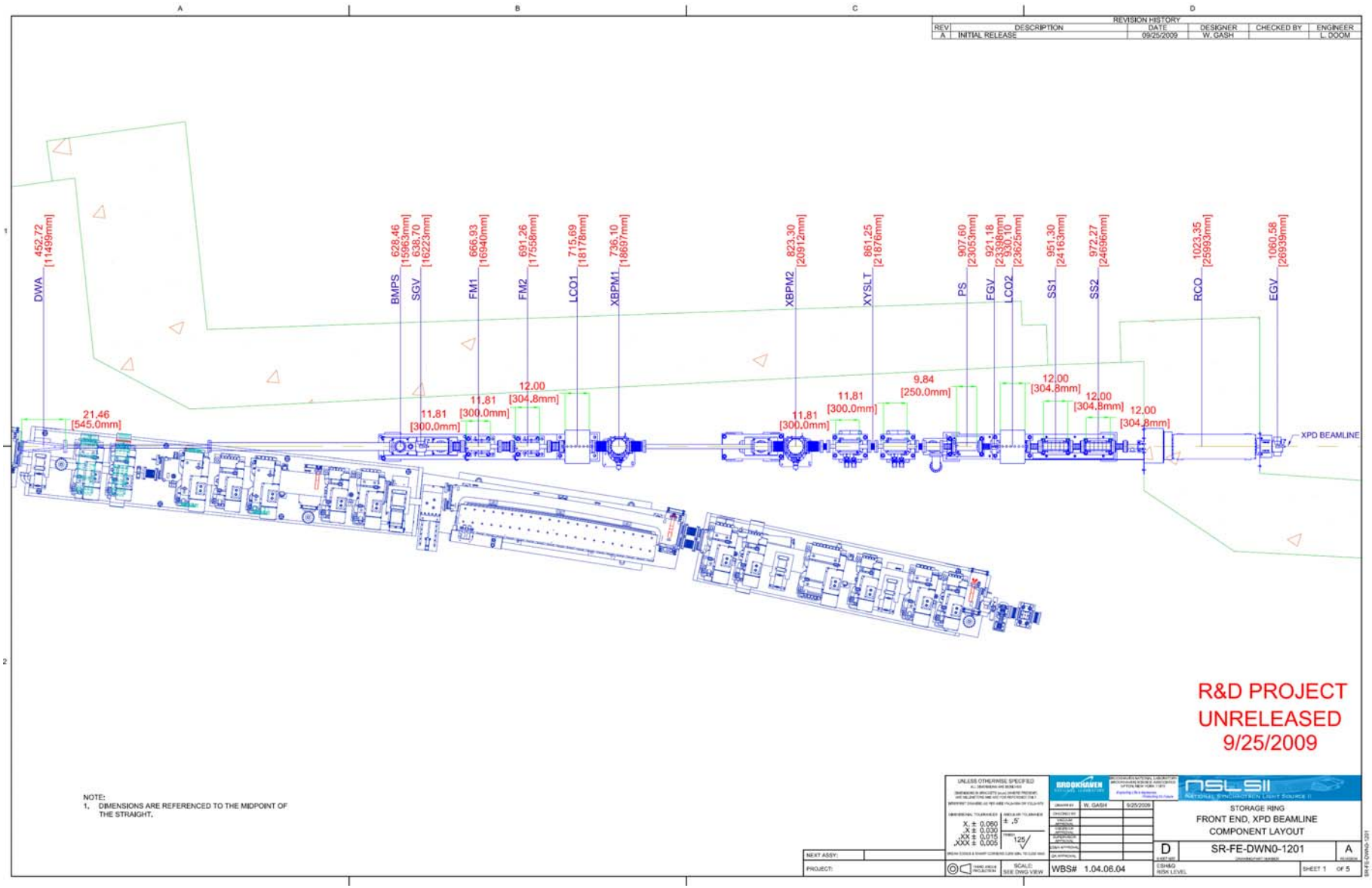

Front-end layout plan of the Front End of XPD (L. Doom).

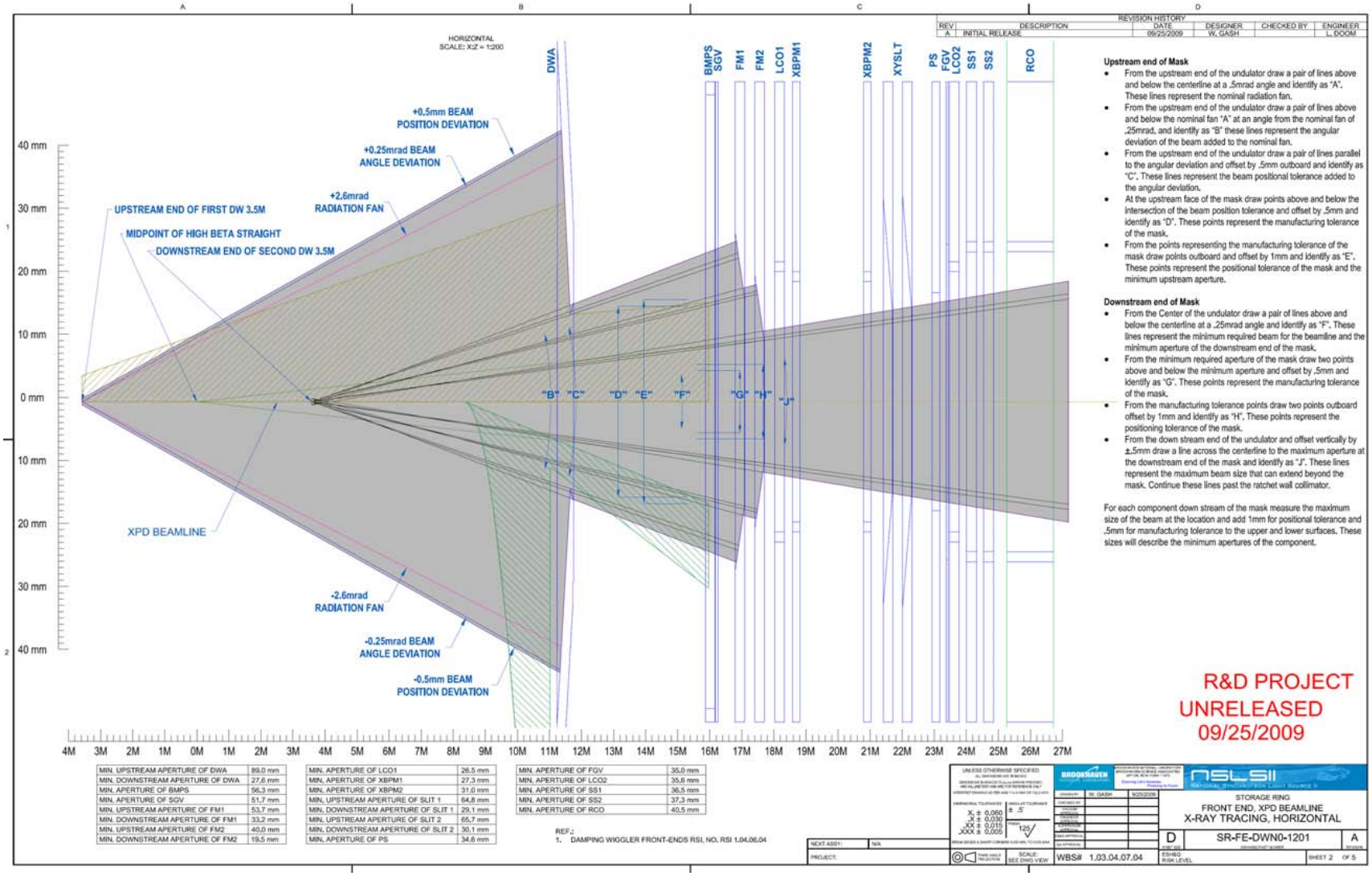

Preliminary Front End x-ray tracings (L. Doom).

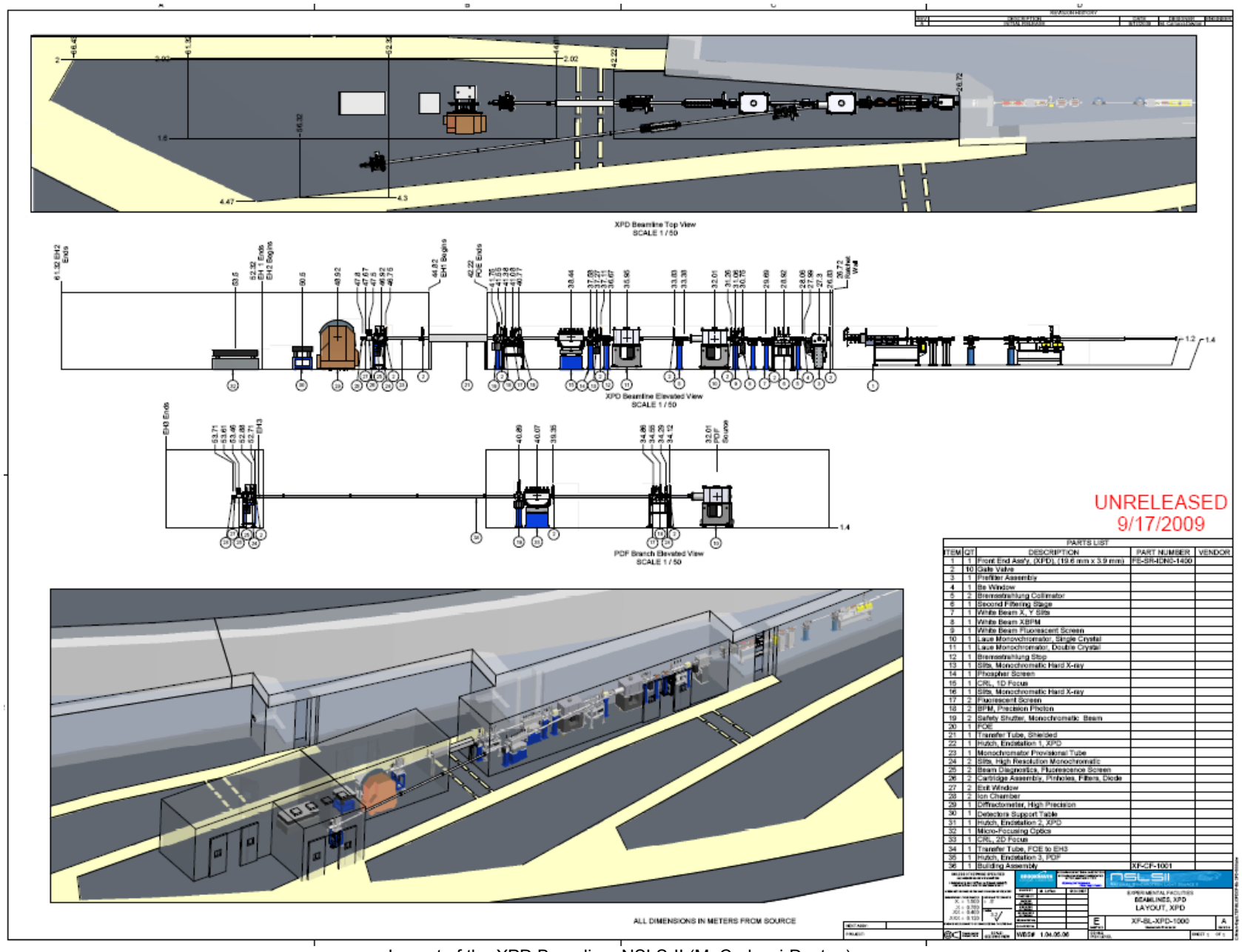

Layout of the XPD Beamline, NSLS-II (M. Carlucci-Dayton).

APPENDIX 3 REPRESENTATIVE EXPERIMENTS

In general, data are required that have the highest possible resolution both in reciprocal space and in real-space. These examples, as well as many more, are described in detail, with references, in the Materials Community White Paper and are provided here by way of example. The XPD Beamline will allow similar studies to be carried out, but under more challenging conditions, moving towards the ability to study these effects *in-operando* in devices that are heterogeneous on the sub-micron scale and where the species of interest are dilute and evolving in time.

a. Encapsulated materials: hydrogen storage

Pivotal to the rational development of host materials with increased H_2 storage capacities (approaching projected DOE targets for practical applications) is the understanding of the nature of the H_2 -framework interaction and the factors that influence H_2 binding strength and storage capacity. However, few structural studies have directly probed the adsorption sites in these systems when loaded with H_2. As such, the principal mechanism for H_2 sorption remains controversial and speculative, with the current views developed from attempts to correlate observed sorption behavior with the structural features and chemical functionality of the apo-host (e.g., surface area and volume; surface polarizability and potential coordination sites). In a recent PDF structural study of local H_2-framework interactions within the H_2/D_2 loaded Prussian Blue analogue, $Mn_3[Co(CN)_6]_2$, both high energy X-ray and neutron scattering data were used together. The results contradicted accepted models by demonstrating there is no evidence for binding interactions with the accessible MnII sites.

b. CO_2 sequestration: in-situ HP powder diffraction

Injection of Carbon (CO_2) as a means of oil recovery is a mature technology and is also seriously considered as a means of effective carbon sequestration. Despite a number of modelling studies there are relatively few experimental studies to examine the chemical processes that may occur down-hole when supercritical CO_2 is injected. One study showed dramatic changes in the solution chemistry raising questions about the long-term stability of injected CO_2 due to changes in the chemical environment. This environment may vary considerably with different minerals, brine concentration, pH, T, P. This has been the subject of an *in operando* study to examining the effects of these variable on the super-critical CO_2-rock interaction by the group of Pam Whitfield. Initial studies in the laboratory using a modified cell, that might serve as a prototype for NSLS and NSLS-II, show high pressure carbonation of wet wollastonite under relatively mild conditions (45-73ºC), followed by quantitative analysis of the data using Rietveld refinement, are consistent with results of thermal analysis results and more time consuming techniques.

c. Accelerated Design of Advanced Structural Ceramics

Once new materials have been identified and the volume and unit cell shape changes as well as transformation temperatures have been identified, structural ceramic composites can be designed and fabricated for *in situ* studies of stress-induced transformation toughening. Specifically, knowing the thermal expansion coefficients of candidate matrices and toughening phases, chemically compatible composites having matched thermal expansion coefficients can be engineered as laminates or fibrous monoliths, or even as fiber-reinforced composites. Bulk samples of such composites can then be prenotched and evaluated by *in situ* straining stage experiments under high energy x-ray radiation. The mechanisms of stress-induced transformation and the resultant redistribution of stress states, clamping forces of a propagating crack tip and overall toughening of the ceramic component can then be demonstrated. A specific example to illustrate such a composite would be transformation weakening of enstatite ($MgO{\bullet}SiO_2$) as a potentially debonding interphase in forsterite ($2MgO{\bullet}SiO_2$). High energy x-rays and small, well defined beams are required for these studies along with the ability to place and manipulate tensile stress equipment in the beam. Such information gives immediate feedback on the mechanism of strain toughening in ceramics that will accelerate the design of new materials.

d. Catalysts and catalysis

Many (if not most) catalysts have different structures while operating than they do at ambient conditions. Attempts to develop structure/activity correlations using only ambient structural information are thus doomed to failure. Development of improved catalysts requires in situ studies of real poly/nanocrystalline materials under operating conditions. Catalytic phases often contain many multiply- and partially-occupied sites, making determination of even their average structures a challenge. Catalytic properties often depend on the surface (not bulk) structure and/or the boundary regions between phases. The ability to point a very small x-ray beam on a desired region in a polycrystalline catalyst sample while operating will be crucial to making progress in understanding industrially-relevant systems. Compared to earth science systems, the temperature and pressure requirements for catalyst studies are modest, but systems for handling potentially-hazardous atmospheres need to be designed into the beamline.

APPENDIX 4 THERMAL CALCULATIONS

A more selective aperturing (central part of the fan), restricting the aperture to ~1mrad (H) × 0.1mrad (V), still leaves almost 6kW. Extreme filtering is being considered, using a multi-filter stage: C (5mm) and Si (8mm) filtering. The figure below shows that the power through a 1x0.1mrad^2 mask is progressively scaled down from 5.7kW to 2.3kW past the 5mm C pre-filter and 0.3kW after the 8mm Si filter stage. The residual incident power is 280W, of which 21W is absorbed in a 0.5mm Si crystal. This filtering strategy reduces the flux by 64% at 50 keV and 46% at 80keV.

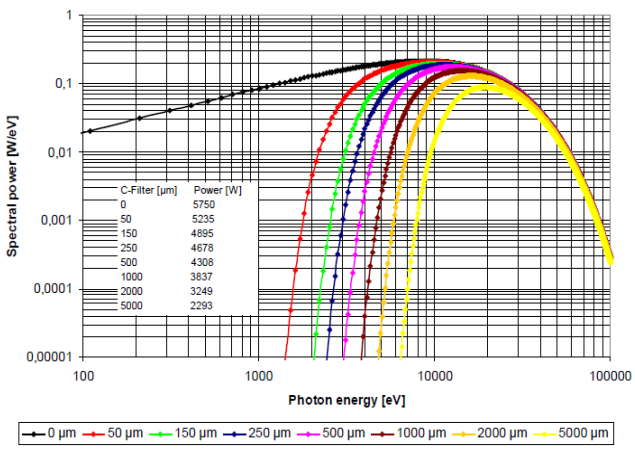

Carbon pre-filter transmission assuming a 1×0.1mrad^2 angular acceptance.

Carbon Pre-Filter Absorption for a 1 mrad by 0.1 mrad beam at 30 m.

Total filter thickness [µm]	Total power after filter [W]	Power density after filter [W/mm²]
0	5750	67.6
50	5235	61.9
150	4896	58.1
250	4678	55.6
500	4308	51.4
1000	3837	46.0
2000	3249	39.2
5000	2293	28.0

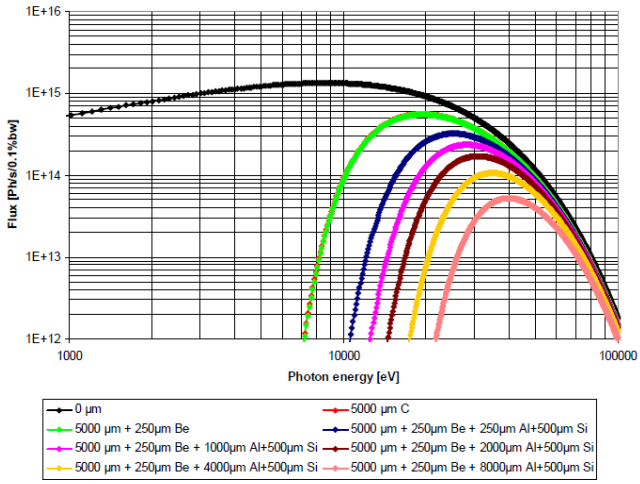

Effect of the second filtering stage on the spectral transmission assuming a 1x0.1mrad^2 angular acceptance.

Preliminary calculations were carried out by V. Ravindranath, assuming the monochromator is located at 25m from the DW source, the aperture size is 1mrad × 0.1mrad, the beam incidence angle = 45°, and the power absorbed by the crystal = 25W. Both sides of the crystal are at 25 °C (water cooling, see figure below). The peak temperature is found to be as high as 169°C. Assuming cryo-cooling (both sides of the crystal at -196°C), the peak temperature is -182°C and the resulting displacement (25nm) and the slope error (2.5µrad) are negligible.

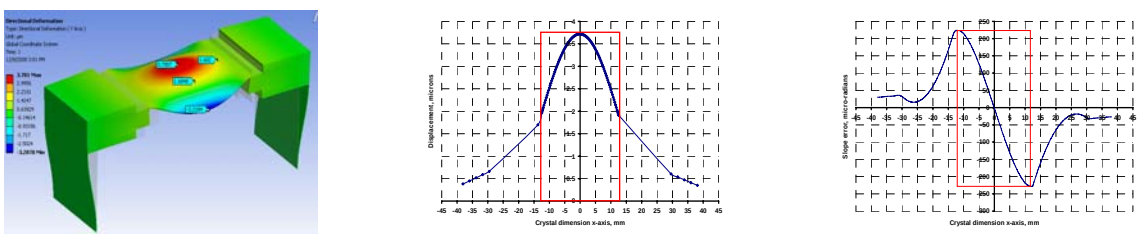

Water-cooled crystal: peak temperature = 170°C, displacement ≈3.8µm,
and slope error ≈225 µrad in the transverse direction.

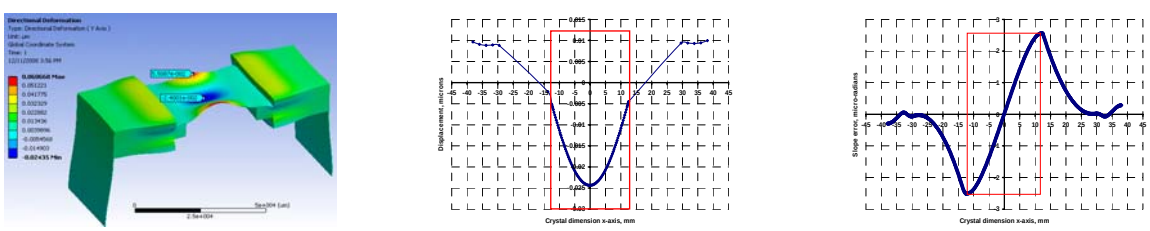

Cryo-cooled crystal: peak temperature = 91°K, displacement ≈25nm
and slope error ≈2.5 µrad in the transverse direction

FEA calculations on the monochromator Silicon first crystal (V. Ravindranath).

APPENDIX 5 LAUE MONOCHROMATIZATION

Horizontal Deflecting Side Bounce Monochromator

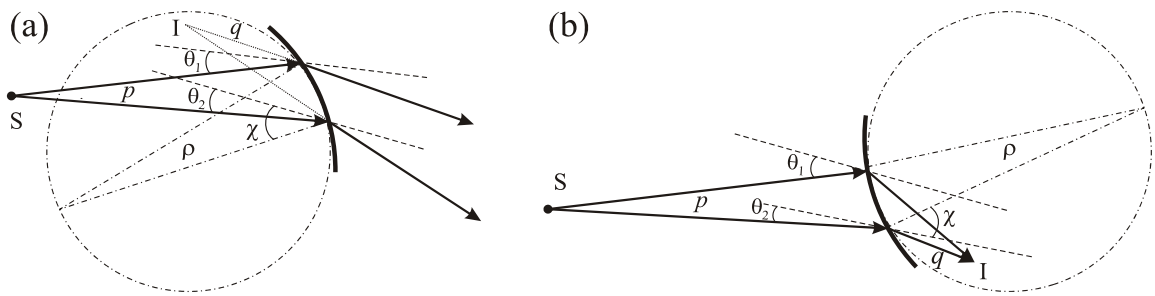

Top views of the horizontal focusing by cylindrically bent Laue crystals.

Two cases of the point-to-point polychromatic focusing by the cylindrically bent Laue crystals are shown: (a) if the incident beam is on the concave side of the crystal, the reflected beam remains diverging, while (b) a real image is obtained if the source is on the convex side. The relation between the bending radius (ρ), the source-to-crystal distance (p = 32m) and the crystal-to-image distance (q) is the following [16,17]:

$$p_o / p + q_o / q = 2 / \rho,$$

where p_o and q_o are those for monochromatic focusing (the source S and the image I are both on the Rowland circle), given by

$$p_o = \rho \cos(\chi \pm \theta_B),$$

$$q_o = \rho \cos(\chi \mp \theta_B).$$

Here θ_B is the Bragg angle and χ is the asymmetric angle between the Bragg planes and the surface normal of the crystal. We should note that these relations are derived for polychromatic focusing, which are the same as in the monochromatic focusing case only in particular cases: the symmetrical reflection or when the Rowland condition is achieved.

The energy bandwidth $\Delta E/E$ of the diffracted X-ray by a bent Laue crystal is given by [4]

$$\Delta E/E = \cot \theta_B \, [\Delta\theta^2 + \omega_0^2 + (\sigma_h/p)^2]^{1/2}$$

where $\Delta\theta$ is the variation of the incident angle due to the horizontal divergence ψ_h of the beam, ω_0 is the intrinsic angular acceptance of the crystal, and σ_h/p is the angular aperture of the horizontal source size. For the Damping Wiggler source at NSLSII, the desired horizontal beam size is small ($\sigma_h \approx 137\mu$m), which will introduce a $\Delta E/E$ less than 10^{-4}. For a flat perfect crystal, ω_0 is simply the Darwin width. For a bent crystal, ω_0 also accounts for the change in the Bragg angle across the crystal thickness (crystal distortion). When the bent is mild (close to the Rowland condition), ω_0 is less than 0.1mrad ($\Delta E/E < 10^{-3}$). Therefore, the energy bandwidth is mainly determined by the divergence term, which, for $\psi_h = h/p$, is given by

$$\Delta\theta = h \, [1/p_o - 1/p].$$

Following these equations, we must optimize (1) the energy bandwidth, (2) the beam spot size and (3) the reflectivity through the combination of the correct reflection plane, the bending radius (ρ), the asymmetry angle (χ) and the thickness of the crystal.

Two possible modes are suggested here: (a) the source is located on the concave side of the crystal. The energy bandwidth is easily reduced by bending the crystal close to the Rowland condition. However, with the 1mrad

horizontal divergence, the beam size will be about several centimeters without applying any slit. (b) The source is on the convex side of the crystal. The beam will converge to a pseudo-focus. However, the energy bandwidth will be too large ($>10^{-2}$). A pre-crystal aperture ($\leq$ 0.2mrad) will be needed in order to reduce $\Delta E/E$ to 5×10^{-3}. As a result, the total flux will be also reduced by 80%. An alternative way will be using another bent crystal after the side bounce as a secondary monochromator. The following discussion will focus on the mode (b).

Since the side bounce angle ($2\theta_B \approx 7^o$) is preselected, four possible optimized energies are calculated using different reflection planes. The ray tracing and calculation were performed using the SHADOW VUI 1.0. The Damping Wiggler source simulated in SHADOW indicates a photon beam size (FWHM) of 0.34mm (h) × 0.013mm (v), and the angular divergence (FWHM) of 2.5mrad (h) × 0.1mrad (v) at the waist for the photon energies above 50 keV. (These spatial properties need to be further verified). In these calculations, the full vertical fan was accepted, and therefore, remained the near-Gaussian profile. By applying the fixed mask aperture, the horizontal aperture was chose to be 0.2 mrad in order to reduce $\Delta E/E$. Contrastable results obtained with 1.0mrad aperture are also listed in the table below (numbers in the parentheses). The horizontal beam size at the crystal is 7.0 mm for 0.2mrad aperture and 35mm for 1mrad aperture. The bending radius ρ was optimized to achieve the smallest horizontal spot size at 8m after the crystal (where the CRL is located). The fluxes per millimeter over the horizontal plane at 8m after the crystal were then calculated using

$$I = I_o\, N_r \Delta E/N_i/E/\delta_h$$

where I_0 is the incident flux, N_i is the number of the incoming rays, N_r is the number of the reflected rays recorded by SHADOW, ΔE is the photon energy bandwidth over which the ray tracing was performed, E is the central photon energy and δ_h is the horizontal spot size at 8m after the crystal. The source fluxes I_0 (ph/s/0.1%BW/mrad) are given in the table.

Side bounce Laue monochromator calculation corresponding to: p = 32m, q = 8m (CRL location), pre-crystal horizontal aperture = 0.2mrad (and 1mrad shown in the parentheses), σ_h = 137μm, crystal thickness T_0 = 0.5mm (X. Shi).

(Reflection)<Crystal cut>	(311) <511>	(331) <100>	(422) <100>	(511) <111>
χ: (°)	60.5	43.5	54.7	51.1
E: (keV)	60	80	90	95
I_0 at E: (ph/s/0.1%BW/mrad)	8.8×10^{13}	1.7×10^{13}	7.2×10^{12}	4.7×10^{12}
$2\theta_B$: (°)	7.24	7.13	7.12	7.16
ρ: (m)	60	35	50	45
$\Delta E/E$: (10^{-3})	4.7 (≈30)	4.5 (≈30)	4.4 (≈30)	5.1 (≈30)
δ_h at 8m after the crystal: (mm)	1.3 (3.8)	1.0 (3.3)	0.96 (3.1)	0.93 (3.1)
I: (ph/s per horizontal mm)	5.1×10^{11} (6.3×10^{11})	7.1×10^{10} (6.7×10^{10})	2.0×10^{10} (1.2×10^{10})	6.0×10^{9} (4.5×10^{9})

In the horizontal plane, for the 0.2mrad aperture, the beam size can be focused by the crystal from 7mm to 1mm, which is similar to the ratio observed at NSLS X17A (from 3mm to 0.5mm). However, the CRL is still needed for further focusing to the sample. In the vertical plane, if we apply the sagittal curvature to the crystal, we can focus the beam to the sample directly.

Sagittally-Focusing Double-Crystal Laue Monochromator

If a point divergent source is used, the distance from the source to the crystal F_1 and the distance from the crystal to the focal point F_2 are then related by:

$$1/F_1 + 1/F_2 = 4 \sin\theta_B \sin\chi / R_s,$$

while ignoring the distance in between the two crystals. In order to increase the energy resolution, both crystals should fulfill the Rowland condition. While R_{m1} can be calculated through eq. (3), R_{m2} is related to R_{m1} through

$$R_{m2}/R_{m1} = \cos(\chi_1-\theta_B)/\cos(\chi_1+\theta_B).$$

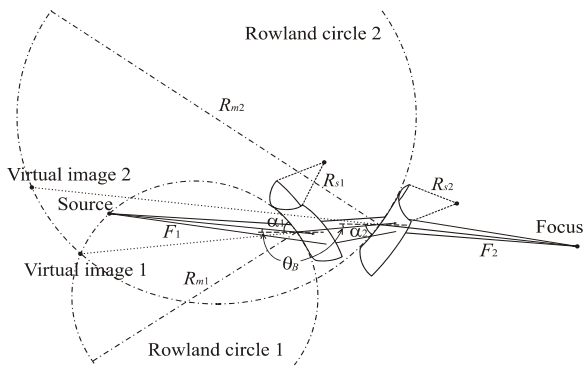

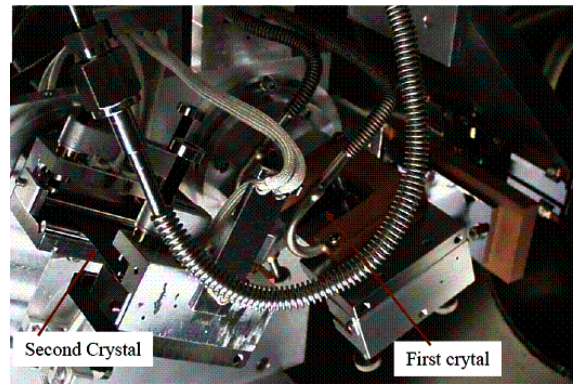

(left) Geometry of a sagittal bent double-Laue monochromator;
(right) Monochromator installed at the NSLS X17B1 beamline.

The bent Laue system provides over an order of magnitude more flux with a reasonably low increase in energy spread. This more than tenfold flux enhancement results from the bending strain-induced broadening of the crystal reflection angular acceptance. The anticlastic bending facilitates the use of the inverse-Cauchois geometry in the meridional plane to provide better energy-resolution and to increase the photon flux. The anticlastic bend radius needs to be properly adjusted so that all rays make the same incidence angle with respect to the crystal planes (the so-called Rowland condition). This new x-ray optics concept makes it possible to focus the large divergence of high-energy x-rays produced by the NSLS-II damping wiggler. For many experiments, with a vertical scattering plane geometry, beam divergence of the order of 0.1-0.2mrad at the sample and the modest 10^{-3} energy spread will be tolerable. A larger divergence (1mrad) in the horizontal plane also is acceptable.

A double-crystal sagittally focusing monochromator has been constructed and tested, and has been in use at the X17B1 beamline for the past two years, providing 67 keV x-rays (figure above). It focuses a horizontal divergence of 3mrad to a brightness-limited horizontal dimension of 0.2mm. The x-ray flux-density at the focus was a few hundred times larger than that of unfocused x rays. A similar design has also been implemented at X7B: our recent tests at X7B show the horizontally focused beam image at E=38.925keV, showing a demagnification factor of ~30.

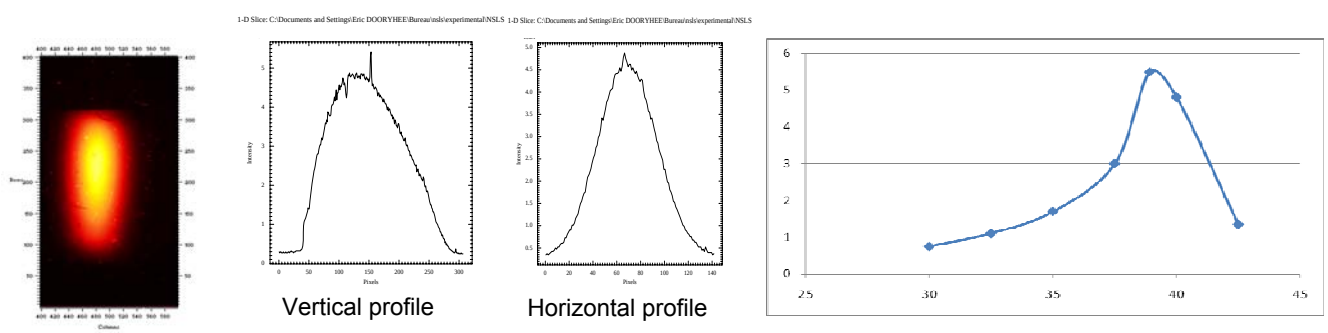

The beam size at the monochromator approximately is 25mm (2mrad horizontal fan) by 2mm (V). The source-to-monochromator distance is 11.026m. The monochromator-to-sample distance is 12.344m. The final optimized focused image at E=38.925keV is shown above: horizontal FWHM ~0.75mm, vertical FWHM ~2mm. With no bending readjustment, the maximum intensity amplitude of these profiles varies by a factor of 7 over the 30 to 42.5keV energy range.

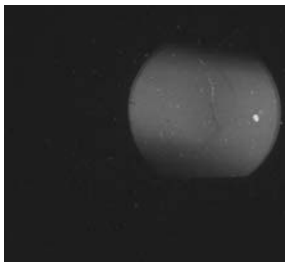

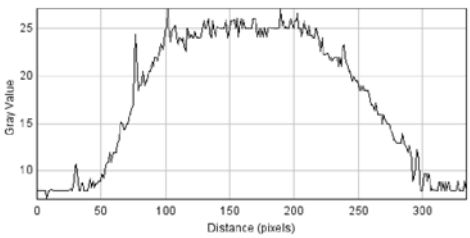

Horizontal Profile at 30keV

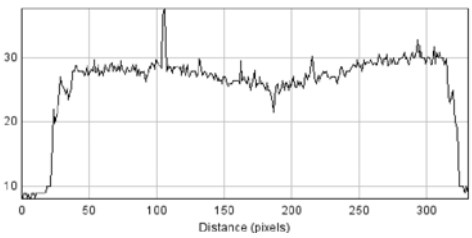

Vertical Profile at 30keV

Out-of-focus image of the beam (collimator truncated) and the corresponding horizontal and vertical profiles at 30keV, keeping the crystal bend setting unchanged between 38.9keV and 30keV.

APPENDIX 6 REFRACTIVE OPTICS

Although the CRL are more suitable for small divergent (undulator) beams, they can match the wiggler beam divergence (up to 100μrad) if they are close enough to the source. We can have them placed before the monochromator for two main reasons:

- The vertical and horizontal beam size has to be tailored to the acceptance of the lenses which typically is 1-2 mm. At a distance of 30 m from the source, the vertical beam size already would be about 3-4 mm. Therefore, moving the CRL closer to the source thus captures a larger proportion of the diverging x-rays. The situation gets far worse in the horizontal direction, *making the development of 1D focusing optics a major request for XPD*.
- Collimating the beam in the vertical beam yields a vertical divergence which better matches the angle acceptance of a high-resolution monochromator first crystal (typically 10μrad at 50keV), improving the performance and flux output of the monochromator.

However, the Laue-Laue monochromator uses the Rowland geometry whereby the anticlastic meridional curvature of the crystals matches the vertical divergence. There is no need for collimating the beam before the monochromator. Therefore, the 1D CRL will be placed after the monochromator (source-to-CRL distance = 38.4m in the main line). *This option relies on the on-going developments regarding 1D focusing and larger acceptance CRL*.

The situation is different in the branchline, for the CRL are placed close to the secondary source produced by the single-bounce monochromator.

In the design of the refractive lenses, we are considering 4 different profiles:

- Parabolic [18]
- Triangular/parabolic saw tooth [9]
- Kinoform profile [19,20]
- Prism [21]

The current proposal would allow for different sets of lenses. The long set will be used to focus (converge) photons with energies larger than 80 keV. The short set will be used to focus (converge) at around 50keV and also can be used to partially collimate the high-energy photons above 80keV. Below we present examples of lenses configurations.

At 80keV main branch	
Number of lenses	~110
Demagnification (p/q)	2.7
Acceptance (mm)	~1
Length (mm)	~150
At 50keV	
Number of lenses	~40
Demagnification (p/q)	2.7
Acceptance (mm)	~1
Length (mm)	~120

The exact parameters of the CRL assembly should be calculated after a final decision on the focal spot sizes and depending on the final position of the lenses and DLCM [9].

APPENDIX 7 DETECTOR DEVELOPMENT

1D and 2D area detectors are increasingly used for powder diffraction. They can considerably improve the detection of very weak signals, and help improve the detection limit to identify intermediate steps in the synthesis or processing of a material. Time resolution takes precedence over angular resolution, requiring a high efficiency photon counting 1-2D detector with sub-sec time resolution. Fast acquisition rate is also required for applications such as diffraction imaging [22] or diffraction tomography [14]. Energy discrimination also is useful in those high-energy measurements where the inelastic (Compton) background could be screened out electronically, and the signal-to-background ratio improved. Higher quality of data can be achieved in the high-Q range.

A good scattering sample only requires a detector image plate, such as the MAR555 (140μm × 140μm pixel size, 430 × 350mm^2, ~1 Hz, 18 bit contrast resolution), be exposed for a few hundred microseconds. Yet the readout of this image (including erase cycle and control macro completion) requires approximately 90s. The MAR345 image plate scanner (circular active area of diameter 345 mm with a pixel size of 150μm or 100μm depending on the readout mode) is also a widespread high-energy detector, but the Point Spread Function deteriorates the pixel size by ~3 and the efficiency at 90keV is as low as 10%.

Faster area detector options are available, including coupling of image intensifiers, or scintillation screens with taper optics, to fast fiber-tapered CCD cameras. However, generally speaking, many of these systems suffer from variable image distortions, low resolution and/or small detection areas.

Mythen strip array detectors (PSI design) are being used at the DIAMOND, SLS and Australian synchrotron facilities and our design will incorporate similar technology; a 7000-element silicon strip detector array (0.014° angle and ~350eV energy resolution, ~1ms readout time) is currently being fabricated at NSLS for in-situ real time material studies. The specifications of the NSLS 1D Si-array are:

- 4mm × 0.125mm strips in arrays of 384 and 640 strips
- Fully-depleted 0.4mm thick detectors
- Pitch matched to ASIC, so simple bonding to form arrays
- 350eV energy resolution @ 5.9keV
- 10^5 cps per strip maximum counting rate
- Readout of 640 strips in few ms.
- Peltier and water cooling

The CMOS-based digital flat-panel detector technology represents a significant step forward for high-energy x-ray diffraction [23-25]. The Pixium 4700 detector [25] combines an amorphous Si panel with a Tl-doped CsI scintillator layer. The detector has a useful pixel array of 1910x2480 pixels with a pixel size of 154 microns, and thus it covers an effective area of 294mm × 379mm. Designed for medical imaging, the detector has good efficiency at high x-ray energies. Furthermore, it is capable of acquiring sequences of images at 7.5 frames per second in full image mode, and up to 60 frames per second in binned region of interest modes. The detector exhibits a narrow point-spread function and a distortion-free image, most appropriate for the acquisition of high-quality diffraction data. In addition, high frame rates and shutterless operation open new experimental possibilities. The sensitivity of the a-Si detector to high-energy X-rays is enhanced, in addition to the increase in experimental efficiency accompanying the virtually continuous exposure/readout.

The General Electric Healthcare detector has similar features [23,24]). Perkin-Elmer also offers a similar design, whose characteristics are 200μm × 200μm pixel size, 410mm × 410mm field of view, 15Hz readout, 16-bit contrast resolution. The scintillator is made of CsI, and proves to perform well at 90keV.

Another relevant development is the photon-counting pixel detector, such as XAMPS (developed at NSLS) or XPAD (CNRS, France [26,27]), MediPIx [28] or PILATUS II (PSI-SLS [29]). A pixelated detector offering a spectrum-per-pixel response, with adequate energy and spatial resolution, opens the breach to simultaneous spectroscopy/diffraction experiments. As an example, the parallel architecture of the XPAD detector design allows

to collect 423 images with less than 10ms exposure (16 bits) or 233 images exposed for more than 10ms (dynamic range=32 bits). In both cases the deadtime between two consecutive images is no more than 2ms; it will be further reduced below 1µsec with buffered output logics in next generation detectors [27]. The full diffraction "movie" is transferred afterwards to the acquisition station after the measurement via a 100MB ethernet link. Some applications of a hybrid pixel detector to powder diffraction is given in reference [30]. Typical pixel size can be 130µm and continues decreasing. For XPAD, the saturation rate is 10^5 photons/s/pixel and the noise level is < 0.1 photon/s/pixel. Replacement of 500µm Si by 700µm CdTe is currently being tested.

The scientific case emphasizes the need for time-resolved/fast studies, and 1kHz acquisition rate is anticipated to become routine work in the future. Recently, Labiche et al. [31] studied the change of iron oxidation:

$$4Fe_2O_3 + 4Fe + NaClO_4 \rightarrow 4Fe_3O_4 + NaCl$$

as a test case, using the FReLoN2k camera: 8,192 diffraction patterns using 64x2048 ROI and 64x2 rebin were collected at a rate of 50Hz, i.e., 19ms integration time and 1ms for data processing and transfer.

The detection (~absorption) efficiency at 100keV of Si 0.5mm, Ge 0.5mm and Ge 1mm is 2%, 14% and 25%, respectively. This drastically limits the efficiency of Si-based detector technology, and the problem arises from the material itself. Thicker scintillators or sensors do not really help: parallax error, lateral spatial resolution degrades with layer thickness, high depletion voltage,… The higher mobility of carriers combined with low effective mass in Ge, as compared to Si, has generated a lot of interest in Ge-based devices. The challenge is having a robust barrier oxide since native Ge oxide is hygroscopic. Other alternatives on semiconductor sensors currently under investigation include: GaAs, CdTe or CdZnTe, n/p Ge, ZrO_2 and HfO_2 on Ge. High-Z scintillating screens from YAG:Ce to LAG:Eu are also being explored.

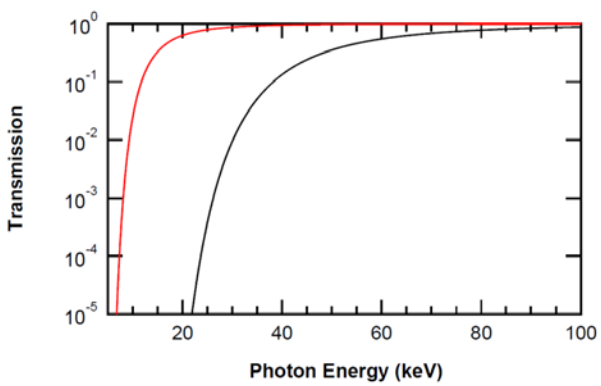

Transmission efficiency of 250µm Si and Ge as a function of x-ray energy.

The technology currently used for making germanium-based sensors is not amenable to making monolithic planar segmented devices such as microstrip detectors. The NSLS Detectors Group is aiming at developing this technology, and subsequently, detectors based on these sensors. *The design of an energy resolving wide-angle photon counting Ge strip detector* (~11 individual modules tiled to provide the necessary angular 100° coverage, 250µradian resolution on 0.5m radius, cryogenic cooling) with good efficiency at around 75keV, would have a tremendous impact on the beamline performance.

For crystallography challenging materials, an important breakthrough can be made with improved detector technology over the high-energy x-ray range. Expected figures in the next 5 years are :

- Time slicing ≤ 1ms or frame rate ≥ 1 kHz (kinetics)
- Pixel size ≈ 100µm × 100µm, i.e. angle resolution ~0.02° 2θ at 0.3m compared to 0.001° 2θ for a point detector with analyzer.
- Active area ≥ letter or A4 format for reaching high Qmax

Using "active" detectors would also be a significant step forward: photon counting with a Poisson statistics for physical interpretation of the data, improved readout schemes (e.g. multiple frame accumulation during the same

data acquisition cycle, using more registers per individual pixel), adjustable gain (counting individual photon up to ~10^{10} photons/s over strong diffracted peaks), image saving only when a random event of interest occurs.

The management of improved detector technology also relies on:

- detector control and interface software
- Integration in data acquisition board and scripts
- data transfer link,
- hard disc writing speed
- size of the available memory
- Data archiving/retrieval and metadata
- On-line data analysis: data screening, assessment
- On-line conversion from detector images into scientific images

Intentionally blank.

LT-XFD_CDR_BLI-00120

NSLS-II Project

CONCEPTUAL DESIGN REPORT for the

BEAMLINES INFRASTRUCTURE at NSLS-II

final draft Sep 2009

Intentionally blank.

Approvals and Reviewers

Compiled by	**Signature**	**Date**
Andrew Broadbent, Beamlines Manager, NSLS-II		
Reviewers		
Nicholas Gmür, ESH Coordinator, NSLS-II		
Sushil Sharma, Mechanical Engineering Group Leader, NSLS-II		
Approvals		
Qun Shen, XFD Director, NSLS-II		

Document Updates

The Conceptual Design Report for the Beamlines Infrastructure at NSLS-II is a controlled document, revised under change control.

Version No.	Date	Authorized by	Changes made
A	9/22/09	A. Broadbent	Initial draft
1	9/30/09		final draft submitted

Intentionally blank.

Contents

1. INTRODUCTION 1

2. SAFETY 1

2.1 Safety Review Process 1

2.2 Radiation Shielding 1

3. CONVENTIONAL FACILITIES INTERFACES 2

3.1 Experimental Floor and Building 2

3.2 Beamline Locations 2

3.3 Utilities 5

3.3.1 General 5

3.3.2 UPS systems 5

3.4 Laboratory Office Buildings (LOBs) 5

3.5 Hard X-ray Nanoprobe Remote Station 8

3.6 Construction Phasing Plan. 9

4. ACCELERATOR SYSTEMS DIVISION INTERFACES 11

4.1 Insertion Devices 11

4.2 Front Ends 11

Acronyms

ASD Accelerator Facilities Division

CDR Conceptual Design Report

CFD Con ventional Facilities Division

CHX Coherent X-ray beamline

CSX Coherent Soft X-ray beamline

DW damping wiggler beamline

ELS Extended Length Straight

EPU Elliptically Polarized Undulator

ES End Station

FOE First Optics Enclosure

HXN Hard X-ray Nanoprobe beamline

ID Insertion Device

IVU In-Vacuum Undulator

IR infrared

IXS Inelastic X-ray Scattering beamline

LOB Lab Office Building

PPS Personnel Protection System

RSI Requirements, Specifications and Interfaces

SOW Statem ent of Work

SRX Submicron Resolution X-ray Spectroscopy beamline

UPS Uninterruptible Power Supply

XFD Experim ental Facilities Division

XPD X-ray Powder Diffraction beamline

3PW 3-pole wiggler beamline

1. INTRODUCTION

This document is written as an accompaniment to the Conceptual Design Reports for each of the six NSLS-II project beamlines. It will describe the infrastructure necessary to support the beamlines, including a number of items outside the formal Experimental Facilities Division (XFD) responsibility, such as insertion devices and front ends (ASD responsibility) and the experimental floor and utility interface points (CFD responsibility). This document also covers the x-ray shielding hutches and the local utilities provisions.

2. SAFETY

2.1 Safety Review Process

The Beamline Safety Review process (and committee) from NSLS was adopted for NSLS-II, with the addition of a review at the Conceptual Design stage. These reviews have all now been held and the presentations and reports are available on request, or at the 09_09_CDR_SafetyReview page of the NSLS-II SharePoint site. Most of the recommendations are currently being implemented. Further reviews will be scheduled in accordance with the NSLS procedure and as shown on the Gantt chart plan below.

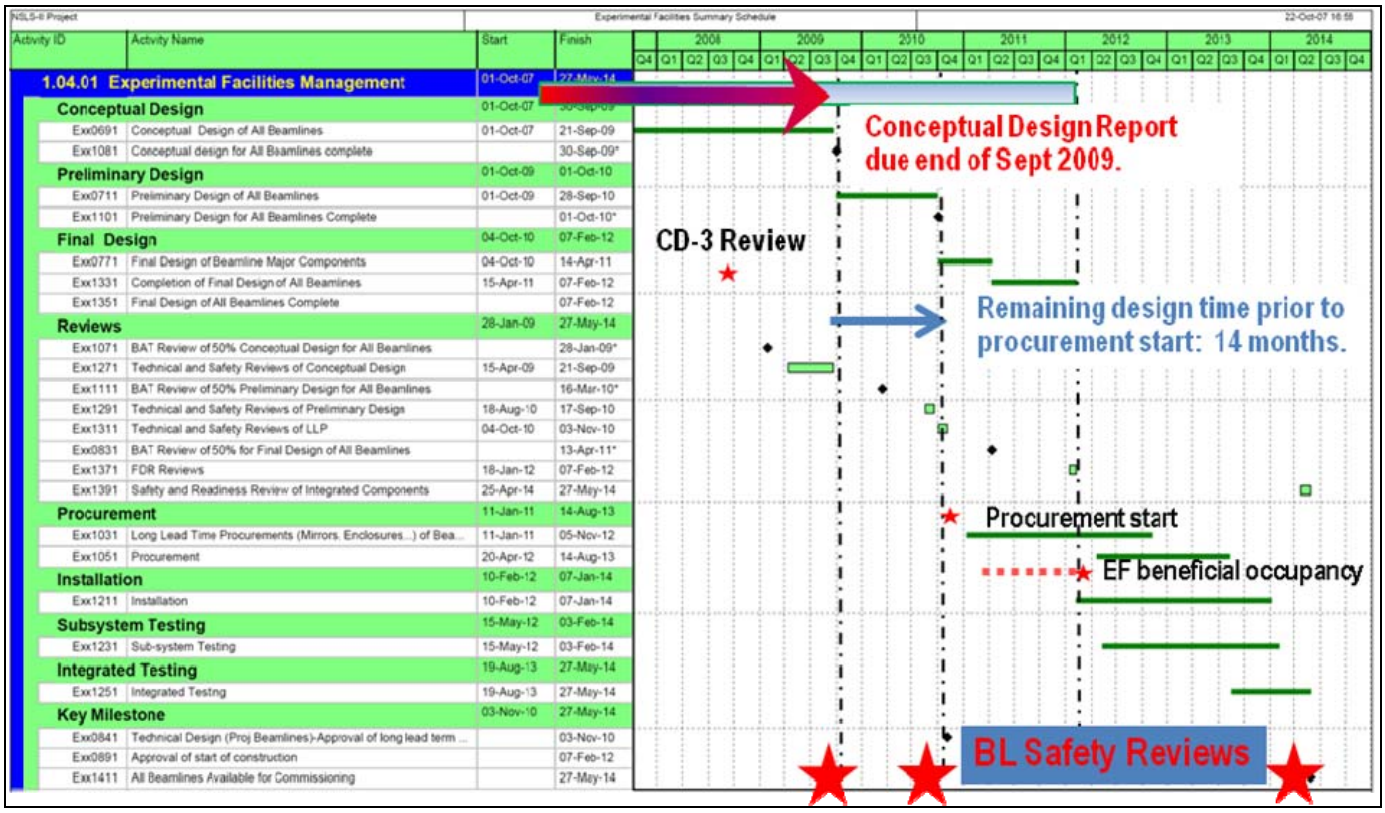

Figure 1. Gantt Chart for the beamline safety review process.

2.2 Radiation Shielding

The radiation shielding at NSLS-II is very similar to that provided at other 3GeV synchrotron sites with lead or steel shielding enclosures ("hutches") designed to ensure that direct radiation from the storage ring and/or radiation scattered by components along the beam line will produce doses external to the hutches that are well within mandated levels. Detailed calculations have been performed by the NSLS-II radiation physicist for a wide range of

generic "standard" configurations, and these calculations will be continued to cover specific beamline situations not covered by the standard configurations. A review committee will evaluate all beam line and front end shielding designs.

A document entitled "Shielding Guidelines for Beamlines" has been written and is available on request. For many standard beamline configurations, lead hutches will be required for First Optics Enclosures (FOEs), with steel hutches used for end stations. Notable exceptions are the requirement for lead hutches on the end stations of damping wiggler beamlines, and no lead requirement for experimental hutches on soft x-ray beamlines; this is in line with practice elsewhere.

A detailed Statement of Work (SOW) has been written for hutch procurement; this is available on request. This SOW will be used to ensure standardization of labyrinths, guillotines, doors, and Personnel Protection System (PPS) interfaces. It is anticipated that a specification sheet and drawing will accompany the general SOW for each hutch to be procured; the specification sheets are relatively short and an example is provided in the Statement of Work.

3. CONVENTIONAL FACILITIES INTERFACES

3.1 Experimental Floor and Building

The general environment for the beamlines is defined in the document "Experimental Facilities Requirements, Specifications and Interfaces for the Ring Building and Experimental Floor." This discusses such important environmental factors as the facility temperature, temperature and humidity stability, as well as ambient noise, vibration, lighting, fire safety, emergency egress and infrastructure, beamline floor territory, accommodation of long beamlines, etc.

The floor layout, including the walkway boundaries between beamlines, is shown in Figure 2. This layout slightly favors insertion device (ID) floor space over floor space for bending magnets (BMs) and three-pole wiggler (3PW) magnets, while allowing access to the front-end access doors in the ratchet wall (for ID front ends only).

Note 1 on the drawing refers to emergency access "duck-unders." These are discussed in a Safety Committee memo dated 3 April 2008.

3.2 Beamline Locations

The beamline locations need to be finalized by the end of March 2010 to enable advanced sequencing of the construction activities to continue. Table 1 documents the absolute beamline location constraints and some of the preferences for beamline locations.

Prior assumptions
Project damping wigglers require three-fold symmetry and are installed on the "8's" (i.e., straights 8, 18, and 28).

Straights reserved for future damping wigglers, also with three-fold symmetry, are installed on the "6's" (i.e., straights 6, 16, and 26).

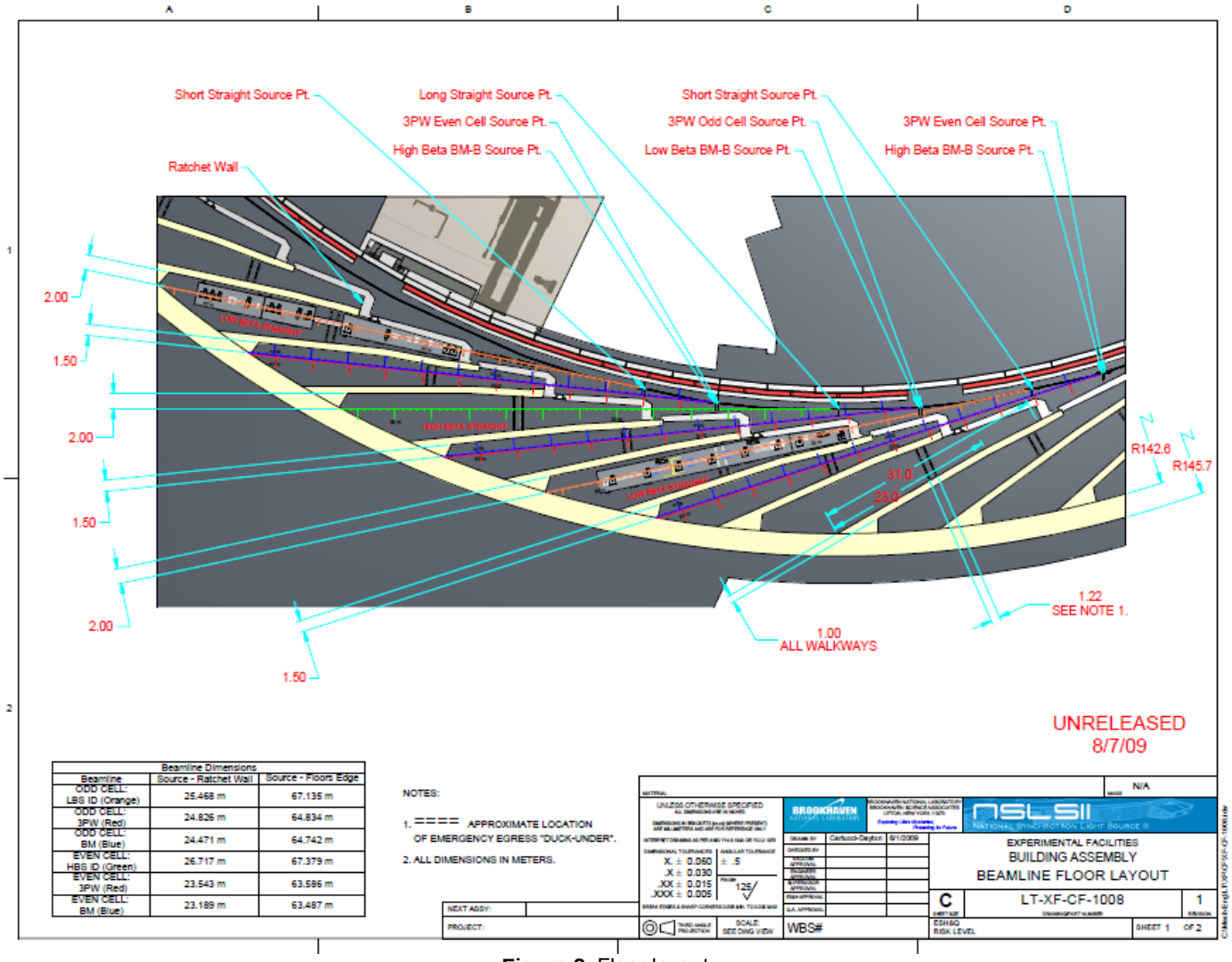

Figure 2. Floor layout.

Table 1: Absolute Beamline Location Constraints and Some Preferences.

Beamline	Straight	Extended experimental floor?	Long beamline?	Location requirements	Options	Location preferences	Preference
IXS	Hi-beta	Y	N	Non damping wiggler straight	4, 10, 12	ELS capability (at least with shorter adjacent straights, even if not with three-fold symmetry).	10-ID
HXN	Low-beta	Not required	Y	Not adjacent to LOB loading docks.	27, 3, 9	Optimized location with low vibration levels.	3-ID
CHX	Low-beta	Y	N	Extended experimental floor to allow emergency duck-under between FOE and ES.	5, 11, 17, 23, 29	None	5-ID
CSX	Low-beta	Y	N	Located away from sources of draughts (exposed optics and end station).	5, 11, 17, 23, 29	Straight 23 is between RF straights and therefore likely to have convenient “parking” space for additional end stations.	23-ID
SRX	Low-beta, canted	N	N	Does not require extended experimental floor.		Ideally near an IR beamline position. Close to bio village.	21-ID
XPD	Hi-beta	Y	N	DW source	18, 28	At beneficial occupancy, there is a long duration between the floor at straight 28 and straight 18 being available.	28-ID

ELS = Extended Length Straight (a future concept to give a single very long straight at the expanse of adjacent straight lengths)
ES = end station
FOE = first optics enclosure
ID = insertion device
LOB = lab office building

3.3 Utilities

3.3.1 General

The strategy with the utility distribution system has been to define a set of convenient interface points for a standardized set of beam line utilities. These interface points will generally serve one or two beamlines. The requirements, specifications, and interfaces (RSI) document entitled "Requirements, Specifications and Interfaces for the Experimental Facilities Utilities" (available on request) defines the utility interfaces and provides information on the estimated utility loads. This document also provides information on how the utilities are to be distributed along the beamline to the various pieces of equipment.

3.3.2 UPS systems

Review committees in the past have commented on the need for, and made recommendations relating to, the inclusion of uninterruptable power supply (UPS) systems. Considerable time has been spent working with the ASD staff and local agents for the large UPS system manufacturers to define systems suitable for the beamlines. The conclusion is that the UPS systems should have a reasonable "whole of life" cost, remote monitoring, high reliability, and low environmental impact while retaining some compatibility with the distributed system proposed for the storage ring controls and data-archiver. Two discussion papers recommend distributed systems and then further analyze the life cycle costs and options. See "Beamline UPS Systems Discussion Sept09.doc" and "UPS discussion document.doc," available on request.

In summary, the reports recommend small, distributed UPS systems sized to provide adequate power for a single beamline. The electrical distribution costs alone dictate against sharing UPS systems over several beamlines, and distributed systems minimize issues of earthing, electrical noise propagation, and safety concerns.

3.4 Laboratory Office Buildings (LOBs)

The laboratory office buildings are on an accelerated schedule, with the 100% design submission due from the architects at the end of September 2009. Considerable interaction with representatives of the user community has occurred to ensure that the standard building footprint planned for all five LOBs is suitable for all communities, including the biology community, who are expected to have a different configuration within the LOB to allow for specific laboratory requirements (including cold rooms, etc.).

The RSI document for the LOBs is available on request. This document defines the number of offices, labs, kitchen areas, etc. within the building; states the intended lab and workshop purposes; and defines the utilities needed by users. A color-coded drawing of the LOB is provided on the following page. Please note:

- The chamfered left-hand end is to allow long beamlines to pass the building.
- Scientists' offices (green) are around the perimeter.
- A wide central atrium links the entrance door with the main door to the Experimental Floor.
- Seating for students and users is perpendicular to the central atrium. Both of these areas have clerestory windows to give good natural light with minimal solar gain.
- A double conference room can be merged to form a single large conference room near the main entrance. There is also another conference room close to the Experimental Floor.
- There is an area for administrative staff (yellow).
- Ten workshops and laboratories plus a small machine shop (blue) are provided.
- The shipping and receiving area with stores space is adjacent to the Experimental Floor at the right-hand end of the LOB.

Images of the LOB are shown overleaf, provided by HDR (Architects) on 10 Sept 2009, 3 weeks prior to 100% design submittal.

Figure 3. Drawing of the LOB floor plan.

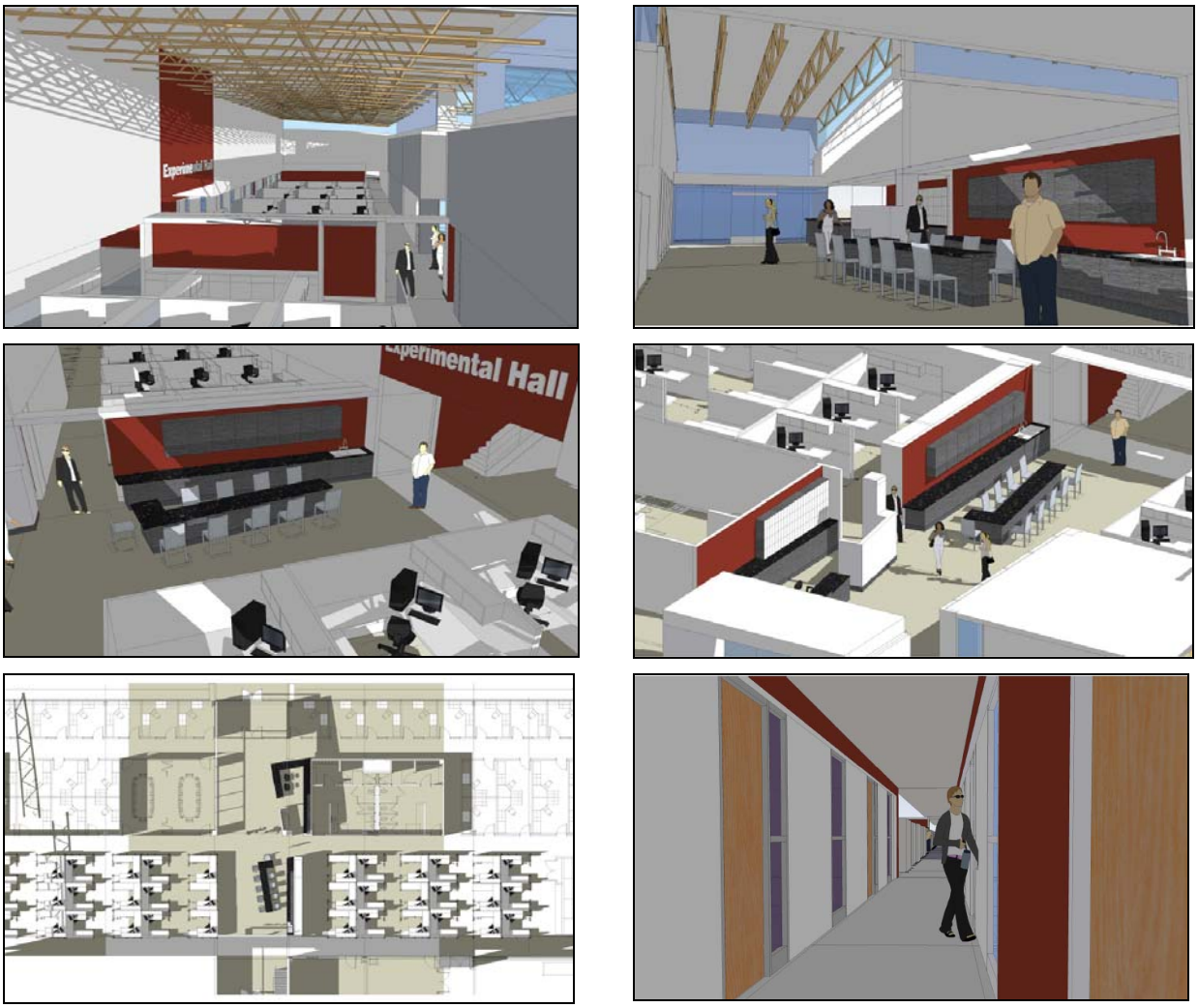

Figure 4. Views of the LOB interior.

Figure 5. The central atrium of the LOB.

3.5 Hard X-ray Nanoprobe Remote Station

The remote station for the nanoprobe is something of a misnomer, since it is located very close to the LOB. Earlier versions of the building were located further away from the storage ring building; the move closer was made for scientific/optics reasons, but there are some engineering benefits including utility connections directly from the LOB and reduced wind loading on the structure.

Very considerable steps have been taken to minimize vibration levels, including holding a workshop at BNL inviting many experts from on site and across the United States, using the services of the CFD vibration expert (Nick Simos), who made many measurements and models to predict the likely impact of traffic, site noise, ocean waves, NSLS-II services, and the filtering effect of the concrete slabs.

A sketch of the proposed building is shown below. Some key points are as follows:

- The building should be completely separate from the storage ring building with no interconnected columns or girders.
- The separation is critical; it will be thick concrete with isolating foam used between the ring building and the satellite building.
- The building will be fully concrete construction based on the "house within a house" concept. The inner "house" is the concrete hutch (8" thick walls – 4" walls required for radiation shielding, doubled to avoid porosity problems). The hutch doors will be steel and the personnel door will incorporate an airlock. (emergency egress requirements are currently being reviewed with BNL staff).
- Connections from the satellite building to the ring building (e.g., for personnel access and for the beampipe) will be done in a lightweight, insulated fabricated steel (or similar) construction material.

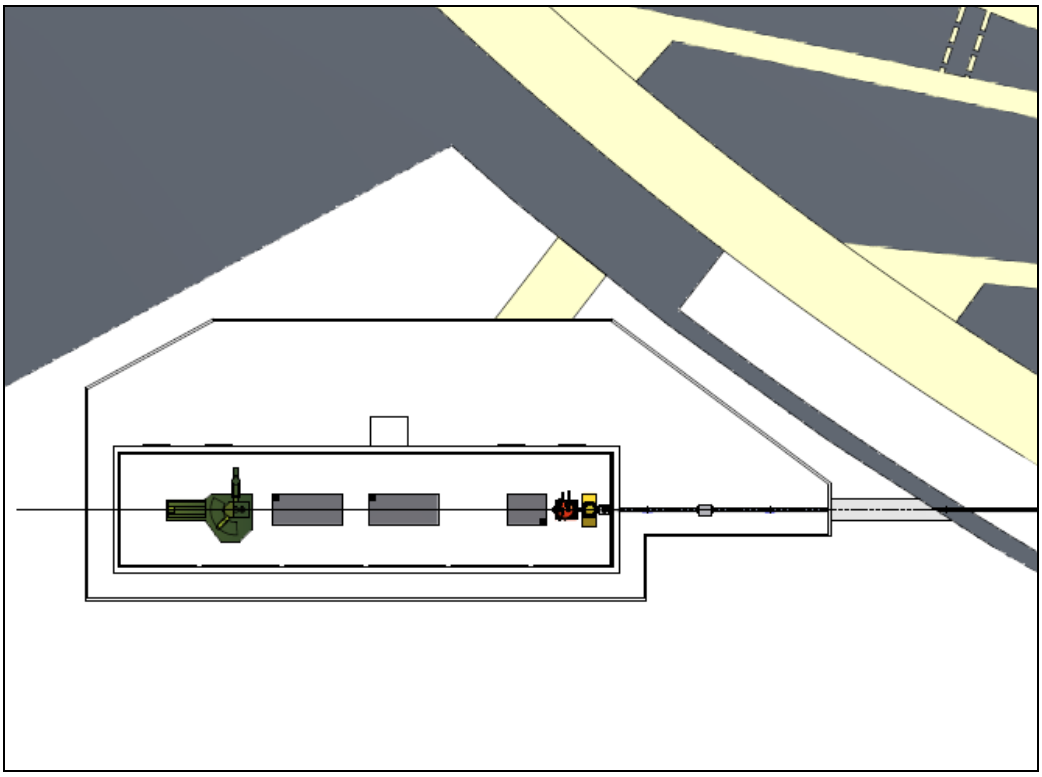

Figure 6. Sketch of the proposed HXN remote station.

3.6 Construction Phasing Plan

One key interface during the facility construction will be the coordination with CFD and ASD activities. Upon beneficial occupancy of each phase, the experimental floor will be used as a staging area for magnet girders and power supplies before they are installed in the storage ring and on the tunnel roof, respectively. Some advanced planning has occurred and this will be further developed over the coming year.

The key points are as follows:

- XFD will try to remain out of the way of ASD installation activities.
- Girders will enter the storage ring building (and be moved onto the experimental floor) through the main entrance, which will not be completed until the whole building is complete. The concrete pad for the entrance lobby will be used for off loading girders from trucks before they are wheeled into the building through a temporary opening. The girders will be towed around the facility on the 10-ft wide walkway (and not via the bypass corridors).
- Current schedules call for hutch installation to start after beneficial occupancy of the whole ring building (a very conservative assumption); we now anticipate gaining earlier access to the floor, in sections, after each individual phase is complete and the ASD activity finishes.
- The first activity after ASD work is completed would be floor painting, prior to hutch erection.

The phasing plan for construction of the synchrotron building, agreed with Torcon, is shown in Figure 7 on the following page.

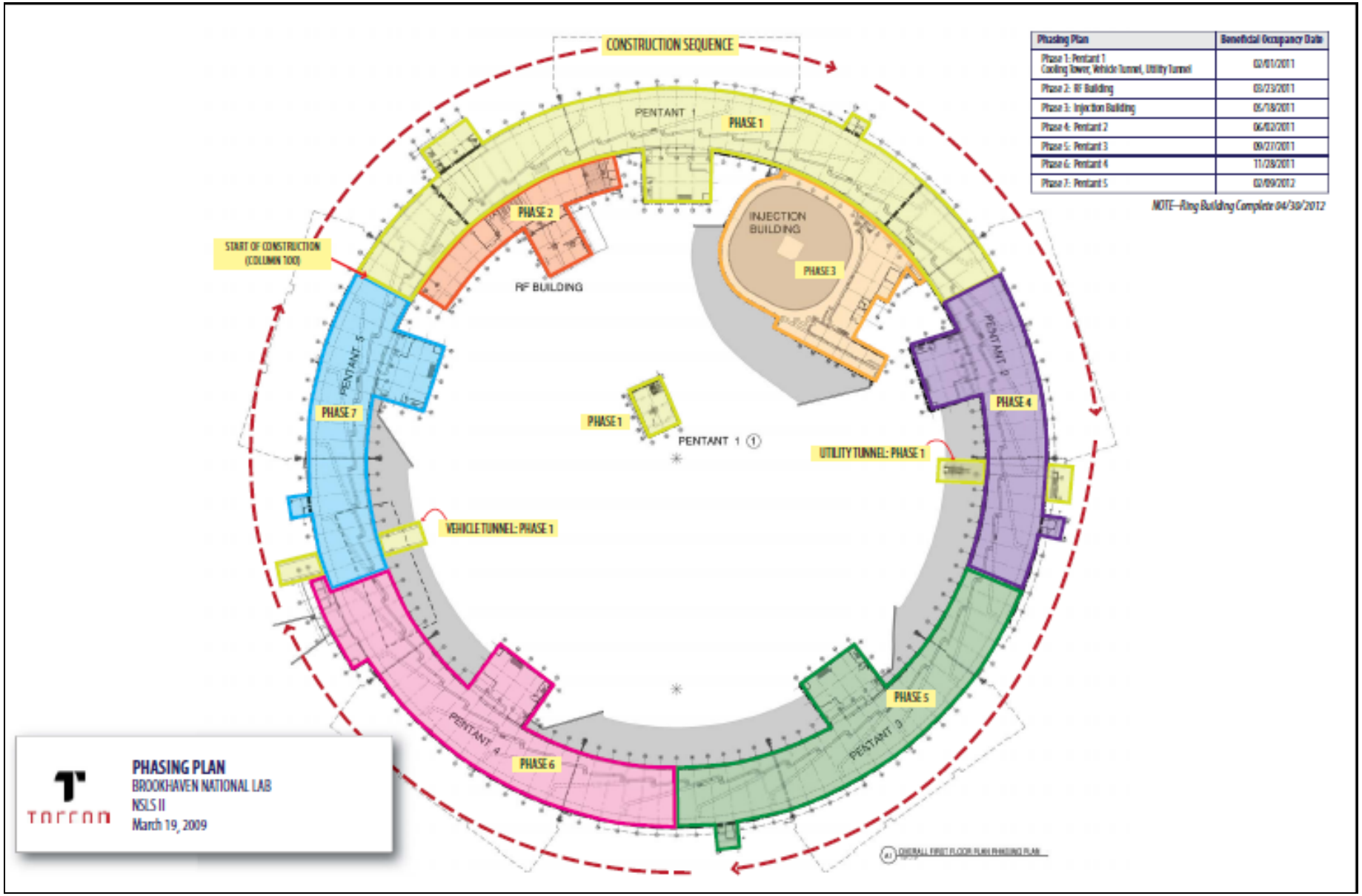

Figure 7. Phasing plan for construction of the synchrotron building.

4. ACCELERATOR SYSTEMS DIVISION INTERFACES

4.1 Insertion Devices

A significant amount of work has been done over the past year to further define and refine the insertion devices for the NSLS-II project beam lines. The standard in-vacuum undulator (IVU) remains the 3 m long U20 device; however, a number of variants are envisaged to optimally meet the scientific requirements of the beamlines while maintaining performance of the storage ring. The elliptically polarized undulator (EPU) has also been optimized to meet the scientific requirements for energy range. The damping wiggler remains the standard device with a 90mm period.

In-vacuum undulators		
IXS Beamline	U22	6m long (probably 2 x 3m devices)
HXN Beamline	U20	3m long – standard device
CHX Beamline	U20	3m long – standard device
SRX Beamline	U21	1.5m long (note; this is one device of a canted pair)
Other insertion devices		
CSX Beamline	EPU 49	2m long
XPD Beamline	DW90	7m long (standard, 2 x 3.5m sections, uncanted).

The Insertion Devices for NSLS-II are described in a document discussing the NSLS-II radiation sources (actually a recent update of Chapter 5 of the NSLS-II Conceptual Design Report), this is available on request.

A paper presented by Chubar et al. at the SRI 09 conference, "Parametric Optimization of Undulators for NSLS-II Project Beamlines," provides further information and detail about the detailed optimization procedure employed, (this is also available on request).

4.2 Front Ends

The front ends for the project beamlines are currently in the design phase. Currently, detailed designs exist for standard hard and soft x-ray undulator beamline front ends, and work is proceeding on the damping wiggler and canted beamline front ends.

The design work has included detailed value engineering studies and the building of prototypes, which have been subjected to life cycle testing (e.g., shutter bellows to >800k cycles). There have also been several formal reviews; this work will continue and it is anticipated that a fully working prototype will be constructed shortly.

A presentation, "Front Ends for NSLS-II" by Lewis Doom, which describes the current status of the front end program, was presented to the BNL Light Sources Beamline Safety Review Committee on 24 August 2009. That presentation and the committee report are available on request.

The standard Front end is shown overleaf.

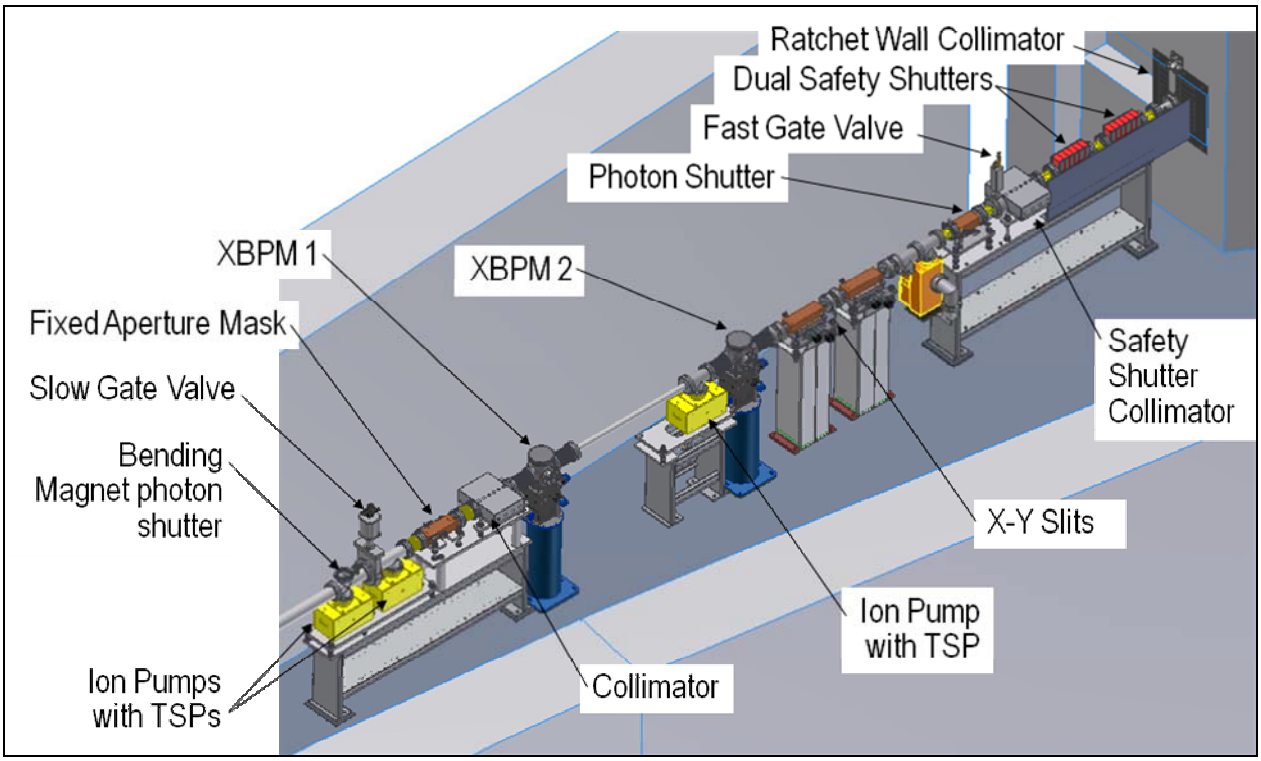

Figure 8. Standard Front End layout.